Interaction behaviour of soil and geosynthetic reinforcement

by:

Alireza Tatari

Department of Civil and Structural Engineering
University of Sheffield

A thesis submitted in partial fulfilment of the requirements for the degree of Doctor of Philosophy

July 2016

Declaration

I, Alireza Tatari, here by confirm that all work presented here is my own. Where information has been used from other sources, I confirm that this has been clearly stated within the thesis.

Signed: **Alireza Tatari**

Date: **01 July 2016**

dedicated to my amazing wife Simin
you are the love of my life

Abstract

The research described in this thesis concerns the use of transparent soil in physical modelling to better understand theoretical and analytical analyses of a geotechnical engineering problem. One of the more recent evolutions in the field of geotechnics is the use of geosynthetic materials as reinforcement to improve the shear resistance of soil, and ultimately provide reinforcement to earth structures. Their application in engineering earthworks has increased significantly in recent years. When designing reinforced earth structures, a vital aspect is to understand the interaction between the reinforcement and the compacted soil as this governs the overall stability. The main function of the reinforcement is to redistribute the stresses within the soil structure in order to enhance the internal stability of the reinforced soil structure. The reinforcement undergoes tensile strain as it transfers loads from unstable to stable zones of the soil.

The most common example of soil-geogrid interaction research is to investigate pull-out capacity. The lack of knowledge of interaction mechanics between soil and reinforcement has considerable impact on the ability to implement rigorous analytical solutions, or to assign suitable parameters for interface elements in numerical modelling. By using classical pull-out, previous researchers have indicated that the interface factors vary between 0.6 - 0.8 (FHWA-NHI-00-043, 2001); hence, it is likely that many designs over predict the possible resistance that may be generated. Furthermore, in the absence of field validation, there is uncertainty as to how representative small scale pull-out tests reflect the likely behaviour that would prevail in the prototype structure.

The transparent soil utilised here is representative of coarse soil and allows non-intrusive measurement of soil displacement on a plane highlighted by a sheet of laser light, captured by a digital camera. This enables the measurement of the displacement of the soil on the target plane by using the image process technique "Particle Image Velocimetry". This technique allows the observation of the interaction between soil and geogrid, and the shear and pull-out boundary which is mobilised around the geogrid.

The principal aim of this research is to investigate the detailed interaction between granular soil and geosynthetics, and to provide a better understanding of the interaction both analytically and numerically.

To achieve this aim, this research is separated into two key areas:

1. Analytical modelling of the interaction between soil and geogrid to assess the degree of uncertainty inherent in the methods;
2. Advanced visualisation element tests using transparent soil technology and Particle Image Velocimetry (PIV) to directly observation of the patterns of strain between the soil and reinforcing material.

Acknowledgement

Firstly, I would like to thank my PhD supervisors, Dr Jonathan A. Black and Dr Colin Smith, without whom this thesis would not have been possible. Their advice and feedback over the last four years has been exceptional. I have learnt so much from them in my short research career so far, and I hope to learn even more in the years to come.

I would like to acknowledge the technical and support staff in the Department of Civil and Structural Engineering. Notably I thank Mr. Paul Osborne, Mr. Mark Foster, Mr. David Callaghan, Mr. Alex Cargill, Mr. Martin Taylor and Dr Paul Bently for their excellent support in the laboratory; they were always eager to help as and when required and for this I am most grateful.

I would also like to thank everyone in the Department of Civil and Structural Engineering. It is incredible how much a friendly atmosphere can encourage you to work better. Being part of such a great research group has always motivated me to achieve the best I can to keep up the sterling reputation of the Geotechnical Research Group and the University of Sheffield.

My parents, my brother and my lovely aunt, Vahideh, thank you for always being there for me. The support I have had from you throughout my life has always made me want to be the best I can possibly be. You are the reason why I wanted to do a PhD, and your advice has always been well placed, reasoned and motivating. I also need to thank my best friend Dr Erfan Shahabpoor Ardakani for his companionship, support and encouragement.

Finally, and most importantly, I would like to thank my dear wife Simin. For everything.

Alireza Tatari,

Friday 1^{st} July, 2016.

Contents

List of Figures

List of Tables

List of Abbreviations

CCD	**C**harge **C**oupled **D**evice
CD	**C**onsolidated **D**rained
DAQ	**D**ata **A**cquisition Device
DI	**D**ifferential Analogy **I**nput
DIC	**D**igital **I**mage **C**orrelation
DLO	**D**iscontinuity **L**ayout **O**ptimisation
FE	**F**inite **E**lement
FFT	**F**ast **F**ourier **T**ransform
ISO	**I**nternational **S**tandardisation **O**rganisation File Speed
LED	**L**ight **E**mitting **D**iode
LVDT	**L**inear **V**ariable **D**isplacement **T**ransducers
MTF	**M**odulation **T**ransfer **F**unction
PI	**P**ixel **I**ntensity
PID	**P**roportional **I**ntegral **D**erivative
PTV	**P**article **T**racking **V**elocimetry
RI	**R**efractive **I**ndex
SE	**S**ingle **E**nded Analogy Input
SLR	**S**ingle **L**ens **R**eflex
ULS	**U**ltimate **L**imit **S**tate
USB	**U**niversal **S**erial **B**us
VI	**V**irtual **I**nstrument

List of Symbols

symbol	name
A	Total area
A_p	Aperture size of geogrid
$\bar{a}_b$	Fraction of grid width available for bearing
α_b	Coefficient of bond
α_c	Interface coefficient between reinforcement and soft soil
α_{ds}	Direct shear sliding coefficient
α_i	Angle to the vertical from centre of rotation to base of slice
$\bar{a}_s$	Fraction of reinforcement plan area that is solid
α	Angle as defined by Bishop (1955)
α_s	Interface coefficient between reinforcement and embankment fill
B	With of a transverse member of a grid taking bearing
B	With of slice
B	Diameter of the soil nail
B_i	Slice width
β	Angle of slope
c'	Cohesion of the soil
c'_{des}	Design cohesion of the soil
C	Compression force
C_c	Coefficient of curvature

C_c	Compression/Swelling index
C_r	Recompression index
C_u	Coefficient of uniformity
c_u	Shear strength of soft soil
C_u	Centroid horizontal coordinate
C_v	Centroid vertical coordinate
D	Thickness of soft soil
D_{10}	The diameter corresponding to 10% finer in the particle-size distribution
D_{30}	The diameter corresponding to 30% finer in the particle-size distribution
D_{50}	Mean particle size
D_{60}	The diameter corresponding to 60% finer in the particle-size distribution
D_{85}	The diameter corresponding to 85% finer in the particle-size distribution
d_{hole}	Diameter of holes nail
δ	Angle of skin friction, soil on planar reinforcement surface
$\delta R^{refraction}$	Refraction correction
$\delta_{u^{tangential}}$	Horizontal tangential distortion
$\delta_{v^{radial}}$	Vertical radial distortion
$\delta_{v^{tangential}}$	Vertical tangential distortion
η	Angle between normal to slip plane and reinforcement
ϵ_f	Maximum strain in the reinforcement
f_b	Bond coefficient between soil and reinforcement
f_x	External force in x direction
FS	Factor of safety
H	Height of embankment
H	Height of slope
ϕ'	Friction angle of soil
ϕ'_{des}	Design friction angle of soil
q	Surcharge

q	Surcharge acting on the surface of the slice
$Q_{1,2}$	Characteristic surcharge force acting on the surface of wedges
$\theta_{1,2}$	Base angle of wedge 1 or 2
γ	Unit weight of soil
$I_{max(I)}$	Maximum pixel intensity of image
$I_{min(I)}$	Minimum pixel intensity of image
$I_{max(O)}$	Maximum pixel intensity of object
$I_{min(O)}$	Minimum pixel intensity of object
I_{search}	Search interrogation patch
I_{test}	Test interrogation patch
J	Tensile stiffness of reinforcement
K_a	Active earth pressure coefficient
k_1	Primary radial distortion coefficient
k_2	Secondary radial distortion coefficient
L	Length of reinforcement
L_a	Length of reinforcement in active soil zone
L_e	Embedded length of reinforcement in stable soil
λ	Refraction scaling component
M	Dummy test patch
M	Bending moment in reinforcement
m	Meter
mm	Millimetre
M_p	Plastic moment of resistance
M_{p1}	Plastic moment of resistance
$M_{driving}$	Driving moment
$M_{resisting}$	Resisting moment
M_{Nails}	Resisting moment of soil nail
M_{Soil}	Resisting moment of soil

N	Newton
N	Lateral resistance per unit length per unit width
N	Lateral resistance
N_1	Lateral resistance per unit length
n	Side slope gradient (nH:1V)
n	Refractive index
Pa	Pascal
p_1	Primary tangential distortion coefficient
p_2	Secondary tangential distortion coefficient
r	Radius of slip circle
r	Radial distance from principle point in recorded image
$R_n(s)$	Normalised cross correlation estimator
$R(s)$	Cross correlation estimator
σ'_b	Effective bearing stress on reinforcement
σ'_h	Horizontal effective stress
σ'_n	Normal effective stress acting to the plane of the reinforcement
σ'_v	Effective stress
R	Rupture strength of reinforcement per unit width
S	Size of aperture in geogrid
s	Displacement of test patch center from original position
S_h	Horizontal nail spacing
T	Pull-out resistance per unit length per unit width
T	Pull-out resistance
T_1	Pull-out resistance per unit length
T_d	Design tension in reinforcement
t_x	Horizontal translation
t_y	Vertical translation
t_z	Depth translation

τ_u	Upper boundary soil/reinforcement interface stress
τ_l	Lower boundary soil/reinforcement interface stress
U	Location of interrogation patch
u	Image space horizontal coordinate
u_i	Pore pressure acting on base of slice
u_0	Image space horizontal principal point coordinate
ε	Reinforcement declination
φ, ω, κ	Eulerian rotation angles
v	Image space vertical coordinate
v_0	Image space vertical principal point coordinate
W	Width of top of embankment
W_i	Self-weight of slice
X	Object space horizontal coordinate
X_A	Project center horizontal coordinate
$X_{apparent}$	Apparent position horizontal coordinate
Y	Object space vertical coordinate
Y_A	Project center vertical coordinate
$Y_{apparent}$	Apparent position vertical coordinate

Chapter 1

Introduction

1.1 Background

Non-soil materials such as reed mats, bamboo fascines, bush and small trees have been used for millenia to aid construction of earthworks such as embankments over soft soil. These materials have been increasingly replaced with geosynthetics over the past few decades to provide the same function (Christopher et al., 2000). The main advantage of this new type of material in comparison to natural materials is durability and a well defined tensile strength. This tensile strength can be incorporated in to the analysis of e.g. embankment stability and adds additional resistance to bearing capacity, settlement and slope stability failure (Christopher et al., 2000).

Early papers on geosynthetics in the 1960s documented their use as filters in the United States and as reinforcement in Europe (Richardson and Koerner, 1990). A 1977 conference in Paris brought together many of the early manufacturers and practitioners, where the name geosynthetics was coined by Dr JP Giroud in a seminal paper (Giroud, 1977).

The use of geosynthetic materials in engineered earthworks has increased significantly in recent years and reinforced soil technology has now become a popular

construction technique. Table 1.1 presents the results of a study carried out by the Freedonia Group Inc. showing the global demand and growth in demand for geosynthetics since 2007 for 10 years (Muller and Saathoff, 2015). The two primary soil reinforcement applications using geosynthetics are: (i) reinforcing the base of embankments constructed on soft foundation soils, and (ii) increasing the stable angle of soil slopes (Jewell, 1996). The main function of the inclusion is to redistribute stresses within the soil mass in order to enhance the internal stability of a reinforced soil structure. Soil has a relatively low tensile strength so that it is not able to transfer all the forces arising in a structure when it is loaded. However, tensile forces can be transferred by using geosynthetic materials (Palmeira and Milligan, 1989).

Table 1.1: World geosynthetics demand (in millions m^2) and percentage of annual growth (Muller and Saathoff, 2015)

Country	2007	2012	2017	Annual growth (%)	
				2007-2012	2012-2017
Geosynthetic demand	2801	3400	5200	4.0	8.9
North America	923	965	1300	0.9	6.1
Western Europe	668	615	725	-1.6	3.3
Asia/Pacific	723	1200	2330	10.7	14.2
Central and South America	124	160	220	5.2	6.6
Eastern Europe	248	305	405	4.2	5.8
Africa/Mideast	115	155	220	6.2	7.3

In order to obtain a better understanding of soil-reinforcement interaction, it is important to identify the different modes of interaction. Palmeira and Milligan (1989) summarised these for a reinforced slope as illustrated in Figure 1.1. The interactions are divided into three areas and listed below with corresponding tests to best characterise the interaction:

1. **Region A**: Sliding of soil over the reinforcement; direct shear test.
2. **Region B**: Shearing soil and reinforcement; direct shear test with inclined reinforcement.
3. **Region C**: Pull-out failure; direct pull-out test.

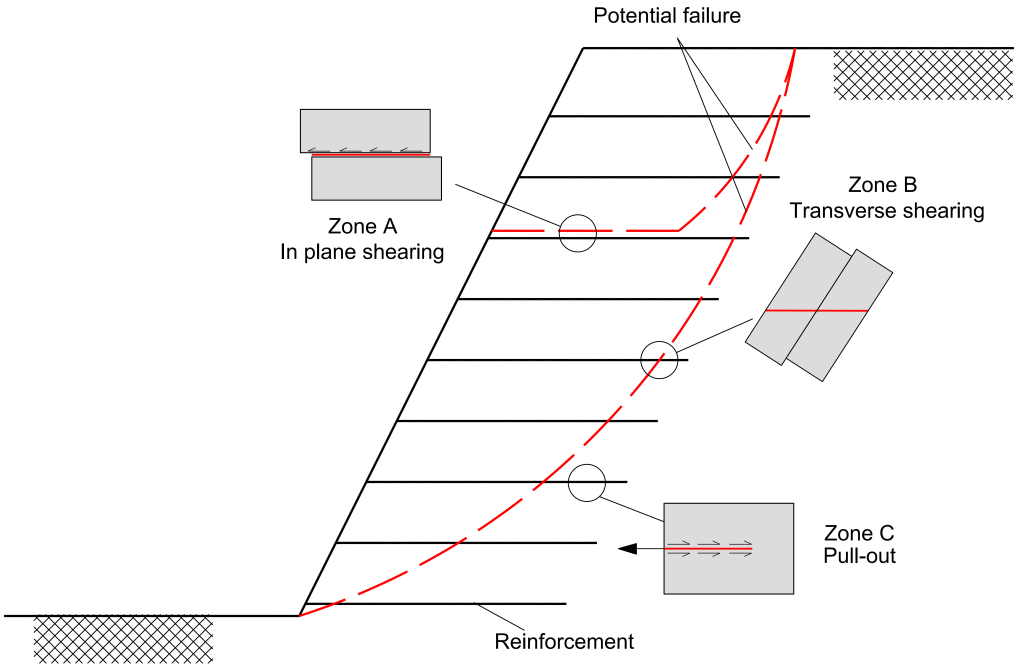

Figure 1.1: Typical interaction mechanisms between soil and geosynthetic material for reinforced slope (after Palmeira and Milligan, 1989)

The most common research into of soil-reinforcement interaction is the investigation of pull-out capacity. However a lack of knowledge of the other interaction mechanics also generates uncertainty in our ability to implement rigorous analytical solutions or assign suitable parameters for reinforcement elements in numerical models.

A perfect pull-out boundary condition between soil and reinforcement would be when full soil strength is mobilised in shear. In previous research the soil - geosynthetic pull-out interaction coefficient was determined either by using theoretical expressions (Jewell et al., 1985; Ghionna et al., 2001 and Palmeira and Milligan, 1989) or by back-calculation from pull-out test results (Ghionna et al., 2001 and Palmeira and Milligan, 1989). Therefore, it is important to describe the role of all the design (and test) parameters on the mobilisation of the pull-out interaction between soil and reinforcement (frictional and passive), including geosynthetic length, L, tensile stiffness, T, geometry and shape, vertical effective stress , σ'_v, (acting at the geosynthetic interface) and soil shear strength, c_u or c', and $\tan\phi'$,

(Moraci and Recalcati, 2006). According to FHWA-NHI-00-043 (2001) engineers can use an interface factor, α, equal to 0.6 and 0.8 for geogrid and geotextile respectively in the absence of test data, where the interface shear strength, τ, is given by; $\tau = \alpha c_u$ or $\tau = \alpha \sigma'_v \tan \phi'$ for undrained and drained soils respectively.

1.2 Objectives and methodology

The principal aim of this research is to investigate the detailed interaction between granular soil and geosynthetics by developing a new pull-out test apparatus and provide a better understanding of the interaction analytically and numerically.

To achieve this aim, this research is separated into two main areas which are:

1. Investigation of the analytical modelling of the interaction between soil and reinforcement to assess the degree of uncertainty and idealisations inherent in the methods.
2. Advanced visualisation element tests using transparent soil technology with Particle Image Velocimetry (PIV). Use of transparent soil allows direct observation of the patterns of strain between the soil and reinforcing material.

To meet this aim the following objectives were developed:

(i) Review and evaluate the analytical interaction models between soil and reinforcement by conducting a thorough review of published literature.

(ii) Model a specific example problem using the limit analysis approach Discontinuity Layout Optimization (DLO) to further evaluate current reinforcement modelling methodology.

(iii) Develop a model test rig and technique of physical modelling using non-intrusive modelling techniques using transparent soil in conjunction with laser aided imaging and coupled with Particle Image Velocimetry (PIV) to visually observe soil geogrid interaction mechanics.

(iv) Use the modelling technique to investigate the specific case of pull-out of a geogrid from soil and develop and enhance an interaction model.

1.3 Thesis structure

Chapter 1 - Introduction: This chapter gives a brief outline of the contents of this thesis, together with a statement of the issues to be investigated.

Chapter 2 - Literature Review: This chapter is separated in two main parts: physical and analytical modelling. The physical modelling part briefly reviews the common type of pull-out test and explains the controlling parameters. The analytical part reviews previous literature on methods of analysing and designing reinforced structures, highlighting gaps in knowledge and idealisations in modelling.

Chapter 3 - Transparent Soil and Geogrid Reinforcement: This chapter covers the history, types of the transparent soil and the results of the physical and mechanical tests on the selected test material: Fused Silica. It also describes the development process of the transparent soil used in this research.

Chapter 4 - Analytical and Numerical Models for Soil-Reinforcement Interaction: This chapter discusses analytical and numerical modelling of the interaction between soil and reinforcement and the inherent assumptions.

Chapter 5 - Experimental Development: This chapter describes the development of the experimental systems and the image based observational methods implemented to evaluate the soil-geogrid performance.

Chapter 6 - Physical Modelling Results: This chapter describes the results of pull-out tests, individually for each type of test including consideration of the effect of confining pressure on displacement, shear and volumetric strains.

Chapter 7 - Results and Discussion: This chapter presents the results of the physical modelling and discusses this in the context of current analytical models.

Chapter 8 - Conclusions and Recommendations: This chapter explains the key conclusion and recommendations for future work.

Appendix A - Limit Analysis of Reinforced Embankment on Soft Soil: This appendix presents a paper which has been published in the Geotextiles and Geomembranes Journal. In this paper comprehensive parametric studies of reinforced and unreinforced embankments were conducted using the general purpose computational limit analysis approach Discontinuity Layout Optimization (DLO).

Appendix B - Transparent Soil to Model Thermal Process: An Energy Pile Example. A paper which has been published in the ASTM Geotechnical Testing Journal is presented in this chapter. This paper explored the hypothesis that temperature change will alter refractive index of the transparent material and therefore progressively reduce its transparency. The development of the experimental methodology was discussed and a relationship between pixel intensity and soil temperature was defined and verified. This research has been conducted along with the main topic of this study while waiting for equipment development.

Chapter 2

Literature Review

2.1 Introduction

The use of geosynthetic materials in engineering earthworks has increased significantly in recent years to provide reinforcement to geotechnical earth structures. Reinforcement develops a bond with the soil through either friction or adhesion for granular soils and cohesive soils respectively. The interaction between soil and reinforcement can be generated through two main modes, either by sliding a block of soil over reinforcement (direct sliding) or pull-out the reinforcement from the soil after mobilising the maximum bond stress (pull-out bond) (Manceau et al., 2012).

In this chapter a review of previous research is carried out in order to investigate fundamental aspects of interface mechanics and evaluate the effects of parameters such as geogrid aperture size, soil particle size distribution, embedment length and confining stress to enhance research design implementation.

When designing reinforced earth structures a vital aspect is to understand the interaction between the reinforcement inclusion and the compacted soil as the interaction governs the overall stability. The main function of the inclusion is to redistribute stresses within the soil mass in order to enhance the internal stability

of the reinforced soil structure. The inclusions undergo tensile strain as they transfer loads from unstable portions of the soil mass into the stable soil zone. The most common research into of soil-reinforcement interaction is pull-out capacity (Palmeira and Milligan, 1989). However there remains a lack of knowledge in the interaction mechanics between soil and reinforcement which has an impact on our ability to implement rigorous analytical solutions or assign suitable parameters for interface elements in numerical modelling of reinforcement.

2.2 Background

The engineer's ability to maximise natural resources has become an important factor in all segments of infrastructure development. Increasingly, designers are faced with the challenge of maximising land use areas that often have both difficult topographic characteristics as well as challenging soil conditions.

One of the first applications of using flexible tensile reinforcement(polymer fabrics) was introduced by Schlosser and Vidal (1969) for use in vertical and inclined retaining slopes. They used flexible galvanised steel strips in horizontal rows in a granular backfill by attaching them to a flexible facing. Geotextile was used for first time in a reinforced wall by Holtz and Broms (1977) and Al-Hussaini and Perry (1976). Pigg and McCafferty (1984) pioneered the use of geogrids for reinforced walls. The first general guide to the nature of polymer reinforcements was given by Christopher and Holtz (1985).

Olivera (1982), Rowe et al. (1984), Rathmayer and Korhonen (1985) and Fowler (1985) used geotextiles for construction of embankments over soft soils. Olivera (1982) and Fowler (1985) have observed the intrusion of fill into the subgrade can reduced by 50% to 80% by using a geotextile under an embankment.

2.3 Soil reinforcement

Soil-reinforcement interaction is the most important aspect in the design and performance of reinforced soil structures and this interaction can be very complex, depending on the nature and properties of the reinforcement and the soil (Palmeira, 2009). In order to better understand the soil-reinforcement interaction different types of test and analytical analyses have been developed.

One of the common geotechnical structures which have been used since in the last decades are reinforced soil slopes. The two main possible types of failure which can happen for reinforced walls are; (i) shearing mass of soil over the reinforcement and (ii) pull-out failure as shown in Figure 1.1 (Palmeira and Milligan, 1989).

2.4 Direct shear test

Different apparatus and boundary condition for the performance of the direct shear test are presented in the literature. In conventional direct shear tests, the bottom box which is fixed can be occupied by the same type of soil as the top, a different type of soil or a rigid block. This test can be modified for investigation of the shear interface properties of a geogrid by placing the geogrid in the shearing plane either by using the same type of soil in both side or a different type of soil. Also, the geogrid can be sheared over a rigid block with different roughness. A more advanced box can place the geogrid with different orientations to the shear plane (Palmeira, 2009).

The main difference between test arrangements is the way the reinforcement is fixed into the box and how the normal stress is applied to the soil sample. The normal stress could be applied over specimen through: (i) a rigid and free top plate, (ii) a rigid top plate not allowed to rotate, (iii) a top plate fixed to the top half of the box, which is desirable for dilative samples and (iv) a flexible bag using bag fluid pressure which is more practical for large scale devices and can guarantee that the distribution of normal stress over the specimen is uniform

(Palmeira, 2009). Another issue is the influence of the boundary conditions on the side wall of the test box particularly for dilative soil which increases the normal stress on the shear plane and consequently the amount of shear strength measured during a test. Figure 2.1 shows the influence of front wall friction in large scale direst shear test on the results reported by Palmeira (2009).

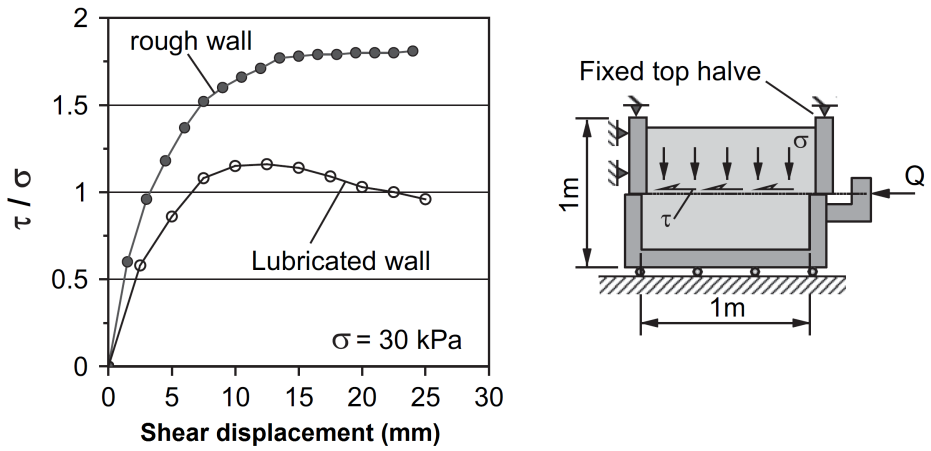

Figure 2.1: Influence of side friction in large scale direct shear tests (Palmeira, 2009)

Palmeira used the results of Dyer (1985) to interpret the results of the direct shear test for inclined specimens. The influence of the boundary on the results of the direct shear test for a reinforced and unreinforced sand sample is shown in Figure 2.2. This study was carried out by Palmeira (1987) using a shear box with inner dimensions 250 mm×250 mm×150 mm whereby soil is reinforced with steel grids. The results of the study show the effect of top boundary condition is larger for a reinforced sample in comparison with a non-reinforced sample.

2.5 Pull-out test

In order to study the effect of interaction behaviour between soil and geosynthetic materials in the anchorage zone of the slope/wall, full scale pull-out tests, laboratory model tests and numerical analysis are valuable (Palmeira, 2009). The results

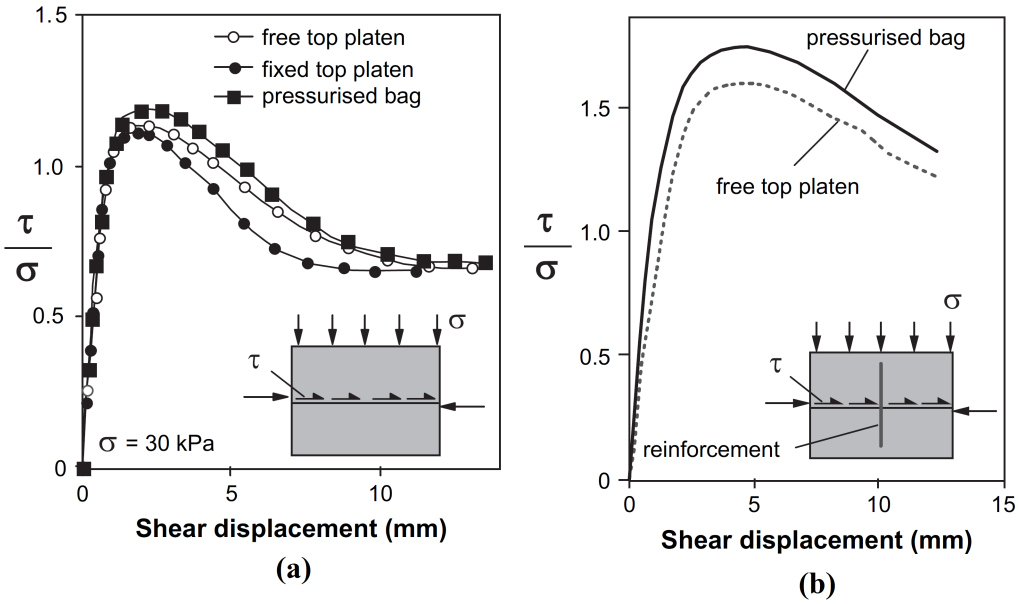

Figure 2.2: The effect of top plate boundary condition on the results of direct shear test for (a) Unreinforced and (b) Reinforced samples (Palmeira, 1987)

of pull-out tests have a direct effect on the design of the structure. British Standard, BS EN 13738:2004 (2004), and American Society for Testing and Materials, ASTM D6706-01 (2001), have published test methods to simulate the condition as close as possible to reality.

Previous research indicates that one of the main aims of the researcher is to modify the pull-out box by changing the dimensions of the box and developing the test method to minimums the effects of the boundary conditions on the test results so as to simulate the test condition as close to reality as possible (Palmeira, 2009).

The results of pull-out box tests are affected by many factors. So, the interpretations of the results of the tests are complex and not easy to understand. A pull-out test device includes: a pull-out box, a vertical load application system which is rigid or flexible, a horizontal force loading system, a clamping system and associated instrumentation for recording the displacement and rate of applying the pull-out load etc.

In order to investigate the pull-out behaviour of geosynthetic materials in different types of soils, the effect of box dimensions on the results and the influence of boundary conditions on pull-out force, several test devices were developed by different researchers (Chang et al., 1977; Palmeira and Milligan, 1989; Ochiai et al., 1996; Alfaro et al., 1995; Lopes and Ladeira, 1996; Raju and Fannin, 1998; Bolt and Duszynska, 2000; Sugimoto et al., 2001; Moraci and Recalcati, 2006 and Nayeri and Fakharian, 2009). Comparing these tests show that the following factors have the most significant effects on the results of a pull-out test:

- Boundary condition at the upper surface of the soil specimen
- Boundary condition at the front wall
- Clamping of the reinforcement

The main difference between researchers is the box dimensions and the method which they used for minimising the effect of boundary condition on the results.

The following equation can describe the pull-out resistance generated along a length of reinforcement: (Palmeira, 2009)

$$P_R = 2\ L\ \sigma_v^{'}\ f_b\ \tan\phi' \tag{2.1}$$

where P_R is the pull-out resistance (per unit width); L the length of reinforcement in the anchorage zone; $\sigma_\nu^{'}$ is the effective stress applied over the specimen; $\phi^{'}$ is the angle of shearing resistance of the soil and f_b is the bond coefficient between soil and reinforcement. Two alternative ways for computing the bond coefficient between soil and geosynthetic materials, are either using theoretical expressions which have been proposed by different researchers or by performing a pull-out test and back analysis to calculate the bond coefficient (Palmeira, 2009).

2.5.1 Boundary conditions at the upper surface of the soil specimen

The boundary condition at the upper surface of the soil specimen could be rigid or flexible, either by using a rigid plate load in contact with the soil or by applying the vertical load through a flexible rubber bag which is filled either with liquid or air. The significant differences between these two types of load application are the distributions of stress on top surface of the specimen (Farrag et al., 1993). The second system of loading allows constant normal stress and the possibility of free vertical displacement at every point of the soil surface contact area (Moraci and Recalcati, 2006).

Figure 2.3 shows the results of pull-out tests reported by Palmeira and Milligan (1989) on galvanized steel for two different top boundary conditions: (i) a fixed rigid rough plate, and (ii) a flexible top plate and bag filled with water. The results show that the peak pull-out force is larger for a rigid boundary than for a flexible application device.

Farrag et al. (1993) demonstrated that a flexible boundary condition at the upper surface of the soil specimen allows a better and more uniform load distribution on the whole contact area and consequently a more uniform distribution of the effective stresses at the specimen upper surface.

2.5.2 Boundary condition at the front wall

The influence of the front boundary condition of the wall has been studied by many researchers (Palmeira, 1987; Palmeira and Milligan, 1989; Johnston and Romstad, 1989; Farrag et al., 1993; Lopes and Ladeira, 1996; Raju, 1995 and Sugimoto et al., 2001). Palmeira (2009) summarised the typical boundary condition which is used by different researchers for doing the pull-out test (Figure 2.4).

In the traditional test arrangement the front wall of the pull-out box is fixed and the soil is in contact with the wall. Therefore, it is important to find the way to

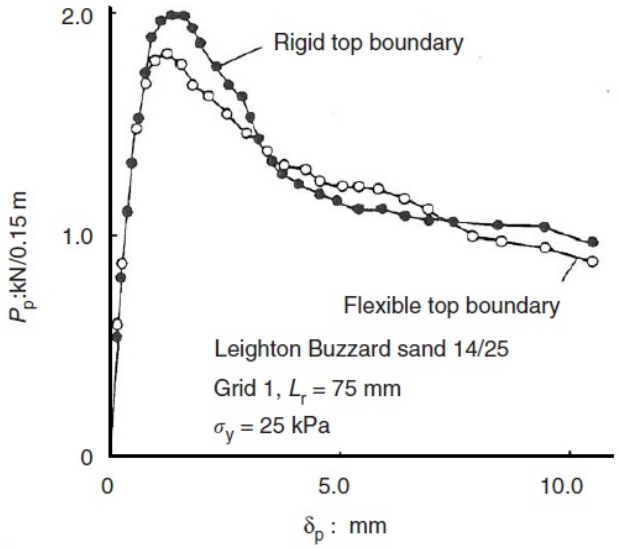

Figure 2.3: The effect of top boundary condition on pull-out tests results (Grid 1: Thickness of bearing member= 1.63 mm, grid size = 12.5×12.5 mm) (Palmeira and Milligan, 1989)

reduce the friction between soil and the front wall to avoid the effect on the results of the test. Palmeira (1987) and Abramento (1993) solved this problem by using layers of plastic films and oil or grease. Another option to reduce the effect of friction on the front wall is to use a sleeve which can cover a few centimeters of reinforcement near the front wall or by placing the reinforcement away from front wall which can be done for a geogrid by removing the frontal transverse members of the grid (Farrag et al., 1993; Wilson-Fahmy et al., 1994; Palmeira, 1987 and Perkins and Cuelho, 1999). Another method to reduce the influence of the front boundary on the results of the test is to use either a flexible face via a pressurised bag or a movable face (Sugimoto et al., 2001).

Sugimoto et al. (2001) presented the results of pull-out test for a rigid and flexible front boundary by using X-ray techniques. The flexible boundary condition was designed by placing two separate unit pressure bags which are filled air between the soil and the front of the wall. They found the distribution of the displacements along the reinforcement length is influenced by the stiffness of the front wall and therefore the mobilisation of the interaction mechanisms. Uniform distribution of

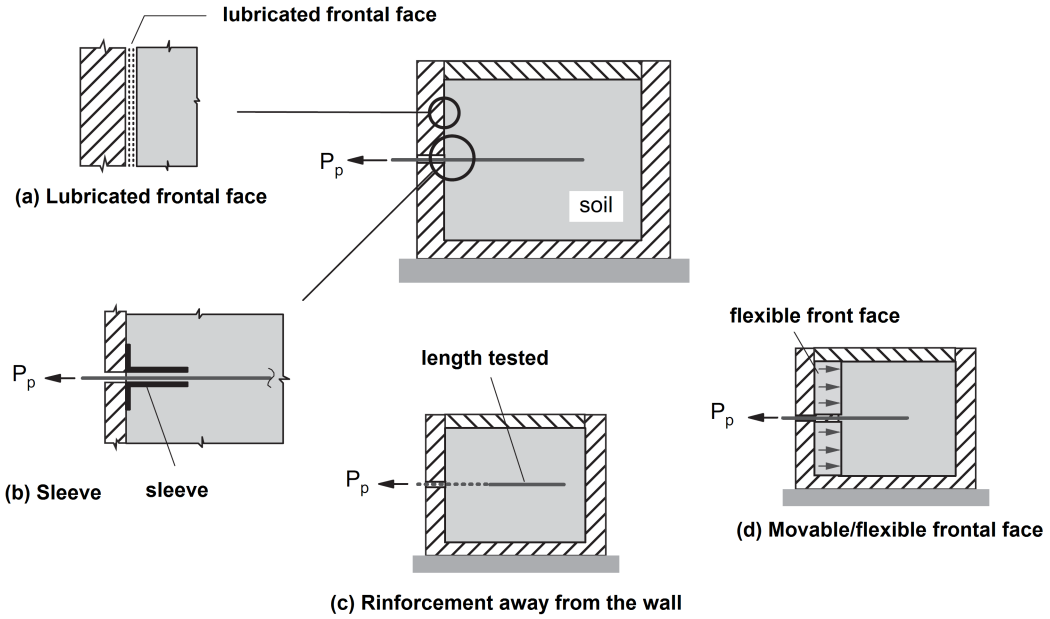

Figure 2.4: Typical boundary conditions of front wall in pull-out test (after Palmeira, 2009)

the interaction mechanisms along the reinforcement were mobilised for a flexible front wall, while with a rigid front wall the interaction mechanisms along the reinforcement are non uniform. Figure 2.5 shows the effects on pull-out force. The pull-out force for a flexible wall is slightly larger than that for a rigid boundary until the point of failure.

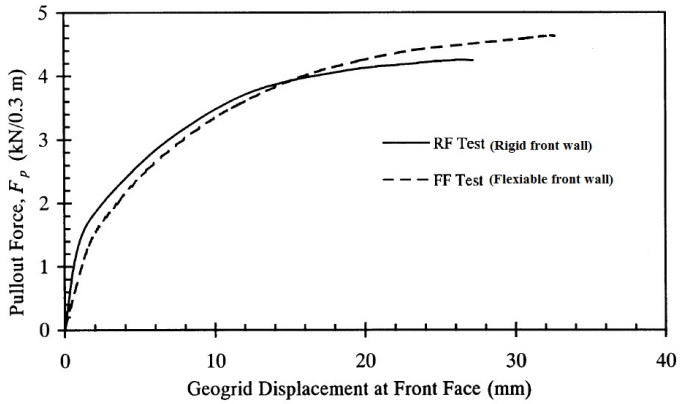

Figure 2.5: Pull-out force versus measured geogrid displacement at the front face (Sugimoto et al., 2001)

Palmeira and Milligan (1989) investigated the effect of friction angle between the soil and the front wall. The results of their study as shown in Figure 2.6 reflect that the friction angle mobilised between wall and soil has a considerable effect on the result of test.

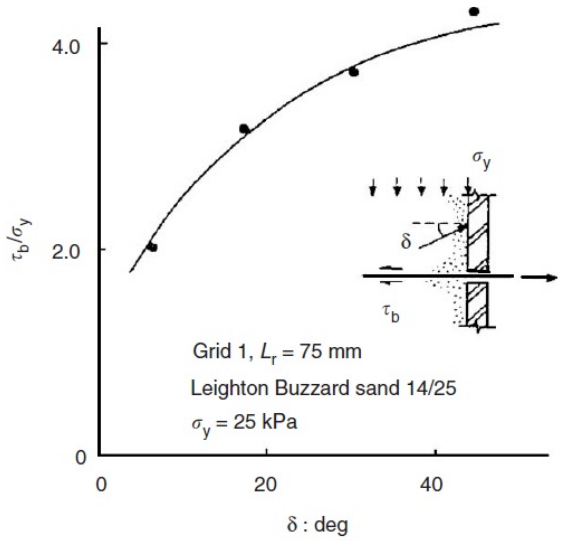

Figure 2.6: The effect of wall roughness on pull-out tests results (Palmeira and Milligan, 1989)

Therefore, it is necessary to consider a way to minimise the influence of wall friction on the results of a test or seek to move the front confined section of reinforcement away from the front of the wall. The results of experimental studies show that the influence of the stiffness of the front wall is less in a large box. Another alternative is to glue low friction materials to the front wall of the box or to fix the specimen between two metal sleeves to move the front confined section away from the front wall (Moraci and Recalcati, 2006). The side wall friction of pull-out box can also change the result of tests by affecting the effective vertical confining stress which is applied over the reinforcement. The friction between the wall and soil reduces the vertical effective confining stress at the soil-reinforcement. Johnston and Romstad (1989) investigated the effect of friction along the side wall of box and reported that the amount of vertical effective confining stress is reduced by 35% in comparison to the net value of vertical stress which is applied over the sample.

ASTM D6706-01 (2001) recommends that a pull-out box should be rectangular or square and be minimum 610 mm long, 460 mm wide and 305 mm deep. The width of the box should be increased by 760 mm for a fully frictional sidewall. In addition, the dimensions of the box depends on the soil particle size and the geometry of the geosymthetic. The minimum width of the box should be greater of 20 times the D_{85} of the soil or 6 times the maximum soil particle size; the minimum length should be should be greater than 5 times the maximum geogrid aperture size. Moreover, the thickness of the soil above or below the geosynthetic should be a minimum of 150 mm and at least 6 times the D_{85} of the soil or 3 times the maximum soil particle size. A significant difference between BS EN 13738:2004 (2004) and ASTM D6706-01 (2001) is on the minimum requirement of the length of the box which is 1.5 m for the British Standard.

2.5.3 Clamping the reinforcement

The clamping device used for transferring load to the specimen is typically made of two pieces of metal which should cover the whole width of the specimen. The reinforcement can be clamped either inside or outside the pull-out box. Farrag and Morvant (2000) studied the effect of the clamping system for both types of device. The advantage of placing the clamping system inside the box is to make sure the confined length of specimen is constant during the whole test and the displacement of clamping device can be used for the first confined section of reinforcement.

In the case of clamping the specimen outside of the box the frictional resistance between clamping plate and reinforcement can be ignored for measuring the pull-out force. By clamping the specimen outside the box it is not possible to apply the confining vertical stress over the specimen. So, the first confined section of reinforcement is measured inside the box instead of at the load application point. In addition, displacements are not affected by the slippage between the specimen and the clamps. The most important part of the design of the clamping system is calibrating the device to investigate the pull-out resistance developed during a test without reinforcement by the two pieces of metal forming the clamp.

2.6 Interaction between soil and reinforcement

The behaviour of a reinforced soil structure is largely governed by interaction mechanism that is developed between the reinforcement inclusions and the back-fill soil. The interface friction angle and adhesion between soil and geosynthetic materials are the main function that redistributes stresses within the soil mass in order to enhance the internal stability of reinforced soil structure. The inclusions undergo tensile strains as they transfer loads from unstable portions of the soil mass into stable soil zone (Teixeira et al., 2007).

Therefore different type of tests and analytical solutions have been developed in order to better understand the interaction between soil and reinforcement. Direct sliding and pull-out are the two main modes of interaction that occur in a returning structure (Jewell, 1996 and Manceau et al., 2012).

2.6.1 Direct sliding coefficient between soil and reinforcement

The modified direct shear test is an ideal way to evaluate the shear strength behaviour when the soil is shearing over geosynthetic materials. The British Standard BS 6906-8:1991 (1991) and American Society for Testing and Materials ASTM D5321 (1991) are published standards which can be used to evaluate the sliding and bond coefficient between soil and geosynthetic materials. The direct shear apparatus is assembled into upper and lower halves in which the reinforcement is supported either on a solid block or the soil in lower half of the box. The shearing force is usually performed at a constant rate of displacement.

In a conventional shear box test for investigating the coefficient of direct sliding between soils and any type of reinforcement material the bottom of the box could be occupied (i) by soil the same as the top, (ii) different types of soil and (iii) a rigid block. In the case of a geotextile a rather uniform shear mechanism develops along the soil-geotextile interface including possibly some interlocking between the soil

particles and geotextile fibres which depends on the dimensions and the shape of the particles and the surface characteristics of the geotextile. However, for geogrid materials, the direct sliding resistance can be generated by sliding between soil over soil through the apertures of the geogrid and soil over the material of the geogrid itself (Jewell, 1996).

2.6.2 Bond coefficient between soil and reinforcement

The bond coefficient between soil and reinforcement is provided by the skin friction over surface of reinforcement, skin friction between soil-soil through the geogrid apertures and passive resistance of the geogrid bearing members.The bond coefficient between soil and geogrid is relative to the size of soil and geogrid apertures and the thickness of members (Jewell, 1996).

2.7 The influence of the particle size of soil on interaction behaviour

One of the factors which has a significant effects on the mechanism of behaviour between soil and geosynthetic is the soil particle size as studied by Jewell (1996); Boyle and Holtz (1994); Chen and Chen (1994); Jewell (1990); Palmeira and Milligan (1989) and Jewell et al. (1984). However, the soil particle size has the largest effect on the geogrid materials since the soil volume can penetrate through the geogrid aperture and mobilise the interlock mechanism. The effect of soil particle size is relative to the geogrid aperture size and thickness of bearing members. When the soil particle is smaller than the geogrid aperture size, it can penetrate through the geogrid. In addition, the particle size of soil should be less than the thickness of the geogrid to generate passive resistance (Jewell et al., 1984). The results of research by Lopes and Lopes (1999) show that the appropriate soil particle size can increase the shear resistance between soil and geogrid by 20%.

Palmeira and Milligan (1989) investigated the influence of the relative sizes of soil particle and geogrid transverse ribs on the bearing stress. Figure 2.7 shows the normalised bearing stress versus the thickness of the transverse ribs normalised by the average of soil particle size. The results of the study show that a transverse member of square or rectangular shape can provide slightly higher bearing strengths in comparison with round sections. The results also indicate that for ratios $B/D_{50} > 12$ the normalised bearing strength starts to be independent of the soil particle size.

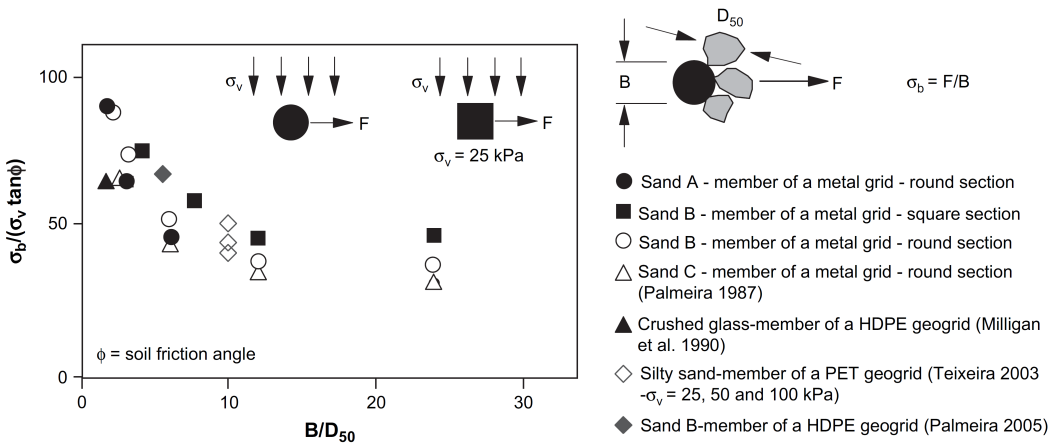

Figure 2.7: The results of pull-out test on isolated transverse geogrid ribs for different cross section shape (after Palmeira and Milligan, 1989)

2.8 Displacement and strain in soil-geogrid reinforcement

Classical pull-out box tests can determine the ultimate pull-out capacity of soil reinforcement for a range of different confining pressures, lengths of embedment, soil particle sizes and geogrid characterization such as rupture strength, shape and size of aperture. However, the geosynthetic-soil interaction mechanisms based on ultimate pull-out capacity is not easy to understand and very complex. Therefore, there is a need to investigate a new method to offer the capability to record the displacement across the sample during the test. To achieve this aim, a few

researchers have used different methods to track soil particles during pull-out tests by adding some artificial objects in soil mass and tracking these instead of soil.

Dyer (1985) and Milligan et al. (1990) used crushed pyrex glass mixed with colourless liquid paraffin together with the photoelasticity method to observe the interaction between soil and metal grid and polymeric materials respectively. Dyer (1985) used the photo-elasticity method to better understand the influence of reinforcement on the distribution of stress in the soil by replacing specimens in different orientations. In his research he used glass ballotini by manufactured of soda and lead glass with refractive indices of approximately 1.51 and 1.60 respectively. Appropriate mixtures of α-bromonaphthalene and colourless liquid paraffin were used to match the RI with glass. The internal dimensions of the pull-out box were 204 mm length, 52 mm width and 150 mm depth. The confining pressure was applied through a rigid platen using a dead load on a hanger. Figure 2.8 shows a schematic of the shear box for single reinforcement.

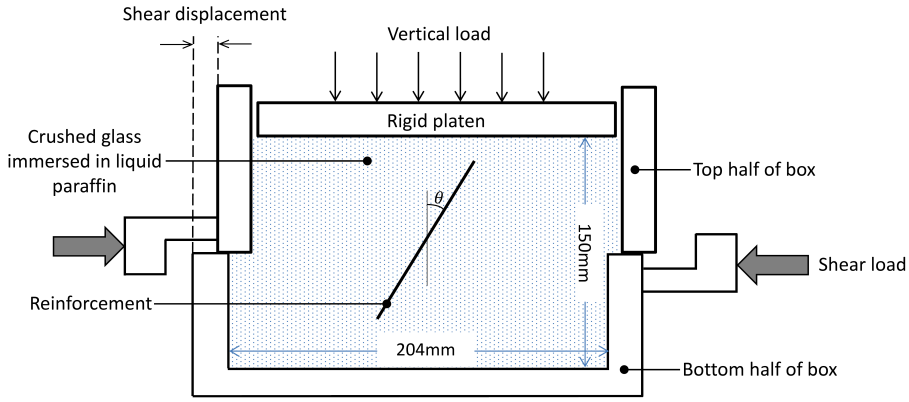

Figure 2.8: Schematic diagram of direct shear box test arrangement for a single reinforcement (after Dyer, 1985)

Figure 2.9 presents the results of his study. The bright areas in the photographs are regions of high compressive stresses and dark areas for low stress levels. The pattern of light obtained shows that the reinforcement significantly changes the mode of distribution of stress on the soil sample.

Figure 2.10 shows the interaction between geogrid transverse members and the surrounding soil during the pull-out test. The results of the study show that for

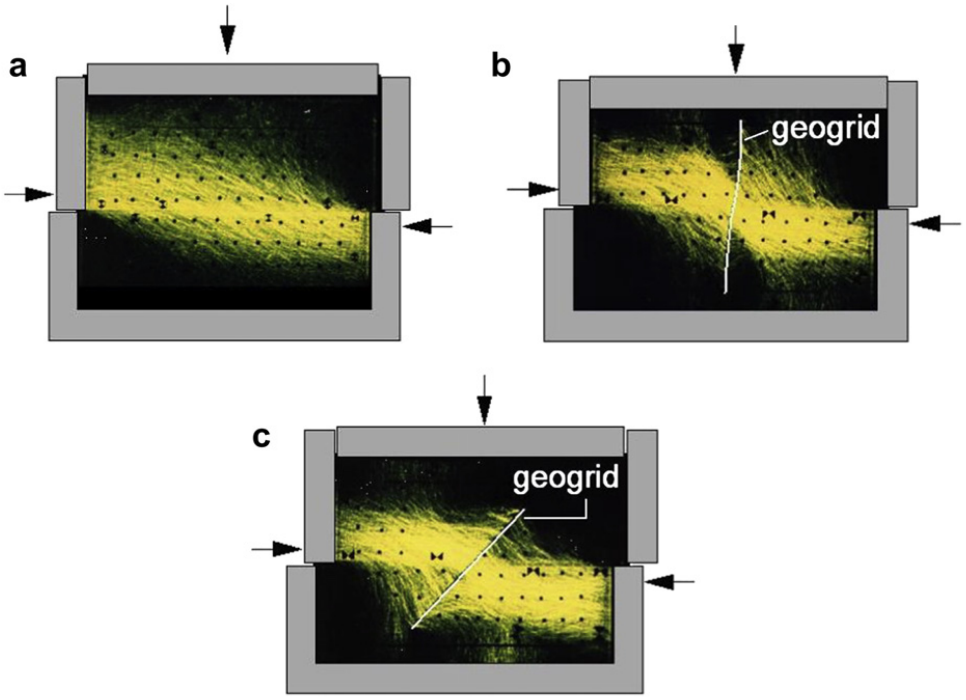

Figure 2.9: Photo-elastic studies in the direct shear test, (a) Unreinforced; (b) Vertical reinforcement and (c) Inclined reinforcement (after Dyer, 1985)

the long spacing between transverse members of a steel grid the load distribution is uniform (Figure 2.10a).

Otani et al. (2001) used other techniques to investigate the interaction between soil and reinforcement using an X-Ray CT scanner which offers superior measurement resolution. The small sample geometry was the problem of their study. Sugimoto et al. (2001) have done a series of laboratory pull-out tests to investigate the effect of the front boundary condition on the pull-out behaviour of geogrids in sand by using X-ray radiography to track lead inclusions in the soil during a pull-out test. The inner dimensions of box were 600 mm×300 mm×625 mm in length, width and height. Figure 2.11 shows the displacement of sand around the geogrid for both rigid and flexible front boundary conditions by tracking lead shots in the soil. The results of the study indicate that the sand movements occur over a larger area with a flexible front boundary in comparison with rigid boundary test. The amount of failure pull-out force for both front wall rigid and flexible boundary condition is not so different. However, the bond stress distribution is larger for

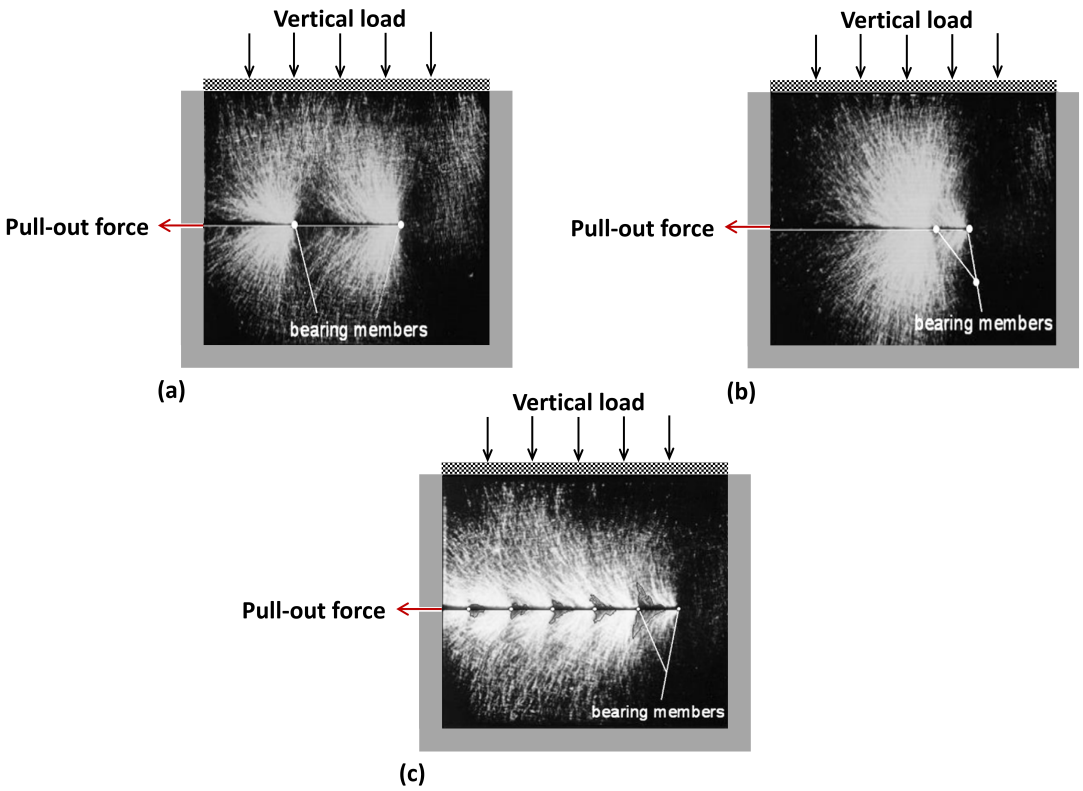

Figure 2.10: Interference between grid transverse members for different spacing between transverse members (a) Large spacing, (b) Short spacing, (c) Test on a longer grid, (after Dyer, 1985)

flexible boundary in comparison with the rigid case. Therefore, the pull-out test with rigid front boundary may provide an underestimated resistance value for the reinforced structures with a constant pressure boundary.

The new non-intrusive modelling technique using transparent soil modelling gives the chance to visually observe soil geogrid interaction mechanics in a special pull-out test apparatus. Ezzein and Bathurst (2011b, 2014) used a transparent coarse granular soil in a large transparent pull-out box apparatus to investigate the interaction between soil and geogrid. The dimensions of the test box were 300 mm high by 800 mm wide by 3700 mm long and it was made with 13 mm aluminium plates. This pull-out equipment was larger than a traditional pull-out box that follows the minimum recommendation of the BS EN 13738:2004 (2004) and ASTM D6706-01 (2001). In addition, in these standards the end of geogrid in the passive

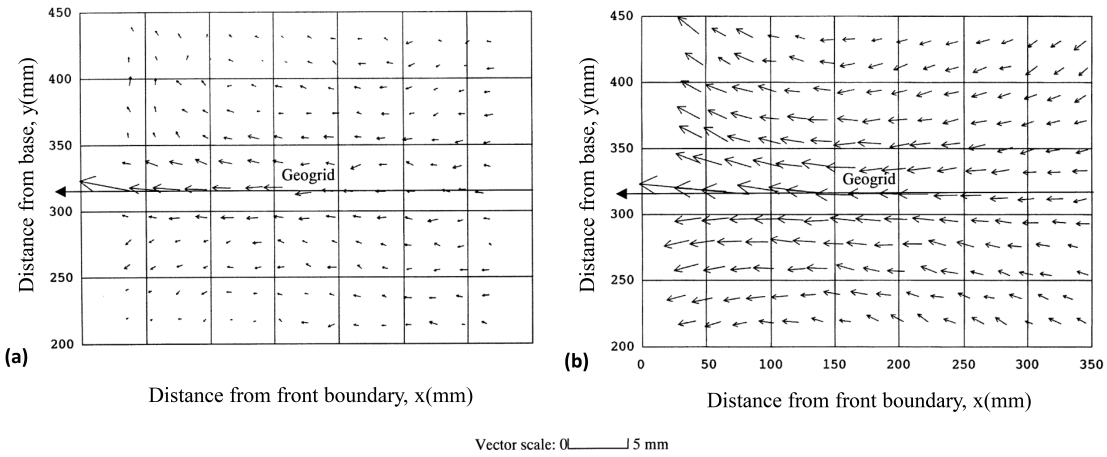

Figure 2.11: Displacement of sand around geogrid for the front boundary of , (a) Rigid front face, (b) Flexible front face (Sugimoto et al., 2001)

zone is free to move whereas it was clamped in their study using a back clamp. Figure 2.12 shows a cross section view of the pull-out box and original image of the biaxial polypropylene geogrid specimen embedded in transparent soil and viewed through the bottom of the pull-out box apparatus.

The transparent soil used particles of crushed fused quartz which are non-porous and incompressible. The fused quartz is classified as SP according to the Unified Soil Classification System with a mean particle size (D_{50}) of 1.68 mm, a coefficient of uniformity of 2.04 and a coefficient of curvature of 0.68. The transparent soil fluid was prepared by mixing two clear mineral oil fluids (Puretol 7 and Krystol 40) together which have a refractive index of 1.4586 at 22°C (Ezzein and Bathurst, 2011a).

Ezzein and Bathurst (2014) and Bathurst and Ezzein (2015) presented displacement profiles for geogrid specimens for different surcharge pressures up to 50 kPa at time intervals until rupturing. The length of geogrid was 2 m for their study with ultimate strength 12.5 kN/m. The authors managed to measure the relative horizontal displacement between the geogrid specimen and painted particles, which were used as targets to track soil displacements, over the length of the geogrid. The results of their study show the zone of influence of the geogrid is around 100 mm from the interface between the specimen and the soil.

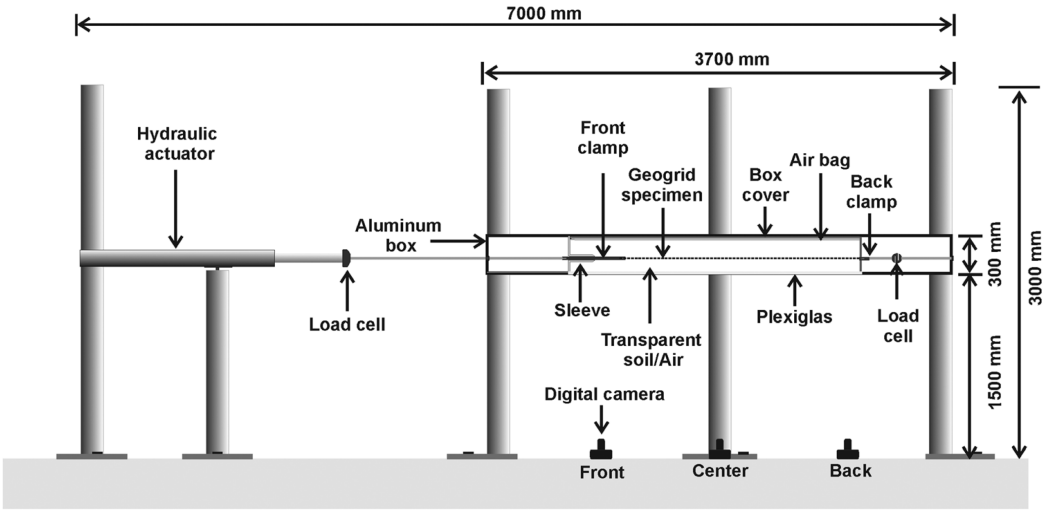

Figure 2.12: (a) Schematic diagram of pull-out box (b) Photo of geogrid taken from bottom of box (Ezzein and Bathurst, 2014)

Ferreira (2013) and Ferreira and Zornberg (2015) presented a new transparent pull-out test for 3D evaluation of soil-geogrid interaction under small displacement and strain which was focused on behaviour at the local level (Figure 2.13). They added additional soil markers in the transparent soil mass which allowed tracking of soil particle displacement during the test. For soil markers they used the same fused quartz painted black. The line of soil markers was placed perpendicularly in the pull-out direction and observed in the plan view at a distance of 51, 31 and 7 mm from the interface (Figure 2.14).

The fused quartz was classified as SP according to the Unified Soil Classification System with a mean particle size (D_{50}) of 3.7 mm, a coefficient of uniformity of 1.6

and a coefficient of curvature of 1.2. They found the zone of influence of geogrid is between 7 and 31 mm which correspond to 2 to $8D_{50}$ of the soil. In addition, they found at small displacement and strain the bearing mechanism along the transverse ribs contributing to soil-geogrid interaction.

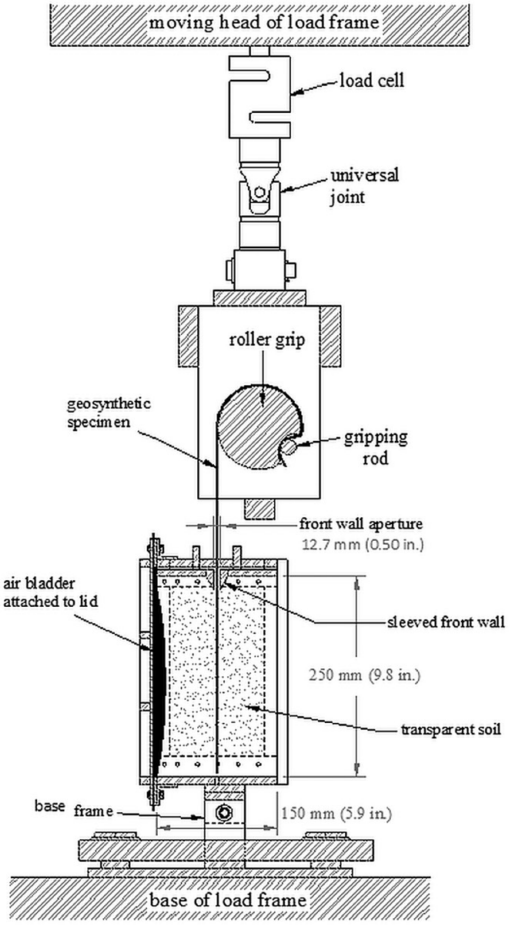

Figure 2.13: Schematic diagram of crosse section of transparent pull-out test setup (Ferreira and Zornberg, 2015)

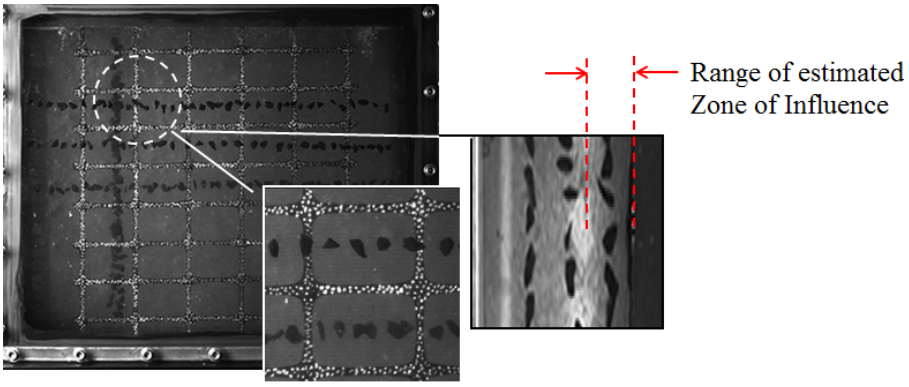

Figure 2.14: Position of soil markers in the pull-out test (Ferreira and Zornberg, 2015)

2.9 Analytical and numerical evaluation of the reinforcement design

Previous literature on methods of designing reinforced structures are summarised in this section highlighting the gaps in knowledge and approximations in modelling methods.

To design a reinforcement soil structure two issues are normally checked: (i) checking the ultimate limit state by examining collapse failure on major damage and (ii) controlling the deformation and settlement in the case of serviceability limit states (Manceau et al., 2012). To model the effect of soil reinforcement on slope stability traditional limit analysis and limit equilibrium method have been modified and various methods are presented in the literature.

Limit equilibrium is a popular method used traditionally for checking the stability of slopes either with or without reinforcement. The main advantage of this method is the capability of modelling the complex soil profile and seepage with different loading conditions (Yu et al., 1998). The main assumption of this method is that the soil follows a Mohr-Coulomb yield behaviour at collapse (Terzaghi, 1943) and that the tensile force mobilised in the reinforcement acts to oppose collapse. A circular slip surface or combination of circular and log spiral or plane surfaces are the common types of assumptions used with most available limit equilibrium

methods (Palmeira et al., 1998). The reinforcement can be applied as a tensile force at the location of the intercept between the reinforcement and slip surface. For instance, Duncan (1996) modelled the reinforcement by using a pre-computed pull-out force which acts to stabilize the construction. An other alternative way is the method of slices which is often used to assess stability. Bishop (1955), Spencer (1967) and Janbu (1973) simulated the reinforcement as a tensile and shear resistance which is applied to each slice. However, additional tensile resistance adds in to the system which is generated from the length of reinforcement that lies beyond the failure mechanism (Clarke et al., 2013).

The limit analysis method is a powerful method for checking slope stability and limit bearing capacity of geotechnical engineering structures. Drucker et al. (1952) first introduced limit analysis based on plastic limit theorems. Chen (1975) used limit analysis in geotechnical engineering for the first time for solving bearing capacity, earth pressure on retaining walls and slope stability problems. In this method soil is modelled as a perfectly plastic material following an associative flow rule. This idealisation of the behaviour of soil allows the use of two plastic bounding theorems which are lower and upper bounds (Drucker et al., 1952 and Chen, 1975).

Using the upper bound theorem a compatible mechanism of collapse is identified and the rate of external work with the rate of internal energy dissipation. The upper bound theory will identify a load that will definitely cause collapse. However, collapse may occur at a lower load. On the other hand, the lower bound theorem identifies an equilibrium distribution of stress that balances the applied load and nowhere violates the yield criterion. The lower bound theorem guarantees that this load will definitely be carried by the body. However, higher loads may be taken without causing collapse. Haliburton et al. (1978) listed the common failure types of embankments and slopes which are due to rupture failure of reinforcement, pull-out failure and excessive deformation of reinforcement.

In the case of soil nail reinforcement different researchers have employed different ways of modelling nail. Juran et al. (1990) used the kinematic limit analysis approach to calculate the maximum shear and tensile forces generated on the soil

nail. However, a modified Bishop (1955) method needs to use to identify the failure mechanism of slope. A continuous stress distribution over the soil nail can be used to find a more accurate approximation of the strength and pull-out and resistance of soil nails. This method developed by Zhu et al. (2005) allows the distribution of the normal stresses acting on soil nails crossing a slip surface.

2.9.1 Analysis of stability

In an internal stability check potential failure mechanisms that either pass through some part of the reinforced area or in front slope all the reinforcement are examined. The output of this check is to find out the best layout of reinforcement. Figure 2.15 presents the potential ultimate limit state modes of failure for slopes which is summarised by BS 8006-2 (2011).

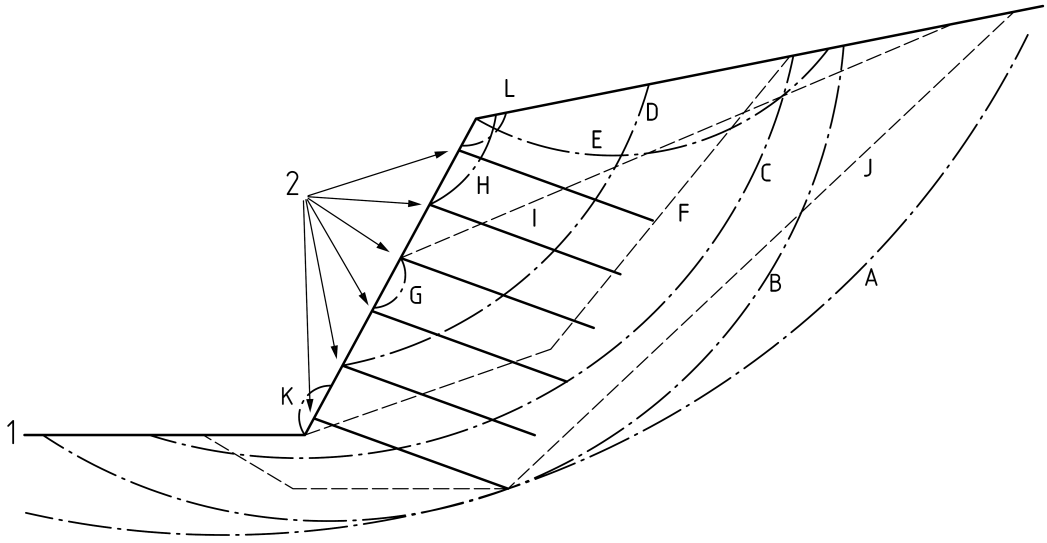

Figure 2.15: Ultimate limit state modes of slope failure; External rotational failures (A,B,E), Internal rotational failures (C,D,H), Internal translational failures (F,I), Internal local face failure (G,L), External translational failure (J), Internal local over stressing of reinforcement, surface (1) and soil reinforcements (2)(after BS 8006-2, 2011)

2.9.1.1 Bishop's simplified method of slices

Bishop's simplified method of slices is the most common method of limit equilibrium analysis methods for the purpose of checking the rotational stability of slope (Bishop, 1955 and Bishop and Morgenstern, 1960). In this method the free body diagram of the slip mechanism is divided into a number of vertical slice as shown in Figure 2.16. The main assumption in this method is that, the shear strength across of the slice boundary is neglected and, the normal force acts through the centre of the base of the slice.

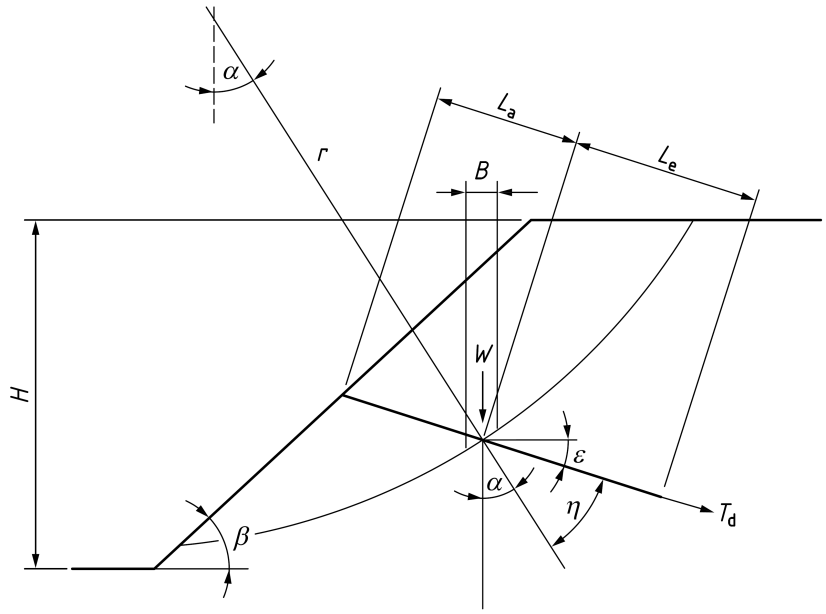

Figure 2.16: Slip circle method of slices (after BS 8006-2, 2011)

This equilibrium equation which is used in this method is based on moment equilibrium and force equilibrium in the vertical direction. This approach is used in British Standard (BS 8006-2, 2011) for designing soil nailing but the process is equivalent for geosynthetic reinforcement. The following equations show the calculation moments either for driving/disturbing moment and resistance about the centre of rotation to obtain the factor of safety.

$$FS = \frac{M_{driving}}{M_{resisting}} \tag{2.2}$$

$$M_{driving} = \sum_{i=1}^{n} [W_i + qB_i] r \sin \alpha_i \tag{2.3}$$

$$M_{resisting} = M_{soil} = \sum_{i=1}^{n} \{ \frac{c^{'} + [W_i + qB_i - u_i B_i] \tan \phi^{'}}{\cos \alpha_i + \sin \alpha_i \tan \phi^{'}} \} r \tag{2.4}$$

where, $\phi^{'}$ and $c^{'}$ are shear resistance of soil, W_i is the self-weight of the slice, q is the surcharge acting on the surface of the slice, u is the pore pressure acting the base of the slice. The geometrical parameters as shown on Figure 2.16 are introduced in Table 2.1.

Table 2.1: Slip circle method of slices geometrical parameters

Symbol	Definition
B	width of slice (m)
H	height of slope (m)
L_a	length of reinforcement to base of slice (m)
L_e	length of embedment zone (m)
r	radius of slip circle (m)
T_d	design tension in reinforcement (kN)
α	angle as defined by Bishop (1955)
β	angle of slope
ε	reinforcement declination
η	angle between normal to slip plane and reinforcement

However, by reinforcing the slope with soil nail the moment resistance of soil nails also contributed to the computation of the safety of factor of slope. Therefore,

$$M_{resisting} = M_{soil} + M_{nails} \tag{2.5}$$

where

$$M_{nails} = \sum_{i=1}^{m} [T_{dj} \cos(\alpha_j + \varepsilon_j + \frac{T_{dj} \sin_{\varepsilon j} \tan \phi^{'}}{\cos \alpha_j + \sin \alpha_j \tan \phi^{'}}] \frac{r}{s_{hj}} \tag{2.6}$$

where, T_d is the designed nail force (in kN) and S_h is the horizontal spacing of the nails.

2.9.1.2 Two-part wedge mechanism

The two-part wedge method is recommended by British Standard BS 8006 (1995) for designing the reinforced soil slopes. This method is essentially the same as the simplified method AASHTO (2004) of design tie-back wedge analysis for geosynthetic reinforced soil walls which are discussed by Allen et al. (2003) and Bathurst et al. (2005). In the two-part wedge method the factor of safety is computed by comparing the restoring and disturbing forces for a prescribed failure mechanism (Clarke et al., 2013).

The Two-part wedge method works by checking the stability of each wedge in terms of a force balance across the boundary of the wedge (Figure2.17) rather than a moment balance which is used in the Bishop's method. This analysis involves less calculation in comparison with Bishop's method of slices and it is easier to follow the calculation (BS 8006-2, 2011). The inter wedge forces are normally assumed to be normal, ignoring friction. The following equations are described in the British Standard (BS 8006-2, 2011):

"The assumption of a frictionless inter-wedge boundary is always likely to be conservative compared to Bishops simple method of slices, while the assumption of full friction on the inter-wedge boundary is always likely to be unconservative."

$$N_{21} = \{\frac{(W_1 + Q_1)(\sin\theta_1 - \cos\theta_1 \tan\phi^{'})}{\cos\theta_1 - \sin\theta_1 \tan\phi^{'}}\}+$$
$$\{\frac{-[\sum \frac{T_{d1}}{S_h}][\cos(\theta_1 + \varepsilon) + \sin(\theta_1 + \varepsilon)\tan\phi^{'}\_k_{d1}}{\cos\theta_1 - \sin\theta_1 \tan\phi^{'}}\} \tag{2.7}$$

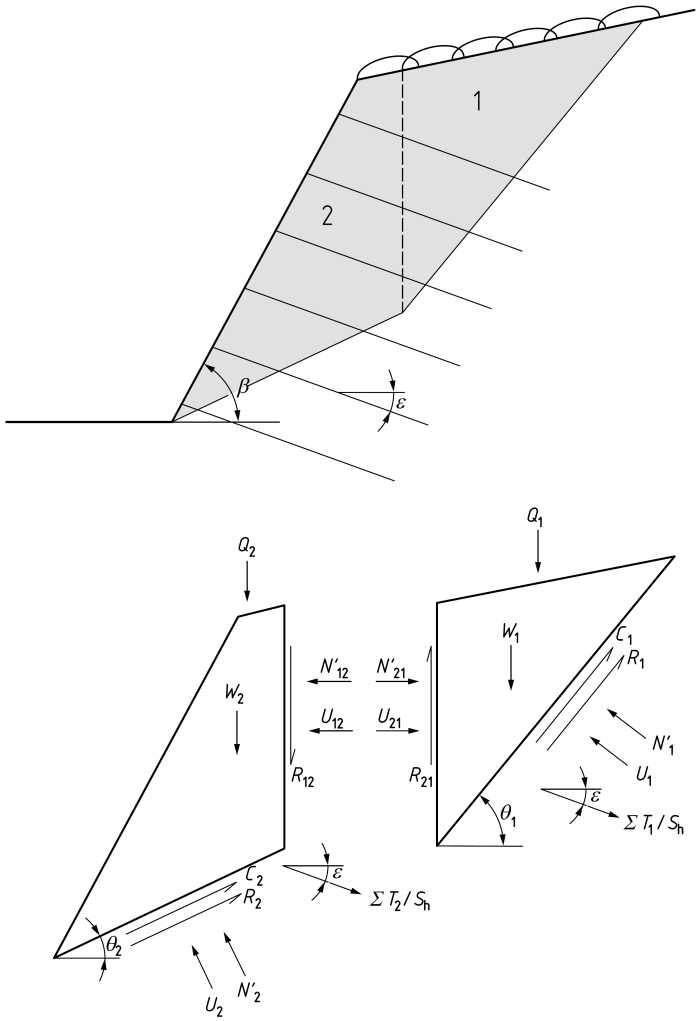

Figure 2.17: Two wedges analysis (after BS 8006-2, 2011)

$$N_{12} = \{\frac{-(W_2 + Q_2)(\sin\theta_2 - \cos\theta_2 \tan\phi')}{\cos\theta_2 - \sin\theta_2 \tan\phi'}\} + \{\frac{-[\sum \frac{T_{d2}}{S_h}][\cos(\theta_2 + \varepsilon) + \sin(\theta_2 + \varepsilon)\tan\phi' - k_{d2}}{\cos\theta_2 - \sin\theta_2 \tan\phi'}\} \tag{2.8}$$

where the various parameters are as indicated in Figure 2.17.

2.9.1.3 Modelling discrete soil reinforcement in numerical limit analysis

In traditional limit analysis and limit equilibrium methods, internal and external stability is checked separately, fewer types of failure mechanisms are considered and the reinforcement is represented by a finite pull-out force. The force is computed from the pull-out strength and the length of reinforcement beyond the slip mechanism. Finally, the resistance to movement of the reinforcement normal to its plane of placement can potentially be modelled, but this is normally neglected in the simpler models (e.g., the two-part wedge method)(Clarke et al., 2013).

However, by using the numerical limit analysis procedures such as finite element analysis (Lysmer, 1970; Sloan, 1988 and Makrodimopoulos and Martin, 2006) or Discontinuity Layout Optimization (DLO) (Smith and Gilbert, 2007a and Gilbert et al., 2010) it is possible to:

1. Determine the critical failure mechanism, without relying on pre-defined mechanism geometries.
2. Model pull-out and lateral resistance for reinforcement.
3. Model the effect of reinforcement on soil failure, regardless of where the reinforcement is located within the soil body.
4. Eliminate the distinction between external and internal stability (i.e., the critical stability state should be identified, whether this involves internal failure, external failure, or some combination of both).

DLO is a computational limit analysis method which can be used to directly compute the collapse load of solid body (Smith and Gilbert, 2007a) and has successfully been employed for a wide range of limit analysis problems, e.g. Gilbert and Smith, 2007; Smith and Gilbert, 2007b, 2008, 2013; Smith, 2012 and Shwan and Smith, 2014 , including those involving soil reinforcement, Clarke et al. (2013). In

that study, the DLO method was calibrated against the two-part wedge analysis method recommended by BS 8006-2 (2011).

The limit analysis problem is formulated in terms of the potential discontinuities that interlink nodes used to discretise the solid body under consideration and involves four key stages as illustrated in Figure 2.18. The critical arrangement of discontinuities (which defines the mechanism of failure that dissipates minimum energy) can be identified using optimisation. In the kinematic formulation these discontinuities represent sliplines and compatibility rigorously enforced everywhere. The accuracy of the method depends on the number n nodes employed which allow the critical mechanism to be selected out of a set of $n(n-1)/2$ potential sliplines.

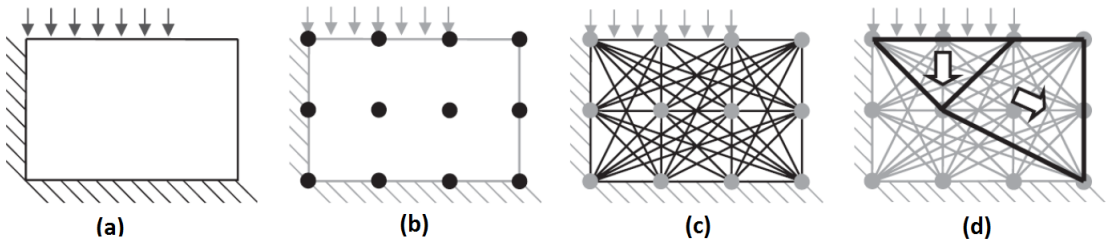

Figure 2.18: Stage in DLO procedure: (a) define problem domain and boundary conditions; (b) discretise domain area with nodes; (c)interconnect every node to every other node with a potential discontinuities; (d) identify critical layout of discontinuities at collapse (after Gilbert et al. 2010).

2.9.2 Modelling geosynthetic reinforcement in DLO

In a conventional limit equilibrium analysis based on the method of slices, a reinforcement element is modeled as a pre-computed pull-out force which acts as a stabilising force on the slice through which it passes into the non-deforming soil (Duncan, 1996; Bishop, 1955 and Spencer, 1967). Interaction within the failing slope mass is not typically modelled and normally the action of the reinforcement in terms of whether it pulls out of the deforming mass or pulls out of the stationary soil is pre-determined before the analysis.

In contrast, in the DLO approach, soil reinforcement can be modelled in a fully general way without any pre-knowledge of whether it will fail by pulling out of the stationary or moving soil mass. Reinforcement is modelled as a one-dimensional element which is able to model failure in bending, tensile rupture and compressive failure controlled by parameters M_p, R, and C respectively, where M_p is the plastic moment of resistance and C is the compressive strength of the reinforcement. The element described by Clarke et al. (2013) was designed to also allow the modeling of soil nails and so had the additional ability to allow soil to 'flow around'the element controlled by a lateral and pull-out resistance. These properties were not required and these resistances were set to ∞. Each engineered element has three parallel components (as shown in Figure 2.19) which comprise: an upper boundary interface, the reinforcement itself and a lower boundary interface. For the purposes of modelling geotextile reinforcement M_p is set to zero to allow free flexure, C is set to zero and the upper and lower boundaries are modelled with Mohr-Coulomb materials with strength $\alpha_s \tan\phi'$ or $\alpha_c c_u$ respectively.

In the equilibrium formulation of DLO, for each discrete element i of the reinforcement, variables are assigned to represent the shear force $\tau_{u,i}, \tau_{l,i}$, on the upper and lower faces respectively, and the tensile force T_i and bending moment M_i in the reinforcement. The set of τ_u, τ_l, M, T are found that give the maximum load on the system that does not violate the following constraints:

1. $\tau_l \leq \alpha_c c_u$
2. $\tau_u \leq \alpha_s(c' + \sigma'_n \tan\phi')$
3. $C \leq T \leq R$
4. $M \leq M_p$

It is noted that even if $M_p = R = C = 0$, the modelled reinforcement will still affect the mechanics of the system in that direct shear displacements are not permitted through the reinforcement element. However this can be represented via element rotations. With sufficiently small segments the same effect is achieved. Use of a

higher nodal density along the reinforcement can therefore be beneficial in some cases.

Note that in a limit analysis formulation such as DLO, yield or rupture of the reinforcement does not lead to breakage or fracture but to unrestricted ductile elongation that still allows transmission of tensile forces along the length of the reinforcement.

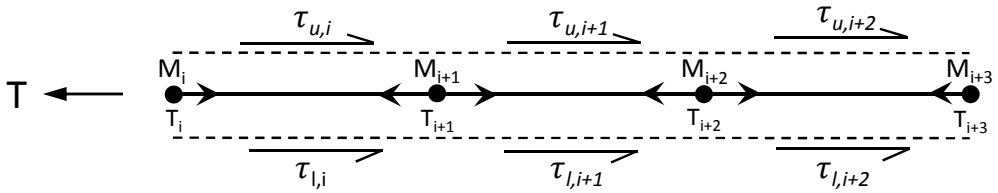

Figure 2.19: Modelling flexible reinforcement in DLO for segment or node i, T: tensile force (kN/m), τ_u: upper boundary soil/reinforcement interface stress (kPa), τ_l: lower boundary soil/reinforcement interface stress (kPa), R: tensile force in reinforcement (kN, per m width), M: bending moment in reinforcement (kN, per m width).

2.10 Transparent Synthetic Soils

Traditionally in an experimental model spatial stresses and strains within the soil have been measured using embedded sensors. While beneficial to offer some understanding of the soil response; disadvantages of this methodology include: (i) a lack of detailed spatial measurement resolution owing to the sparse number of measurement locations within the soil and (ii) local stiffening of the soil in the vicinity of the sensors leading to stiffness compliance errors. Transparent synthetic soil has been developed in recent decades to allow direct internal observation of axisymmetric and three dimensional geotechnical problems (Iskander, 2010). Since its inception many forms of transparent soil analogues have been successfully developed to represent a broad spectrum of both fine and coarse grained soil for modelling purposes. Visualisation capabilities have also advanced considerably in terms of material quality and image capture /measurement observation techniques.

Early pioneers sought to directly capture the location of isolated embedded targets visible within the soil (similar to lead shot X-Ray methods) which has evolved to full field resolution using laser aided imaging methods harnessing advanced automated digital image correlation methods. The work reported in the thesis relates to granular based soils thus a review of granular transparent materials previously developed is summarised in the following sections.

Figure 2.20 contains two sets of images from the testing conducted. Early experiments in transparent soil adopted back illumination to silhouette embedded target markers to capture the mechanical response of the soil and a geostructure by Gill (1999) and recent works by using laser aided imaging in conjunction with digital image correlation by Kelly (2013). This demonstrates the advance of the experimental technique to other enhance resolution measurement.

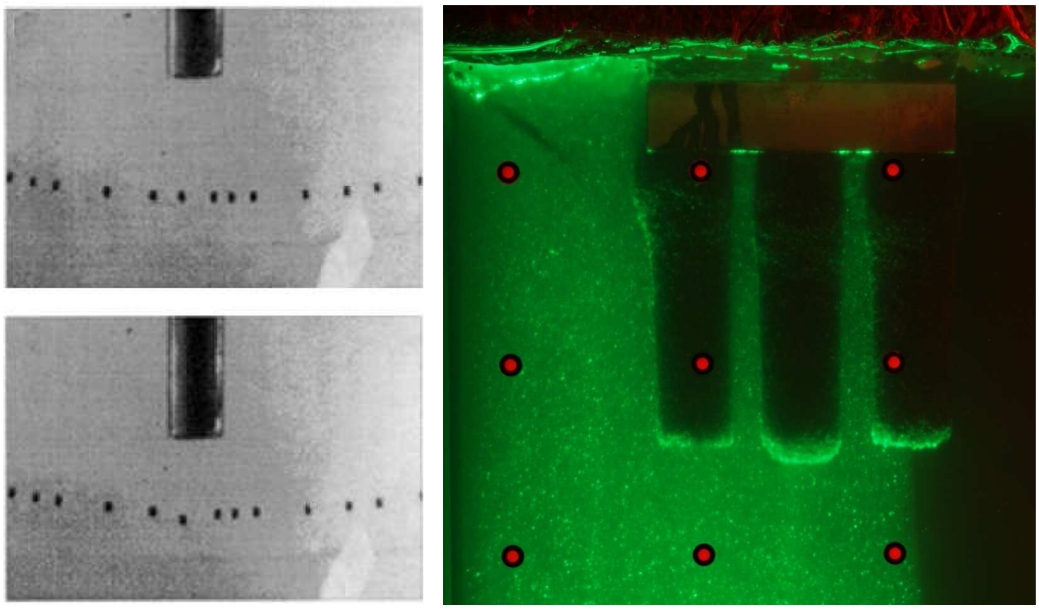

Figure 2.20: Images from investigations conducted by (a) Gill (1999) and (b) Kelly (2013)

2.10.1 Coarse grained transparent synthetic soils

2.10.1.1 Crushed glass

One of the first experimental programmes that used transparent soil was by Allersma (1982) which used crushed borosilicate glass submerged in a white oil pore fluid to examine the stress and strain distributions developed during the installation of a penetrometer. The particle size of crushed glass was specified in two ranges of 1-2 mm and 2-3 mm in diameter. Several concerns prevent this material being adopted for the present research, (i) the susceptibility of crushing the glass particles during the loading process which is reported by Allersma (1982), (ii) internal micro fractures within the crushed particles diminish the visual depth within the model that can be viewed, and (iii) the particle shape of the crushed glass is highly angular and thus may offer increased frictional resistance compared to natural granular soil under pull-out. Indeed Allersma reported the friction angle of crushed glass in a medium-dense sample as 33° and 40° for particle sizes between 1-2 mm and 2-3 mm respectively, which is larger than typical values for fine sand and gravel respectively.

2.10.1.2 Silica gel

The geotechnical properties of silica gel are presented by Sadek et al. (2002). This type of material has been used for modelling sand and originates from a colloidal form of silica. It is available in a wide range of particle size from 0.5 mm to 5 mm. Silica gel is an amorphous highly porous, partially hydrated form of silica, which is a substance made from silicon and oxygen (Iskander, 2010).

The specific gravity of silica gel is approximately 20% less than the specific gravity of natural silica sands which is 2.2 (Weast, 1986) and the dry unit weight is typically between 6-9 kN/m^3. Sadek et al. (2002) carried out triaxial compression and direct shear tests on dry and saturated specimens to investigate shear strength of silica gel and stiffness. The stress-strain behaviour for fine and coarse particle size are presented in Figure 2.21 and summarised in Table 2.2. The strain associated

with the peak strength of dense silica gel in the triaxial test is higher than natural dense sand owing to the greater compressibility of silica gel.

Table 2.2: Frictional properties of fine and coarse silica gel for statured specimen (Sadek et al., 2002)

Silica gel	Density	Particle Size (mm)	Friction angle (ϕ)	
			Triaxial Test	Direct shear test
Fine angular	Loose	0.5-1.5	29°-36°	32°-46°
	Dense		31°-42°	37°-52°
Coarse round	Loose	2.0-5.0	29°-33°	36°-43°
	Dense		33°-36°	38°-53°

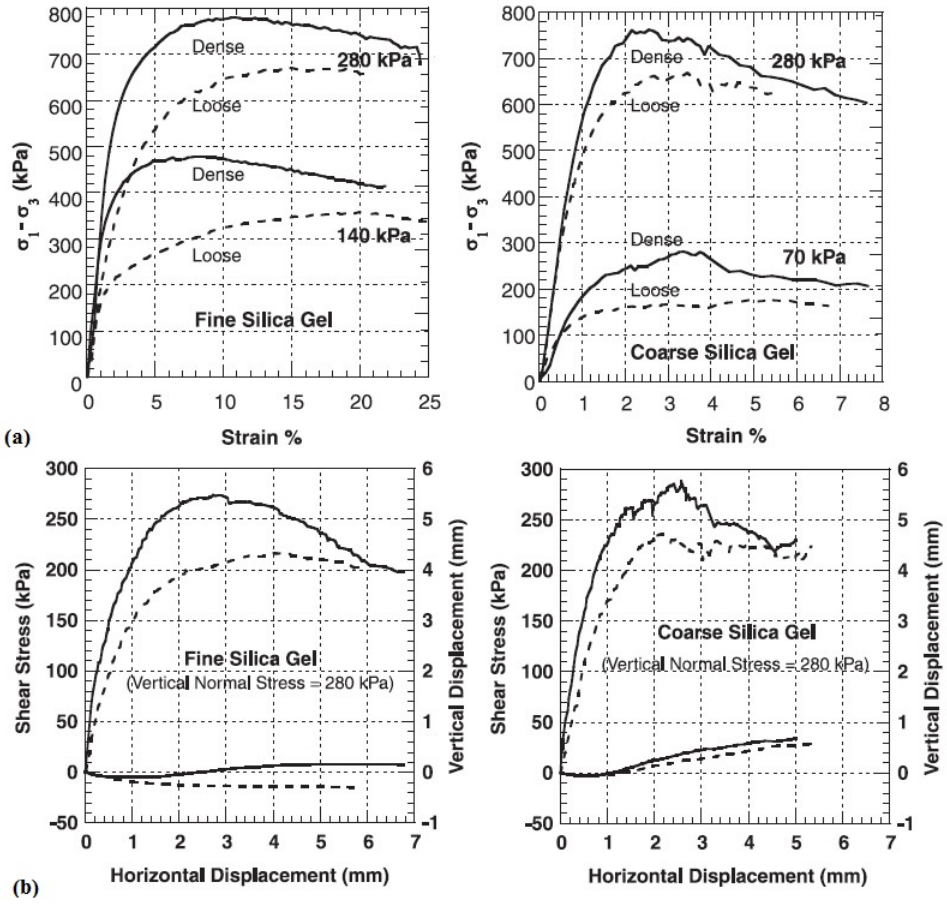

Figure 2.21: Typical results of (a) Stress-strain curve for consolidated drained triaxial tests and (b) Direct shear test on loose (dashed) and dense (solid) on specimen of silica gel (Sadek et al., 2002)

2.10.1.3 Fused silica

Ezzein and Bathurst (2011a) introduced the most recent type of transparent granular soil based on fused silica aggregate which is shown in Figure 2.22. Fused silica is a noncrystalline which is made from silica dioxide (SiO_2) quartz sand. The material is manufactured by melting natural quartz crystals present in quartzite sand in high temperature around 2000°C, and cooling. The fused silica particles are impermeable and non-absorbent. A series of laboratory tests were carried out to investigate the properties of fused silica transparent soil by Ezzein and Bathurst (2011a) to assess its suitability for modelling natural soils. Table 2.3 shows the sieve analysis of fine and coarse fused quartz samples used by Ezzein and Bathurst (2011a).

Figure 2.22: Fused quartz particles (Ezzein and Bathurst, 2011a)

The shear strength of fused quartz materials was determined by direct shear tests for dry and saturated conditions with either water or mineral oil (Table 2.4). The results of the tests are shown in Figure 2.23.

The results of one-dimensional compression tests over fine and coarse fused quartz compared with uniform natural sand is presented in Figure 2.24 with the influence of fluid type. The main advantage of using this type of material for modelling granular soils in compression compared to silica gel beads is that the particles

of fused quartz are hard with negligible breakage. Furthermore, trial tests by Ezzein and Bathurst (2011a) indicated no adverse chemical reaction occurred between the aggregate and pore fluid that would compromise its visual clarity. In fact, as described later, examination of the various aggregates sourced for this project indicted that fused quartz offered superior optical properties i.e. greater transparency which could be advantageous in allowing larger model geometries.

Table 2.3: Particle size of fused quartz samples (Ezzein and Bathurst, 2011a)

Property		Coarse particle	Fine particle
Particle size (mm)	D_{60}	2.10	0.39
	D_{50}	1.68	0.33
	D_{30}	1.21	0.22
	D_{10}	1.03	0.11
Coefficient of curvature	C_c	0.68	1.16
Coefficient of uniformity	C_u	2.04	3.65

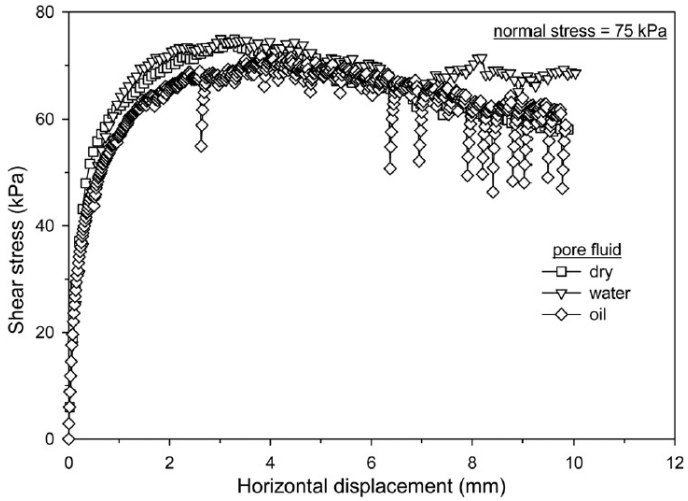

Figure 2.23: Influence of type of fluid on the results of direct shear test for coarse fused quartz (Ezzein and Bathurst, 2011a)

Table 2.4: Peak shear strength of fine and coarse fused quartz from direct shear tests for $c = 0$ (Ezzein and Bathurst, 2011a)

Pore fluid	Particle type	Peak friction angle (ϕ)
Dry	Fine	42°
	Coarse	43°
Water	Fine	44°
	Coarse	45°
Oil	Fine	43°
	Coarse	44°

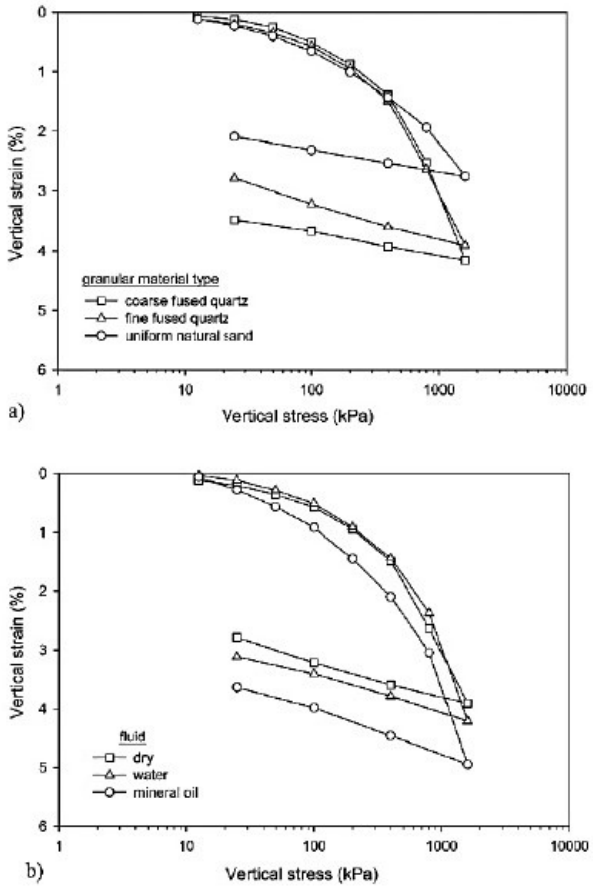

Figure 2.24: Result of one-dimensional test (a) over coarse and find fused silica and natural soil in dry condition, (b) influence the type of fluid on fine particle specimen (Ezzein and Bathurst, 2011a)

Chapter 3

Transparent Synthetic Soils and Geogrid Reinforcement

3.1 Transparent soil used in this research

Following the literature survey it is clear that material properties, particle size - reinforcement compatibility and optical clarity are all important factors in the selection of a suitable aggregate material. Based on the superior mechanical and optical qualities of fused silica introduced by Ezzein and Bathurst (2011a) it was decided to implement a similar aggregate type for this research. The following sections outline details of the specific material used and highlight the relevant mechanical and optical properties.

3.1.1 Fused silica

The fused silica adopted in this work was manufactured by Xuzhou New Hitech Silica Materials Co.,Ltd in China. It is produced from high purity Quartz Sand which is melted at high temperature between $1800-2000^{o}$C, cooled and crushed to produce a granular aggregate (Figure 3.1). Once submerged in suitable refractive matched index fluid the aggregate particles become transparent. This material

and supplier were selected as the manufacturer was able to produce the material in a desired range of both large and small aggregate sizes.

Figure 3.1: Fused silica particles

The size of soil particles selected for the project is between 10-15 mm with the mean particle size (D_{50}) of 7.42 mm which is classified as GP according to the unified soil classification system. The coefficient of uniformity, C_u is 1.342 and the coefficient of curvature, C_c is 1.009. The particle size distribution of this material is presented in Figure 3.2. The aspect of particle crushing was investigated by conducting a sieve analysis before and after triaxial shear tests (Figure 3.2). Particle crushing was not found to be significant and thus given the lower global stress conditions in the experimental pull out tests minimal particle breakage is anticipated.

Optical transmission of the soil is critical to ensure optimum viewing of the particles illuminated by the laser sheet and thus the precise mixture ratios have been carefully calibrated at 20°C. The matched RI pore fluid is blended from two mineral oils: technical white oil (Foodlink 15 supplied by Lincol oil) and Paraffin (N-Paraffin C10-C13 supplied by Aztec Oil) that are mixed at 80 : 20 ratio by volume (Figure 3.3).

Conventional consolidated drained (CD) triaxial tests have been used to determine the mechanical properties of this fused silica aggregate. Stress-strain curves from tests on dry and wet samples of this fused silica aggregate which are presented

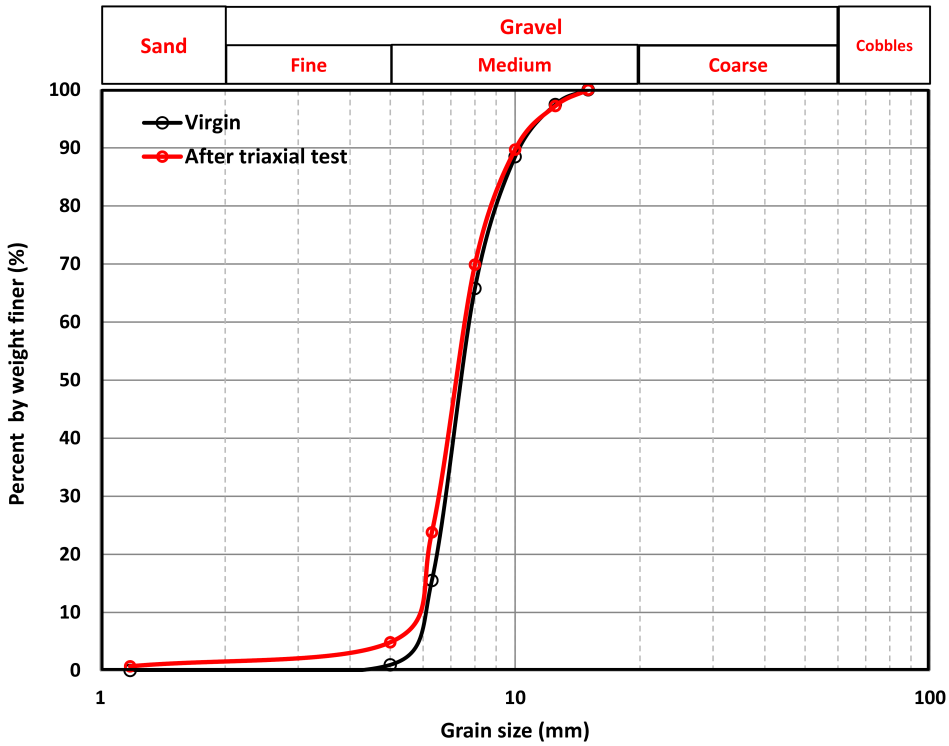

Figure 3.2: Particle crushing curve of wet fused silica after triaxial testing

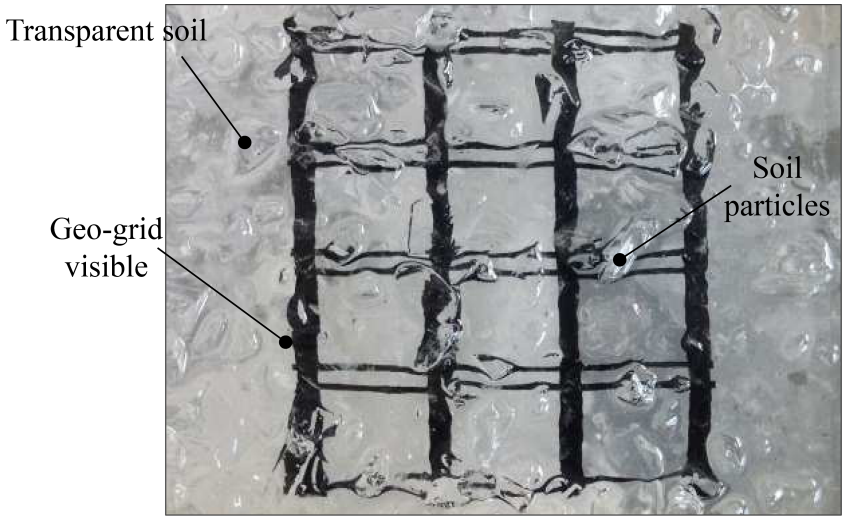

Figure 3.3: Photograph showing geogrid in transparent soil under natural light

in Figures 3.4 and 3.5. All tests were conducted on specimens 100 mm in diameter and with 200 mm in height.

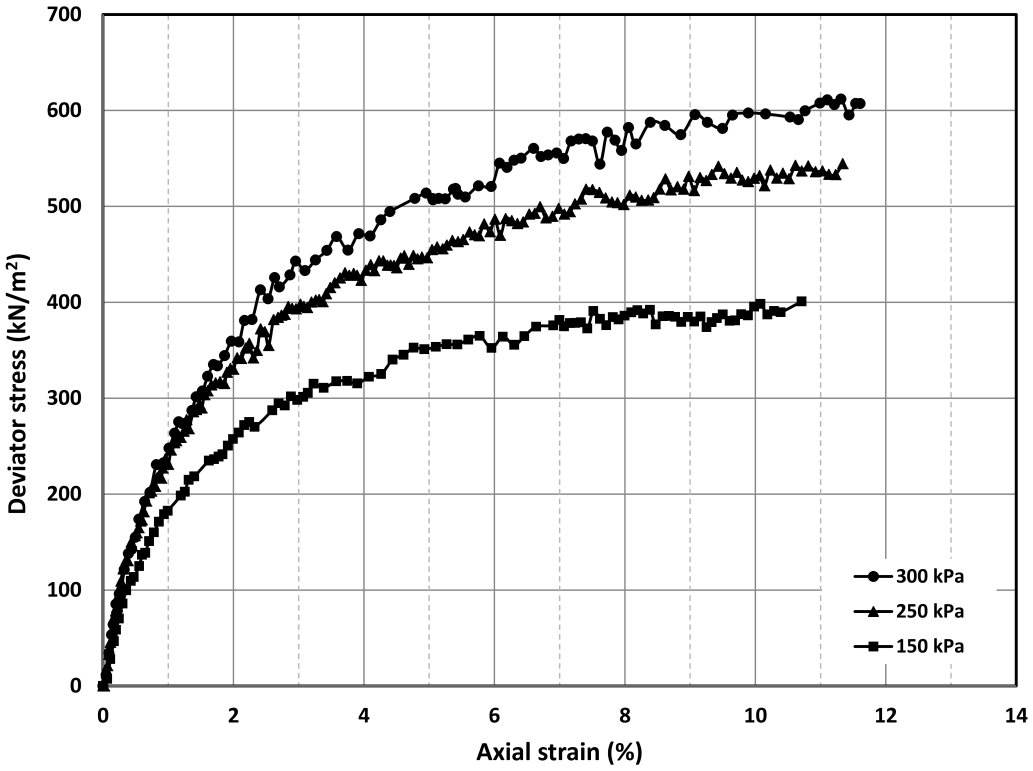

Figure 3.4: Stress-strain curves from conventional triaxial test on dry under three different cell pressures value

Figure 3.6 shows peak shear strength data from triaxial test for saturated sample. The strength data may be interpreted in several ways:

- A best fit tangential line gives strength parameters: $c' = 80$ kN/m^2 and $\phi' = 23^o$.
- It is not possible to make a good straight line fit through the origin. Hence the tangent to the smallest Mohr-circle through the origin has been selected. This gives $c' = 0$ kN/m^2 and $\phi' = 37^o$.
- A power-law fit is normally assumed, especially at low stress levels. While there is insufficient data to determine parameters with accuracy, an estimate is made here for use for low stress levels of the order of 12-50 kN/m^2. The

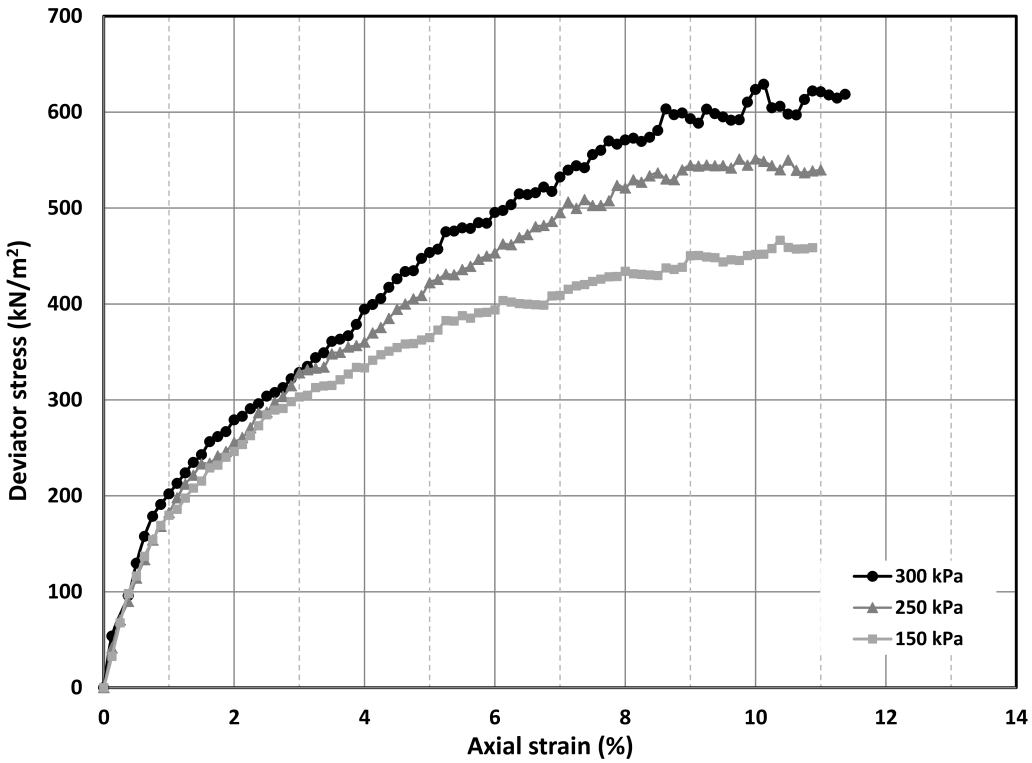

Figure 3.5: Stress-strain curves from conventional triaxial test on saturated under three different cell pressures value

indicative curve shown in Figure 3.6 gives a friction angle of $\sim 45^{o} - 50^{o}$. For the purposes of later interpretation an estimated value of $\phi' = 48^{o}$ will be adopted in saturated condition.

The average dry unit weight of fused silica specimens in these tests was 12 kN/m^3.

It should be noted that the values of cell pressure for triaxial testing were chosen based on a preliminary test programme for pull-out tests at the concept phase of this research. However, after manufacturing the box and the way of designing the structure of the box, it came to the author's attention that it was not possible to apply this amount of pressure as a surcharge. This is the reason that the stress levels used between the triaxial testing and pull-out testing were different.

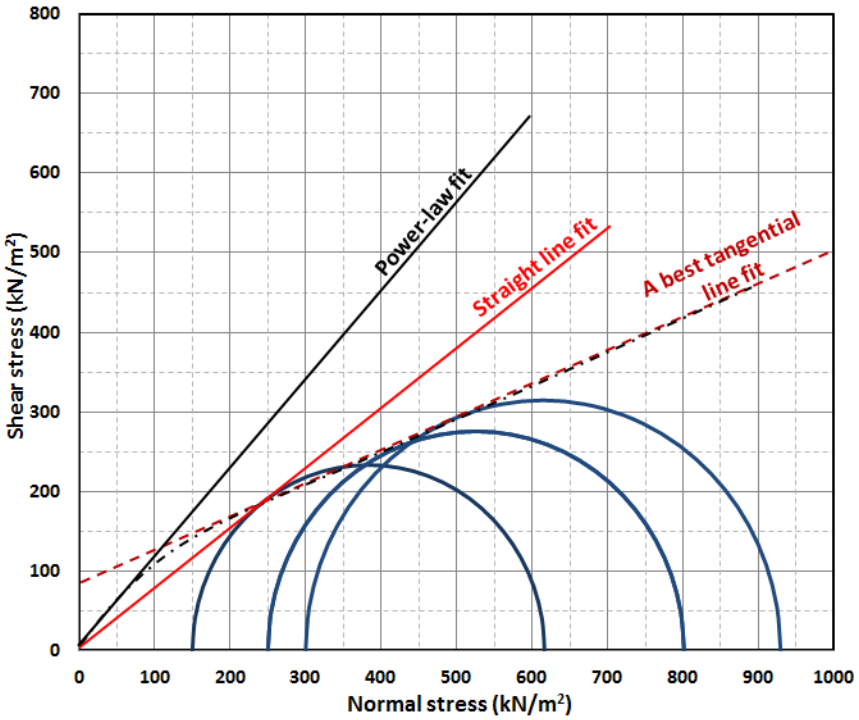

Figure 3.6: Peak shear strength envelopes for saturated samples from triaxial testing

3.1.2 Optical clarity assessment

To assess the optical transparency of the fused silica the "modulation transfer function"(MTF) approach was used as reported by Black and Take (2015). MTF works by relating the pixel contrast that is transferred from an object to an image and is commonly used to calibrate an optical system (Equation 3.1). The concept of MTF is shown in Figure 3.7. By way of an example, consider viewing a calibration target consisting of black and white contrasting lines through a translucent soil body. A soil with high optical quality will enable distinct observation of maximum and minimum pixel contrast between the black the white alternating lines to be well defined in an image. However, if the calibration target were viewed through a material of lower optical quality (i.e. poorly refractivity matched soil), the maximum and minimum contrast would be less well defined such that the line edges appear blurred or become indistinguishable and merge to a single pixel intensity.

$$MTF = \frac{\text{Modulation of image}}{\text{Modulation of object}} = \frac{(I_{max(I)} - I_{min(I)})/(I_{max(I)} + I_{min(I)})}{(I_{max(O)} - I_{min(O)})/(I_{max(O)} + I_{min(O)})} \tag{3.1}$$

where $I_{max(I)}$ and $I_{min(I)}$ are the maximum and minimum intensity as captured in an image of an actual object with repeating structure having maximum and minimum intensity $I_{max(O)}$ and $I_{min(O)}$.

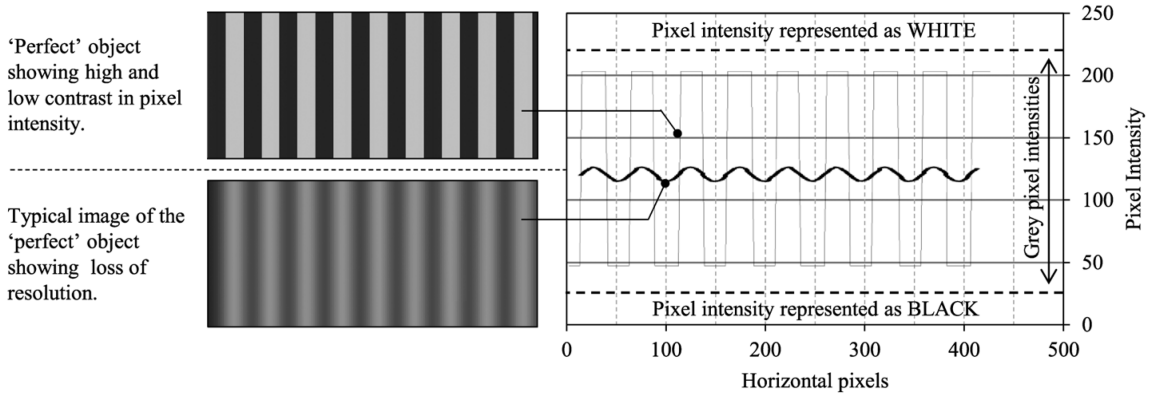

Figure 3.7: Concept of using MTF (after Black and Take, 2015)

The test card shown in Figure 3.8 represents a number of cycles per pixel (c/p) in the range of 0.02 c/p (low frequency) to 1.00 c/p (high frequency). As the spatial frequency changed from low to high, the ability to visually resolve individual line pairs reduces (Black and Take, 2015). By capturing images of each calibration target of increasing spatial frequency submerged in the saturated transparent soil, it is possible to determine the optimum resolution of the soil-pore fluid mixture.

The MTF method was conducted to investigate two aspects, (i) the optimum blend of pore fluid mix ratio (ii) the maximum possible depth of viewing that detail in the model could be resolved. The latter aspect was critical as it would dictate the possible size of the experimental test chamber that could be achieved for the aggregate materials. Figure 3.9 shows the test set up for calibrating the transparency of the fused silica.

The calibration test cards were viewed through a Perspex box at three different depths of 100 mm, 125 mm and 150 mm. The test was conducted for a range of

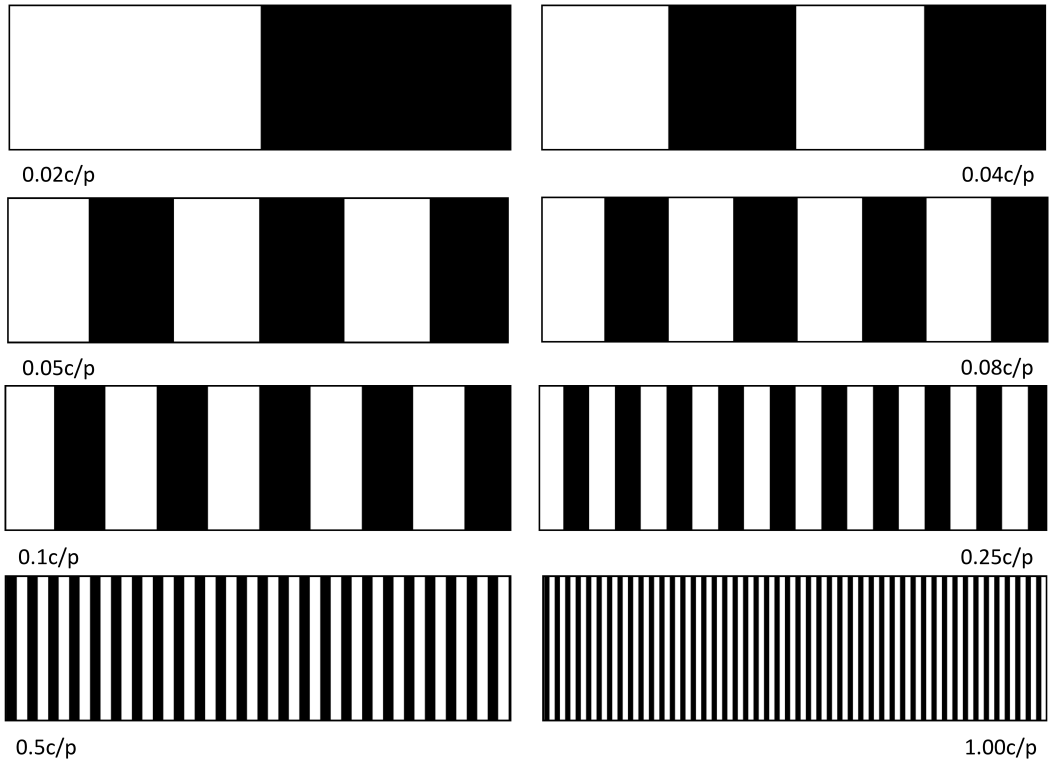

Figure 3.8: Calibration target used to assess transparency of transparent soil through the MTF method

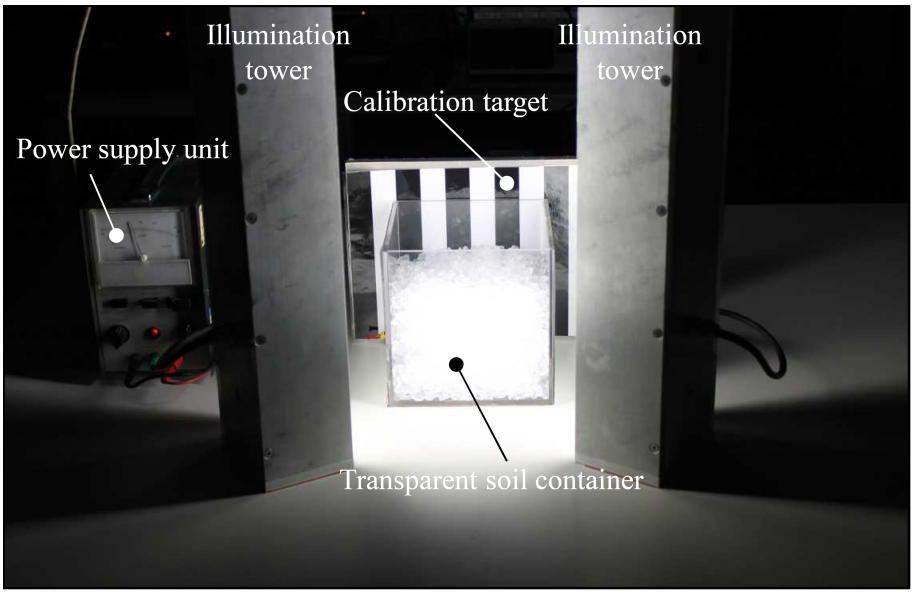

Figure 3.9: Test set up for calibrating the transparency of the fused silica (Note: aggregate is not saturated)

pore fluid with aggregate at 20°C (Figure 3.10). The results of study indicate that the maximum depth of view for optimum ratio of mixing of pore fluid is 100 mm which has the higher value of MTF (Figure 3.11).

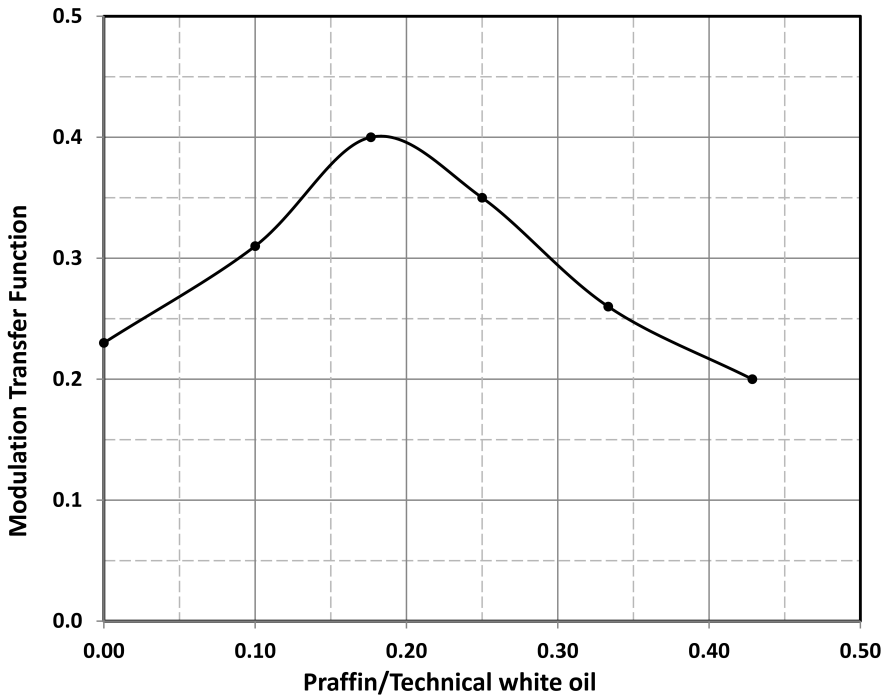

Figure 3.10: Transparency of fused silica transparent soil through 100 mm depths of material for different ratio of pore fluid

No fused silica aggregate is perfectly transparent and it is common for particles to have minor inclusions such as trapped air or minor internal stress fractures resulting from non-uniform cooling during the manufacturing process. Some minor inclusions were observed in this aggregate particles which was later determined to yield small errors in the image processing methods during data analysis. In brief, some individual particles with inclusions could be seen in front of the plane of interest which compromised the tracking of particles on the illuminated plane behind. A novel colour spectrum filtering image analysis method was deployed to mitigate this effect using image extraction techniques which is described in detail in Section 5.2.3.

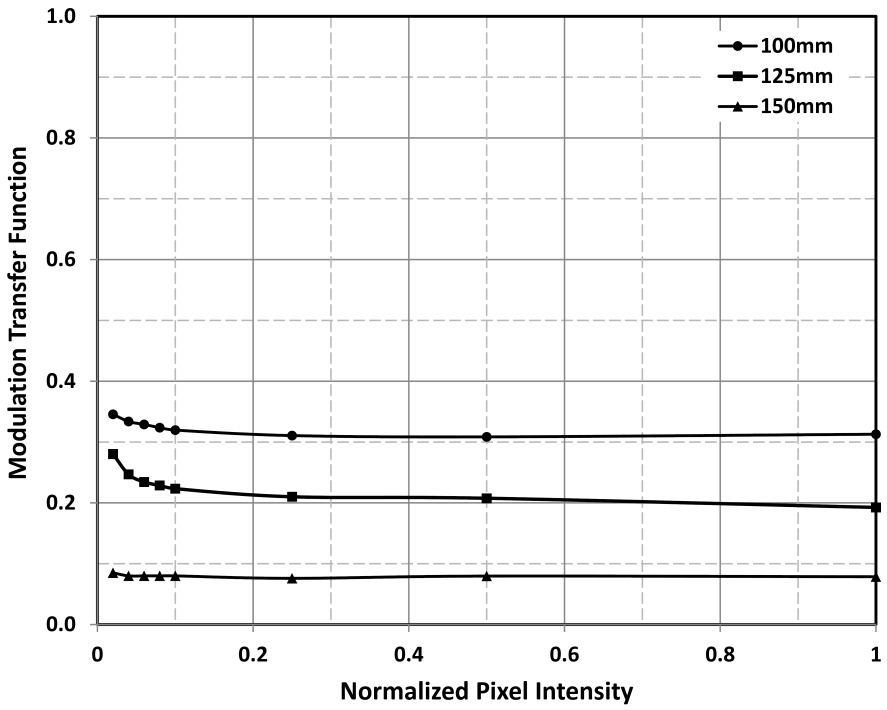

Figure 3.11: Transparency of fused silica transparent soil for three different depths of view at mixed ratio of 80 (Technical white oil):20 (Paraffin)

3.2 Geogrid reinforcement

The geogrid used in this research was selected in consideration of the nominal average particle size of the soil that could be sourced. As outlined in Chapter 3, the size of soil particles varied between 10-15 mm with the D_{50} = 7.42 mm. Reflecting on literature (Lopes and Lopes, 1999) the geogrid aperture size needs to be considerably larger than the soil particles to allow the particles to embed in between the apertures to mobilise the passive resistance in the bearing members.

Also, Sarsby (1985) investigated the influence of aperture size on the size of soil particles for maximum frictional efficiency (or efficiency against pull-out). According to Sarsby (1985) study, the highest efficiency occurs when:

$$A_p > 3.5D_{50} \tag{3.2}$$

Thus according to Equation 3.2 for the transparent soil particle size range available a geogrid aperture of 30 mm would be compatible. Three types of biaxial geogrid used in this research which are manufactured by HUESKER Synthetic GmbH Company. The nominal specifications of three geogried products used by this researcher are presented in Tables 3.1, 3.2 and 3.3. Note, in this research only the effect of rupture strength\stiffness on the performance of the geogrid during pull-out test is evaluated; other variables such as shape of the apertures and thickness of the geogrid are not considered.

Table 3.1: Geogrid material properties of Fortrac R150/30-30 (from manufacture's website)

Property	**Type or value**	
Raw Material		PET
Coating		Polymer
Weight (EN ISO 9864)		$\backsim$ 600 g/m^2
Ultimate tensile strength (EN ISO 10.319)		
	Longitudinal	$\geq$ 150 kN/m
	Transversal	$\geq$ 30 kN/m
Strain at nominal tensile strength (EN ISO 10.319)		
	Longitudinal	$\leq$ 12.5%
Stiffness		$\backsim$ 1200 kN/m
Mesh size		30 $\times$ 30 mm

Table 3.2: Geogrid material properties of Fortrac R200/30-30 (from manufacture's website)

Property	**Type or value**	
Raw Material		PET
Coating		Polymer
Weight (EN ISO 9864:2005)		$\backsim$ 680 g/m^2
Ultimate tensile strength (EN ISO 10.319)		
	Longitudinal	$\geq$ 200 kN/m
	Transversal	$\geq$ 30 kN/m
Strain at nominal tensile strength (EN ISO 10.319)		
	Longitudinal	$\leq$ 13%
Stiffness		$\backsim$ 1600 kN/m
Mesh size		31 $\times$ 28 mm

Table 3.3: Geogrid material properties of Fortrac R400/50-30 (from manufacture's website)

Property	**Type or value**	
Raw Material		PET
Coating		Polymer
Weight (EN ISO 9864:2005)		$\backsim$ 1300 g/m^2
Ultimate tensile strength (EN ISO 10.319)		
	Longitudinal	$\geq$ 400 kN/m
	Transversal	$\geq$ 50 kN/m
Strain at nominal tensile strength (EN ISO 10.319)		
	Longitudinal	$\leq$ 14%
Stiffness		$\backsim$ 2900 kN/m
Mesh size		30 $\times$ 25 mm

Chapter 4

Analytical and Numerical Models for Soil-Reinforcement Interaction

4.1 Introduction

The shearing resistance of soil can be improved by reinforcement, and reinforcement acts most effectively when placed in a direction in which tensile strain develops in the soil (Jewell, 1996). The main purpose of such inclusions is to redistribute stresses within the soil mass so as to increase the internal stability of reinforced soil. The inclusions undergo tensile strain as they transfer loads from unstable portions of the soil mass into stable soil zones. The redistribution of stresses within a reinforced soil mass is dependent on the stiffness and the shear strength properties of the soil, the tensile properties of the reinforcement, and the stress transfer mechanism taking place between soil and reinforcement (Teixeira et al., 2007).

The two most common applications of reinforcement are for slope stabilisation and for constriction of embankments over soft soil. Herein a simple analytical calculation demonstrating the effect of reinforcement for increasing the stability of these two geostructures is presented.

Figure 4.1 illustrates the effects of reinforcement on the stability of a slope. The self-weight loading of the soil generates a shear force, P_s , that acts on the section of the shear surface as shown in Figure 4.1a. For an unreinforced slope, this force is resisted by the available soil frictional resistance, $P'_n \tan \phi'$, along the failure surface.

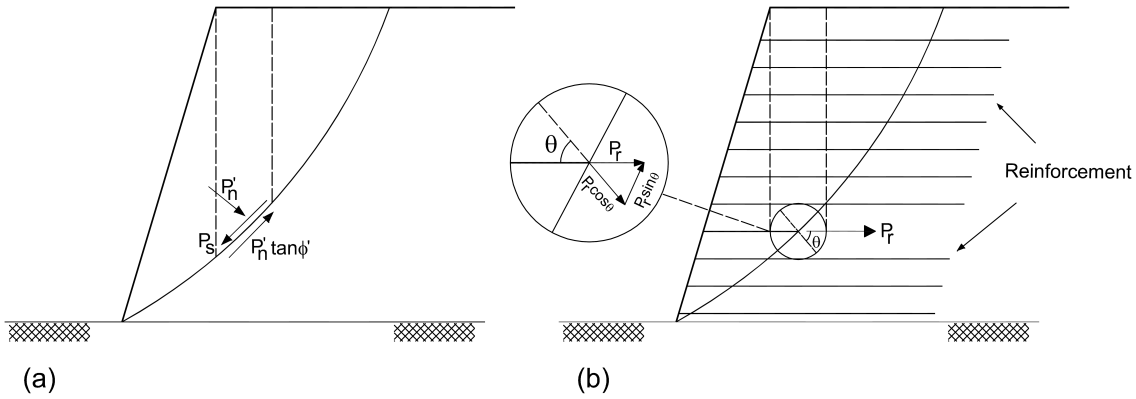

Figure 4.1: Effects of reinforcement on equilibrium (a) unreinforced slope and (b) reinforced slope (after Jewell, 1996)

However, for the reinforced slope, shown in Figure 4.1b, shear deformation in the soil will generate a tensile force in the reinforcement, P_r. This force provides two additional components of resistance to the reinforced slope. The first component is $P_r \sin \theta$ which acts along the failure surface against the disturbing shear force. The second component mobilises additional frictional shear resistance against slip failure, $P_r \cos \theta \tan \phi'$.

Figure 4.2 shows the distribution of forces in an unreinforced and reinforced embankment. Jewell (1996) divided the main loading which is applied from an embankment to the underlying soft soil into two parts; (i) the vertical self-weight of the embankment (Figure 4.2a), and (ii) the outward directed lateral force cased by horizontal stress in the fill (Figure 4.2b). As Figure 4.2c illustrates the lateral outward force acts over the surface of the base layer which acts to reduce the bearing capacity of the soil. Therefore, the primary role of reinforcement is to generate resistance against this outward force (Figure 4.2d).

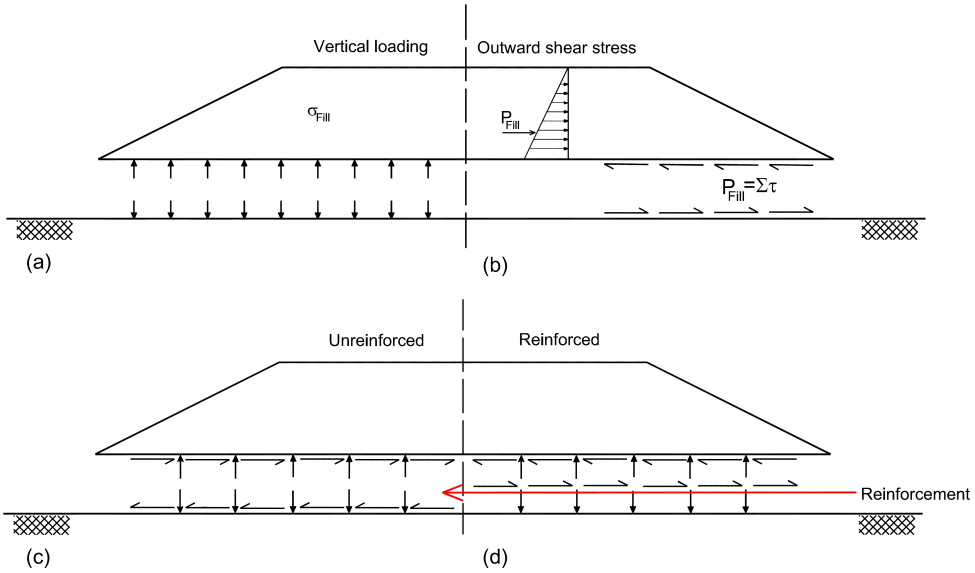

Figure 4.2: Disturbing forces in an unreinforced and reinforced embankment (after Jewell, 1996)

The traditional way of checking the stability of a reinforced soil structure is based on the limit equilibrium method. Michalowski (1998) states that this technique was used for the first time for reinforced soil analysis in the late 1980s using the following two approaches:

- Soil and reinforcement are modelled as homogenised materials (de Buhan et al., 1989 and Sawicki and Lesniewska, 1989)
- Reinforcement is modelled as a separate structural element. The soil is modelled as a continuum and the reinforcement consider as a discrete element (Anthoine, 1989 and de Buhan and Salencon, 1993)

Michalowski (1998) used the kinematic approach of limit analysis which is based on the construction of kinematically admissible collapse mechanisms, and the balance of the work rate in an incipient failure process. Since limit analysis leads to a rigorous bound on the reinforcement strength, limit loads, or a safety factor, the geometry of the failure mechanisms considered can be optimised, so that the best bound is obtained. A dual formulation of kinematic limit analysis is possible in

terms of limit force equilibrium (Salencon, 1990), but the former is preferable since the kinematics of collapse mechanisms appeals to engineering intuition more than the distribution of forces.

Both analysis methods discussed above depend on specific model of soil reinforcement interaction.

4.2 Embankment failure mechanisms

A reinforced embankment can fail via a variety of mechanisms such as shearing, pull-out and incline shearing. A comprehensive parametric study of reinforced and unreinforced embankments was conducted using the general purpose computational limit analysis approach Discontinuity Layout Optimization (DLO). This study identified four distinct mechanisms of failure as shown in Figure 4.3. These mechanisms can be described as follows:

1. Lateral sliding failure (surface failure).
2. Deep seated global failure.
3. Lower layer failure (squeezing/extrusion failure) with sinking.
4. Lower layer failure (squeezing/extrusion failure) with 'snapping'.

For a high strength lower stratum, failure is in the shoulders of the embankment only (Figure 4.3a). For low strength reinforcement the dominant failure mechanism is a deep seated global failure accompanied by yield of the reinforcement (Figure 4.3b). In this type of failure, significant shearing happens in the main body and side slopes of the embankment. For high strength reinforcement significant 'squeezing' deformation is primarily seen in the lower stratum. The embankment itself either undergoes very localised shearing and vertical 'sinking' translation (Figure 4.3c) or rotational 'snapping' (Figure 4.3d). The latter mechanism is more likely to occur and need not involve any significant deformation/yielding of the reinforcement which simply rotates. To the authors knowledge, the latter type of failure has not been previously examined in the literature.

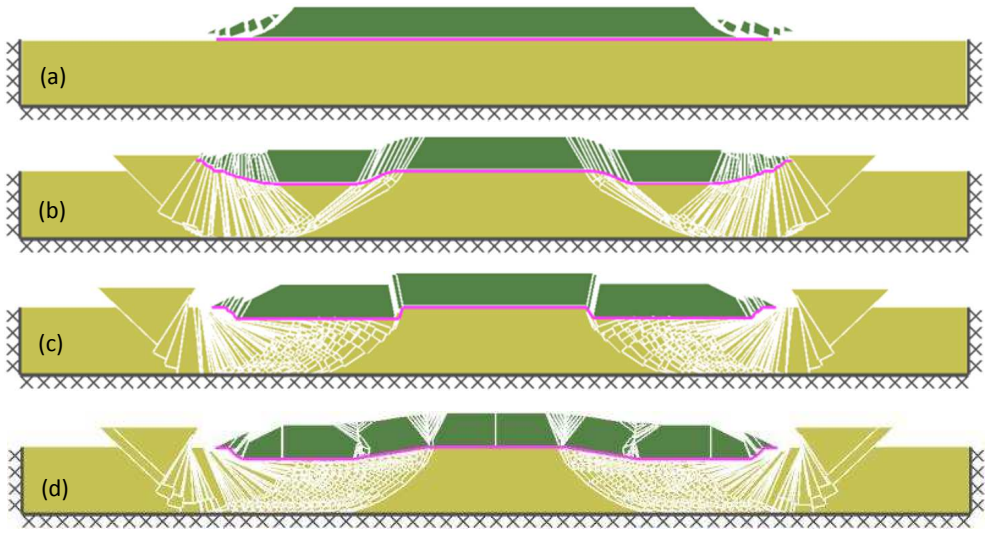

Figure 4.3: Failure mechanisms of embankment over soft soil (exaggerated), (a) lateral sliding failure (surface failure), (b) deep seated global failure, (c) lower layer extrusion with sinking and (d) lower layer extrusion with 'snapping'

4.2.1 Reinforcement Strength

Two values of $R/\gamma H^2$ were employed in the generic parametric study, 0.1 and 1.0. This was intended to cover a broad range from very weak reinforcement (0.1) and strong reinforcement (1.0). To investigate the effect of reinforcement on stability, specific studies were undertaken over a broad range of values of $R/\gamma H^2$. Figures 4.4a and b show how $c_u/\gamma H$ varies with reinforcement strength $R/\gamma H^2$ for a particular parameter set. It can be seen that for the no surcharge case, the solutions are independent of $R/\gamma H^2 > 1.0$ (this value will be defined as the limiting value $R_L/\gamma H^2$, at which the embankment will be said to be fully reinforced), and that there is a generally linear relationship between the parameters between $R/\gamma H^2$=0 to 0.7. Therefore if it is necessary to interpolate for R, a conservative approximation is to linearly interpolate between the values of $R = 0$ to R_L. An example interpolation is indicated in Figure 4.4b. In order to ensure conservative results, it can be seen that there will be a small error in the interpolation which is maximum between around $0.5R_L$ to $0.6R_L$. This maximum error is around 8% in c_u or around 20% in R.

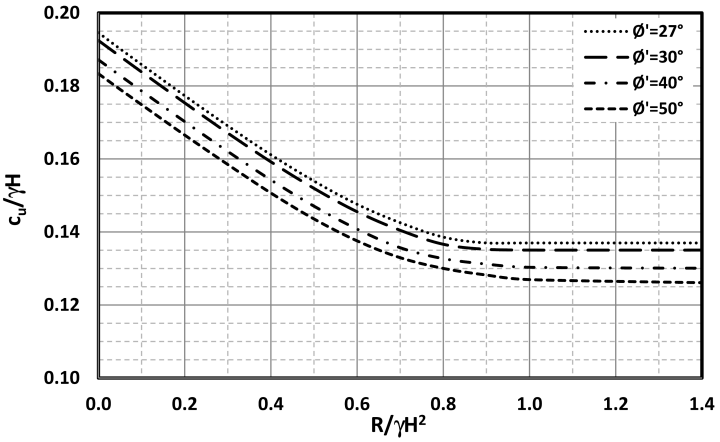

(a) With surcharge, $q/\gamma H = 0.1$

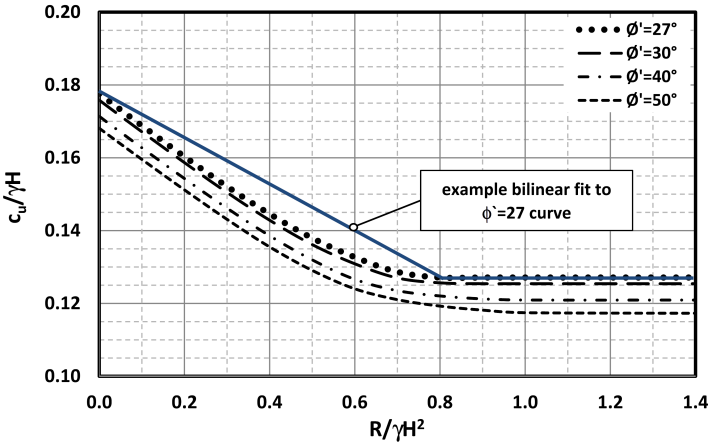

(b) Without surcharge

Figure 4.4: Required undrained shear strength for stability plotted against reinforcement strength($H/D = 0.5$, 1V:2H, $c' = 0$ and $\alpha = 0.8$).

4.2.2 Simplified design envelopes

The study also generated a new design chart that allow critical heights and reinforcement strengths to be rapidly determined based on soft soil strength and depth, and shows how the balance between soft soil strength and reinforcement strength combines to affect overall stability. This is shown in Figure 4.5. In Figure 4.5a for $\phi' = 30^o$ and $c'/\gamma H = 0.0$ and Figure 4.5b for $\phi' = 50^o$ and $c'/\gamma H = 0.1$.

Two curves are given. Above the upper value the system is always stable (this corresponds to $R = 0$). Below the lower limit, it is generally always unstable (though minor gains may be made with stronger fill) and this corresponds to $R = R_L$. Values of $R_L/\gamma D^2$ are given on the same graph. In between the values the more detailed design charts must be used, or, as discussed in Section 4.2.1, a linear interpolation can be used to provide a good estimate of R.

Note that for these graphs the values of c_u and R_L have been normalised using D rather than H since this is expected to be an independent variable. Overall it can be seen that the use of reinforcement allows an embankment of a given size to be constructed on soft soil of around 50-100% the strength of that on which an unreinforced embankment could be constructed, depending on the value of H/D. It can also be seen that stronger fill has a marginal effect on the performance of a reinforced embankment, but a more significant effect on the stability of an unreinforced embankment.

Figure 4.5b also indicates that, for this example, an almost unlimited height of a fully reinforced embankment is possible for $c_u/\gamma D > \sim 0.16$ which may seem paradoxical, however this arises because the mechanism of failure is squeezing of the (relatively thin) confined soft soil layer which occurs over a width that extends beyond the embankment crest. Since the side slope width increases in tandem with the height, the bearing resistance in the soft soil layer also increases. It is noted that the reinforcement strength must also increase significantly with the height.

4.3 General interaction modes between soil and reinforcement

The behavior of reinforced soil structures is largely governed by interaction mechanisms that develop between the reinforcement inclusions and the backfill soil. The interface coefficient between reinforcement and soil is an important factor required to compute the accurate pull-out resistance of reinforcement. Palmeira and Milligan (1989) characterized the typical soil-reinforcement interaction mechanism as (i) shearing soil over reinforcement, (ii) transverse shear or (iii) pulling

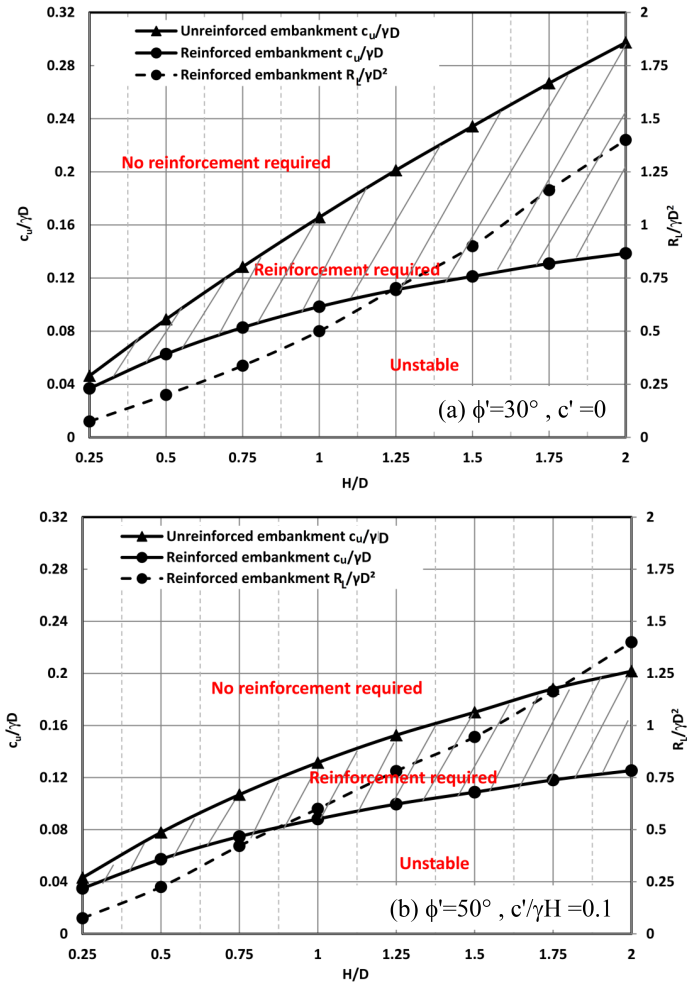

Figure 4.5: Simplified design domains ($\alpha = 0.8$, $q = 0$ and $n = 2$). The reinforced embankment case uses reinforcement with rupture strength R_L the value of which is given in the same plot. The shaded zone is the design domain where reinforcement is required. Below this zone stability is not possible with a single layer of reinforcement

out the reinforcement through the soil as indicated in Figure 4.6. Based on the embankment study discussed in Section 4.2 the transverse shear mechanism can be subdivided into (ii) a discrete shear band (Figure 4.3c) and (ii) a diffuse shearing (Figure 4.3d). While pull-out tests provide invaluable information on the soil-reinforcement interaction, additional understanding of the other mechanisms that occur during pull-out testing is still needed and can provide valuable insight into the behaviour of reinforced soil structures (Teixeira et al., 2007).

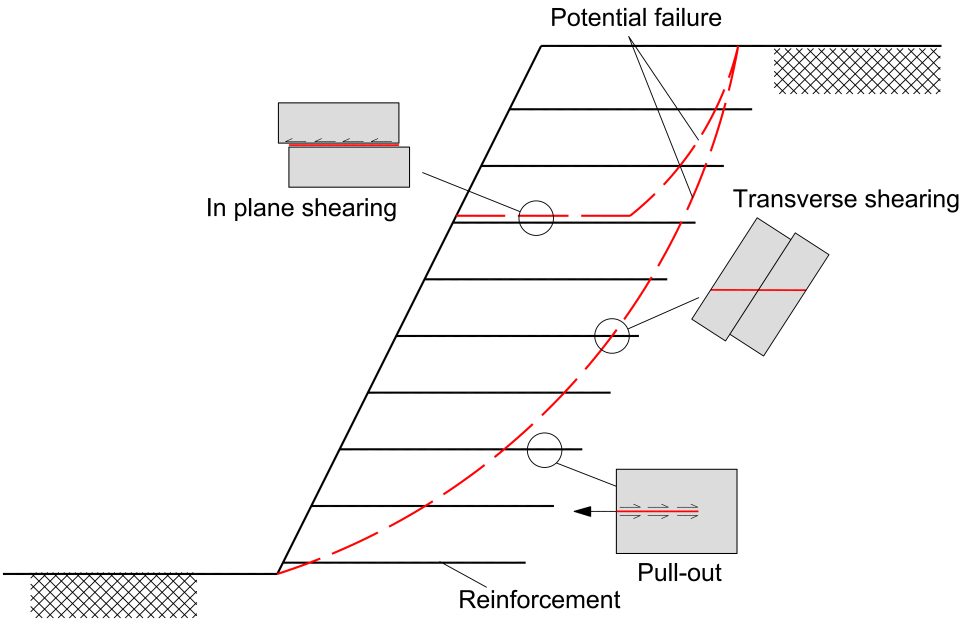

Figure 4.6: Typical interaction mechanisms between soil and geogsynthetic material (after Palmeira and Milligan, 1989)

4.4 Geogrid pull-out

As mentioned in Section 2.6, the pull-out interaction mechanisms between soil and geogrid reinforcements are more complex than those between soil and geotextile reinforcements. This is because the pullout resistance of geogrids includes two components: (i) the interface shear resistance that takes place along the longitudinal ribs and to a lesser extent along the transverse ribs and (ii) the passive resistance that develops against the front of the transverse ribs (Jewell, 1996). Although the interface shear resistance can be quantified using parameters achieved from modified direct shear tests, the passive resistance can only be evaluated using pull-out tests. Jewell mentioned that the ultimate pull-out resistance results from the summation of the passive and interface shear components. The passive pull-out resistance that develops against the transverse ribs can result from several types of failure mechanisms. These failure mechanisms are listed as: (i) general shear failure (Peterson and Anderson, 1980), (ii) punching failure (Jewell et al., 1984) and (iii) modified punching failure (Chai, 1992).

Previous studies have reported that the interaction between soil and geogrid reinforcement depends on the geometry of geogrid, soil grain size distribution, shape of soil particles, and density of soil. However, Jewell (1996) reported that the geogrid pull-out failure mechanism is a function of the ratio between transverse rib spacing S and the transverse rib diameter and the average particle size D_{50}. He identified limiting values of the S/D_{50} ratio that characterize either interface shear or interface shear plus passive resistance.

Jewell (1996) introduced a theoretical expression for direct shear sliding coefficient, α_{ds}, which is a function of the geometry reinforcement type and soil's properties (Equation 4.1).

$$\alpha_{ds} \ \tan\phi' = \overline{a}_s \ \tan\delta + (1 - \overline{a}_s) \ \tan\phi' \tag{4.1}$$

where $\tan\delta$ is the skin friction between soil and planar surface of the reinforcement, ϕ' is the friction angle of soil and $\bar{a}_s$ is the fraction of the grid surface area that is solid which equals 1 for geotextiles and for most geogrids this ratio is 0.5.

He also introduced the theoretical expression for computing the coefficient of bond, α_b, between soil and geosynthetic materials (Equation 4.2). The coefficient of bond is the contribution between skin friction over the planar surface area, α_s, skin friction between soil, $\tan\delta$, and the passive resistance of geogrid bearing members.

The theoretical expression for bond is:

$$\alpha_b \ \tan\phi' = \overline{a}_s \ \tan\delta + (\frac{\sigma_b^{'}}{\sigma_n^{'}})(\frac{\bar{a}_b B}{2S}) \tag{4.2}$$

where $\sigma_b^{'}$ is the effective bearing stress on reinforcement, $\sigma_n^{'}$ is the normal effective stress acting in the plane of the reinforcement, B is the width of the transverse member of a geogrid and $\bar{a}_b$ is a fraction of the grid width available for bearing resistance (in the case of geotextile $\bar{a}_s$=1.0 and $\bar{a}_b$=0.0 because it has no openings in the structure). The parameters which are used in Equation 4.2 are shown in Figure 4.7.

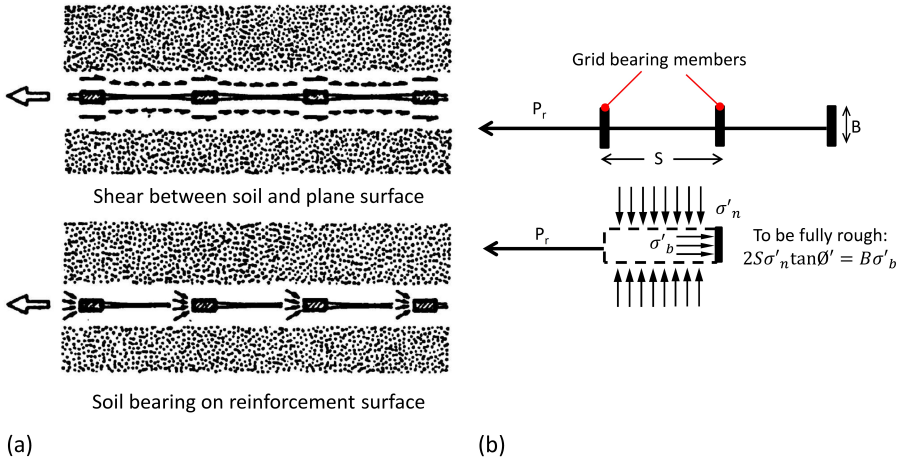

Figure 4.7: The interaction between soil and reinforcement; (a) contribution of mechanisms and (b) definitions for analysis (after Jewell et al., 1984)

Previous research in this area by Dyer (1985) and Milligan et al. (1990) indicated that the pull-out bond for a geogrid is combined from three types of resistance which are generated during the pull-out; (i) partly through concentration of bearing stress against the transverse members of the grid, whilst they develop direct sliding resistance (ii) partly by shear of soil over planar geogrid surface areas, and finally (iii) somewhat by shear of soil over soil through the apertures (Jewell, 1996).

4.5 Transverse shearing

Another aspect which needs to be considered, is the complex mechanism of failure at the point of intersection between failure surface and reinforcement. Consideration of the kinematic shows that, after a small increment of deformation, the reinforcement is no longer horizontal at a failure surface, and the direction of the limit force in the reinforcement taken in the analysis is then not well-defined as discussed by Wright and Duncan (1991) in the context of the limit equilibrium methods as applied to reinforced slopes. Figure 4.8 indicates the schematic of tensile force before and after small displacement. This introduces a moment into the system which must be locally resisted by the soil.

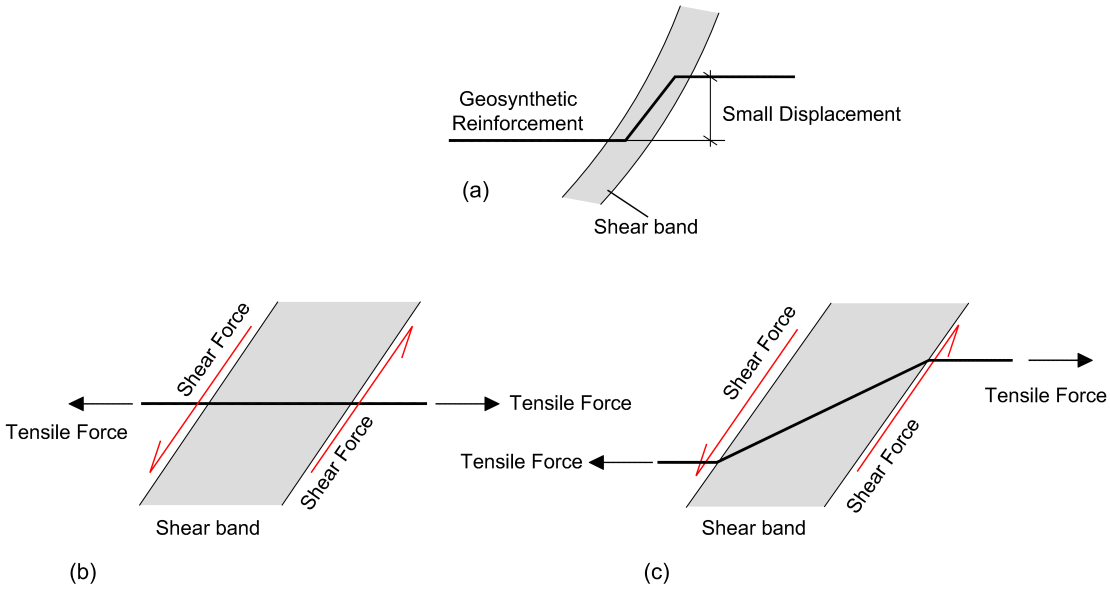

Figure 4.8: Schematic of tensile force which is generated in reinforcement; (a) small displacement of geosynthetic in shear bond, (b) horizontal reinforcement and (c) inclination reinforcement (after Michalowski, 1998)

4.6 What needs to be researched?

As discussed earlier in this chapter, uncertainties remain concerning the interface coefficient between reinforcement and soil. Figure 4.9 presents, as an example, a non-dimensional chart generated for better clarification of the effect of the interface coefficient on the required soil properties to build embankments over soft soil. The figure presents the required soil properties for the embankment which is reinforced by a high rupture strength reinforcement. The results of the study show that by changing the perfect boundary condition between soil and reinforcement to 0.6, the required shear strength of the soft soil needs to increase by 20%.

In numerical modelling the interface coefficient between soil and reinforcement is modelled by following the concept of sliding soil over the full plan area of reinforcement. This is achieved by using a very thin layer of soil between soil and reinforcement with lower shear strength properties in comparison to the surrounding soil. It follows that the interaction between soil and reinforcement for geotextile reinforcement for bond is simply twice that of sliding. However, this mechanism becomes more complex for geogrid type reinforcement. The reason is that the

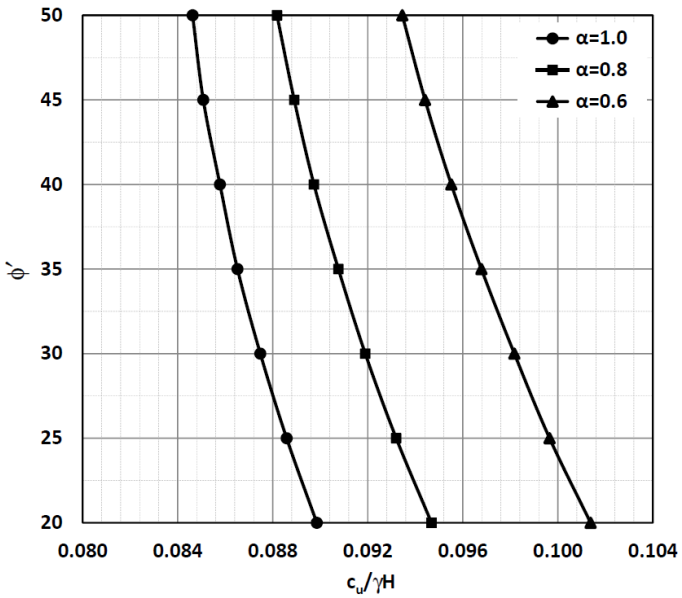

Figure 4.9: Required soil properties for embankment to achieve the safety of factor on strength of material equals one for different values of interface coefficient ($H/D = 1$, $1V : 2H$, $c'/\gamma H = 0.1$)

contact area of soil and geogrid is non uniform and soil particles can penetrate through the apertures of geogrid. Therefore, the interaction between soil and geogrid is a combination of different parameters; sliding soil over soil, sliding soil over a plane surface of geogrid and passive bearing capacity in front of geogrid ribs. This needs to be correctly captured in a numerical model in such a way that pull-out and sliding are correctly modelled. In addition, the effect of the extensibility of the specimen does not affect conventional calculation of pull-out and shear calculations. The interaction between soil and reinforcement, particularly geogrid needs to be investigated to specify or at least formulate a better representation of current unknowns:

- The influence of soil particle interlock over open spacing in geogrid (geogrid apertures).
- The effect of soil properties such as shape, particle size distribution, shear properties on the interaction behaviour.
- The influence of material properties of geogrid such as stiffness, dimensions and shape of aperture, size of longitudinal and transverse members.

Chapter 5

Experimental Development

5.1 Introduction

It is evident from the adjoining literature and numerical implementation that there is uncertainty surrounding soil and geo-reinforcement interaction that governs the local resistance and global failure mechanics. To enhance knowledge in this field a novel experimental methodology is proposed to enable direct visualisation of internal interaction mechanics using advanced non-intrusive transparent soil modelling methods. Ezzein and Bathurst (2011b, 2014) pioneered the early adoption of transparent soil modelling to investigate geo-reinforcement and successfully characterised the strain distribution in the reinforcement during pull-out. Ferreira (2013) verified these observations, albeit at a smaller scale, but also sought to detect the relative soil movement during pull-out using visible embedded tracer particles. However, owing to the low number of particles the measurement resolution in the model was sporadic and quantification of precise interaction mechanics proved elusive. The work presented herein builds on these contributions but advocates the use of laser aided imaging to illuminate a planar cross-section of soil particles in a model to detect high resolution full field soil interaction characteristics in the immediate vicinity of the reinforcement. To deliver this ambitious objective a new experimental test system is required. The design of this apparatus is outlined fully in the following sections along with the image based deformation

measurement techniques implemented to determine the soil-geogrid interaction characteristics.

5.2 Image based deformation measurement methods

Spatial deformation measurement within a soil body has been the subject of continued research for many decades. Roscoe et al. (1963), James (1965) and Bransby (1968) where the first to utilise X-rays to measure internal displacement of embedded lead shot targets to evaluate strain patterns in large scale physical models and shear box tests. The method consists of burying a grid of lead markers within the soil and exposing radiographs at different stages of the test to reveal the soil-structure behaviour. Bransby and Milligan (1975) applied this method to cantilever sheet pile walls defining the position of the lead shot with an accuracy of $\pm 34\mu m$ over the measurement field. More recent imaging advances in the medical field such as Magnetic Resonance Imaging (MRI) and X-Ray CT have opened up new opportunities for geotechnical interaction studies at considerably higher resolutions than previously thought possible; although this has yet to be been applied to geo-reinforcement problems.

The advance of modern camera technology and photographic methods in the mid 1970's revolutionised physical model testing and gave rise to plane strain modelling techniques whereby surface targets exposed through a perspex window were used to resolve soil displacement and strain behaviour. Butterfield et al. (1970) introduced stereo-photogrammetry to observe soil movements during cone penetration stating an accuracy of approximately $10\mu m$. Early forms of stereo-photogrammetry where conducted by hand matching however the rise of computer based automatic target recognition improved computational efficiency and accuracy. A distinct advantage of this technique compared to X-Ray methods was that it mitigated health and safety concerns surrounding radiation exposure and it did not require expensive experimental systems.

Both the aforementioned methods are reliant on discrete target markers for displacement measurement which has several inherent limitations; (i) low measurement resolution, (ii) stiffness compliance issues within the soil affecting the soil stress field and (iii) pre-determined locations for strain measurement during model construction. The above difficulties in conjunction with the continued improvements in digital imaging capabilities motivated White et al. (2003) to develop a new image based deformation measurement system using only the natural soil texture for tracking. They implemented Digital Image Correlation (DIC) on methods established by Adrian (1991), adapting Particle Image Velocimetry (PIV), to track soil movement throughout a series of digital images to resolve displacement and strain fields using only the natural texture of the soil for measurement. This mitigated the need for artificial targets and offered increased resolution; hence, it has found favour among geotechnical researchers for a wide range of geotechnical problems in the lab (White et al., 2003) and field. Ni et al. (2010) and Stanier et al. (2012) were among the first to harness GeoPIV image processing capabilities and transparent soil laser aided imaging methods to determine internal displacement mechanics of CFA's and helical screw piles respectively.

5.2.1 GeoPIV

GeoPIV is a program which implements Particle Image Velocimetry (PIV) to measure deformation of soil from sequences of digital images captured during tests. For succinctness only a brief overview of GeoPIV is presented herein; however, comprehensive information can be found in Take (2003), White (2002) and White et al. (2001a). The PIV method uses a cross-correlation function to track soil texture in a reference image throughout a series of subsequent images captured during a displacement event. An image is initially subdivided into a mesh of individual patches (I_{test}) that each having a unique soil texture signature that is recorded as an intensity matrix with known patch centre U. Each patch within the reference image is compared with subsequent images in the event sequence within a designated search zone (I_{search}) as shown in Figure 5.1. The cross correlation estimator $R(s)$ is specified by Equation 5.1, given that U is the location of the test patch and s is the displacement experienced by the patch.

$$R(s) = \sum_{(U)} I_{test}(U).I_{search}(U+s) \tag{5.1}$$

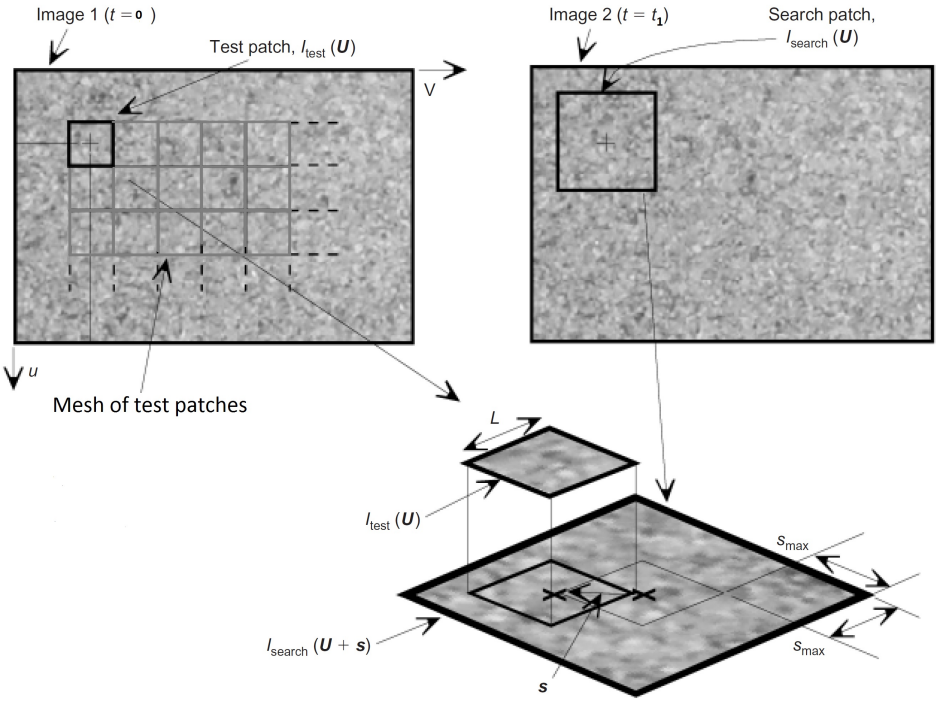

Figure 5.1: PIV image analysis technique (after White et al., 2003)

To reduce the computational requirement for multiple patches, the tracking algorithm is implemented in the frequency domain by Fast Fourier Transform (FFT) in preference to the spatial domain. The matching algorithms provide a map of 'degree of the match' over the chosen search zone. The highest peak of the map gives the displacement vector to single-pixel precision and subsequent bi-cubic spline interpolation around this point of best match is used to assess the displacement to sub-pixel precision.

5.2.2 Photogrammetry and image error

Photogrammetry is the series of mathematical transformation functions which allow conversion of image space pixel data into real world coordinates (object

space). GeoPIV executes an inbuilt pinhole camera model (Figure 5.2) which is used to convert between image and object space using the methods described by Heikkila and Silven (1997). This method is based on the principle of collinearity such that each point in object space is projected by a straight line through the lens into projection centre in the image plane. The transformation between object points is described by a 6 degree of freedom rigid-body rotation and translation matrix. Camera properties can be determined using calibration toolboxes available in $MATLAB^{TM}$ such as (Heikkila, 2000). The camera rotation with respect to X, Y and Z axis is described Eulerian rotation angles ω, φ and κ which are defined by Slama (1980). High contrast black on white control target markers positioned within the field of view of each image enable calibration of the image reference framework.

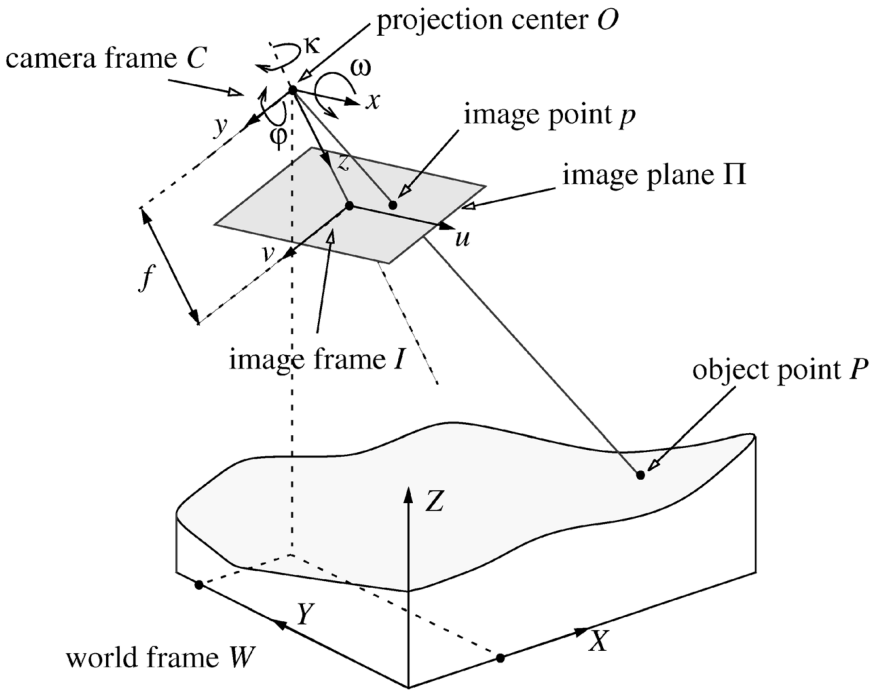

Figure 5.2: Pinhole camera model (Heikkila, 2000)

In the current work, a further refraction correction is necessary as in transparent soil modelling the calibration control markers and the plane of interest of soil displacement are non-conplanar (i.e. control markers and the laser illumination plane occur at different distances from the camera); hence, a refraction correction

model is required to account for distortion of light rays passing through the Perspex viewing window and saturated soil (Figure 5.3). Details of this calibration process are described in Section 5.6 later in this chapter.

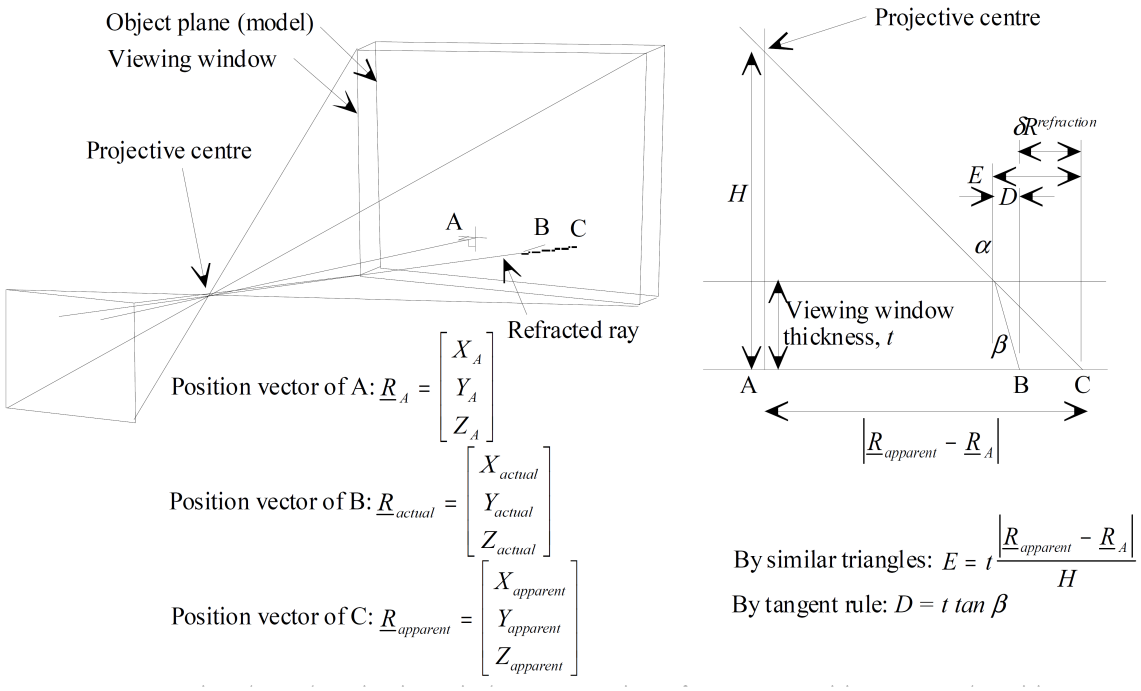

Figure 5.3: Mathematical framework for refraction through a viewing window (White, 2002)

5.2.3 RGB imaging

Visualisation experiments are best conducted in a dark room environment to ensure that the test exposure can be carefully controlled. As discussed previously in Chapter 3, high quality image measurement requires conversion of pixel data to real co-ordinates (i.e. mm). Within the framework of GeoPIV this is conducted using control markers located on the viewing window. Hence, owing to the dark conditions it is difficult to distinguish high contrast black on white control targets as any control marker on the viewing window is silhouetted by the background laser illumination plane. Hence, some front illumination is necessary.

Previous transparent soil tests in dark room conditions conducted by Stanier (2011) attempted to use LED's as target markers however the LED glow proved difficult to determine the precise centroid as the LED 'flared' in the captured image. In this work it was proposed to use front illuminating LED panels to highlight the control markers directly. As outlined in Chapter 3, some particles had minor inclusions resulting from the manufacturing process and thus were not 100% perfectly transparent. It was considered to use white light to illuminate the control markers on the front of the test box; however, it was observed that some of these non-perfect soil particles reflected the white light and thus were visible in an image. This poses a problem as these particles are in front of the desired internal plane illuminated by the laser and thus would affect the image correlation process. As general white light contains a blend of Red, Green and Blue colour spectrum this left little opportunity to control the light conditions if ambient light used to illuminate the control markers.

For this reason, it was decided to utilise filtered light of a known frequency to highlight the control markers. Doing so would ensure that erroneous particles visible in front of the target plane illuminated by the filtered light could then be eliminated from subsequent images for analysis processing runs by extracting the specific wavelength from the image. Owing to the laser being in the green and blue spectrum, red light was selected as the suitable light frequency to use as the control illumination channel in Figure 5.4.

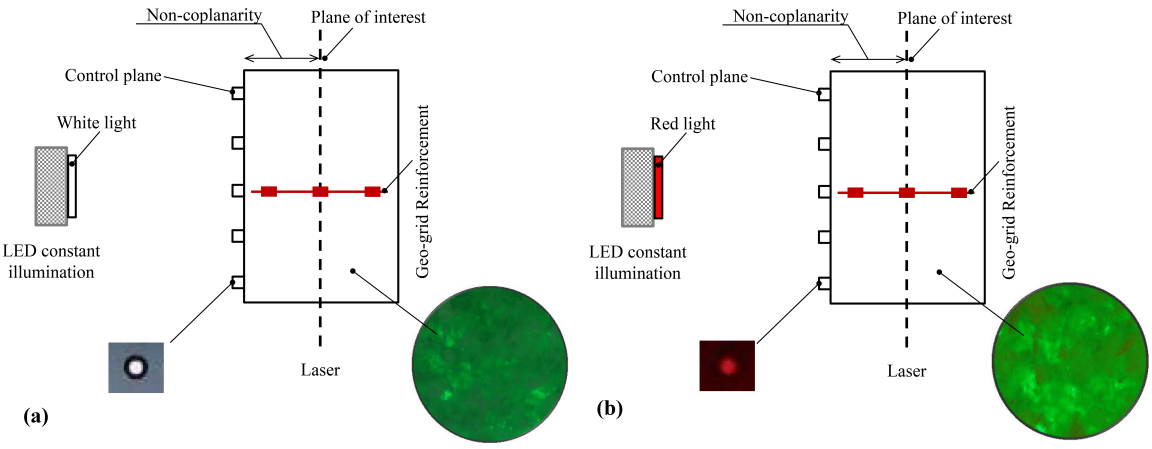

Figure 5.4: LED light illumination, (a) White light (b) Red light

5.3 Development of interaction pull-out test system

The design of reinforced earth is based on effective load transfer between soil and the reinforcement (Hryciw and Irsyam, 1993). Similar to previous investigations (Ezzein and Bathurst, 2011b, 2014 and Ferreira and Zornberg, 2015) it is proposed to evaluate interaction mechanics between the soil and geo-reinforcement material using a classical pull-out approach BS EN 13738:2004 (2004) and ASTM D6706-01 (2001), with the distinct advancement of visualising the soil-geogrid interaction using transparent soil laser aided imaging to observe soil particle movement. Figure (5.5) show a typical overview of the transparent soil modelling application.

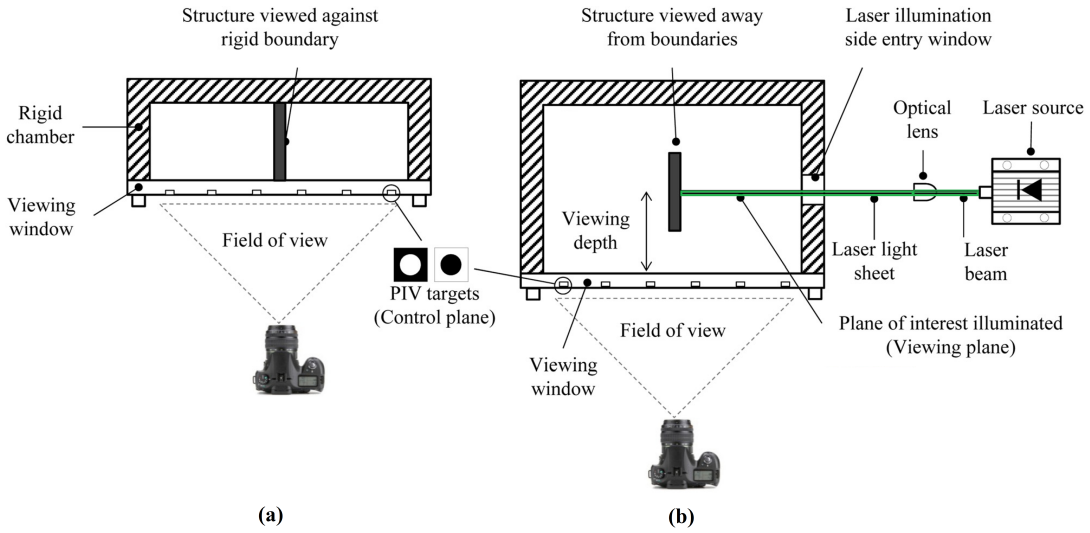

Figure 5.5: Physical modelling methods, (a) plane strain modelling and (b) transparent soil non-intrusive modelling (after Black, 2015)

Considerable experience has been gained in previous studies at The University of Sheffield (Stanier, 2011 and Kelly, 2013). Many of these investigations using laser illumination have used a single point beam laser source in conjunction with a diverging optical lens to produce an illuminated plane within a model. While this is perhaps the simplest configuration to generate a light sheet, the diverging beam often leads to non-uniform illumination intensity which can compromise the image analysis. A further limitation of this method is that it can lead to shadowing/loss of

laser light when an opaque object is present in the transparent model, for example geogrid reinforcement. When investigating interaction effects of stone column groups, Kelly (2013) devised a novel methodology of using a scanning beam box to produce a parallel beam of highly uniform light that minimised shadow effects. This laser generation methodology is highly suitable for this study also and thus the development of the experimental pull-out box was developed on this basis. A conceptual diagram of the laser, scanning beam box projection system and test chamber are shown in Figures 5.6 and 5.7, each of which are fully described in the following sections.

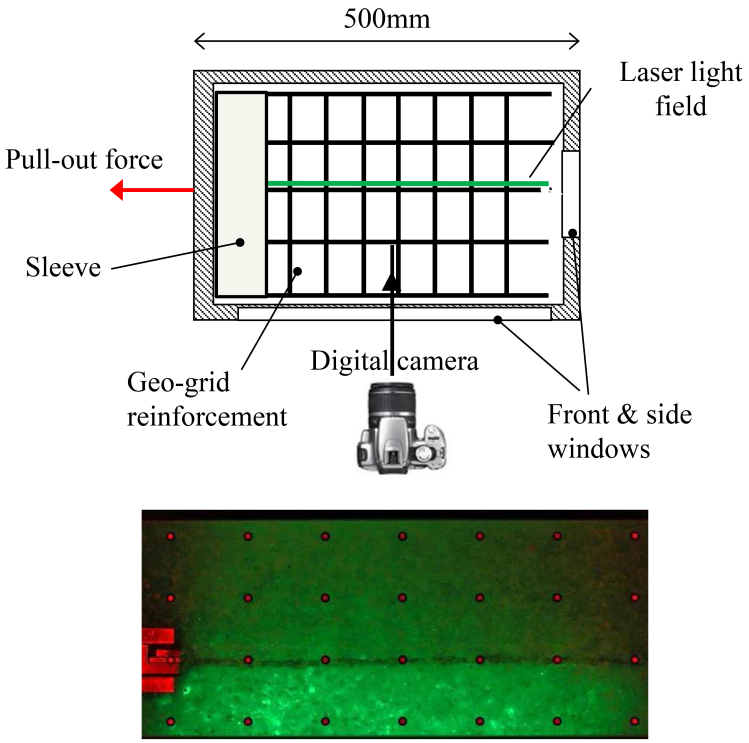

Figure 5.6: Schematic illustration of technique adopted for pull-out test, plan view

5.4 Pull-out experimental box

The test pull-out box with internal visualisation capabilities was designed in Solid-Works 3D to ensure full integration of components prior to fabrication. Each plate

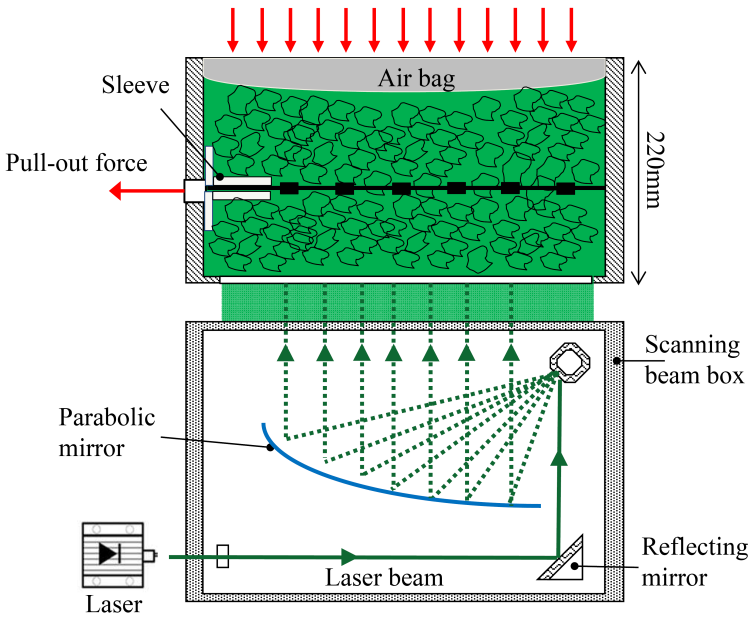

Figure 5.7: Schematic illustration of technique adopted for pull-out test, cross sectional view

was constructed from 20 mm thick aluminium which was sufficiently stiff to minimise deflections/strain of the boundary under the proposed working stresses. The chamber was mounted on a base plate 730 mm in length and 300 mm in width. Vertical plates bolted to the base formed the box sides producing an internal sample dimension of the 500 mm (L)×200 mm (W)×200 mm (H). Each plate was anodised black to minimise laser light reflection. To observe the interaction performance of the soil and reinforcement during a pull-out event it was necessary to incorporate several Perspex windows into the box design. A viewing window 440 mm long×140 mm high was incorporated into the front plate to enable visual observation of the exposed internal soil plane within the model. A strip window 440 mm long×50 mm wide was incorporated into the base plate to enable the introduction of the laser illumination from beneath as shown in Figures 5.8 and 5.9. Fluid lines were also located on the base plate to enable filling of the test box from a header tank.

According to the literature, one of the important parameters, which has significant effect on the pull-out force, is the friction between the soil and the front wall.

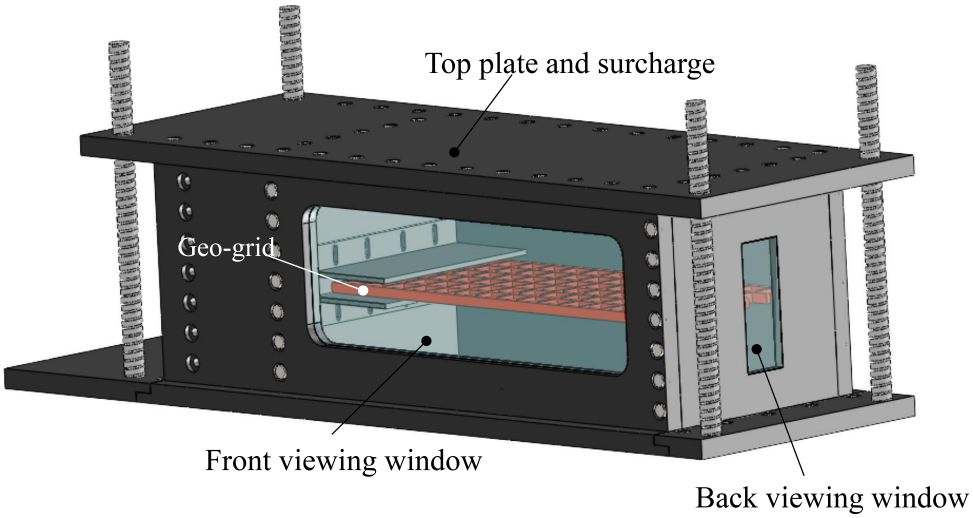

Figure 5.8: Design of pull-out box test in SolidWorks

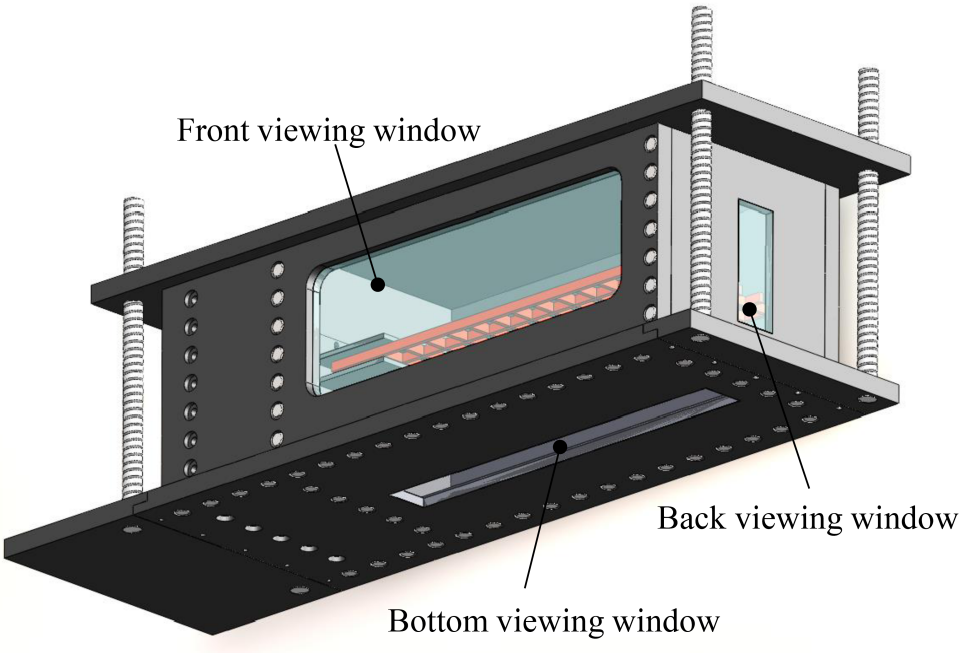

Figure 5.9: Location of three viewing windows in pull-out box

Therefore, to better understand this influence on the results of the test, the pull-out box was simulated by LimitState:GEO software. The friction of front wall decreases the magnitude of the vertical stress, which is applied on the top boundary of the box hence the result of the pull-out test is slightly lower than that for a frictionless boundary condition. Figure 5.10 shows the result of pull-out test which is normalised by the length of specimen and vertical stress versus the different friction angle of the front wall. The results of this study shows the friction angle mobilised between front wall and soil has a considerable influence on the result of the pull-out test. Therefore, it is important to find a way to reduce the friction between soil and front wall to avoid the effect on the results of the test.

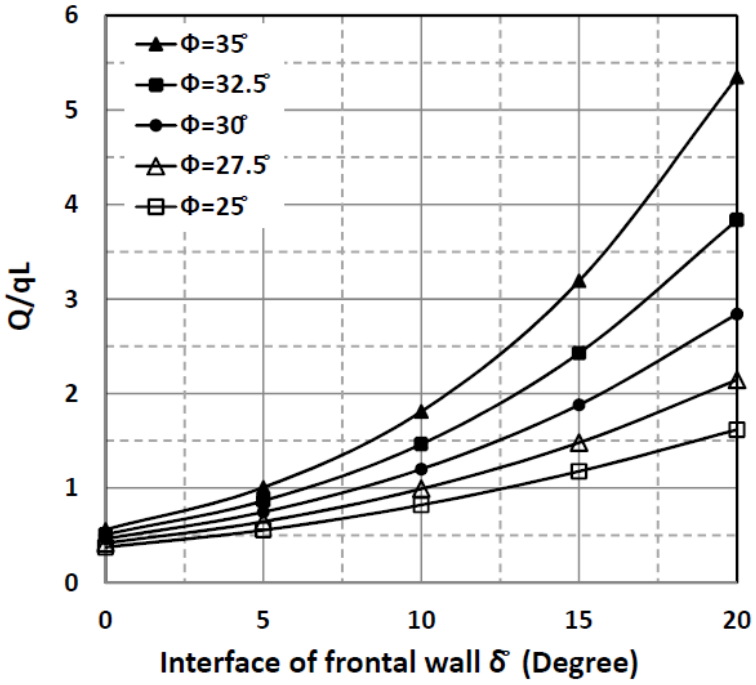

Figure 5.10: Effect of wall roughness on the results of pull-out test

The front wall of the chamber accommodated the attachment of upper and lower friction sleeves (of length 100 mm) that minimised the resistance between the load system and front wall during pull-out as recommended by Bolt and Duszynska (2000), Farrag et al. (1993), Lopes and Ladeira (1996) and Raju and Fannin (1998) (Figure 5.11). A 19.5 mm diameter hole and bush assembly, complete with 'O'-ring seals, allowed the load ram (19 mm steel bar) to enter the chamber through which the pull-out force was applied.

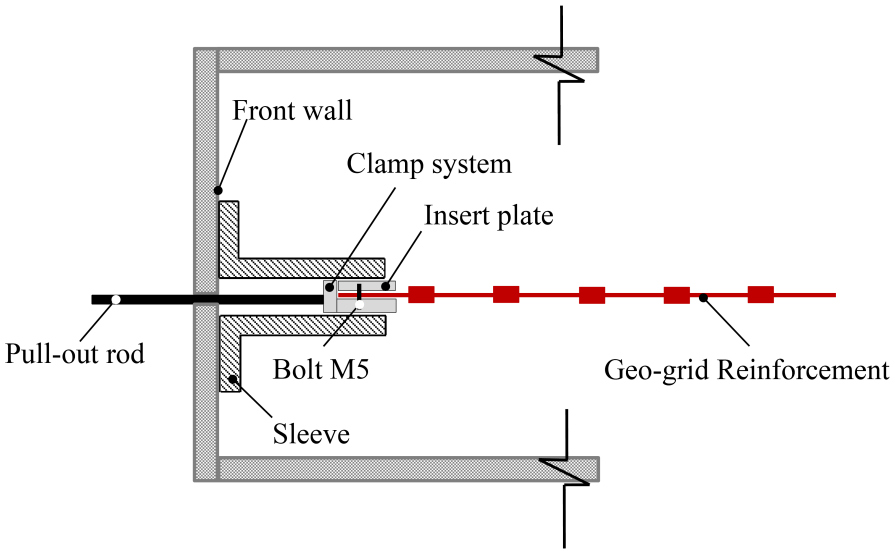

Figure 5.11: Schematic illustration of clamping system

To simulate difference stress conditions at the soil reinforcement interface it was necessary to apply vertical confining stress. After some consideration it was decided to apply the vertical stress via a flexible rubber membrane rather than a rigid plate, in accordance with recommendations by Palmeira and Milligan (1989). This would ensure that the applied stress was more uniform across the wide of the sample and also prevent detrimental interaction effects with the chamber walls which would be more pronounced for a rigid boundary. This aspect was confirmed using numerical simulations to evaluate the likely boundary effects during the design stage of the test system. The results of the analyses which have been done by LimitSate:GEO emphasised that by applying the flexible vertical load on the top surface boundary of the pull-out box, the stress is distributed uniformly over the surface of the specimen. Figure 5.12 illustrates the mechanism of failure and distribution of stress for rigid and flexible top boundary. The flexible boundary was achieved using an air bag that was filled with fluid and pressurised to simulate various surcharge conditions. To restrain the air bag a 20 mm thick aluminium plate was bolted to the top of the box so that it could be pressurised.

The geogrid is placed in the mid-height of box between the friction sleeves and secured using a clamping system. This clamping system was crucial to ensure that it was able to transfer the necessary pull-out force from the actuator to

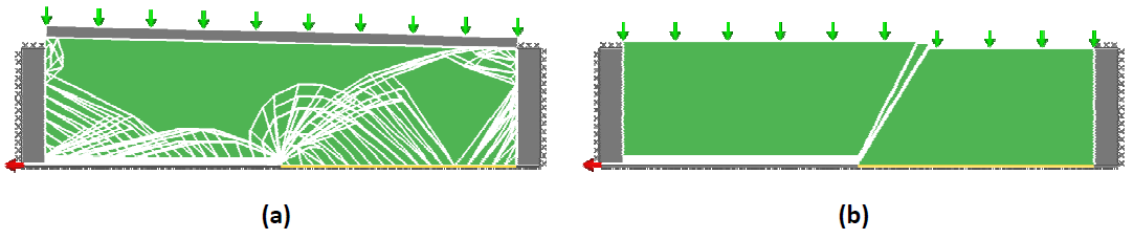

Figure 5.12: Load distribution, (a) Rigid, (b) Flexible

the geo-reinforcement uniformly without local rupturing. The clamp body was manufactured from 10 mm aluminium plate and a smaller insert plate of thickness 4 mm clamped the geogrid when fastened together using M5 countersunk socket cap bolts (Figure 5.11). The clamp system is attached to the load bar and a load cell that is interfaced with the liner screw actuator.

5.4.1 Drive system

The drive system for pulling out the geogrid incorporates an electronic actuator (K91G40NC-T) is coupled with a right angled planetary gear box that yields a gear ratio of 24 : 1. Motor torque is converted to linear force using a linear screw such that the actuator can generate a pull-out force of up to 10 kN and travel at a rate of 1.7 mm/min up to a total stroke of 100 mm. The load assembly is shown in Figure 5.13.

5.4.2 Laser and optical systems

5.4.2.1 Laser

The laser utilised in this research was a class IV Argon laser manufactured by Laser Quantum Opus 532 serial No 11142 (2011) with 2W maximum power output and a wavelength range of 514-532 nm (green spectrum). The laser provided a beam of polarized collimated light 1.85 mm diameter. For safety compliance it was fully enclosed in matt black plywood shuttering to prevent accidental harmful radiation

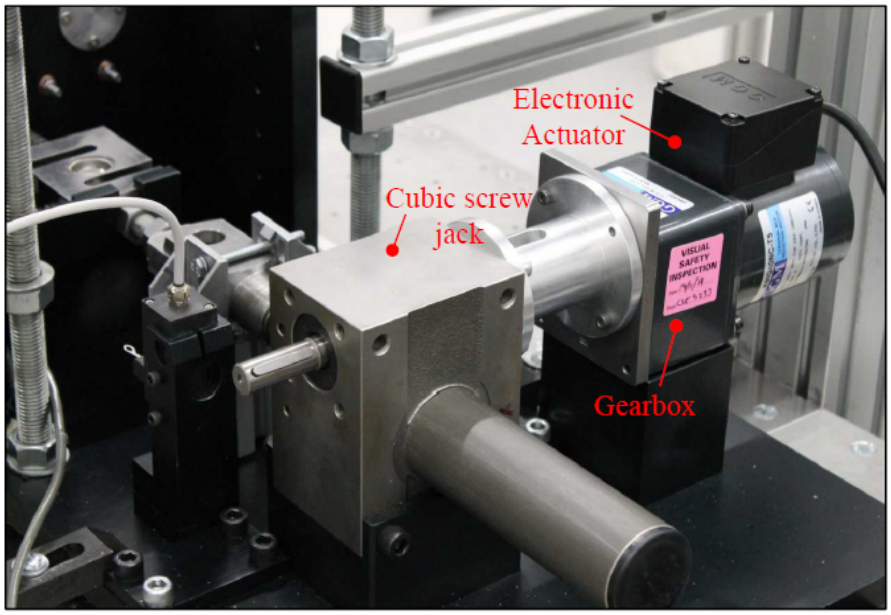

Figure 5.13: Actuator system of pull-out box

exposure. The laser was mounted on an adjustable platform to enable alignment with the scanning beam box entrance.

The scanning beam box was manufactured by Optical Flow System Ltd. The device incorporates a motor driven polygon mirror to reflect and disperse the laser beam onto a parabolic mirror which in turn produces a parallel, continuous sheet of vertical laser illumination. The admissible energy input for the box is 20W, while the scanning period can be set from 0.5 ms to 12.7 ms by varying the RPM of the polygon mirror. Calibration of laser power and scanning beam box RPM, in conjunction with camera settings, were conducted to obtain the optimum exposure for soil tracking performance as described in Section 5.6.

5.4.2.2 Camera

A digital camera is used to capture the soil displacement behavior during the pull-out event. The camera is fixed in front of the test chamber 1000 mm away from the front Perspex viewing window. The camera is a CANON EOS 1100D Digital Single Lens Reflex (DSLR) with an 18-55 mm lens and a summary of its specification

is reported in Table 5.1. The camera was controlled by an integrated National Instruments data acquisition hardware and LabVIEW to trigger the camera at a predetermined time interval.

Table 5.1: Canon EOS 1100D Digital Camera Specification

Image Sensor	
Type	CCD
Maximum Resolution	4872×2848
Effective Pixels	10.0 M
Size	22 ×14.7
Image Ratio (W:H)	3:2
Image Stabilisation	Gyroscopic
Lens	
Focal Length Range	18.0-55.0 mm
Aperture Range	F3.5-38.0
Exposure Control	
Shutter Speeds	1/4000 sec to 1/60 sec
ISO Speed	Auto. ISO 100-6400

5.4.2.3 LED illumination panels

As described in Section 5.2.3 , it was determined that a suitable method to minimize the impact of lower quality particles whilst ensuring the control targets would be visible would be to use filtered light. To achieve this two LED illumination panels were fabricated, 450 mm high and 100 mm wide. Three individual 12V DC illumination panels consisting of 30 surface mount diodes (SMD) were positioned in each tower. Brightness was controlled using a dimmer circuit. In front of each LED tower a white diffuser was located followed by a red LED Perspex filter that allowed controlled light, wavelength red light is 600-750 nm at 400-484 Hz to below 500 nm, to illuminate the front of the test chamber.

5.4.3 Data acquisition and instrumentation

In addition to the visual deformation data stream captured by the camera of the soil and geo-reinforcement within the test chamber, additional external measurements of applied force and displacement during pulling were also recorded. A data acquisition module was built using National Instruments hardware and integrated LabVIEW user interface and is described in the following sections and a schematic overview of the system electronics is shown in Figure 5.14.

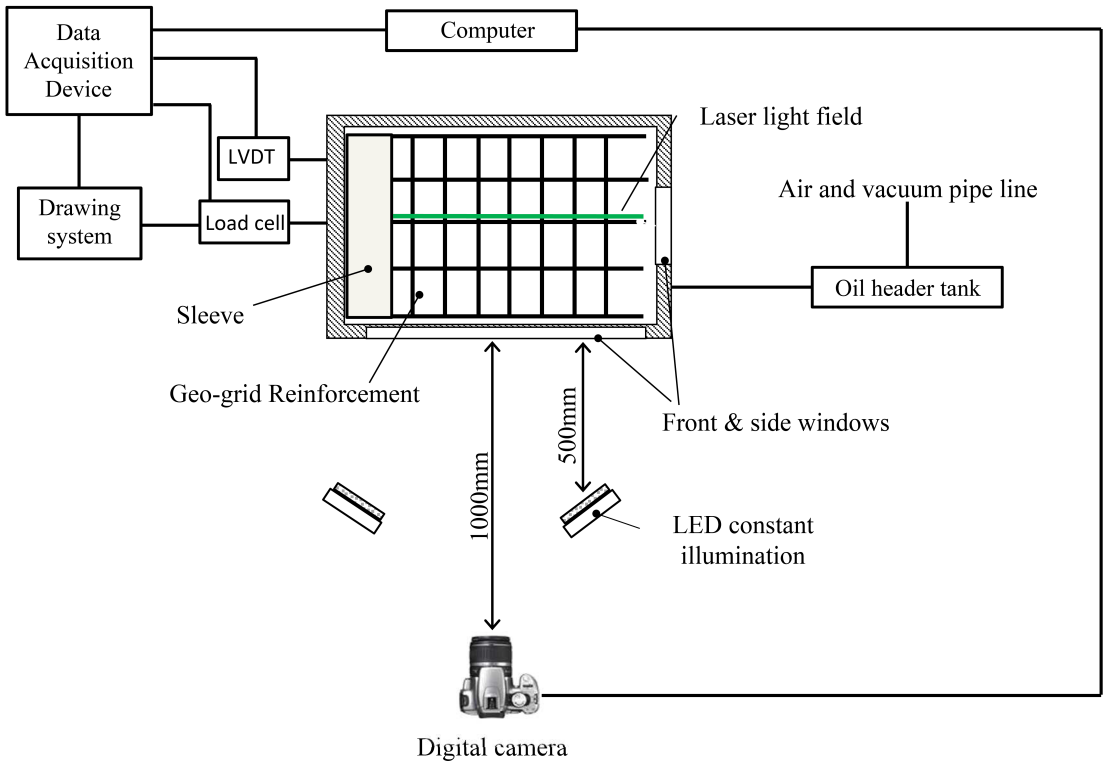

Figure 5.14: Schematic of instrumentation

5.4.3.1 Load cell

An S-type stainless steel tension-compression load cell from Vishay Precision Group, Inc. was chosen to monitor the load applied for pulling out the geogrid. The transducer was certified with a capacity of ±10 kN. The transducer was provided with an excitation of 12V DC, which was within the recommended supply

voltage of 10-15 V, and generated an output signal of 2 mV/V with tolerance 0.0035 ± mV/V. The load cell was connected to the actuator and clamping system using a pair of stainless steel connectors of 32 mm diameter, half threaded with $M16T$ as shown in Figure 5.15.

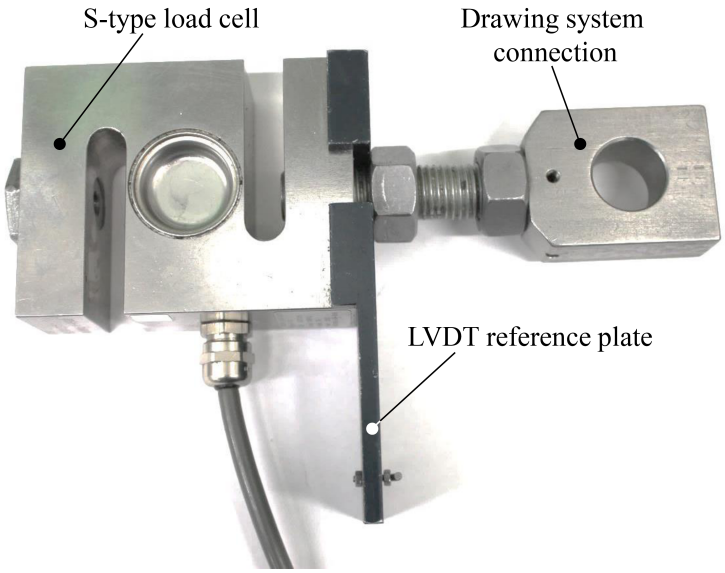

Figure 5.15: 10 kN tension-compression load cell

A SHIMADZU AGS-X series 10 kN reaction frame was used to calibrate the load cell in both compression and tension and the result is shown in Figure 5.16. A linear correlation was observed with a least square regression analysis (R^2) of 0.9996. At the end of the experimental programme the load cell calibration was re-checked for drift which did not occur.

5.4.3.2 Draw wire transducer

An ASM WS31C draw-wire LVDT transducer was used to measure the applied displacement of the linear actuator. This transducer had a range of 500 mm and was mounted in front of the box and adjacent to the plate which is located on load cell Figure 5.17. The transducer was provided with an excitation of 12V DC, which was within the recommended supply voltage of 10-15 V, and generated an output signal of 24 mV/mm with tolerance ±0.35 % full scale. Figure 5.18 shows

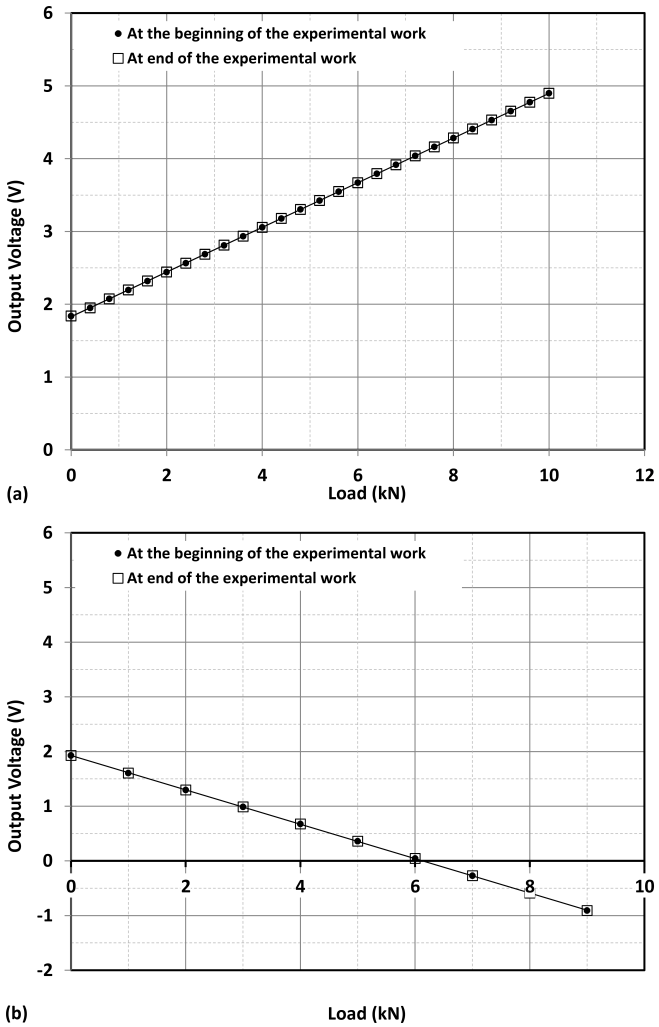

Figure 5.16: Load cell calibration, (a) compression (b) tension

the results of calibration at the beginning and end of the tests. A strong linear correlation was observed with a least square regression analysis (R^2) of 0.98.

5.4.3.3 Data acquisition system

A National Instrument NI USB-6229 Data Acquisition Device (DAQ) was utilised to record input signals from the transducers. This device had 16 differential or 32 single ended analogue inputs in the range of ±0.2V to ±10V with a maximum sampling rate of 250 kS/s and 16 bit resolution. The NI DAQ was packaged into

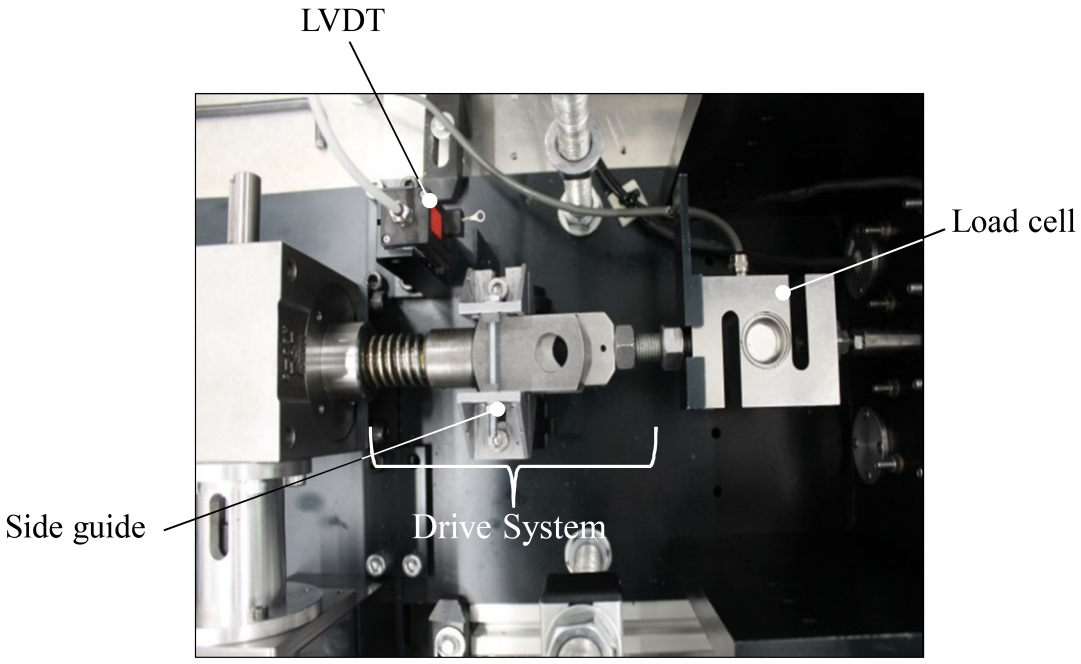

Figure 5.17: Photo of actuator system include load cell and LVDT

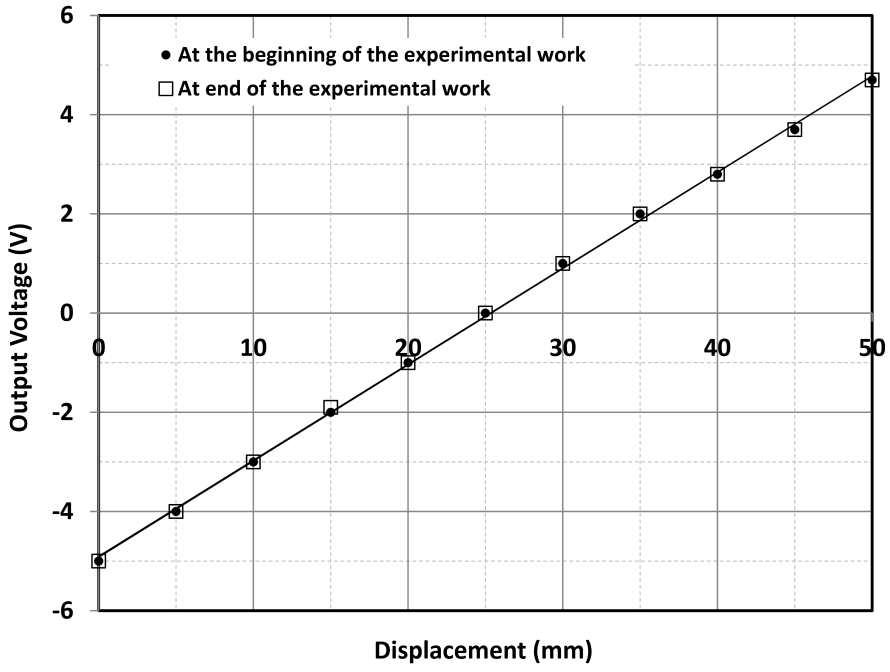

Figure 5.18: Draw-wire LVDT transducer calibration

an IP66 rated water proof protective housing that also incorporated a $12V$ DC Traco power supply that provided sensor excitation. External surface mount 9-way D-sub terminal connectors interfaced with the incoming sensors. The NI USB DAQ also featured Digital Input and Output (I/O) channels one of which was used to trigger the DSLR camera automatically at a predetermined time interval. A time of 5 seconds between successive images was deemed suitable to provide a comprehensive image bank over the duration of the pull-out event ensuring that 1.7 mm of movement occurred between subsequent image frames (Figure 5.19).

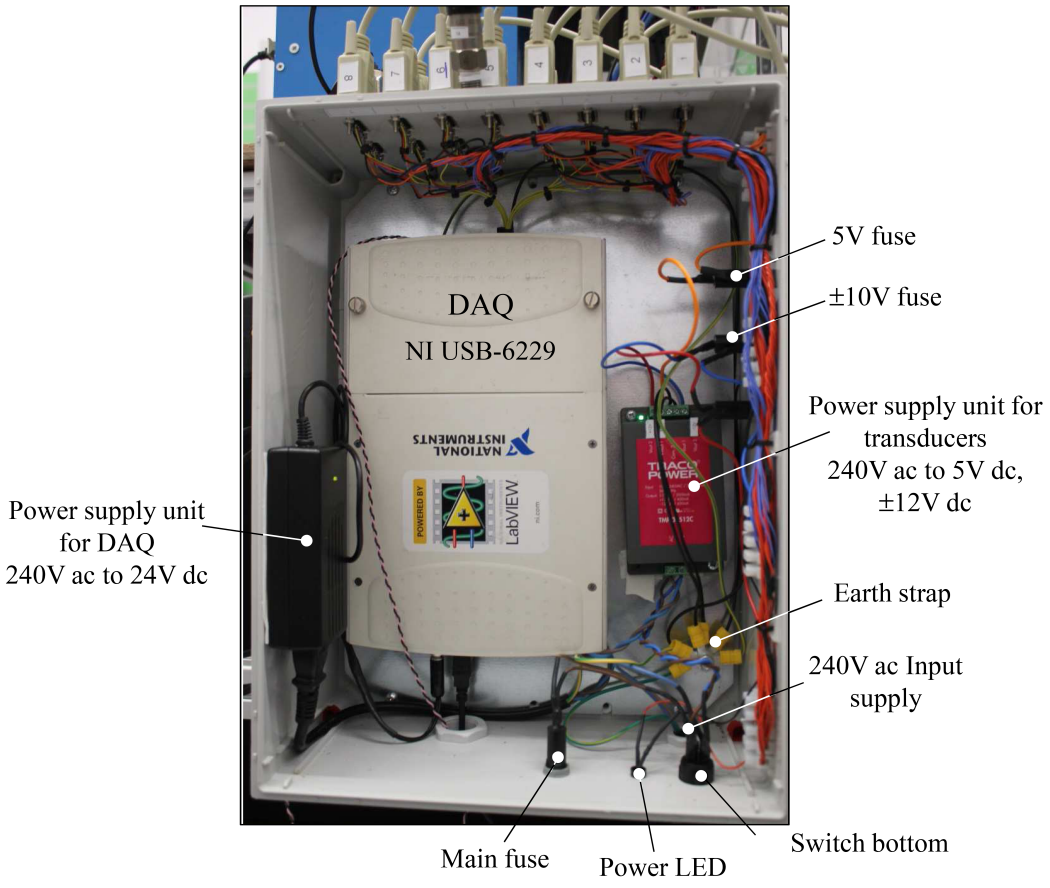

Figure 5.19: Data Acquisition System

A front end user Virtual Instrument (VI) interface was developed in LabVIEW to control the DAQ and display real time data feedback of all sensors during a test. The VI included graphical output of force and displacement with time, force vs displacement and test input information as shown in Figure 5.20.

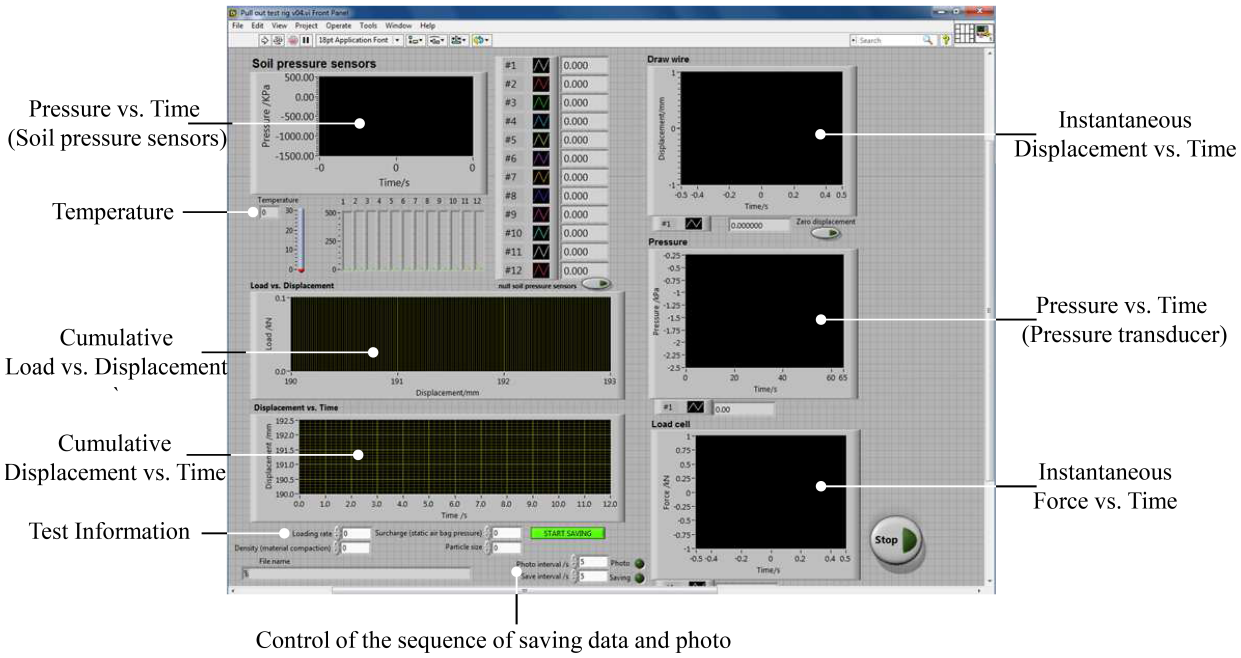

Figure 5.20: LabVIEW control software interface for data sampling and real time control of pull-out test

5.5 Experimental procedures and methodology

5.5.1 Sample preparation

Material properties of the fused silica used in this investigation are reported in Chapter 3, Section 3.1. Prior to use, the material was thoroughly washed and air dried to remove surface dust residue produced by the crushing process during manufacture. This pre-screening stage is essential as contaminants on the particles discolour the refractivity matched pore fluid and compromise the image data quality. Clean dry fused quartz was placed into the test chamber in 50 mm layers in loose relative density. The box was filled up to the lower friction sleeve and levelled in preparation for the geo-reinforcement to be laid horizontally at the mid-height of the chamber.

The geo-reinforcement specimen was prepared by trimming it to 420 mm (L) $\times$90 mm (W) and fastened securely within the clamping system described in Section 5.4. The load rod, connected to the clamp, was fed through the bush assembly in

the side plate and attached to the lead screw drive assembly. The reinforcement was placed over the aggregate, pulled taut and checked to ensure that the vertical plane of interested that would be illuminated by the laser aligned with the cross member rib. Two further 50 mm layers of aggregate were placed into the box ensuring not to disturb the alignment of the reinforcement. Once filled, the rubber membrane used to apply the flexible confining stress was placed on the soil and the chamber sealed by securing the rigid top backing plate.

The soil should be fully saturated to ensure optimum transparent to the plane of interest. To aid saturation a vacuum was applied to evacuate air from the compacted sample and the pour fluid was slowly drawn in under suction from the header tank. This process proved highly successful in removing air pockets trapped at the particle contact interface.

Once the sample was assembled the test was conducted by the following steps:

1. The front viewing window was thoroughly cleaned and the control target marker panel attached.
2. The light panels were positioned to provide uniform illumination of the targets on the control panel.
3. The camera was mounted to the support frame, f-stop and aperture set to $f/8$ and 1/10 sec respectively, and connected to the automatic trigger of the DAQ. At the same time the laser as switched on and the camera manually focused to provide the optimum clarity of the illuminated soil particles.
4. All sensors were connected to the DAQ, LabVIEW VI launched and the system energised for 10 minutes to allow stabilisation of electrical resistances.
5. Data acquisition was started, logging at a rate of 1Hz and the camera triggered capture an image every 5 seconds.
6. Confining pressure was applied to the sample via the flexible membrane.
7. Pull-out was initiated at a rate of 1.7 mm/min until a displacement of 40 mm was achieved.

5.6 Experimental system calibration and validation

Prior to conducting the main body of tests it was necessary to confirm the suitability of the developed experimental systems with respect to the aspects such as (i) the achievable measurement resolution and error associated with the image base observations and (ii) confirm the repeatability of the pull-out system.

5.6.1 Laser calibration

The calibration process conducted to assess the accuracy of GeoPIV in tracking a known displacement was similar to that employed by White et al. (2003). The images translated 10 pixels in horizontal direction using the $MATLAB^{TM}$ toolbox. Then, computing the displacement between original image and manipulated one using GeoPIV and comparing the results for different patches with upper bound estimate of the standard error in image space generated with White (2002). It should be noted that for this calibration process, the 'search zone' parameter was raised to 20 pixels to allow accurate computation of the displacements. Patch sizes from 10 to 100 pixels in 10 pixel increments were calibrated and compared in all case. All calibrations are presented here in image space units (pixel) since no photogrammetric correction processes were conducted at this stage. The error was quantified in all cases as the standard deviation of the displacement measurement errors, so that the results were comparable with the upper bound proposed by White (2002). Figure 5.21 shows the results of calibration of different power of the laser, indicating that the standard error for patch size of 100 pixels was near upper bound of White (2002). From the results the optimum power of the laser is 0.5 W for the test conditions considered. A patch size of 100 pixels was adopted for the analysis process, while creating patch overlap by maintaining a spacing of 50 pixels, further improves performance.

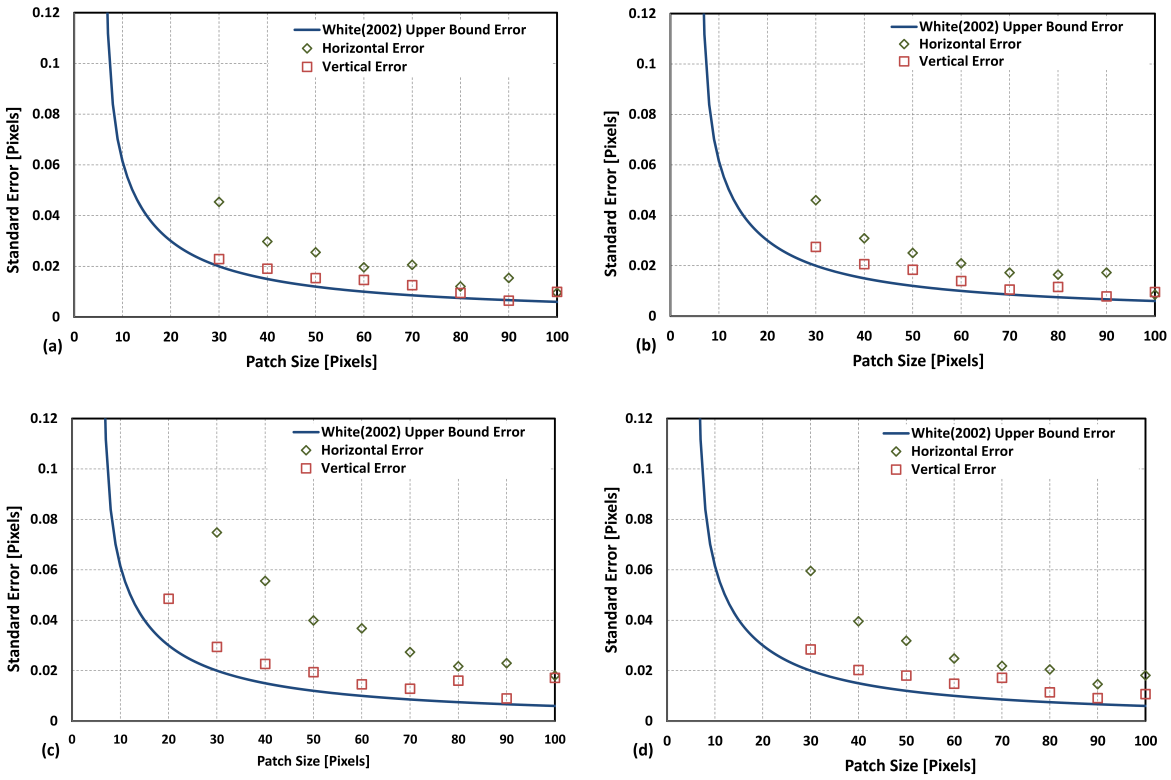

Figure 5.21: Standard error of tracking soil particles for different laser power; (a)0.5W, (b)1.0W, (c)1.5W and (d)2.0W

5.6.2 Camera calibration

A calibration target was fabricated at the University of Sheffield from Perspex which is shown in Figure 5.22. The target was drilled with 252 3mm diameter blind holes to an accuracy of ± 10 μm at 15mm centres in square grid arrangement. The target was then painted matt black before the blind holes were backfilled with white Tipp-Ex^{TM} fluid to generate the control points.

The resolution of data can be assessed by using a single image from calibration target since the center position of holes is clear. The accuracy achieved in the present work is 42 μm for vertical measurement and 32 μm.

The calibration of the camera was conducted in accordance with the Heikkila analysis toolbox for $MATLAB^{TM}$ (Heikkila, 2000). Three images of the calibration panel were taken at different angles and positions relative to the camera in each

Figure 5.22: Calibration target

as show in Figure 5.23. The camera settings remained the same as those used in validation and testing. Table 5.2 contains the camera calibration parameters derived by using Heikkila camera calibration toolbox.

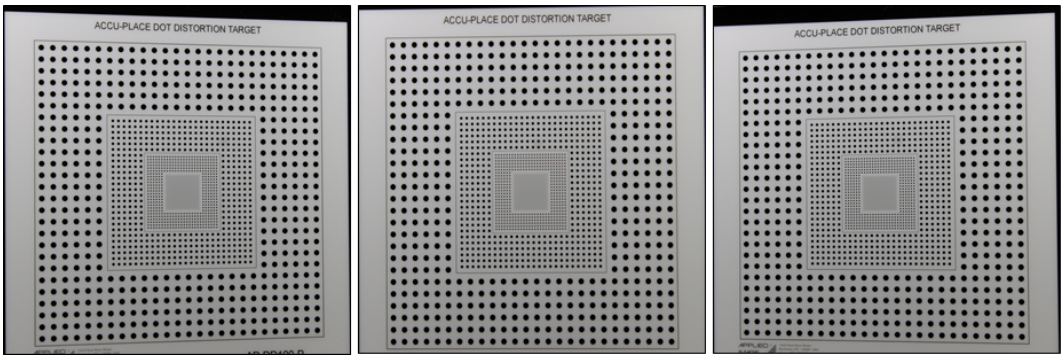

Figure 5.23: Calibration target images

Table 5.2: Camera calibration parameters derived using calibration target

Parameter	Output
α	0.9976
u_0	2166.9250
v_0	1511.4221
k_1	-1.933974×10^{-5}
k_2	-3.942701×10^{-8}
p_1	-9.178687×10^{-5}
p_2	-5.541610×10^{-5}

5.6.3 Time dependency

As the test to be conducted requires the camera to be placed in continuous trigger mode it is necessary to check the temporal error that is generated with the test apparatus and also the processing steps. For checking the movement of the camera itself during tests, 500 photos were captured of a box filled with the transparent soil and highlighted by the laser light sheet. GeoPIV was then used to track the movement of these photos which is shown in Figure 5.24.

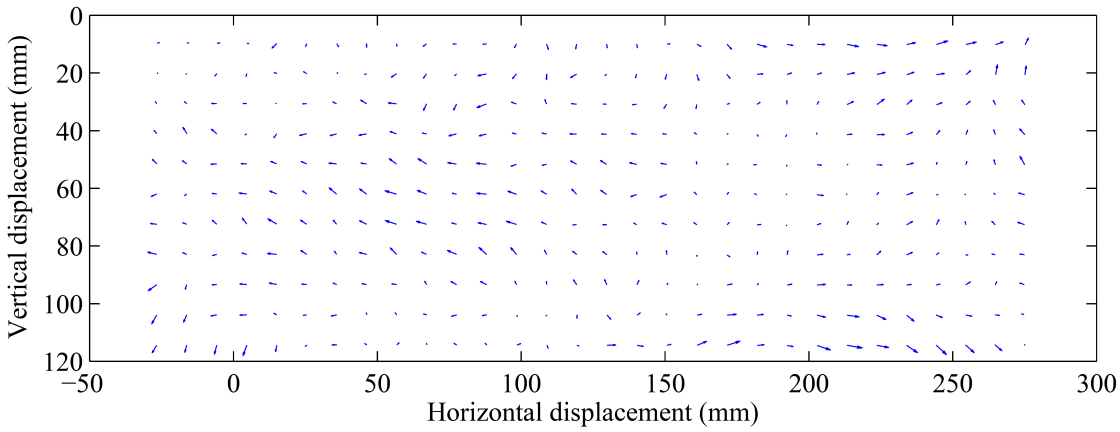

Figure 5.24: Camera movement vectors after capturing 500 images (vectors amplified by 10)

5.6.4 Calibration test set up

In order to calibrate the experimental system pullout response and the image acquisition a simulated reinforcement element was used. A sheet of steel was cut in the same dimensions and aperture as the geogrid selected for the research such that it would provide a fully rigid body pullout in the soil (Figure 5.25a). A second calibration condition also attempted to verify the resistance of the drive systems under different confining pressures. In this instance a complete sheet of steel was used in order to isolate the particle interaction effects (Figure 5.25b).

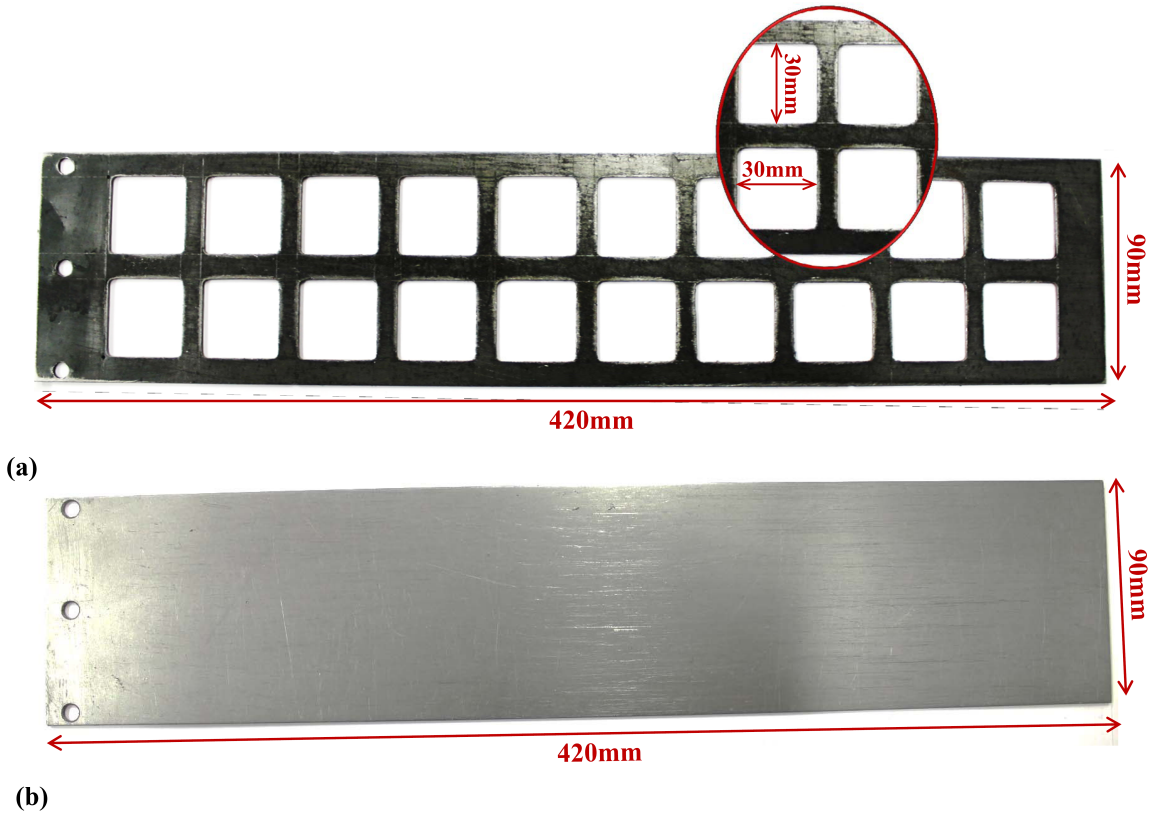

Figure 5.25: Configuration of steel reinforcement; (a) steel with holes, (b) sheet of steel

The results of the experimental study can be categorised into two sets, external and internal. External results relate to the force-displacement results measured with the load cell and the LVDT transducer. The internal results are the output of post processing of the images of the illuminated soil plane within the model. These

results present soil interaction behaviour by plotting the soil velocity and horizontal trajectory, vertical displacement, shear strain and volumetric strain contours of local interaction effects soil particles. These sets of graphs indicate the region of soil movement, zone of influence, for local and global response (cumulatively and incrementally).

For reference the convention for labelling of the graphical output, in horizontal displacement contour plots, negative contours indicate that the soil particle is moving in the same direction of pull-out force and positive contours show rightward movement which is against the pull-out force. Similarly, in the vertical displacement contour plots, positive contours indicate settlement and negative contours show dilation or heave.

5.6.4.1 Steel reinforcement with holes

The results of load-displacement under three different confining pressures (12.5 kN/m^2, 25 kN/m^2 and 50 kN/m^2) are presented in Figure 5.26. The maximum pull-out force obtained at each test were 35 kN/m, 60 kN/m and 69 kN/m for confining pressure of 12.5 kPa, 25 kPa and 50 kPa respectively. The results for all three different values of confining pressures show the initial elastic region of the load-displacement response of the pull-out behaviour is independent of the value of confining pressure and the magnitude of the pull-out force is sharply increased with small displacement.

The cumulative PIV results at 40 mm axial displacement of geogrid under three different values of confining pressures (12.5 kPa, 25 kPa and 50 kPa) are presented in Figures 5.27 to 5.29. The figures show the movement of soil particles along the reinforcement is almost uniform confirming the fact of the rigid body transition and mobilisation of the soil resistance at the same strain magnitude in the test.

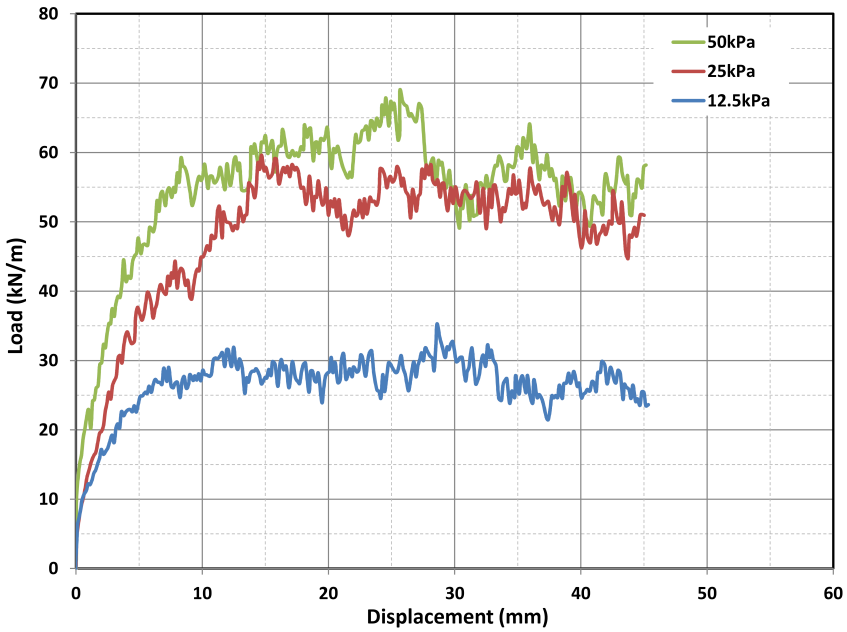

Figure 5.26: Load-displacement plots of steel with holes

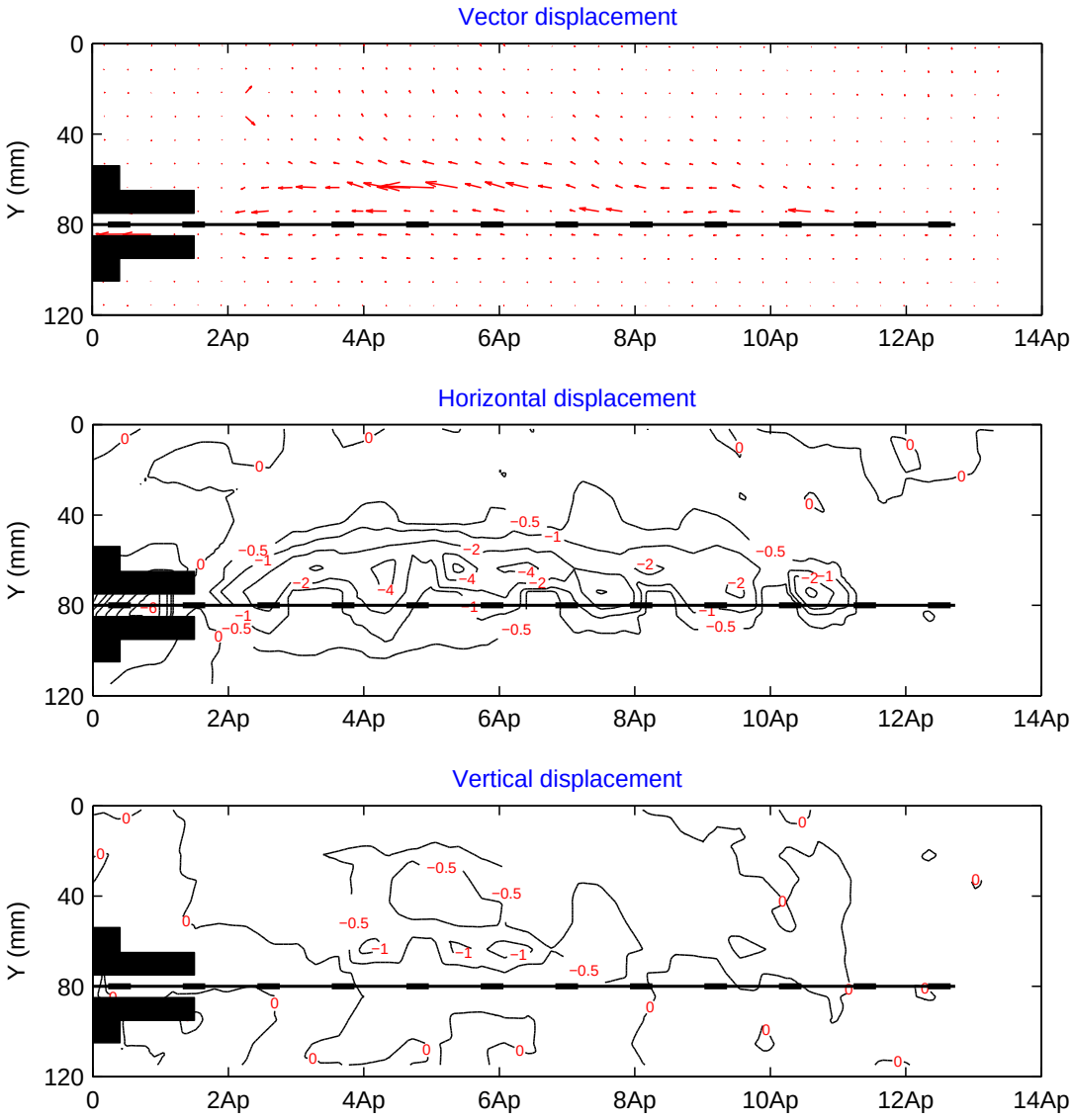

Figure 5.27: Cumulative PIV results at 40 mm axial tensile displacement of steel with holes for 12.5 kPa confining pressure

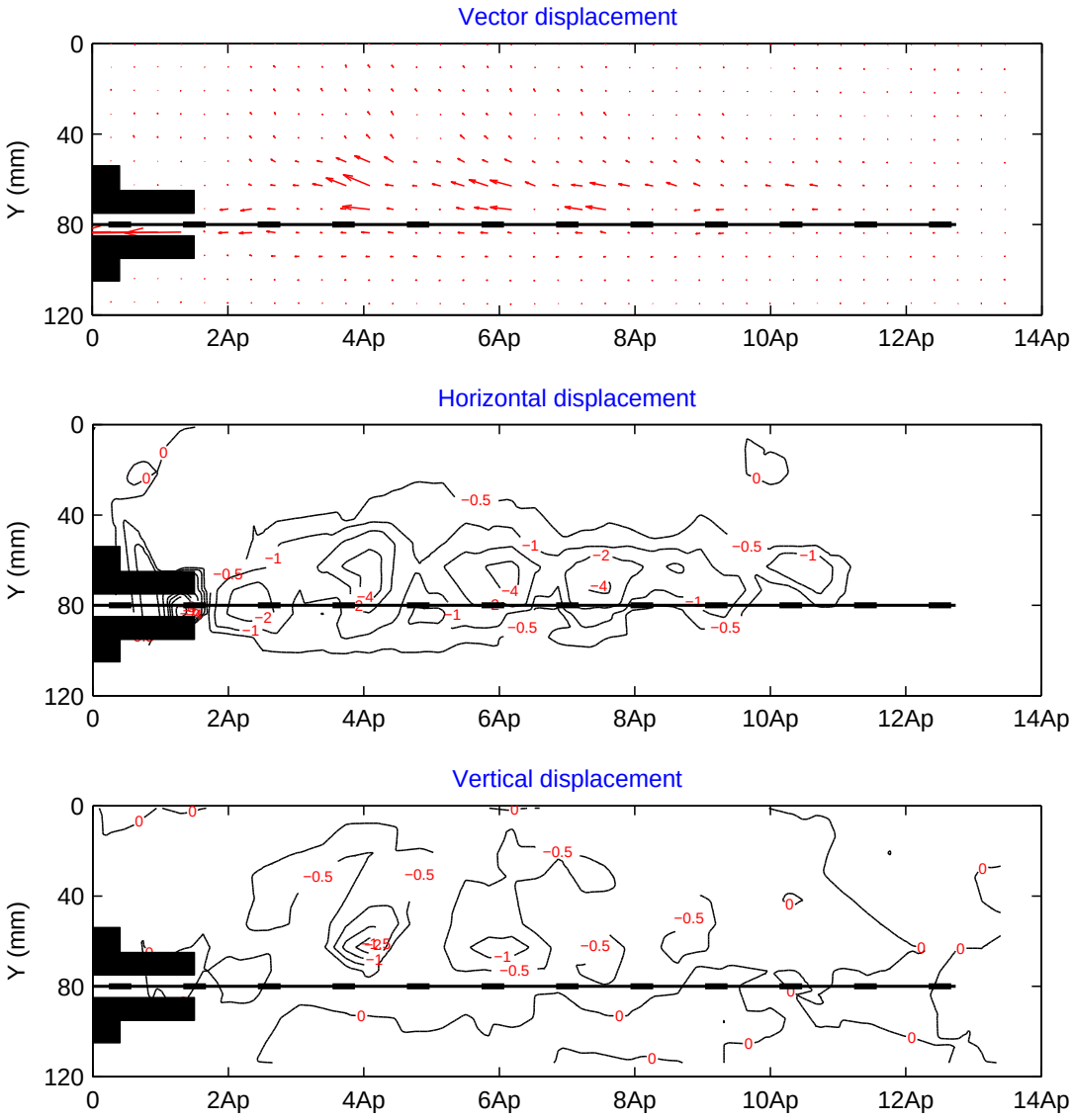

Figure 5.28: Cumulative PIV results at 40 mm axial tensile displacement of steel with holes for 25 kPa confining pressure

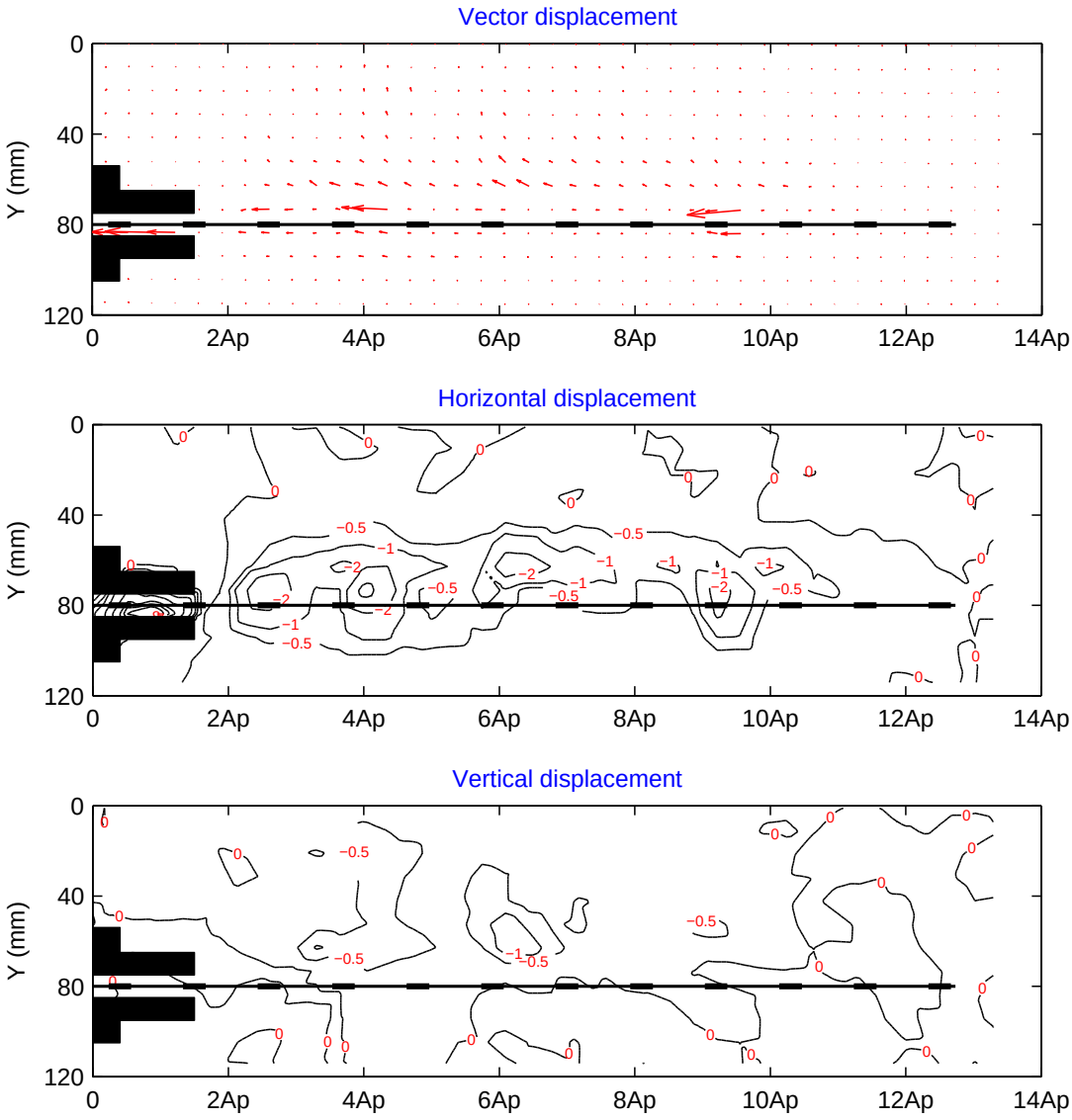

Figure 5.29: Cumulative PIV results at 40 mm axial tensile displacement of steel with holes for 50 kPa confining pressure

5.7 Sheet of steel reinforcement

The purpose of using the sheet of steel reinforcement is also to calibrate the system and look at the friction between the components. The results of load-displacement graph for three different confining pressures (12.5 kPa, 25 kPa and 50 kPa) presented in Figure 5.30. The maximum pull-out forces obtained at each test were 6.5 kN/m, 7.6 kN/m and 10.6 kN/m for confining pressure of 12.5 kPa, 25 kPa and 50 kPa respectively.

The graph shows exactly after starting the test the amount of load increased sharply. The reason is that no interlocking between soil particles is generated at the boundary of the interface and it is simply sliding through the soil. For the first 5 mm movement of steel the shear strength of between steel and soil particles mobilised which is the case to show the higher loading capacity. Then, the amount of pull-out load starts to reduce because the shear strength between soil and specimen start to release.

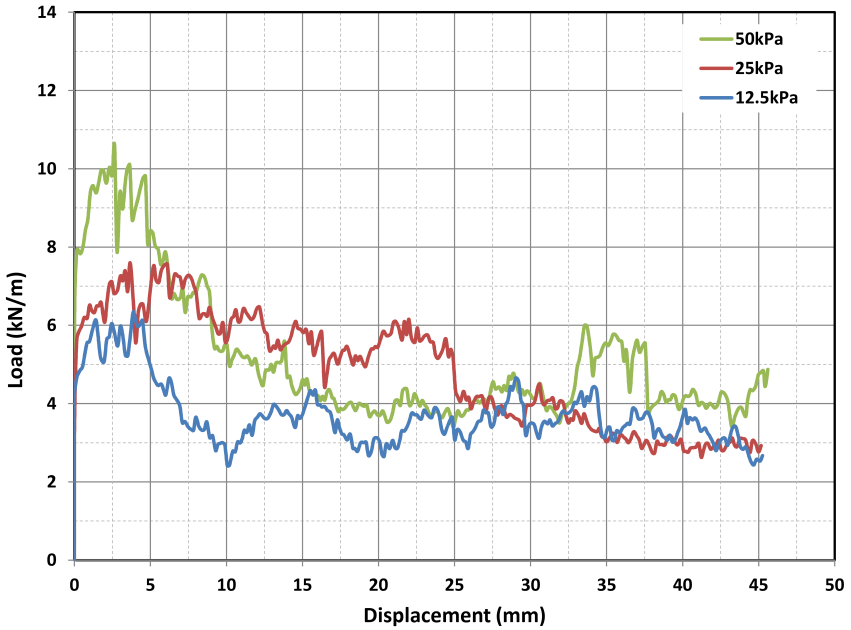

Figure 5.30: Load-displacement plots of sheet of steel

Chapter 6

Physical Modelling Results

The results from the laboratory element pull-out testing are presented in this chapter. In addition to the classic force-displacement pullout relationship, horizontal and vertical displacement, shear strain, volumetric strain are also possible due to the internal visualsation and PIV method implemented. Section 6.1 introduces the test plan in this research. Section 6.2 presents the output data from pull-out test for three different types of geogrid under different confining pressures. Repeatability of test system and experimental data are presented in Section 6.3.

6.1 Test programme

The tests conducted as part of this research are summarised in Tables 6.1. The aim of these tests is to evaluate the effect of rupture strength\stiffness of the geogrid on the pull-out mechanics at different confining pressures in the interaction behaviour between soil and geogrid. In each test the camera, laser and LED light parameters were fixed as described in Chapter 5. Also, as mentioned in Section 5.4.1, the rate of pull-out of the reinforcement was constant at 1.7 mm/min during which images were captured at a frequency of 5 sec. Typically, around 300 images were captured by the digital camera which enabled displacement, shear strain and volumetric strain fields to be derived from PIV analysis.

Table 6.1: Test programme for pull-out test

Test No.	Stiffness of geogrid (kN/m)	Confining pressure (kN/m^2)
1	∽ 1200	12.5
2	∽ 1200	25
3	∽ 1200	50
4	∽ 1600	12.5
5	∽ 1600	25
6	∽ 1600	50
7	∽ 2900	12.5
8	∽ 2900	25
9	∽ 2900	50

The cumulative displacements, shear strain and volumetric strain fields are presented for axial tensile displacement of geogrid at 10, 20, 30 and 40 mm. In addition, incremental results are shown for 10-20 mm, 20-30 mm, 30-40 mm axial tensile displacement of reinforcement to show the evident of interaction performance.

6.2 Pull-out test results

6.2.1 Test1: Stiffness of geogrid = 1200 kN/m

6.2.1.1 External results

The stiffness of the geogrid specimen used in this test is 1200 kN/m. A series of three tests were carried out to study the effect of confining pressure (12.5 kPa, 25 kPa and 50 kPa) on the load-displacement response of the geogrid and the results are presented in Figure 6.1. The maximum pull-out force obtained in each test were 50 kN/m, 60 kN/m and 68 kN/m under confining pressure of 12.5 kPa, 25 kPa and 50 kPa respectively.

A peak pull-out resistance was not observed in any of the three values of confining pressures as shown in Figure 6.1. The results of the tests also show that the initial elastic region of the load-displacement graph is independent from the value

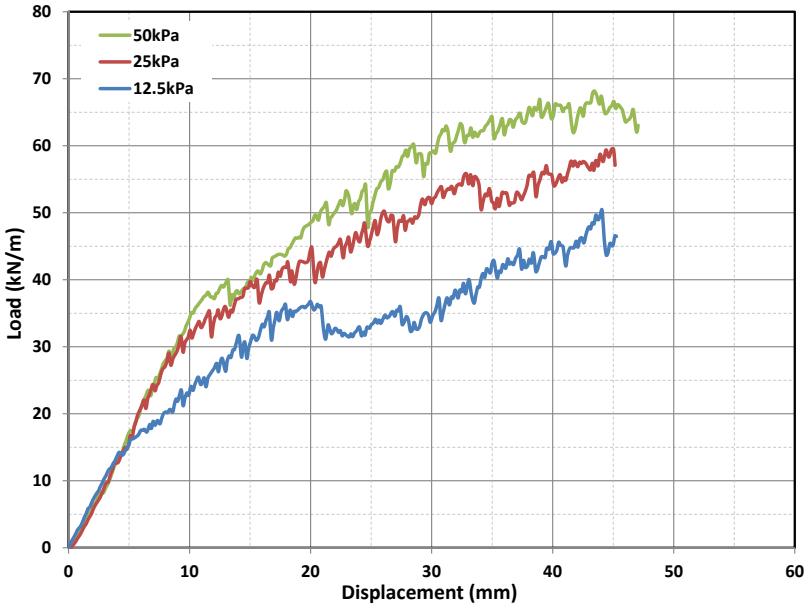

Figure 6.1: Load-displacement plots of geogrid specimen with stiffness of 1200 kN/m

of confining pressure for low stiffness geogrid. This could be because the geogrid itself is not strong enough to resist the pull-out force, but after initial stretching of the geogrid and increasing the interaction between soil and geogrid, the test with the higher confining pressure has stiffer behaviour in comparison with the low confining pressure. As the figure above shows the load-displacement response for the displacements smaller than 5 mm is linear for the confining pressure 12.5 kPa which is extended to 9 mm and 10 mm for 25 kPa and 50 kPa confining pressure respectively. This linear response indicates that the pull-out load is transferred directly to the geogrid generating minimal interaction with the surrounding soil particles. This viewpoint can be verified by reviewing the contours of soil displacement in these regions. Horizontal displacement contours of soil particle displacement in Figures 6.3, 6.9 and 6.13 show almost no soil deformations prior to 5 mm pull-out under 12.5 kPa confining pressure. For the first 10 mm of displacement for two others tests at 25 kPa and 50 kPa. The amount of transmitted force to the geogrid is about 15 kN/m, 30 kN/m and 35 kN/m for low to high confining pressures.

Figure 6.2 shows the picture of the geogrid specimen retrieved at the end of test for

three different confining pressures. It is observed that the transverse members of the geogrid under higher value of confining pressure deformed more in comparison with other ones.

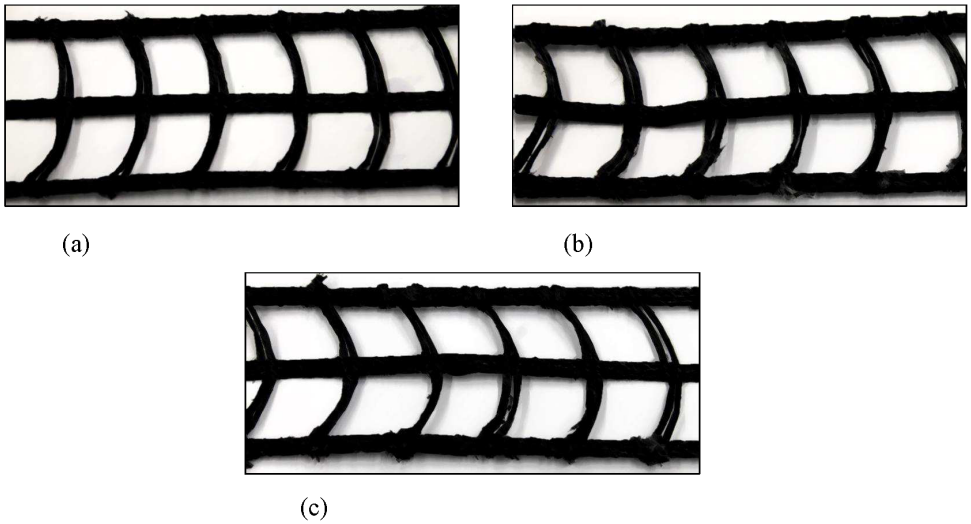

Figure 6.2: Deformation of geogrid transverse members at the end of test for different value of confining pressure, (a) 12.5 kPa, (b) 25 kPa and (c) 50 kPa (J=1200 kN/m)

6.2.1.2 Internal results

The output indicated soil interaction behaviour by showing the velocity trajectory vectors and presented the region of soil movement, a zone of influence and local and global response with plotting the cumulatively and incrementally horizontal and vertical contours of soil displacement. The following sections explain the behaviour of soil-geogrid interaction which is observed from pulling out the geogrid through the transparent soil.

6.2.1.2.1 Displacement contours

The cumulative horizontal and vertical displacement of soil particles under three different confining pressures (12.5 kPa, 25 kPa and 50 kPa) are presented in Figures 6.3-6.16. The local behaviour of soil-geogrid interaction under three different values of confining pressure at the end of the test are explained separately bellow:

Confining Pressure=12.5 kPa

As Figure 6.3 shows, for the first 5 mm movement of the geogrid, the pull-out tensile force generated is produced by pre-tensioning of the geo-grid as negligible levels of soil movement are observed upon the initial pullout. However, as the geogrid is mobilised further the onset of interaction between soil and geogrid commences as evidenced in Figure 6.4. As the geogrid pull out advances the interaction zone propagates along the full length of the reinforcement confirming that the geogrid is mobilising the soil capacity generated by the interlocking soil particles and geogrid. Larger magnitudes of horizontal displacement around the transverse cross rib members indicates that passive bearing capacity of these elements is mobilised. This could be the reason for vertical movement of the soil particles in advance of the transverse members as they are rotating clear of the interaction zone. The vertical contours demonstrate that the soil has started to dilate. Figure 6.7 presents the results at the end of the pull-out test and indicated the pull-out resistance between soil and geogrid is fully mobilised. The largest horizontal displacement contours are generated near the rib position that confirms the capacity of the transverse members has been released.

The magnitude of maximum horizontal displacement contours of soil particles is -4 mm which was generated in the proximity of the geogrid ribs location. The value of the horizontal displacement reduces with distance from the surface of the geogrid. The maximum vertical displacement contours of soil displacement are -2 mm which occurred over the ribs location near the loading place. The direction of vector displacement shows that the soil was dilating during the test. The post processing analysis showed the initial horizontal displacement of soil particle happened after 5 mm of

geogrid movement whereas 20 mm was required to generate initial vertical displacements.

Confining Pressure=25 kPa

For the first 7.5 mm of movement of the geogrid, the pull-out force is directly transferred into the geogrid with nominal interaction between soil and the geogrid (Figure 6.8). However, after 10 mm movement of the geogrid, as it is shown in Figure 6.9, the passive resistance of the transverse members has started to mobilise. At this stage of the test, the passive pull-out resistance in front of the transverse members has been mobilised and soil particles have started to move vertically. As Figure 6.11 demonstrates, dilatation occurs after the passive resistance of the transverse members is mobilised.

The maximum horizontal displacement contour of soil particles is -4 mm which was concentrated around the geogrid ribs location. This value reduced to -2 mm for the area around geogrid. The maximum displacement of the soil particle is -1.5 mm in the vertical direction which was mobilised above the geogrid. The initial horizontal and vertical movement of soil particle occurred after 9 mm and 15 mm of movement of the geogrid respectively.

Confining Pressure=50 kPa

The soil interaction behaviour of this test is similar to the 12.5 kPa and 25 kPa conditions. As Figure 6.13 shows, for the first 10 mm of movement of the geogrid, the pull-out force is stretching the geogrid without transferring into the soil particles. The interaction between soil and the geogrid is fully mobilised at 30 mm displacement of the geogrid as shown in Figure 6.15. However, as Figure 6.16 indicates, the magnitude of dilation of soil particles is less than two other tests. This is due to only confining pressure resistance the upward rotational movement more compacted and it is difficult for them to move.

The magnitude of maximum horizontal contours is -2 mm which was happened around the geogrid ribs position. This number is reduced to -1 mm for the vertical movement with dominate the movement equals -0.5 mm. The initial horizontal and vertical movement of soil particles was around 12 mm and 15 mm of geogrid movement respectively.

The results of the tests indicate that the largest horizontal displacement of soil particles was consistently adjacent to the geogrid location concentrating near the rib positions. The magnitude of horizontal displacement of soil particles increase by reducing the amount of confining pressure whereby the soil particles have more movement in the direction of loading for lower confining pressure. The reason is that the resisting pressure of the soil is less so soil particles can move easily with generating the lower resistance against the movement. Other observations can be made by evaluating the reduction in magnitude of horizontal displacement across the specimen. The soil near the loading place has more movement in comparison with the soil located near the rear wall which indicates the pattern of distribution of pull-out force along the specimen. Also, as the value of the confining pressure increases the initial movement of the soil particles occurs for the bigger pull-out force and displacement of the geogrid which is further evidence that the interaction between soil and geogrid is directly related to the value of confining pressure.

By looking at the direction of the vector of displacement in Figures 6.3-6.16 it is evident that dilation occurs for all tests with different confining pressure values and that greater dilation occurs in the tests with lower confining pressure.

From the horizontal displacement contours can be observed that the boundary of the zone of influence of the geogrid was observed to be at a distance from the interface of 4 times the D_{50} of the soil.

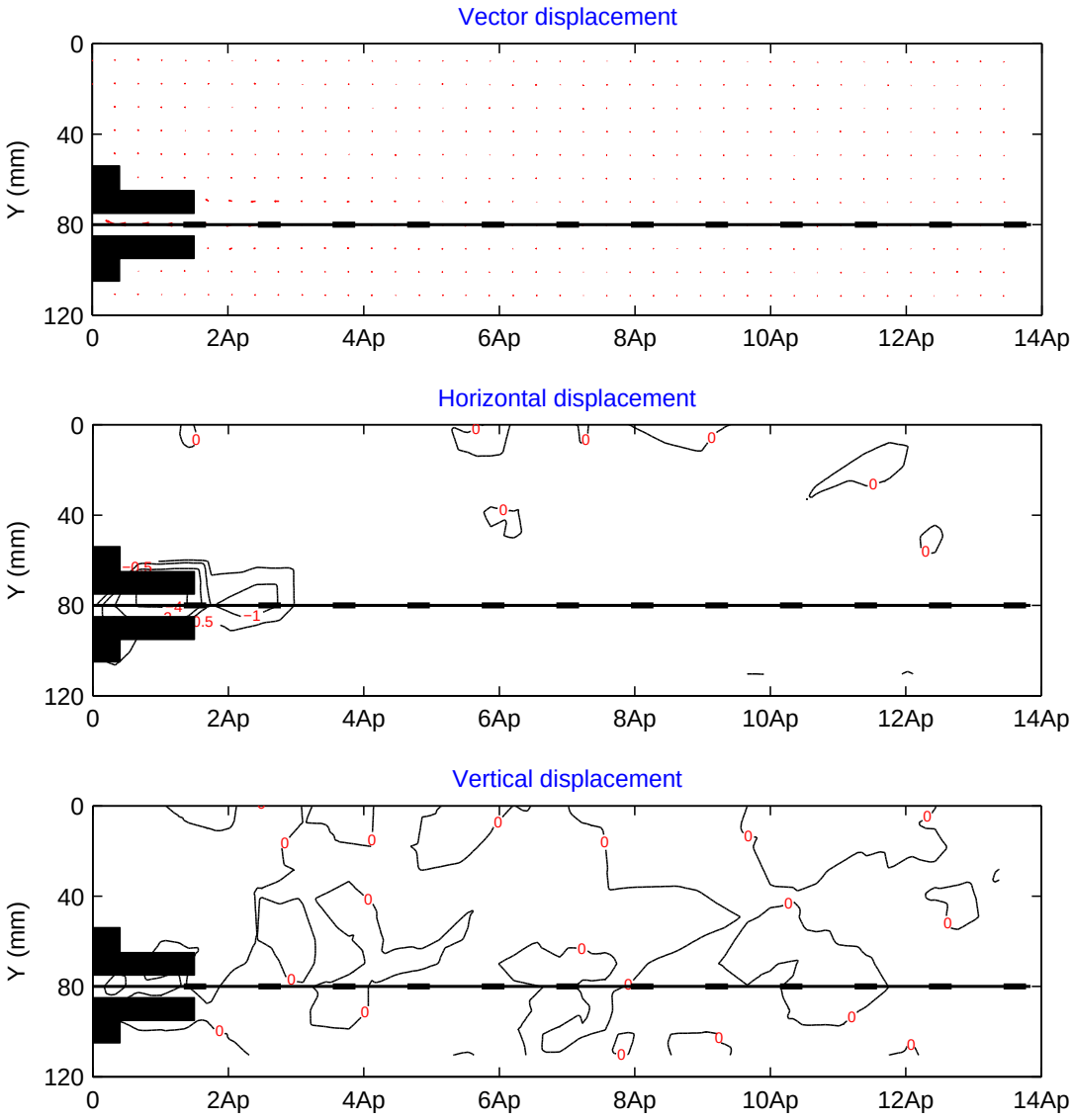

Figure 6.3: Cumulative PIV results at 5 mm axial tensile displacement of geogrid with 1200 kN/m stiffness under 12.5 kPa confining pressure

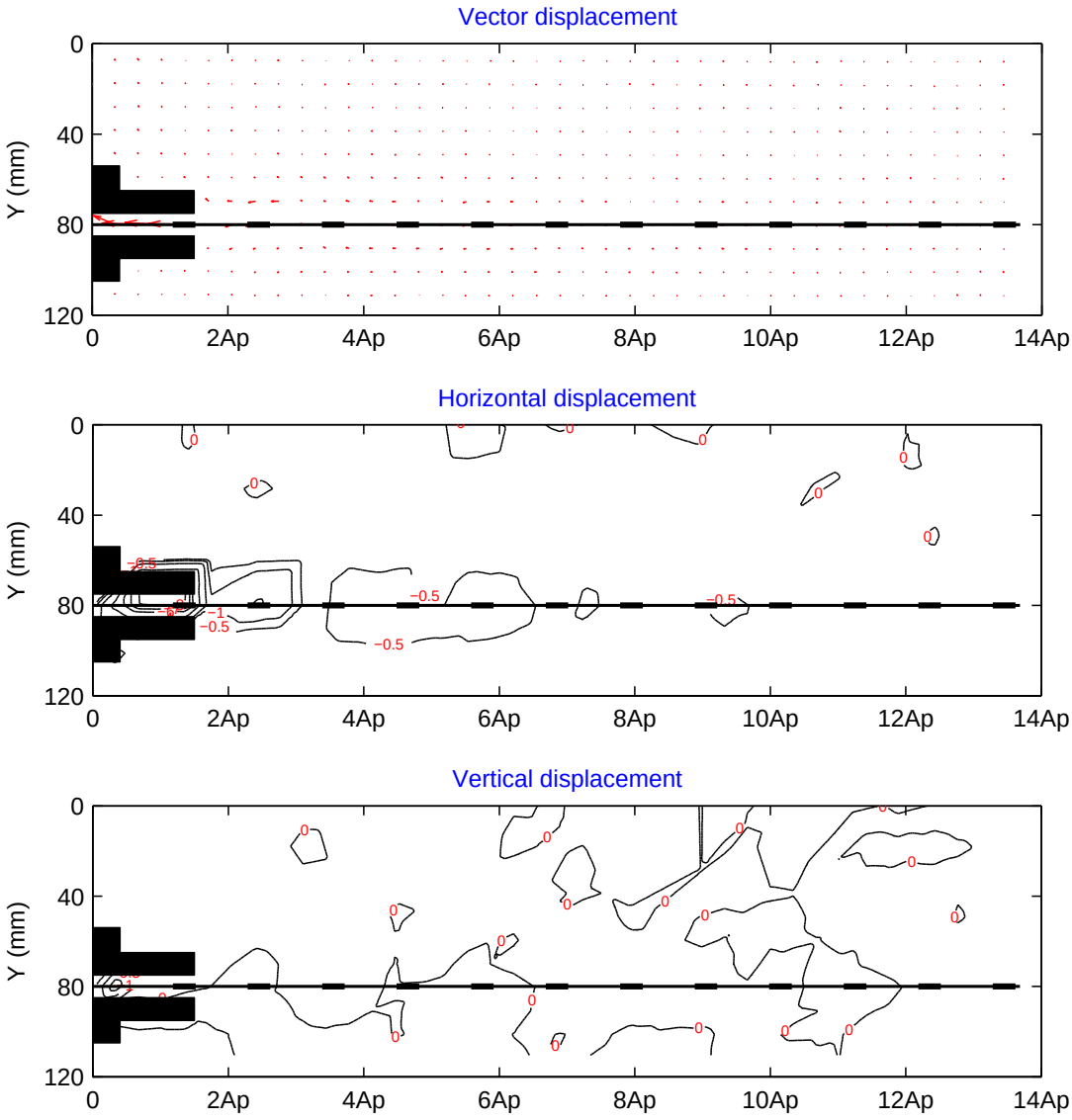

Figure 6.4: Cumulative PIV results at 10 mm axial tensile displacement of geogrid with 1200 kN/m stiffness under 12.5 kPa confining pressure

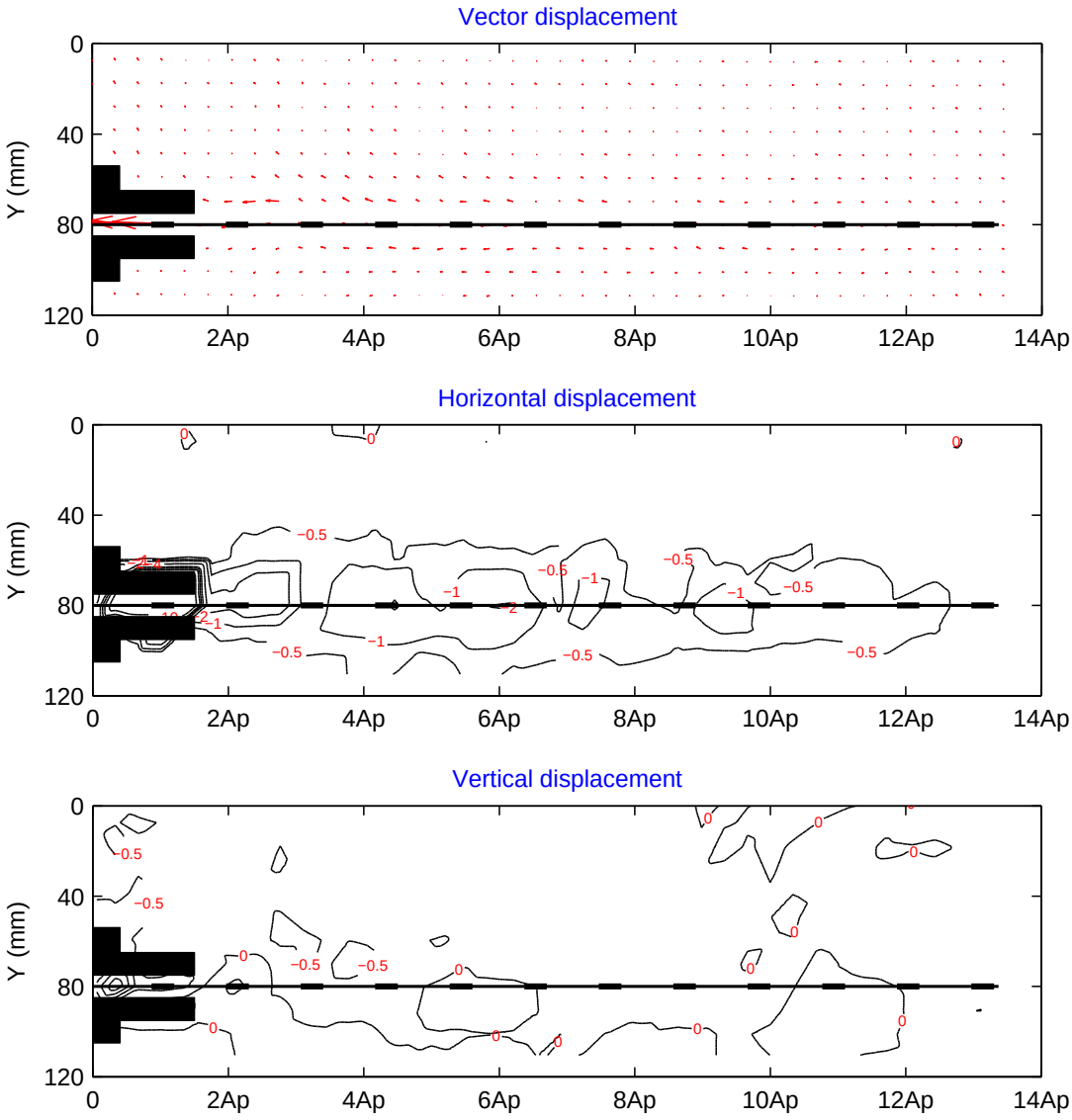

Figure 6.5: Cumulative PIV results at 20 mm axial tensile displacement of geogrid with 1200 kN/m stiffness under 12.5 kPa confining pressure

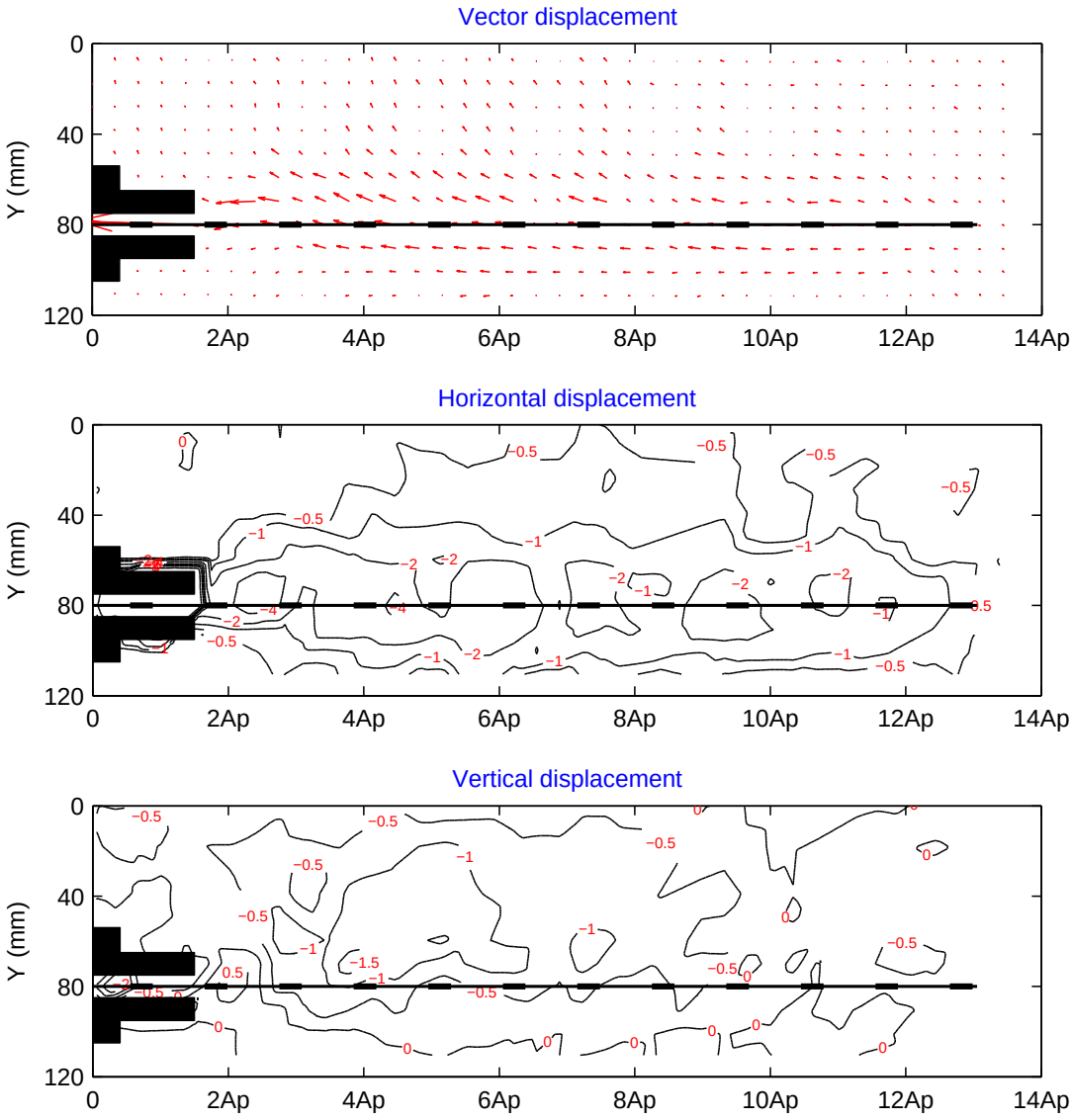

Figure 6.6: Cumulative PIV results at 30 mm axial tensile displacement of geogrid with 1200 kN/m stiffness under 12.5 kPa confining pressure

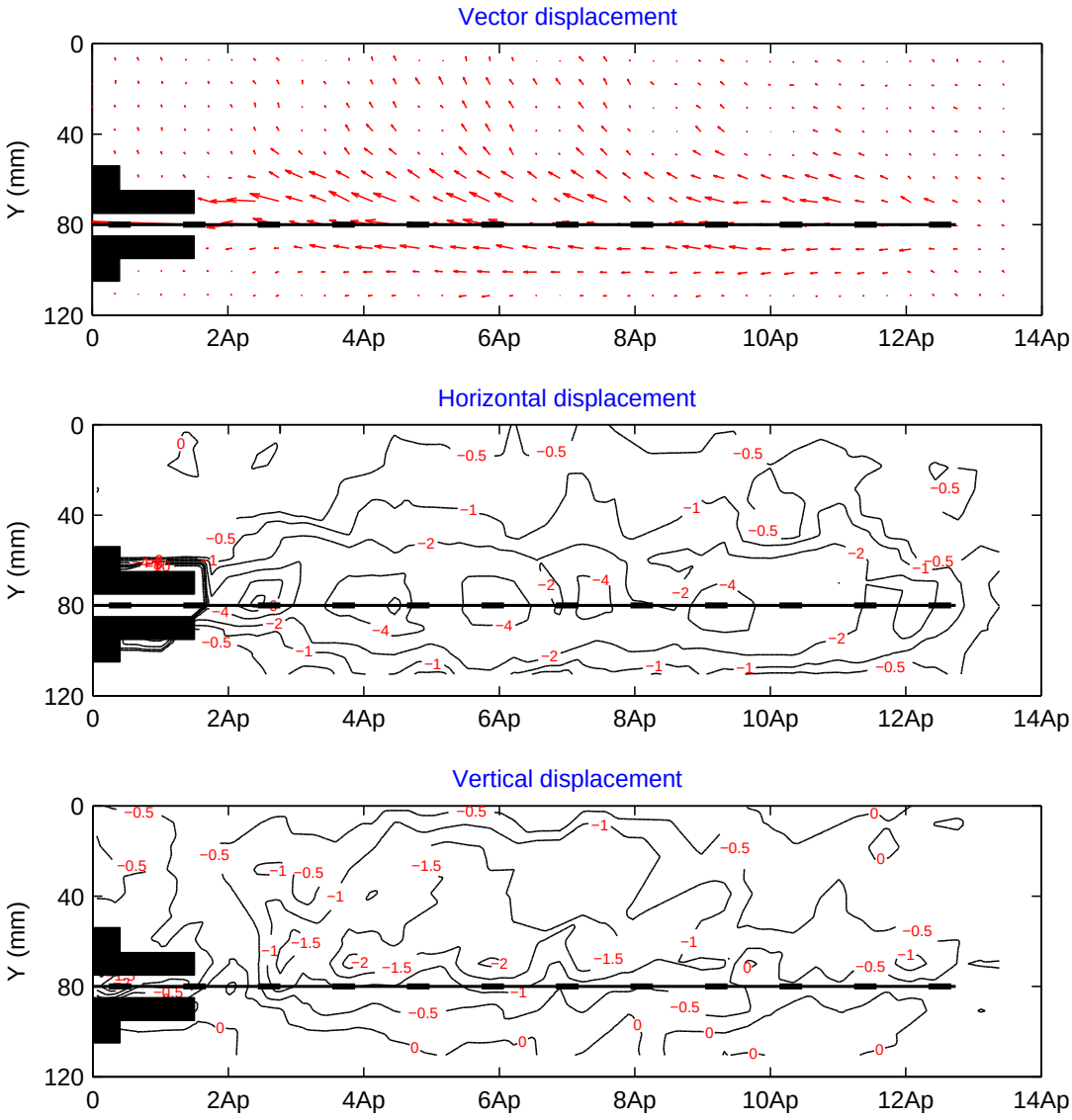

Figure 6.7: Cumulative PIV results at 40 mm axial tensile displacement of geogrid with 1200 kN/m stiffness under 12.5 kPa confining pressure

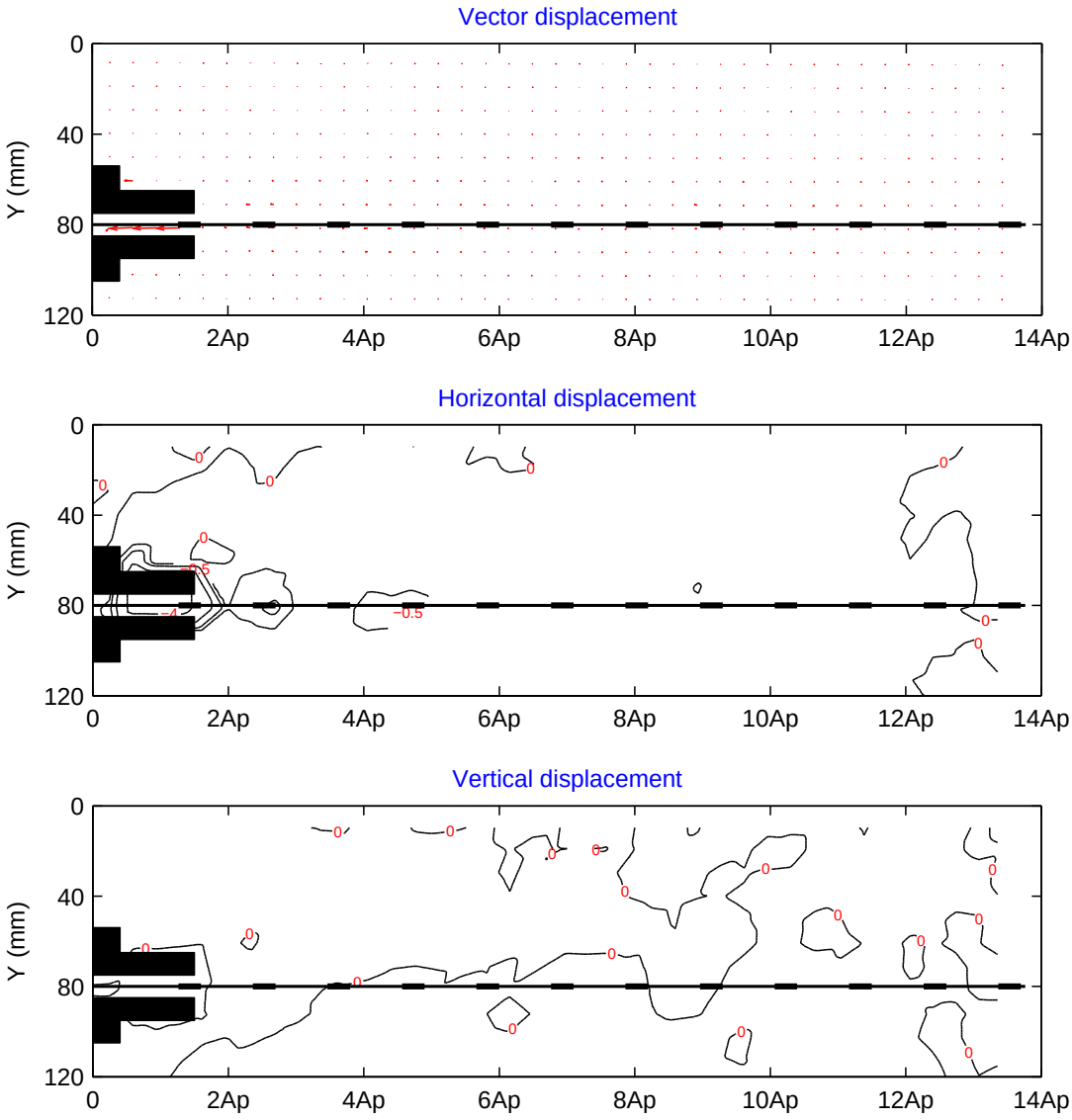

Figure 6.8: Cumulative PIV results at 7.5 mm axial tensile displacement of geogrid with 1200 kN/m stiffness under 25 kPa confining pressure

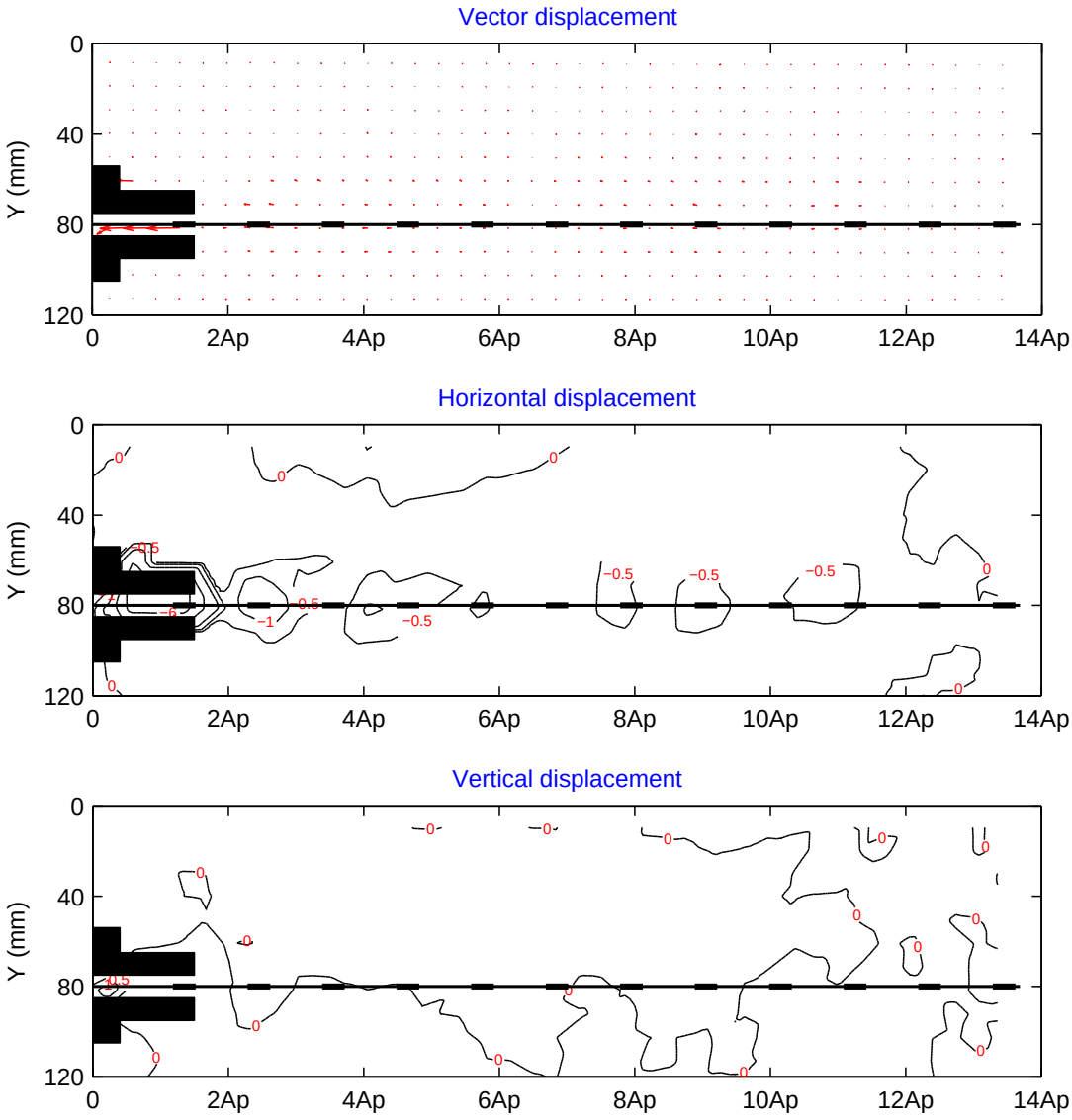

Figure 6.9: Cumulative PIV results at 10 mm axial tensile displacement of geogrid with 1200 kN/m stiffness under 25 kPa confining pressure

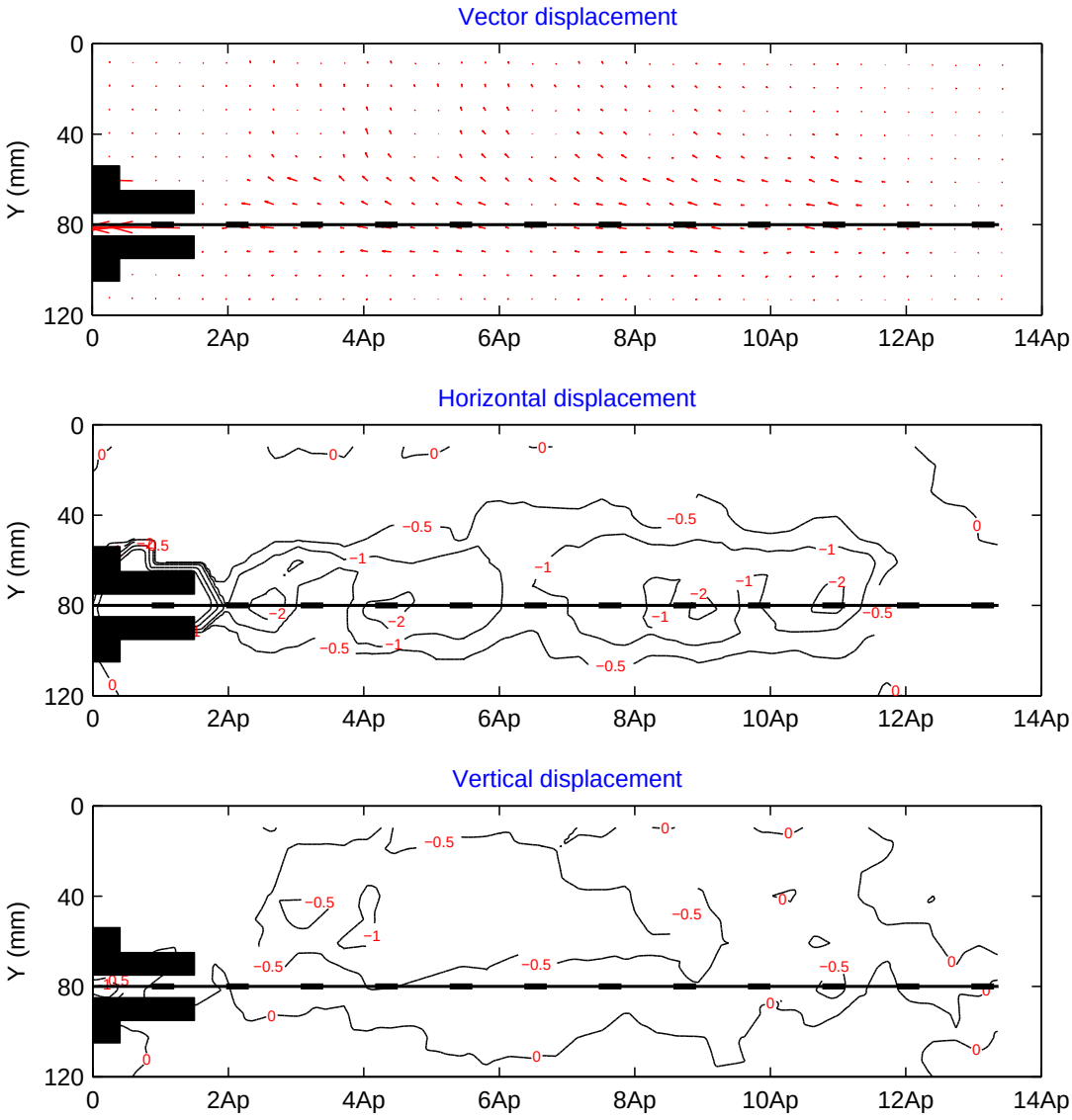

Figure 6.10: Cumulative PIV results at 20 mm axial tensile displacement of geogrid with 1200 kN/m stiffness under 25 kPa confining pressure

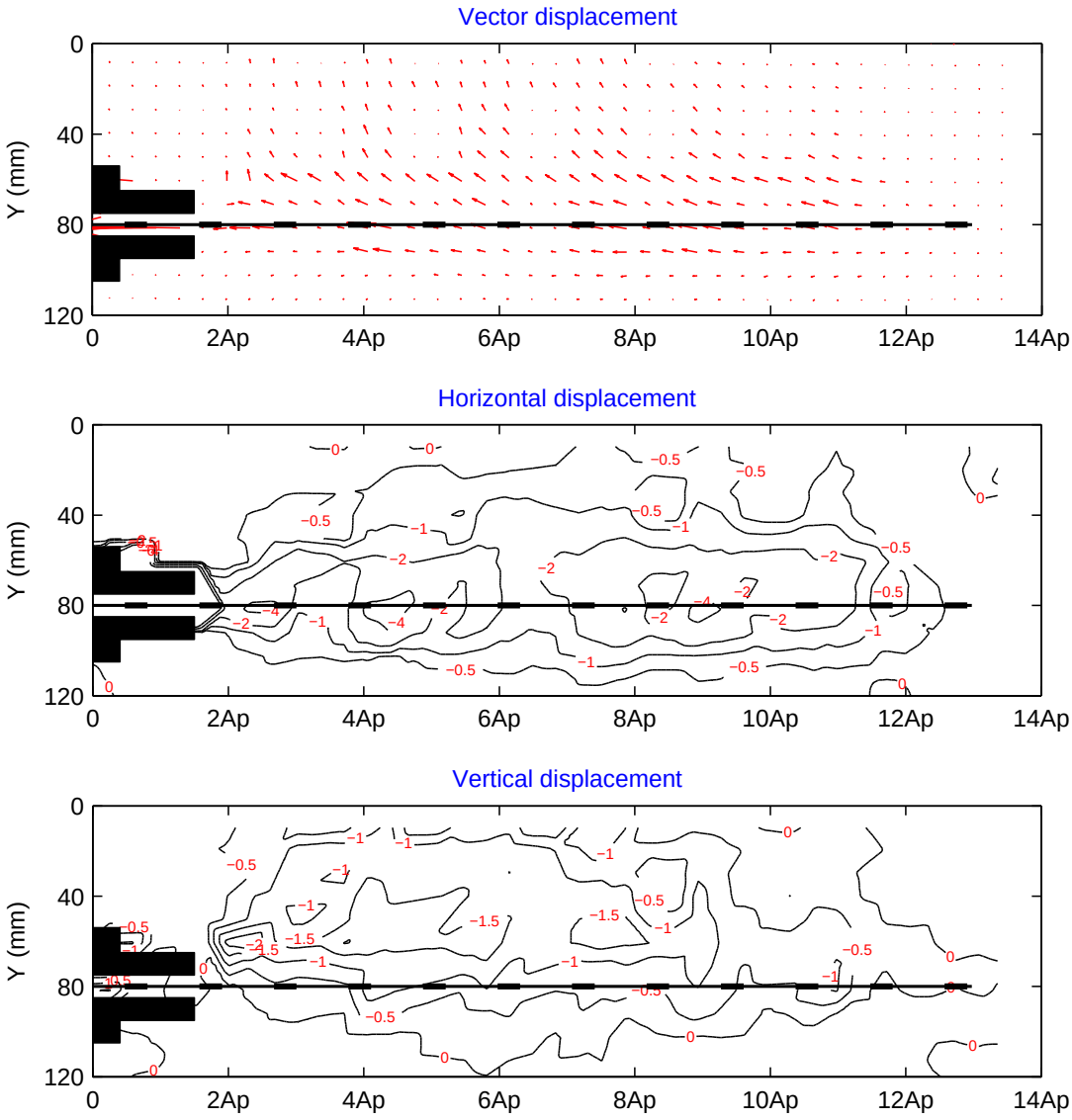

Figure 6.11: Cumulative PIV results at 30 mm axial tensile displacement of geogrid with 1200 kN/m stiffness under 25 kPa confining pressure

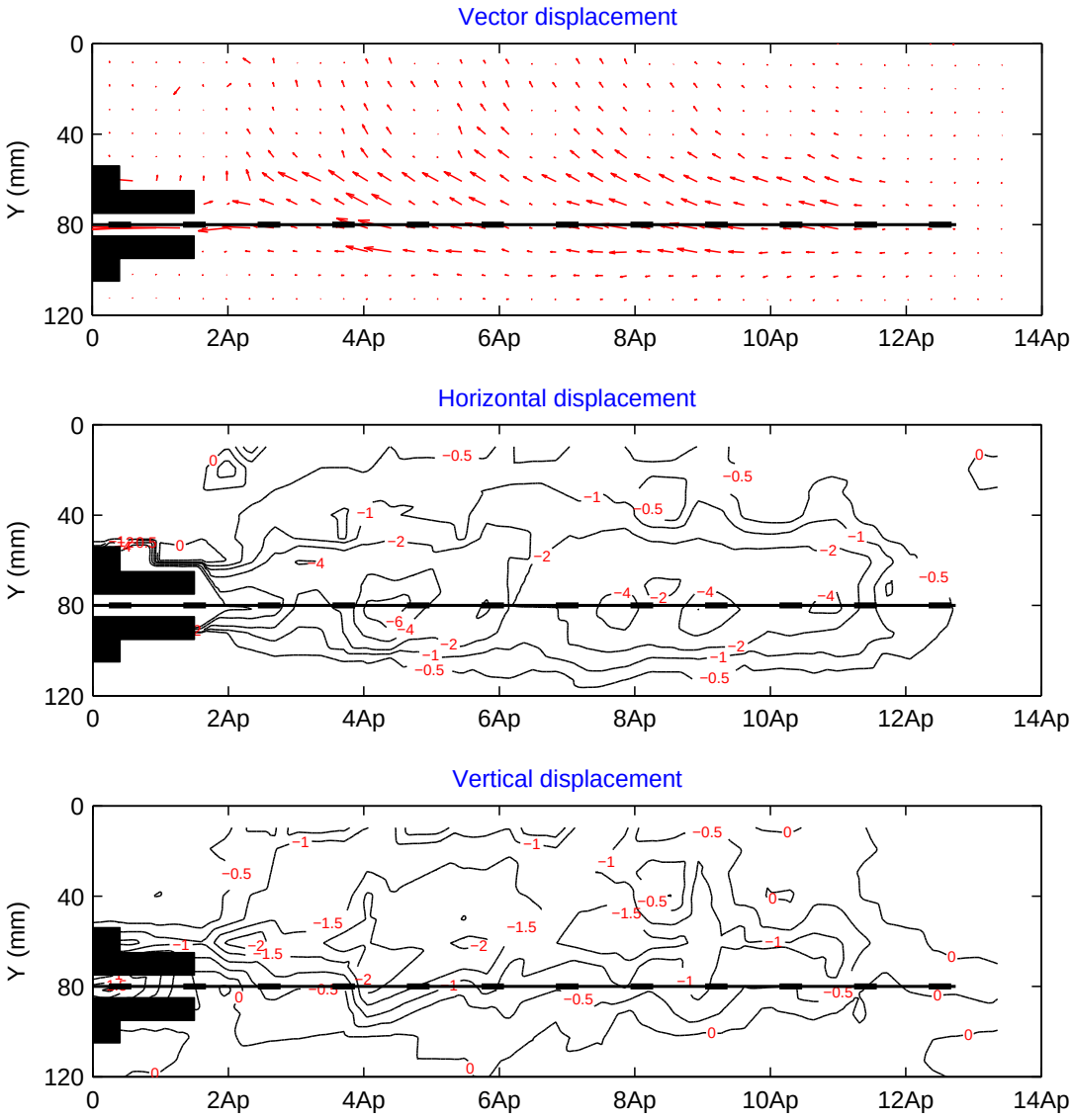

Figure 6.12: Cumulative PIV results at 40 mm axial tensile displacement of geogrid with 1200 kN/m stiffness under 25 kPa confining pressure

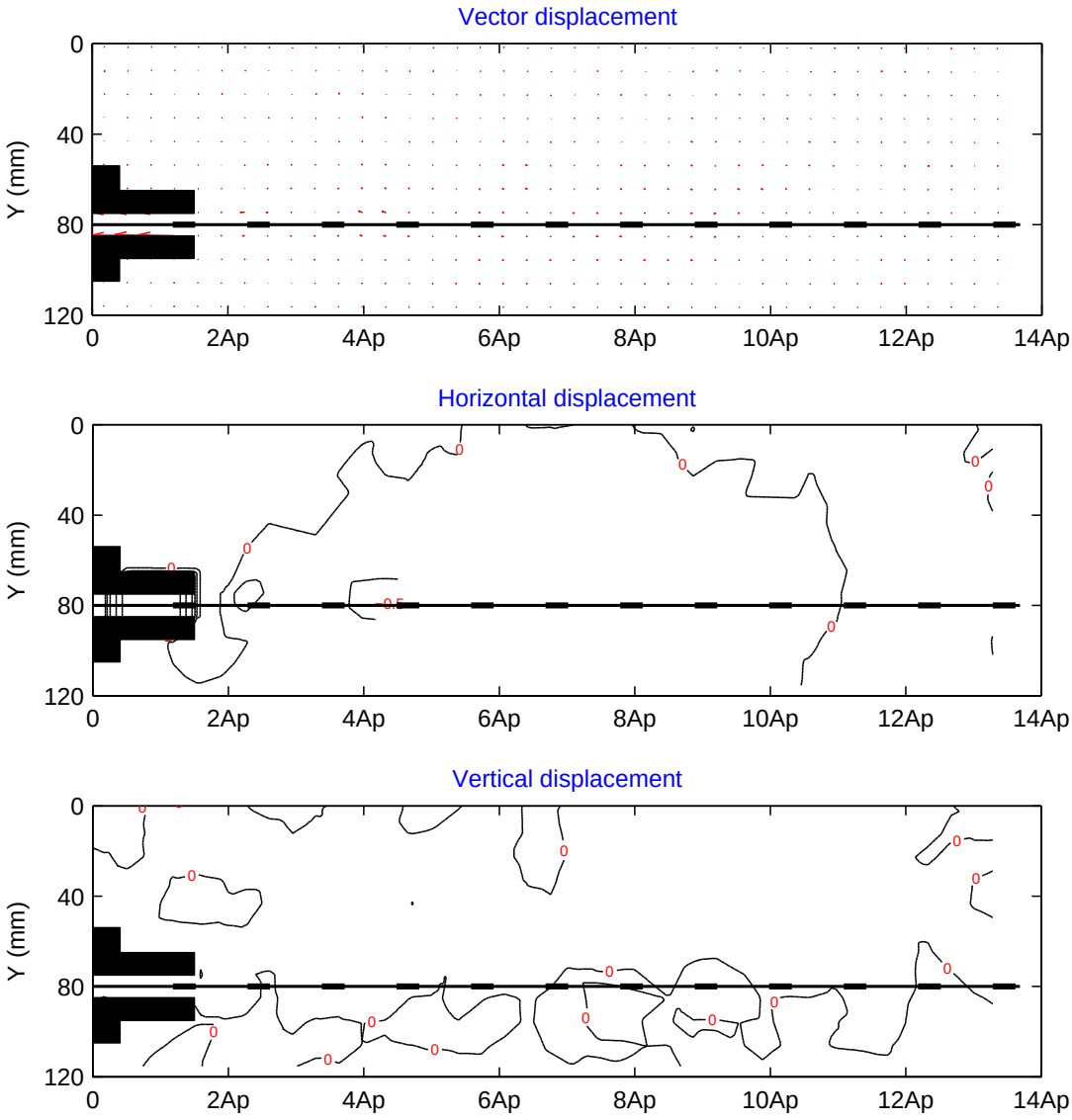

Figure 6.13: Cumulative PIV results at 10 mm axial tensile displacement of geogrid with 1200 kN/m stiffness under 50 kPa confining pressure

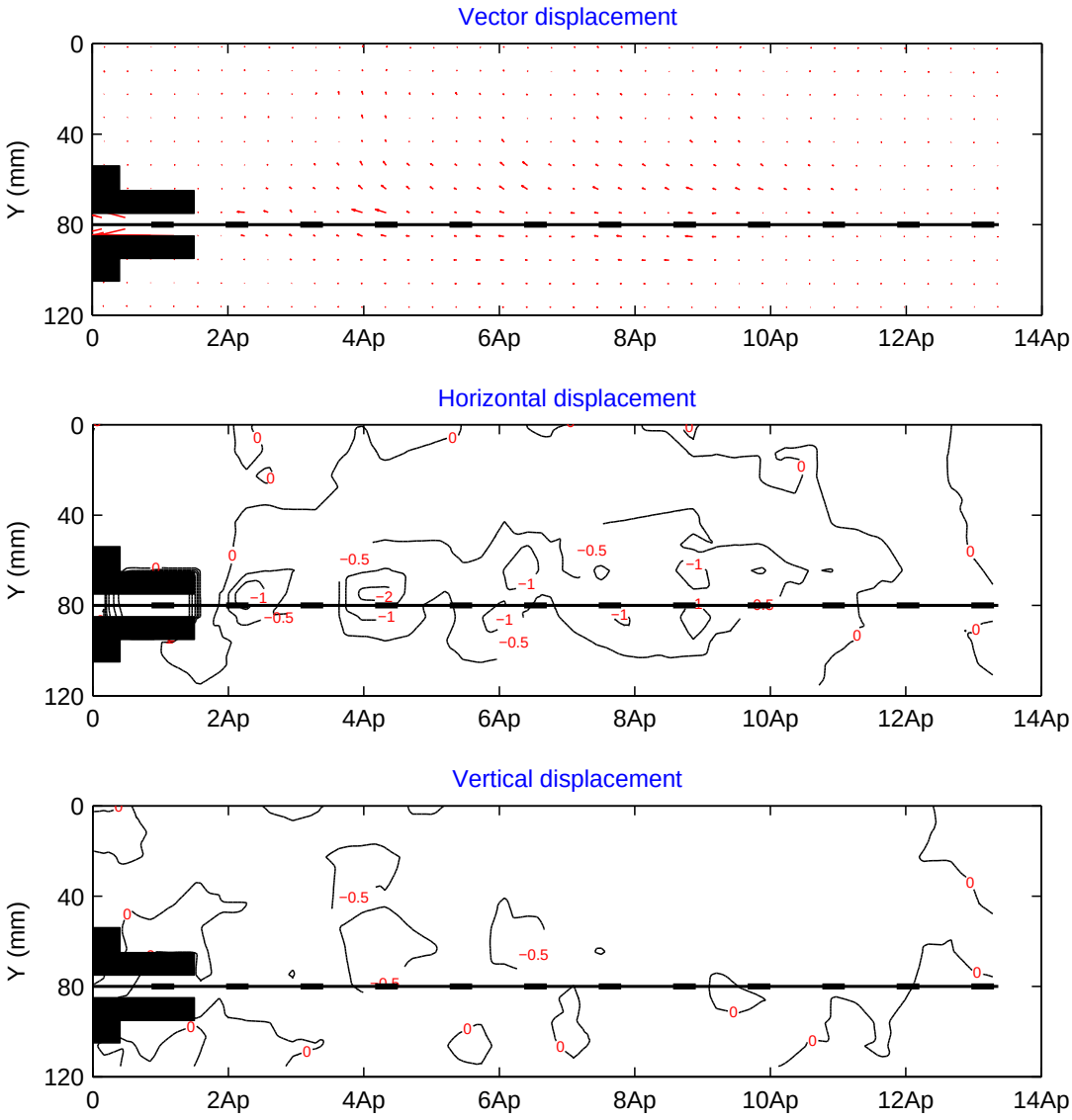

Figure 6.14: Cumulative PIV results at 20 mm axial tensile displacement of geogrid with 1200 kN/m stiffness under 50 kPa confining pressure

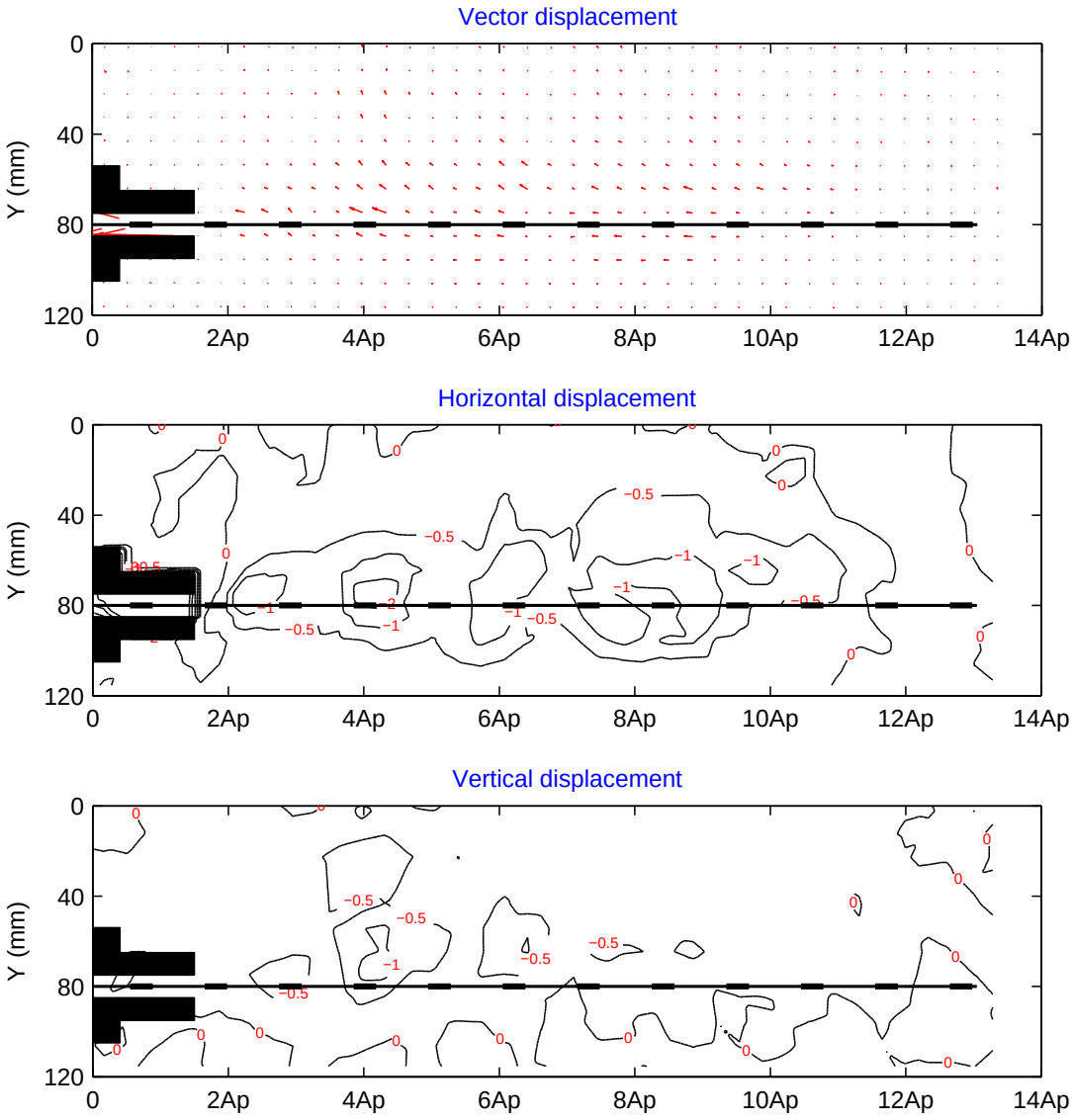

Figure 6.15: Cumulative PIV results at 30 mm axial tensile displacement of geogrid with 1200 kN/m stiffness under 50 kPa confining pressure

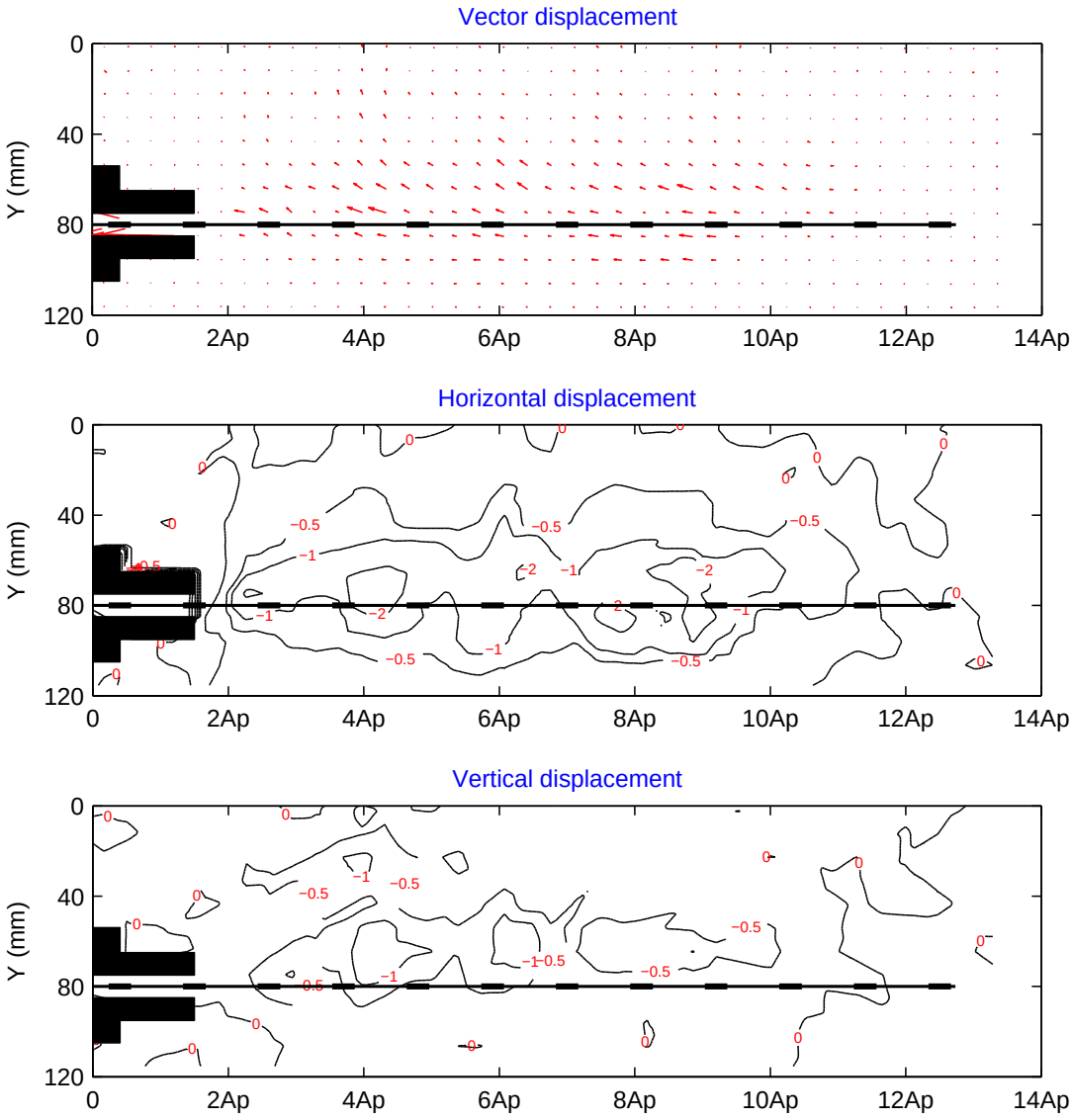

Figure 6.16: Cumulative PIV results at 40 mm axial tensile displacement of geogrid with 1200 kN/m stiffness under 50 kPa confining pressure

The incremental PIV results from 0 to 40 mm for 10 mm increments for a vector of horizontal and vertical displacement under three different values of confining pressure (12.5 kPa, 25 kPa and 50 kPa) show in Figures 6.17-6.28.

Incremental PIV results of the displacement contours for 12.5 kPa confining pressure indicate for the first 10 mm movement of geogrid, the maximum soil particles

displacement in the horizontal direction is -0.5 mm and -0.25 mm which was generated around the geogrid near the loading place and close to rear wall respectively.

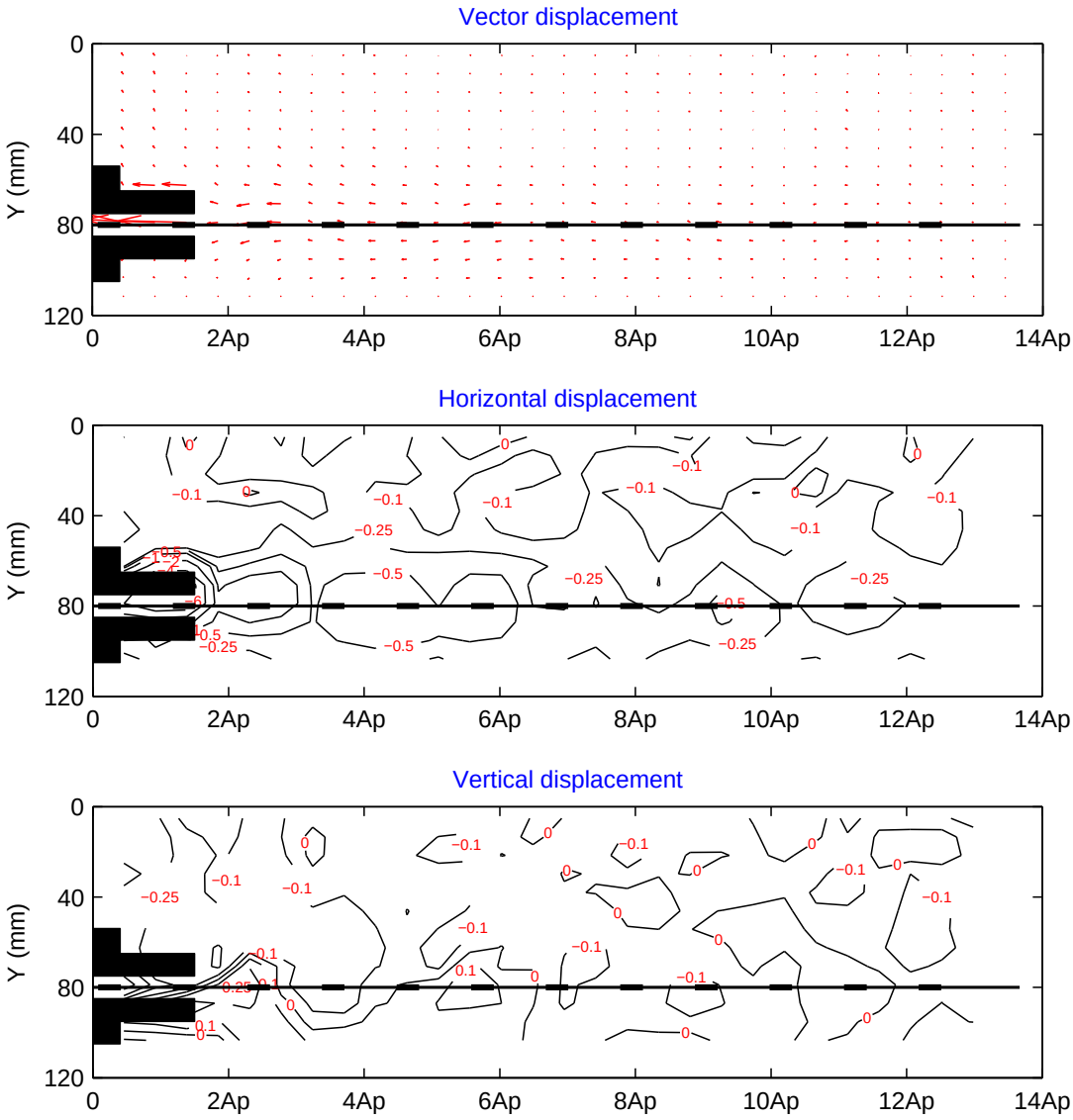

Figure 6.17: Incremental PIV results from 0 mm to 10 mm axial tensile displacement of geogrid with 1200 kN/m stiffness under 12.5 kPa confining pressure

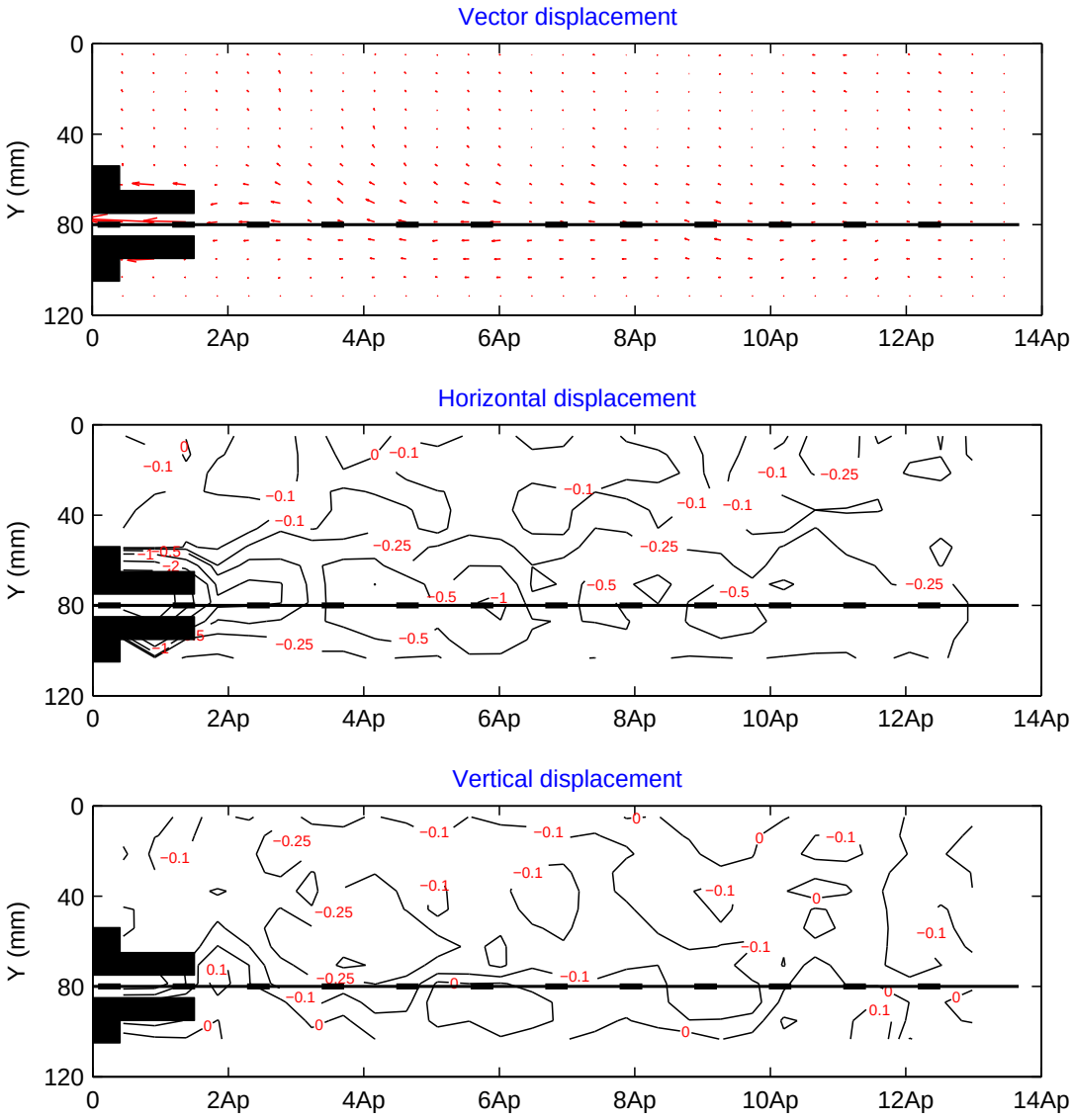

Figure 6.18: Incremental PIV results from 10 mm to 20 mm axial tensile displacement of geogrid with 1200 kN/m stiffness under 12.5 kPa confining pressure

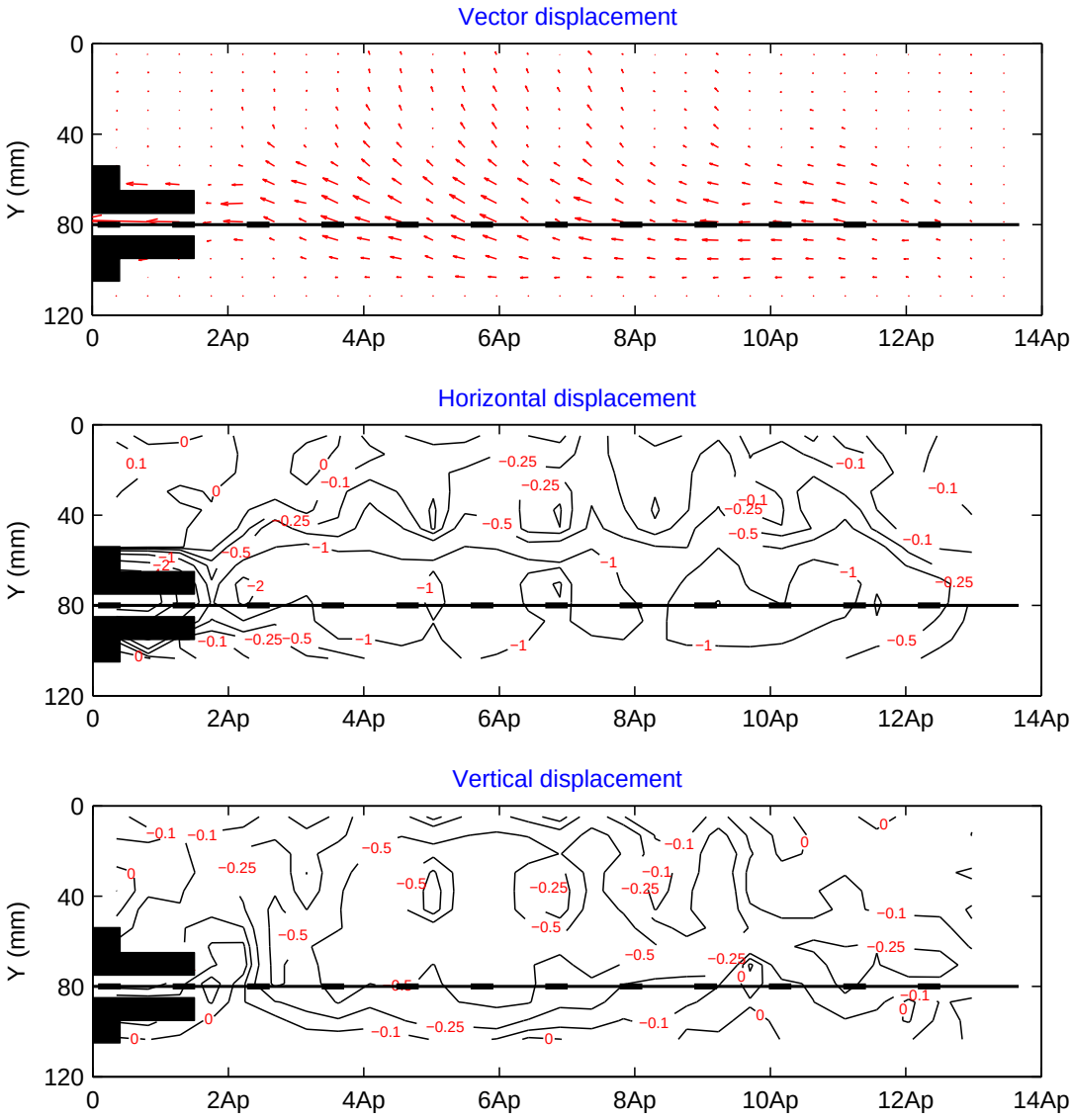

Figure 6.19: Incremental PIV results from 20 mm to 30 mm axial tensile displacement of geogrid with 1200 kN/m stiffness under 12.5 kPa confining pressure

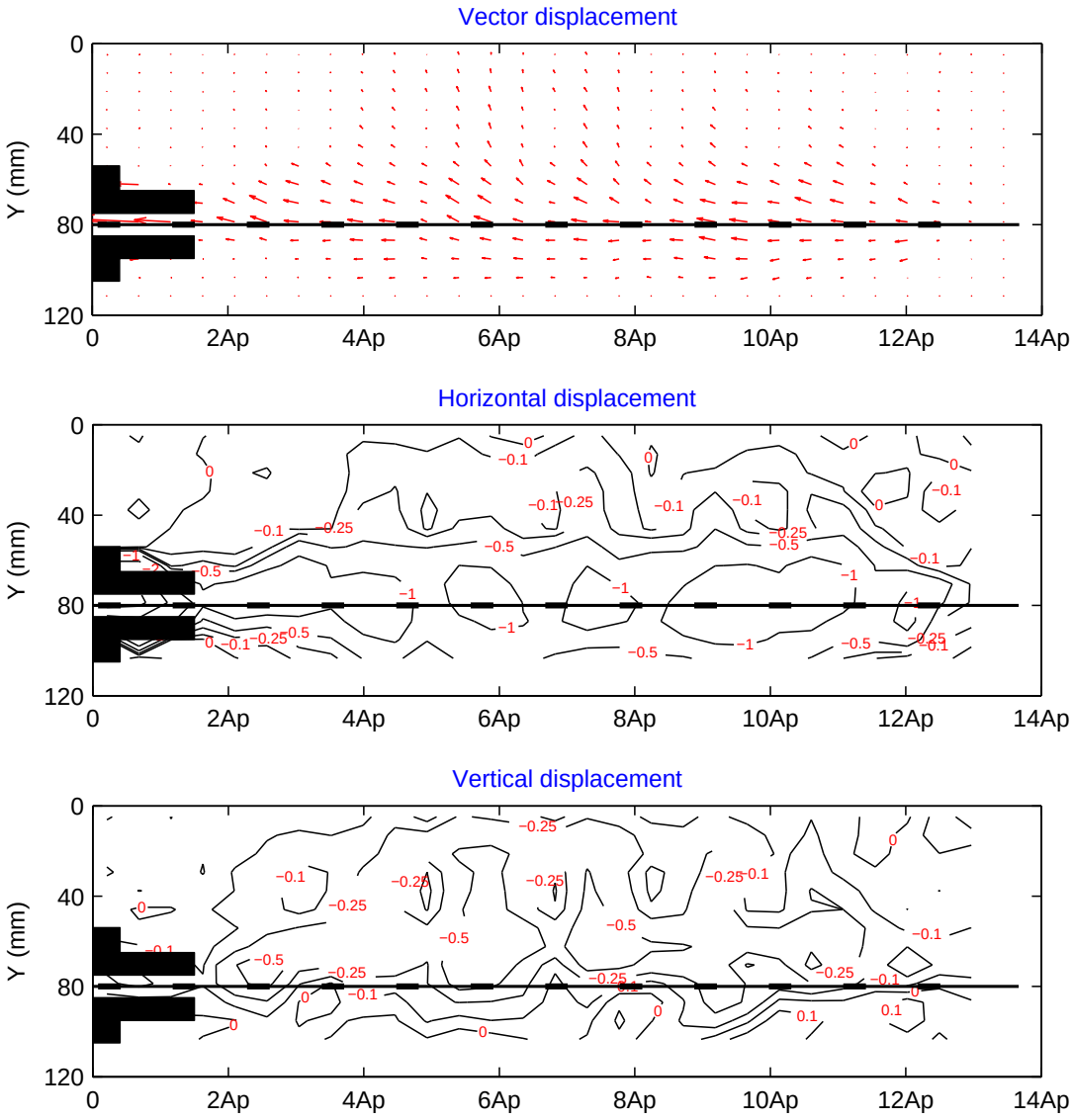

Figure 6.20: Incremental PIV results from 30 mm to 40 mm axial tensile displacement of geogrid with 1200 kN/m stiffness under 12.5 kPa confining pressure

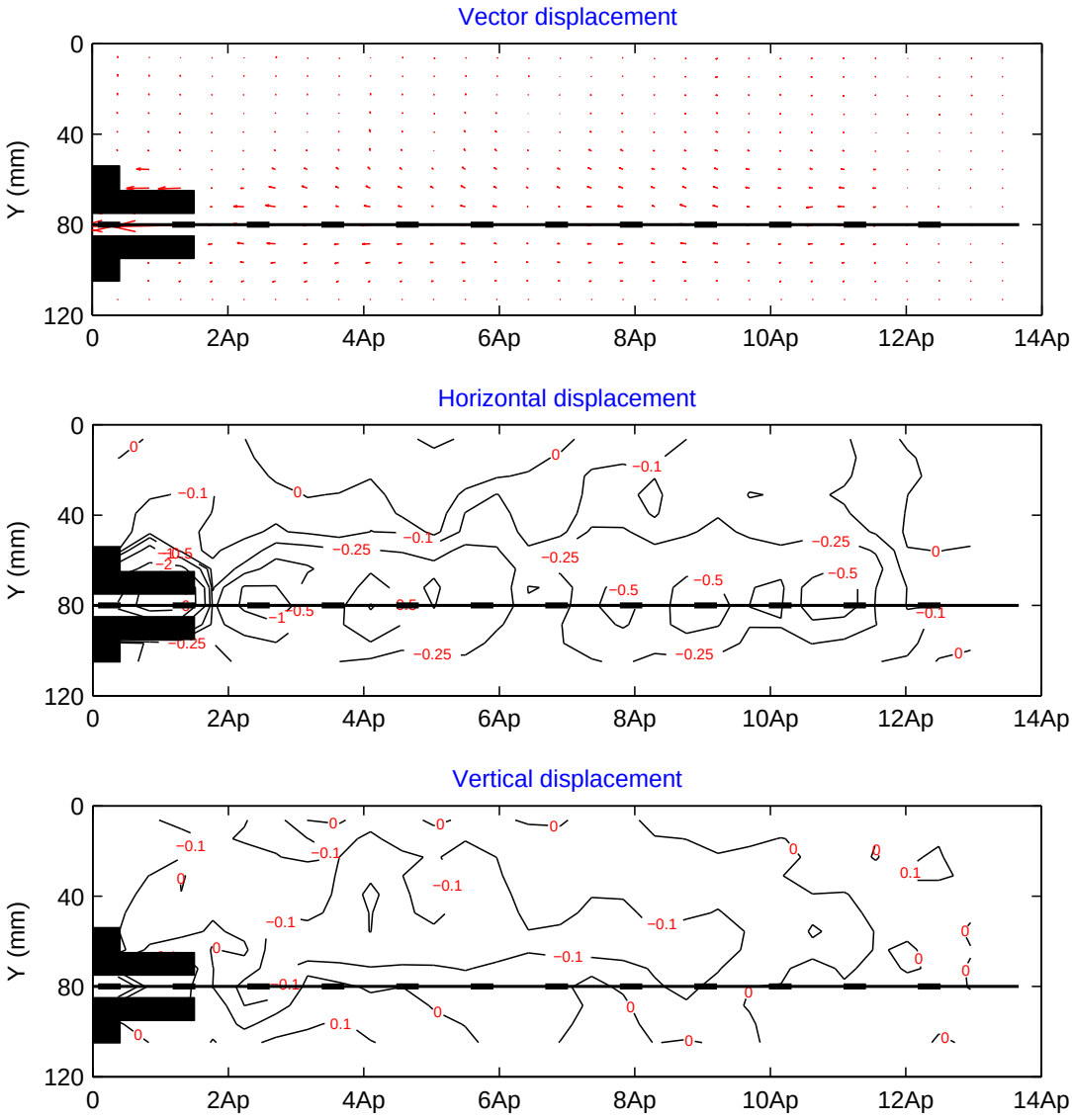

Figure 6.21: Incremental PIV results from 0 mm to 10 mm axial tensile displacement of geogrid with 1200 kN/m stiffness under 25 kPa confining pressure

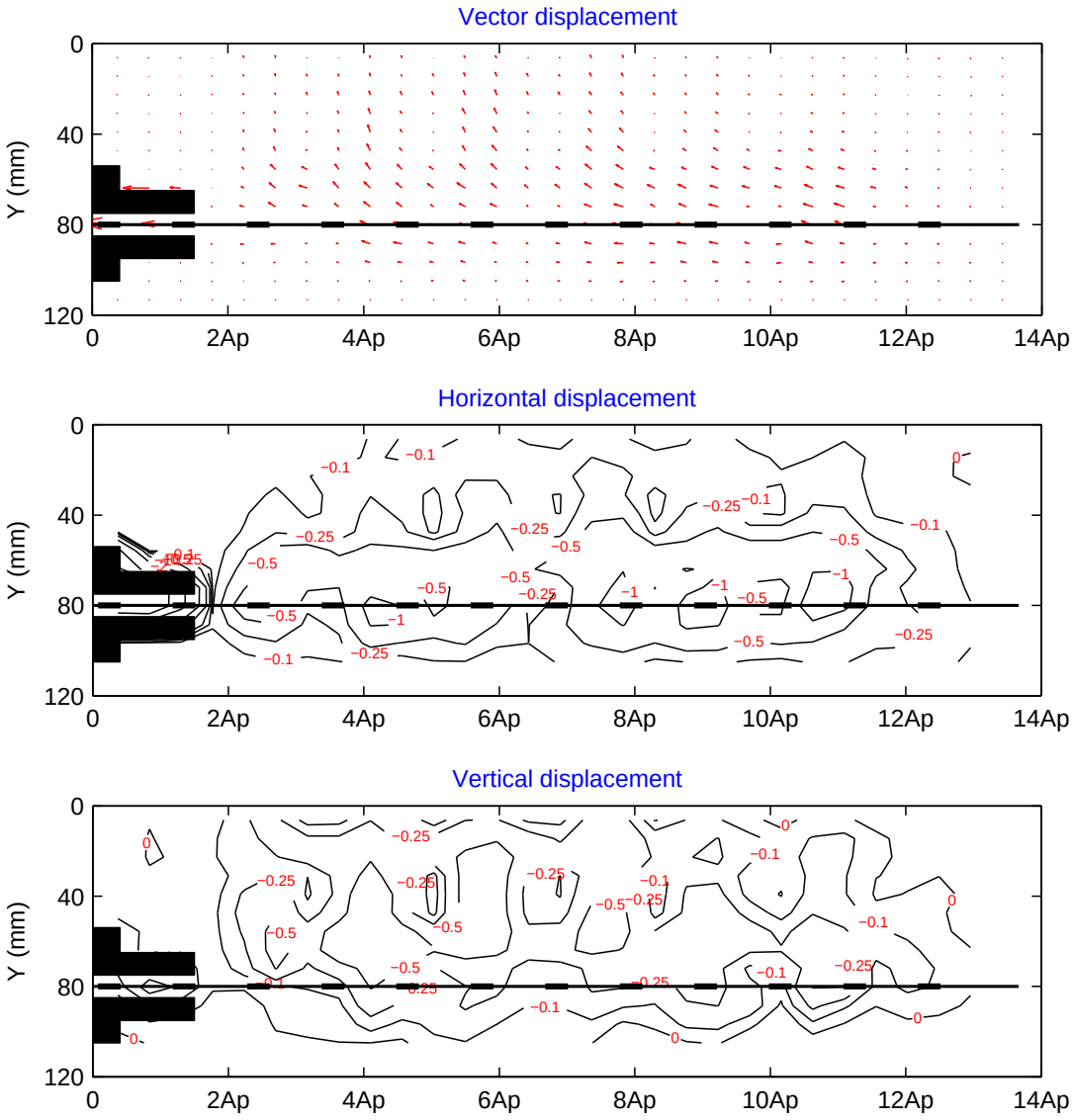

Figure 6.22: Incremental PIV results from 10 mm to 20 mm axial tensile displacement of geogrid with 1200 kN/m stiffness under 25 kPa confining pressure

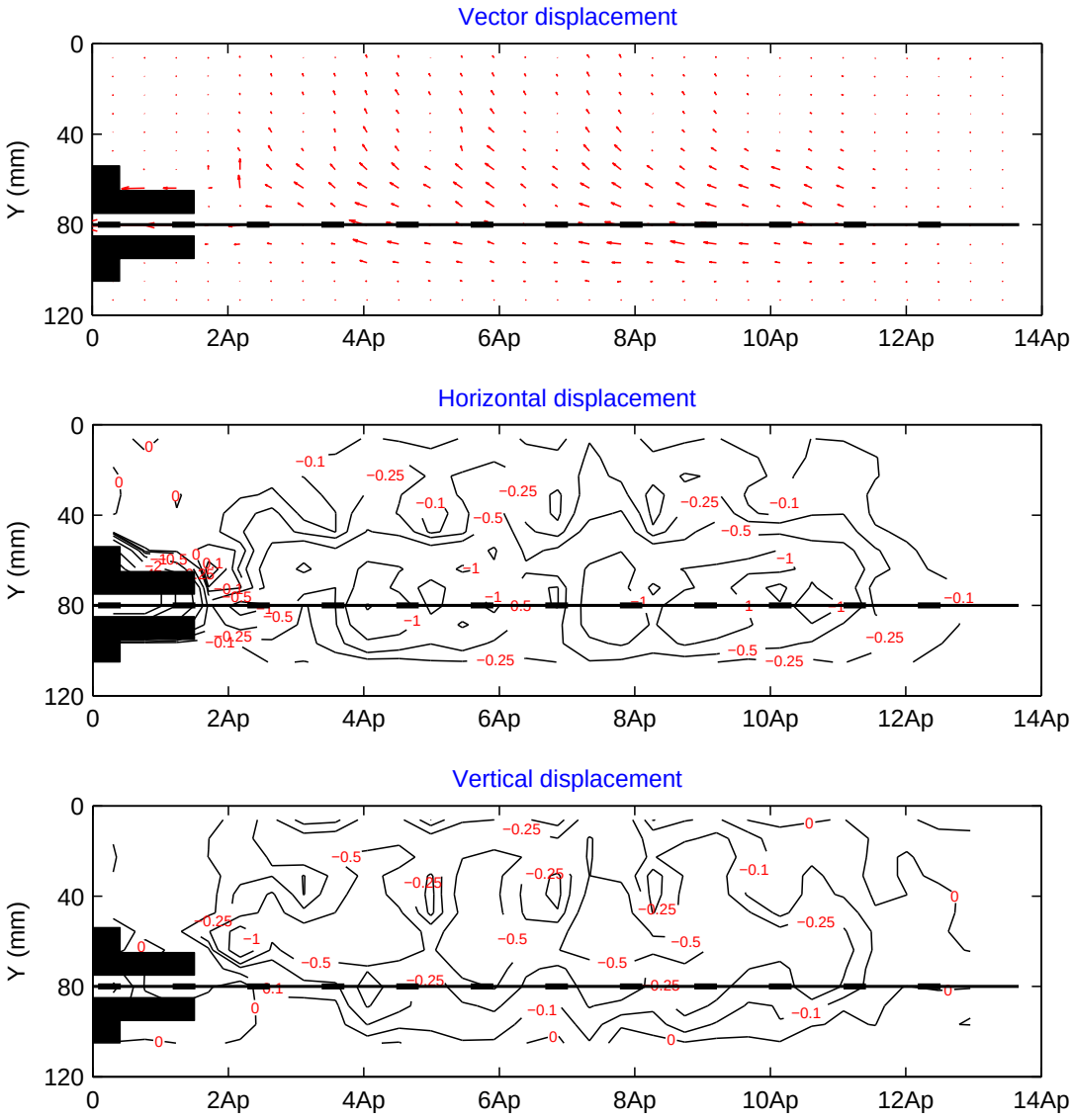

Figure 6.23: Incremental PIV results from 20 mm to 30 mm axial tensile displacement of geogrid with 1200 kN/m stiffness under 25 kPa confining pressure

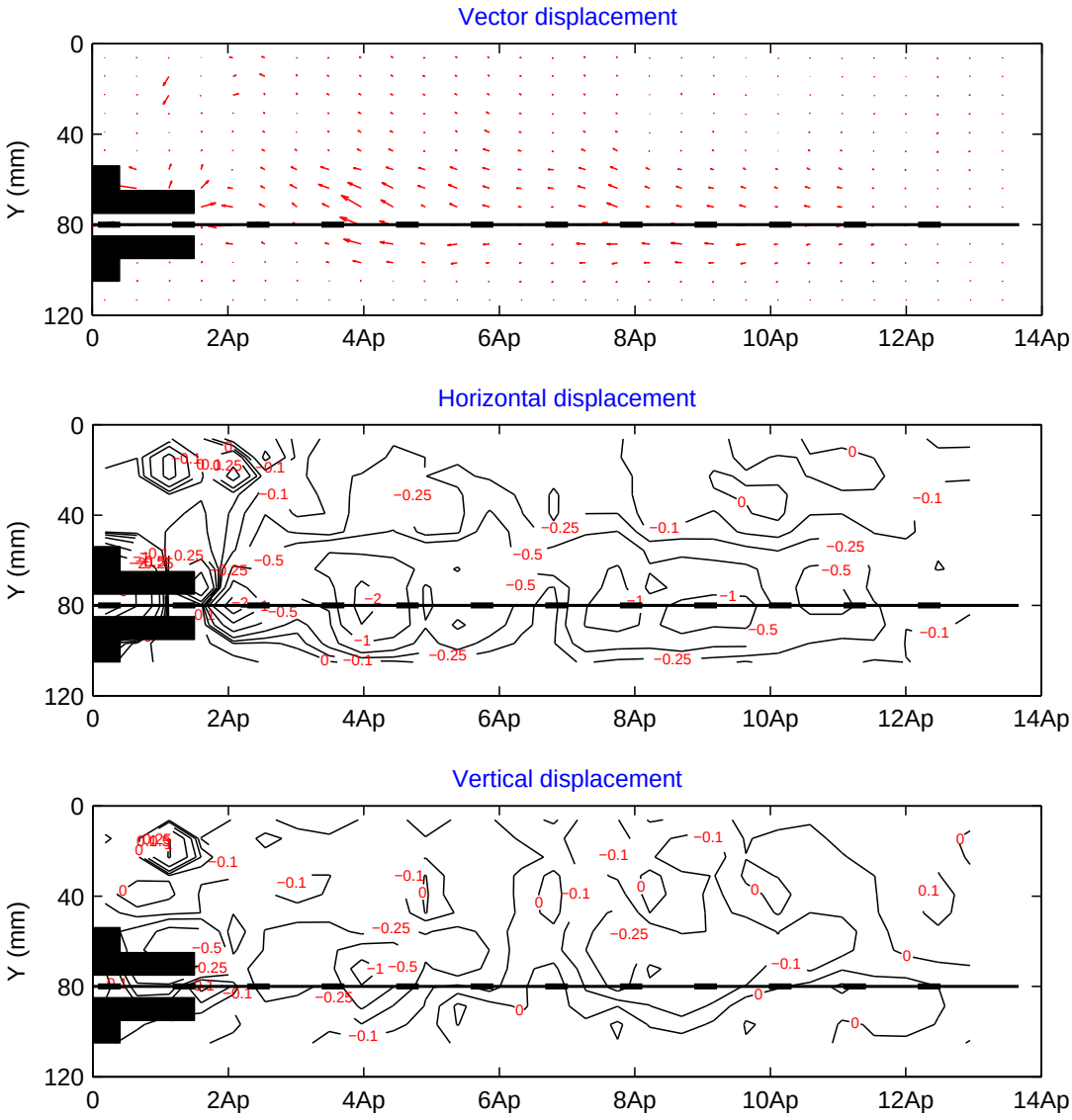

Figure 6.24: Incremental PIV results from 30 mm to 40 mm axial tensile displacement of geogrid with 1200 kN/m stiffness under 25 kPa confining pressure

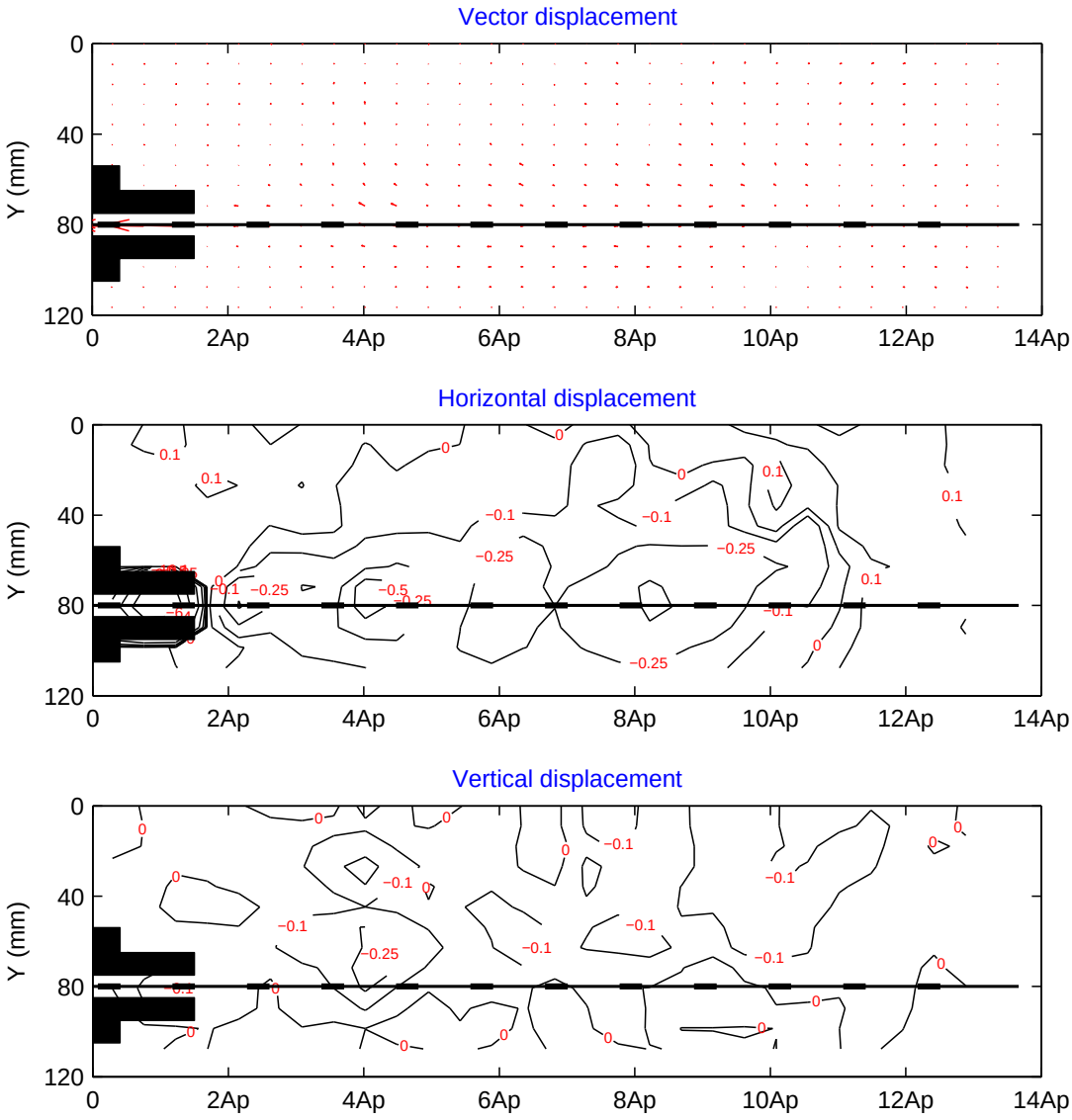

Figure 6.25: Incremental PIV results from 0 mm to 10 mm axial tensile displacement of geogrid with 1200 kN/m stiffness under 50 kPa confining pressure

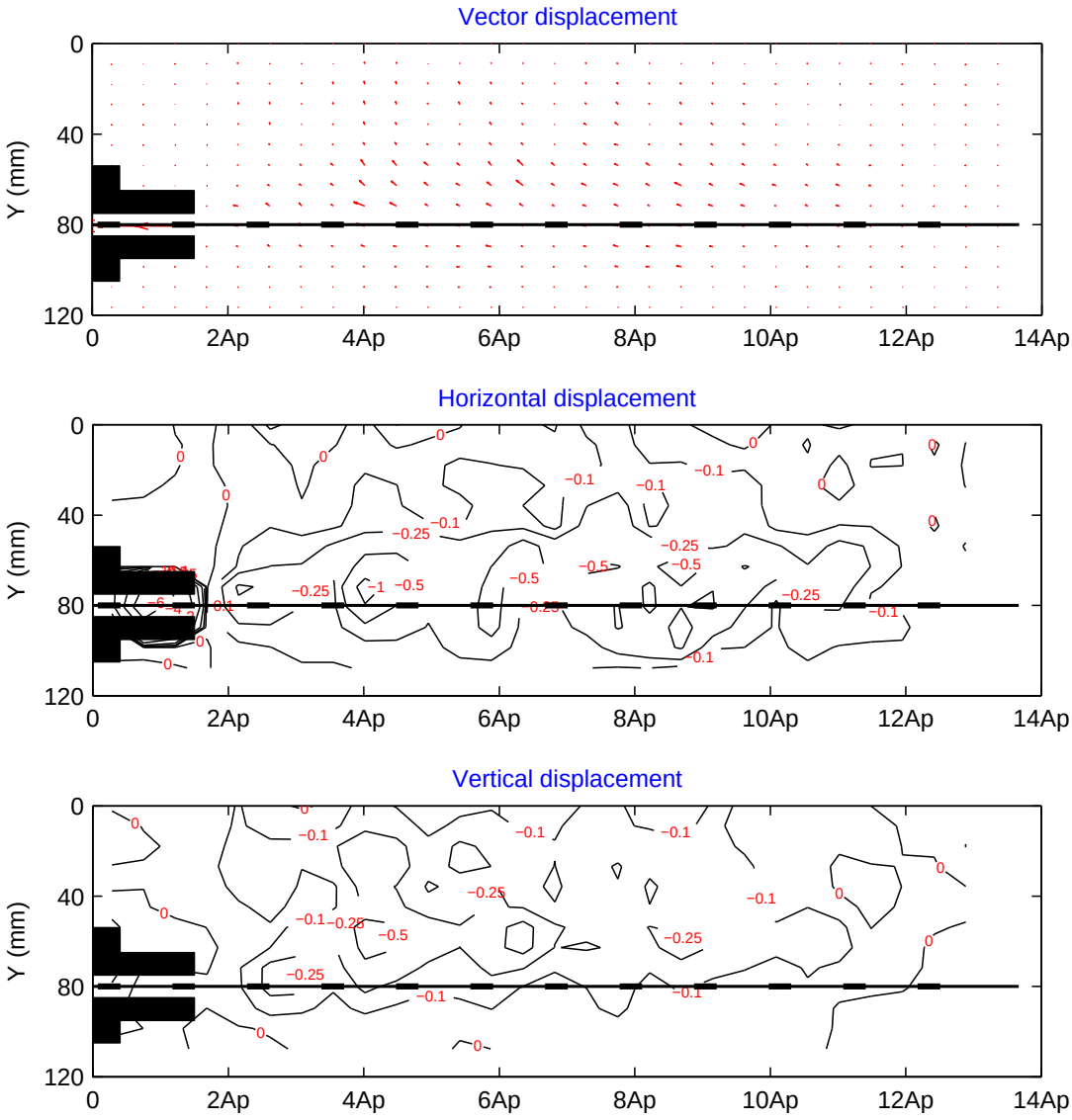

Figure 6.26: Incremental PIV results from 10 mm to 20 mm axial tensile displacement of geogrid with 1200 kN/m stiffness under 50 kPa confining pressure

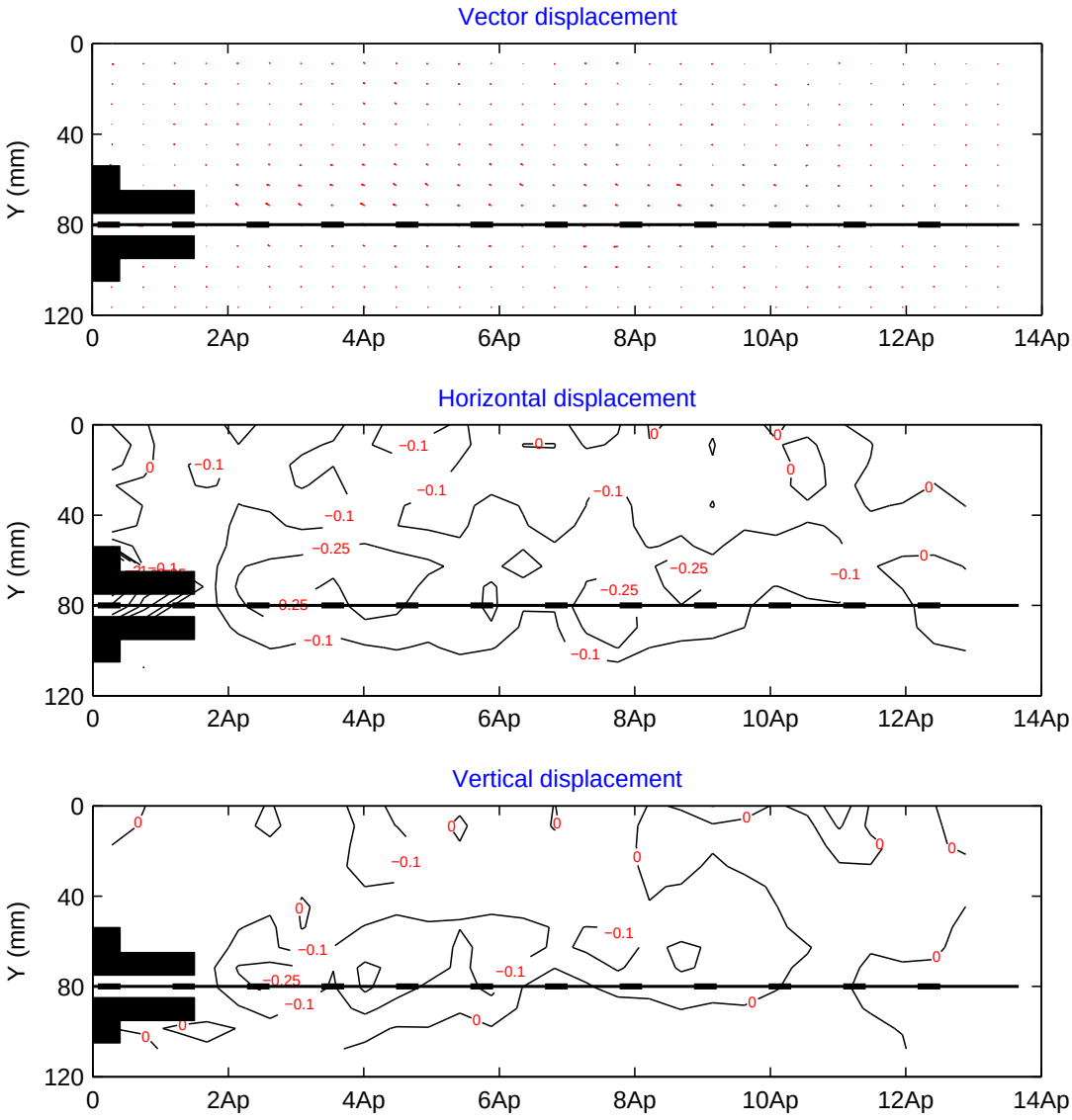

Figure 6.27: Incremental PIV results from 20 mm to 30 mm axial tensile displacement of geogrid with 1200 kN/m stiffness under 50 kPa confining pressure

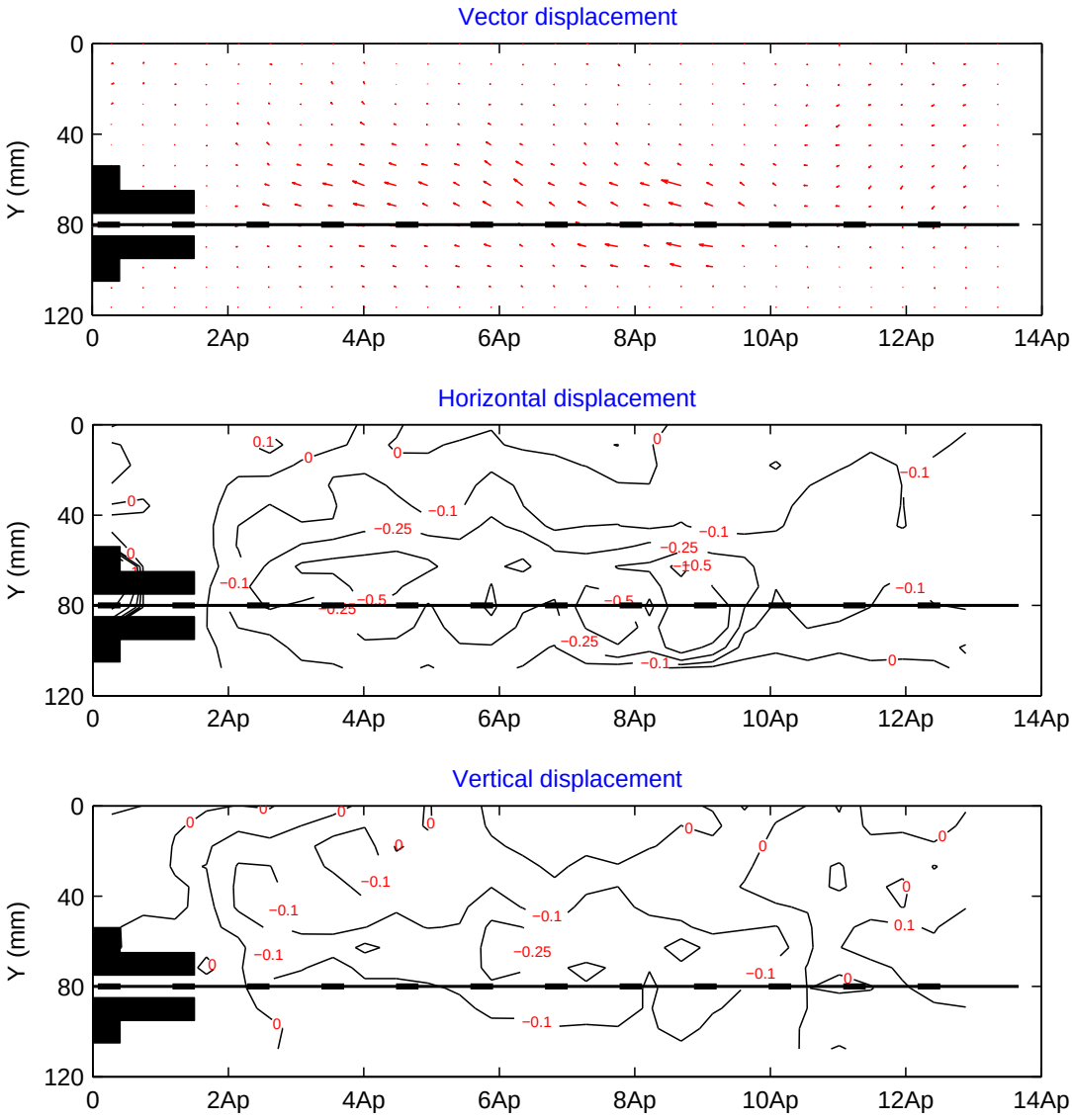

Figure 6.28: Incremental PIV results from 30 mm to 40 mm axial tensile displacement of geogrid with 1200 kN/m stiffness under 50 kPa confining pressure

6.2.1.2.2 Total shear strain contours

The interaction between soil and geogrid is a result of interlocking of particles, friction between soil particles and surface skin of the geogrid and the passive bearing capacity generated in front of the geogrid ribs. Due to interlocking, particulate material may expand or contract in volume as it is subject to shear strains.

Figures 6.29, 6.30 and 6.31 present the shear strains caused by pulling out the geogrid from soil under three different amounts of confining pressures 12.5 kPa, 25 kPa and 50 kPa. The results show that the maximum shearing is apparent around the geogrid with more concentration around geogrid ribs position with the zone of influence around 30 mm from the interface of geogrid which is equal with $4D_{50}$ of the soil particle. Of most interest is the comparison of shear strains induced by pulling out the geogrid from soil for two amounts of confining pressures 12.5 kPa and 25 kPa is not significantly different. The reason for this could be because the magnitude of the two lowest confining pressures is small in comparison with the stiffness of the geogrid. From the results of PIV analyses the maximum shear strain of these two tests is 20% which is reduced to half for higher confining pressure, 50 kPa.

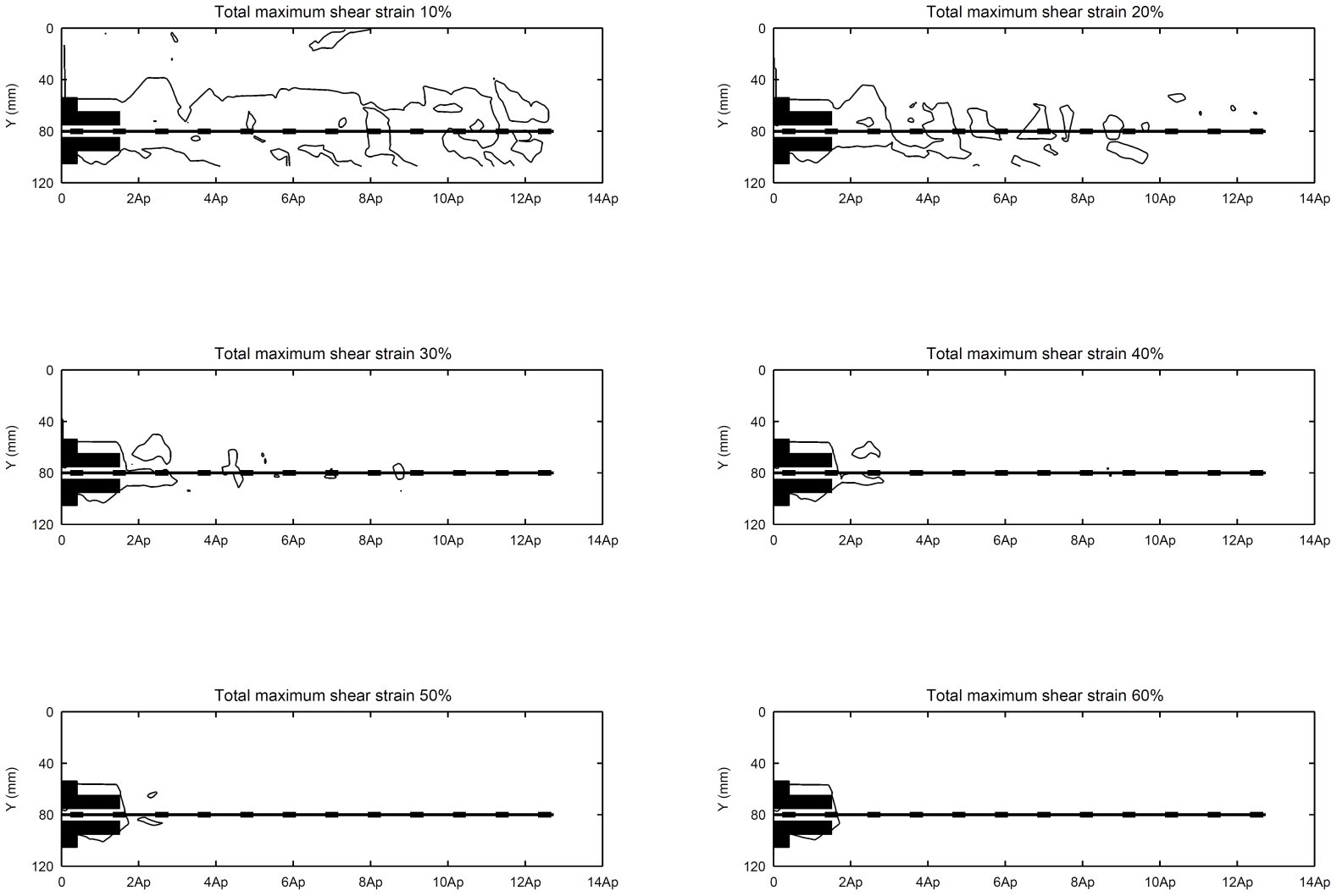

Figure 6.29: Cumulative shear strain for 40 mm axial tensile displacement of geogrid with 1200 kN/m stiffness under 12.5 kPa confining pressure

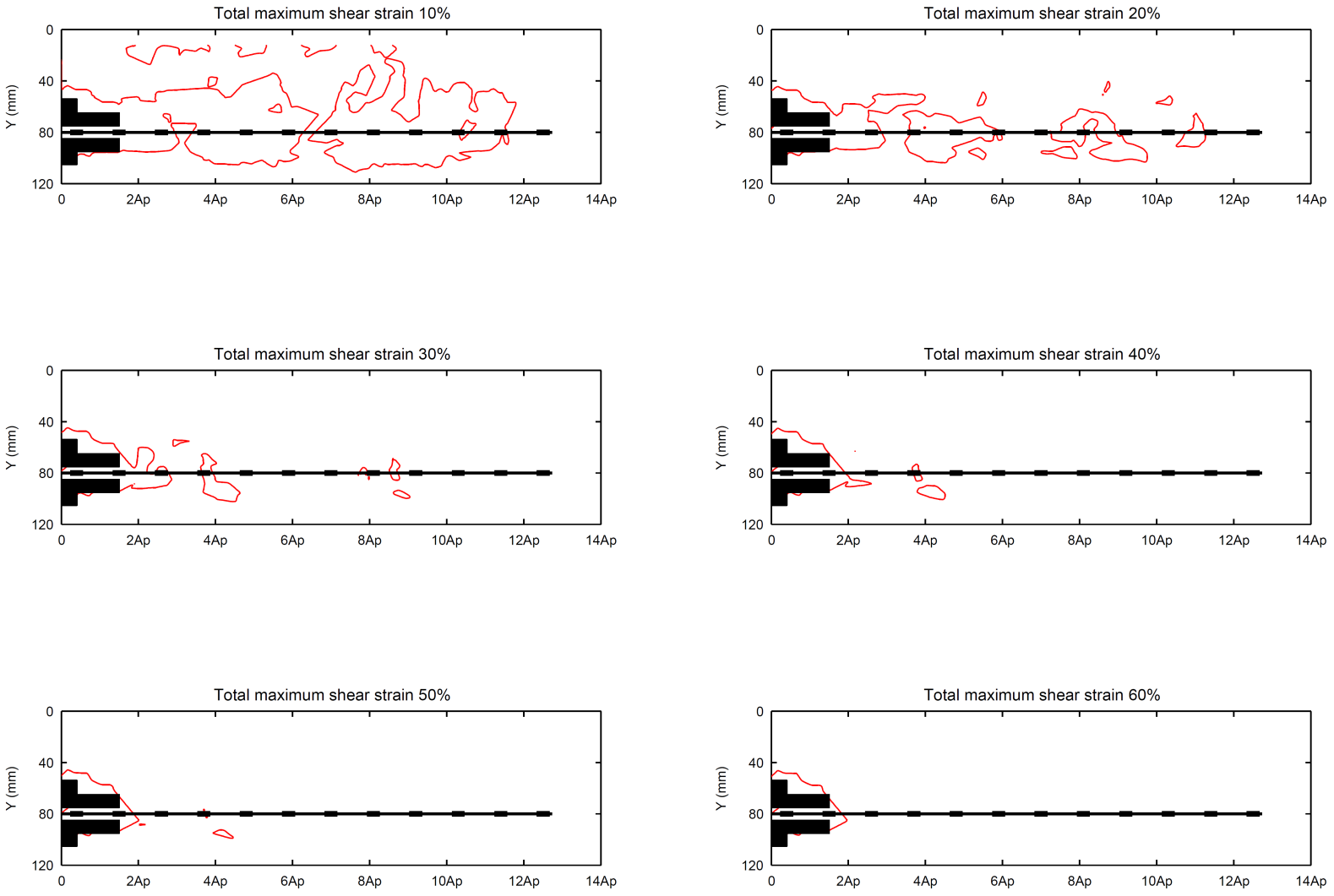

Figure 6.30: Cumulative shear strain for 40 mm axial tensile displacement of geogrid with 1200 kN/m stiffness under 25 kPa confining pressure

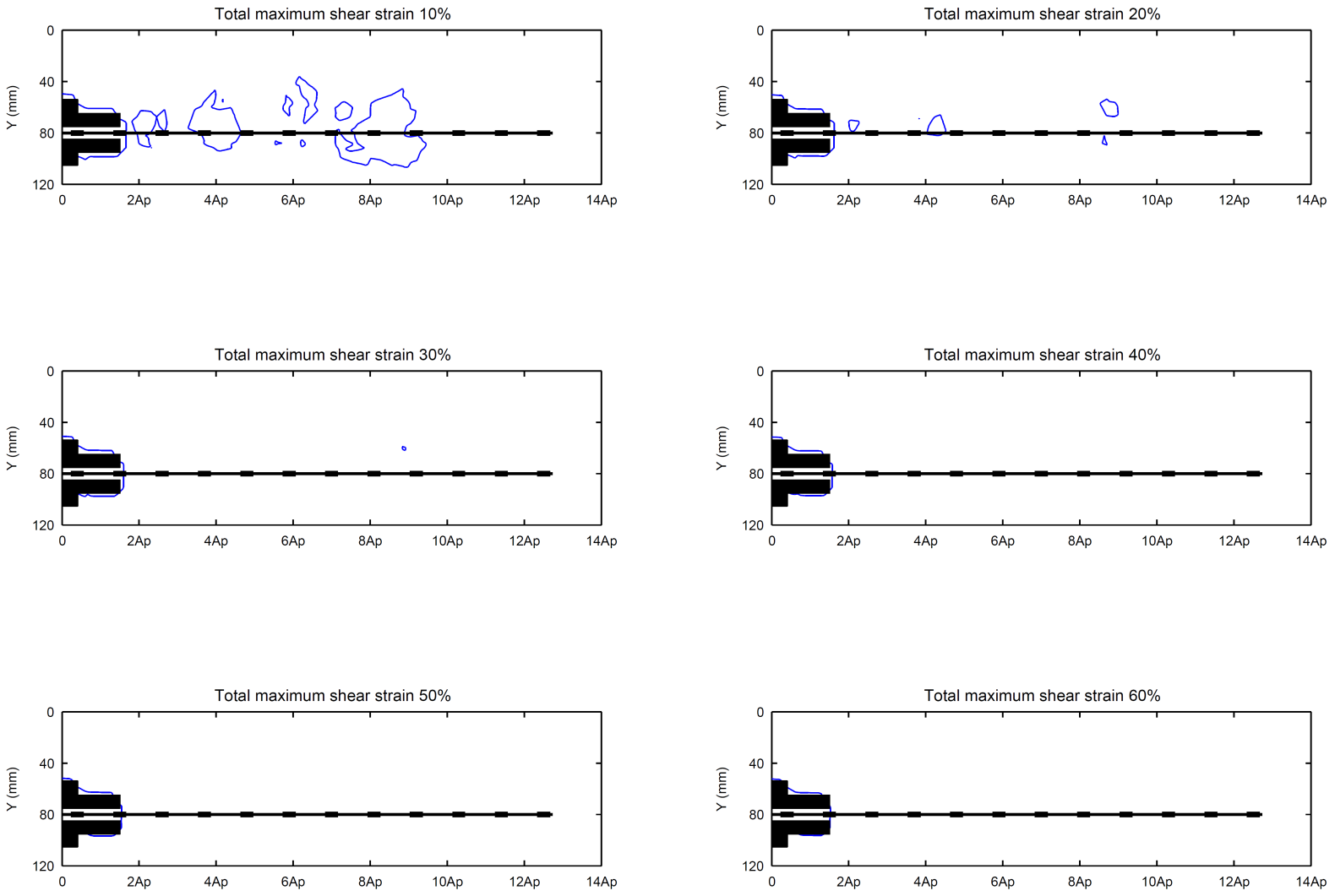

Figure 6.31: Cumulative shear strain for 40 mm axial tensile displacement of geogrid with 1200 kN/m stiffness under 50 kPa confining pressure

6.2.1.2.3 Total volumetric strain contours

Figures 6.32, 6.33 and 6.34 present of the volumetric strains caused by pulling out the geogrid from soil under different amount of confining pressure 12.5 kPa, 25 kPa and 50 kPa. The results of the study show the volumetric strain for 12.5 kPa and 25 kPa confining pressure is not significantly different and maximum amount volumetric strain is around 10%. However, this number is reduced to 5% for higher confining pressure. The results of the analysis show a higher percentage of volumetric strain occurred around the position of geogrid ribs which is evidence of mobilising the passive bearing resistance generated in front of the ribs.

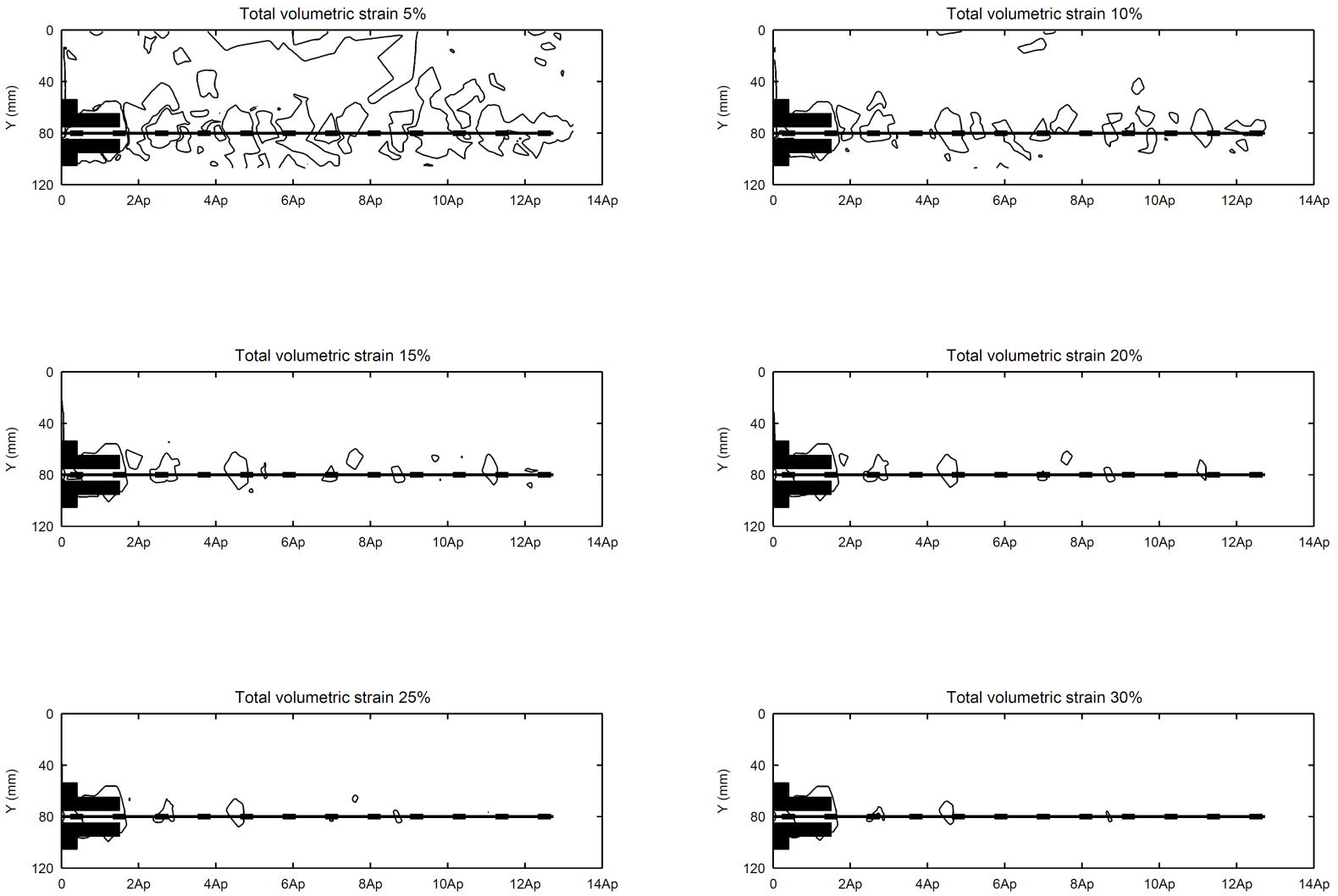

Figure 6.32: Cumulative volumetric strain for 40 mm axial tensile displacement of geogrid with 1200 kN/m stiffness under 12.5 kPa confining pressure

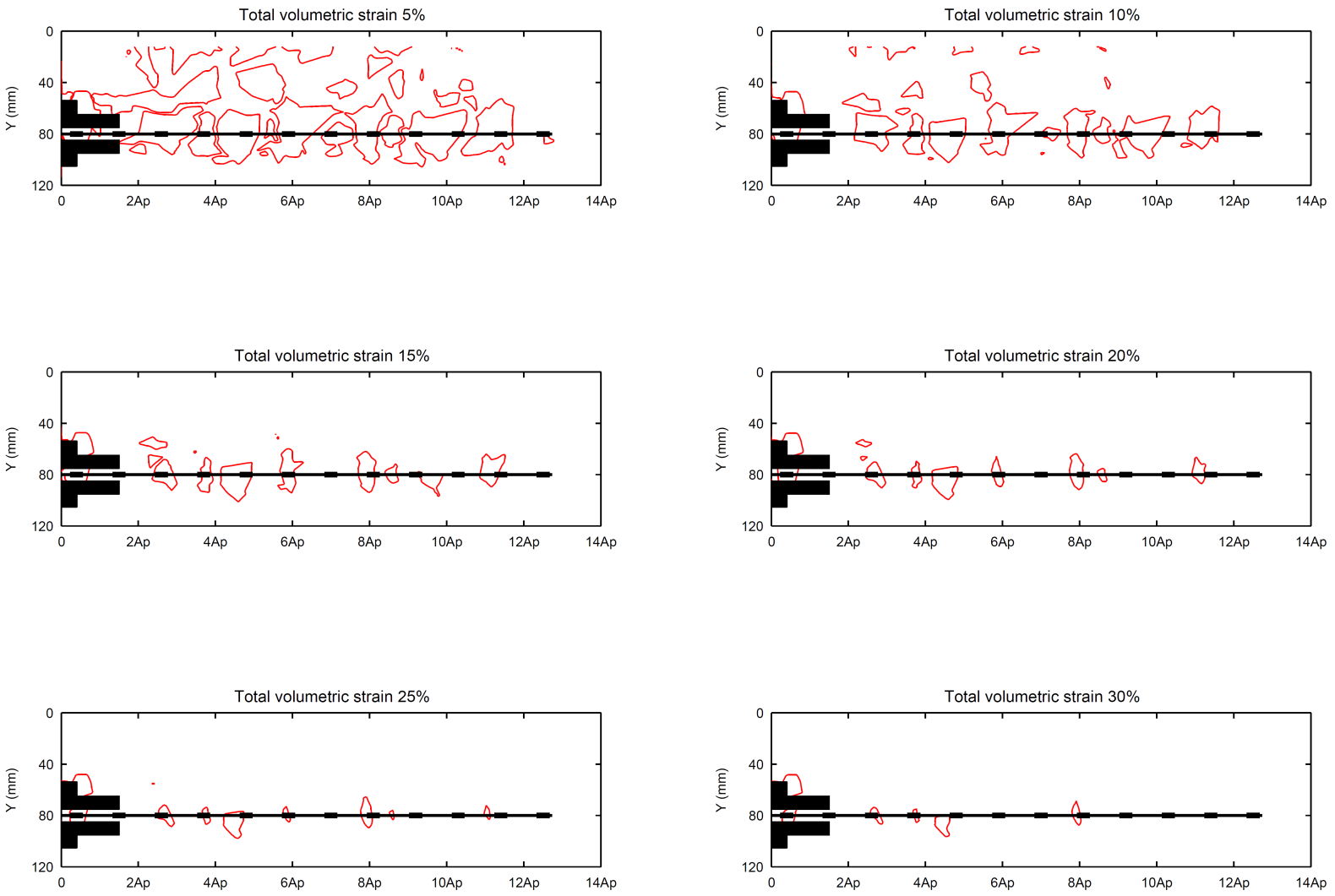

Figure 6.33: Cumulative volumetric strain for 40 mm axial tensile displacement of geogrid with 1200 kN/m stiffness under 25 kPa confining pressure

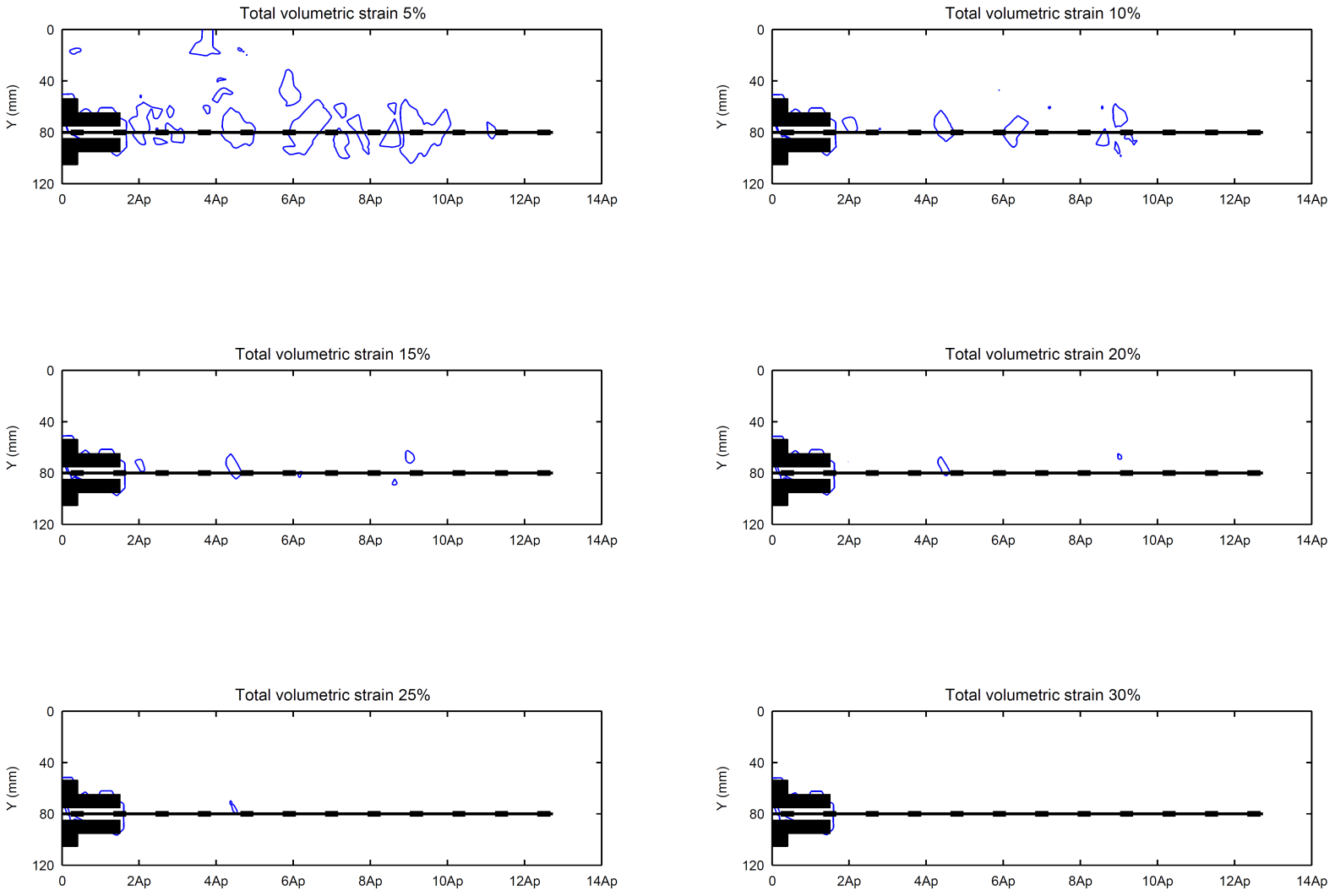

Figure 6.34: Cumulative volumetric strain for 40 mm axial tensile displacement of geogrid with 1200 kN/m stiffness under 50 kPa confining pressure

The observed soil-geogrid interaction was similar for all three types of geogrid. Therefore, in order to avoid repetition, description has only been provided for the first set of the results. For the other two sets, only the internal and external graphs have been presented.

6.2.2 Test2: Stiffness of geogrid=1600 kN/m

Figure 6.35 shows the results of pull-out load-displacement for three different confining pressures.

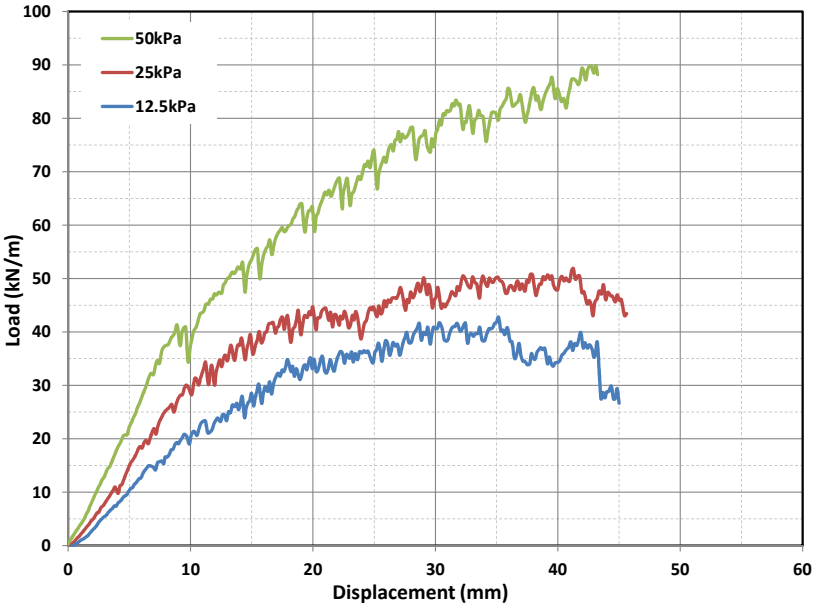

Figure 6.35: Load-displacement plots of geogrid specimen with stiffness of 1600 kN/m

The cumulative vector of displacement with horizontal and vertical displacement under three different values of confining pressures (12.5 kPa, 25 kPa and 50 kPa) at the end of the test presented in Figures 6.36-6.47.

The zone of influence of geogrid and transparent soil is observed from the horizontal contours between 35 - 40 mm which corresponds to 4 to 5.5 times the soil particles. The results of the study show that the lowest confining pressure has a bigger zone of influence.

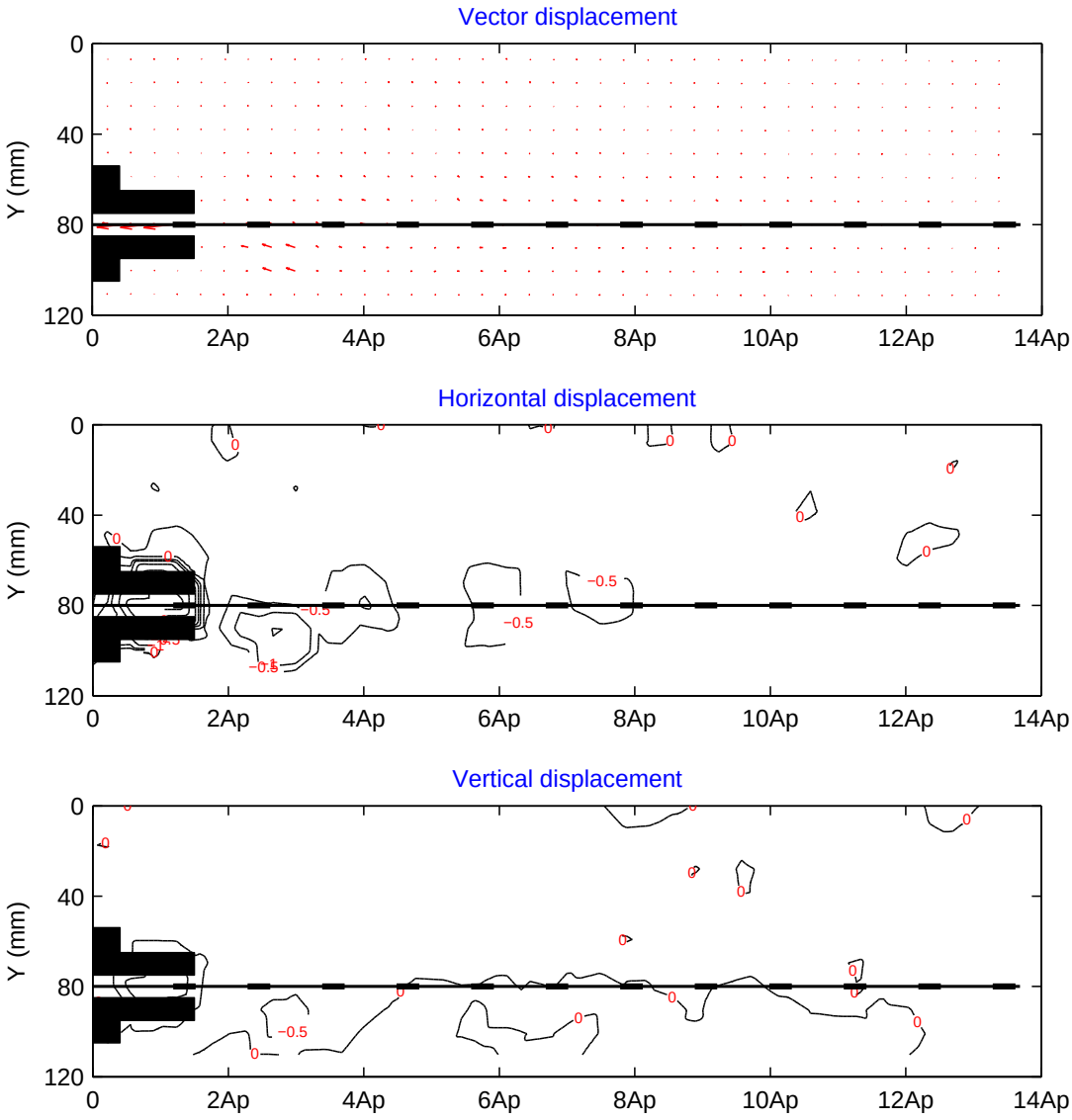

Figure 6.36: Cumulative PIV results at 10 mm axial tensile displacement of geogrid with 1600 kN/m stiffness under 12.5 kPa confining pressure

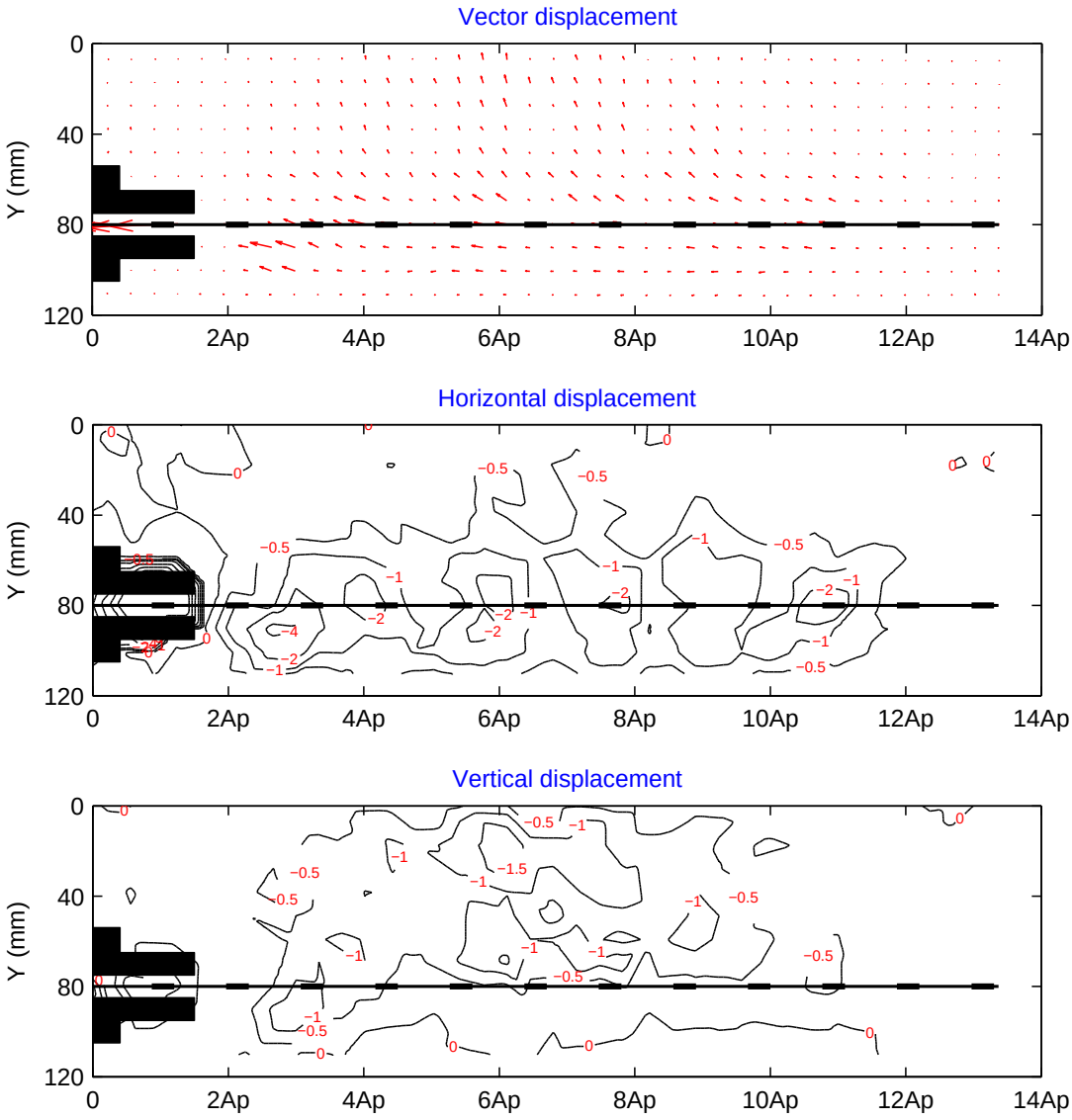

Figure 6.37: Cumulative PIV results at 20 mm axial tensile displacement of geogrid with 1600 kN/m stiffness under 12.5 kPa confining pressure

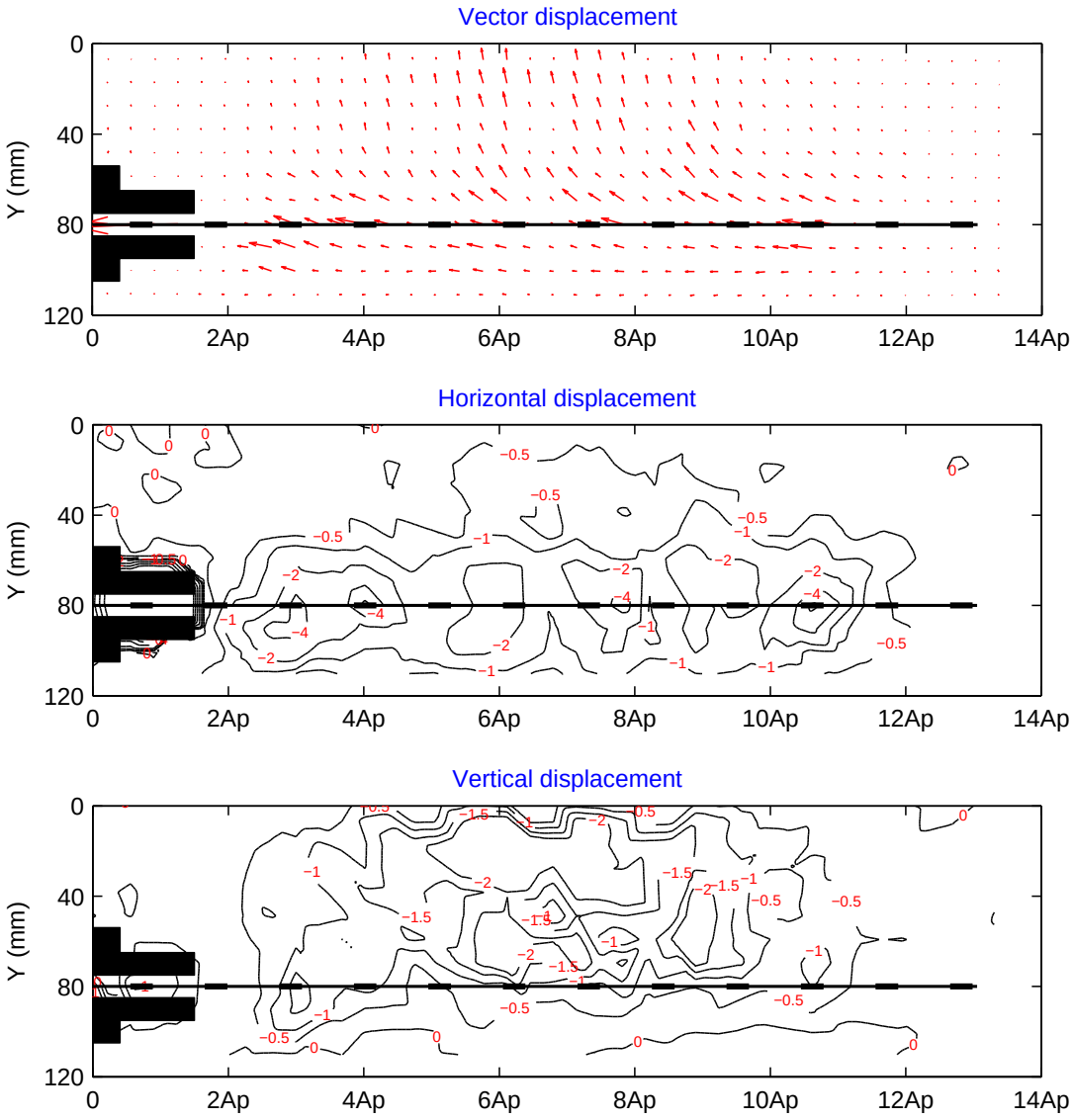

Figure 6.38: Cumulative PIV results at 30 mm axial tensile displacement of geogrid with 1600 kN/m stiffness under 12.5 kPa confining pressure

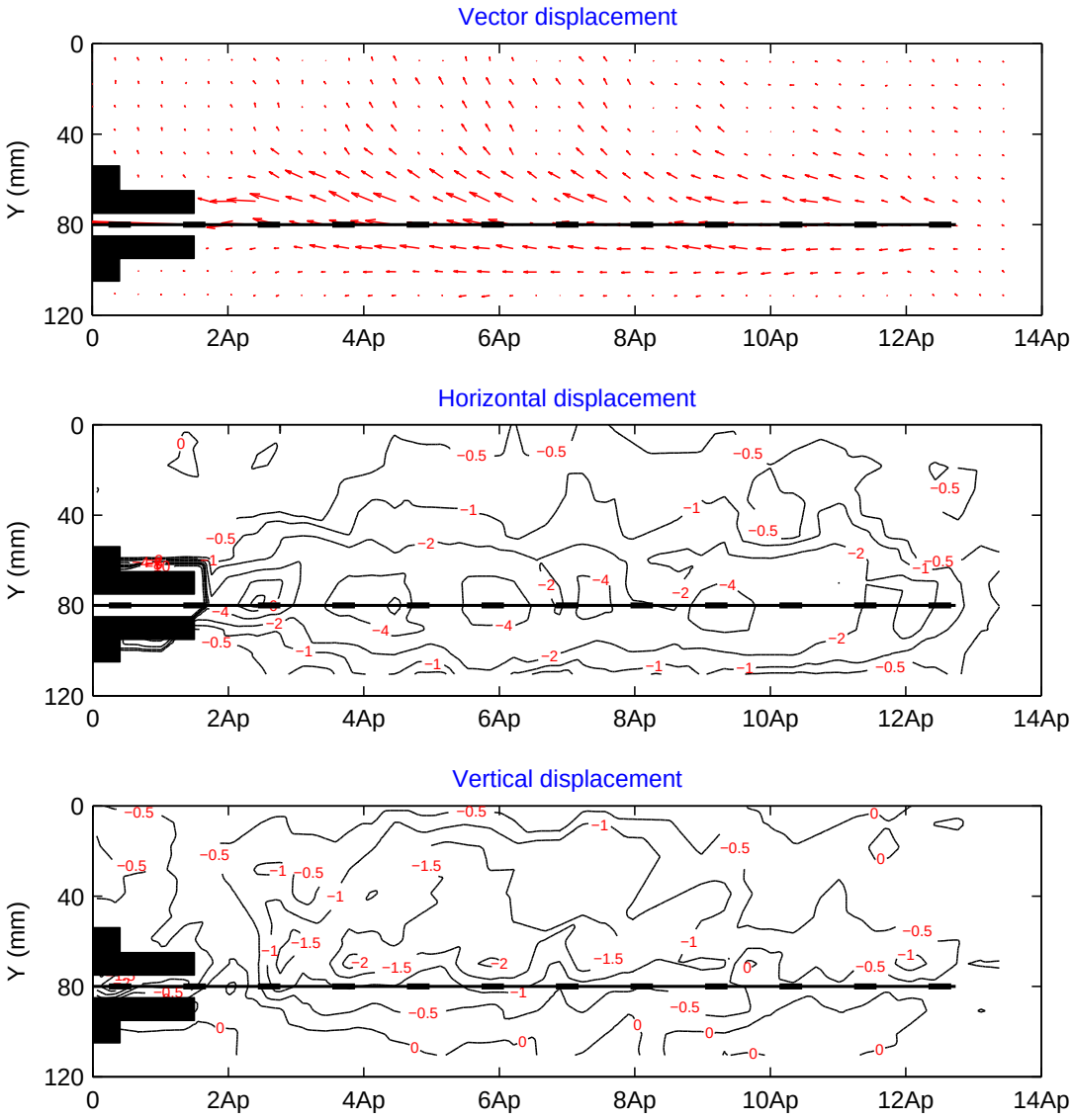

Figure 6.39: Cumulative PIV results at 40 mm axial tensile displacement of geogrid with 1600 kN/m stiffness under 12.5 kPa confining pressure

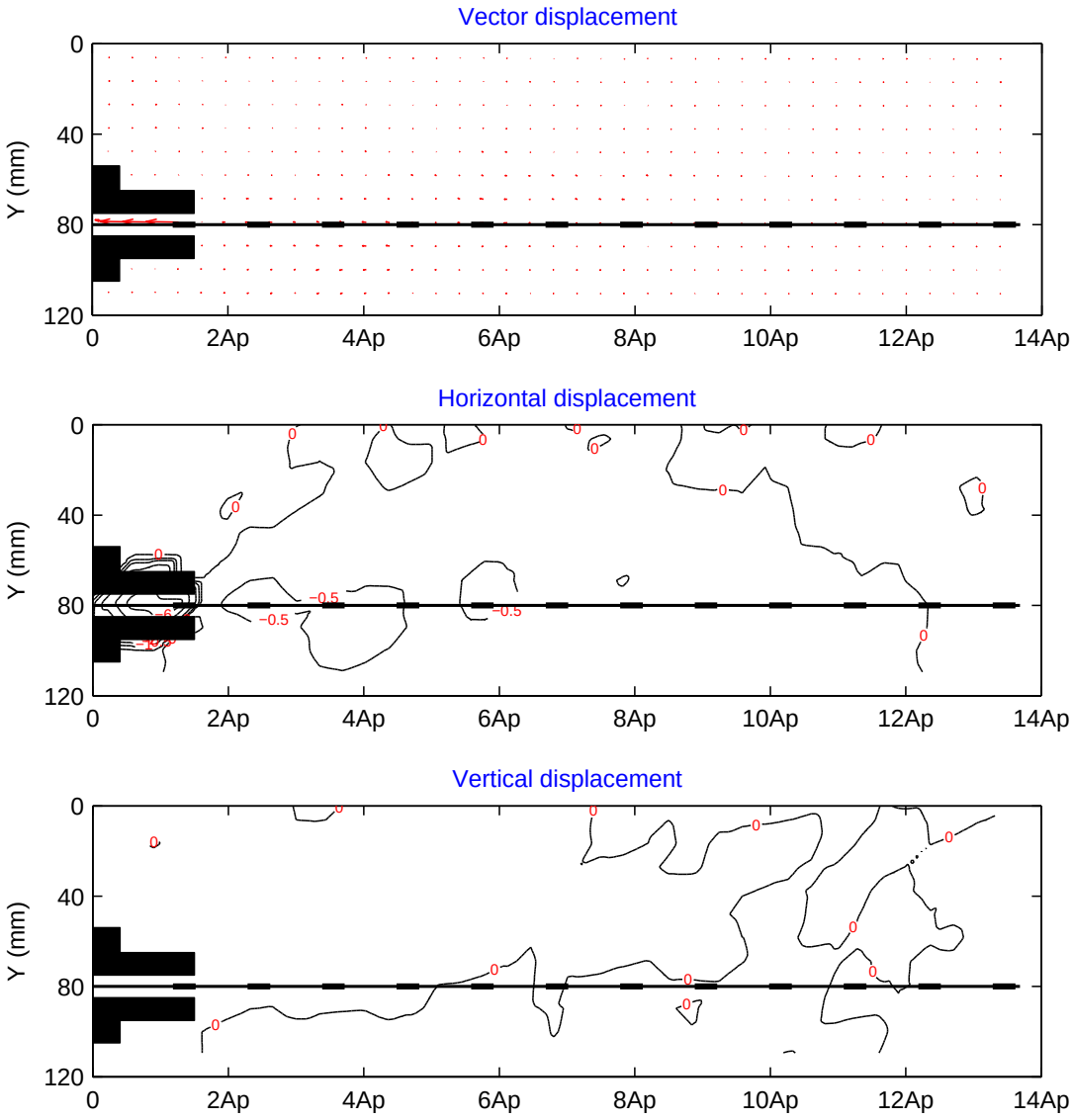

Figure 6.40: Cumulative PIV results at 10 mm axial tensile displacement of geogrid with 1600 kN/m stiffness under 25 kPa confining pressure

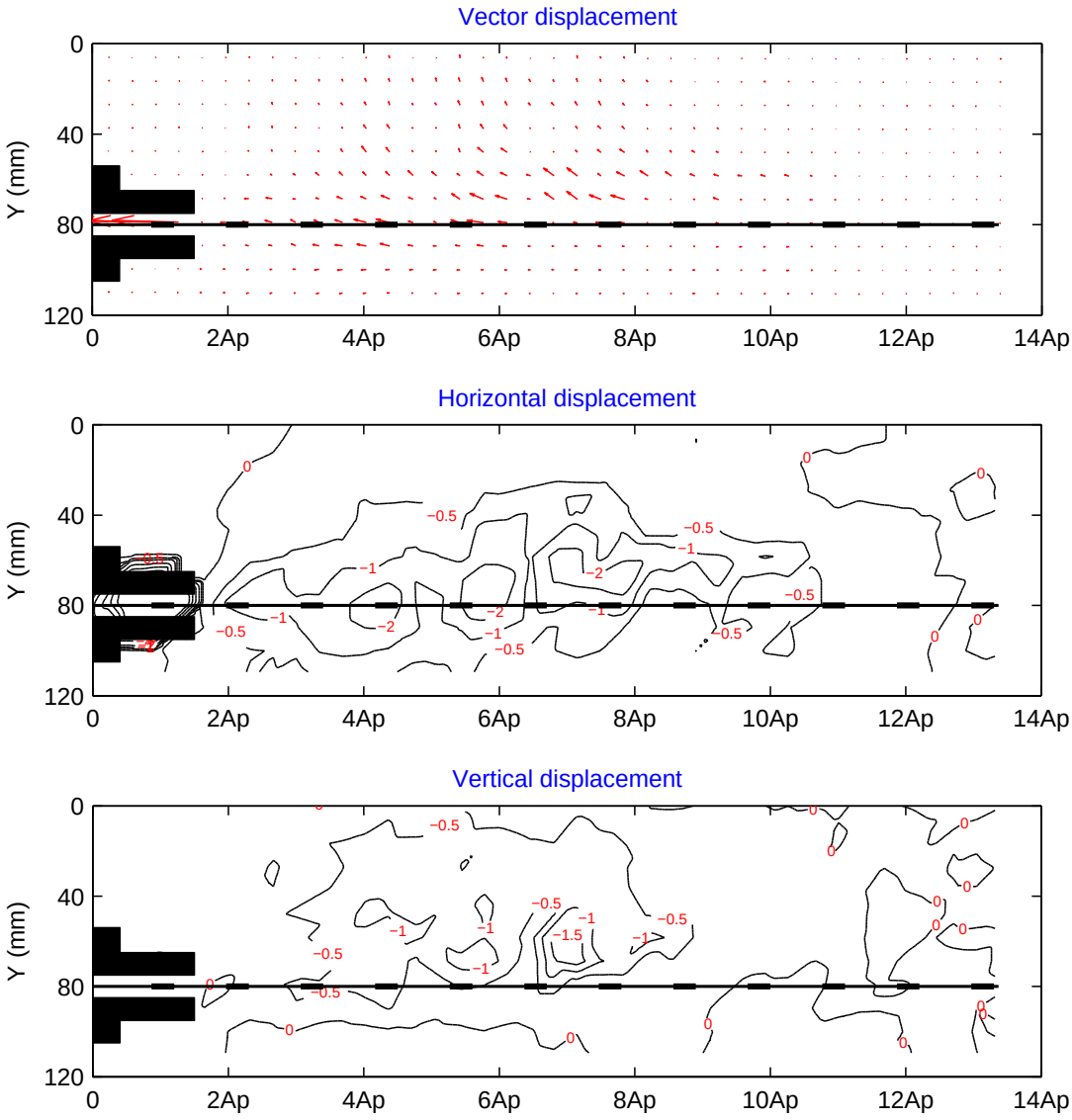

Figure 6.41: Cumulative PIV results at 20 mm axial tensile displacement of geogrid with 1600 kN/m stiffness under 25 kPa confining pressure

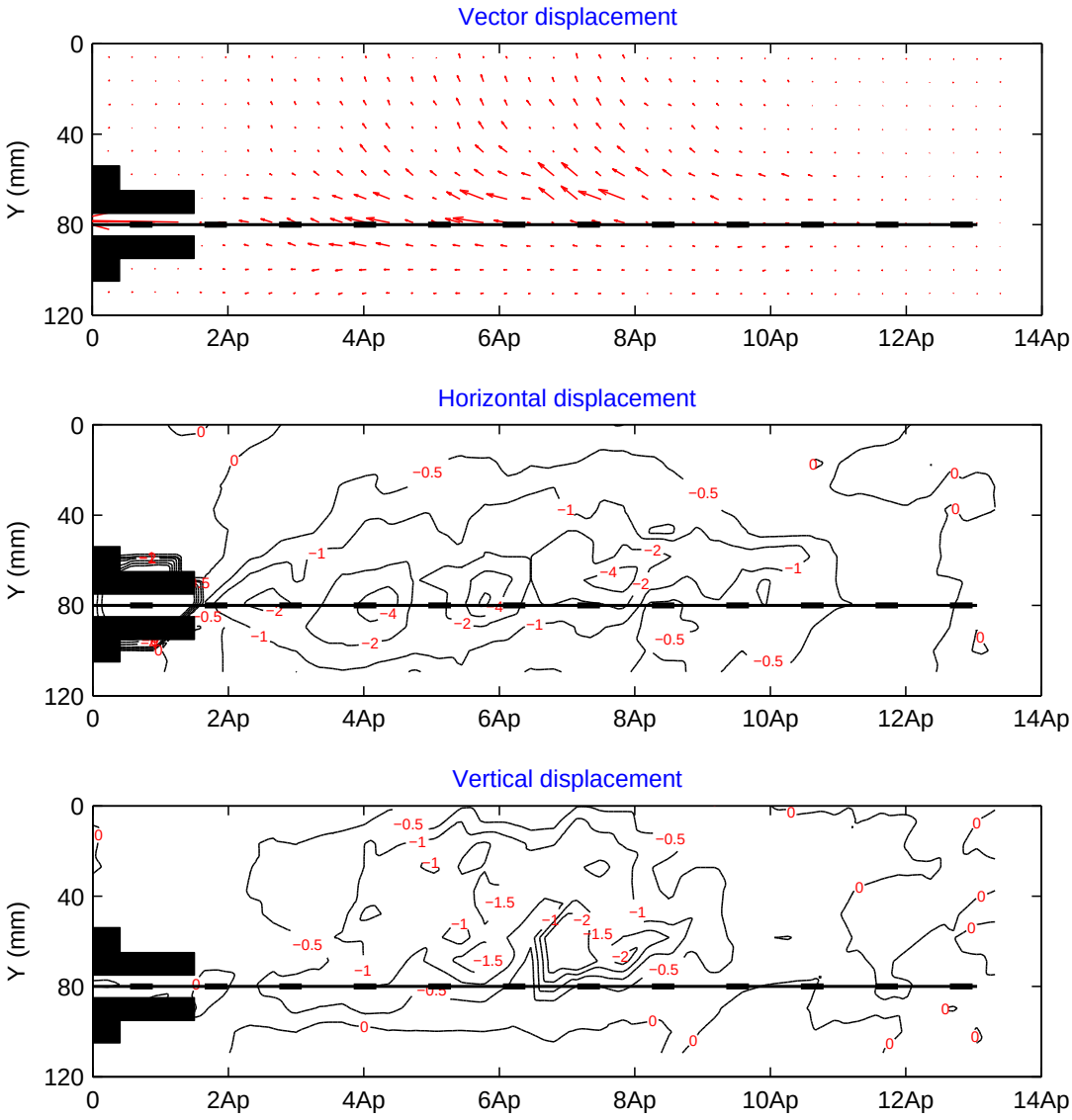

Figure 6.42: Cumulative PIV results at 30 mm axial tensile displacement of geogrid with 1600 kN/m stiffness under 25 kPa confining pressure

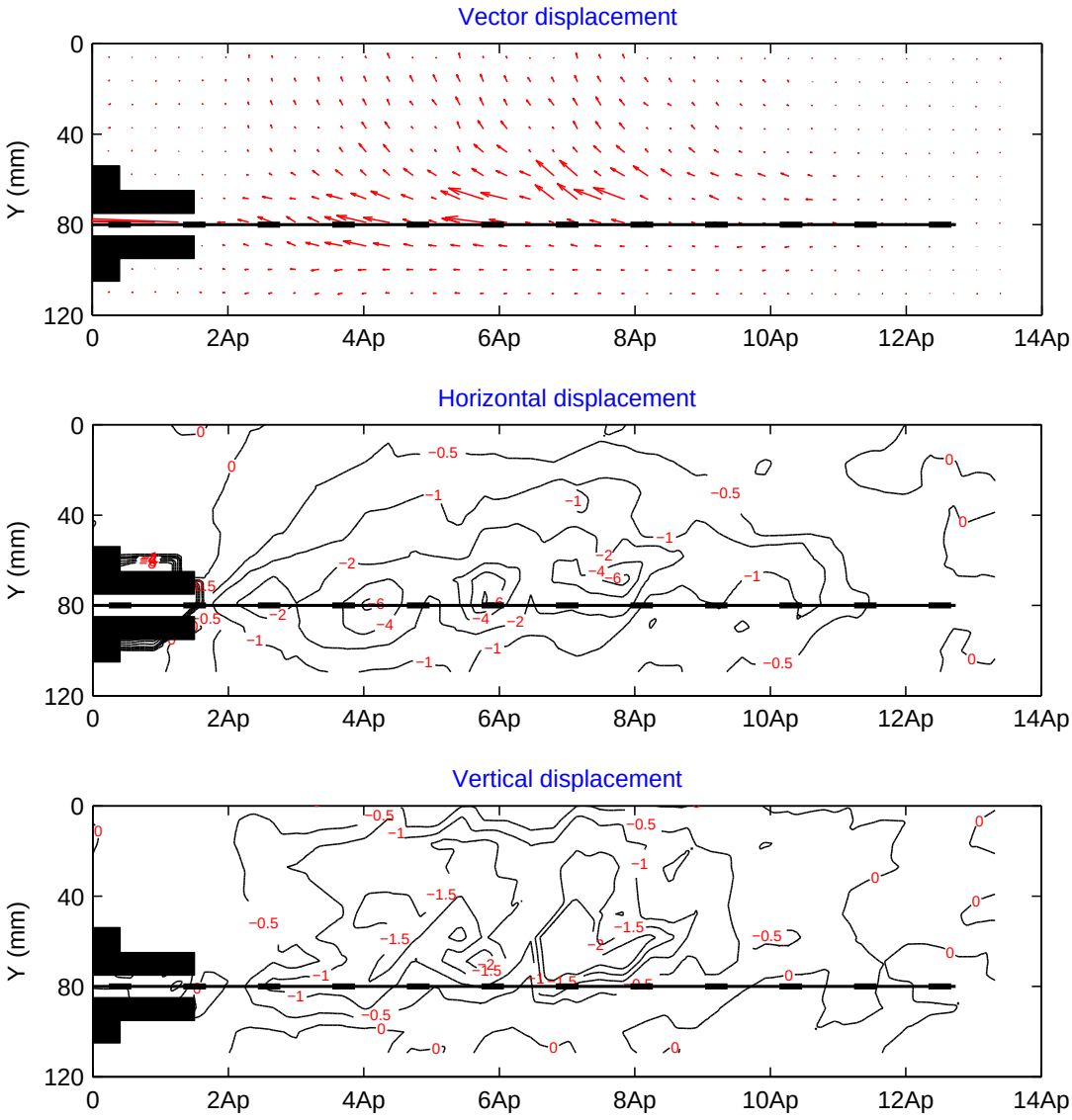

Figure 6.43: Cumulative PIV results at 40 mm axial tensile displacement of geogrid with 1600 kN/m stiffness under 25 kPa confining pressure

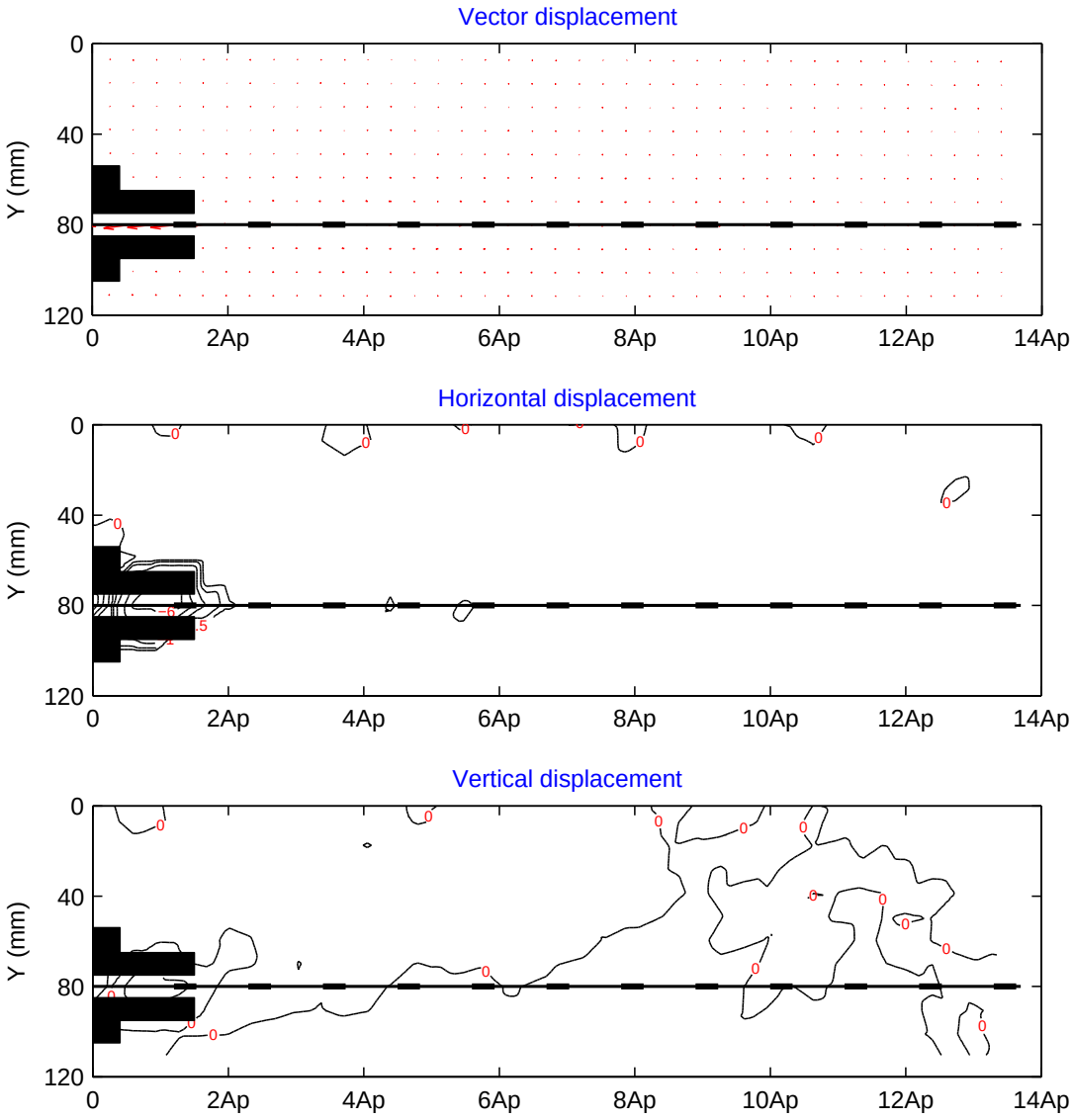

Figure 6.44: Cumulative PIV results at 10 mm axial tensile displacement of geogrid with 1600 kN/m stiffness under 50 kPa confining pressure

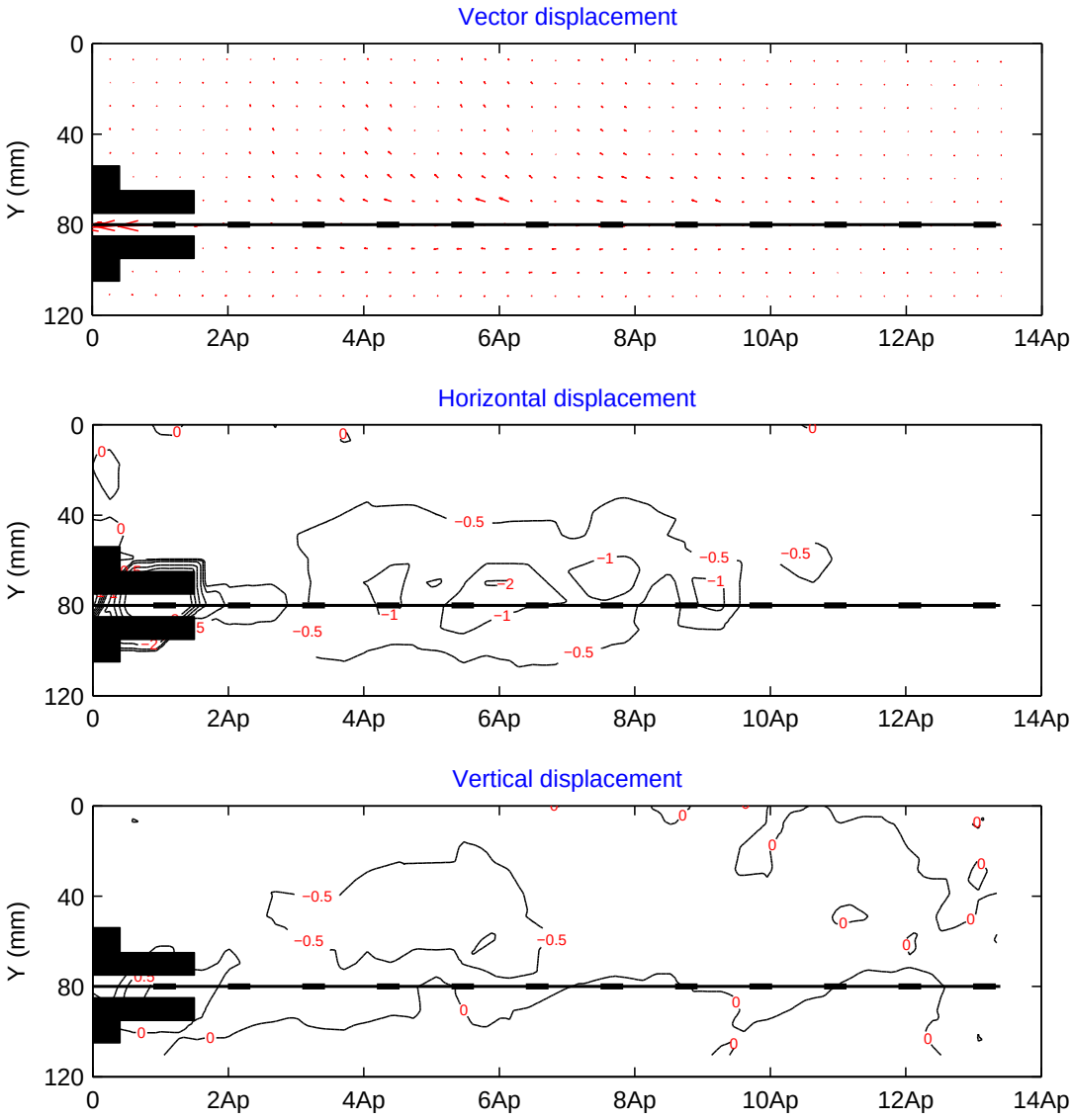

Figure 6.45: Cumulative PIV results at 20 mm axial tensile displacement of geogrid with 1600 kN/m stiffness under 50 kPa confining pressure

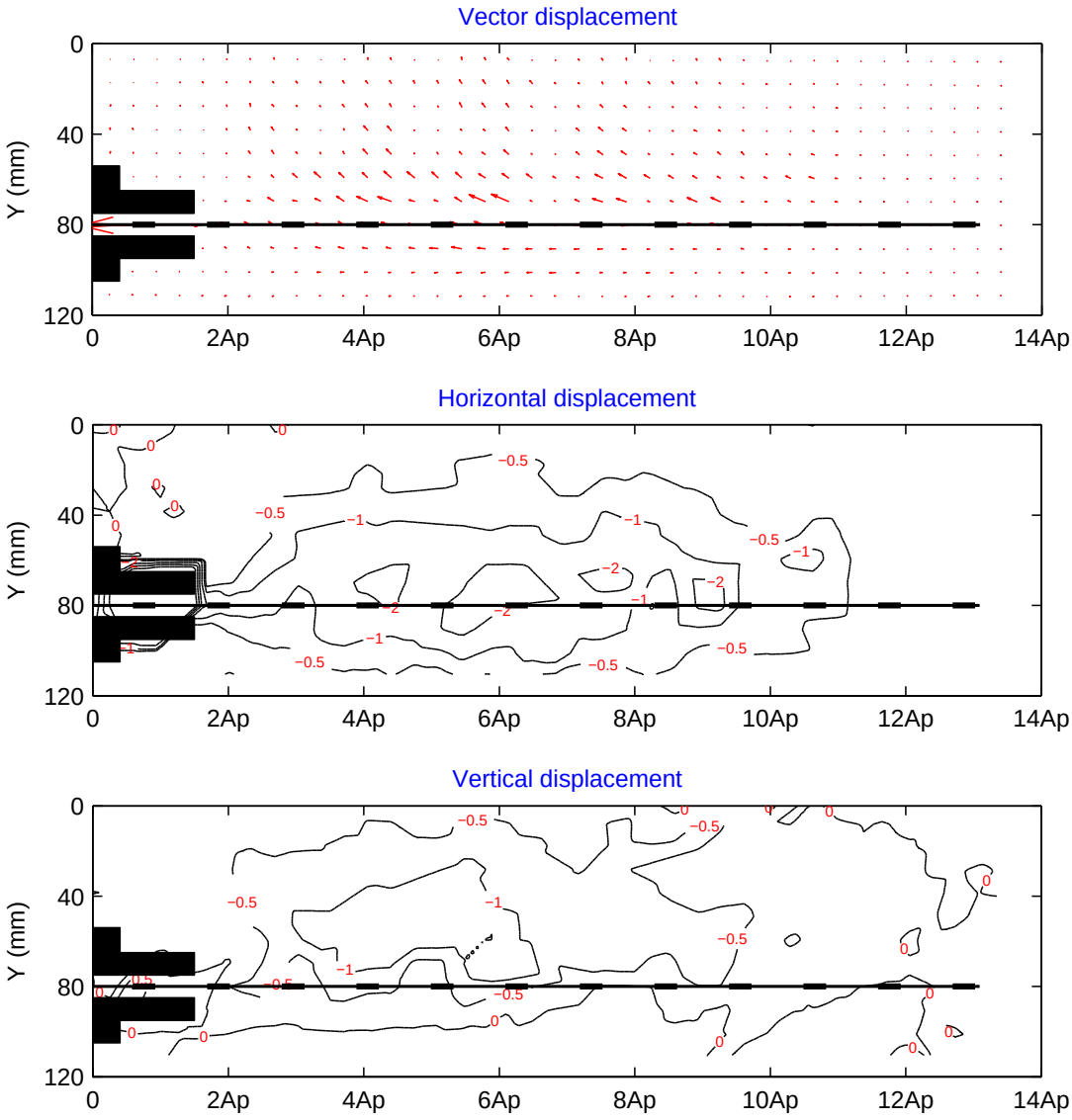

Figure 6.46: Cumulative PIV results at 30 mm axial tensile displacement of geogrid with 1600 kN/m stiffness under 50 kPa confining pressure

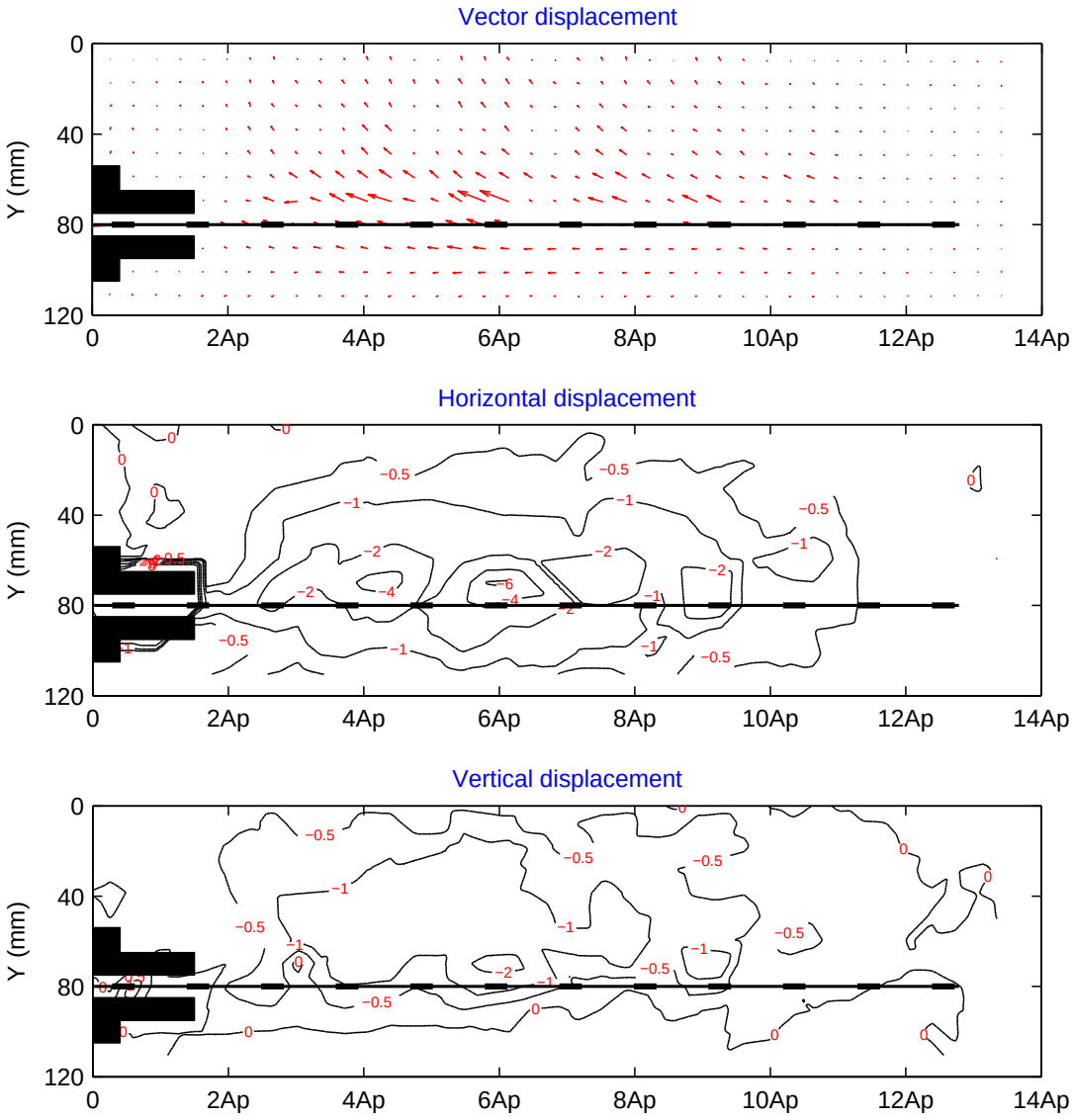

Figure 6.47: Cumulative PIV results at 40 mm axial tensile displacement of geogrid with 1600 kN/m stiffness under 50 kPa confining pressure

The incremental PIV results from 0 to 40 mm for 10 mm increments for a vector of horizontal and vertical displacement under three different values of confining pressure (12.5 kPa, 25 kPa and 50 kPa) show in Figures 6.48-6.59.

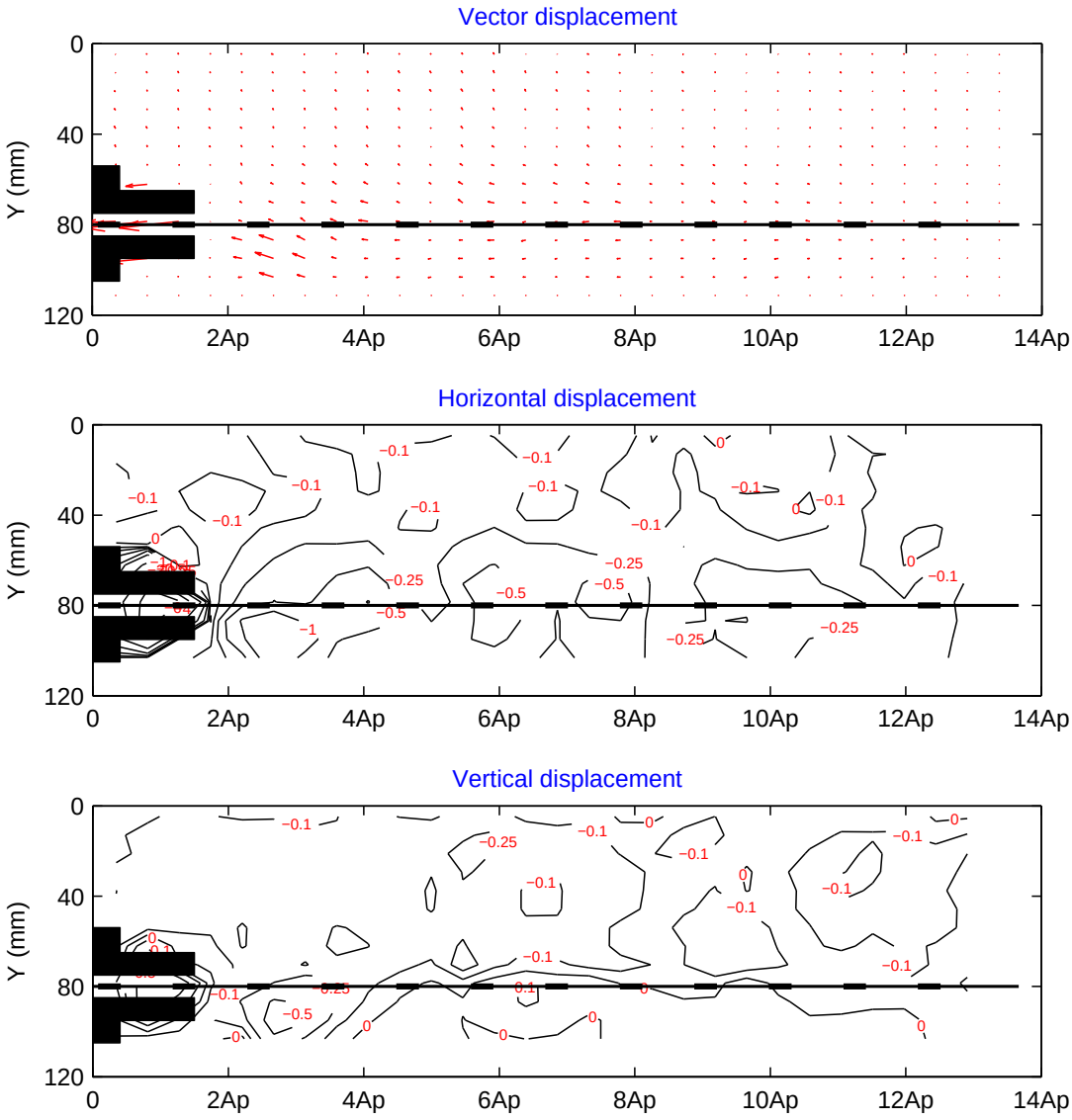

Figure 6.48: Incremental PIV results from 0 mm to 10 mm axial tensile displacement of geogrid with 1600 kN/m stiffness under 12.5 kPa confining pressure

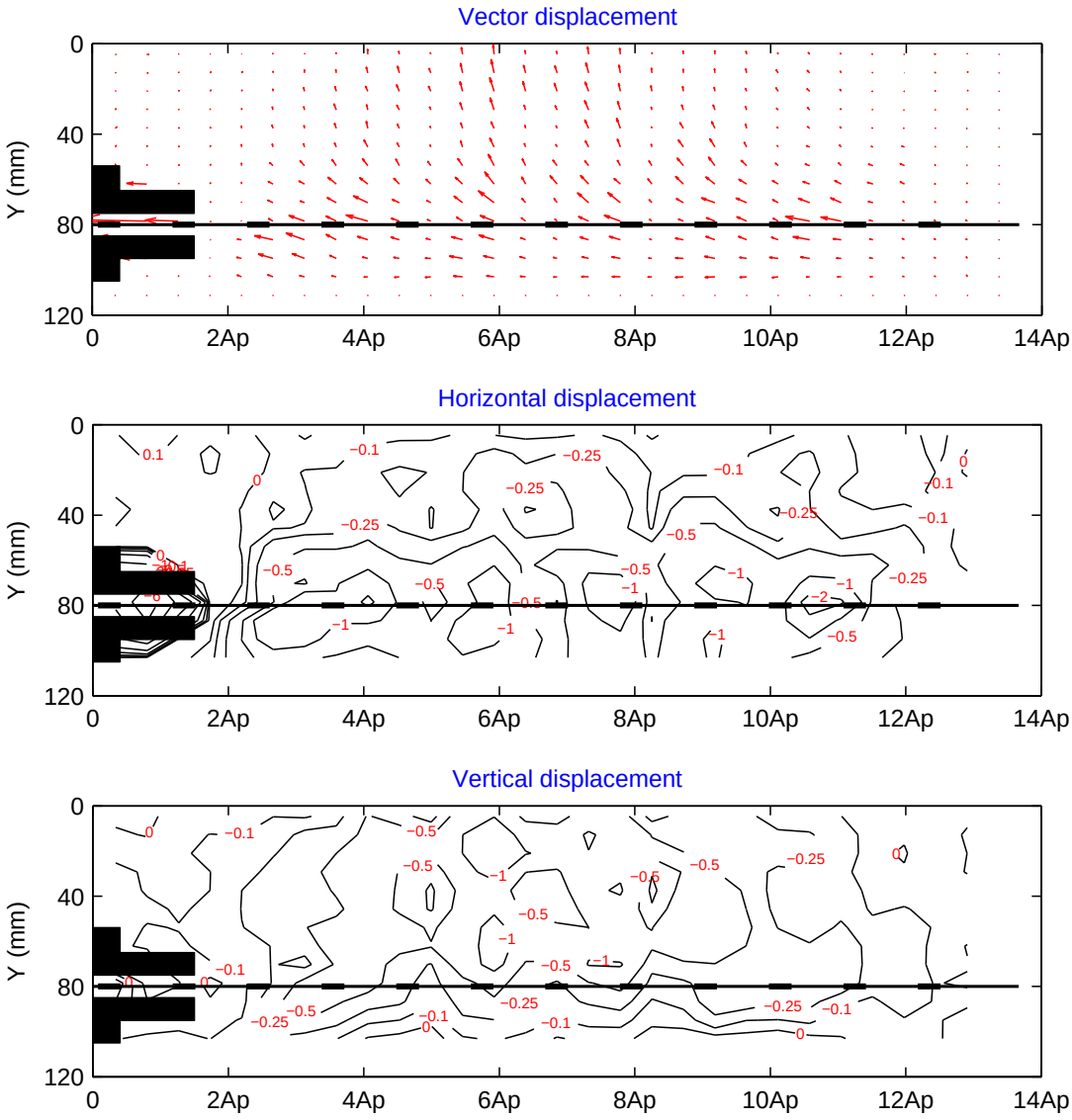

Figure 6.49: Incremental PIV results from 10 mm to 20 mm axial tensile displacement of geogrid with 1600 kN/m stiffness under 12.5 kPa confining pressure

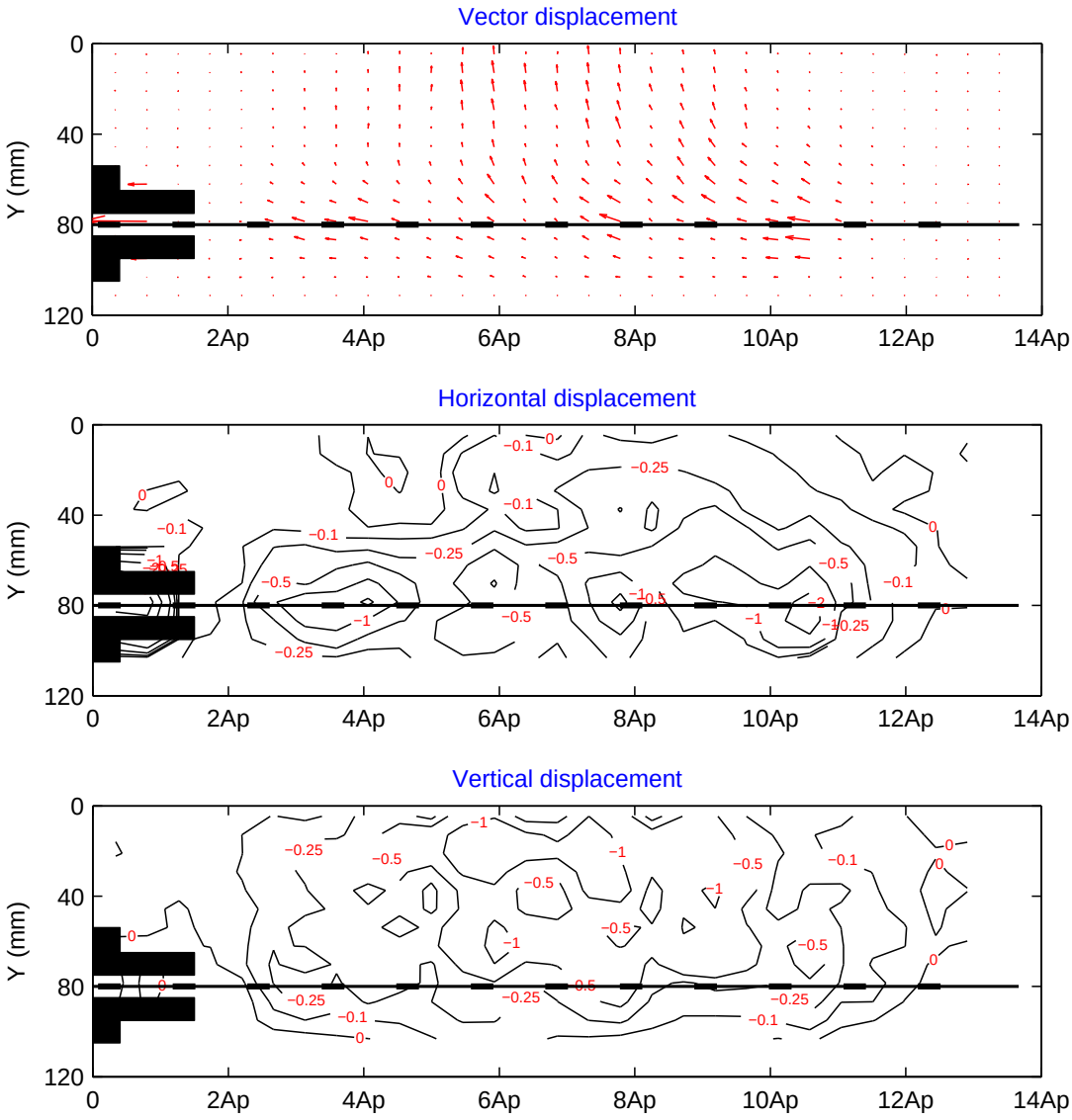

Figure 6.50: Incremental PIV results from 20 mm to 30 mm axial tensile displacement of geogrid with 1600 kN/m stiffness under 12.5 kPa confining pressure

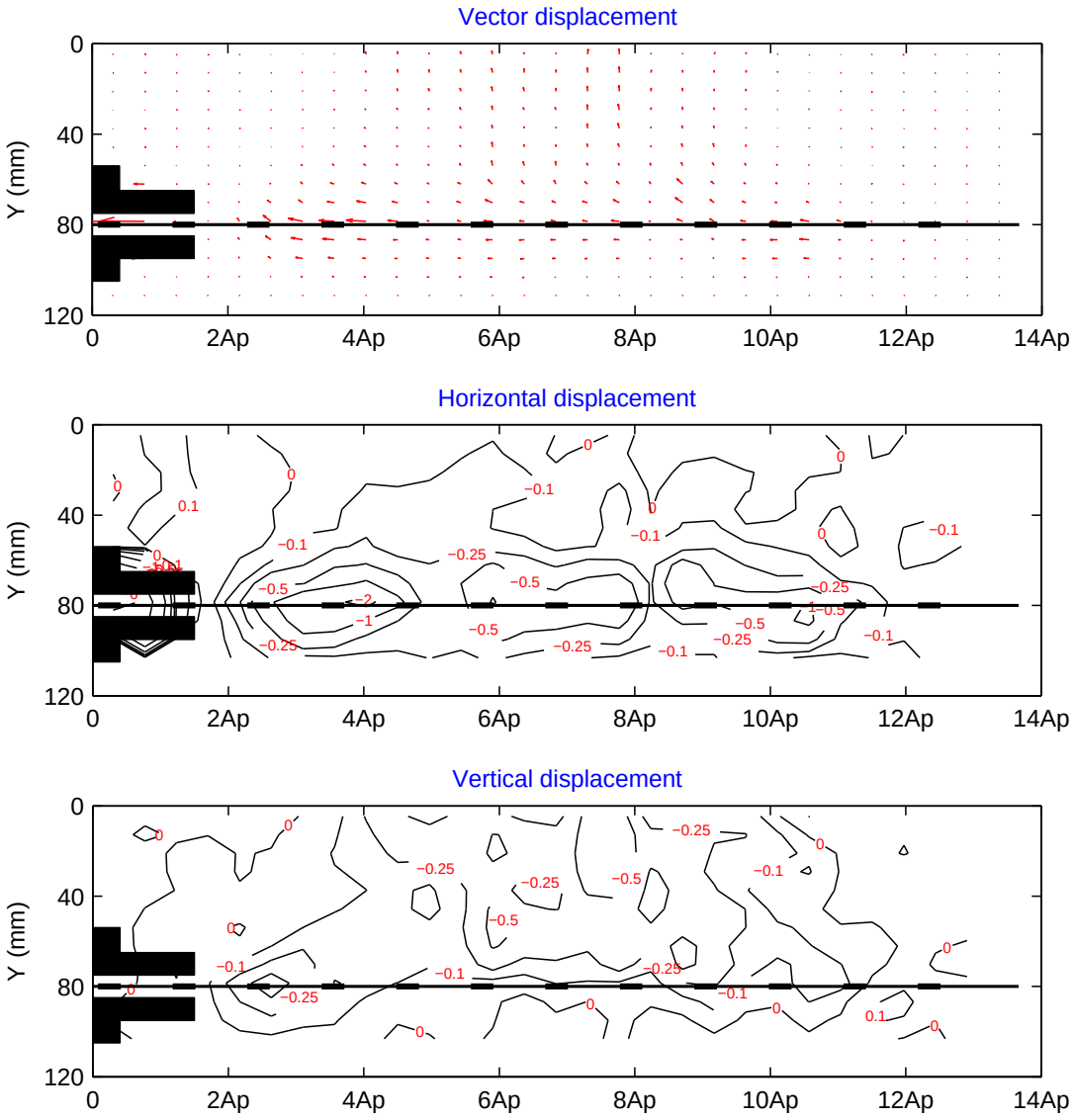

Figure 6.51: Incremental PIV results from 30 mm to 40 mm axial tensile displacement of geogrid with 1600 kN/m stiffness under 12.5 kPa confining pressure

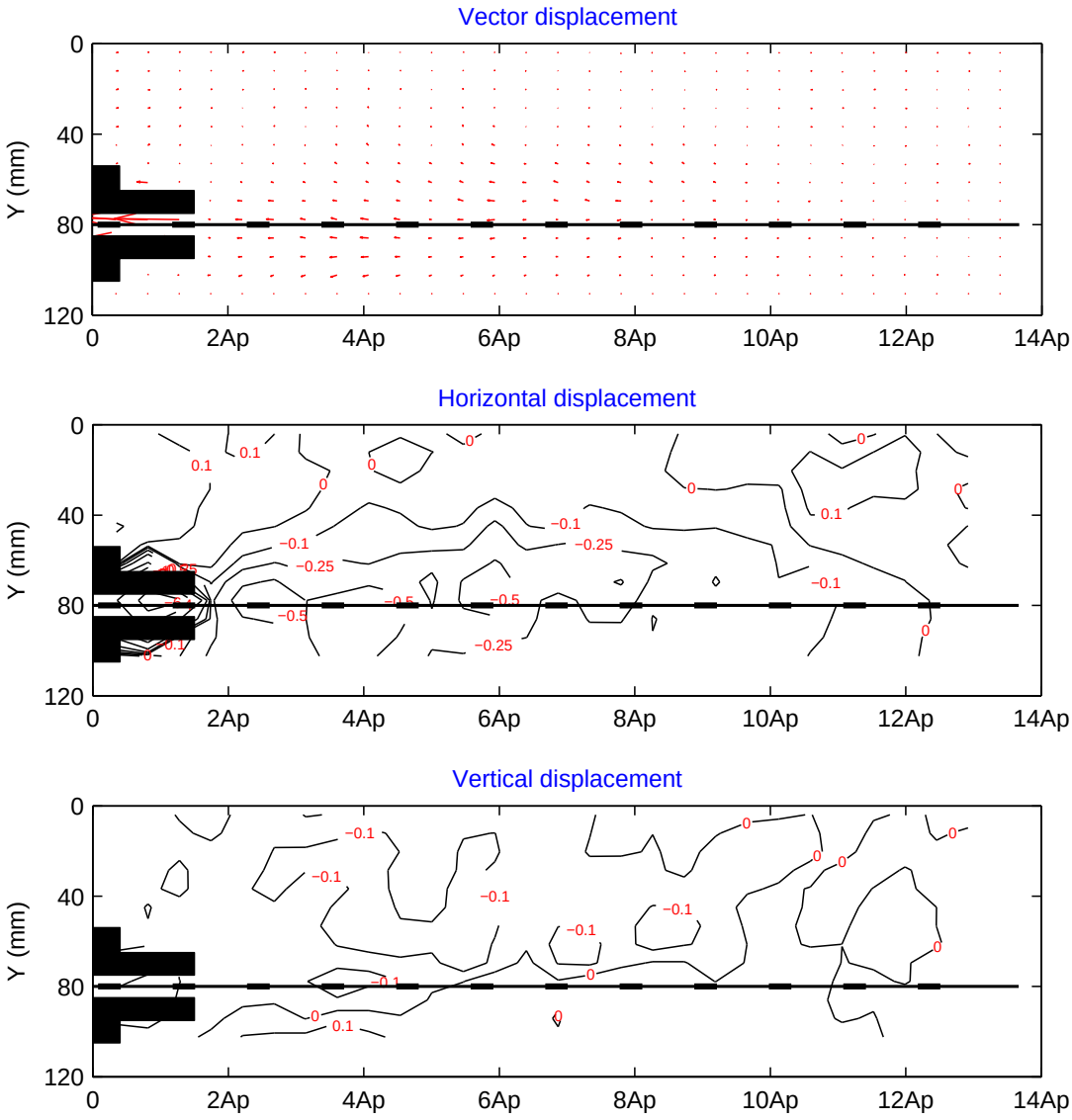

Figure 6.52: Incremental PIV results from 0 mm to 10 mm axial tensile displacement of geogrid with 1600 kN/m stiffness under 25 kPa confining pressure

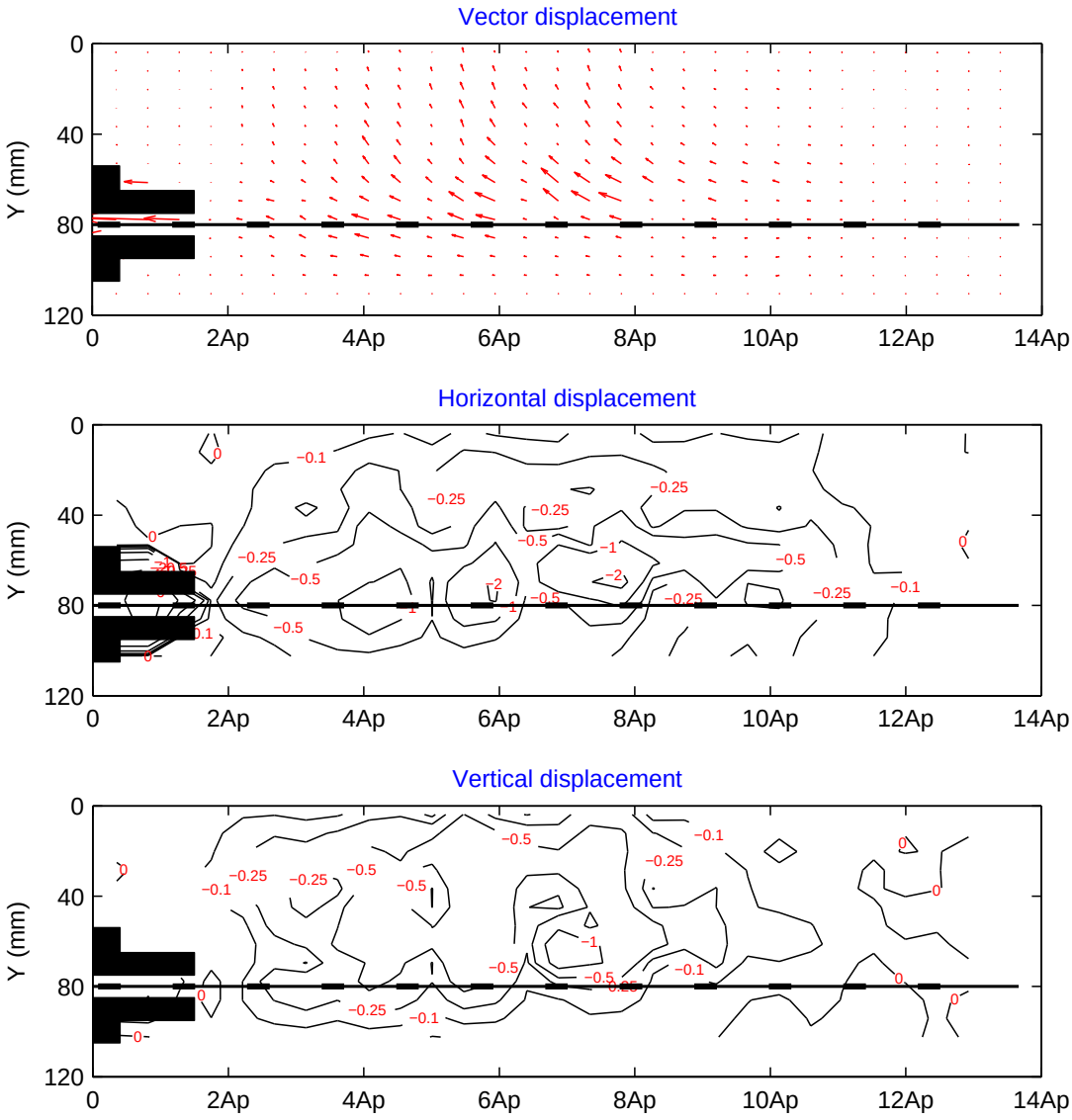

Figure 6.53: Incremental PIV results from 10 mm to 20 mm axial tensile displacement of geogrid with 1600 kN/m stiffness under 25 kPa confining pressure

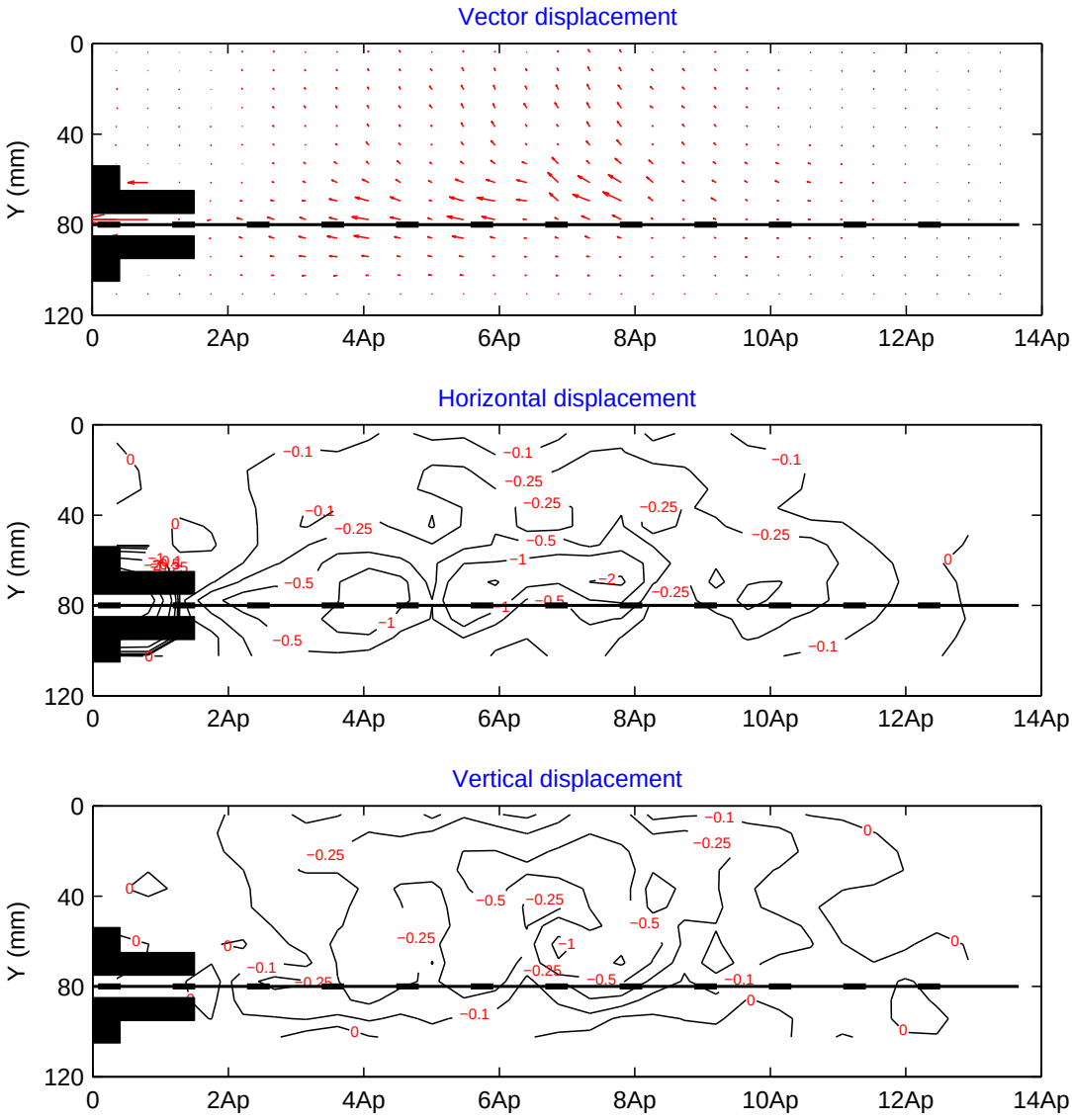

Figure 6.54: Incremental PIV results from 20 mm to 30 mm axial tensile displacement of geogrid with 1600 kN/m stiffness under 25 kPa confining pressure

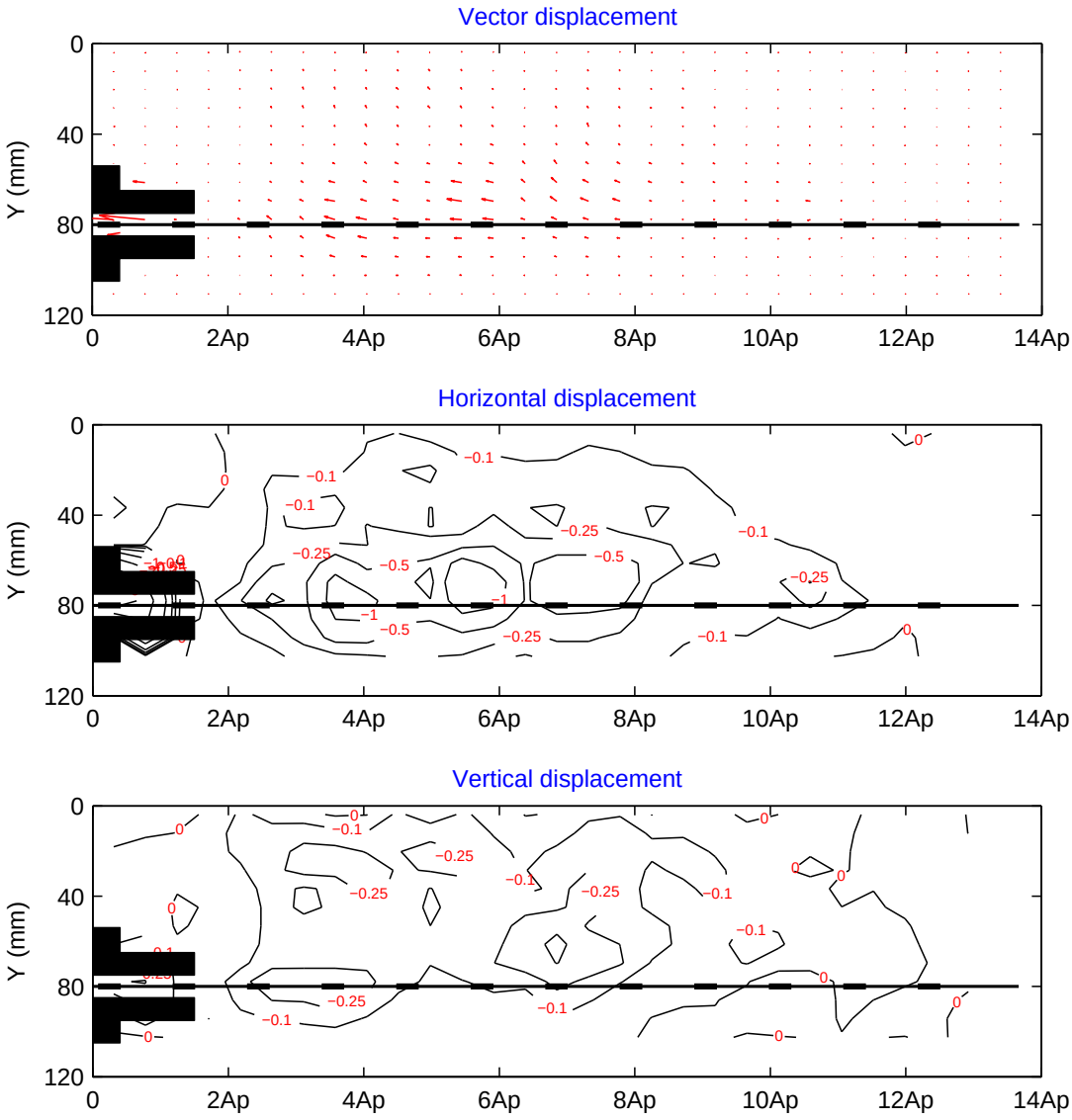

Figure 6.55: Incremental PIV results from 30 mm to 40 mm axial tensile displacement of geogrid with 1600 kN/m stiffness under 25 kPa confining pressure

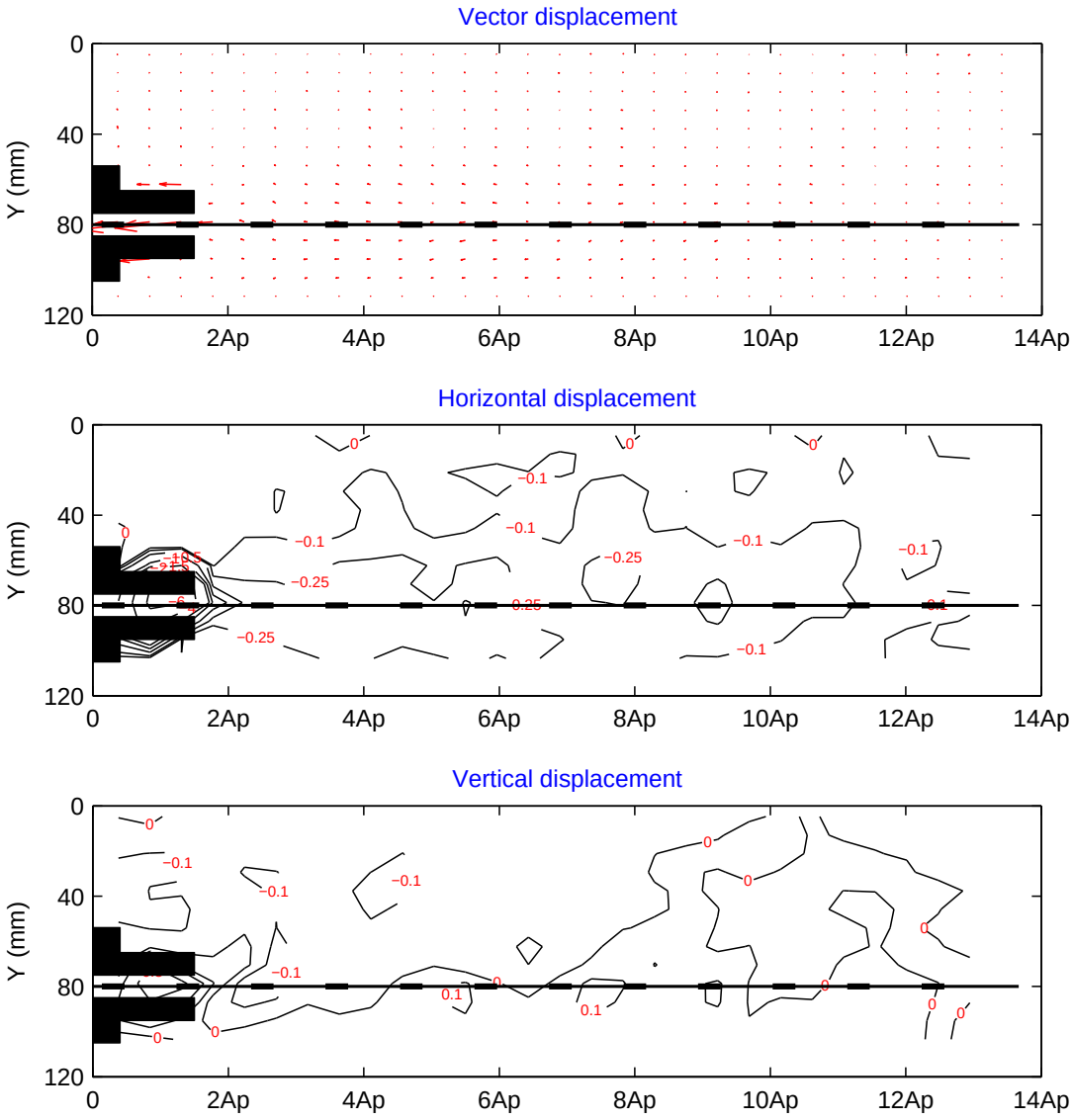

Figure 6.56: Incremental PIV results from 0 mm to 10 mm axial tensile displacement of geogrid with 1600 kN/m stiffness under 50 kPa confining pressure

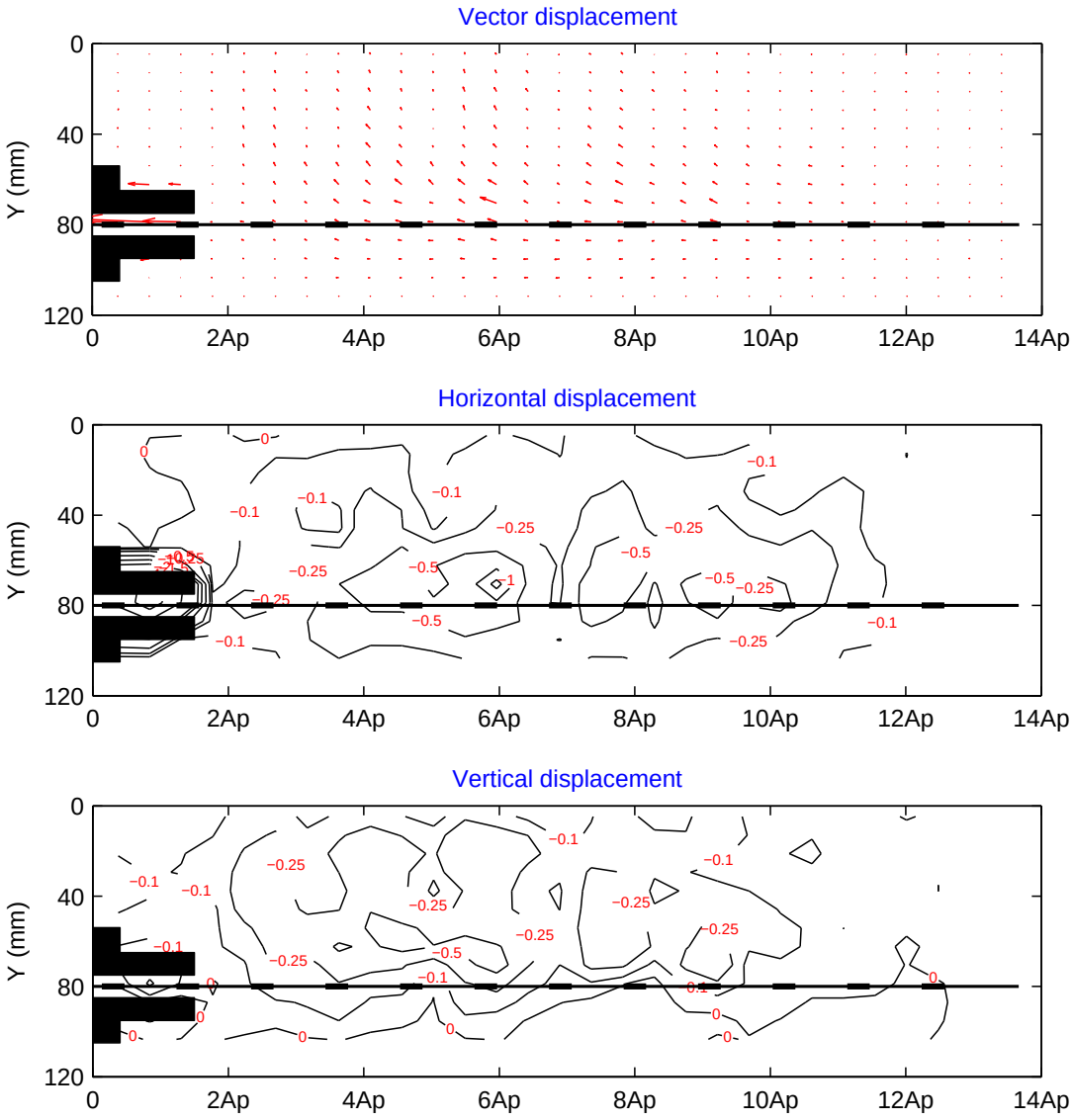

Figure 6.57: Incremental PIV results from 10 mm to 20 mm axial tensile displacement of geogrid with 1600 kN/m stiffness under 50 kPa confining pressure

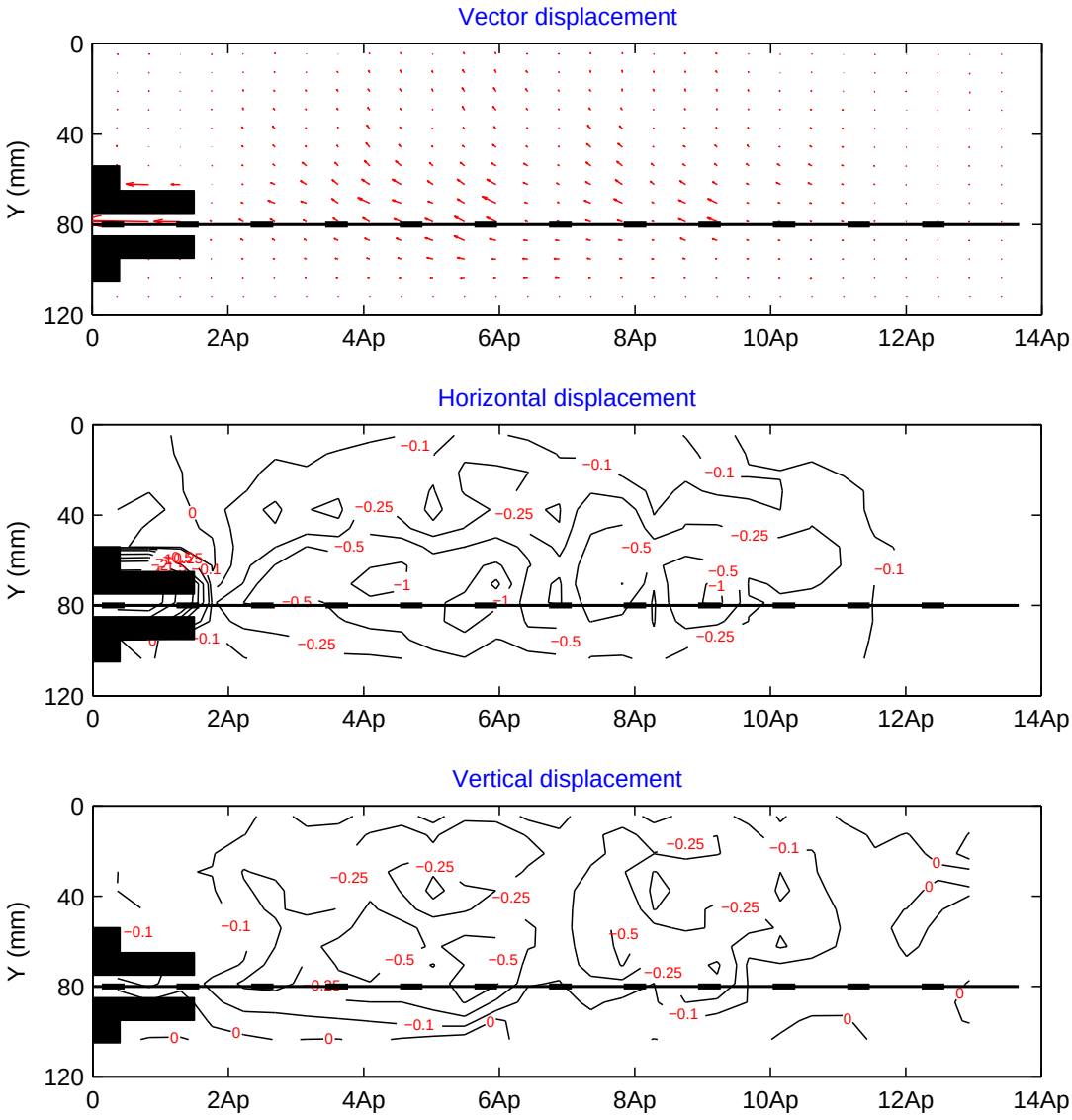

Figure 6.58: Incremental PIV results from 20 mm to 30 mm axial tensile displacement of geogrid with 1600 kN/m stiffness under 50 kPa confining pressure

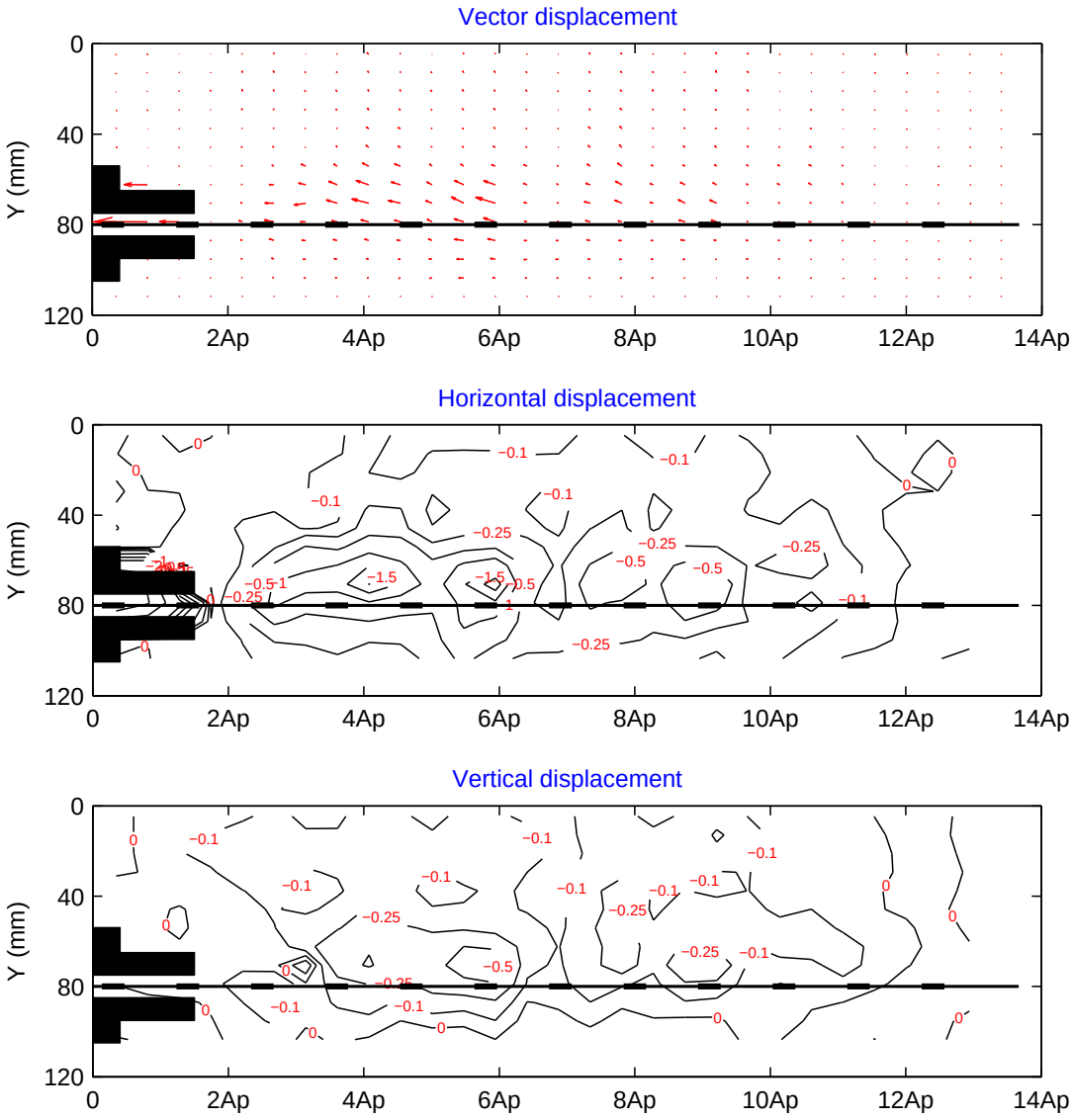

Figure 6.59: Incremental PIV results from 30 mm to 40 mm axial tensile displacement of geogrid with 1600 kN/m stiffness under 50 kPa confining pressure

Figures 6.60, 6.61 and 6.62 show the shear strains caused by pulling out the geogrid from soil under three different amounts of confining pressures (12.5 kPa, 25 kPa and 50 kPa).

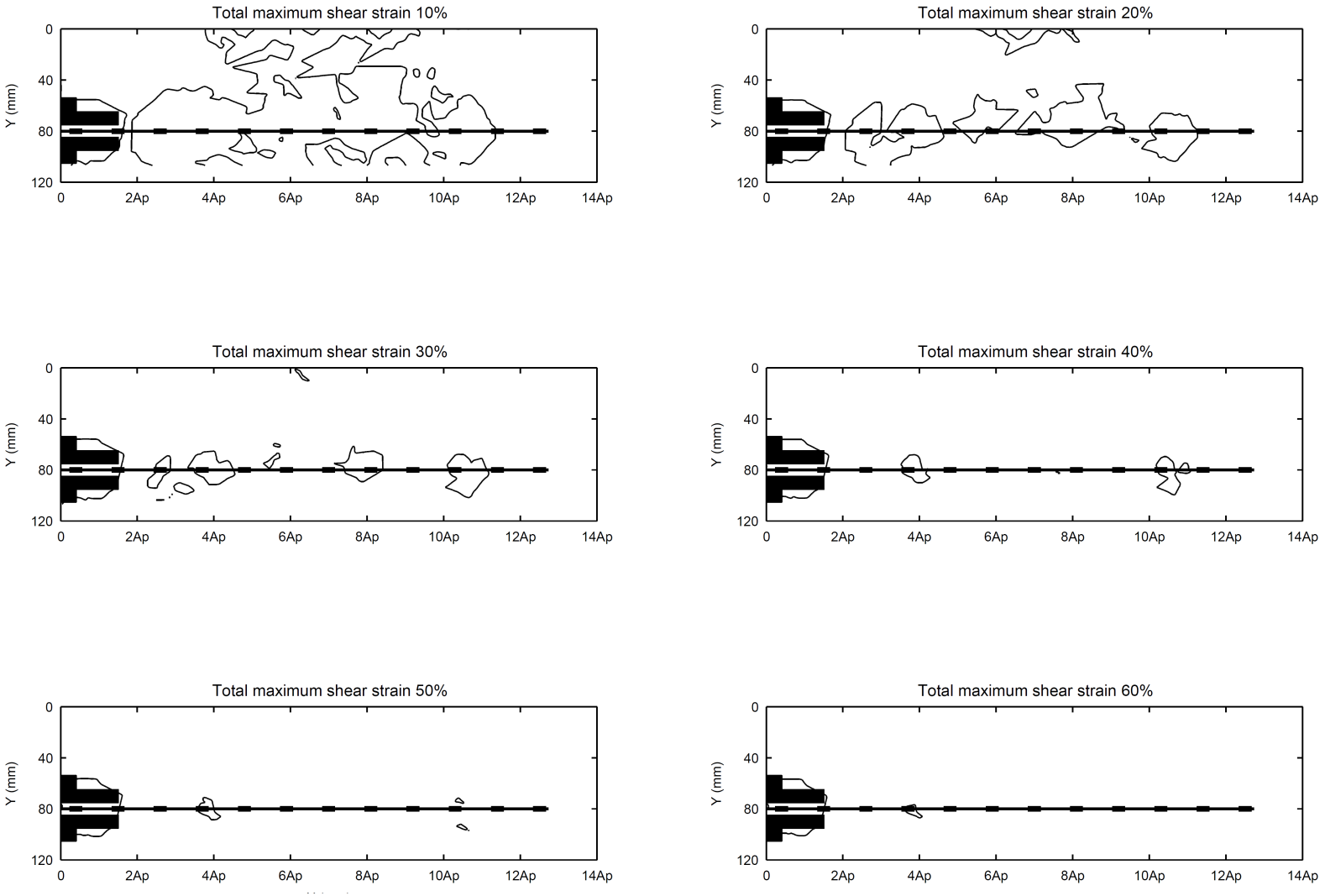

Figure 6.60: Cumulative shear strain for 40 mm axial tensile displacement of geogrid with 1600 kN/m stiffness under 12.5 kPa confining pressure

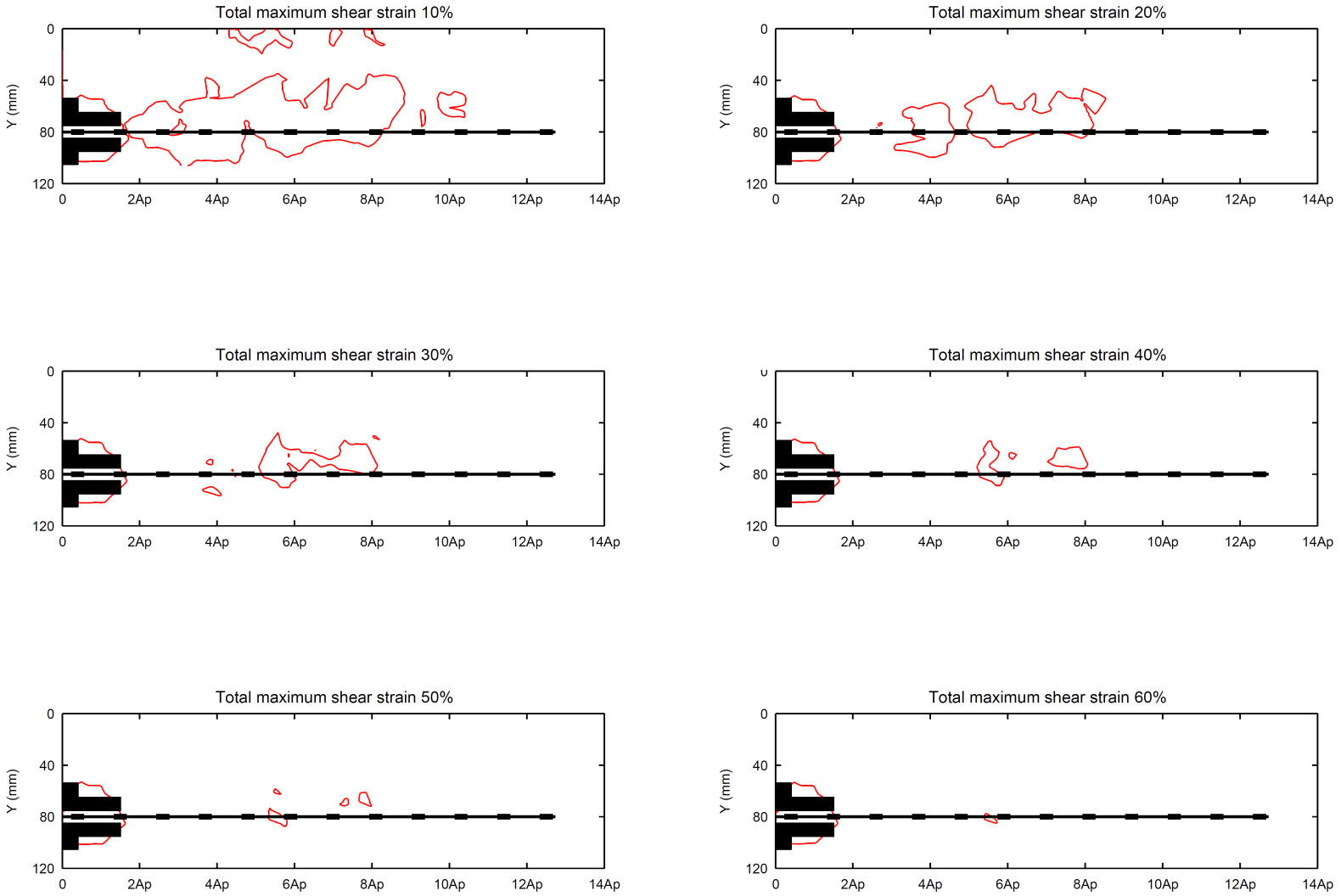

Figure 6.61: Cumulative shear strain for 40 mm axial tensile displacement of geogrid with 1600 kN/m stiffness under 25 kPa confining pressure

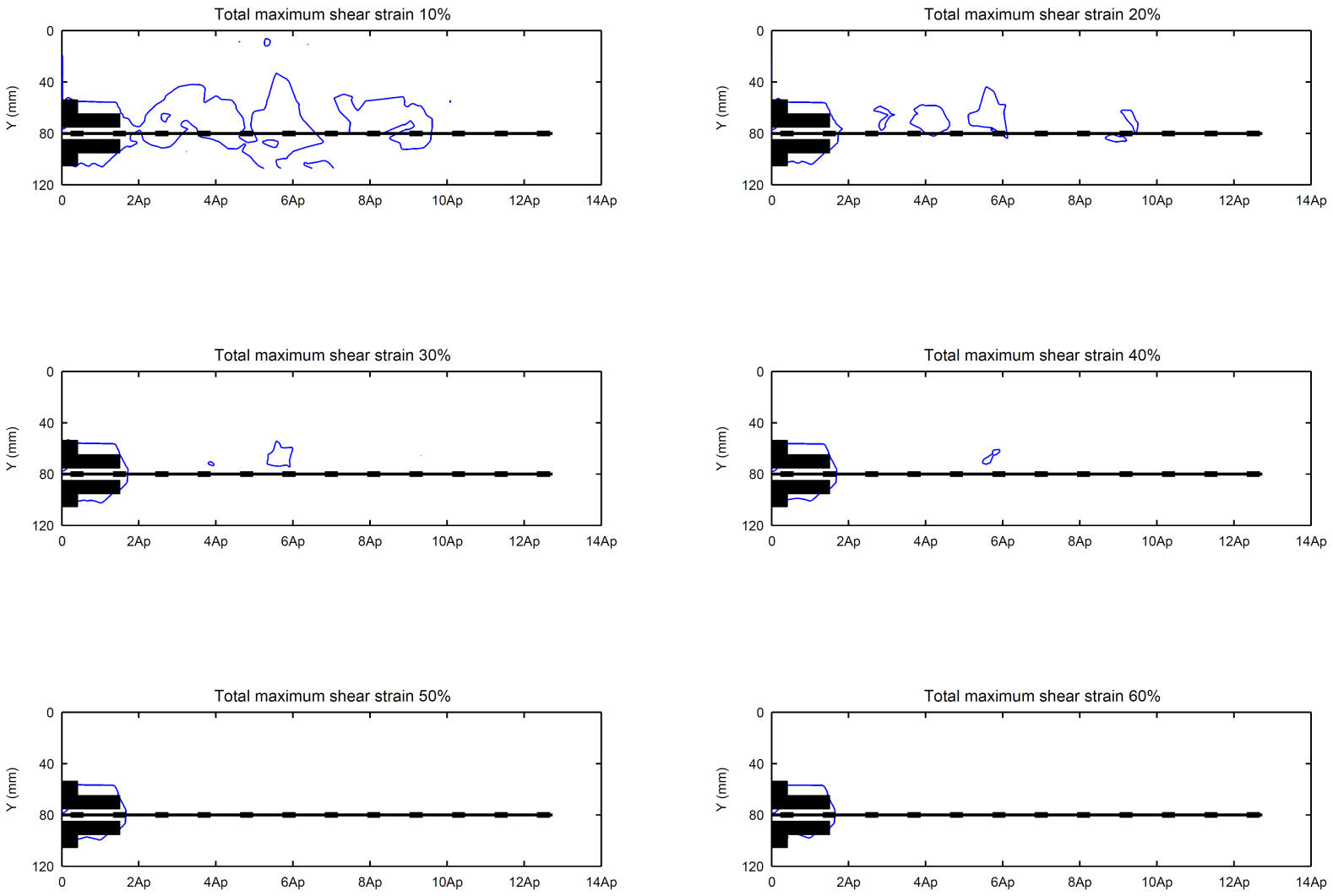

Figure 6.62: Cumulative shear strain for 40 mm axial tensile displacement of geogrid with 1600 kN/m stiffness under 50 kPa confining pressure

Figures 6.63, 6.64 and 6.65 show the volumetric strains caused by pulling out the geogrid from soil for different amount of confining pressure 12.5 kPa, 25 kPa and 50 kPa.

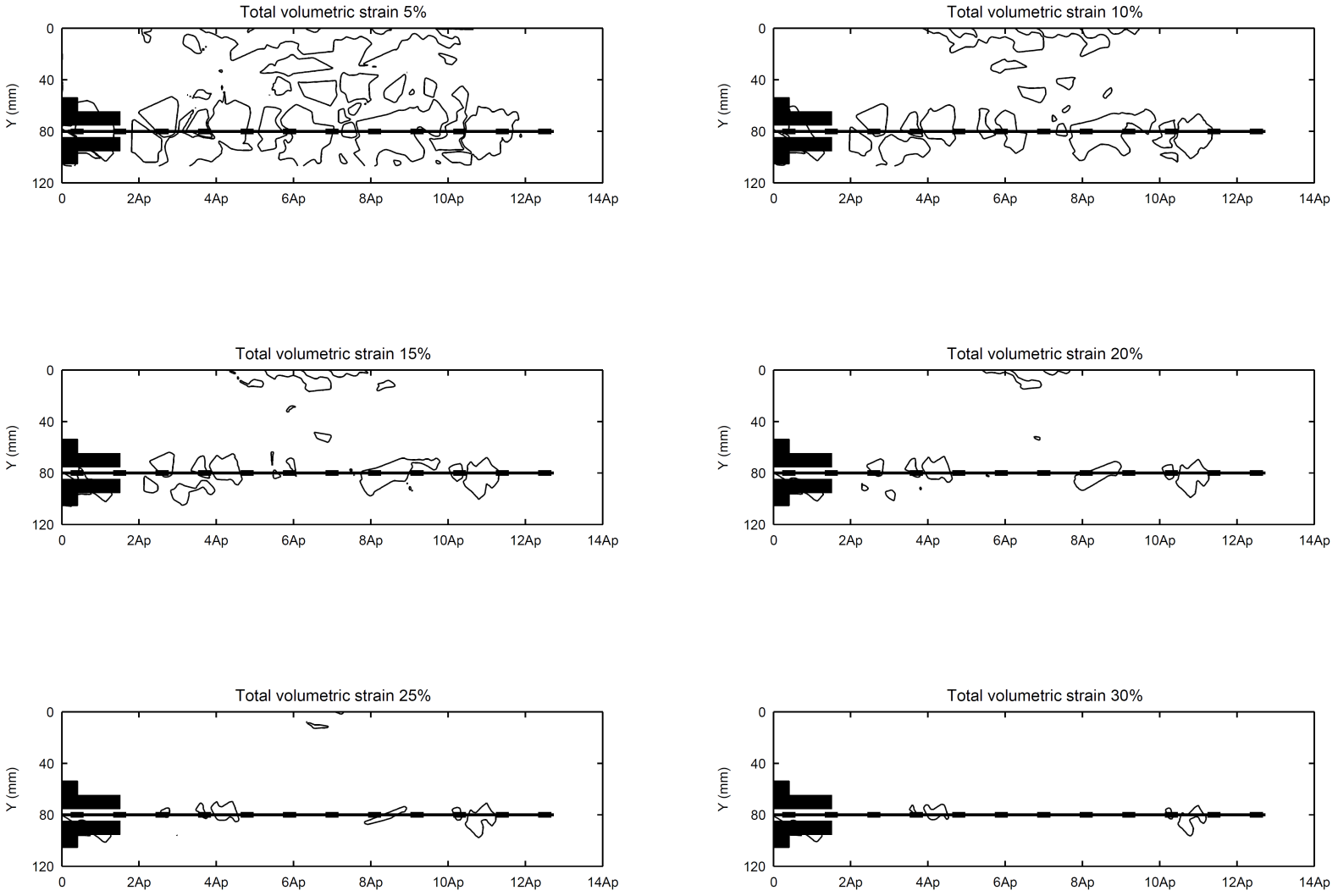

Figure 6.63: Cumulative volumetric strain for 40 mm axial tensile displacement of geogrid with 1600 kN/m stiffness under 12.5 kPa confining pressure

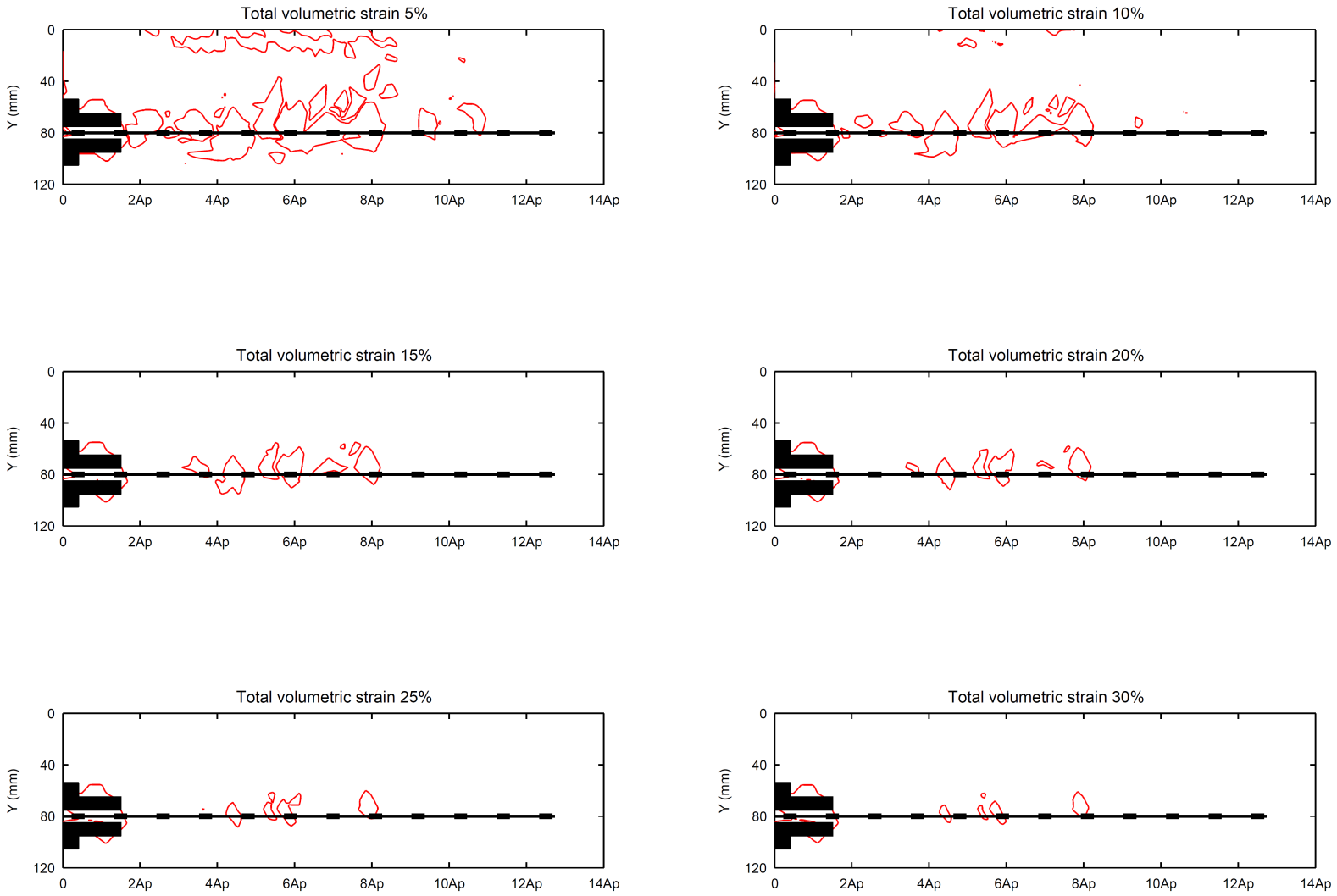

Figure 6.64: Cumulative volumetric strain for 40 mm axial tensile displacement of geogrid with 1600 kN/m stiffness under 25 kPa confining pressure

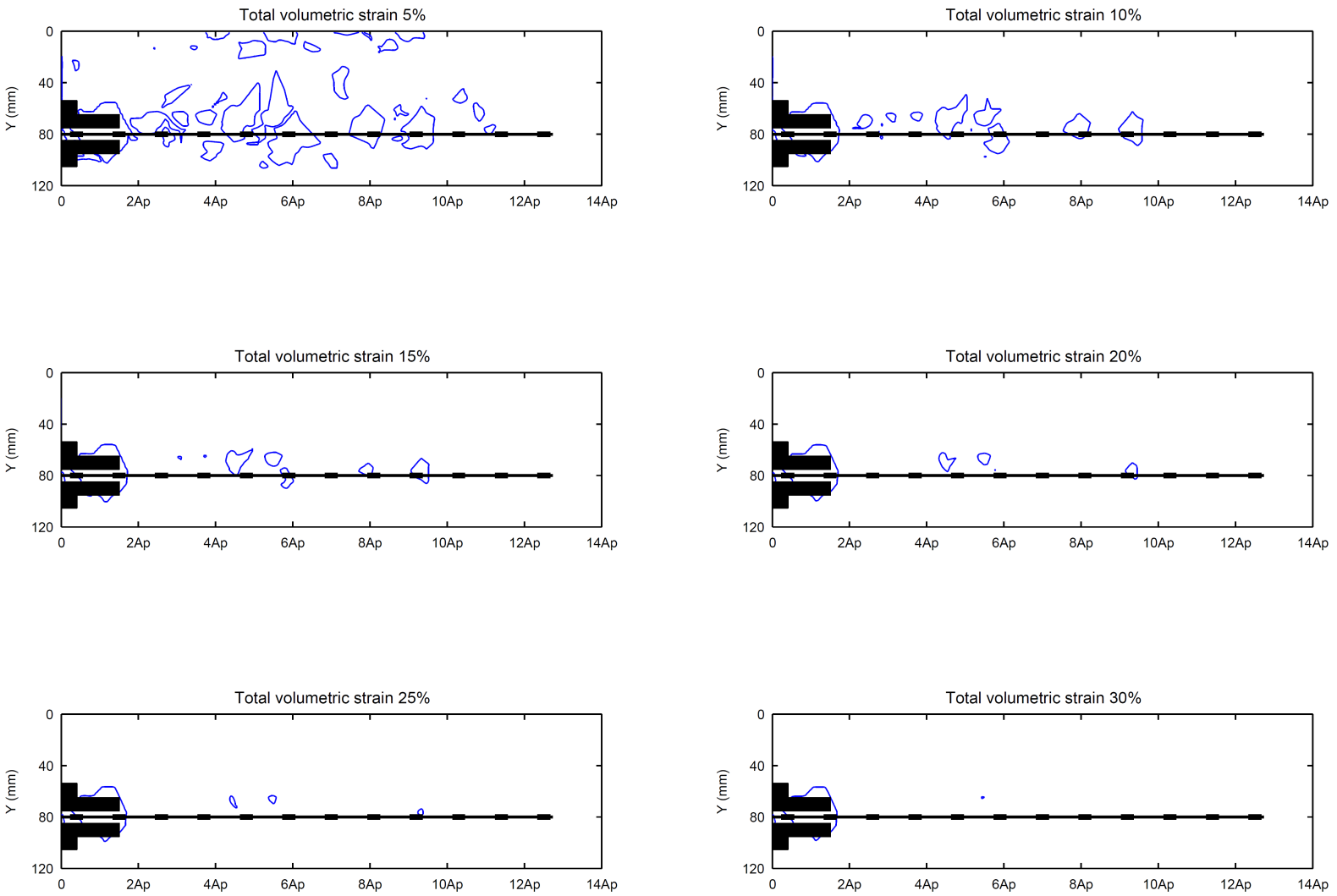

Figure 6.65: Cumulative volumetric strain for 40 mm axial tensile displacement of geogrid with 1600 kN/m stiffness under 50 kPa confining pressure

6.2.3 Test3: Stiffness of geogrid=2900 kN/m

Figure 6.66 presents the results of the load-displacement under 12.5 kPa, 25 kPa and 50 kPa confining pressures.

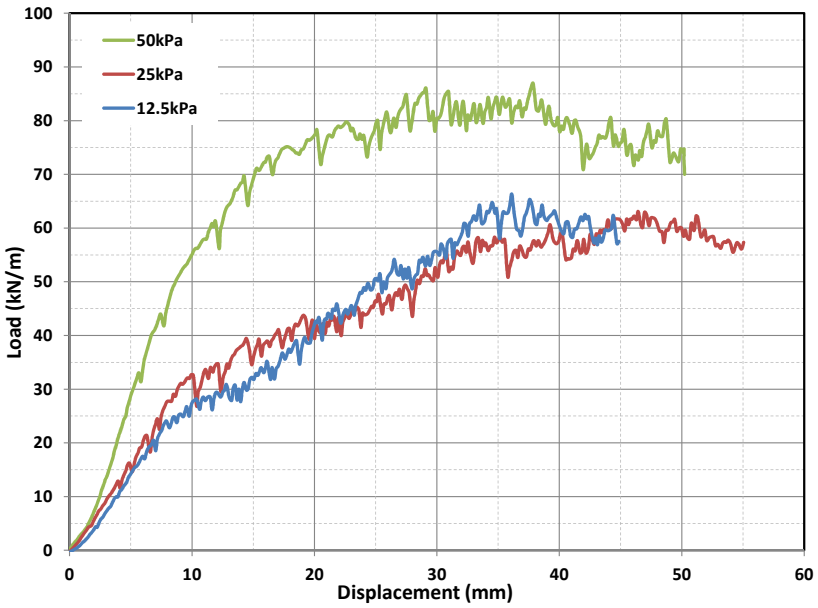

Figure 6.66: Load-displacement plots of geogrid specimen with stiffness of 2900 kN/m

The cumulative vector of displacement with horizontal and vertical displacement under three different confining pressures (12.5 kPa, 25 kPa and 50 kPa) at the end of the test is presented in Figures 6.67-6.78.

The zone of influence of geogrid and transparent soil is observed from the horizontal contours between 35 - 40 mm which corresponds to 4 to 5.5 times the soil particles. The results of the study show that the lowest confining pressure has a bigger zone of influence.

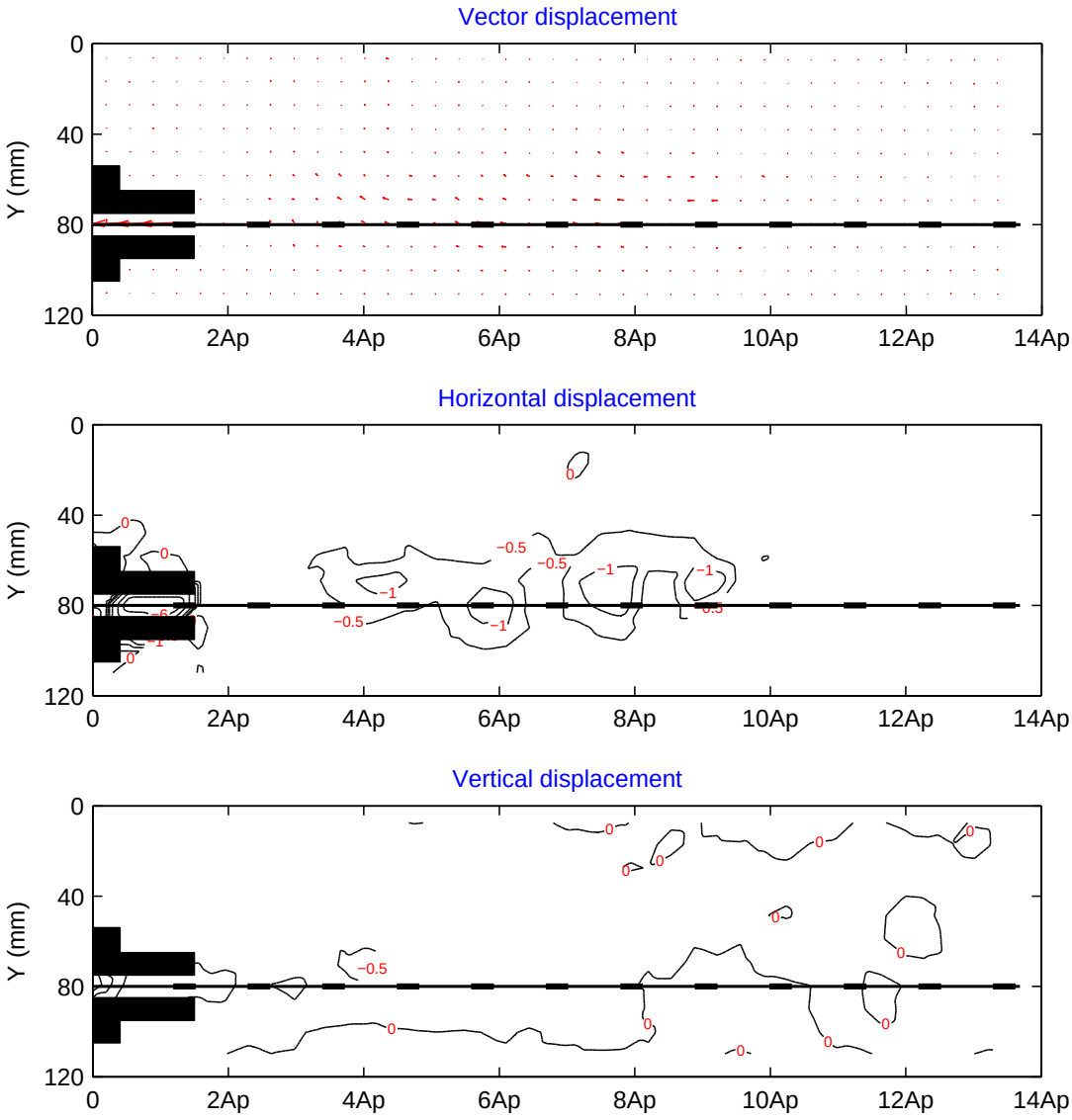

Figure 6.67: Cumulative PIV results at 10 mm axial tensile displacement of geogrid with 2900 kN/m stiffness under 12.5 kPa confining pressure

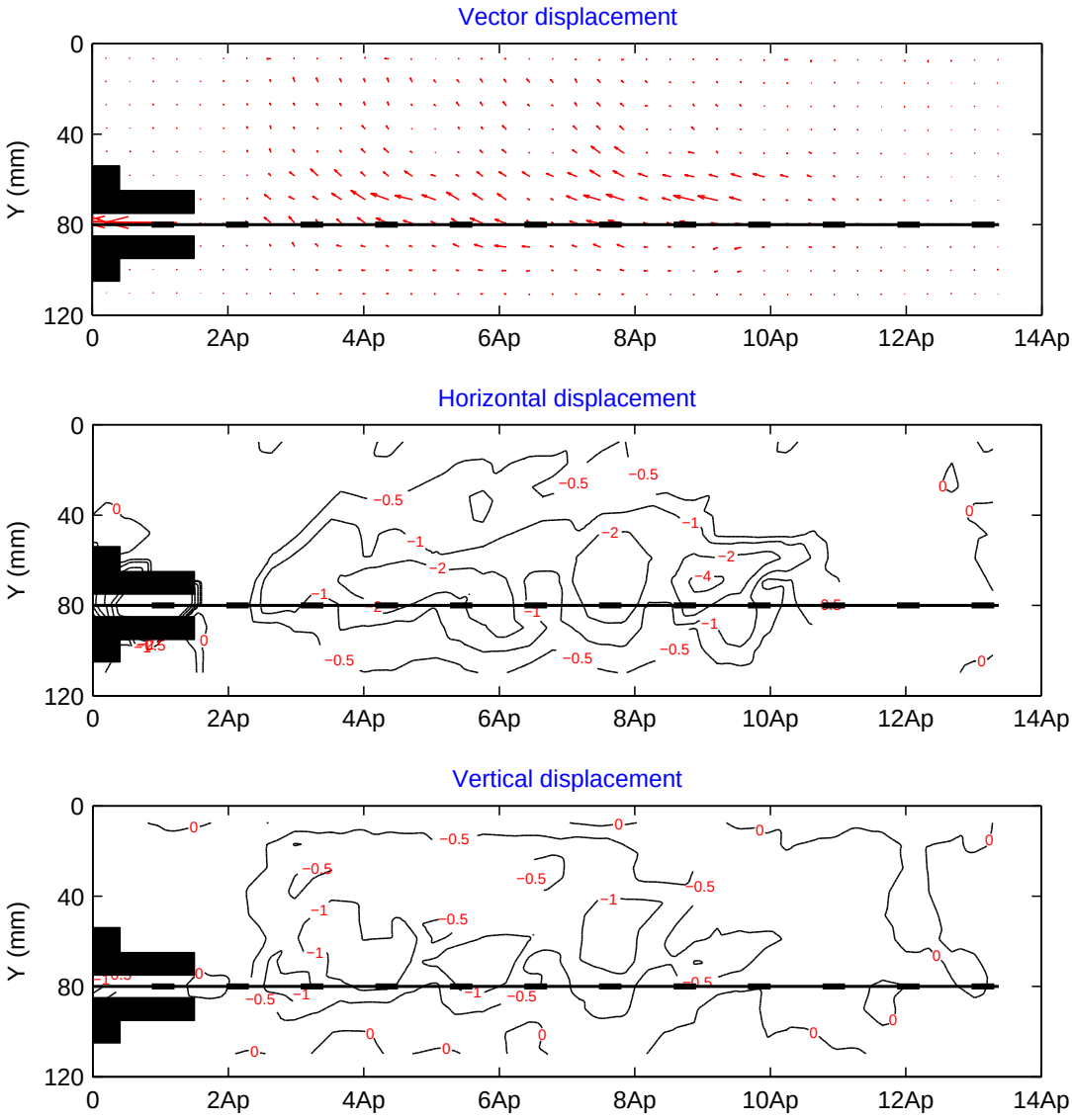

Figure 6.68: Cumulative PIV results at 20 mm axial tensile displacement of geogrid with 2900 kN/m stiffness under 12.5 kPa confining pressure

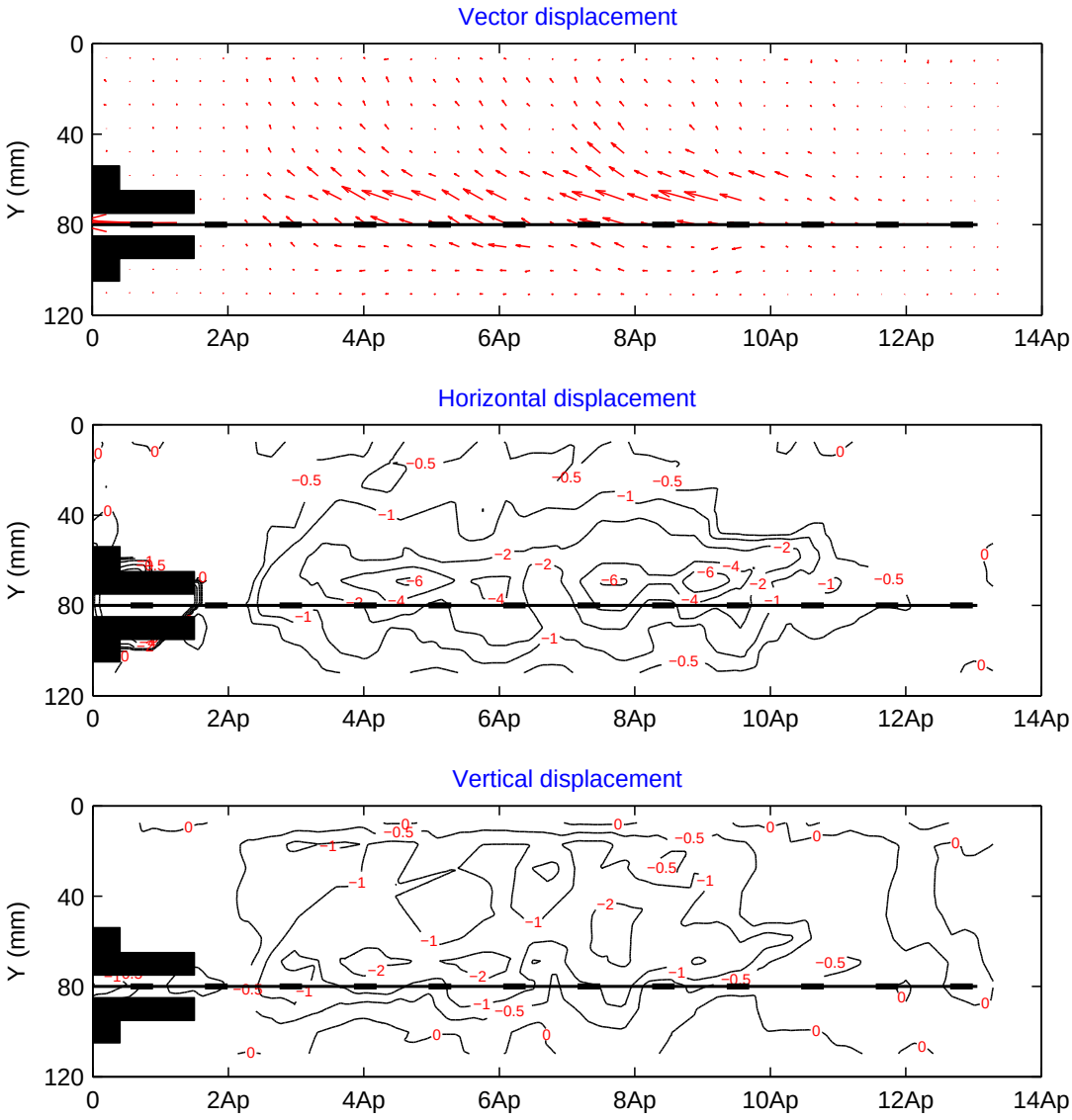

Figure 6.69: Cumulative PIV results at 30 mm axial tensile displacement of geogrid with 2900 kN/m stiffness under 12.5 kPa confining pressure

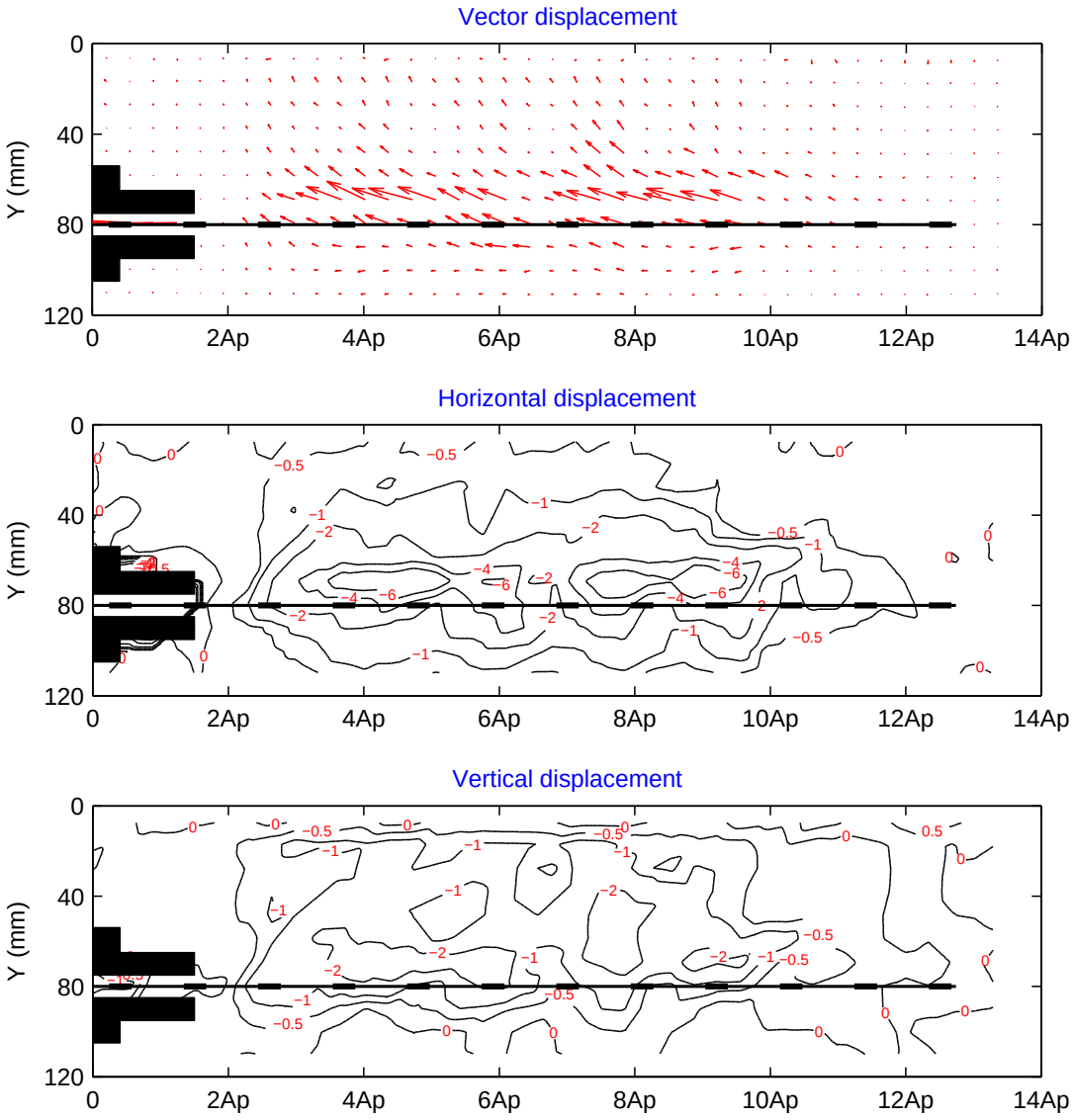

Figure 6.70: Cumulative PIV results at 40 mm axial tensile displacement of geogrid with 2900 kN/m stiffness under 12.5 kPa confining pressure

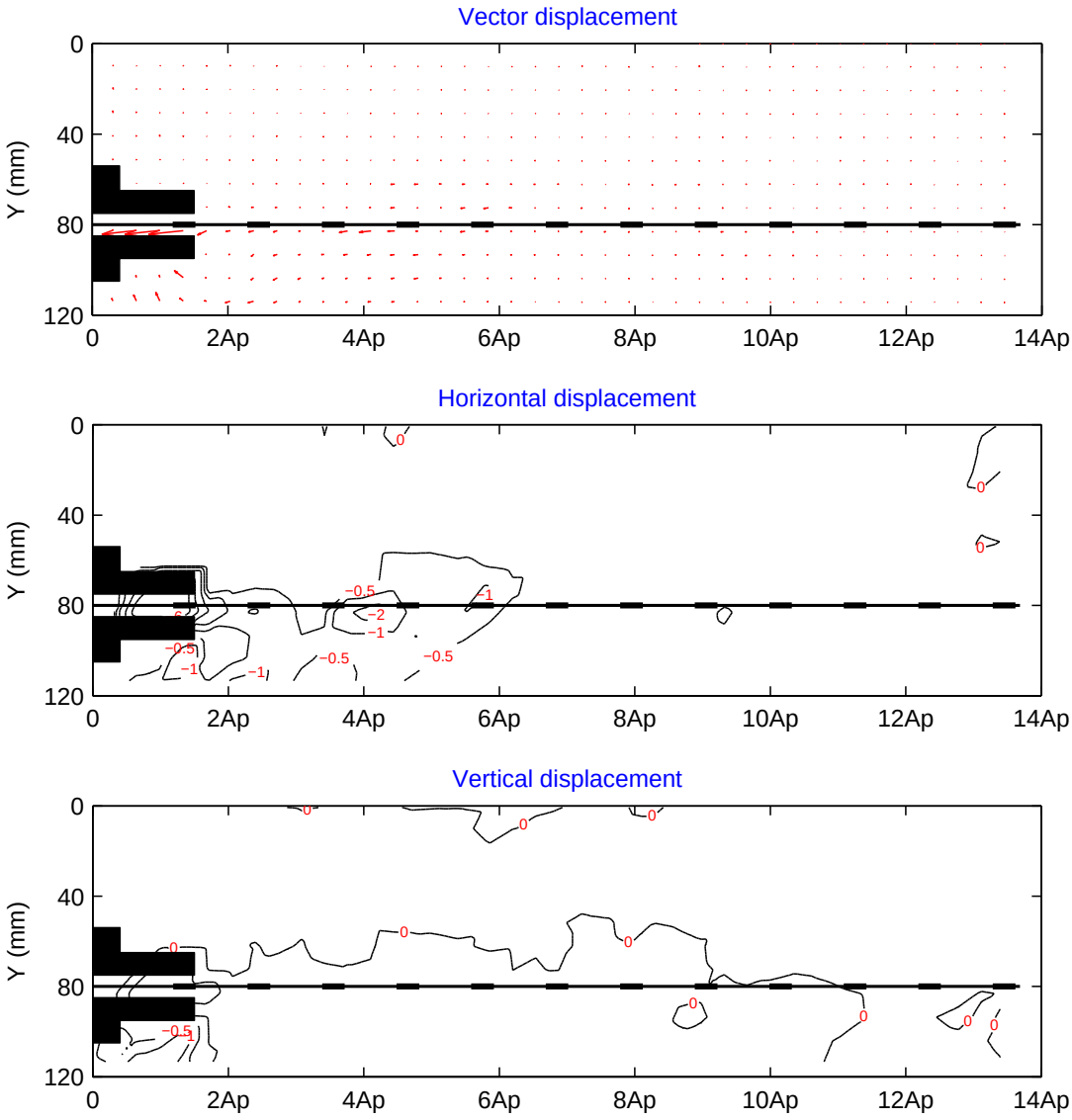

Figure 6.71: Cumulative PIV results at 10 mm axial tensile displacement of geogrid with 2900 kN/m stiffness under 25 kPa confining pressure

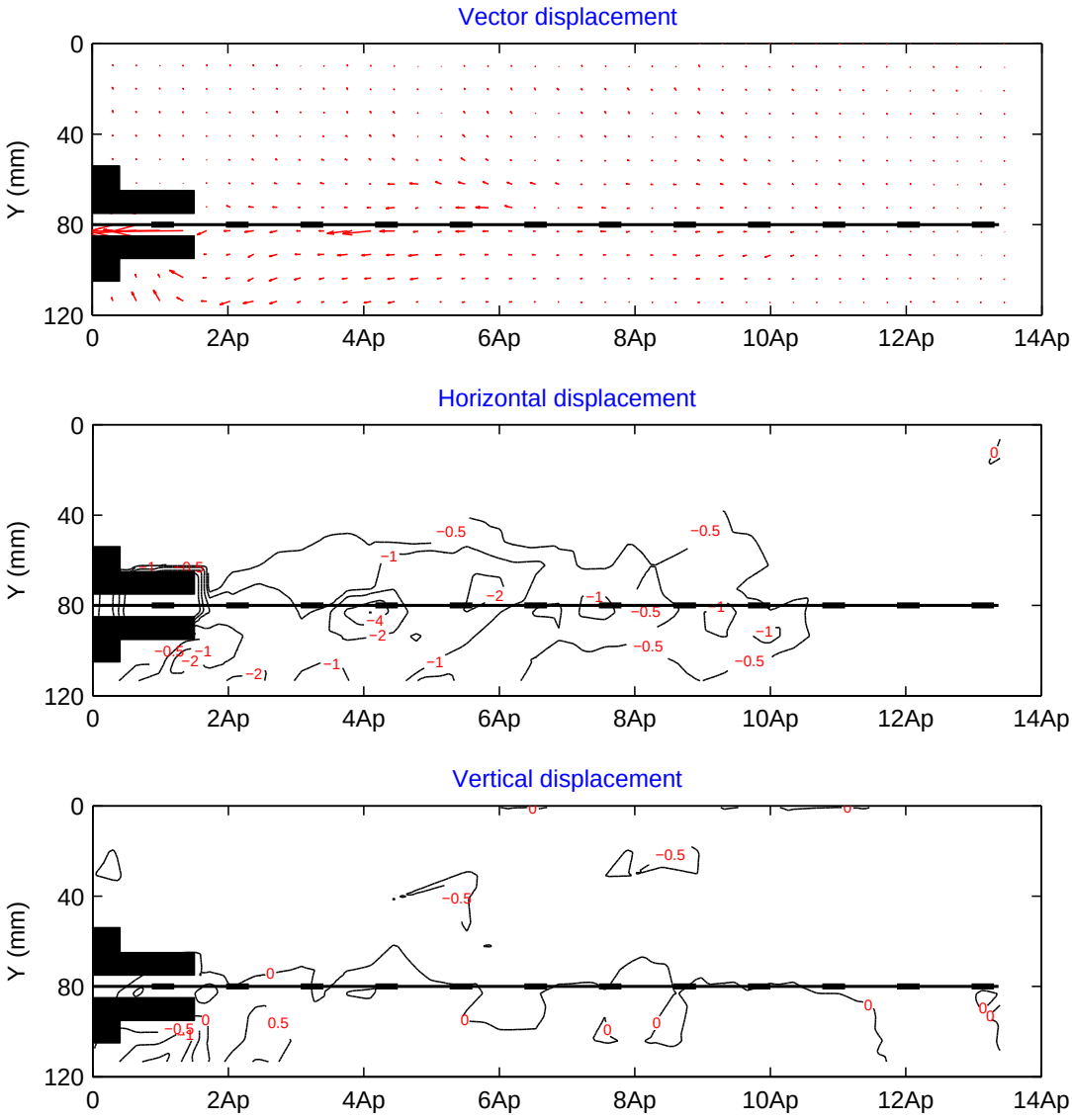

Figure 6.72: Cumulative PIV results at 20 mm axial tensile displacement of geogrid with 2900 kN/m stiffness under 25 kPa confining pressure

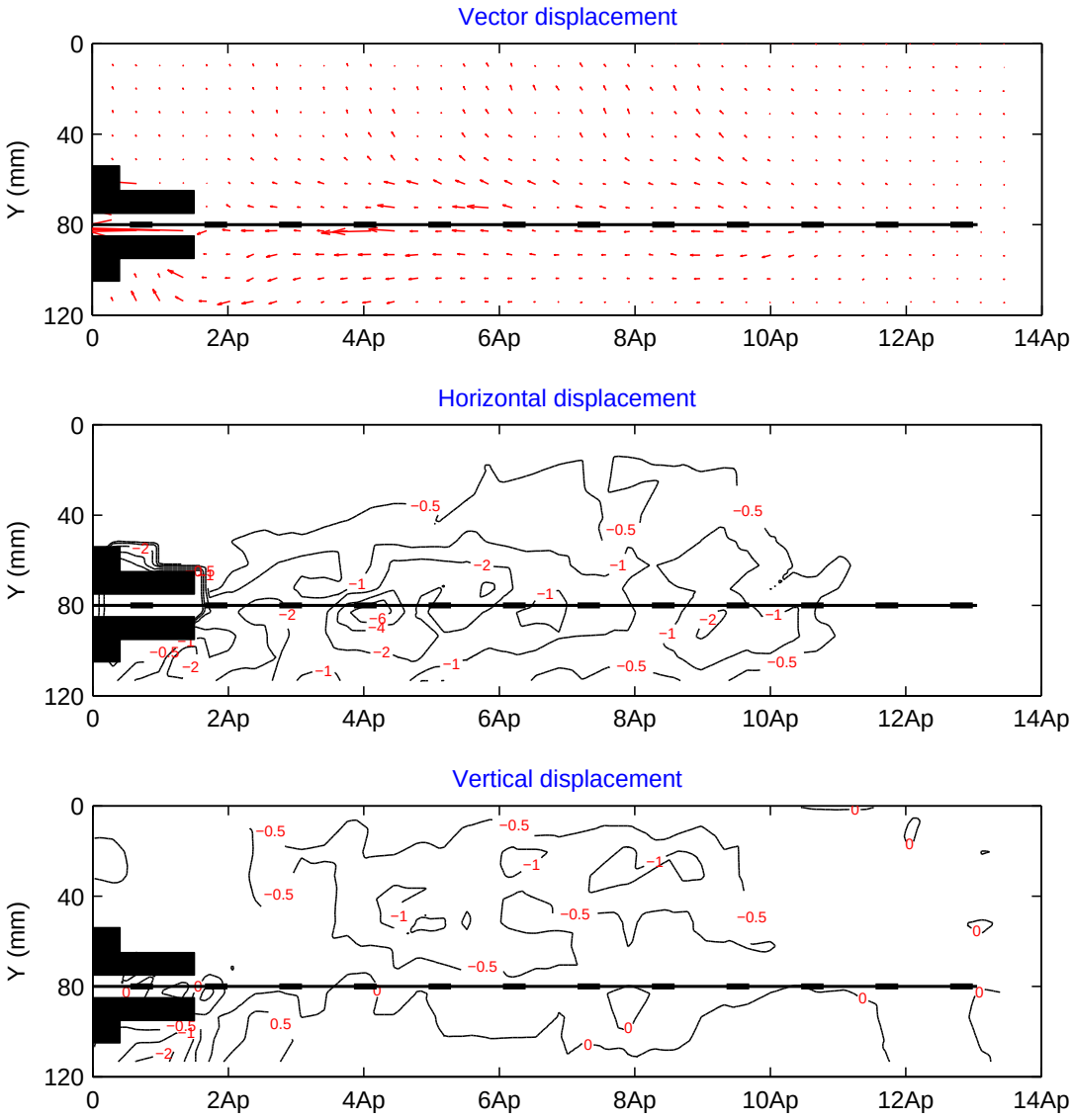

Figure 6.73: Cumulative PIV results at 30 mm axial tensile displacement of geogrid with 2900 kN/m stiffness under 25 kPa confining pressure

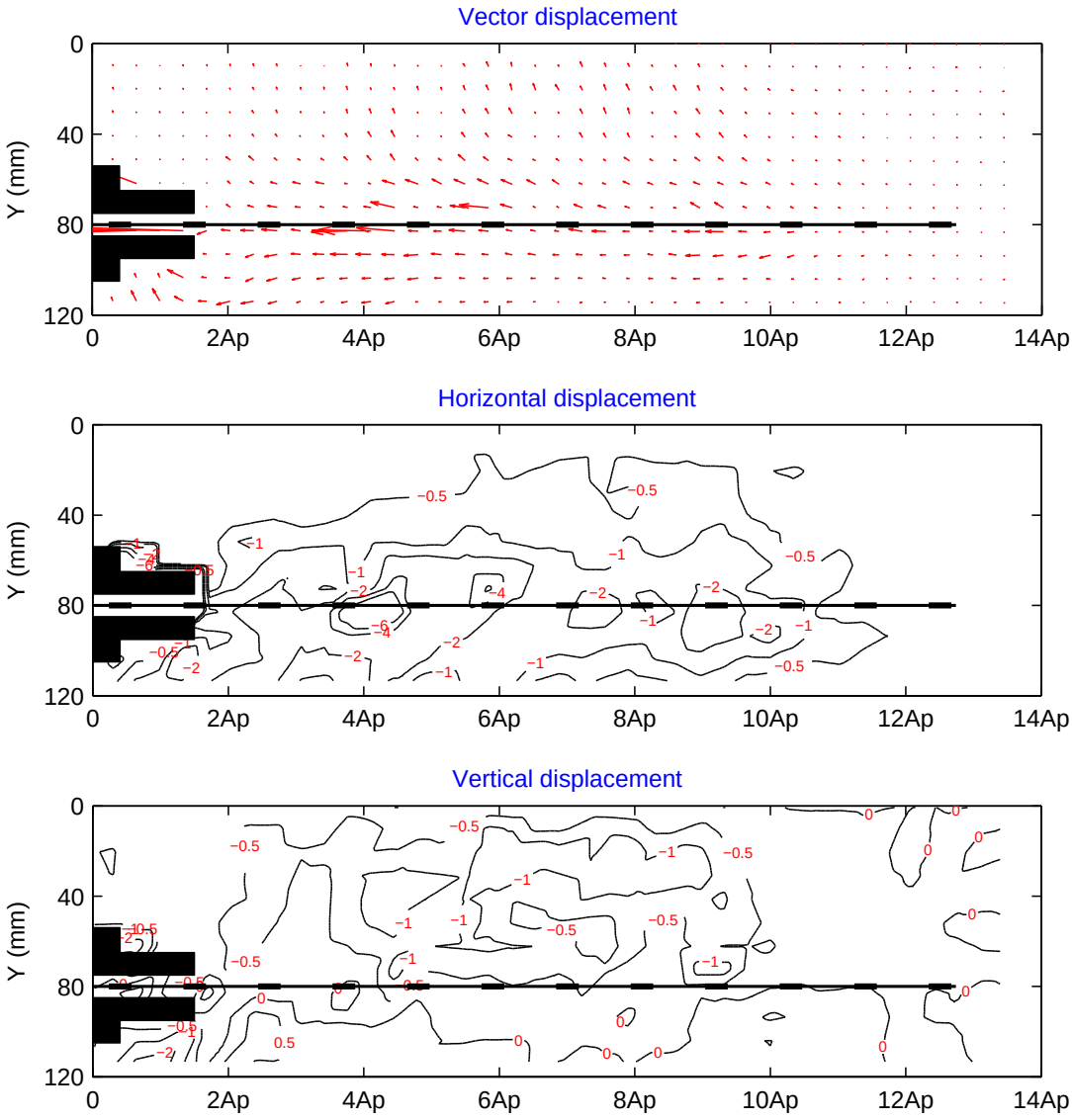

Figure 6.74: Cumulative PIV results at 40 mm axial tensile displacement of geogrid with 2900 kN/m stiffness under 25 kPa confining pressure

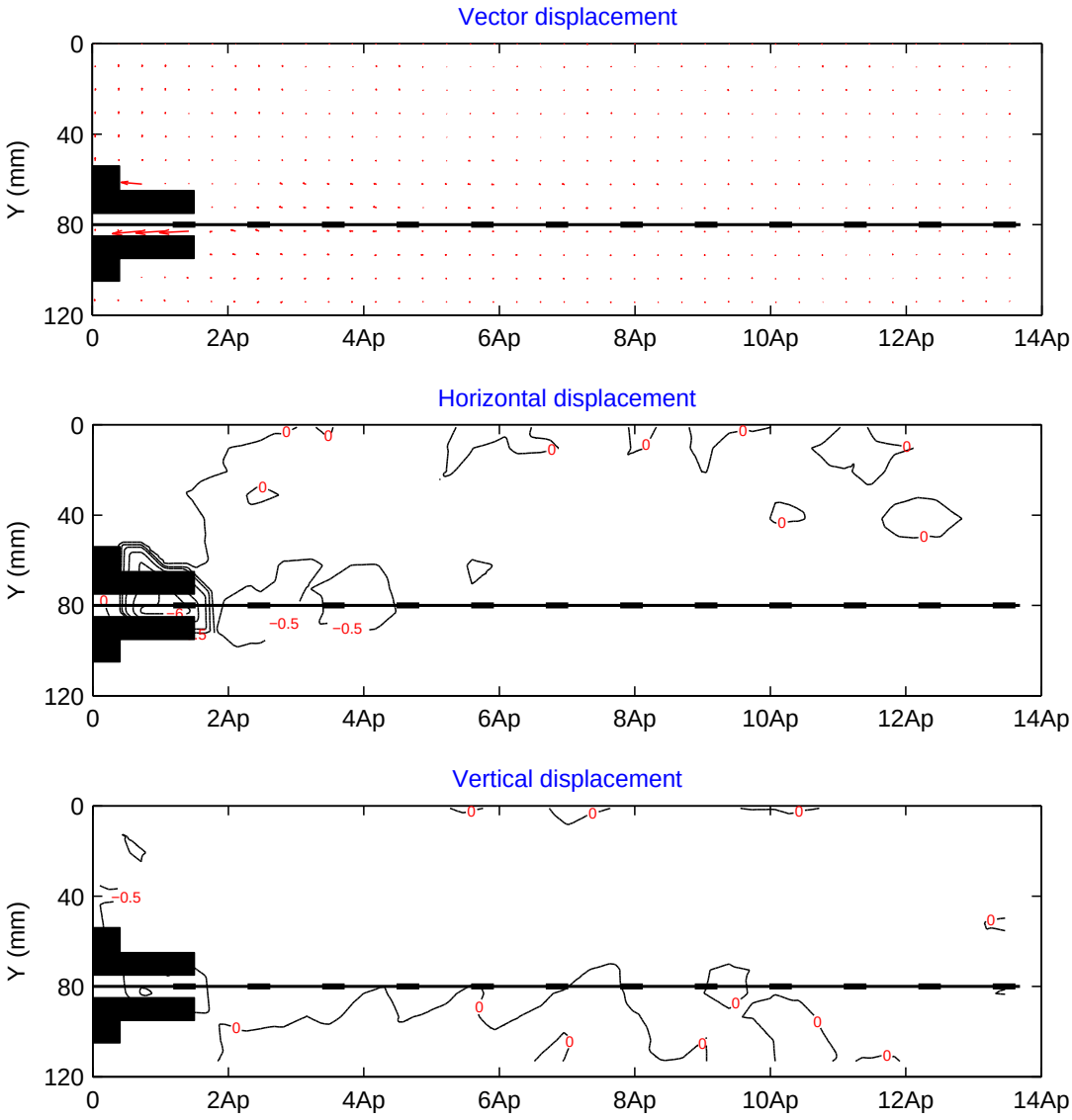

Figure 6.75: Cumulative PIV results at 10 mm axial tensile displacement of geogrid with 2900 kN/m stiffness under 50 kPa confining pressure

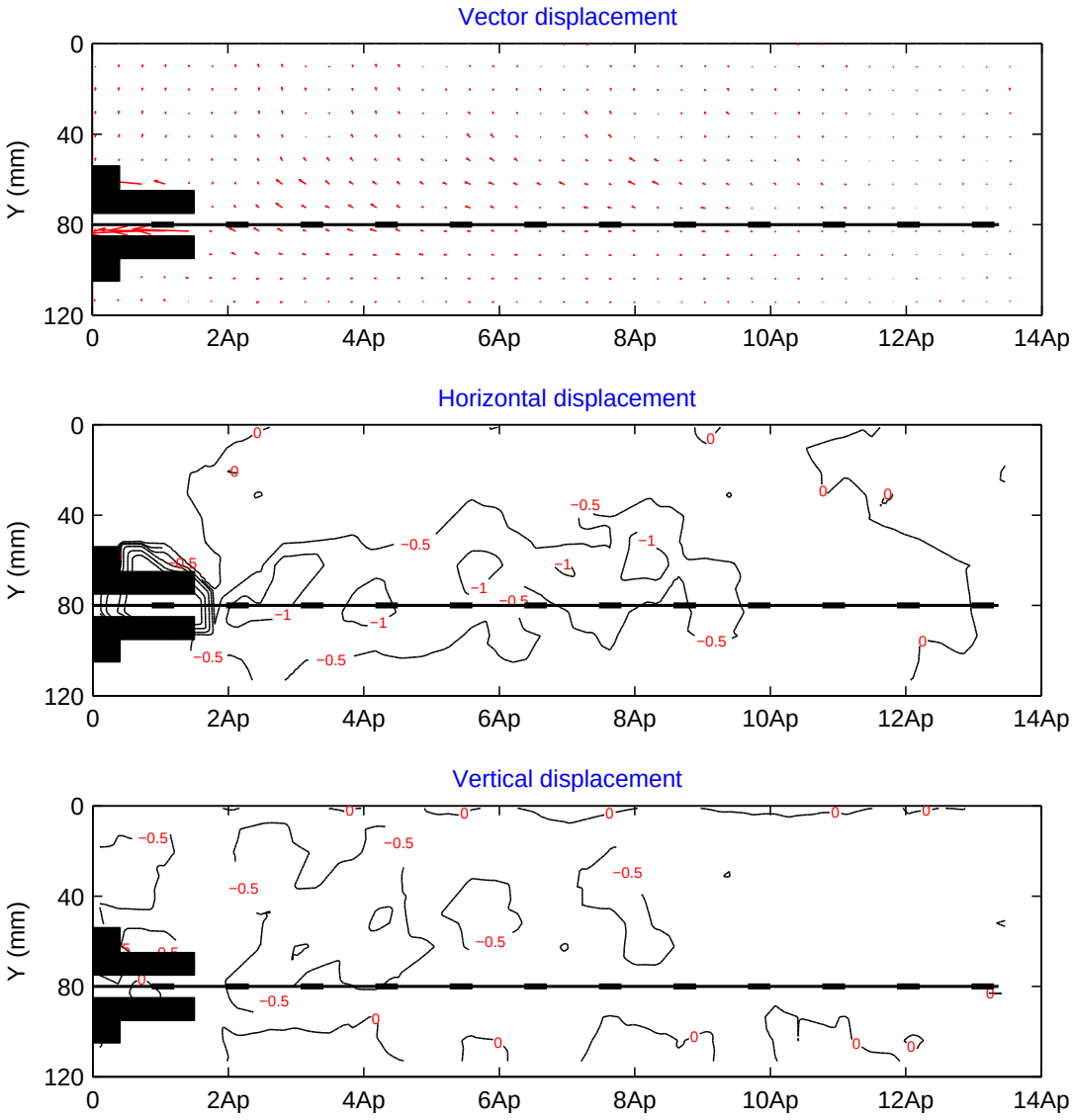

Figure 6.76: Cumulative PIV results at 20 mm axial tensile displacement of geogrid with 2900 kN/m stiffness under 50 kPa confining pressure

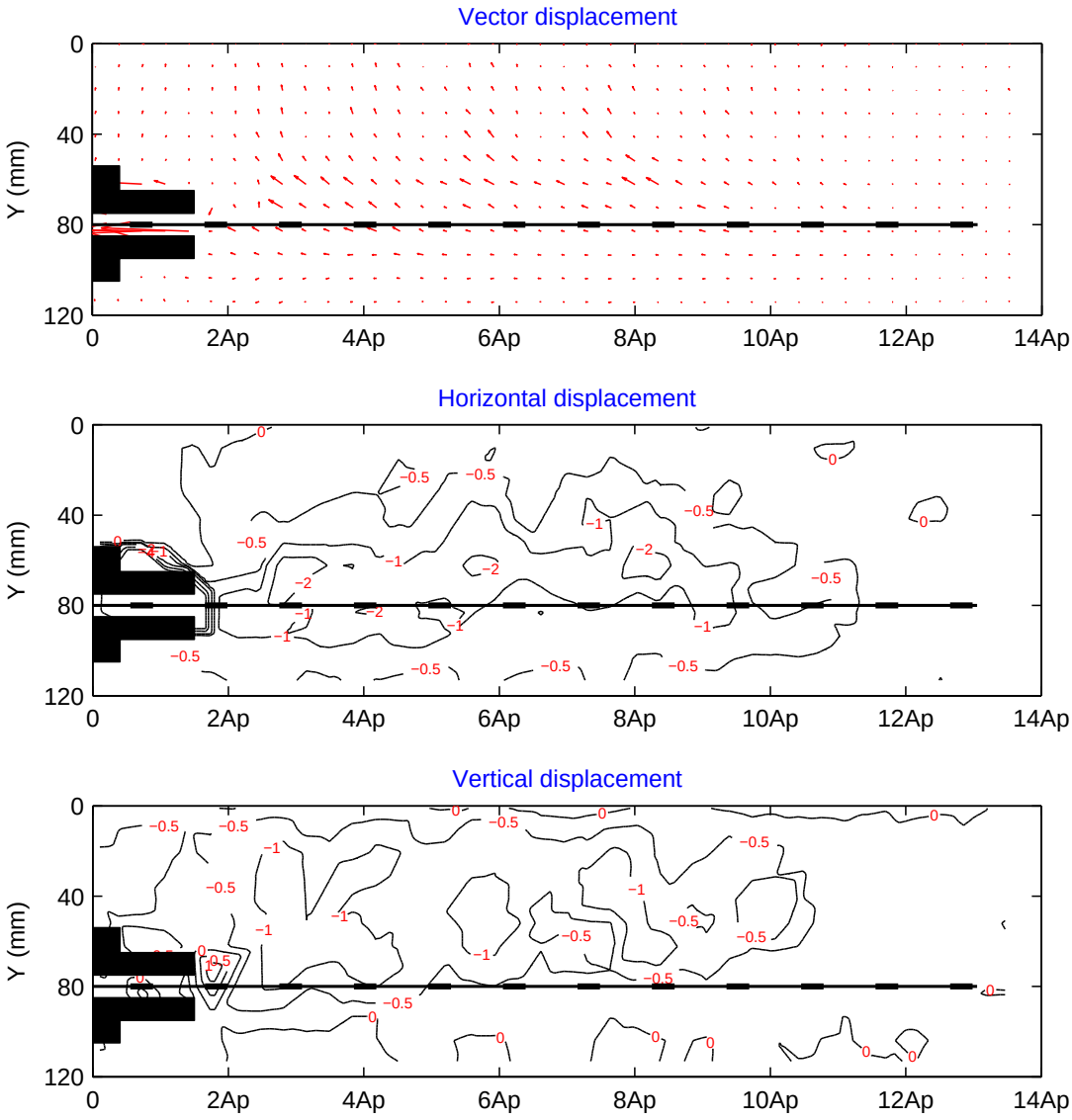

Figure 6.77: Cumulative PIV results at 30 mm axial tensile displacement of geogrid with 2900 kN/m stiffness under 50 kPa confining pressure

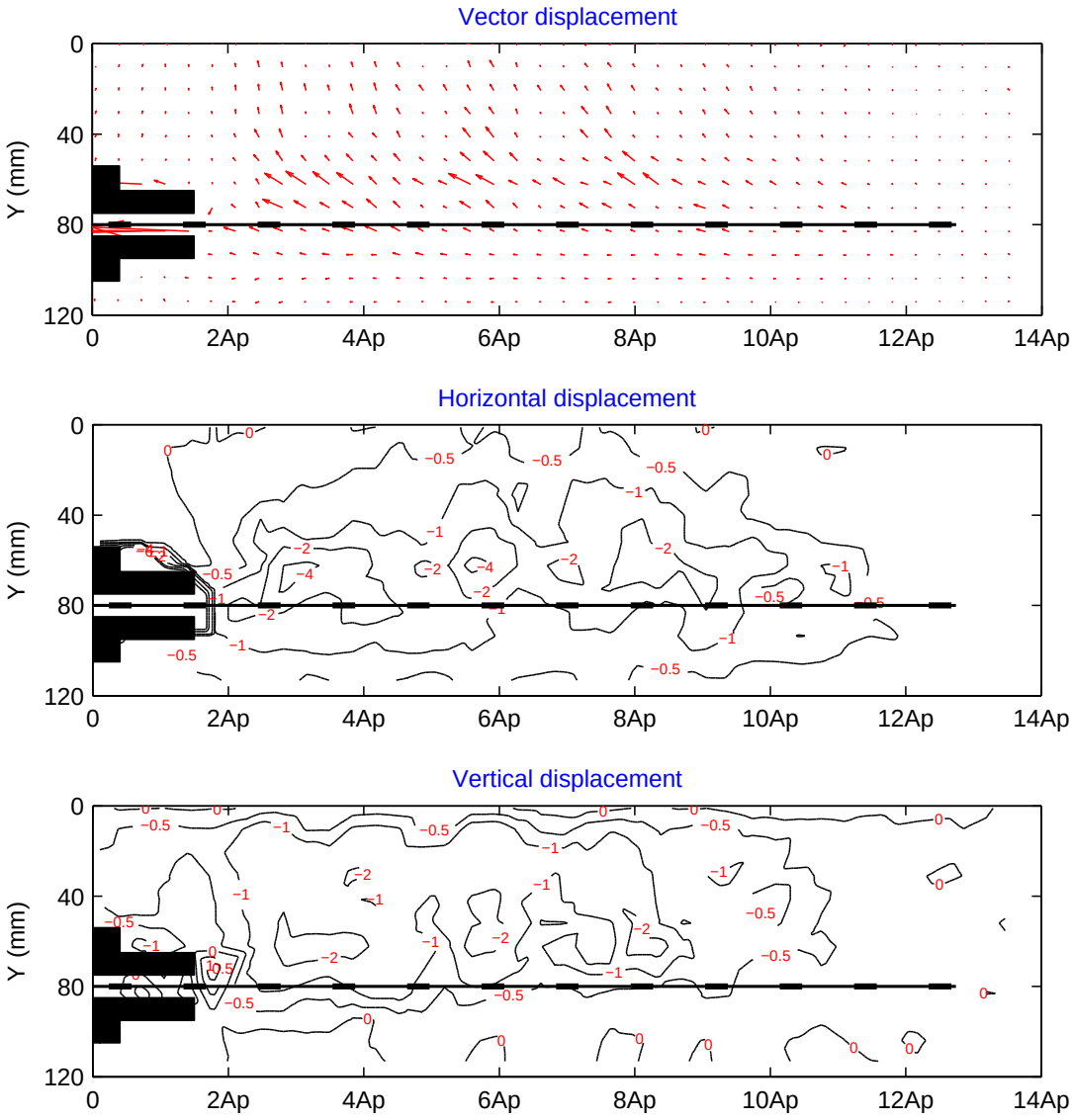

Figure 6.78: Cumulative PIV results at 40 mm axial tensile displacement of geogrid with 2900 kN/m stiffness under 50 kPa confining pressure

The incremental PIV results from 0 to 40 mm for 10 mm increments for a vector of horizontal and vertical displacement under three different values of confining pressure (12.5 kPa, 25 kPa and 50 kPa) show in Figures 6.79-6.90.

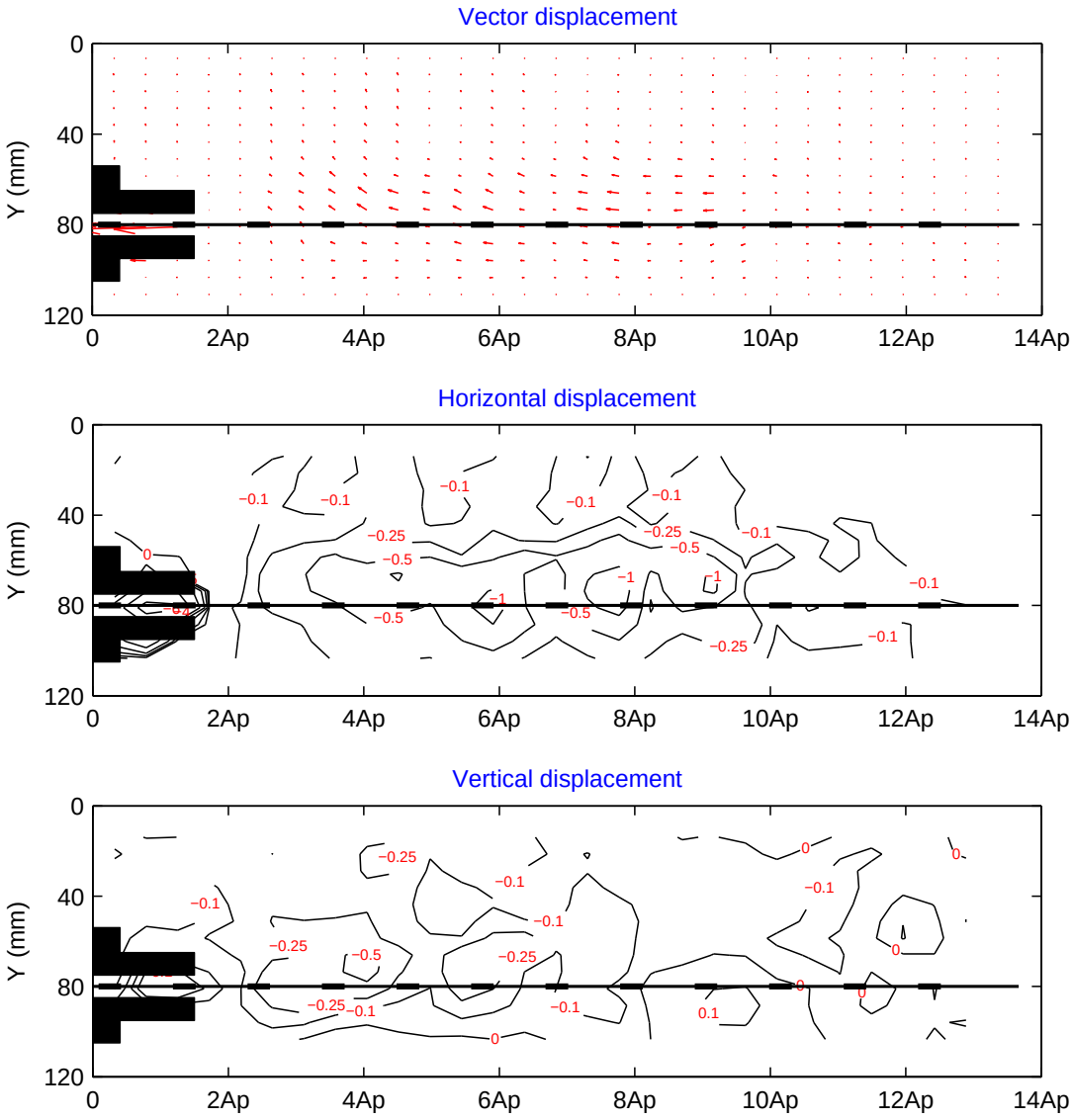

Figure 6.79: Incremental PIV results from 0 mm to 10 mm axial tensile displacement of geogrid with 2900 kN/m stiffness under 12.5 kPa confining pressure

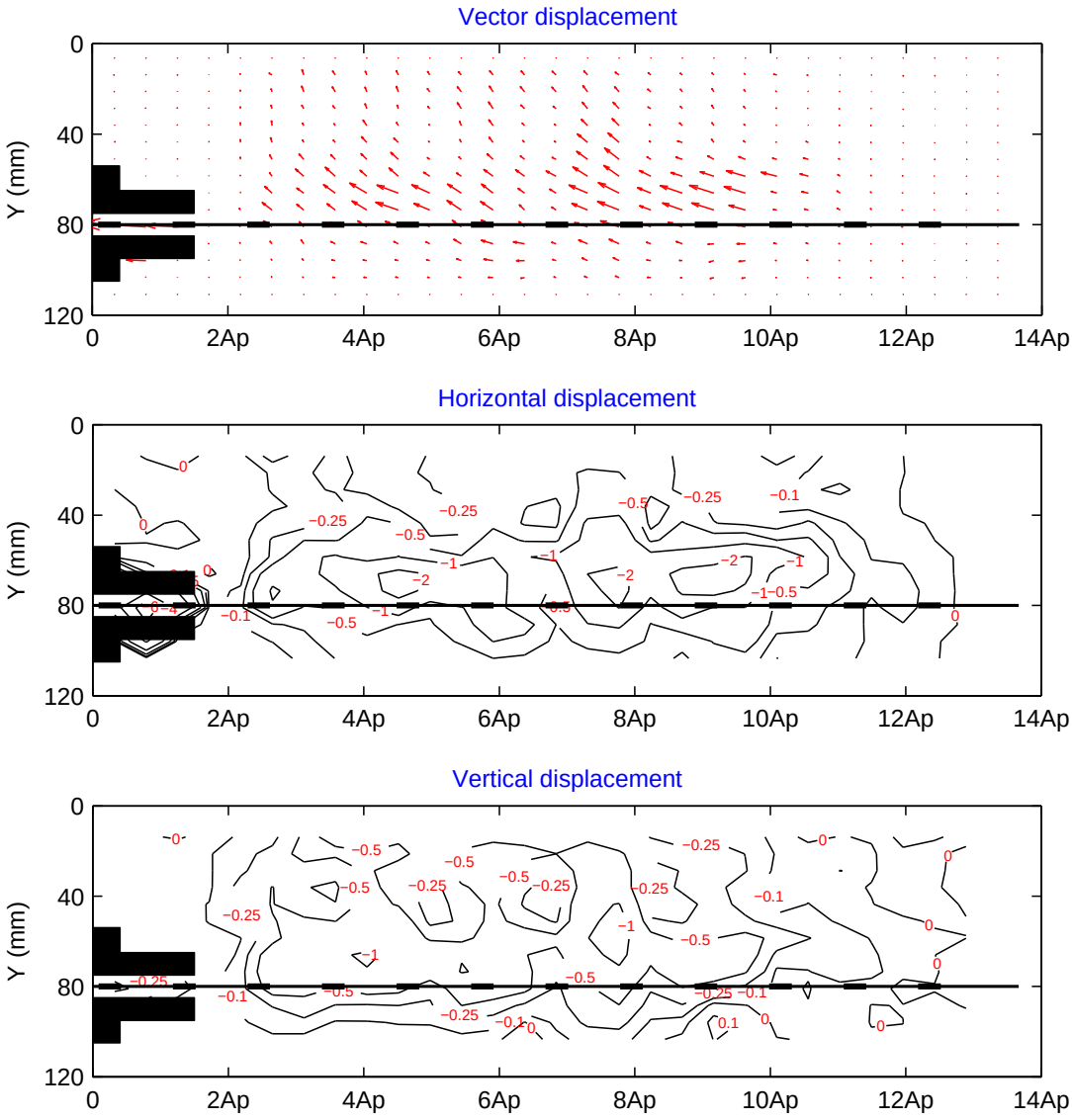

Figure 6.80: Incremental PIV results from 10 mm to 20 mm axial tensile displacement of geogrid with 2900 kN/m stiffness under 12.5 kPa confining pressur

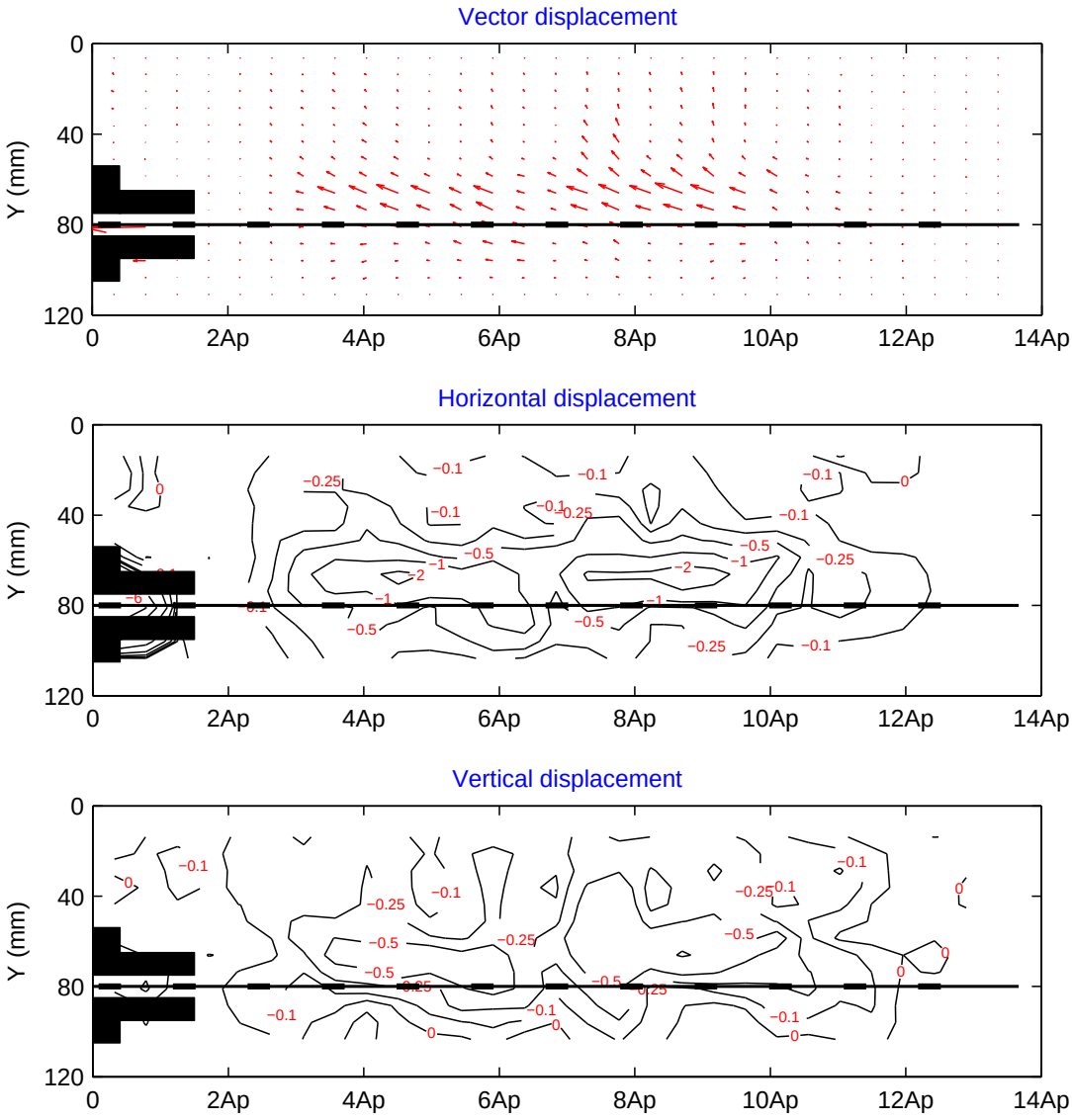

Figure 6.81: Incremental PIV results from 20 mm to 30 mm axial tensile displacement of geogrid with 2900 kN/m stiffness under 12.5 kPa confining pressur

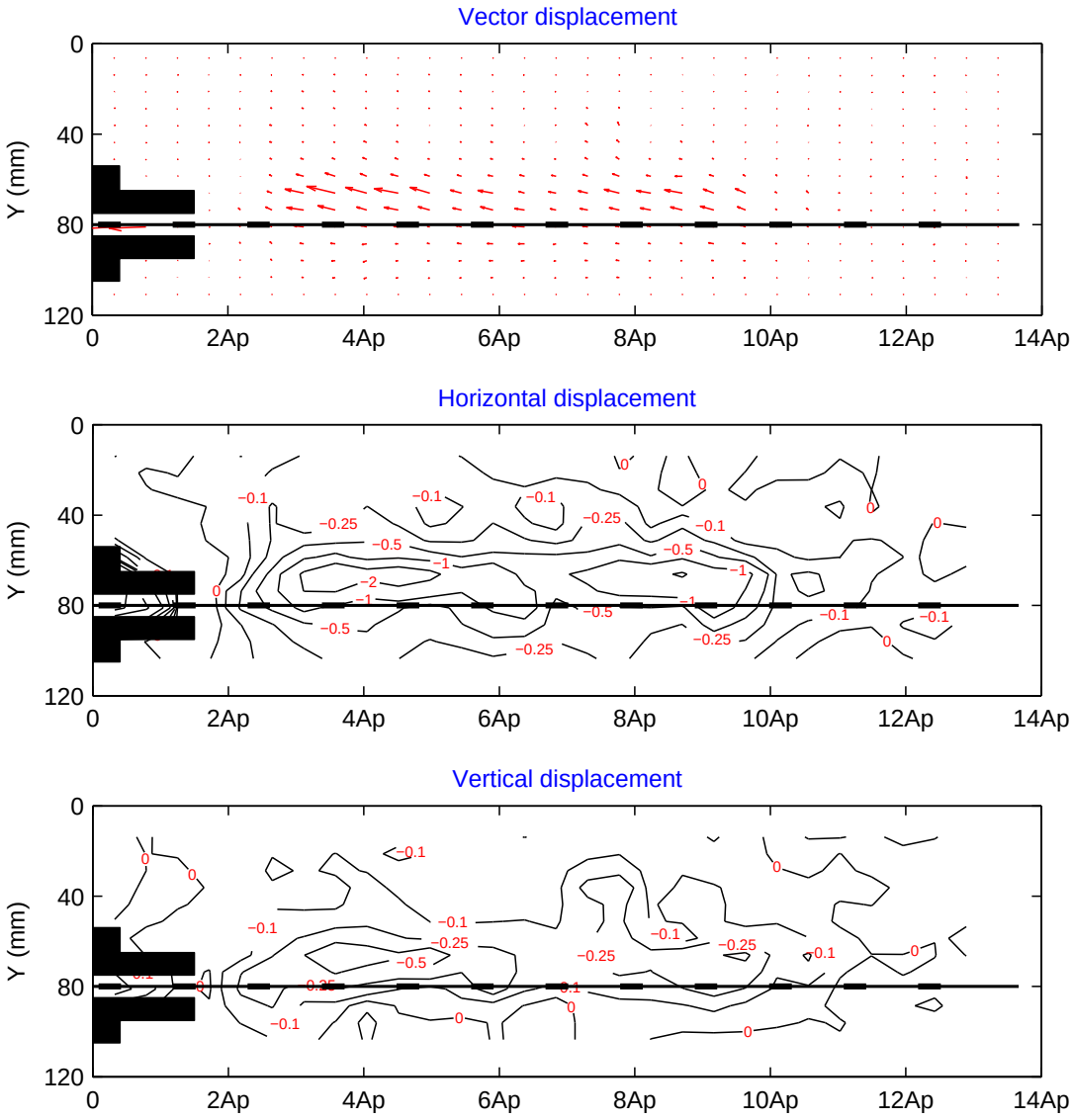

Figure 6.82: Incremental PIV results from 30 mm to 40 mm axial tensile displacement of geogrid with 2900 kN/m stiffness under 12.5 kPa confining pressure

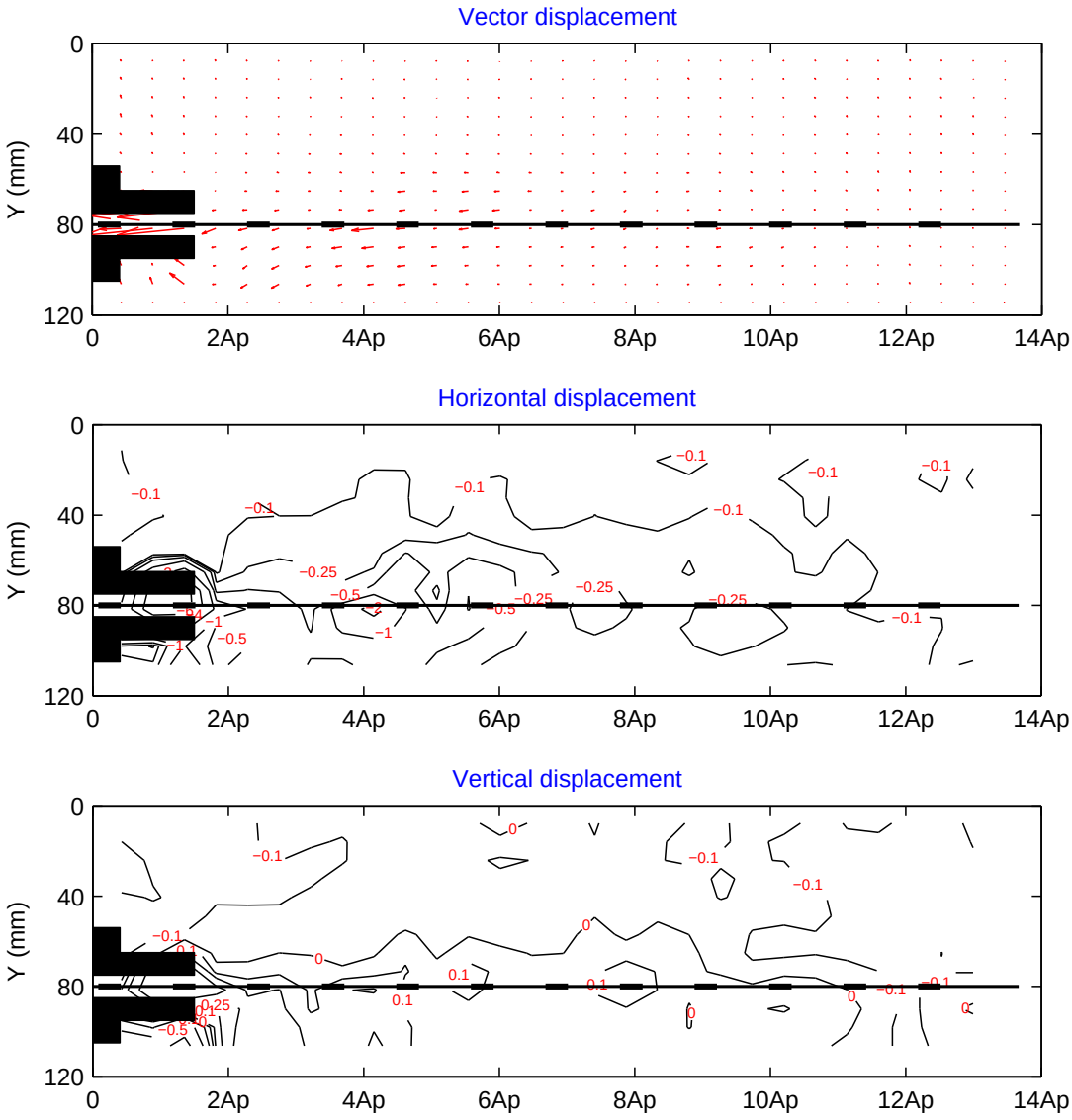

Figure 6.83: Incremental PIV results from 0 mm to 10 mm axial tensile displacement of geogrid with 2900 kN/m stiffness under 25 kPa confining pressure

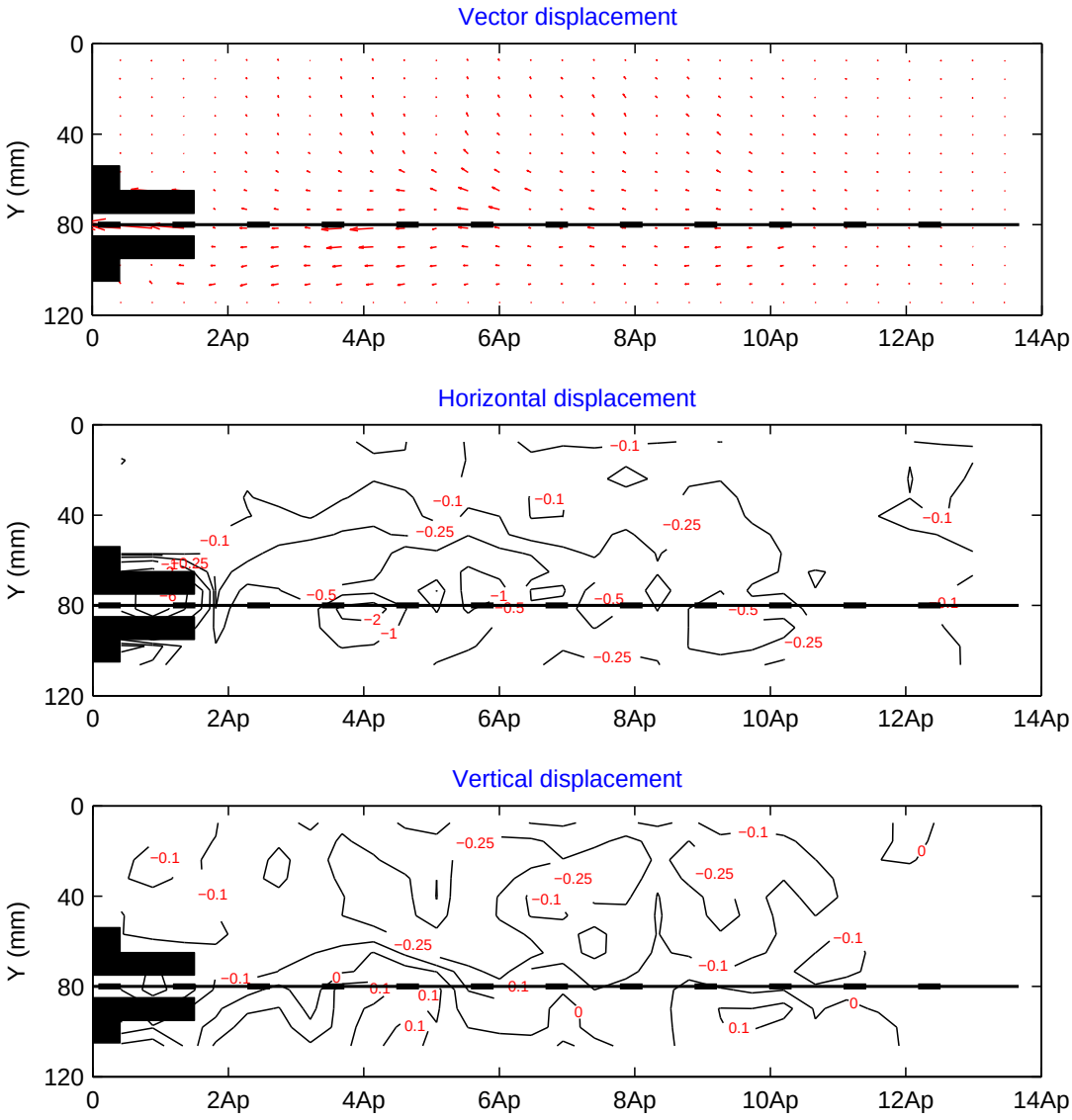

Figure 6.84: Incremental PIV results from 10 mm to 20 mm axial tensile displacement of geogrid with 2900 kN/m stiffness under 25 kPa confining pressure

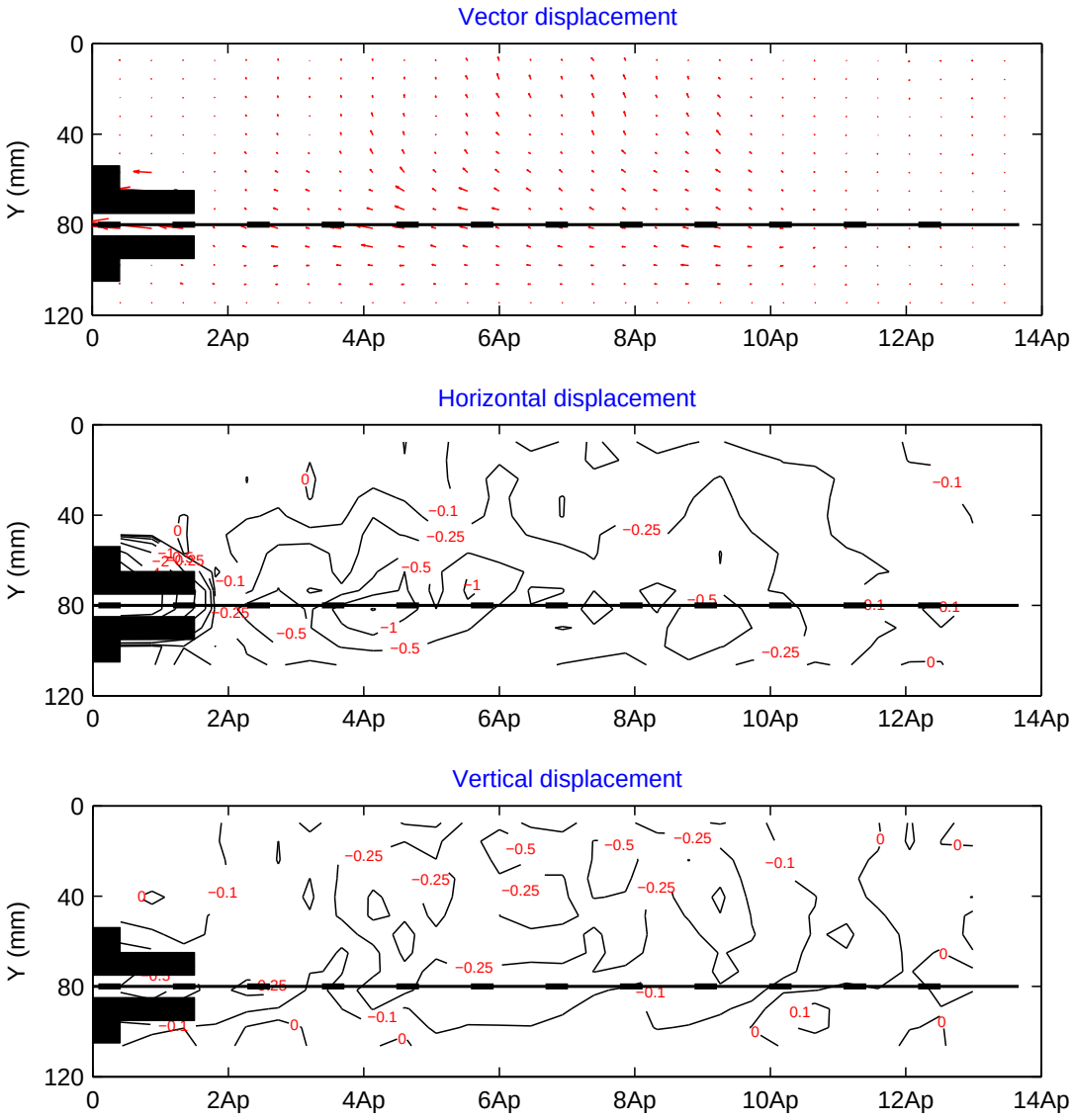

Figure 6.85: Incremental PIV results from 20 mm to 30 mm axial tensile displacement of geogrid with 2900 kN/m stiffness under 25 kPa confining pressure

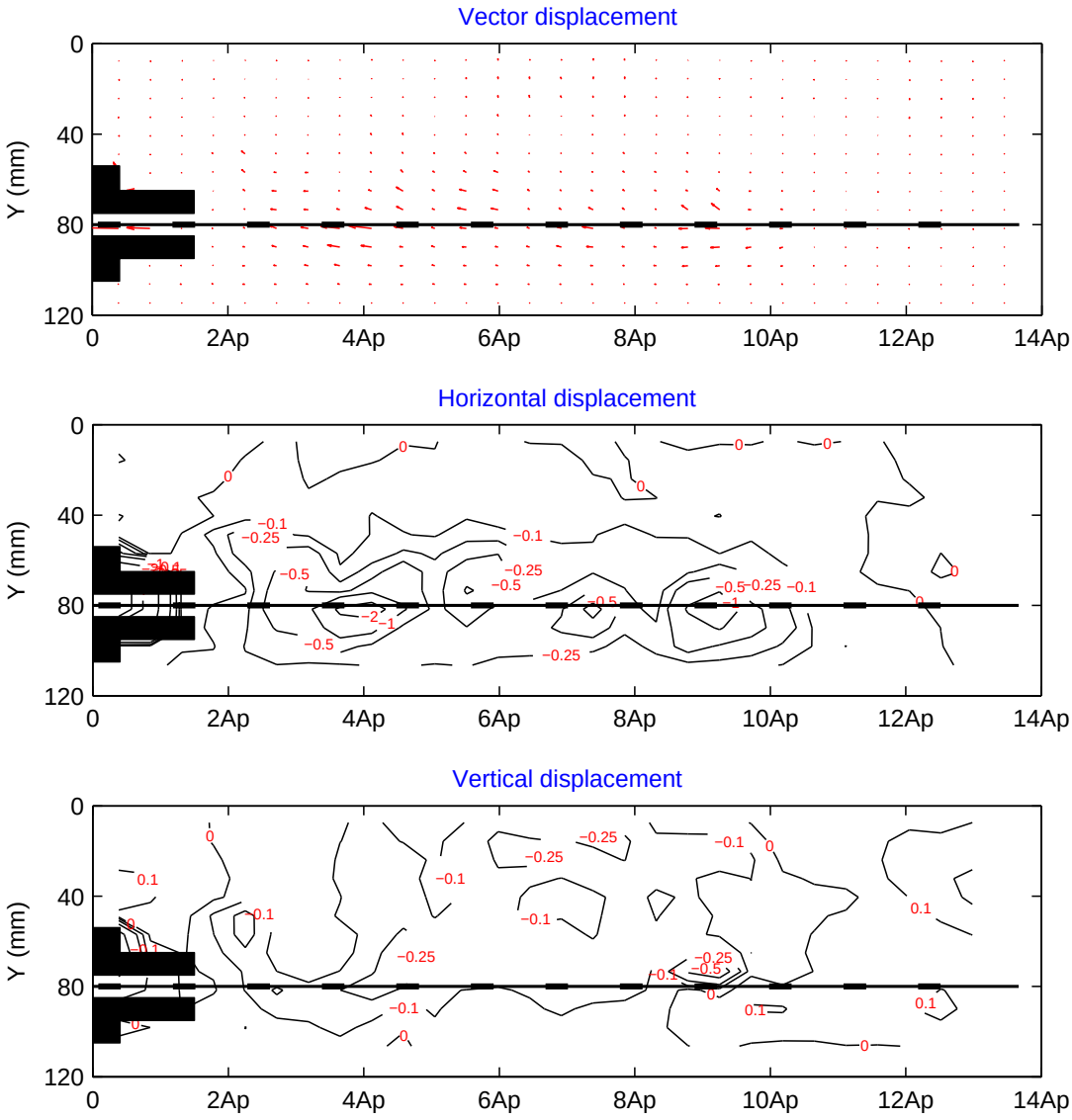

Figure 6.86: Incremental PIV results from 30 mm to 40 mm axial tensile displacement of geogrid with 2900 kN/m stiffness under 25 kPa confining pressure

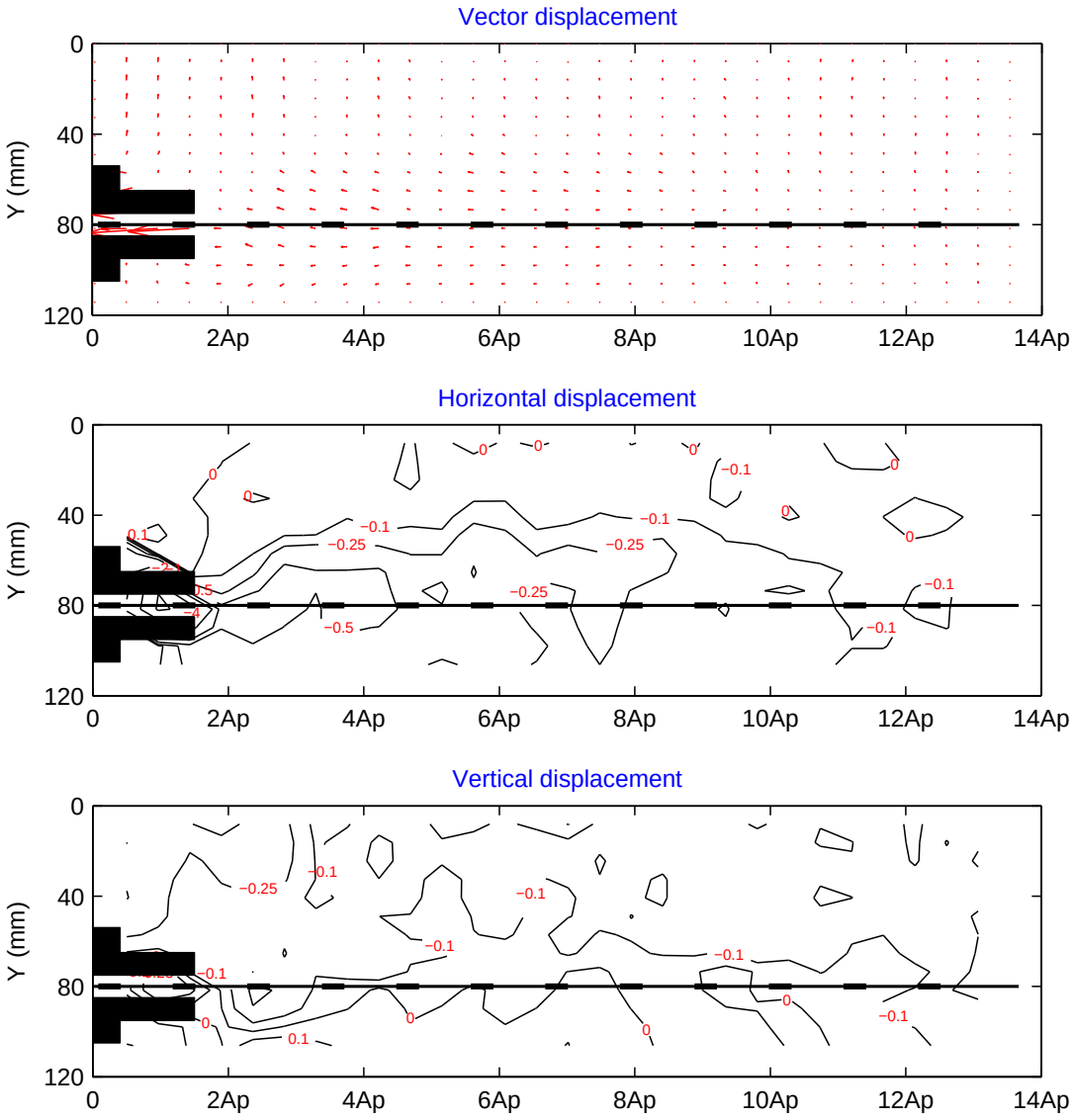

Figure 6.87: Incremental PIV results from 0 mm to 10 mm axial tensile displacement of geogrid with 2900 kN/m stiffness under 50 kPa confining pressure

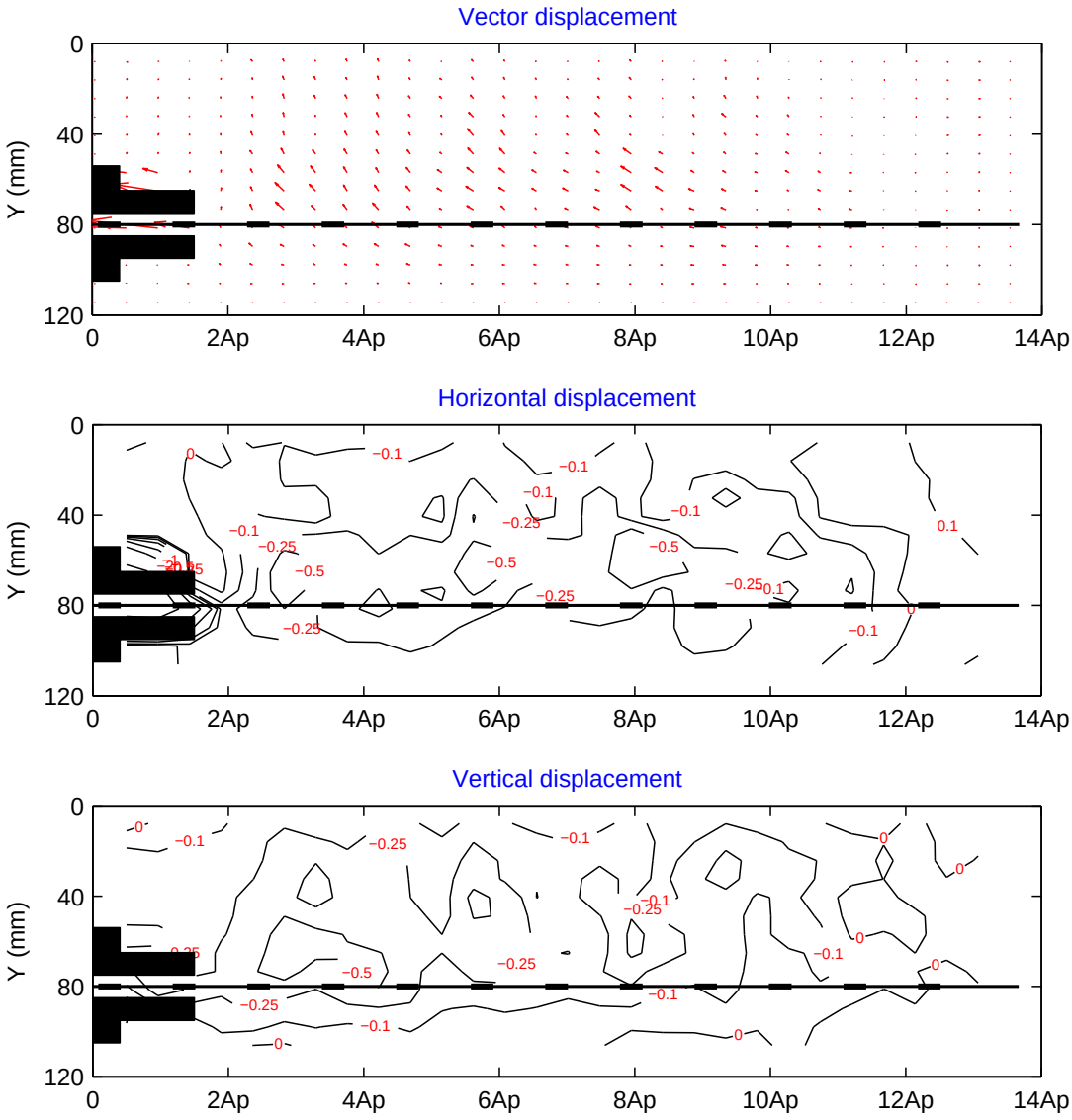

Figure 6.88: Incremental PIV results from 10 mm to 20 mm axial tensile displacement of geogrid with 2900 kN/m stiffness under 50 kPa confining pressure

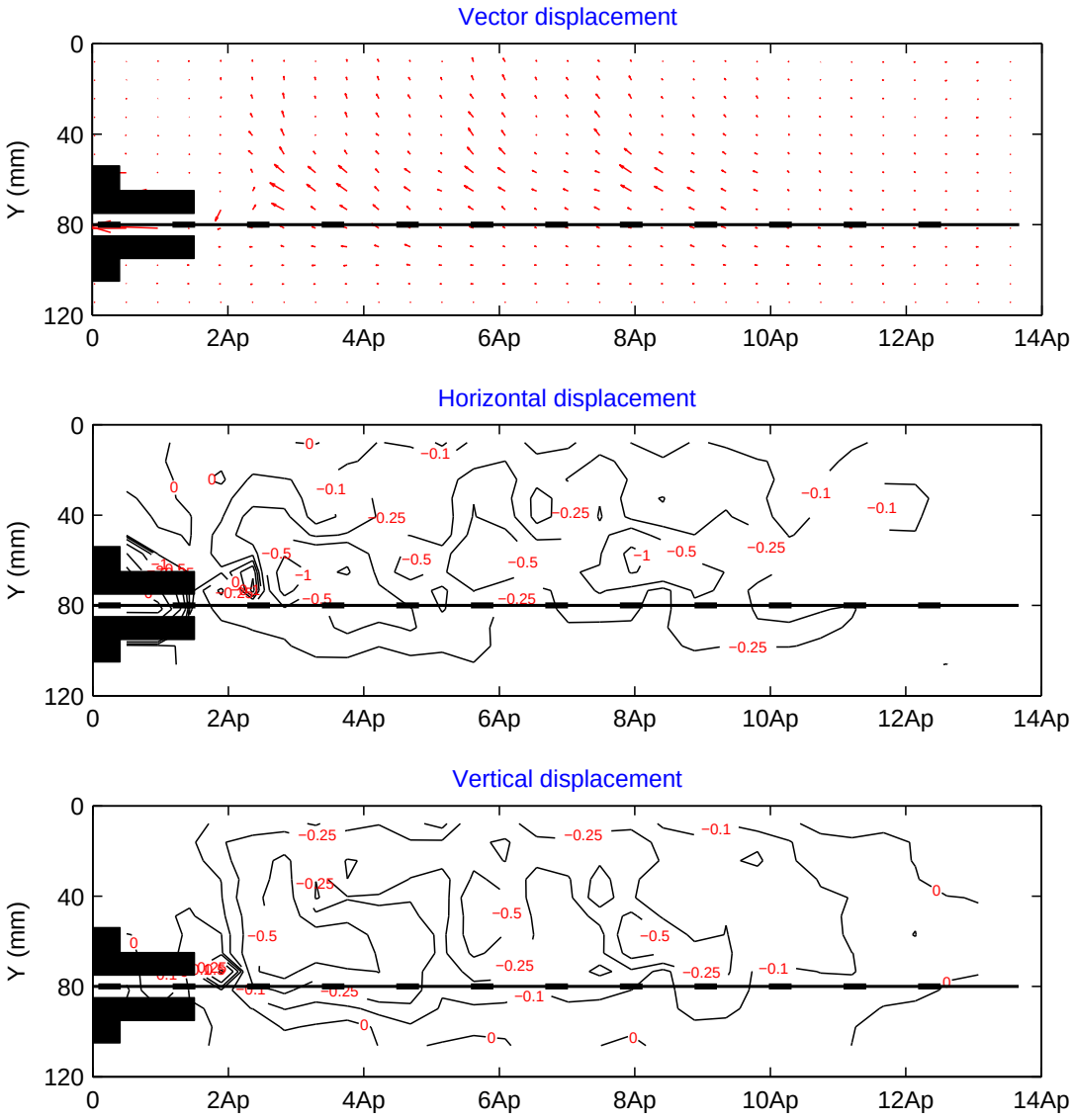

Figure 6.89: Incremental PIV results from 20 mm to 30 mm axial tensile displacement of geogrid with 2900 kN/m stiffness under 50 kPa confining pressure

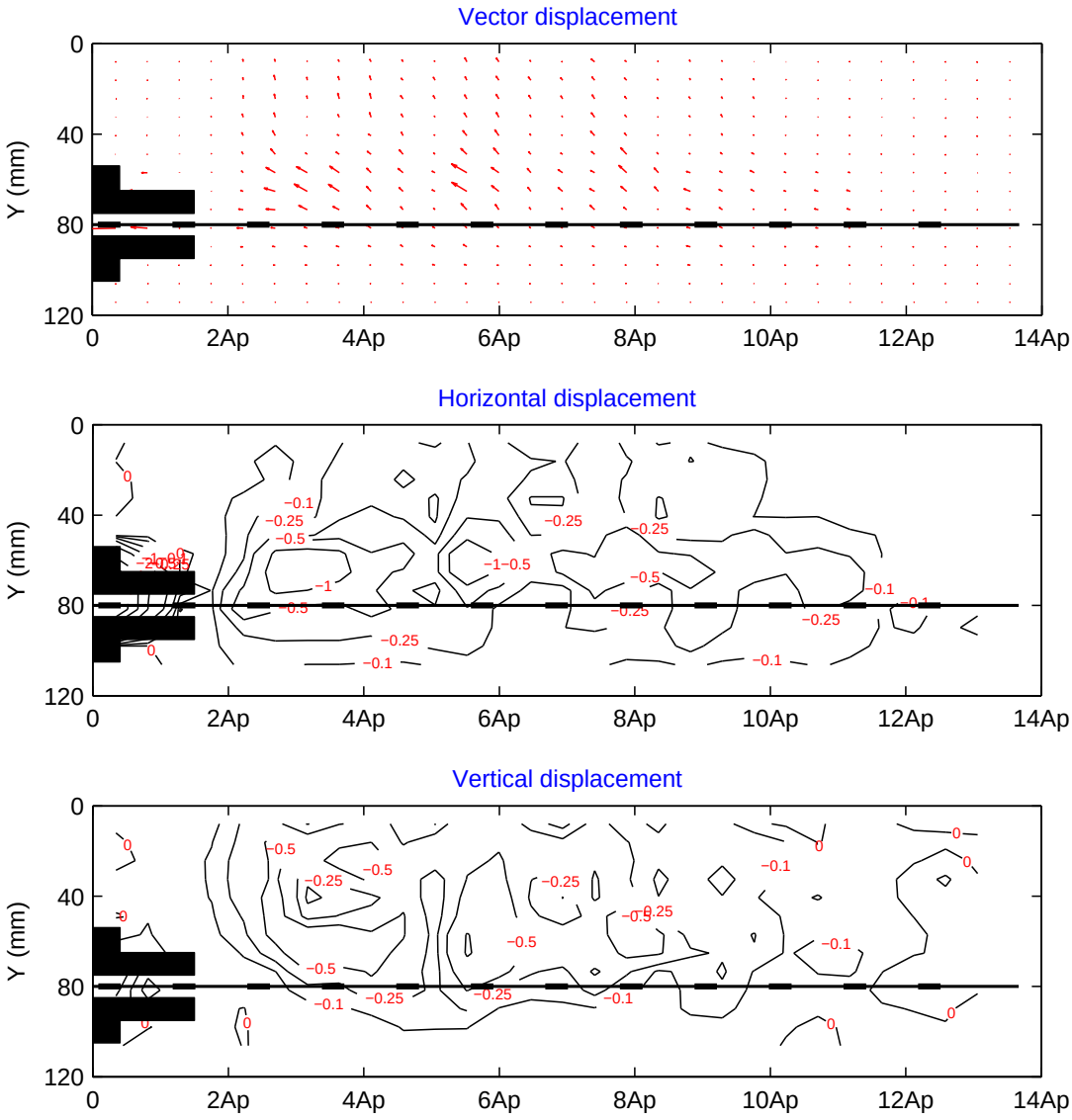

Figure 6.90: Incremental PIV results from 30 mm to 40 mm axial tensile displacement of geogrid with 2900 kN/m stiffness under 50 kPa confining pressure

Figures 6.91, 6.92 and 6.93 show the shear strains caused by pulling out the geogrid from soil for different amount of confining pressure 12.5 kPa, 25 kPa and 50 kPa.

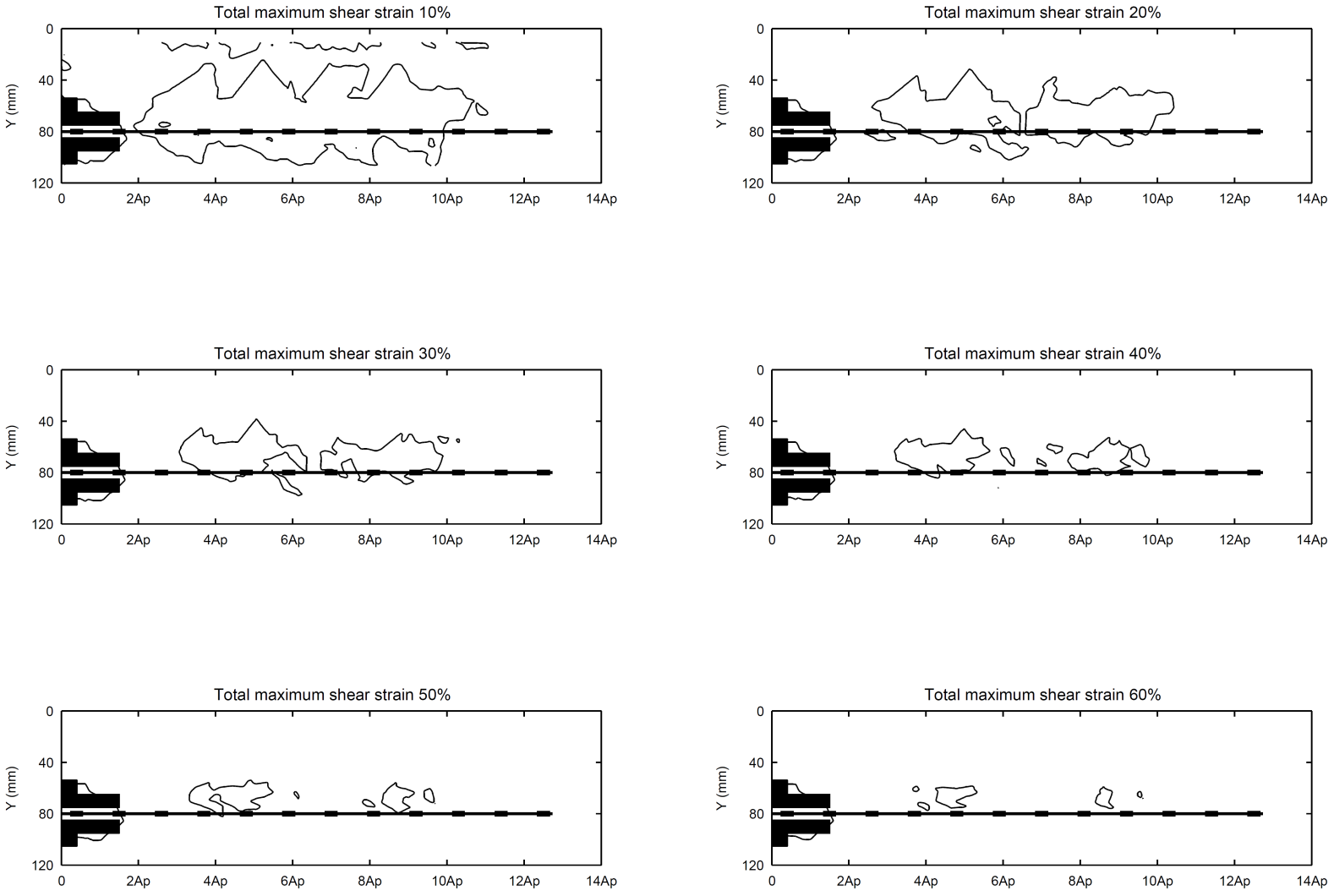

Figure 6.91: Cumulative shear strain for 40 mm axial tensile displacement of geogrid with 2900 kN/m stiffness under 12.5 kPa confining pressure

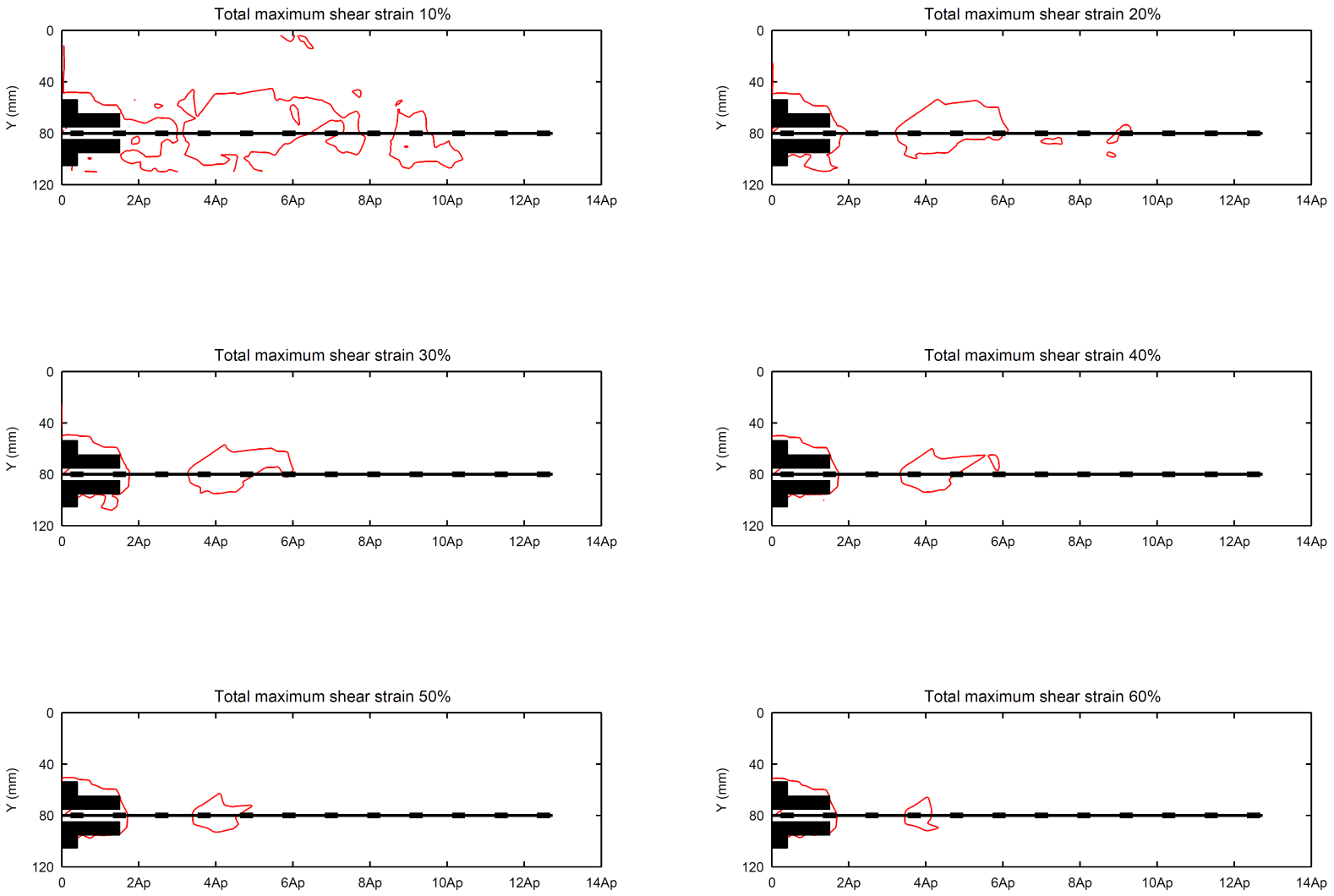

Figure 6.92: Cumulative shear strain for 40 mm axial tensile displacement of geogrid with 2900 kN/m stiffness under 25 kPa confining pressure

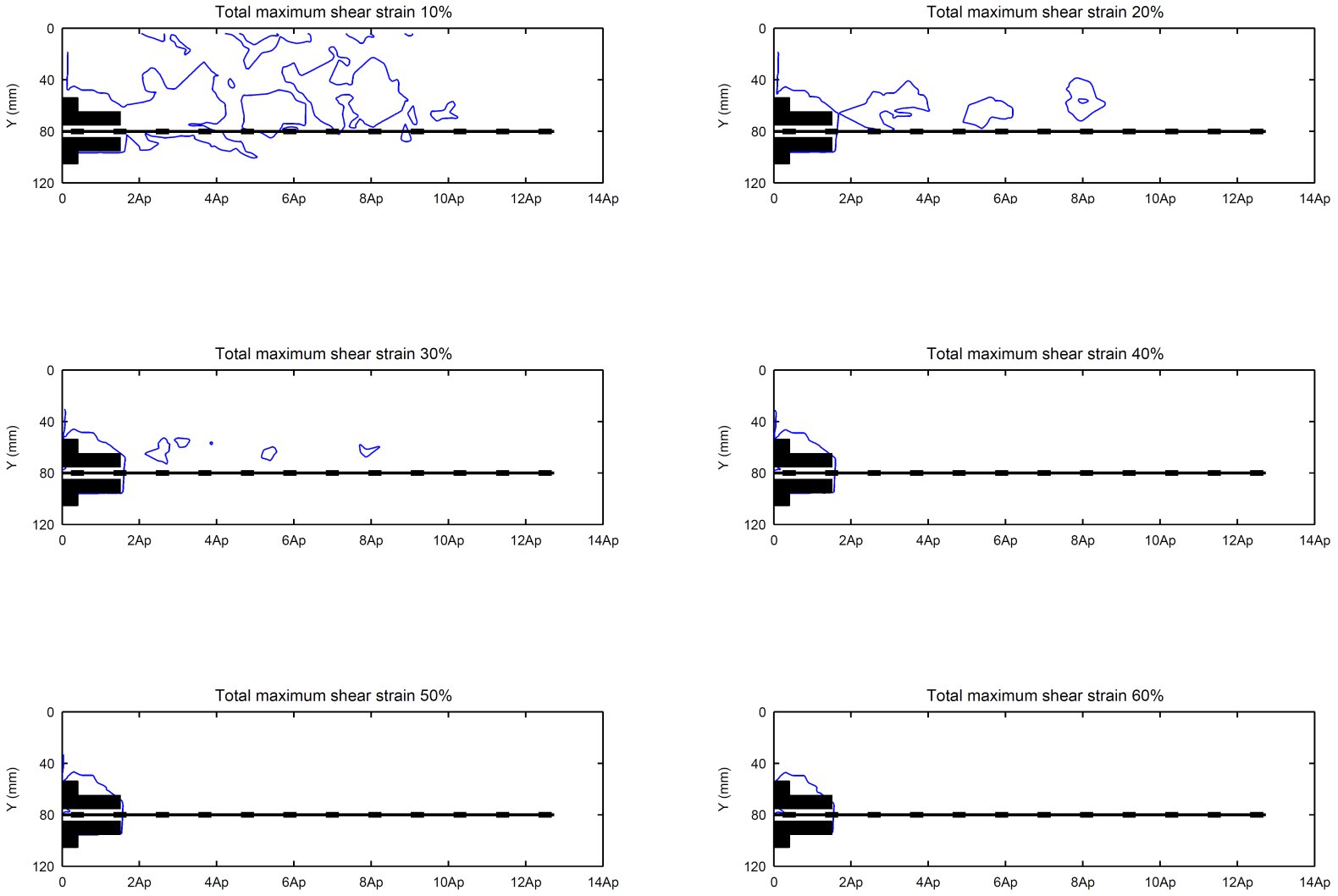

Figure 6.93: Cumulative shear strain for 40 mm axial tensile displacement of geogrid with 2900 kN/m stiffness under 50 kPa confining pressure

Figures 6.94, 6.95 and 6.96 show the volumetric strains caused by pulling out the geogrid from soil for three confining pressures are 12.5 kPa, 25 kPa and 50 kPa.

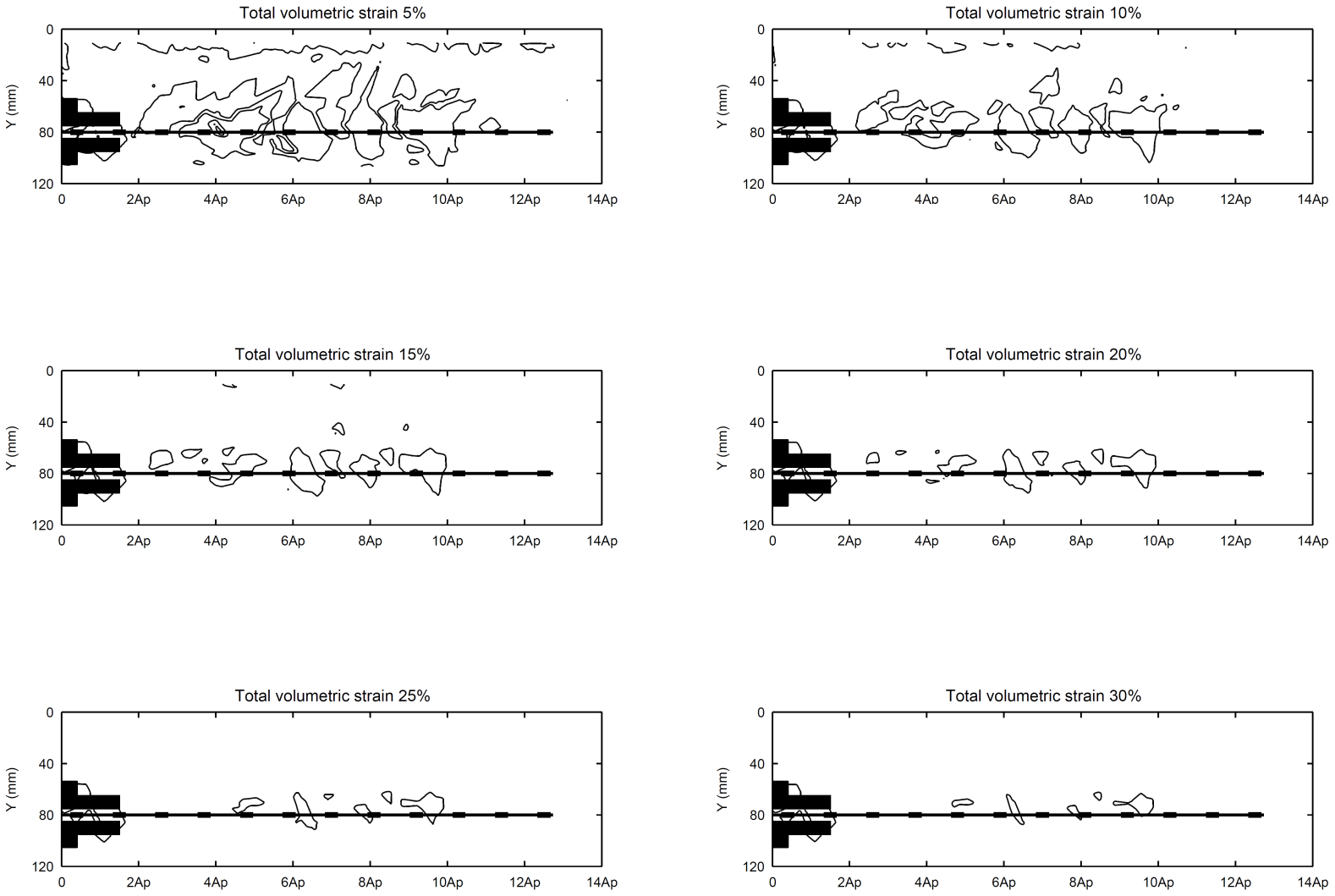

Figure 6.94: Cumulative volumetric strain for 40 mm axial tensile displacement of geogrid with 2900 kN/m stiffness under 12.5 kPa confining pressure

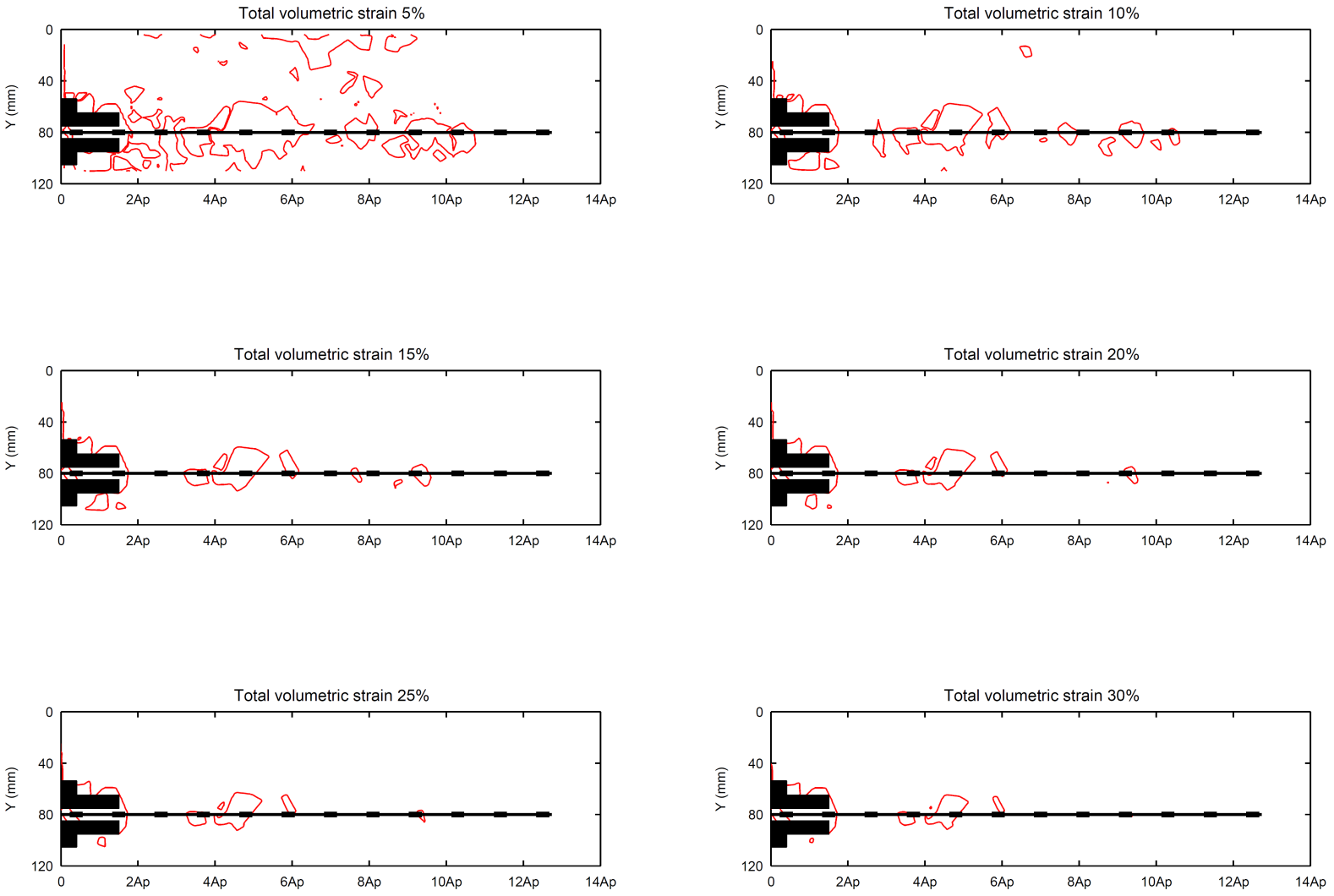

Figure 6.95: Cumulative volumetric strain for 40 mm axial tensile displacement of geogrid with 2900 kN/m stiffness under 25 kPa confining pressure

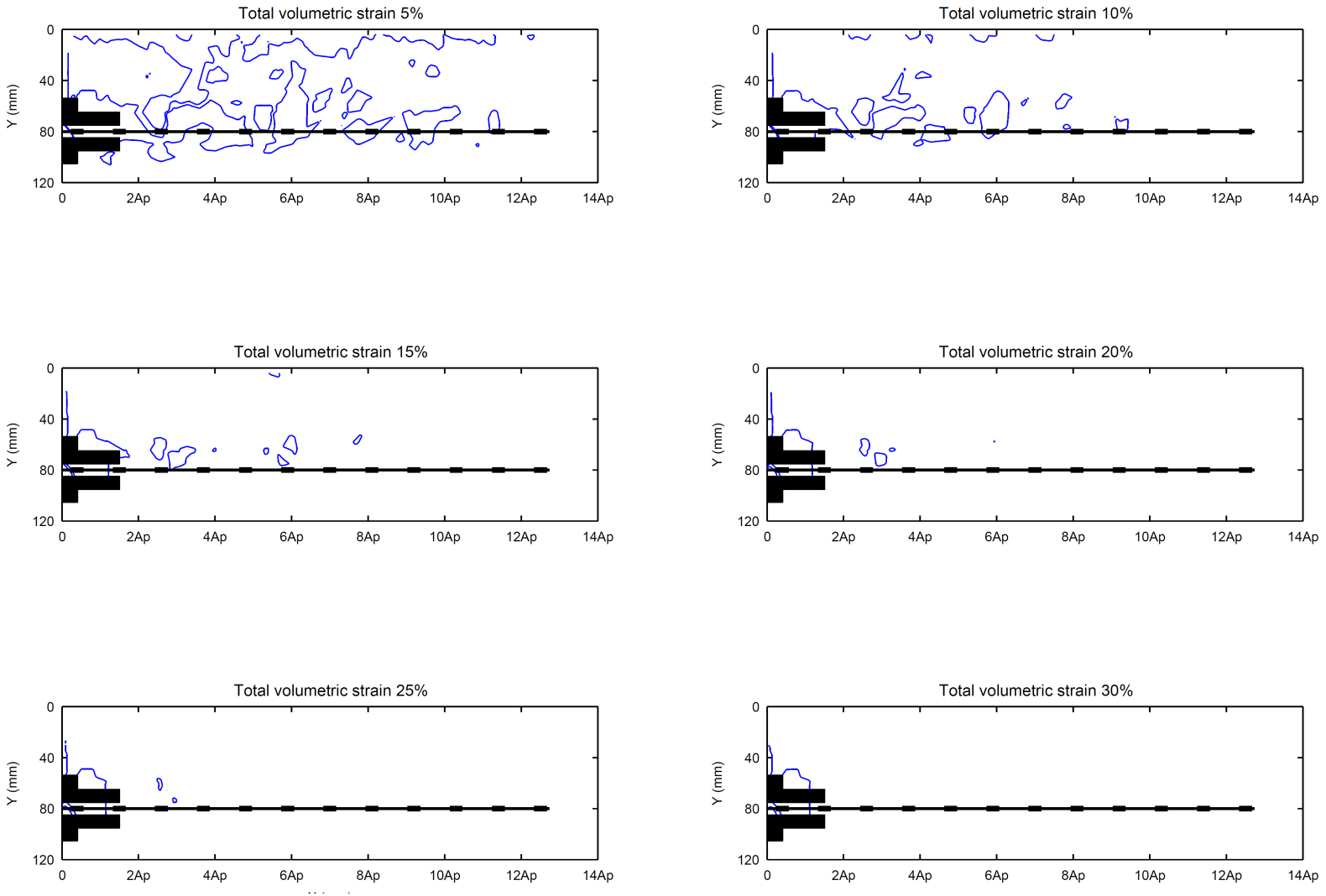

Figure 6.96: Cumulative volumetric strain for 40 mm axial tensile displacement of geogrid with 2900 kN/m stiffness under 50 kPa confining pressure

6.3 Repeatability of test data

Assessment of the repeatability considered by comparing of the external load-displacement results and the internal results image analysis. The pull-out test has been repeated three times for the geogrid with 1600 kN/m stiffness with confining pressure of 25 kPa. The results of tests presented as follow:

6.3.1 Force-displacement results

Figure 6.97 indicates the graph of load-displacement of three tests. The external results of these three tests are matched together which verified the repeatability of these results by using the measurement instrument, load cell and LVDT wire displacement.

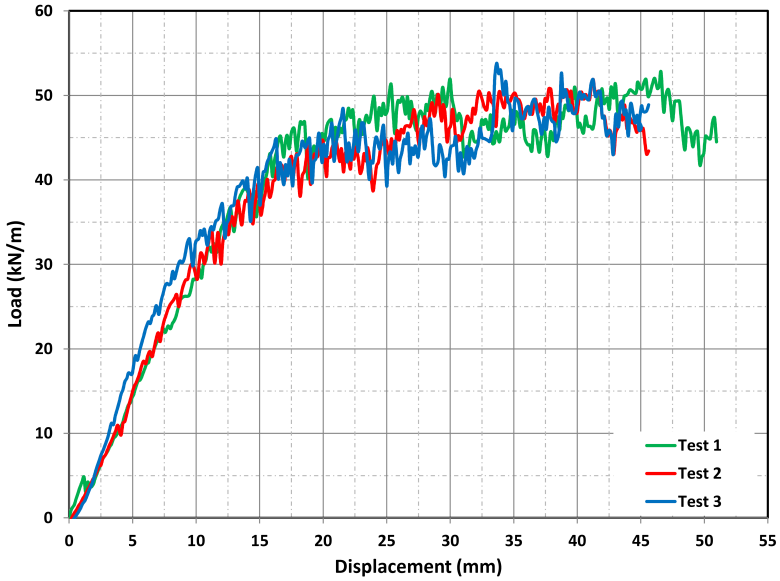

Figure 6.97: Load-displacement graphs for checking the repeatability of external results (J = 1600 kN/m and Confining pressure = 25 kPa)

6.3.2 Displacement contours

Figure 6.98 presents the comparison between the cumulative horizontal displacement of soil particles after 40 mm movement of geogrid. The displacement contour are generally very similar for these two tests which gave confidence that the image processing method used in this research is repeatable.

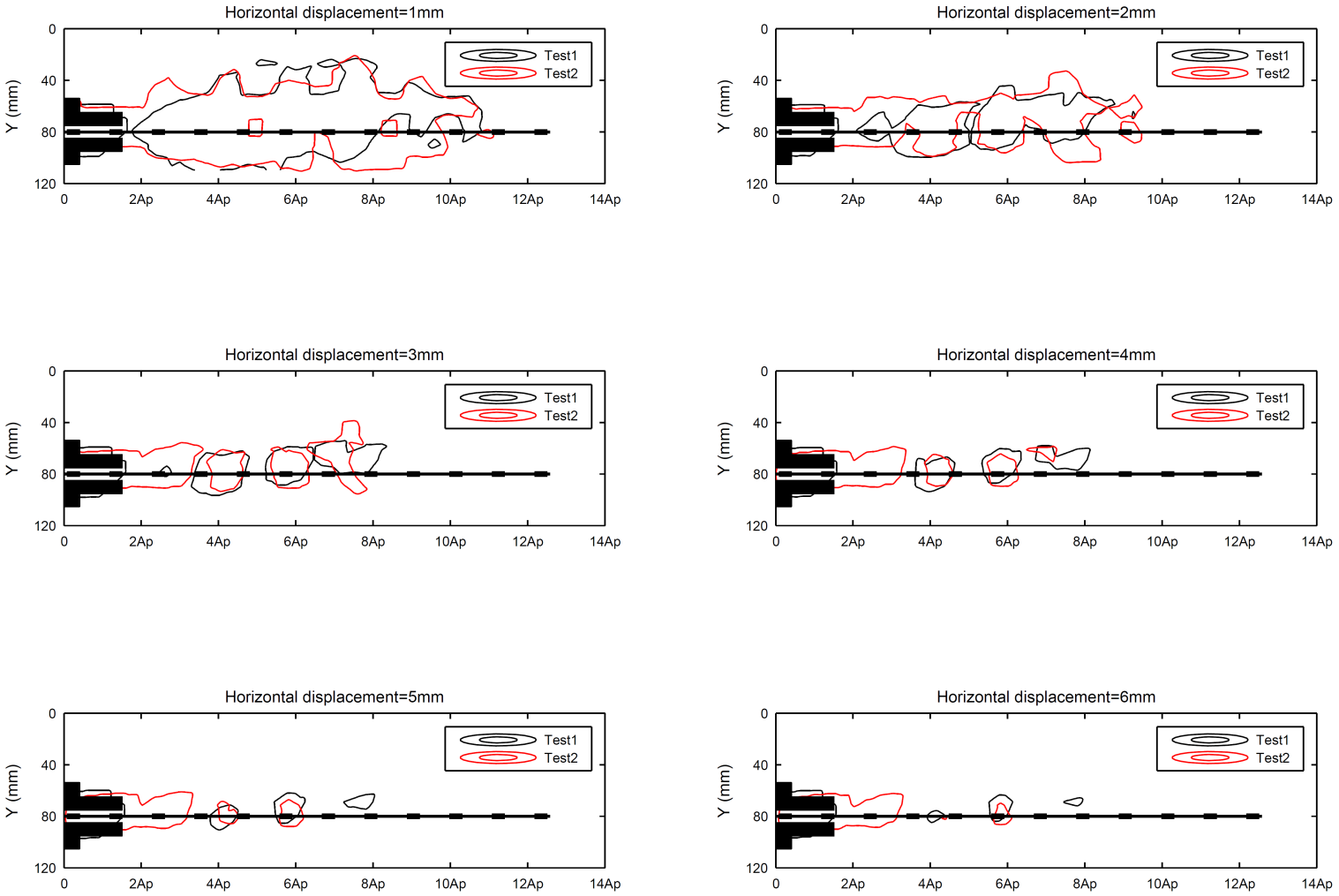

Figure 6.98: Comparison of cumulative horizontal displacement contours after 40 mm movement of geogrid

Chapter 7

Results and Discussion

7.1 Introduction

The interaction behaviour between soil and geogrid reinforcement is a complex phenomenon and it is not well understood. The pull-out resistance of a geogrid is a combination of skin friction which is generated by soil passing over soil, and over geogrid members and the bearing resistance of transverse ribs (Jewell, 1996). However, the mechanism of interaction between the soil and geogrid depends on several factors such as soil type and size of soil particles, density of soil, geometry of geogrid, strength, stiffness and surface roughness of the geogrid (Palmeira, 2004).

The overall behaviour of pull-out tests for different test conditions was presented in Chapter 6. This chapter focuses on reviewing the local interaction of soil and reinforcement and load displacement data to evaluate the impact of aspects such as:

- Confining (surcharge) pressure
- Stiffness of reinforcement
- Transverse members of the geogrid

7.2 The effect of confining pressure on interaction behaviour between soil and reinforcement

The tests were carried out under three confining pressures of 12.5 kPa, 25 kPa and 50 kPa. The following figures in this section present the influence of confining pressure on the interaction behaviour between soil and reinforcement determined from internal visualisation. Figures 7.1 and 7.2 indicate the distribution of horizontal and vertical displacement of soil particles at the end of the pull-out tests under three different confining pressures respectively. It is clearly evident that greater horizontal movement is observed for a confining pressure of 12.5 kPa compared to 50 kPa. Furthermore, the measurement profile is more concentrated along the length of the reinforcement whereas for the confining pressure of 50 kPa, movements are concentrated only in the immediate vicinity of the transverse members.

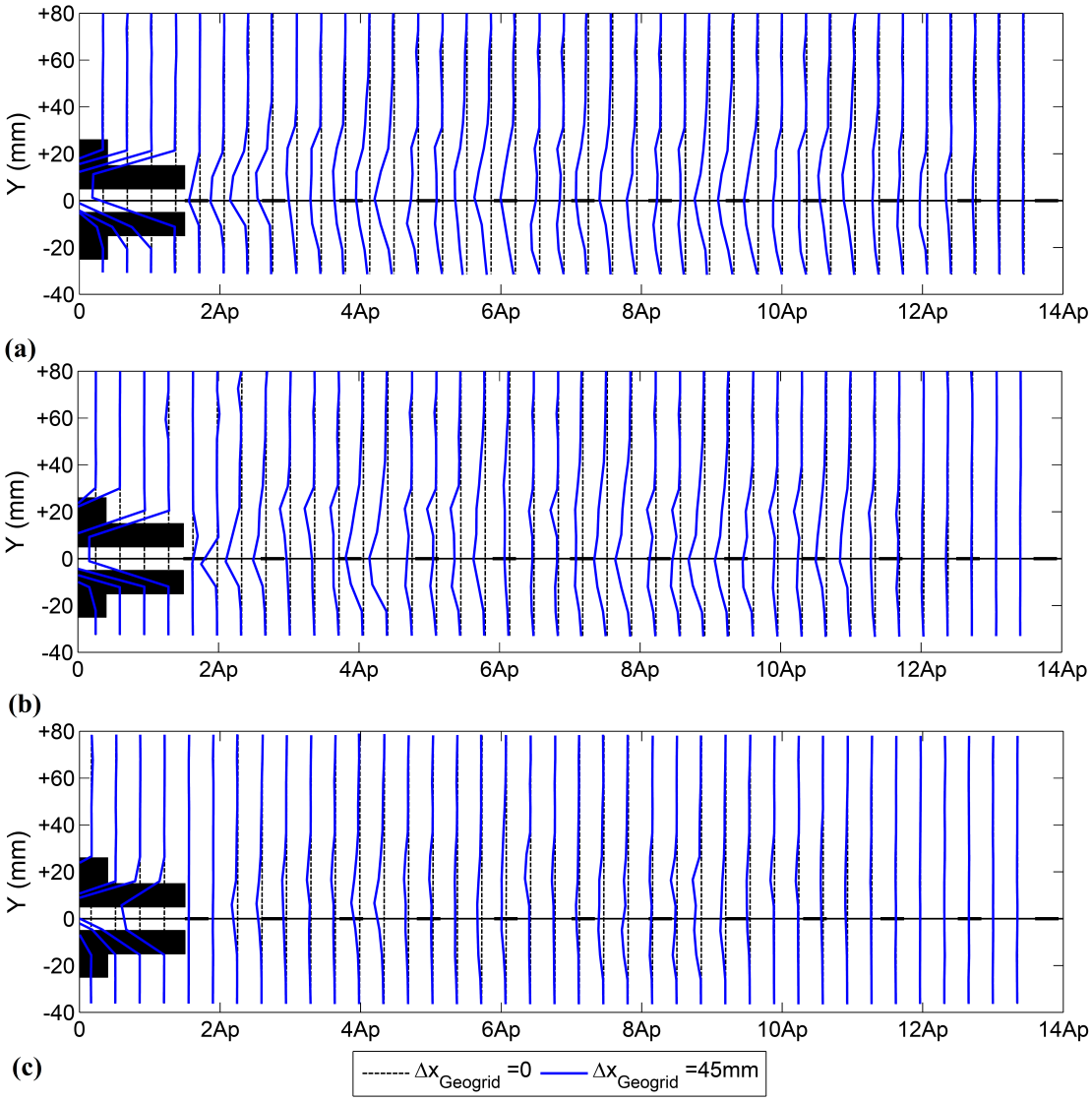

Figure 7.1: Distribution of horizontal displacement, $\triangle x$, of soil particles plotted against vertical position,Y, at the end of test under three different value of confining pressures; (a)12.5 kPa, (b)25 kPa and (c)50 kPa (J=1200 kN/m)

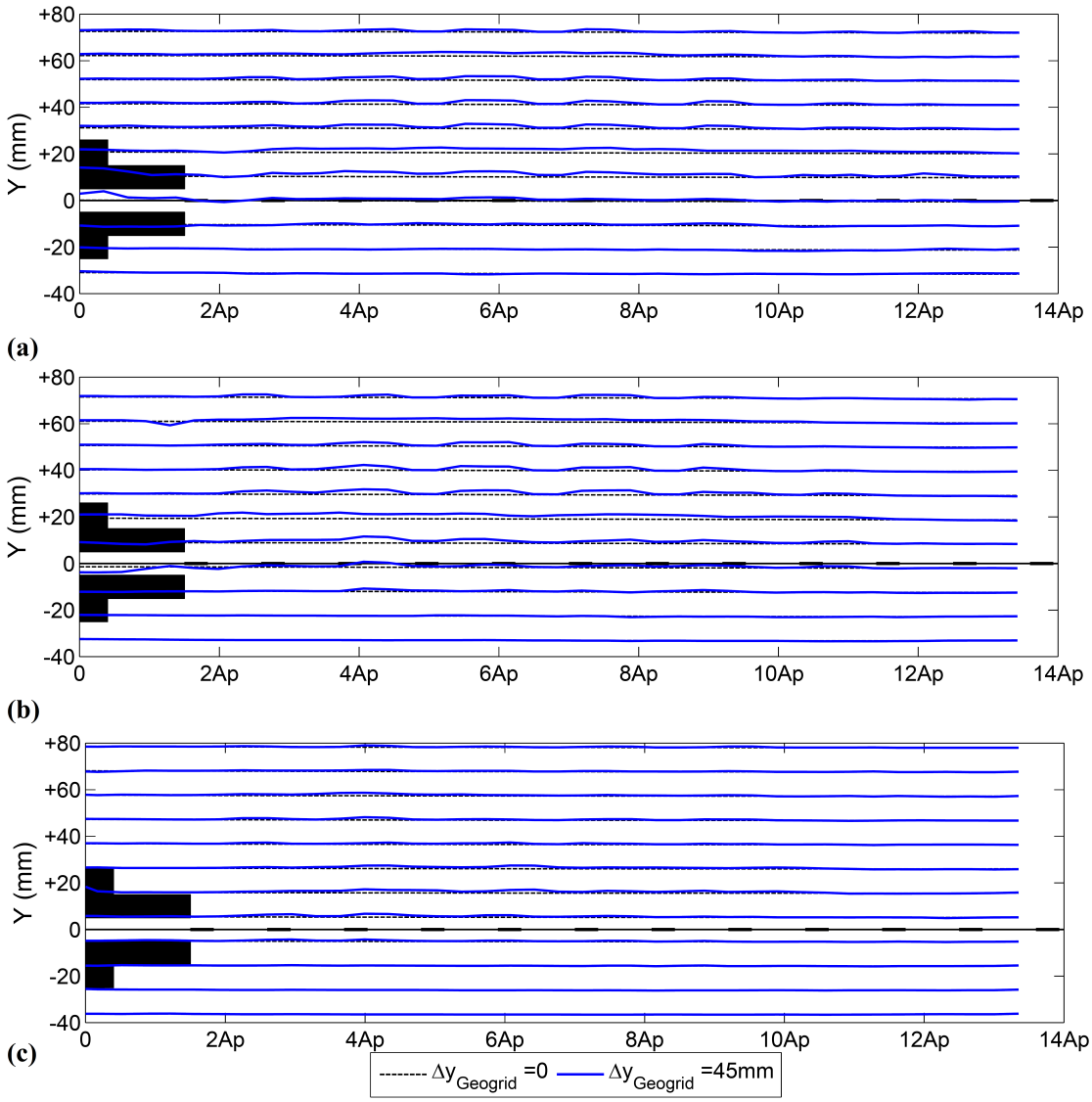

Figure 7.2: Distribution of vertical displacement, $\triangle y$, of soil particles plotted against vertical position,Y, at end of the test under three different value of confining pressures; (a)12.5 kPa, (b)25 kPa and (c)50 kPa (J= 1200 kN/m)

The horizontal displacement of soil particles based on the position of the apertures of the geogrid is presented in Figures 7.3 to 7.5. The results show that a large horizontal displacement of soil particles is consistently apparent adjacent to the geogrid location; with the largest displacement near the rib positions. The magnitude of the horizontal displacement of the soil particles has an inverse relation to the amount of confining pressure. By increasing the confining pressure the interlock between soil particles is increased so that the movement of soil particles by sliding, shearing or rotation is restricted more than at lower confinement.

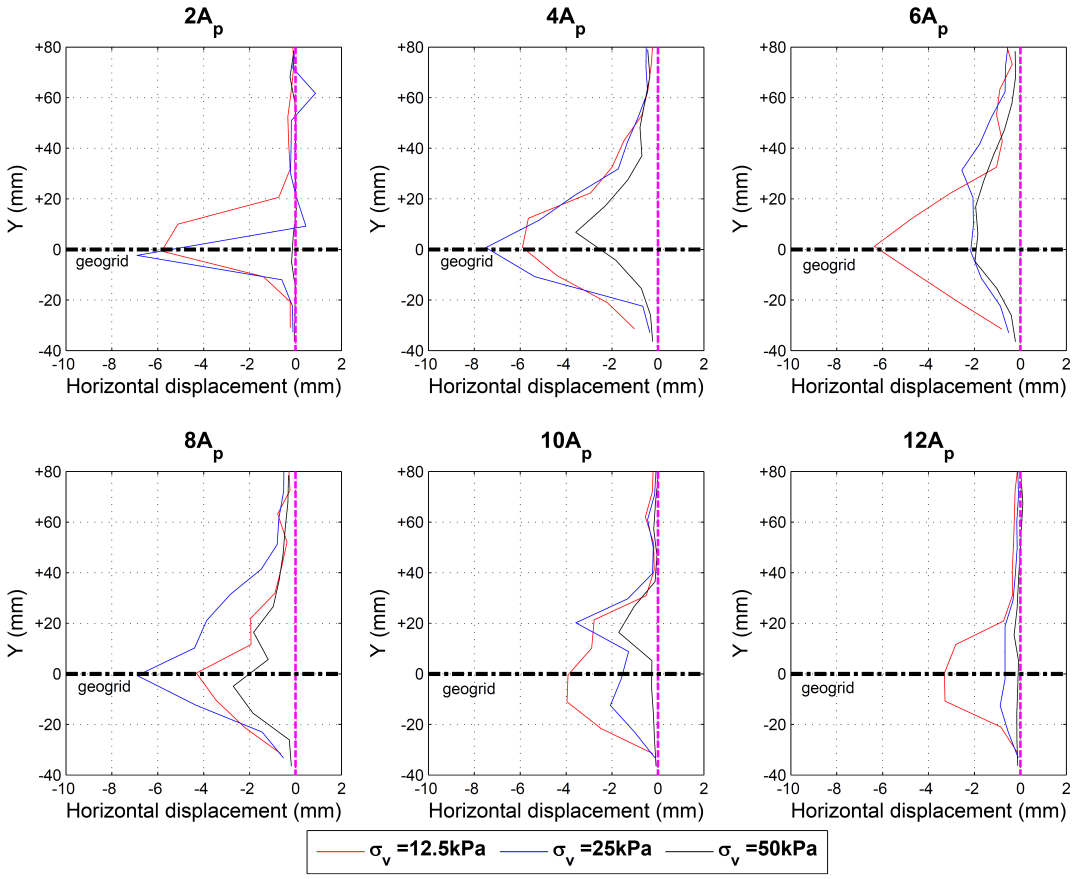

Figure 7.3: Comparison of the horizontal displacement of soil particles at end of the test for the geogrid with 1200 kN/m stiffness under different confining pressures for different distances from the clamp (A_p:aperture size of geogrid)

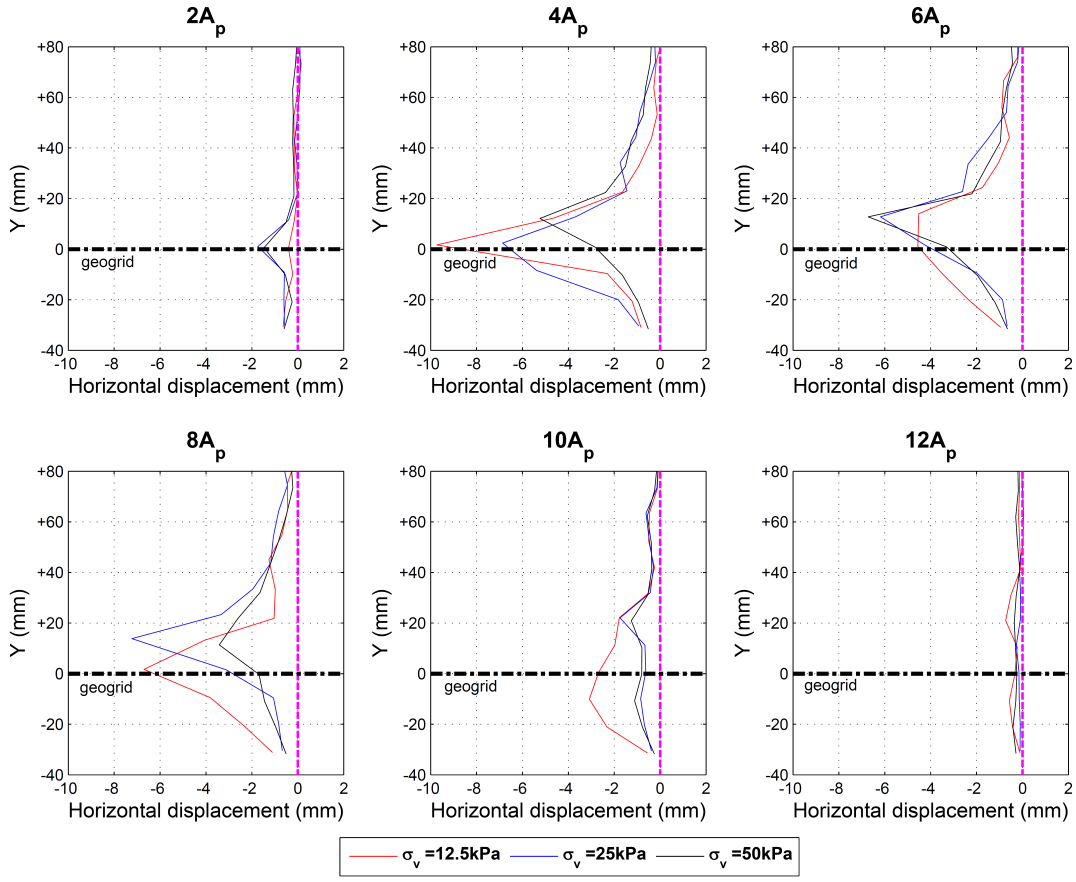

Figure 7.4: Comparison of the horizontal displacement of soil particles at end of the test for the geogrid with 1600 kN/m stiffness under different confining pressures for different distances from the clamp (A_p:aperture size of geogrid)

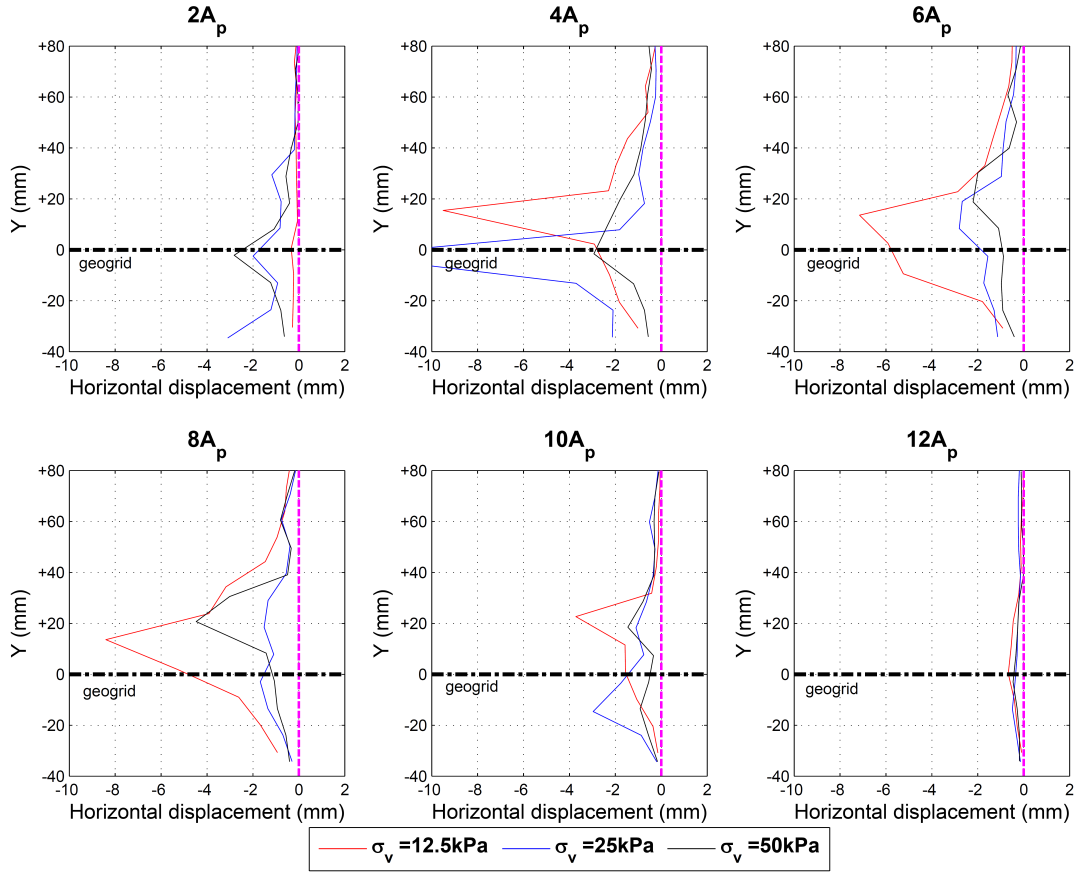

Figure 7.5: Comparison of the horizontal displacement of soil particles at end of the test for the geogrid with 2900 kN/m stiffness under different confining pressures for different distances from the clamp (A_p:aperture size of geogrid)

Figures 7.6 to 7.8 present the vertical displacement of soil particles for different vertical distances from the geogrid based on the mean particle size of soil. The contours show that locations further from the geogrid undergo smaller vertical displacements than those closer. The dilation phenomenon occurred for all tests under different values of confining pressures. This indicates that dilation occurs adjacent to the geogrid due to particles being "locked" within the geogrid apertures, while contraction due to shearing is occurring further away from the grid. This would be consistent with a "loose" sample produced due to the placement technique.

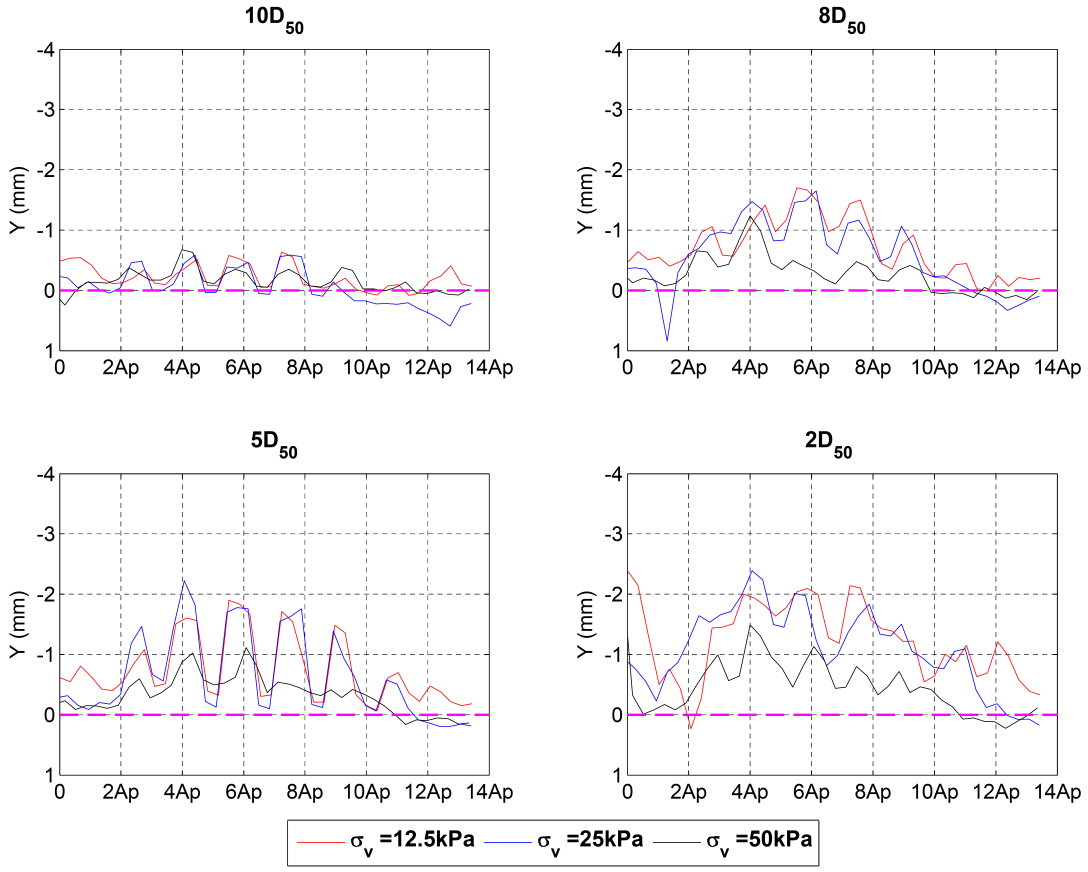

Figure 7.6: Comparison of the vertical displacement of soil particles above the geogrid specimen at end of the test for the geogrid with 1200 kN/m stiffness under different confining pressures and for different vertical distance from the geogrid given as multiplies of mean particle size, D_{50}

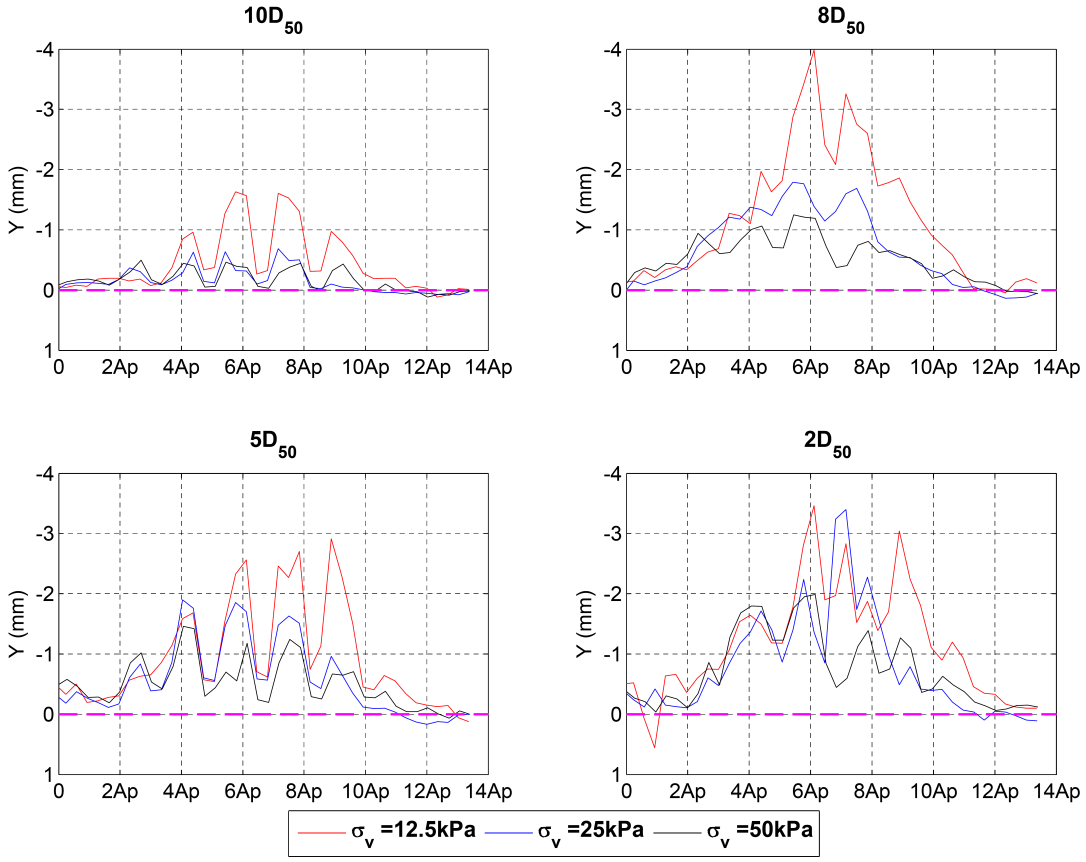

Figure 7.7: Comparison of the vertical displacement of soil particles above the geogrid specimen at end of the test for the geogrid with 1600 kN/m stiffness under different confining pressures and for different vertical distance from the geogrid given as multiplies of mean particle size, D_{50}

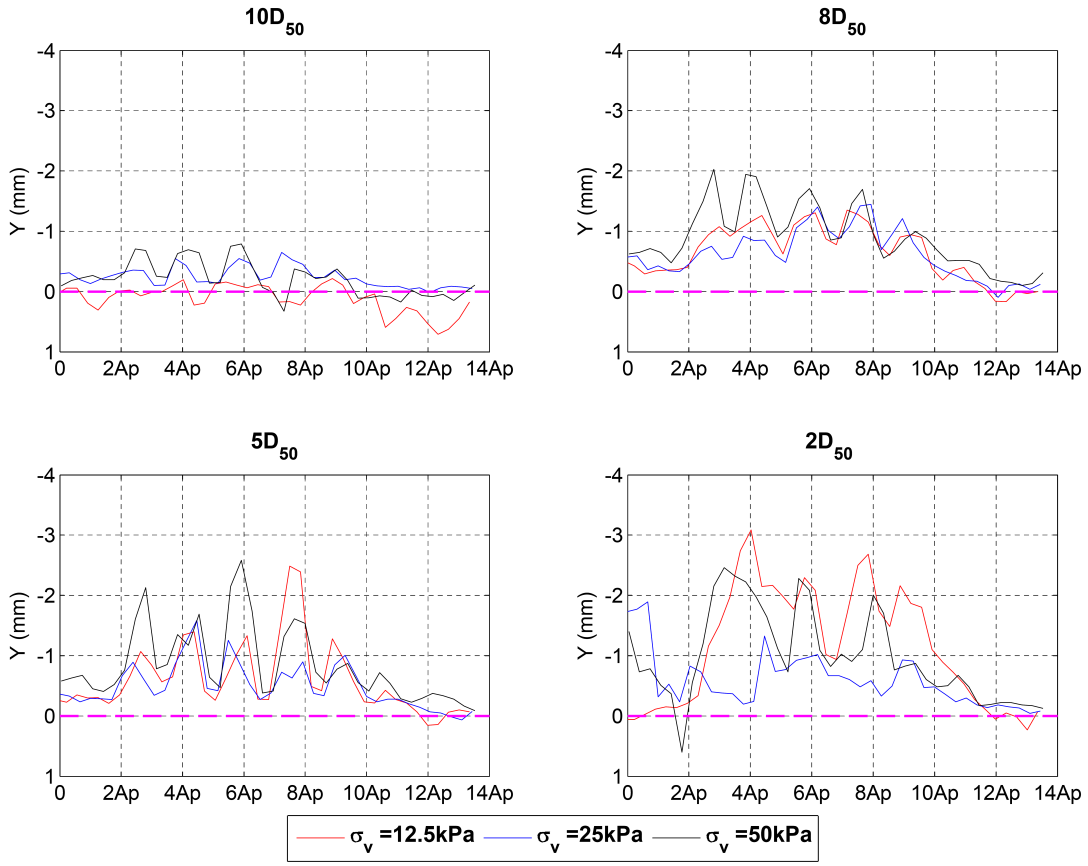

Figure 7.8: Comparison of the vertical displacement of soil particles above the geogrid specimen at end of the test for the geogrid with 2900 kN/m stiffness under different confining pressures and for different vertical distance from the geogrid given as multiplies of mean particle size, D_{50}

Figures 7.9 to 7.11 show the zone of influence of geogrid for three different values of stiffness under different confining pressures. The magnitude of horizontal displacement of soil particles was scaled by 10 to illustrate the zone of influence of the geogrid with higher accuracy. The boundary of the zone of influence of the geogrid observed from these figures was at a distance from the interface of 4 to 5.5 times the D_{50} of the soil. The soil particles beyond the zone of influence has less than %5 of the movement of the soil which happens adjacent to the geogrid.

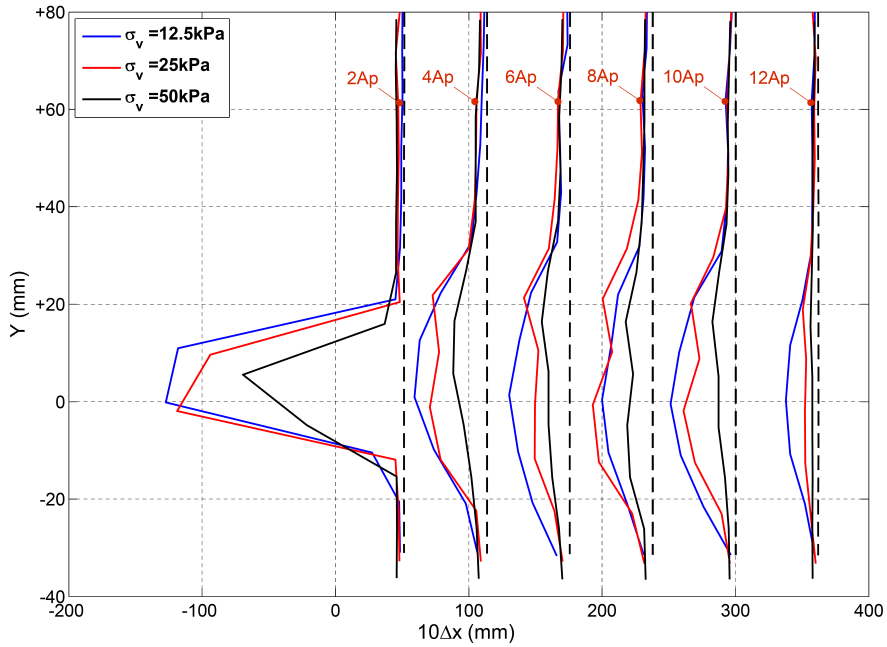

Figure 7.9: Comparison of the horizontal displacement of soil particles at the end of the test for the geogrid with 1200 kN/m stiffness under different confining pressures

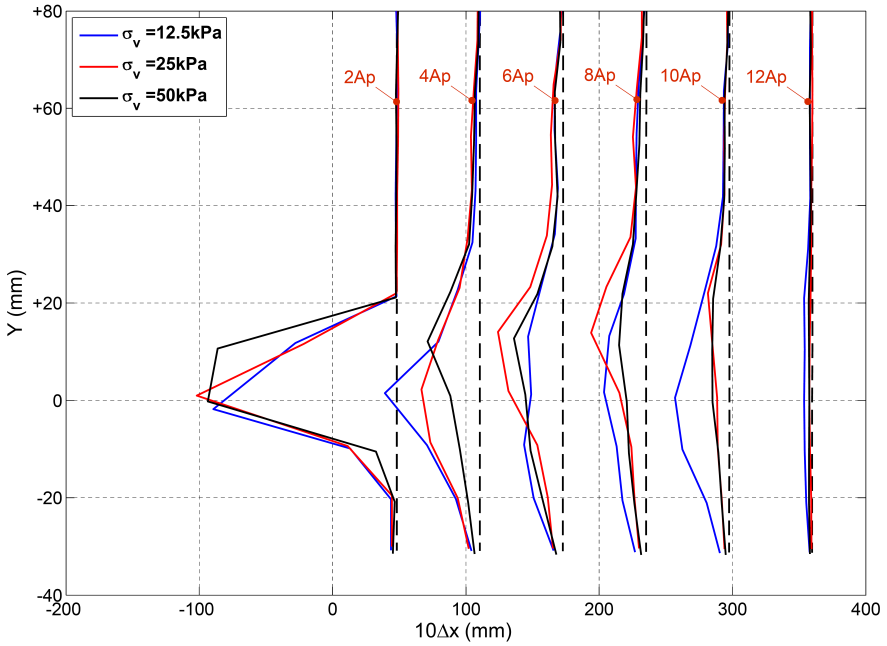

Figure 7.10: Comparison of the horizontal displacement of soil particles at the end of the test for the geogrid with 1600 kN/m stiffness under different confining pressures

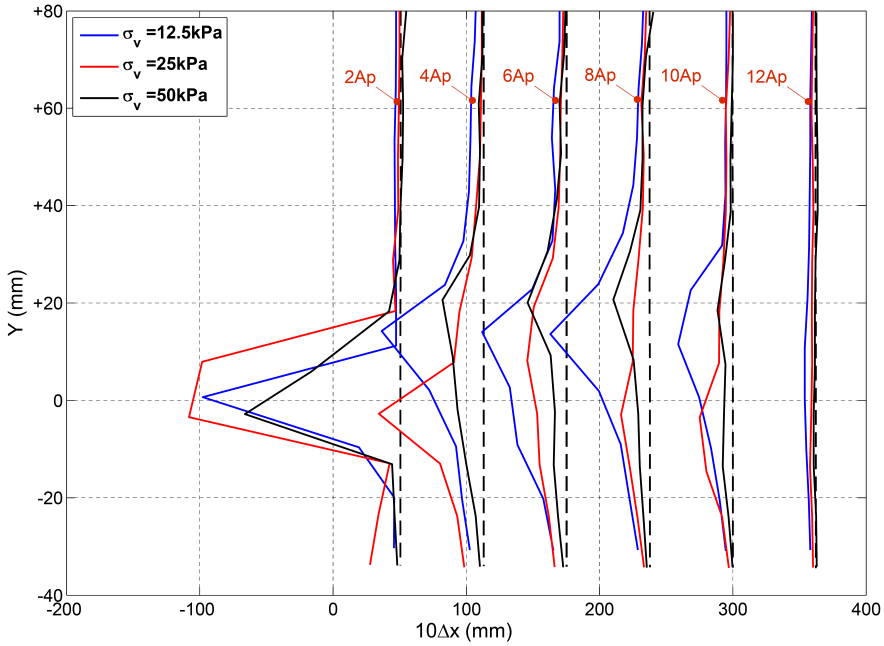

Figure 7.11: Comparison of the horizontal displacement of soil particles at the end of the test for the geogrid with 2900 kN/m stiffness under different confining pressures

7.3 The effect of stiffness of reinforcement on soil interaction behaviour

Figures 7.12 to 7.14 present the load-displacement response of the pull-out test for the confining pressures considered with respect to the rupture strength\the stiffness of the geogrid. The results of the study show that for low values of confining pressure (12.5 kPa and 25 kPa) the load-displacement response was independent of the rupture strength\the stiffness of the specimen. However, for the higher value of confining pressure (50 kPa), the geogrid with the higher value of rupture strength\ stiffness has a higher pull-out resistance. It is inferred that, the magnitude of the two lowest confining pressures, 12.5 kPa and 25 kPa, is small in comparison to the stiffness of the geogrid, the stiffness of geogrid exceeds the stiffness of the geogrid/soil resistance.

As Figures 7.12 and 7.14 show, for the geogrid with the lowest value of stiffness strength (1200 kN/m), did not display a peak pull-out resistance whereas for the

two other types of geogrid (1600 kN/m and 2900 kN/m) a peak pull-out resistance was observed. This occurred for all samples with the exception of the sample with 1600 kN/m stiffness under a high value of confining pressure, 50 kPa.

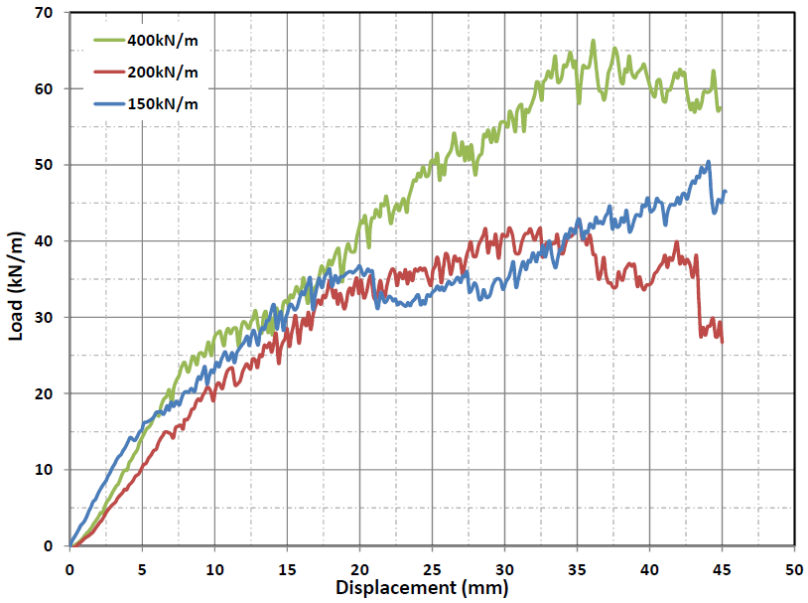

Figure 7.12: Load-displacement plot for three different types of geogrid under confining pressure 12.5 kPa

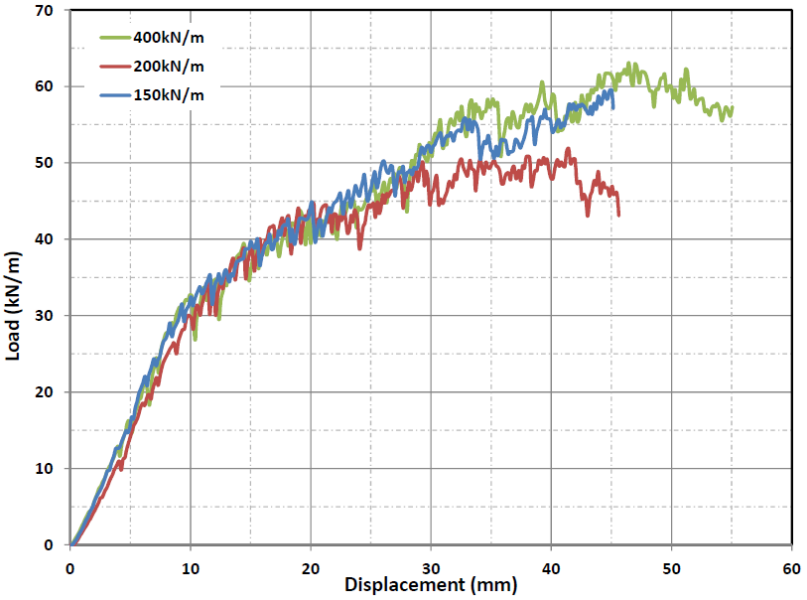

Figure 7.13: Load-displacement plot for three different types of geogrid under confining pressure 25 kPa

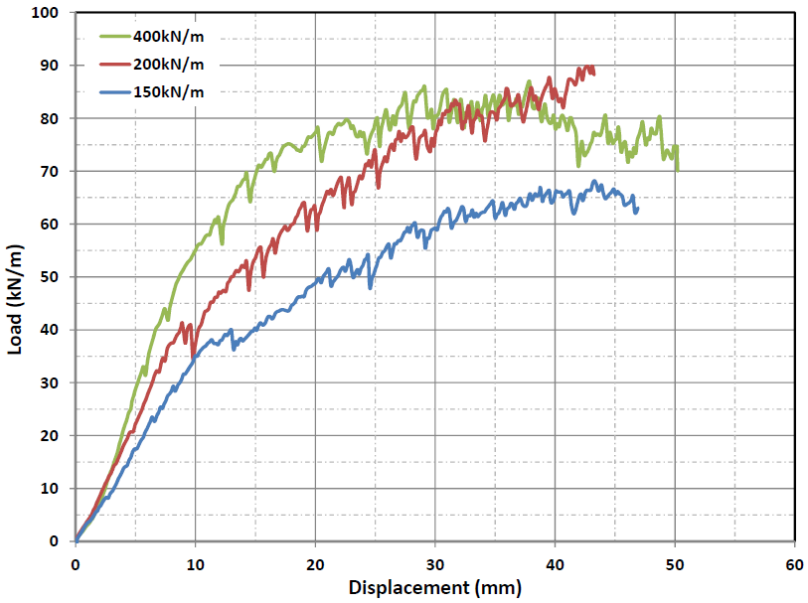

Figure 7.14: Load-displacement plot for three different types of geogrid under confining pressure 50 kPa

Figures 7.15 to 7.17 illustrate the comparison between the magnitude of horizontal displacement of soil particles for three values of geogrid rupture strengths. The results of the study show that the zone of influence is similar for three types of geogrid under constant confining pressure which is around 4 to 5.5 times the D_{50} of the soil away from the interface of geogrid.

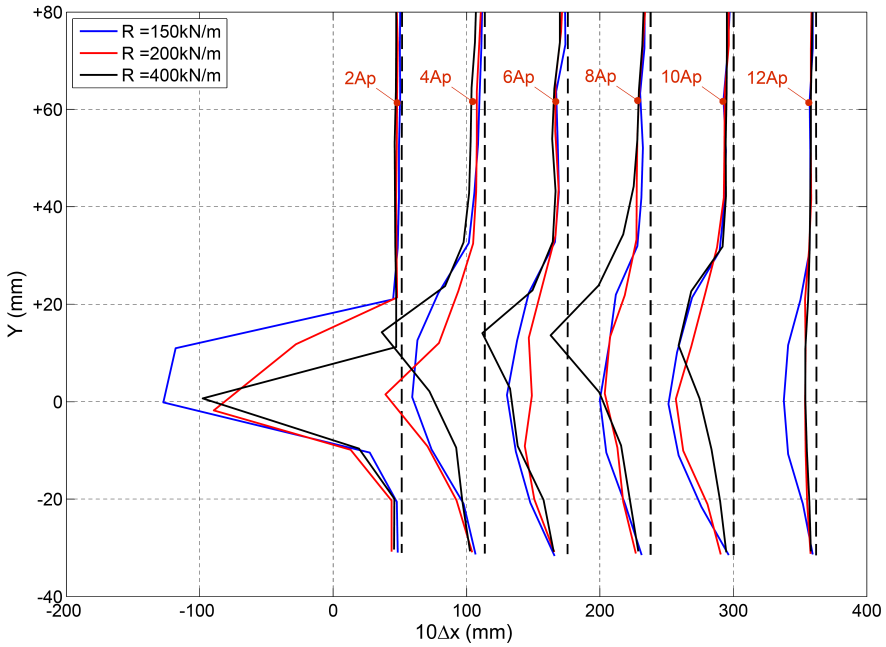

Figure 7.15: Comparison of the horizontal displacement of soil particles at end of the test for the geogrid under constant value of confining pressure, 12.5 kPa, for three different types of geogrid

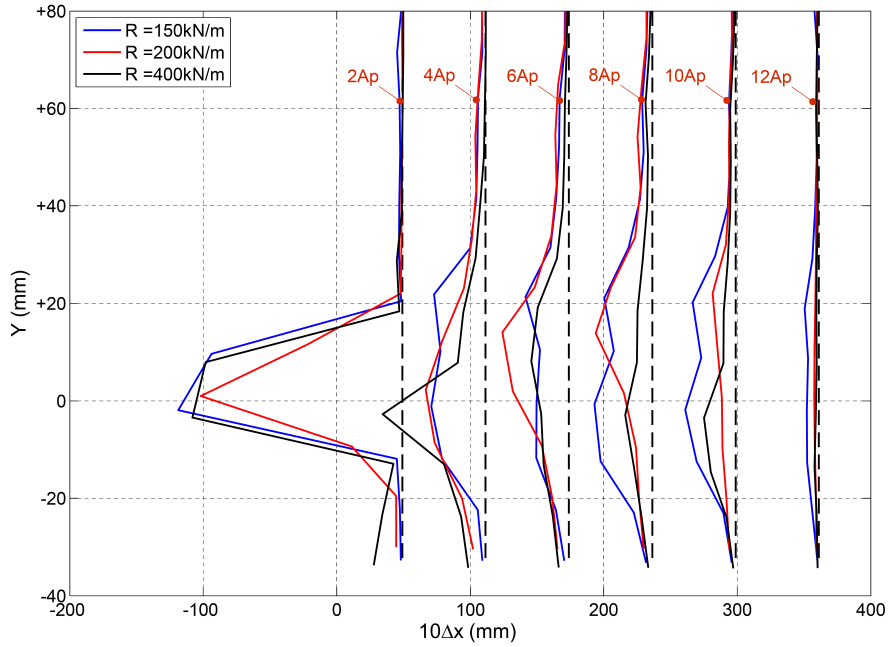

Figure 7.16: Comparison of the horizontal displacement of soil particles at end of the test for the geogrid under constant value of confining pressure, 25 kPa, for three different types of geogrid

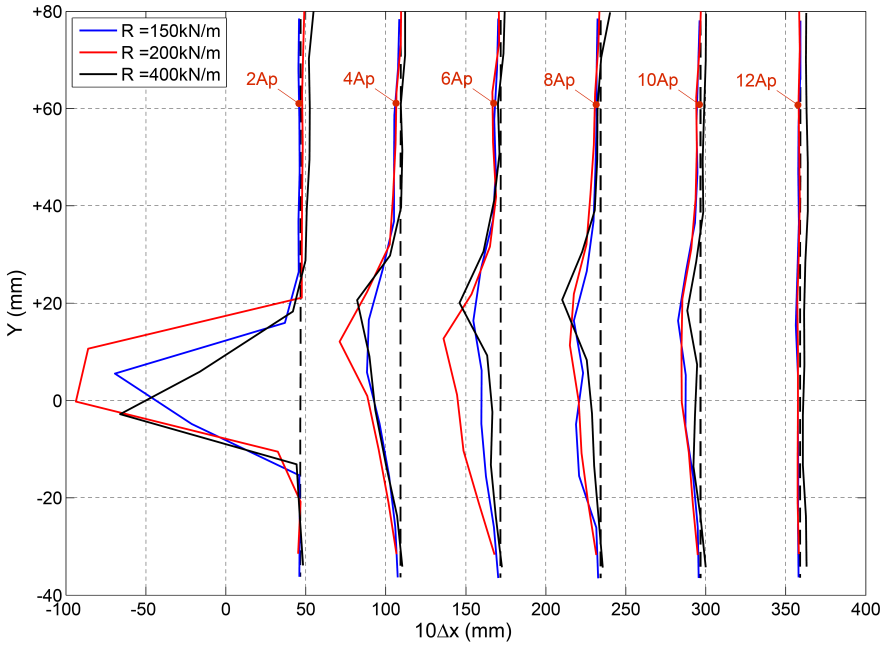

Figure 7.17: Comparison of the horizontal displacement of soil particles at end of the test for the geogrid under constant value of confining pressure, 50 kPa, for three different types of geogrid

7.4 The effect of transverse members of geogrid on soil interaction behaviour

Jewell (1996) proposed that the interaction between soil and geogrid reinforcement is the combination of the skin friction between soil over soil, soil over geogrid and bearing stress against the transverse members of the geogrid. There, the soil particles located in front of the transverse members should move more than other areas.

Figures 7.18 and 7.19 present the horizontal displacement of soil particles through the reinforcement at the location of the transverse ribs and between them after 20 mm axial tensile movement of geogrid and at the end of the test respectively. The results of the test show the soil particles have more movement in the front area of the ribs.

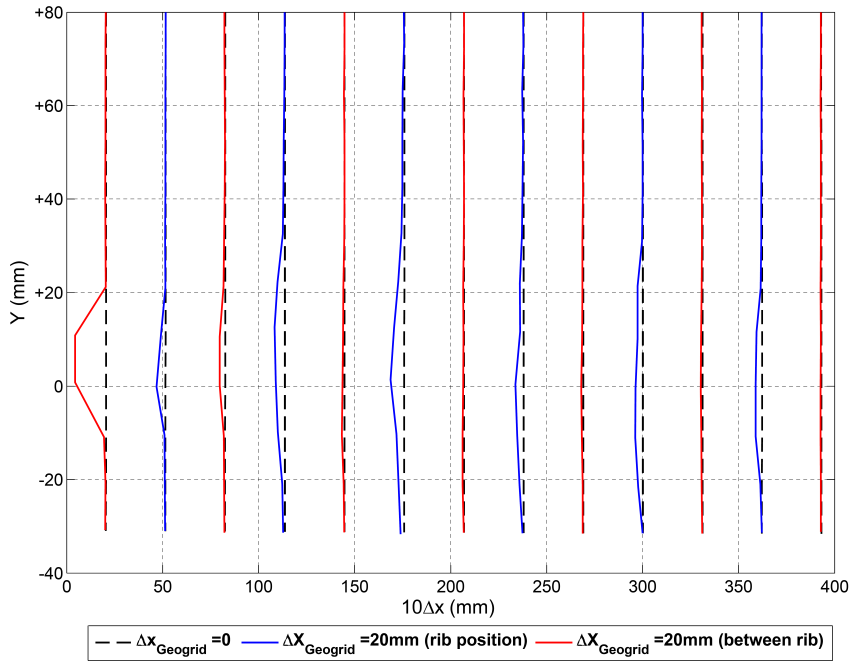

Figure 7.18: Comparison the effect of ribs to generate the horizontal movement of soil particles after 20 mm movement of geogrid (stiffness of geogrid is 1200 kN/m under confining pressure of 12.5 kPa

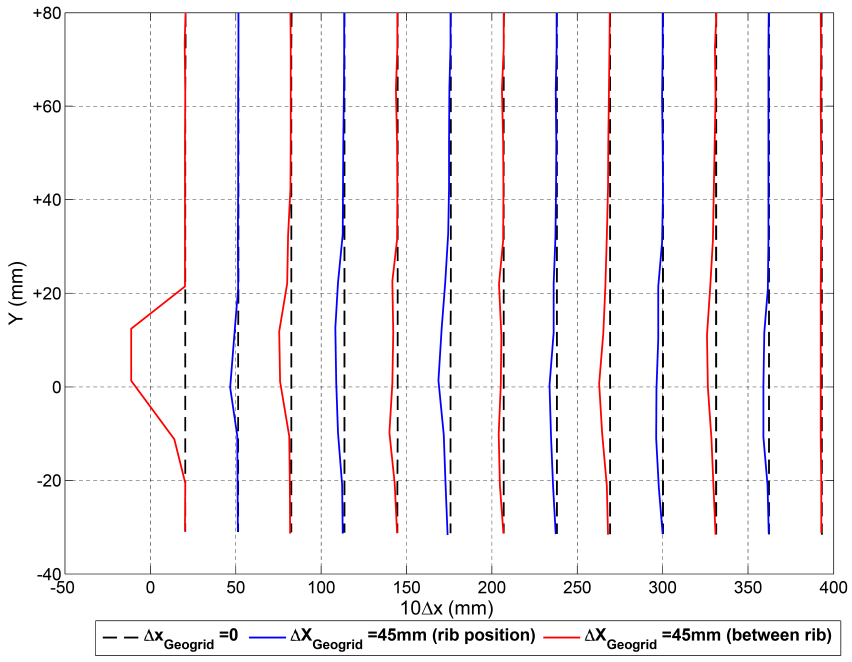

Figure 7.19: Comparison the effect of ribs to generate the horizontal movement of soil particles at the end of the test (stiffness of geogrid is 1200 kN/m under confining pressure of 12.5 kPa

7.5 Calculating displacement along geogrid specimens

One of the main advantages of this current state of the art using transparent materials and the DIC image analysis method is that it provides a capability of observing the soil-geogrid interaction response along the length of the reinforcement during pull-out test rather than relying on a simple load-deflection response. Displacement profiles along the geogrid specimens in the pull-out test were obtained by tracking the transverse members of geogrid by monitoring the movement of them during tests from beginning of the test until the end. Figures 7.20 to 7.22 show displacement-time plot recorded at different distance from the clamp. The solid line which is marked with a circle in the plot is the displacement-time record for the clamp which was advanced at a rate of about 1.7 mm/min, which was the reference rate for the tests in this investigation. The plots show that the displacement at the same location were diminished with increasing confining pressure. However, the results of the tests illustrated that the displacement at the same location for the three different types of geogrid is very close together.

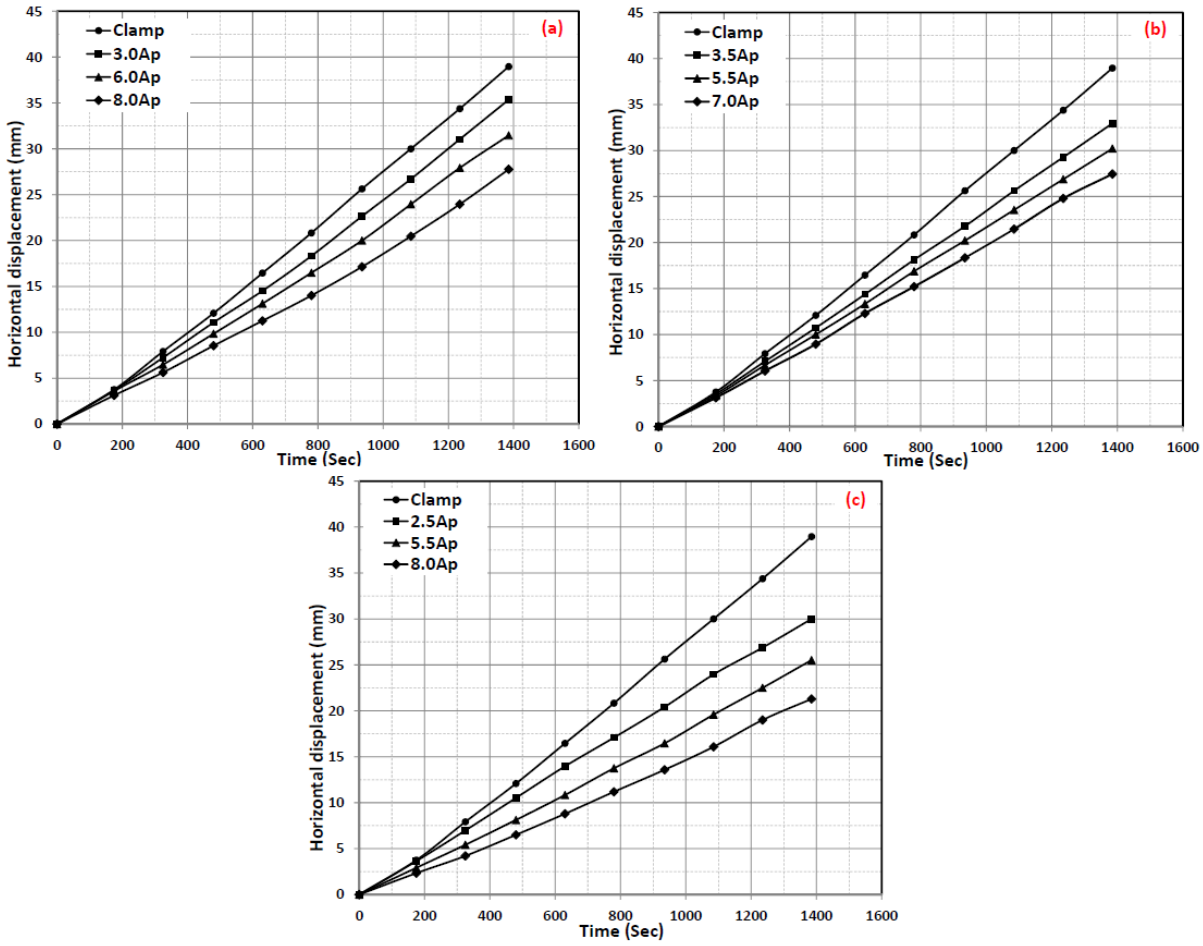

Figure 7.20: Displacement-time plot at different location behind the clamp under different value of confining pressures for the geogrid with 1200 kN/m stiffness; (a) 12.5 kPa, (b) 25 kPa and (c) 50 kPa (A_p:aperture size of geogrid)

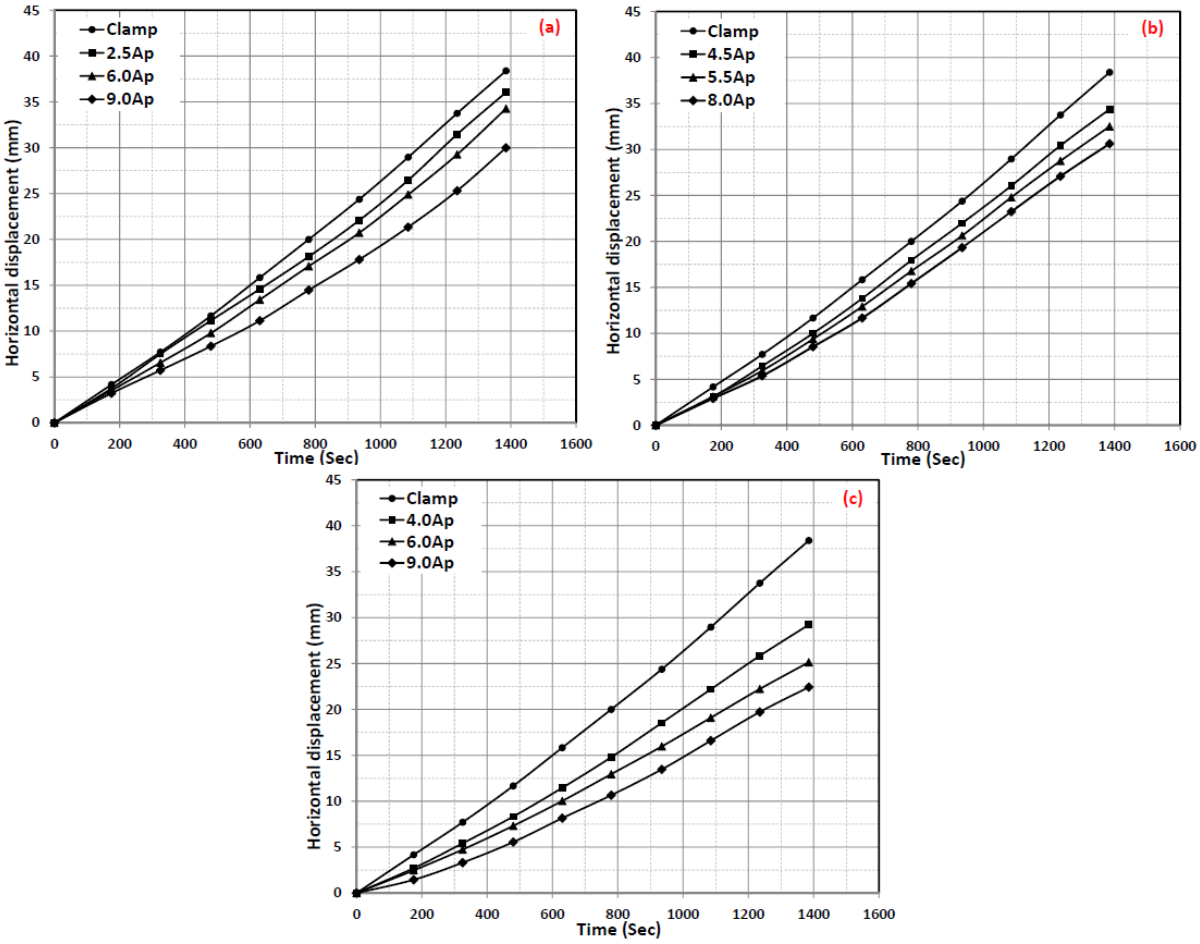

Figure 7.21: Displacement-time plot at different location behind the clamp under different value of confining pressures for the geogrid with 1600 kN/m stiffness; (a) 12.5 kPa, (b) 25 kPa and (c) 50 kPa (A_p:aperture size of geogrid)

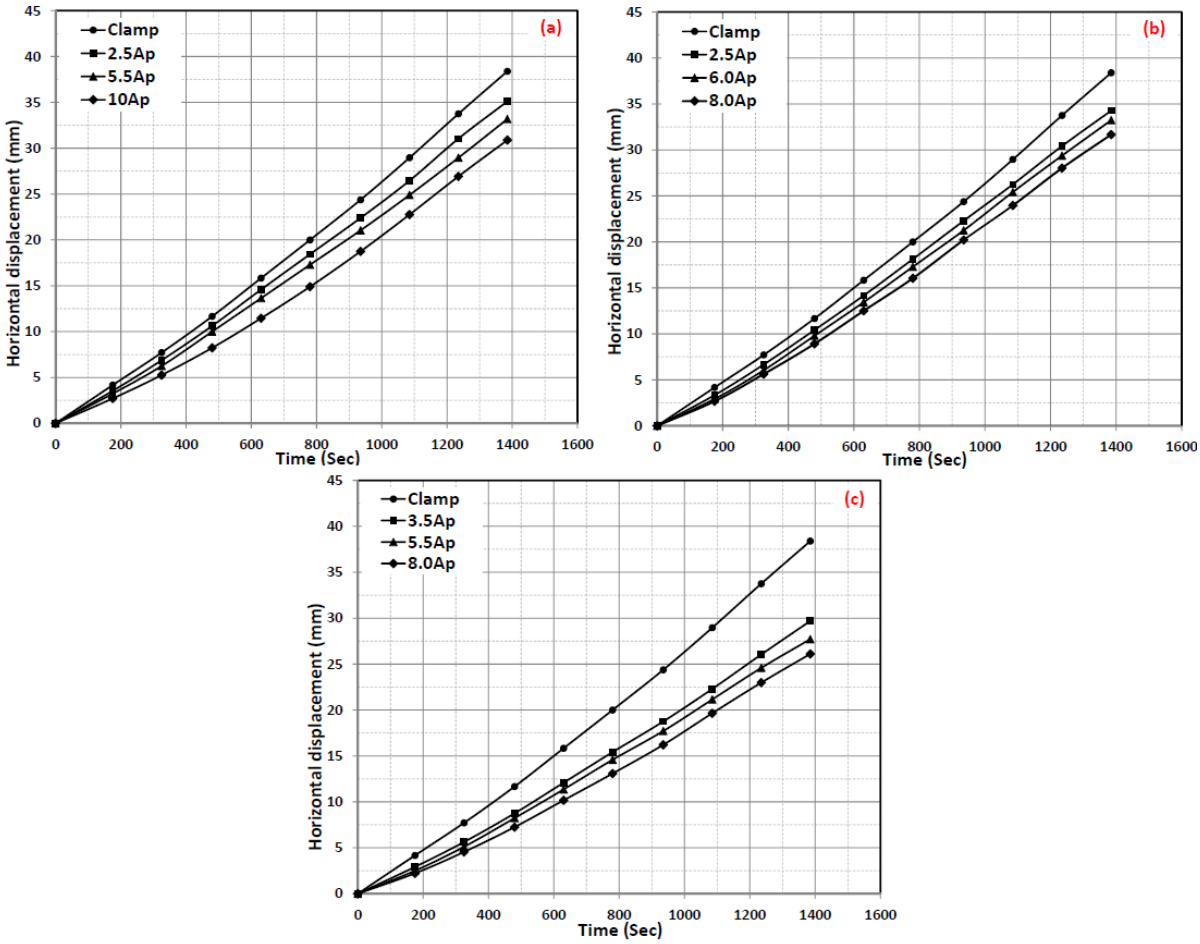

Figure 7.22: Displacement-time plot at different location behind the clamp under different value of confining pressures for the geogrid with 2900 kN/m stiffness; (a) 12.5 kPa, (b) 25 kPa and (c) 50 kPa (A_p:aperture size of geogrid)

The measured data points together with the best polynomial fit of the normalised displacement profiles of the geogrid under different confining pressures along the length of the reinforcement are shown in Figure 7.23 to 7.25. These indicate that the differential displacement between the fixed end and the free end is greater for higher confining pressure. The smallest differential displacement was observed for the geogrids with the stiffness equal to 2900 kN/m under low confining pressure.

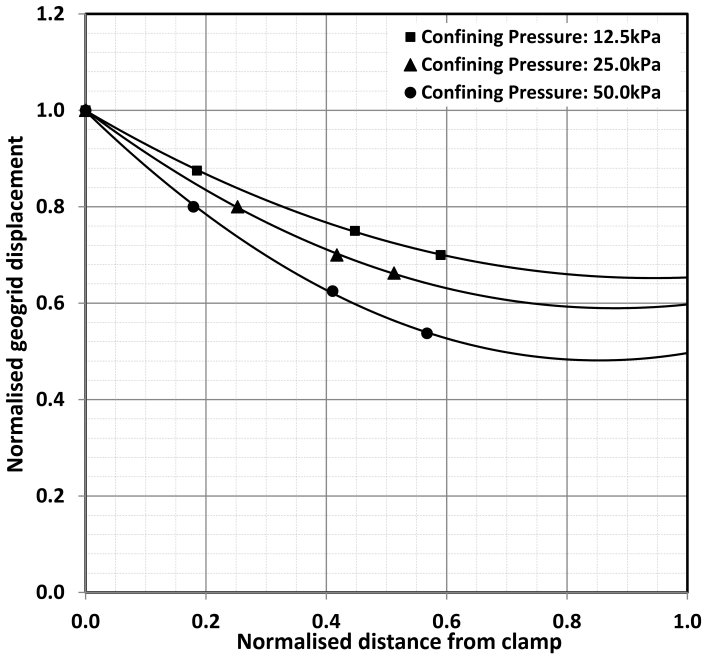

Figure 7.23: Normalised displacement of geogrid with 1200 kN/m stiffness under different normal stresses (markers indicate experimental data and solid line is best fit curve).

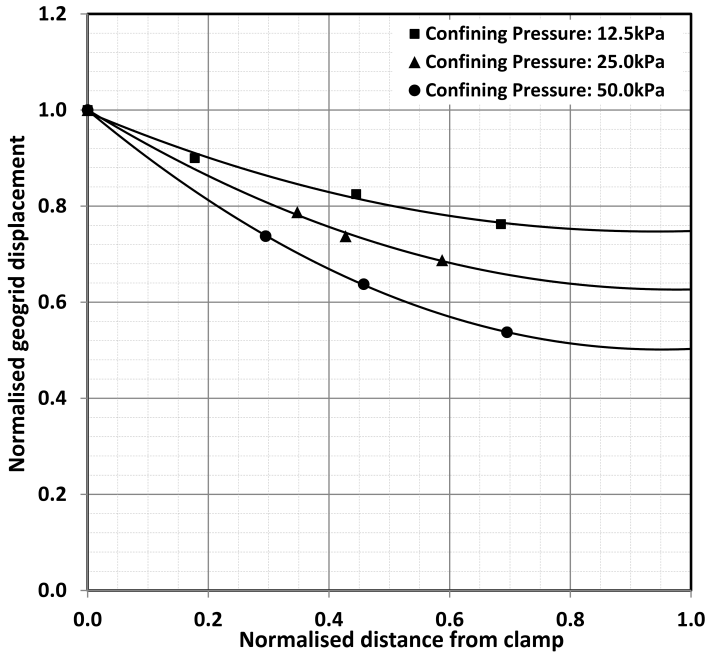

Figure 7.24: Normalised displacement of geogrid with 1600 kN/m stiffness under different normal stress (markers indicate experimental data and solid line is best fit curve).

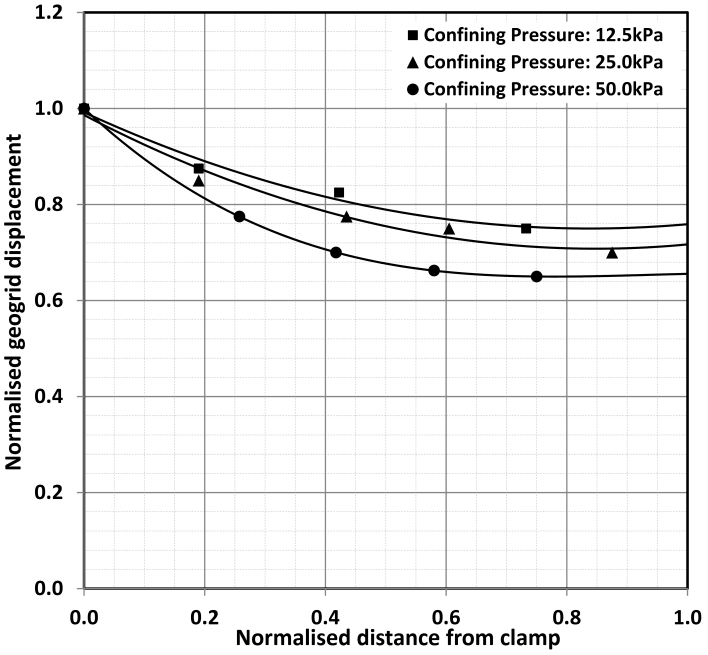

Figure 7.25: Normalised displacement of geogrid with 2900 kN/m stiffness under different normal stress (markers indicate experimental data and solid line is best fit curve).

7.6 Interaction between soil and geogrid

The interface coefficient between soil and geogrid can be calculated using the classical pull-out resistance equation :

$$P_R = 2\ L\ \sigma_v^{'}\ \tan\delta'\ = 2\ L\ \sigma_v^{'}\ \alpha \tan\phi' \tag{7.1}$$

where P_R is the pull-out resistance (per unit width); L the length of reinforcement in the anchorage zone; $\sigma_\nu^{'}$ is the effective stress applied over the specimen; δ' is the interface friction between soil and geogrid; $\phi^{'}$ is the angle of shearing resistance of the soil and α is the bond coefficient between soil and reinforcement.

Figure 7.26 shows the value of the interface coefficient for the three types of geogrid, the steel reinforcement with holes and the sheet of steel under different confining pressures calculated based on the peak pull-out strength. The α values are based on the assumption of a fixed value of $\phi' = 48°$ (Section 3.1).

The value of α is significantly larger than that normally expected (typical values in the literature are 0.6 - 0.8). It is postulated that this is due to 3D edge effects where dilation of soil above and below the geogrid is resisted by the soil mass to the sides of the geogrid leading to an overall greater resistance. This may lead to the 2-3 times increase in value of α seen for the $\sigma_v^{'}$=25 and 50 kPa results. However, the $\sigma_v^{'}$=12.5 kPa results are hard to explain, particularly the value for the 2900 kN/m stiffness geogrid and require further investigation. The latter value may be an anomalous data point since the observed load-displacement behaviour for the corresponding test was inconsistent with all the other test data.

The data also indicates that $\tan\delta$ (and therefore either α or ϕ' or both) increases at low confining pressure. This is attributed to enhanced dilation, corroborated by the PIV data in Chapter 6. The results of the test also show that the interface coefficients for the geogrid and steel reinforcement with holes are similar at $\sigma_v^{'}$=25 and 50 kPa, though diverge $\sigma_v^{'}$=12.5 kPa. The value for α for the plain steel sheet is consistent with the literature and potentially implies a reduced 3D effect due to low dilation as the sheet simply slides between the particles.

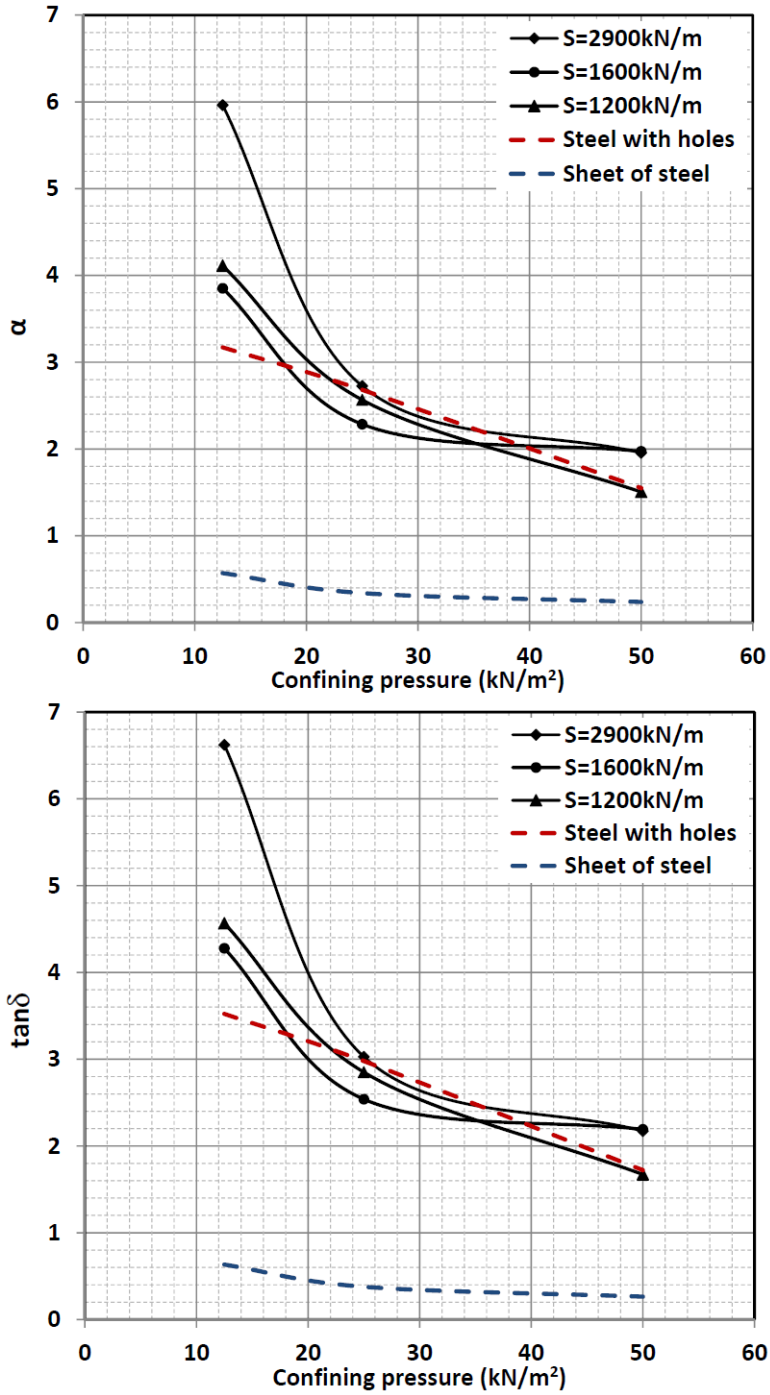

Figure 7.26: Interface coefficient of shear resistance for geogrid and steel reinforcement based on peak strength observed in the load-displacement results (S: stiffness of geogrid, kN/m)

Figures 7.27 to 7.29 show horizontal displacement of soil particles along the length of the geogrid under different confining pressures for three different types of geogrid. As the figures show, the magnitude of horizontal displacement of soil is reduced with increasing the value of confining pressure. In addition, the trend of the graphs show that the movement of soil particles has become less from the front of the box to the end of the box. This happens for higher values of confining pressure. For low values of confining pressure the distribution of soil movement is more or less uniform along the length of the specimen.

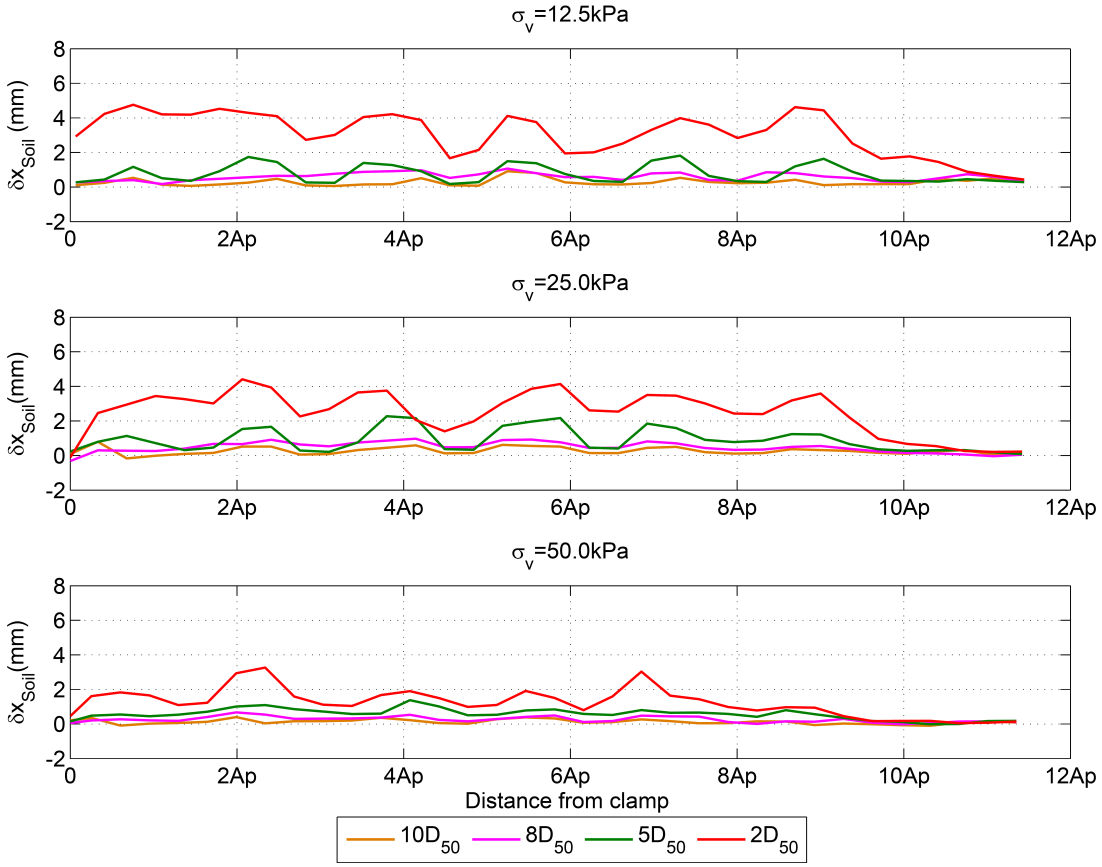

Figure 7.27: The horizontal displacement of soil particles at the end of pull-out test under three different values of confining pressures for the geogrid with stiffness equals 1200 kN/m

The results of this study indicate that a large horizontal displacement of soil particles is consistently apparent adjacent to the geogrid location with the largest displacement concentrated near the rib positions. The magnitude of the horizontal displacement of the soil particles has an inverse relation with the amount of

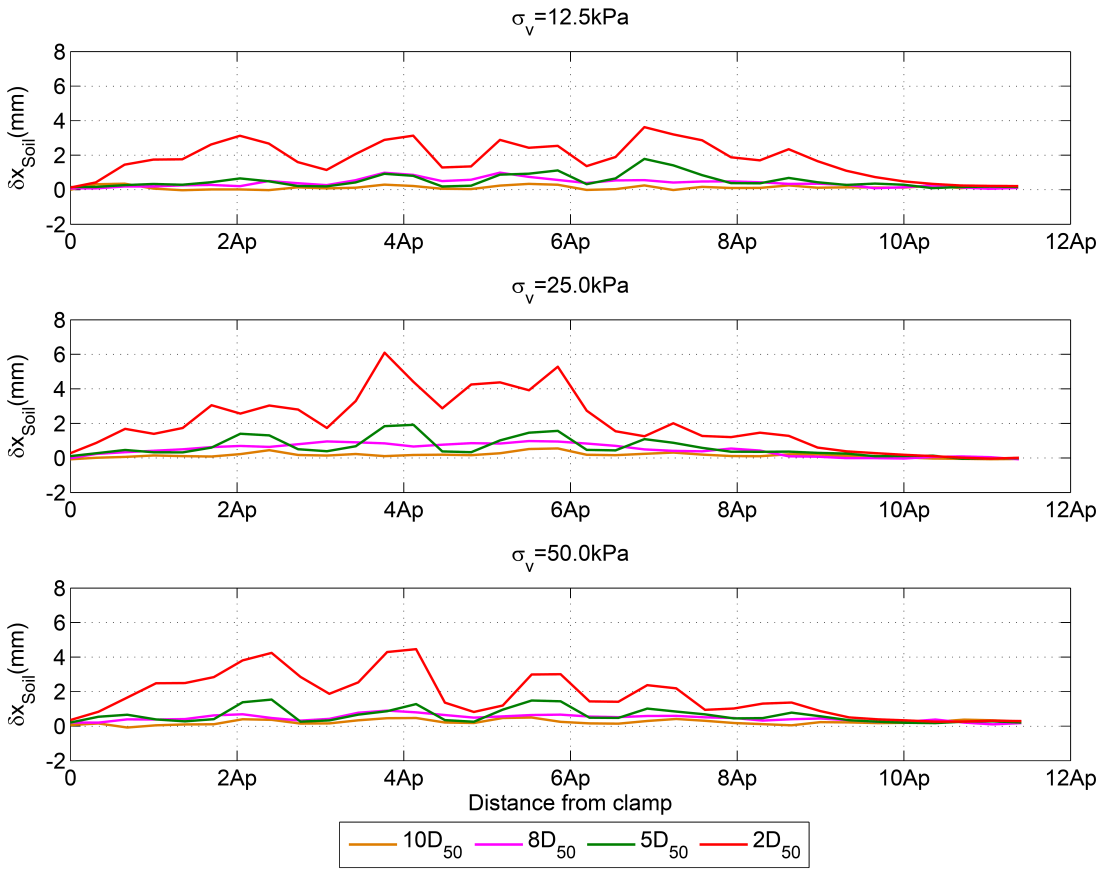

Figure 7.28: The horizontal displacement of soil particles at the end of pull-out test under three different values of confining pressures for the geogrid with stiffness equals 1600 kN/m

confining pressure. The soil particles is located further from the geogrid undergo smaller vertical displacements than those closer. The dilation phenomenon occurred for all tests under different values of confining pressures. However, the magnitude of dilation is greatest near to the geogrid. The reason for this is assumed to be that the interlock between soil particles near the geogrid is greater due to the soil particles located within the geogrids apertures, but the soil particles beyond the shear bond have a lower interlock so the particles simply shear over each other.

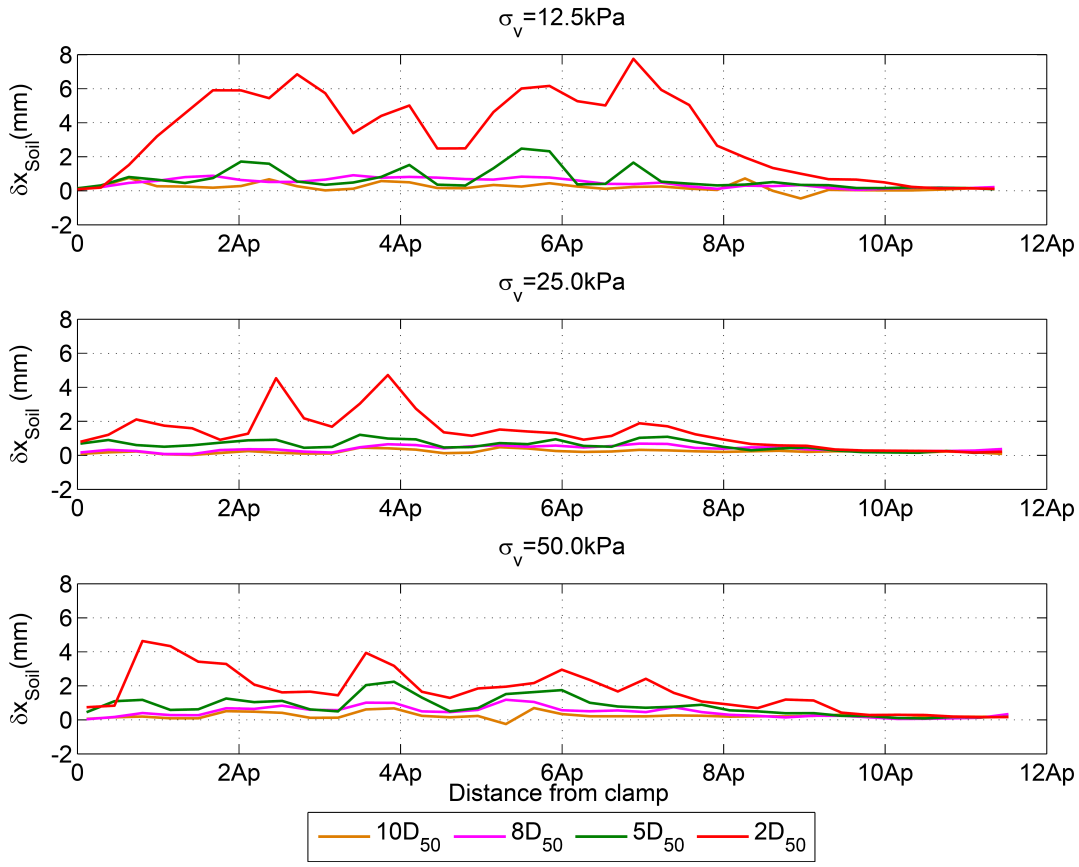

Figure 7.29: The horizontal displacement of soil particles at the end of pull-out test under three different values of confining pressures for the geogrid with stiffness equals 2900 kN/m

7.7 Qualitative conceptual model

The purpose of this research was to develop a new pull-out box and to introduce a new technique of evaluation for the mechanism of interaction between the soil and geogrid. Therefore, the generation of a comprehensive model of this interaction is beyond the scope of this work. However, by using the result of the pull-out tests performed herein, a tentative simple qualitative conceptual model is presented here to give a better understanding of the interaction mechanism between soil and geogrid.

As explained in the earlier chapters previous researchers have attributed, the pull-out resistance of a geogrid to a combination of three different components: (i)

skin friction over surface of geogrid; (ii) skin friction between soil-soil through the geogrid apertures and; (iii) passive resistance developed in front of the transverse members of geogrid.

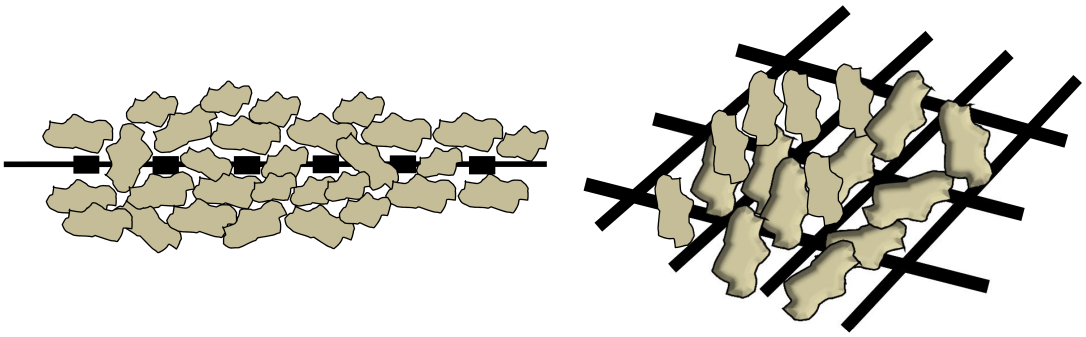

Figure 7.30: Particle distribution around a geogrid

This appears valid for soils when $D_{50} << A_p$, however an alternative conceptual model appears necessary for situations where $D_{50} \backsim A_p$.

- As shown in Figure 7.30, significant numbers of particles are "locked" in the geogrid apertures.
- On pullout, these particles are restricted in their degree of freedom of movement and therefore cause enhanced dilation of the adjacent particle assemblage, as they try to " push" past the adjacent particles, even if the soil body is initially loose. No "bearing capacity" type mechanism around geogrid transverse members as postulated by Jewell (1996) for finer grained soils is expected.
- For a " loose" soil body, the shearing induced by the geogrid pullout is transmitted vertically upwards and downwards. Away from the geogrid, this becomes contractive, therefore the absolute upwards movement induced by the dilation around the geogrid, diminishes with distance from the geogrid. There is therefore a zone of influence of absolute vertical displacement around the geogrid. In the experiments conducted this was around 4 to 5.5 times D_{50} of the soil.
- Overall there is a zone of soil shearing adjacent to the geogrid, where soil particles are locally dragged with the geogrid, but at a certain distance,

particles are unaffected. In the experiments conducted this was also found to be around 4 to 5.5 times D_{50} of the soil.

- During pullout, the geogrid stretches. This increases the degree of freedom of movement and locally reduces the averaged shear stress between geogrid and adjacent soil. Hence at higher confining pressures, rather than pull out uniformly along its length, it will stretch at the loaded end, locally reducing friction and transmitting more of the load to the end of the geogrid. This mode of behaviour will depend on the relative stiffness of the geogrid and the stressed, confining soil mass. However this may not alter the overall load capacity.
- The interface friction between soil and geogrid is not constant, but is a function of confining pressure. This may be entirely due to a variation in friction angle of the soil itself with confining stress, but may also include a variation in interface coefficient with confining stress.
- For a narrow strip of geogrid (width $\backsim 2A_p$), 3D effects around the edges can give significant gain to pullout capacity relative to a steel strip. This is attributed to dilation induced by the geogrid that is resisted by the soil to the sides of the grid.

7.8 Implications for numerical limit analysis and limit equilibrium models

For the modelling of geogrids with where $D_{50} \backsim A_p$, the following tentative observations can be made in relation to the discussion presented in Chaper 4;

- There is no distinction between bond and friction. The interaction is essentially frictional/dilational. This can be modelled using a conventional α value.
- The interface friction will vary with confining stress. This is not normally represented in conventional limit equilibrium models, but can be modelled

numerically using a non-linear yield envelope rather than a linear Mohr-Coulomb envelope. It is most likely to affect shallow buried geogrids up to 2-3 m deep.

- Dilation during pullout may be an issue if modelling an otherwise rigidly confined soil mass. This is an issue that arises in any case for limit analysis which assumes all the behaviour is dilational and that the frictional component can be approximated as dilational.

As mentioned earlier in Section 4.6, the required shear strength of soft soil needs to be increased by 20 % by changing the boundary condition between soil and reinforcement from 1 to 0.6. This could be one of the main reasons for future researchers to evaluate the accurate interface factor between soil and reinforcement. This should be followed by investigating the main parameteres which have influence on this factor.

Chapter 8

Conclusions and Recommendations

8.1 Introduction

The primary aim of this research was to develop new techniques and a new pull-out test apparatus to evaluate the interaction mechanism between soil and reinforcement and to investigate the effect of rupture strength\stiffness and confining pressure on pull-out. A further aim was to investigate the detailed interaction between granular soil and geosynthetic materials both analytically and numerically. To achieve these aims, this research is separated into two main areas which are; (i) analytical and numerical models for soil-reinforcement interaction and (ii) advanced visualisation element tests using transparent soil technology with Particle Image Velocimetry (PIV). A series of research objectives were outlined in Chapter 1. The following section revisits these objectives and summarises the key findings and conclusions.

8.2 Research outcomes

8.2.1 Analytical and numerical modelling

The study into the stability of embankments described in the paper presented in Appendix A:

1. Undertook a comprehensive parametric study of reinforced and unreinforced embankments using the general purpose computational limit analysis approach Discontinuity Layout Optimization (DLO).
2. Identified 4 distinct mechanisms of failure for an embankment constructed over soft soil which are: (i) lateral sliding failure, (ii) deep seated failure, (iii) lower layer failure (squeezing/extrusion failure) with sinking and (iv) lower layers failure (squeezing/extrusion failure) with 'snapping'. The latter mechanism is more likely to occur than mechanisms (iii) and need not involve any significant deformation/yielding of the reinforcement which simply rotates. This has not been previously examined in the literature.

Based on the above work and drawing in previous literature, the following distinct modes of soil/reinforcement interaction were identified: (i) shearing soil over reinforcement, (ii) transverse shear or (iii) pulling out the reinforcement through the soil. However, because of time constraints this current research is focused only on pull-out interaction mechanism. This is covered in Section 8.2.3.

The embankment study also had the following outcomes:

1. The DLO analysis was shown to find more critical failure mechanisms compared with other limit equilibrium results in the literature for most cases. It was also able to identify a previously unreported bearing type failure mechanism which involves rotational 'snapping'of the embankment.
2. The use of reinforcement allows an embankment of a given height H to be constructed on a depth D of soft soil of around 50-100 % the strength of that on which an unreinforced embankment could be constructed, depending on

the value of H/D. Use of very strong compared to lower strength embankment fill has only a marginal additional effect of allowing construction on a soft soil of around 10% lower strength.

3. Design charts have been presented that can be used for determining the maximum stable height and required reinforcement strength for fully reinforced (where the reinforcement is not taken to yield) and unreinforced embankments resting over soft soil and the transition between these two states which is shown to result in an approximately linear relationship between the required reinforcement rupture strength and the undrained shear strength of the soft soil.

4. It is recommended that embankments be designed at the point where the reinforcement is not taken to yield to avoid an observed sensitivity to the soft soil strength for cases where reinforcement and soil yield together.

8.2.2 Physical modelling

1. Triaxial tests and sieve analysis showed that the coarse grained transparent fused silica used in the current study can be used as a surrogate for gravels. The size of soil particles was between 10-15 mm with the mean particle size (D_{50}) of 7.42 mm. This is classified as *GP* according to the unified soil classification system. Conventional consolidated drained (CD) triaxial test indicated a shear friction angle of 47° in a dry condition and 48° in a saturated condition.

2. The optical "modulation transfer function method"(MTF) method introduced by Black and Take (2015) was shown for the first time to perform well for the transparency of a coarse grained transparent soil. This allows the evaluation of the optimum depth of viewing.

3. A new transparent pull-out box to evaluate the interaction behaviour between soil and geogrid reinforcement was developed using transparent soil coupled laser aided imaging to illuminate a vertical cross section within the transparent soil. This allows visualisation of the movement of transparent soil particles within the entire plane of interest.

8.2.3 Gravel-geogrid interaction mechansim

The test programme was grouped into three sets of pull-out tests. The first group of tests involved 9 experiments using a geogrid as reinforcement. Three different types of geogrid under different confining pressures were tested in this research study to evaluate the effect of rupture strength\stiffness on the interaction between soil and reinforcement. The second group of tests (total of 3) used a sheet of steel as reinforcement with similar size/shape of those in the geogrid. The objective of these tests was to investigate the effect of rigidity/flexibility of reinforcement on distribution of soil particles movement and the interaction behaviour between soil and reinforcement. Lastly, 3 tests at different confining pressures were performed on a sheet of steel without manufactured grids. The objective of these tests was to evaluate the effect of particles "locked" within the grids on the interaction between soil and reinforcement. It should be noted, due to the number of tests performed in this research project, the observed results may not generalisable to scenarios beyond the experimental series performed here. Analysis of the test results led to the following conclusions:

1. Pull-out tests under different confining pressures (12.5 kPa, 25 kPa and 50 kPa) for the geogrid with the lowest value of stiffness (1200 kN/m), did not display a peak pull-out resistance whereas for the two other types of geogrid (1600 kN/m and 2900 kN/m) a peak pull-out resistance was observed. This occurred for all samples with the exception for the sample with 1600 kN/m stiffness under a high value of confining pressure (50 kPa).
2. For low values of confining pressure (12.5 kPa and 25 kPa) the load-displacement response was independent of the rupture strength\the stiffness of the specimen. However, for the higher value of confining pressure (50 kPa), the geogrid with the higher value of rupture strength\stiffness has a higher pull-out resistance.

   It is inferred that, the magnitude of the two lowest confining pressures, 12.5 kPa and 25 kPa, is small in comparison with the stiffness of three types of geogrid, so the stiffness of geogrid far exceeds the stiffness of the geogrid/soil resistance.

3. A large horizontal displacement of soil particles is consistently apparent adjacent to the geogrid location with the largest displacement concentrated near the rib positions. The magnitude of the horizontal displacement of the soil particles has an inverse relation with the amount of confining pressure.
4. Vertical displacement contours show that locations further from the geogrid undergo smaller vertical displacements than those closer. The dilation phenomenon occurred for all tests under different values of confining pressures. However, the magnitude of dilation is greatest near to the geogrid. The reason for this is assumed to be that the interlock between soil particles near the geogrid is greater due to the soil particles located within the geogrid's apertures, but the soil particles beyond the shear bond have a lower interlock so the particles simply shear over each other. The greatest amount of dilation occurs for a geogrid with the highest stiffness (2900 kN/m) under the lowest confining pressure (12.5 kPa).
5. For geogrid strips, 3D effects are apparent, where it is postulated the area around the edges provides restraint again soil dilatancy around the geogrid. This is increases the pull-out resistance and the magnitude of interface coefficient between soil and geogrid by a factor of 2-3 for the specimen tested.
6. The boundary of the zone of influence of the geogrid was observed to be at a distance from the interface of 4 to 5.5 times the D_{50} of the soil.
7. The horizontal displacement profiles of the geogrid under different confining pressures along the length of the reinforcement reveal that the differential horizontal displacement between the fixed end and the free end is greater for higher confining pressure. The smallest differential horizontal displacement was observed for the geogrids with the stiffness equal to 2900 kN/m under low confining pressure. For each case the rate of pulling out the geogrid was constant.

8.3 Limitation of the current research

The quality of fused silica used in this research was not as high as desired. The fused silica grains are therefore not fully transparent. When immersed in mineral

mixed oil, small cracks form a foggy area around each grain leading to a poor quality of transparency. The amount of fogginess was more than initially anticipated. Therefore, for future studies it is recommended that higher quality fused silica should be used where available.

8.4 Recommendations for future research

There remain areas related to the research presented here that require further development. These potential avenues for further work encompass both further investigations into interaction behaviour between soil and reinforcement and the modelling techniques employed here and include:

1. PIV analysis for tracking the geogrid can be improved by allocating markers at the location of each rib. These markers can be tracked during the test which allows the calculation of the magnitude of strain along the length of the geogrid with higher accuracy.

2. A comprehensive study of the influence of the geometric and physical characteristics of geogrids on soil-geogrid interaction. Geometric characteristics of geogrids such as the distance between transverse members, the distance between longitudinal members, the shape of the aperture of the geogrid (square, rectangular or triangular); and the thickness and width of transverse and longitudinal members can be studied. Physical characteristics of geogrids include stiffness and strength of the different types of polymers that constitute geogrids; and stiffness and strength of the junctions. It is also useful to perform an additional study to investigate the effect of physical and mechanical properties of soil (particle size, density and etc) on the soil-geogrid interaction.

3. Modifying the front wall from fixed position to mobile wall to investigate a 45^{o} shear failure which passes through the reinforcement (Figure 8.1).

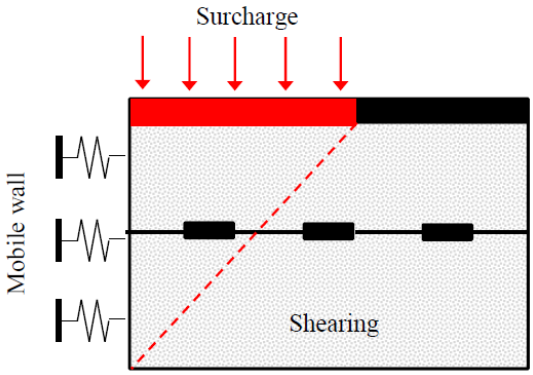

Figure 8.1: Mobile front wall to investigate 45^{o} shearing passing through the reinforcement

References

AASHTO (2004). *AASHTO LRFD bridge design specifications.*, 3rd edn, American Association of State Highway and Transportation Officials, Washington, D.C.

Abramento, M. (1993). *Analysis and measurement of stresses in planar soil reinforcements*, PhD thesis, Massachusetts Institute of Technology, USA.

Adrian, R. (1991). Particle-image techniques for experimental fluid mechanics, *Annu. Rev. Fluid mechanics* **23**: 261–304.

Ahmed, M. & Iskander, M. (2010). Analysis of tunnelling induced ground movements using transparent soil models, *Journal of Geotechnical and Geoenvironmental Engineering* **137**, 5: 525–535.

Al-Hussaini, M. & Perry, E. (1976). Effect of horizontal reinforcement on stability of earth masses, *Technical report No. S-76-11, U.S.Army Engineer, Waterways Experiment Station, Vicksburg.* .

Alfaro, M., Miura, N. & Bergado, D. (1995). Soil-geogrid reinforcement interaction by pullout and direct shear tests, *Geotechnical Testing Journal* **18**: 157–167.

Allen, T. M., Bathurst, R. J., Holtz, R. D., Walters, D. & Lee, W. F. (2003). A new working stress method for prediction of reinforcement loads in geosynthetic walls, *Canadian Geotechnical Journal* **40**, 5: 976–994.

Allersma, H. (1982). Photoelastic investigation of the stress distribution during penetration, 2nd European Symposium on Penetration Testing, pp. 411–418.

Anthoine, A. (1989). Mixed modelling of reinforced soils within the framework of the yield design theory, *Computers and Geotechnics* **7**, 1-2: 67–82.

ASTM D5321 (1991). *Standard test method for determining the coefficient of soil and geosynthetic or geosynthetic and geosynthetic system by the direct shear method*, ASTM, USA.

ASTM D6706-01 (2001). *Standard test method for measuring geosynthetic pullout resistance in soil*, ASTM, USA.

Bathurst, R. J. & Ezzein, F. (2015). Geogrid and soil displacement observations during pullout using a transparent granular soil, *Geotechnical testing Journal* **38**, 5: 673–685.

Bathurst, R. J., Allen, T. M. & Walters, D. L. (2005). Reinforcement loads in geosynthetic walls and the case for a new working stress design method, *Geotextiles and Geomembranes* **23**, 4: 287–322.

Bishop, A. W. (1955). The use of the slip circle in the stability analysis of slopes, *Geotechnique* **5**, 1: 7–17.

Bishop, A. W. & Morgenstern, N. (1960). Stability coefficients for earth slopes, *Geotechnique* .

Black, A. J. (2015). Centrifuge modelling with transparent soil and laser aided imaging, *ASTM Geotech Testing journal* **38**, 631-644: 5.

Black, J. A. (2012). Ground displacement during press-in piling using transparent soil and piv, pp. 1–8. presented at the International Press-In Association, 4th IPA Workshop, Singapore, Dec 67, International Press-In Association, Tokyo, Japan.

Black, J. A. & Take, W. (2015). Quantification of optical clarity of transparent soil using the modulation transfer function, *ASTM Geotech Testing journal* **38**, 5: 588–602.

Bolt, A. & Duszynska, A. (2000). Pull-out testing of geogrid reinforcement, Vol. 2, Proceeding of the Second European Geosynthetics Conference,, Bologna, Italy-EUROGEO, pp. 939–943.

Boudali, M., Leroueil, S. & Srinivasa Murthy, B. (1994). Viscous behaviour of natural clays, Vol. 1, pp. 411–416. Proceedings of the 13th International Conference on Soil Mechanics and Foundation Engineering, New Delhi, India.

Bourne-Webb, P., Amatya, B., Soga, K., Amis, T.and Davidson, C. & Payne, P. (2009). Energy pile test at lambeth college, london: Geotechnical and thermodynamic aspects of pile response to heat cycles, *Gotechnique* **59**, 3: 237–248.

Boyle, S. & Holtz, R. (1994). Deformation characteristics of geosynthetic-reinforced structures, Vol. 1, Fifth International Conference on Geotextiles, Geomembranes and Related Products, Singapore, pp. 361–364.

Brandl, H. (2006). Energy foundations and other thermo-active ground structures, *Gotechnique* **56**, 2: 81–122.

Bransby, P. (1968). *Stress and strain in sand caused by rotation of a model wall*, Phd, Cambridge University.

Bransby, P. & Milligan, G. (1975). Soil deformations near camtilever sheet pile walls, *Geotechnique* **25**, 2: 175–195.

British Standard BS 8006 (1995). *Code of practice for strengthened/reinforced soils and other fills*, British Standard BS 8006:1995. British Standards Institution, London.

Britto, A., Savvidou, C., Maddocks, D., Gunn, M. & Booker, J. (1989). Numerical and centrifuge modelling of coupled heat flow and consolidation around hot cylinders buried in clay, *Geotechnique* **39**, 1: 13–25.

BS 6906-8:1991 (1991). *Method of test for Geotextiles-Part 8: Determination of sand-geotextile frictional behaviour by direct shear*, British Standard.

BS 8006-2 (2011). Code of practice for strengthened/reinforced soils, part2: Soil nail design,, *British Standards Institution* .

BS EN 13738:2004 (2004). *Geotextiles and geotextile - related products - Determination of pullout resistance in soil*, British Standard.

Busby, J., Lewis, M., Reeves, H. & Lawley, R. (2009). Initial geological considerations before installing found source heat pump systems, *Quarterly Journal of Engineering Geology and Hydrogeology* pp. 295–306.

Butterfield, R., Harkness, R. & Andrawes, K. (1970). A stereo-photogrammetric method for measuring displacement fields, *Getechnique* **20**, 3: 308–314.

Campanella, R. & Mitchell, J. (1968). Influence of temperature variations on soil behaviour, *Journal of the Soil Mechanics and Foundations Division, ASCE* **94**: 709–734.

Cekerevac, C. & Laloui, L. (2004). Experimental study of thermal effects on the mechanical behaviour of a clay, *Int. J. Numer. Anal. Methods Geomech* **28**, 3: 209–228.

Chai, J. C. (1992). *Interaction between grid reinforcement and cohesivefrictional soil and performance of reinforced wall/embankment on soft*, PhD thesis, Asian Institute of Technology, Bangkok, Thailand.

Chai, J. C. & Bergado, D. (1993). Some techniques for finite element analysis of embankments on soft ground, *Canadian Geotechnical Journal* **30**, 4: 705–715.

Chang, J., Hannon, J. & Forsyth, R. (1977). Pullout resistance and interaction of earthwork reinforcement and soil, *Technical report*, National Research Council, Washington, DC, 01-07.

Chen, R. & Chen, C.-C. (1994). Investigation of pull-out resistance of geogrids, Vol. 1, Fifth International Conference on Geotextiles, Geomembranes and Related Products, Singapore, pp. 461–464.

Chen, W. F. (1975). *Limit analysis and soil plasticity*, Elsevier Science Publishers, BV, Amsterdam, The Netherlands.

Christopher, B. R. & Holtz, R. D. (1985). Geotextile engineering manual, *Federal Highway Administration report, Washing D.C.* .

Christopher, B. R., Holtz, R. D. & Berg, R. R. (2000). Geosynthetic reinforced embankments on soft foundations, *in* J. L. Hanson & R. J. Termaat (eds), *Proceedings of the soft ground technology conference*, United engineering foundation, The Geo-Institute of the American Society of Civil Engineers, pp. 206–236.

Clarke, S., Smith, C. & Gilbert, M. (2013). Modelling discrete soil reinforcement in numerical limit analysis, *Canadian Journal of Civil Engineering* **50**, 7: 705–715.

Cui, P., Li, X., Man, Y. & Fang, Z. (2011). Heat transfer analysis of pile geothermal heat exchanges with spiral coils, *Applied Energy* **88**, 11: 4113–4119.

de Buhan, P. & Salencon, J. (1993). A comprehensive stability analysis of soil nailed structures, *European journal of mechanics. A. Solids* **12**: 325–345.

de Buhan, P., Mangiavacchi, R., Nova, R., Pellegrini, G. & Salenion, J. (1989). Yield design of reinforced earth walls by a homogenization method, *Geotechnique* **39**, 2: 189–201.

Demars, K. & Charles, R. (1982). Soil volume changes induced by temperature cycling, *Canadian Geotechnical Journal* **19**: 188–194.

Drucker, D. C., Greenberg, H. J. & Prager, W. (1952). Extended limit design theorems for continuous media, *Quarterly of Applied Mathematics* **9**: 381–389.

Duncan, J. M. (1996). State of the art: limit equilibrium and finite-element analysis, *Journal of Geotechnical Engineering* **122**, 7: 577–596.

Duncan, J. M. & Schaefer, V. R. (1988). Finite element consolidation analysis of embankments, *Computers and Geotechnics* **6**, 2: 77–93.

Duncan, J. M., Buchignani, A. L. & De Wet, M. (1987). An engineering manual for slope, *Virginia Polytechnic Institute and State University* . Reproduced by the University of Wisconsin-Madison with permission and courtesy of the Virginia Polytechnic Institute and State University.

Dyer, M. R. (1985). *Observation of the stress distribution in crushed glass with applications to soil reinforcement*, PhD thesis, University of Oxford, UK.

Ezzein, F. & Bathurst, R. (2011a). A transparent sand for geotechnical laboratory modeling, *Geotechnical testing journal* **34**, 6: 590–601.

Ezzein, F. & Bathurst, R. J. (2011b). Development of a geosynthetic pullout test apparatus with transparent granular soil, *Pan-American Canadian Geotechnical Society Geotechnical Conference, Toronto, Canada.*

Ezzein, F. & Bathurst, R. J. (2014). A new approach to evaluate soil-geosynthetic interaction using a novel pullout test apparatus and transparent granular soil, *Geotextiles and Geomembranes* **42**: 246–255.

Farrag, K. & Morvant, M. (2000). Effect of clamping mechanism on pullout and confined extension tests, *ASTM SPT 1379, American society fo rtesting and materials* pp. 89–96.

Farrag, k., Acar, Y. & Juran, I. (1993). Pull-out resistance of geogrid reinforcements, *Geotextiles and Geomembranes* **12**: 133–159.

Ferreira, J. A. Z. (2013). *Evaluation of Soil-Geogrid Interaction at Different Load Levels Using Pullout Tests and Transparent Soil*, PhD thesis, The University of Texas at Austin.

Ferreira, J. A. Z. & Zornberg, J. G. (2015). A transparent pullout testing device for 3d evaluation of soil-geogrid interaction, *Geotechnical Testing Journal* **38**, 5: 686–707.

FHWA-NHI-00-043 (2001). *Mechanically stabilized earth walls and reinforced soil slopes, Design Construction Guidelines*, NHI-00-0043 edn, Department of Transportation Federal Highway Administration, U.S.

Forlati, G. & Black, J. A. (2014). Impact of pile geometry on the installation of open ended press-in piles. Proceedings of the 8th International Conference on Physical Modeling in Geotechnics. Perth, Australia.

Fowler, J. (1985). Building on muck, *Civil Engineering* **55**, 5. ASCE.

Gao, J., Zhang, X., Liu, J., Li, K. & Yang, J. (2008). Thermal performance and ground temperature of vertical pile-foundation heat exchangers: A case study, *Applied Energy* **86**: 2295–2304.

Ghionna, V. N., Moraci, N. & Rimoldi, P. (2001). Experimental evaluation of the factors affecting pull-out test results on geogrids, Proceedings of International Symposium: Earth Reinforcement. Fukuoka, Kyushu, Japan.

Gilbert, M. & Smith, C. (2007). Discontinuity layout optimization: a new numerical procedure for upper bound limit analysis, pp. 170–173. In IX International Conference on Computational Plasticity: COMPLAS IX, Barcelona.

Gilbert, M., Smith, C., Haslam, I. & Pritchard, T. (2010). Application of discontinuity layout optimization to geotechnical engineering., Proceedings of the 7th European Conference on NumericalMethods in Geotechnical Engineering.

Gill, D. (1999). *Experimental and theoretical investigations of pile and penetrometer installation in clay*, PhD thesis, Trinity College, Dublin.

Giroud, J. P. (1977). Commentaire sur la comparaison des armatures mtalliques et armatures textiles, Vol. 3, Proceedings of the International Conference on the Use of Fabrics in Geotechnics, Paris, p. 38. (in French).

Goode III, J., Zhang, M. & McCartney, J. S. (2014). Centrifuge modeling of energy foundations in sand and clay, Vol. 7, 8th International Conference on Physical Modelling in Geotechnics (ICPMG2014), Perth, Australia. Junuary 14-17, 2014, pp. 729–735.

Habibagahi, K. (1977). Temperature effects and the concept of effective void ratio, *Indian Geotechnical Journal* **7**: 14–34.

Haliburton, T. A., Anglin, C. C. & Lawmaster, J. D. (1978). Testing of geotechnical fabric for use as reinforcement, *Geotechnical Testing Journal* **1**: 203–212.

Heikkila, J. (2000). *Camera calibration toolbox for Matlab Version 3.0 at http://www.vision.caltech.edu/bouguetj/calib˙doc/*.

Heikkila, J. & Silven, O. (1997). A four-step camera calibration procedure with implicit image correction, Proceedings of the 1997 Conference on Computer Vision and Pattern Recognition, pp. 1106–1112.

Hepbasli, A., Akdemir, O. & Hancioglu, E. (2003). Experimental study of a closed loop vertical ground source heat pump system, *Energy Conservation and Management* **44**: 527–548.

Hird, C. C. (1986). Stability charts for reinforced embankment on soft ground, *Geotextiles and Geomembranes* **4**: 107–127.

Hird, C. C. & Kwok, C. M. (1989). Finite element studies of interface behaviour in reinforced embankments of soft ground, *Computers and Geotechnics* **8**, 2: 111–131.

Hird, C. C., Pyrah, I. C. & Russell, D. (1990). Finite element analysis of the collapse of reinforced embankments on soft ground, *Geotechnique* **4**, 40: 633–640.

Hird, C., Ni, Q. & Guymer, I. (2008). Physical modeling of displacements around continuous augers in clay, Vol. 1, Proc. 2nd British Geotechnical Association International Conference on Foundations, pp. 565–574.

Holtz, R. D. & Broms, B. B. (1977). Walls reinforced by fabrics-results of model tests., *Int.Conf. on the use of fabrics in geotechnics, Paris.*

Houston, S. L., Houston, W. N., & Williams, N. D. (1985). Thermo-mechanical behaviour of seafloor sediments, *Journal of Geotechnical Engineering* **111**, 11: 1249–1263.

Hryciw, R. D. & Irsyam, M. (1993). Behavior of sand particles around rigid ribbed inclusions during shear, *Soils and Foundations* **33**, 3: 1–13.

Hueckel, T. & Baldi, G. (1990). Thermoplasticity of saturated clays: experimental constitutive study, *J. Geotech. Engng* **61**, 10: 831–844.

Hueckel, T. & Pellegrini, R. (1992). Effective stress and water pressure in saturated clays during heating-cooling cycles, *Canadian Geotechnical Journal* **29**, 6: 1095–1102.

Hueckel, T., Francois, B. & Laloui, L. (2011). Temperature-dependent internal friction of clay in a cylindrical heat source problem, *Geotechnique* **61**, 10: 831–844.

Hueckel, T., Laloui, L. & Francois, B. (2009). Implications of thermal sensitivity of the static internal friction angle, pp. 104–115. Proc. 1st Int. Symp. on Computational Geomechanics, Juan les Pins.

Iskander, M. (2010). *Modelling with Transparent Soils, Visualizing Soil Structure Interaction and Multi Phase Flow, Non-Intrusively*, Springer.

Iskander, M., Lai, J., Oswald, C. & Mannheimer, R. (1994). Development of a transparent material to model the geotechnical properties of soils, *ASTM Geotechnical Testing Journal, GTJODJ* **17**, 4: 425–433.

Iskander, M., Liu, J. & Sadek, S. (2002). Transparent amorphous silica to model clay, *Journzl of geotechnical and geoenvironmental engineering* **128**, 3: 262–273.

James, R. (1965). *Stress and strain fields in sand*, Phd, Cambridge University.

Janbu, N. (1973). *Slope stability computations. In Embankment dam engineering, Casagrande memorial volume*, Edited by E. Hirschfield and S. Poulos. John Wiley Sons, New York. pp. 4786.

Jewell, R. (1990). Reinforced bond capacity, *Geotechnique* **40**, 3: 513–518.

Jewell, R. (1996). *Soil reinforcement with geotextiles*, London: Construction Industry Research and Information Association (CIRIA).

Jewell, R. A. (1988). The mechanics of reinforced embankment on soft soils, *Geotextiles and Geomembranes* **7**: 237–273.

Jewell, R. A., Milligan, G. W. E., Sarsby, R. W. & Dubois, D. (1985). Interaction between soil and geogrids, Proceedings from the Symposium on Polymer Grid Reinforcement in Civil Engineering, Ed. Thomas Telford, London, pp. 18–30.

Jewell, R., Milligan, G., Sarsby, R. & DuBois, D. (1984). Interaction between reinforcement and geogrids, Polymer Grid Reinforcement, London, UK,, pp. 18–30.

Johnston, R. & Romstad, K. (1989). Dilation and boundary effects in large scale pull-out tests, Vol. 2, Rio DeJaneiro, Brasil, pp. 1263–1266.

Juran, I., Baudrand, G., Farrag, K. & Elias, V. (1990). Kinematical limit analysis for design of soil nailed structures, *Journal of Geotechnical Engineering* **116**, 1: 54–72.

Kelly, P. (2013). *Soil Structure Interaction and Group Mechanics of Vibrated Stone Column Foundation*, PhD thesis, University of Sheffield. PhD Thesis.

Laloui, L., Moreni, M. & Vulliet, L. (2003). Comportement d'un pieu bi-fonction, fondation et changeur de chaleur., *Canadian Geotechnical Journal* **40**, 2: 388–402.

Laloui, L., Nuth, M. & Vulliet, L. (2006). Experimental and numerical investigations of the behaviour of a heat exchanger pile, *IJNAMG* **30**, 8: 763–781.

Leshchhinsky, B. (2015). Bearing capacity of footings placed adjacent to c'-ϕ' slopes, *Journal of Geotechnical and Geoenvironmental Engineering* **141**: 04015022.

Leshchinsky, D. (1987). Short-term stability of reinforced embankment over clayey, *Soil and Foundation* **29**, 3: 105–114.

Leshchinsky, D. & Smith, D. S. (1989). Deep seated failure of a granular embankment over clay: Stability analysis, *Soil and Foundation* **27**, 3: 43–57.

Leshchinsky, D., Vahedifard, F. & Leshchinsky, B. A. (2012). Revisiting bearing capacity analysis of mse walls, *Geotextiles and Geomembranes* **34**: 100–107.

LimitState (2014). *LimitState:GEO Manual Version 3.2.a, june 2014 edn, LimitState Ltd.*

Liu, J., Iskander, M. & Sadek, S. (2002). Optical measurement of deformation under foundations using a transparent soil model, pp. 155–159. International Conference on Physical Modeling in Geotechnics: ICPMG.

Liu, J., Iskander, M. & Sadek, S. (2003). Consolidation and permeability of transparnet amorphous silica, *Geotechincal testing journal* **26**, 4: 1–12.

Lopes, M. & Ladeira, M. (1996). Role of specimen geometry, soil height and sleeve length on the pull-out behaviour of geogrids, *Geosynthetics International* **3**, 6: 701–719.

Lopes, M. & Lopes, M. (1999). Soil-geosynthetic interaction- influence of soil particle size and geosynthtic structure, *Geosynthetics International* **6**, 4: 261–282.

Loveridge, F. & Powrie, W. (2012). Pile heat exchangers: thermal behavior and interactions, Vol. 166, pp. 178–196. Proceedings of the Institution of Civil Engineers, Ground Engineering.

Lysmer, J. (1970). Limit analysis of plane problems in soil mechanics, *Journal of the Soil Mechanics and Foundations Division* **96**, 4: 1311–1334. ASCE.

Makrodimopoulos, A. & Martin, C. M. (2006). Lower bound limit analysis of cohesive-frictional materials using second-order cone programming., *International Journal for Numerical Methods in Engineering* **6**, 4: 604–634.

Manceau, S., Macdiarmid, C. & Horgan, G. (2012). Design of soil reinforced slopes amd structures, *in* J. Burland, T. Chapman, H. Skinner & M. Brown (eds), *ICE manual of geotechnical engineering, Volume II geotechnical design, Construction and verification., first edn, ICE Publishing.*, pp. 1093–1107.

Michalowski, R. L. (1998). Limit analysis in stability calculations of reinforced soil structures, *Geotextiles and Geomembranes* **16**: 311–331.

Milligan, G. W. E., Earl, R. F. & Bush, D. I. (1990). Observations of photo-elastic pullout tests on geotextile and geogrids, *In: Proceedings of the 4th International Conference on Geotextiles, Geomembranes and Related Products*, Vol. 2, The Hague, The Netherlands, pp. 747–751.

Mitchell, J. (1964). Shearing resistance of clay as a rate process, *J. Soil Mech. Fdns., Am Soc. Civ.* **90**: 29–61.

Moraci, N. & Recalcati, P. (2006). Factor affecting the pullout behaviour of extruded geogrids embedded in a compacted granular soil, *Geotextiles and Geomembranes* **24**, 2: 220–242.

Muller, W. W. & Saathoff, F. (2015). Geosynthetics in geoenvironmental engineering, *Science and Technology of Advanced Materials* **16**: 034605(20pp).

Nayeri, A. & Fakharian, K. (2009). Study on pullout behaviour of uniaxial hdpe geogrids under monotonic and cyclic loads, *International Journal of Civil Engineering* **7**, 4: 211–223.

Ng, C. W. W., Shi, C., Gunawan, A. & Laloui, L. (2014). Centrifuge modelling of energy piles subjected to heating and cooling cycles in clay, *Geotechnique Letters* **4**: 310–316.

Ni, Q., Hird, C. & Guymer, I. (2010). Physical modelling of pile penetration in clay using transparent soil and particle image velocimetry, *Geotechnique* **60**, 2: 121–132.

Ochiai, H., Otani, J., Hayashic, S. & Hirai, T. (1996). The pull-out resistance of geogrids in reinforced soil, *Geotextiles and Geomembranes* **14**: 19–42.

Olivera, A. (1982). Use of non-woven geotextiles to construct a deep highway embankment over swamp soil, *2nd Int. Conf. on geotextiles, Las Vegas* **3**: 625–630.

Otani, J., Miyamoto, K. & Mukunoki, T. (2001). Visualization of interaction behaviour between soil and reinforcement using x-ray ct, *International Journal of Physical Modelling in Geotechnics* **2**: 15–22.

Pahud, D. & Hubbuch, M. (2007). Measured thermal performances of the energy pile system of dock of the midfield at zurich airport, *Proceedings of the European Geothermal Congress, Unterhaching, Germany, 30th May-1st June.*

Palmeira, E. M. (1987). *The study of soil-reinforcement interaction by means of large scale laboratory tests.*, PhD thesis, University of Oxford, UK.

Palmeira, E. M. (2004). Bearing force mobilisation in pull-out tests on geogrids, *Geotextiles and Geomembranes* **22**: 481–509.

Palmeira, E. M. (2009). Soil-geosynthetic interaction: Modelling and analysis, *Geotextiles and Geomembranes* **27**: 368–390.

Palmeira, E. M. & Milligan, G. W. E. (1989). Scale and other factors affecting the results of pull-out tests of grids buried in sand, *Geotechnique* **39**, 3: 511–524.

Palmeira, E. M., Pereira, J. H. F. & Silva, A. R. L. d. (1998). Backanalyses of geosynthetic reinforced embankments on soft soils, *Geotextiles and Geomembranes* **16**: 273–292.

Perkins, S. W. & Cuelho, E. V. (1999). Soil-geosynthetic interface strength and stiffness relationships from pullout test, *Geosynthetics Internatinal* **6**, 5: 321–346.

Peters, S. B., Siemens, G. & Take, W. A. (2011). Characterization of transparent soil for unsaturated applications, *ASTM Geotechnical Testing Journal Special Issue on Innovations in Characterizing the* **34**, 5: 445–456.

Peterson, L. M. & Anderson, L. R. (1980). Pullout resistance of welded wire mats embedded in soil, *Technical report*, Research Rep., Submitted to Hilfiker Co., Civil and Environmental Engineering Dept., Utah State Univ., Logan, Utah.

Pigg, D. R. & McCafferty, W. R. (1984). The design and construction of a reinforced soil retaining wall at low southwick., *Symp. on polymer grid reinforcement in civil engineering, London.* .

Plum, R. & Esrig, M. (1969). Some temperature effects on soil compressibility and pore water pressure, effects of temperature and heat on engineering behaviour of soils, pp. 231–242.

Raju, D. & Fannin, R. J. (1998). Load-strain-displacement response of geosynthetics in monotonic and cyclic pullout, *Canadian Geotechnical Journal* **35**: 183–193.

Raju, D. M. (1995). *Monotonic and cyclic pullout resistance of geosynthetic*, PhD thesis, University of british Columbia, Canada.

Rathmayer, H. G. & Korhonen, O. E. (1985). Geotextile reinforced land reclamation in the bay of river vantaa, helsinki, *Proc. 11th ICSMFE, Helsinki* **3**: 1795–1800.

Richardson, G. N. & Koerner, R. M. (1990). *A Design Primer: Geotextiles and Related Materials*, Industrial Fabrics Association International.

Roscoe, K. H., Arthur, J. R. F. & James, R. G. (1963). The determination of strains in soils by an x-ray method, *Civil Engng and Public Works* **58**, 7: 873–876.

Rowe, R. & Li, A. L. (2005). Geosynthetic-reinforced embankments over soft foundation, *Geosynthetics International* **12**, 1: 50–85.

Rowe, R. K. & Hinchberger, S. D. (1998). The significance of rate effects in modelling the sackville test embankment, *Canadian Geotechnical Journal* **35**, 3: 500–516.

Rowe, R. K. & Li, A. L. (1999). Reinforced embankment over soft foundations under undrained and partially conditions, *Geotextiles and Geomembranes* **17**: 129–146.

Rowe, R. K. & Soderman, K. (1987). Stabilization of very soft soils using high strength geosynthetics: the role of finite element analyses,, *Geotextiles and Geomembranes* **6**: 53–80.

Rowe, R. K. & Soderman, K. L. (1985). An approximate method for estimating the stability of geotextile reinforced, *Canadian Geotechnical Journal* **22**: 392–398.

Rowe, R. K., MacLEAN, M. D. & Barsvary, A. K. (1984). The observed behaviour of a geotextile reinforced embankment constructed on peat, *Conadian geotechnical Journal* pp. 289–304.

Sabhahit, N., Basudhar, P. K., Madhav, M. R. & Miura, N. (1994). Generalized stability analysis of reinforced embankment on soft clay, *Geotextiles and Geomembranes* **13**: 765–780.

Sadek, S., Iskander, M. & Liu, J. (2002). Geotechnical properties of transparent silica, *Canadian geotechnical journal* **39**, 1: 111–124.

Sadek, S., Iskander, M. & Liu, J. (2003). Accuracy of digital image correlation for measuring deformations in transparent media, *American Society of Civil Engineers, ASCE, Journal of Computing in Civil Engineering* **17**, 2: 88–96.

Salencon, J. (1990). An introduction to the yield design theory and its applications to soil mechanics, *European Journal of Mechanics - A/Solids* **9**, 5: 477–500.

Sarsby, R. W. (1985). The influence of aperture size/particle size on the efficiency of grid reinforcement, Second Canadian Symposium on Geotextiles and Geomembranes., Edmonton, Alberta, Canada, pp. 7–12.

Savvidou, C. (1988). Centrifuge modelling of heat transfer in soil, *Proceedings International Conference Centrifuge 88, Paris, Cort (ed.), Balkema, Rotterdam*, pp. 583–591.

Sawicki, A. & Lesniewska, D. (1989). Limit analysis of cohesive slopes reinforced with geotextiles, *Computers and Geotechnics* **7**, 1-2: 53–66.

Schlosser, F. & Vidal, H. (1969). Reinforced earth, *Bulletin de Liaison des Laboratories Routiers, Ponts et Chaussees* , 40.

Shwan, B. J. & Smith, C. (2014). Application of limit analysis in unsaturated soils: Numerical and experimental study of bearing capacity, Vol. 2, pp. 1757–1762. Unsaturated Soils: Research and Applications - Proceedings of the 6th International Conference on Unsaturated Soils, UNSAT 2014.

Siemens, G., Peters, S. & Take, W. A. (2010). Analysis of a drawdown test displaying the use of transparent soil in unsaturated flow applications, *5th Int. Conf. on Unsat. Soils, Barcelona.*

Slama, C. (1980). *Manual of photogrammetry*, 4 edn, American Society of Photogrammetry: 105 North Virginia Avenue, Falls Church, VA.

Sloan, S. W. (1988). Lower bound limit analysis using finite elements and linear programming, *International Journal for Numerical and Analytical Methods in Geomechanics* **12**, 1: 61–77.

Smith, C. (2012). Limit loads for a shallow anchor/trapdoor embedded in a non-associative coulomb soil, *Gotechnique* **62**, 7: 563–571.

Smith, C. & Gilbert, M. (2007a). Application of discontinuity layout optimization, *Royal Society A:Mathematical, Physical and Engineering* **463**, 2086: 2461–2484.

Smith, C. & Gilbert, M. (2007b). New upper bound solutions for layered soil bearing capacity problems using discontinuity layout optimization, 10th Australia New Zealand Conference on Geomechanics, Brisbane, pp. 250–255.

Smith, C. & Gilbert, M. (2008). Limit analysis of the stability of foundations on inclined ground, pp. 1683–1692. In 2nd International Conference on Foundations, ICOF 2008, Dundee.

Smith, C. & Gilbert, M. (2013). Identification of rotational failure mechanisms in cohesive media using discontinuity layout optimization, *Geotechnique: International Journal of Soil Mechanics* **63**, 14: 1194–1208.

Spencer, E. (1967). A method of analysis of the stability of embankments assuming, *Geotechnique* **17**, 1: 11–26.

Stanier, S. (2011). *Modelling the behaviour of helical screw piles*, PhD thesis, Department of Civil and Structural Engineering, University of Sheffield.

Stanier, S. A., Black, J. A., & Hird, C. C. (2013). Modelling helical screw piles in clay and design implications. Proc. Inst. Civ. Eng.: Geotech. Eng. (available online).

Stanier, S. A., Black, J. A. & Hird, C. C. (2012). Enhancing accuracy and precision of transparent synthetic soil modeling, *International Journal of Physical Modeling in Geotechnics* **12**, 4: 162–175.

Stewart, M. A., & McCartney, J. S. (2012). Strain distributions in centrifuge model energy foundations, *ASCE GeoCongress 2012. Oakland, CA. March 25-29th 2012.*

Stewart, M. A., & McCartney, J. S. (2014). Centrifuge modelling of soil-structure interaction in energy foundations, *Journal of Geotechnical and Geoenvironmental Engineering* **140**, 4.

Sugimoto, M., Alagiyawanna, A. & Kadoguchi, K. (2001). Influence of rigid and flexible face on geogrid pullout tests, *Geotextiles and Geomembranes* **19**: 257–277.

Take, W. (2003). *The influence seasonal moisture cycles on clay slopes*, PhD thesis, Churchill College, University of Cambridge.

Tandjiria, V., Low, B. K. & Teh, C. I. (2002). Effect of reinforcement force distribution on stability of embankments, *Geotextiles and Geomembranes* **20**: 423–443.

Teixeira, S., Bueno, B., Zomberg, J. & ASCE, M. (2007). Pullout resistance of individual longitudinal and transverse geogrid ribs, *Journal of Geotechnical and Geoenvironmental Engineering* **133**, 1: 37–50.

Terzaghi, K. (1943). *Theoretical soil mechanics*, John Wiley Sons, Inc., New York.

Towhata, I., Kuntiwattanaul, P., Seko, I. & Ohishi, K. (1993). Volume change of clays induced by heating as observed in consolidation tests, *Soils and Foundations* **33**: 170–183.

Vahedifard, F., Leshchinsky, B. A., Sehat, S. & Leshchinsky, D. (2014). Impact of cohesion on seismic design of geosynthetic-reinforced earth structures, *Journal of Geotechnical and Geoenvironmental Engineering* **140**, 6: 04014016–12.

Weast, R. (1986). *Handbook of Chemistry and Physics*, 66 edn.

White, D. (2002). *An investigation into the behaviour of pressed-in piles*, PhD thesis, Churchill College, University of Cambridge.

White, D., Take, W. & Bolton, M. (2001a). Measuring soil deformation in geotechnical models using digital images and piv analysis, Proc. 10th International Conference on Computer Methods and Advances in Geomechanics, Tucson, Arizona. 997-1002 pub. Balkema, Rotterdam.

White, D., Take, W. & Bolton, M. (2003). Soil deformation measurement using prticle omage velocimetry (piv) and photogrammetry, *Geotechnique* **53**, 7: 619–631.

Wilson-Fahmy, R. F., Koerner, R. M. & Sansone, L. J. (1994). Experimental behaviour of polymeric geogrids in pullout, *Journal of Geotechnical Engineering* **120**, 4: 661–677. ASCE, USA.

Wood, C. J., Liu, H. & Riffat, S. B. (2010). An investigation of the heat pump performance and ground temperature of a pile foundation heat exchanger system for a residential building, *Energy* **35**, 12: 3932–3940.

Wright, S. G. & Duncan, J. M. (1991). Limit equilibrium stability analyses for reinforced slopes, *Transportation Research Board* **1330**: 40–46.

Yu, H. S., Salgado, R., Sloan, W. & Kim, J. M. (1998). Limit analysis versus limit equilibrium for slope stability, *Journal of geotechnical and geoenvironmental engineering* pp. 1–11.

Zhang, N., Shen, S. L., Wu, H. N., Chai, J. C., Xu, Y. S. & Yin, Z. Y. (2015). Evaluation of effect of basal geotextile reinforcement under embankment loading on soft marine deposits, *Geotextiles and Geomembranes* **43**: 506–514.

Zhu, D. Y., Lee, C. F., Chan, D. H. & Jiang, H. D. (2005). Evaluation of the stability of anchor-reinforced slopes, *Canadian Geotechnical Journal* **45**, 5: 1342–1349.

Appendix A

Limit Analysis of Reinforced Embankment on Soft Soil

This paper is published in the Geotextiles and Geomembranes Journal:

Smith, C.C. and Tatari, A. (2016). "Limit Analysis of Reinforced Embankments on Soft Soil." *Geotextiles and Geomembranes Journal*, 44(**4**):504-514.
doi:10.1016/j.geotexmem.2016.01.008

Abstract

Previous work on the problem of the stability of a reinforced embankment founded on soft soil have presented limited studies based on a narrow range of assumed failure mechanisms. In this paper comprehensive parametric studies of reinforced and unreinforced embankments were conducted using the general purpose computational limit analysis approach Discontinuity Layout Optimization (DLO). Comparisons with previous Limit Equilibrium and FE results in the literature showed good agreement, with the DLO analysis generally able to determine more critical failure mechanisms. Simplified, summary design envelopes are presented that allow critical heights and reinforcement strengths to be rapidly determined based on soft soil strength and depth, and shows how the balance between soft soil strength and reinforcement strength combines to affect overall stability.

Keywords: Geosynthetics, discontinuity layout optimization, limit analysis, failure, reinforcement, safety factor.

A.1 Introduction

The use of geosynthetic reinforcement as basal reinforcement for an embankment constructed on soft soils can significantly enhance stability and allow construction to heights substantially higher than could be achieved without reinforcement (Rowe and Soderman, 1987). Two common analysis methods used by geotechnical engineers to check the stability of embankments over soft soil are (i) conventional limit equilibrium such as Coulomb wedge or the method of slices and (ii) the finite element (FE) method. The general concept of the former method is to find the most critical slip surface with the lowest factor of safety. This may be defined as the shear strength of the soil divided by shear stress required for equilibrium, Duncan (1996).

Most limit equilibrium methods indirectly model the reinforcement as a single representative force which acts at the intersection between the reinforcement and the failure mechanism. The failure mechanism may be modelled as a slip-circle using the method of slices (e.g. Rowe and Soderman (1985); Hird (1986); Sabhahit et al. (1994)), or as a log-spiral (e.g. Leshchinsky (1987); Leshchinsky and Smith (1989)) or using a translational mechanism (e.g. Jewell, 1988).

While limit equilibrium is simple and straightforward it makes an assumption about the nature of the failure mechanism which can lead to inaccuracy. In contrast FE methods can accurately model both working conditions and failure modes, representing the reinforcement as a structural membrane with an axial stiffness and negligible flexural rigidity. More recent in the literature has focused on this method Rowe and Soderman (1985); Rowe and Soderman (1987); Duncan and Schaefer (1988); Hird and Kwok (1989); Hird et al. (1990); Chai and Bergado (1993); Rowe and Hinchberger (1998); Rowe and Li (2005) and Zhang et al. (2015). However, modelling the embankment problem by finite elements typically requires significant time and is more complex with regard to choosing the problem parameters in comparison with limit equilibrium methods (Duncan, 1996).

Recently the advent of numerical direct methods has allowed the solution of limit analysis problems using optimization techniques in a fully general way. These provide a middle way between the simplification in limit equilibrium analysis and the relative complexity of the FE method. An elasto-plastic analysis typically requires many increments in order to find the critical factor of safety in contrast to a computational limit analysis approach which can directly determine the collapse state through optimization. One of the main advantages of limit analysis over FE methods is it requires only two strength parameters for any material modelled: the cohesion, c' or c_u, and the angle of shearing resistance, ϕ', of the soil. Computational limit analysis approaches have been recently used to analysis a range of reinforced soil problems Leshchinsky et al. (2012), Clarke et al. (2013) and Vahedifard et al. (2014). These papers utilise the Discontinuity Layout Optimization method (Smith and Gilbert, 2007a), which is adopted in this paper to undertake a parametric study of embankment stability.

The aim of this paper is to illustrate how reinforced embankments can be modelled in limit analysis; to investigate the range of failure modes that can occur and to produce a series of non-dimensional design charts for different geometries of embankment which allows the necessary minimum embankment soil strength and reinforcement strength required for stability to be determined in terms of the embankment geometry, base soil strength, soil/geotextile interface coefficient and surcharge. This provides a significantly more comprehensive set of charts compared to previous works that have utilised Limit Equilibrium such as Leshchinsky and Smith (1989), Duncan et al. (1987), Leshchinsky (1987) and Hird (1986) without using an analysis which typically adopts only one mode of failure.

A.2 Mechanics of reinforced embankments

Manceau et al. (2012) recommend three ULS states should be considered as follows: (i) deep-seated failure, (ii) lateral sliding (iii) extrusion. While deep seated failure requires an analysis such as method of slices or equivalent, the latter two mechanisms can be analysed relatively simply using limit equilibrium. Jewell (1988), presented simple analytical equations based on force equilibrium for the analysis

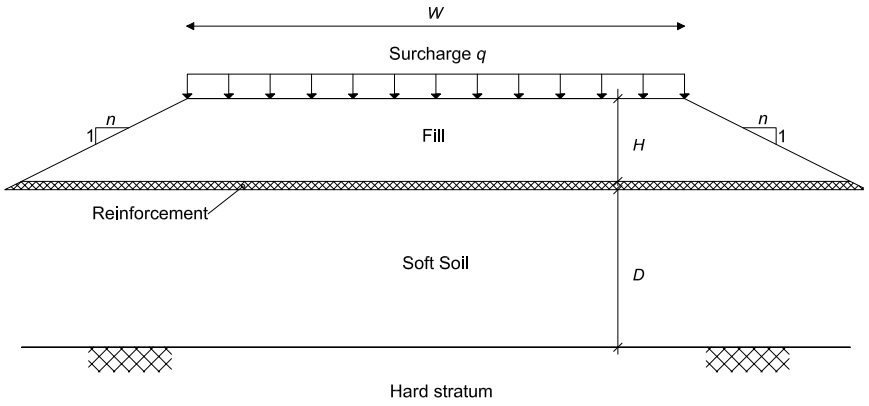

Figure A.1: geometry of embankment model

of reinforced and unreinforced embankments of geometry depicted in Figure A.1 and described by the parameters listed in Table A.1 (in the analysis $c' = 0$ was assumed). These provide useful equations for calibration and a conceptual model of two of the main mechanisms of collapse.

Table A.1: Reinforced embankment analysis parameters

Symbol	Definition
c'	cohesion of the soil of embankment fill
ϕ'	friction angle of soil of embankment fill
γ	unit weight of soil of embankment fill
c_u	shear strength of soft soil
R	rupture strength of reinforcement per unit width
H	height of embankment
W	width of top of embankment
D	thickness of soft soil
q	surcharge
n	side slope gradient ($1V : nH$)
α_c	interface coefficient between reinforcement and soft soil
α_s	interface coefficient between reinforcement and embankment fill

In Figure A.2a, the reinforcement provides resistance against lateral failure of the embankment itself with friction on the upper reinforcement surface of $\alpha_s \tan \phi'$

where α_s is the reinforcement interface coefficient. Equilibrium analysis gives the following required side slope gradient n for stability:

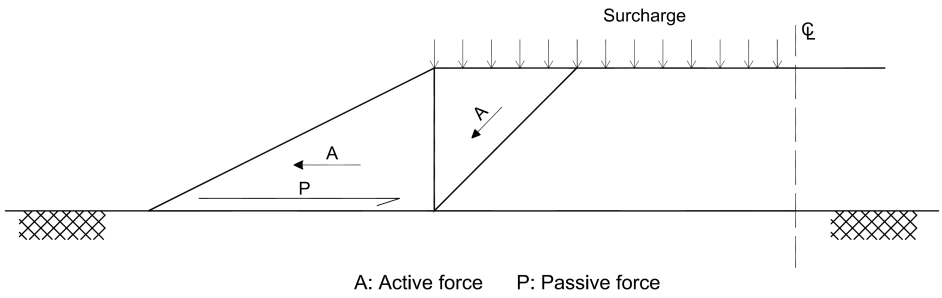

(a) Lateral sliding

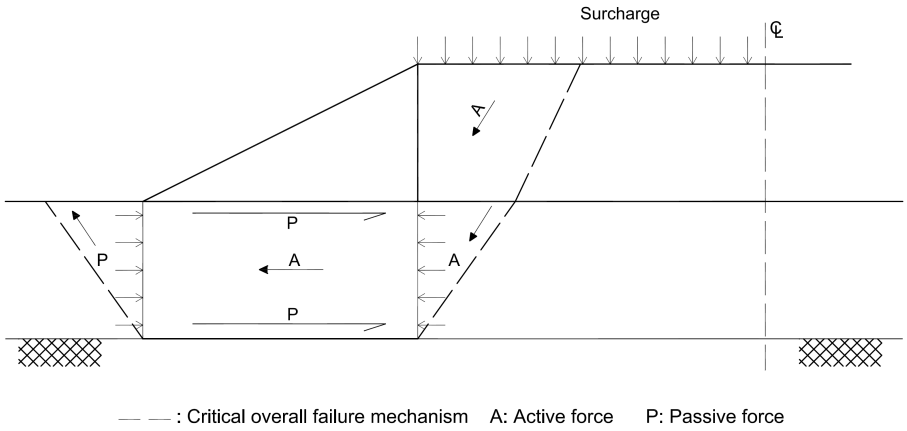

(b) Extrusion

Figure A.2: The mechanism of failure of embankment over soft soil (after Jewell, 1996)

$$n > \frac{K_a}{\alpha_s \tan\phi'}(1 + \frac{2q}{\gamma H}) \tag{A.1}$$

where the design value of active earth pressure coefficient, $K_a = \frac{1-\sin\phi'}{1+\sin\phi'}$.

In Figure A.2b the reinforcement provides shear resistance against lateral squeezing of the soft soil beneath the embankment. Equilibrium analysis of the deep failure mechanism gives the factor of safety F_s on the soft soil strength as follows:

$$F_s = \frac{c_u}{q + \gamma H}(4 + (1 + \alpha_c)\frac{nH}{D}) \tag{A.2}$$

The minimum force R within the reinforcement required to provide the stability for the failure mechanism in Figure A.2b is given by equation A.3:

$$R = \gamma H^2 \left(\frac{\alpha n D}{4D + (1 + \alpha) nH} + \frac{K_a}{2} \right) \tag{A.3}$$

Jewell also presented the following equation for checking the stability of an unreinforced embankment the failure mechanism is not present here):

$$F_s = \frac{c_u}{\gamma H} \left(\frac{8D + 2nH}{2D + K_a} \right) \tag{A.4}$$

Such limit equilibrium equations have the value of simplicity and clarity but it is not necessarily clear whether these are conservative or non-conservative in all cases.

A.3 Discontinuity layout optimisation (DLO)

A.3.1 Geotechnical analysis

Discontinuity layout optimization is a computational limit analysis method which is able to identify the critical failure mechanism and collapse load for any geotechnical stability problem. Examples of this analysis approach applied to soil only problems (with no reinforcement) may be found in Smith and Gilbert (2007b, 2013) and Leshchhinsky (2015). Figure A.3 illustrates the stages in the DLO procedure for finding the layout of sliplines that form the critical collapse mechanism

(after Gilbert et al. 2010). The accuracy of the method depends on the number n nodes employed which allow the critical mechanism to be selected out of a set of $n(n-1)/2$ potential sliplines. Using the principles of duality, the DLO formulation may be presented in either a kinematic energy form or an equilibrium and yield form.

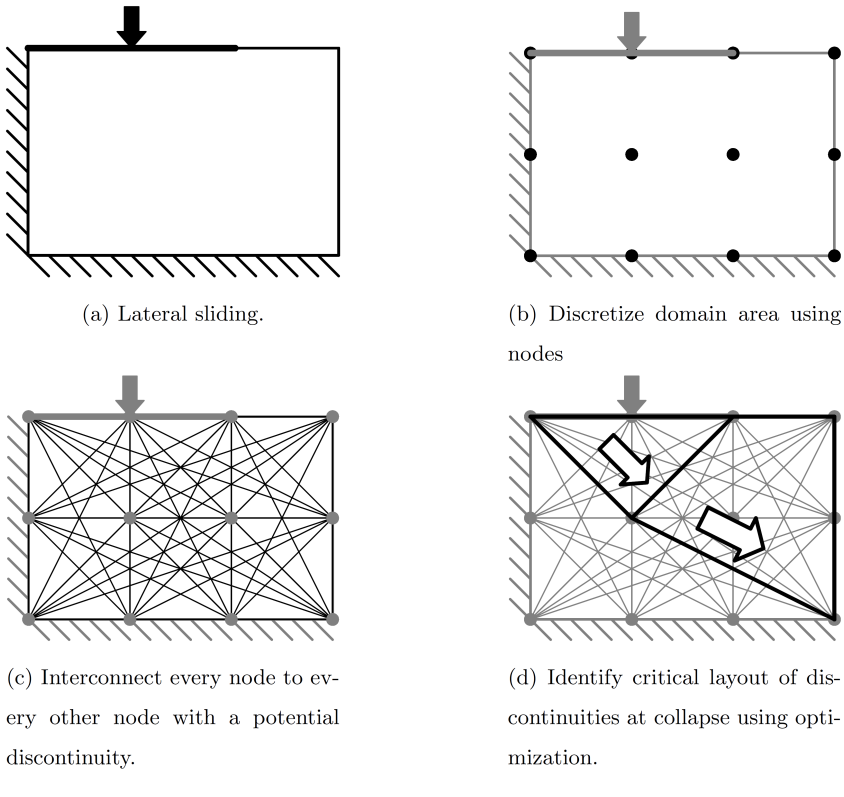

(a) Lateral sliding.

(b) Discretize domain area using nodes

(c) Interconnect every node to every other node with a potential discontinuity.

(d) Identify critical layout of discontinuities at collapse using optimization.

Figure A.3: Stages in DLO solution procedure (after Gilbert et al., 2010).

A.3.2 Modelling reinforcement in DLO

Reinforcement is modelled as a one dimensional element similar to that described by Clarke et al. (2013). This element is able to model failure in bending, tensile rupture and compressive failure controlled by parameters M_p, R, and C respectively, where M_p is the plastic moment of resistance and C is the compressive strength of the reinforcement. The element described by Clarke et al. (2013) was

designed also to allow the modeling of soil nails and so had the additional ability to allow soil to 'flow around' the element controlled by a lateral and pullout resistance. In this paper these properties were not required and these resistances were set to ∞. Each engineered element has three parallel components (as shown in Figure A.4) which comprise: an upper boundary interface, the reinforcement itself and a lower boundary interface. For the purposes of modelling geotextile reinforcement M_p is set to zero to allow free flexure, C is set to zero and the upper and lower boundaries are modelled with Mohr-Coulomb materials with strength $\alpha_s \tan\phi'$ and $\alpha_c c_u$ respectively.

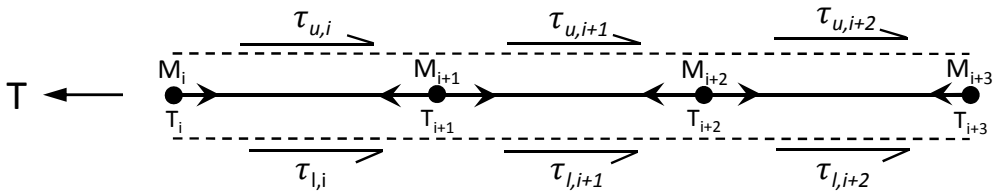

Figure A.4: Modelling flexible reinforcement in DLO for segment or node i, τ_u: upper boundary soil/reinforcement interface stress (kPa), τ_l: lower boundary soil/reinforcement interface stress (kPa), T: tensile force in reinforcement (kN, per m width), M: bending moment in reinforcement (kN, per m width).

In the equilibrium formulation of DLO, for each discrete element i of the reinforcement, variables are assigned to represent the shear stress $\tau_{u,i}, \tau_{l,i}$, on the upper and lower faces respectively, and the tensile force T_i and bending moment M_i in the reinforcement. The set of τ_u, τ_l, M, T are found that give the maximum load on the system that does not violate the following constraints:

1. $\tau_l \leq \alpha_c c_u$
2. $\tau_u \leq \alpha_s(c' + \sigma'_n \tan\phi')$
3. $C \leq T \leq R$
4. $M \leq M_p$

where σ'_n is the effective normal stress acting on the reinforcement.

It is noted that even if $M_p = R = C = 0$, the modelled reinforcement will still affect the mechanics of the system in that shear displacements are not permitted directly through the reinforcement element. However this can be represented via element rotations. With sufficiently small segments the same effect is achieved. Use of a higher nodal density along the reinforcement can therefore be beneficial in some cases.

Note that in a limit analysis formulation such as DLO, yield or rupture of the reinforcement does not lead to breakage or fracture but to unrestricted ductile elongation that still allows transmission of tensile forces along the length of the reinforcement.

A.4 Embankment modelling

A.4.1 Numerical model

Analysis was carried out using the implementation of DLO within the software LimitState:GEO Version 3.2a (LimitState, 2014). In the model, the boundary nodal spacing was set to be half that within the internal solid bodies as is recommended (LimitState, 2014). A series of internal vertical boundaries were also modelled within the embankment to allow 'bending' (or 'snapping') failure of the embankment. A simple example of this is shown in Figure A.5d. Selected models across the parameter space were evaluated using nodal spacings on a square grid of $H/1$ to $H/10$. Typical results are shown in Section A.9. Based on these an accuracy of 1-2% in terms of the factor of safety on soil strength would be achieved with a nodal spacing of $H/5$. This spacing was selected as a compromise between accuracy and speed.

A.4.2 Failure mechanisms

Four distinct mechanisms of failure were generated by the DLO analysis and are shown in Figure A.5. These mechanisms can be described as follows:

1. Lateral sliding failure (surface failure).
2. Deep seated global failure.
3. Lower layer failure (squeezing/extrusion failure) with sinking.
4. Lower layer failure (squeezing/extrusion failure) with 'snapping'.

For a high strength lower stratum, failure is in the shoulders of the embankment only (Figure A.5a). For low strength reinforcement the dominant failure mechanism is a deep seated global failure accompanied by yield of the reinforcement (Figure A.5b). In this type of failure, significant shearing happens in the main body and side slopes of the embankment. For high strength reinforcement significant 'squeezing' deformation is primarily seen in the lower stratum. The embankment itself either undergoes very localised shearing and vertical 'sinking' translation (Figure A.5c) or rotational 'snapping' (Figure A.5d). The latter mechanism is more likely to occur and need not involve any significant deformation/yielding of the reinforcement which simply rotates. To the authors' knowledge, the latter type of failure has not been previously examined in the literature.

A.4.3 Verification

A.4.3.1 Translational failure mechanisms

To permit direct comparison between the analytical solutions of Jewell (1988) and the DLO method for the analysis of surface failure (equation A.1 and figure A.2a), a simplified constrained model was first set up in DLO, setting the boundaries of the model to coincide exactly with the mechanism geometry used by Jewell. The relevant soil properties were applied to these boundaries while the solid bodies between the boundaries were assigned a rigid material of the same unit weight as the soil. This ensures failure can only occur along the pre-defined boundary lines, thus forcing the mechanisms to match those of Jewell's. The results, given in Figure A.6, show, as expected, that the constrained DLO analysis exactly matches the analytical solution (which can be regarded as an upper bound analysis) while

(a) Lateral sliding failure (surface failure)

(b) Deep seated global failure

(c) Lower layer extrusion with sinking

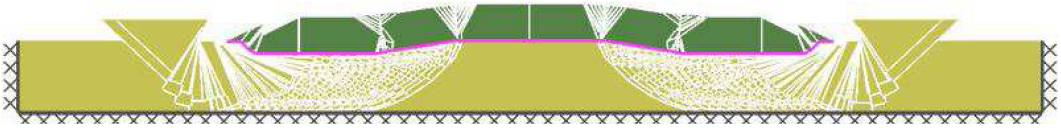

(d) Lower layer extrusion with 'snapping'

Figure A.5: Failure mechanisms of embankment over soft soil (exaggerated)

the unconstrained DLO analysis, results also given in Figure A.6, give more critical results.

Figure A.7 illustrates the comparison between the results of DLO and equations A.2 and A.4 for deep seated failure of reinforced and unreinforced embankments respectively. The results of analyses show a good match. However the DLO results are not consistently more critical as might be expected. This can be attributed to the form of the analytical equations which are based on limit equilibrium rather than limit analysis and, while probably not adopting an optimal mechanism, do neglect soil strength in various parts of the system.

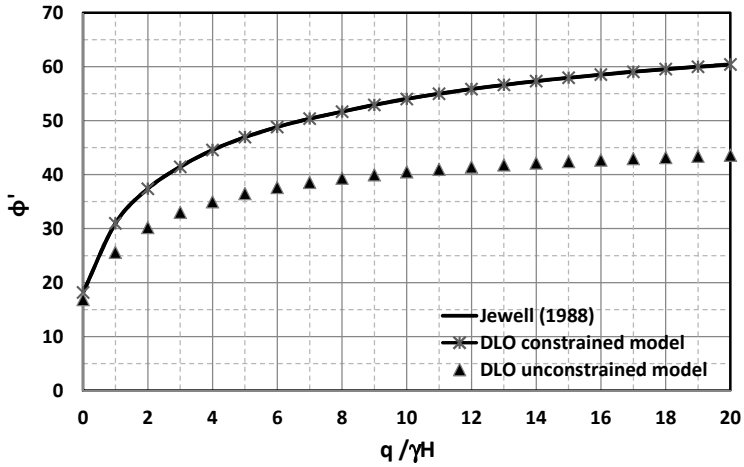

Figure A.6: Plot of ϕ' required for factor of safety of 1.0 against $q/\gamma H$ for Jewell's analytical method (1988) and the current approach ($n = 2$ and α_s= 0.8).

A.4.3.2 Rotational mechanisms

Leshchinsky and Smith (1989) used an upper bound log-spiral rotational analysis for checking the factor of safety of an unreinforced embankment constructed on soft clay. The results were expressed in terms of a stability number:

$$N_m = \frac{1}{\gamma H}\frac{c_u}{F_s} \tag{A.5}$$

where F_s is the required factor of safety.

The comparison of DLO analyses with those of Leshchinsky and Smith shown in Figure A.8 show close agreement, with DLO generally able to identify a more critical case as would be expected, since it is not restricted to one single failure mode. However the specific mechanism utilised Leshchinsky and Smith outperformed the DLO analysis marginally in two of the cases considered. This is not unexpected for circumstances where their mechanism closely matches the exact solution.

Figure A.9 compares results of the DLO and the log-spiral limit analysis of Leshchinsky (1987) for a stability of embankment over soft soil. Leshchinsky (1987)checked bearing failure and deep seated failure. The results of the study showed that DLO

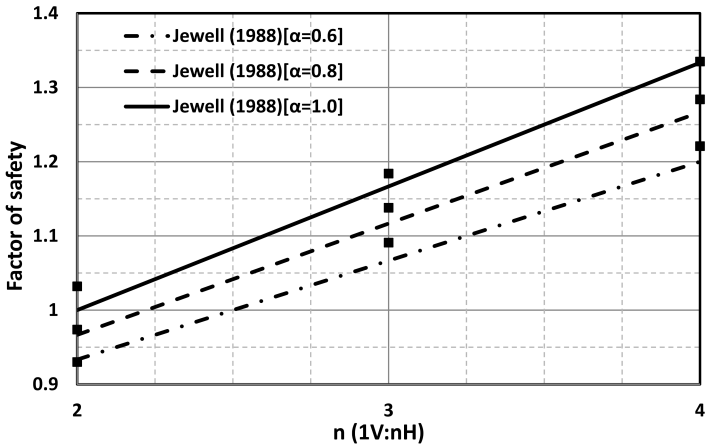

(a) Reinforced embankment over soft soil

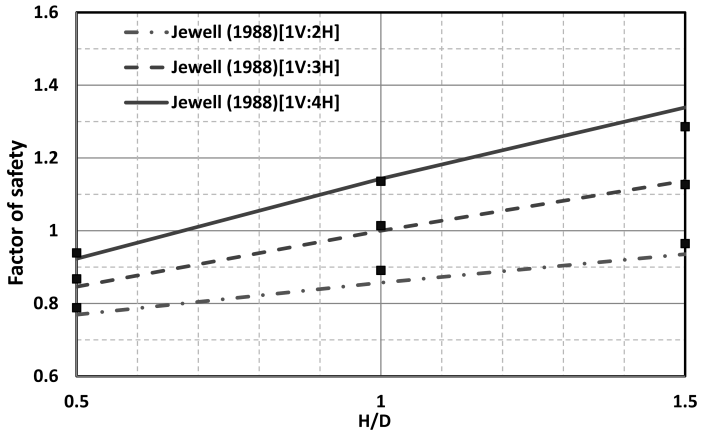

(b) Unreinforced embankment over soft soil

Figure A.7: Plot of factor of safety against side slope gradient (n) for Jewell's analytical method (1988) and the current method (square markers) ($c_u = 15\text{kPa}$, $\gamma = 18\text{kN/m}^3$, $\phi' = 30^\circ$)

was able to identify a more critical failure mechanism for all the above modes and in addition for surface lateral sliding.

Hird (1986) produced a series of non-dimensional charts for cohesive and cohesionless reinforced embankments over soft soil using the limit equilibrium method of slices in which the reinforcement was modelled by applying a horizontal force to the sliding mass of soil. Figure A.10 again shows good agreement, though since

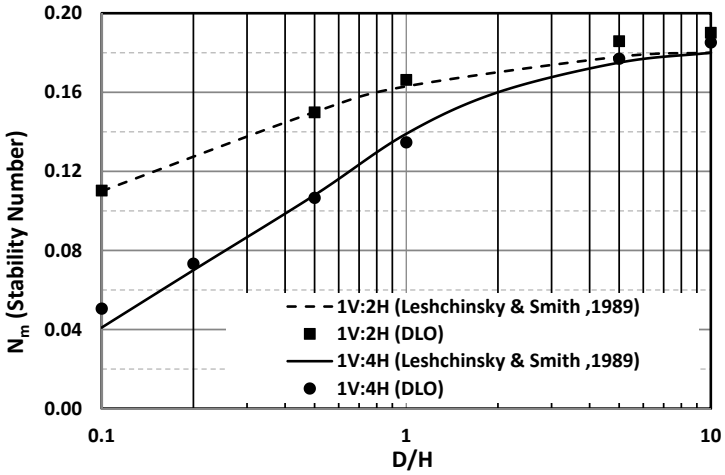

Figure A.8: Comparison the result of DLO and Leshchinsky and Smith (1989) for an unreinforced embankment over soft soil. ($\phi' = 30°$)

the work by Hird was based on Limit Equilibrium it is not possible to comment specifically on the relative magnitudes.

A.4.3.3 FE analysis

Rowe and Li (1999) and Rowe and Soderman (1987) investigated reinforced embankment problems by using finite element analysis. They investigated the required tensile stiffness of reinforcement (J: kN/m) for a given embankment height to achieve a factor of safety of one, and reported the maximum strain (ϵ_f) in the reinforcement at that point. A Limit Analysis method such as DLO cannot model elastic stiffness. Therefore to enable comparisons, the equivalent rupture strength R is calculated from the following equation:

$$R = J\epsilon_f \tag{A.6}$$

This limits the mobilised tensile stress in the reinforcement to the maximum value modelled in the FE analysis. However while in the FE model, this value represents the peak mobilised strength, possibly at one location only, in the DLO LA

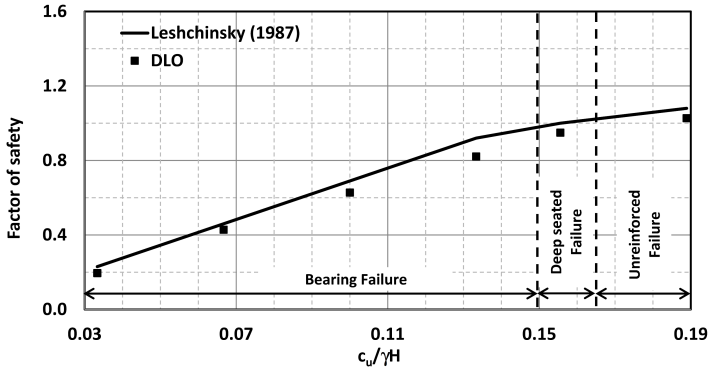

(a) H/D=0.1

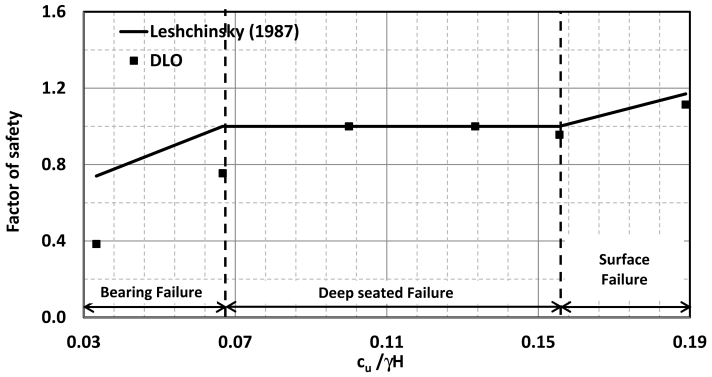

(b) H/D=1.0

Figure A.9: Comparison of DLO and Leshchinsky (1987) for an embankment with slope 1V:2H over soft soil for ($\phi' = 30°$). The factor of safety was on the shear strength of the soil. The mechanism description is based on the DLO analysis.

model, the mobilised strength is free to be distributed along the length of the reinforcement.

The model parameters investigated are given in Table A.2. Figure A.11 shows the corresponding maximum height H of the embankment for a variety of reinforcement rupture strengths. The results of the study shows that the FE method generally found more critical results (i.e. higher required rupture strengths) in comparison with DLO. This is attributed to the DLO model being able to redistribute the yield stress within the reinforcement, while the corresponding value in

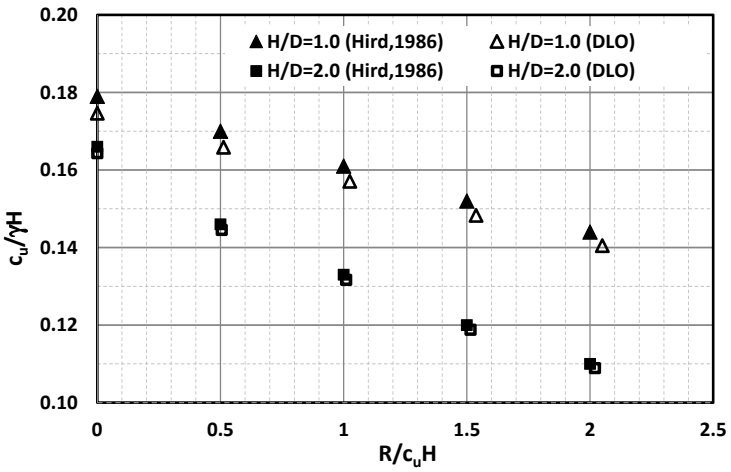

Figure A.10: Plot of normalised undrained shear strength of soft soil required for stability against normalised reinforcement resistance for current method and Hird (1986) ($1V : 1.75H$, H=5m, γ=18kN/m^3, ϕ'=30^o).

the FE model may only be a single peak value. However it is observed that this does not fully agree with the results of Tandjiria et al. (2002) who modelled the same scenarios using limit equilibrium and achieved closely similar results to the FE models with a range of different distributions of mobilised strength along the length of the reinforcement.

Table A.2: FE model comparison. Reinforced embankment analysis parameters. The undrained strength c_u varies linearly with depth z below the soft soil surface.

Parameter	**Embankment 1** (**Rowe and Soderman, 1987**)	**Embankment 2** (**Rowe and Li, 1999**)
W	30m	27m
n	2	2
ϕ'	32^o	37^o
γ	20 kN/m^3	20 kN/m^3
c_u (z=0m)	10kN/m^2	5.0kN/m^2
c_u (z=15m)	40kN/m^2	27.5kN/m^2
D	15m	15m
α_c	1.0	1.0
α_s	1.0	1.0

In summary the results show generally very good agreement with previous work, validating the DLO approach but also indicates that DLO is able to find more critical mechanisms in most cases.

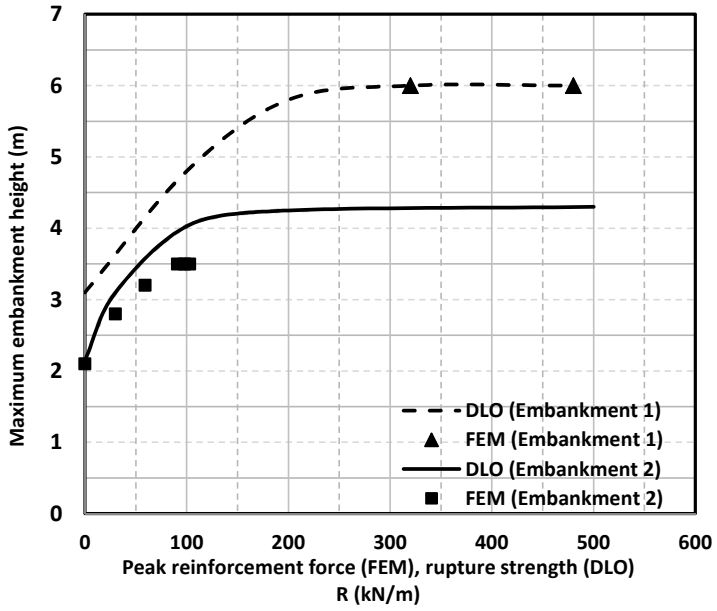

Figure A.11: Comparison of the maximum height H of embankment versus reinforcement rupture strength R for current method, and peak reinforcement force for Rowe and Soderman, 1987 (Embankment 1) and Rowe and Li, 1999 (Embankment 2). Model parameters are given in Table A.2.

A.5 Parametric study

A.5.1 Non-dimensional charts

The parametric study employed in this study investigated the geometry depicted in Figure A.1 and the parameters given in B.1.1. For a horizontal stratum of soil, the unit weight has no effect in undrained collapse, therefore the weight of the soft soil need not be considered. To efficiently cover a wide range of possible parameters, the study was conducted using the following 8 independent non-dimensional

groups:

$c'/\gamma H$, $c_u/\gamma H$, $R/\gamma H^2$, $q/\gamma H$, H/D, n, α and ϕ'

H was chosen as a normalising parameter for the first four groups since an increase in height of the embankment is expected to have the most significant effect on the stability. It was assumed that the embankment was sufficiently wide to avoid the collapse mechanism involving the centre. Based on the numerical model results, minimum values of W/D of approximately $4 + 2H/D$ are required for this assumption to hold true for most typical parameter sets. A comprehensive set of 72 charts were generated and are available in Section A.10.

Different charts are presented for different values of:

- surcharge $q/\gamma H$ (0.0, 0.1),
- Interface coefficient α (0.6, 0.8, 1.0),
- Ratio of height of embankment and thickness of soft soil H/D (0.5, 1.0, 1.5),
- Angle of side slope 1V:nH (2, 3, 4),
- Low or high rupture strength of reinforcement $R/\gamma H^2$ (0.1, 1.0).

An example non-dimensional chart is presented in Figure A.12 in terms of ϕ' vs $c_u/\gamma H$ for a range of values of $c'/\gamma H$. All graphs shared the same qualitative pattern.

According to FHWA-NHI-00-043 (2001) the normal interface factor for geogrid and geotextiles varies between 0.6 and 0.8 respectively. In most design guidelines and work examples, the interface coefficient for both top and bottom part of reinforcement is selected to be the same which has been done in this paper. Therefore the stated three interface coefficient values were modelled: 0.6, 0.8 and 1.0. It was necessary to model this only for the high rupture strength reinforcement because the dominant failure mechanism for weak reinforcement is global failure which is

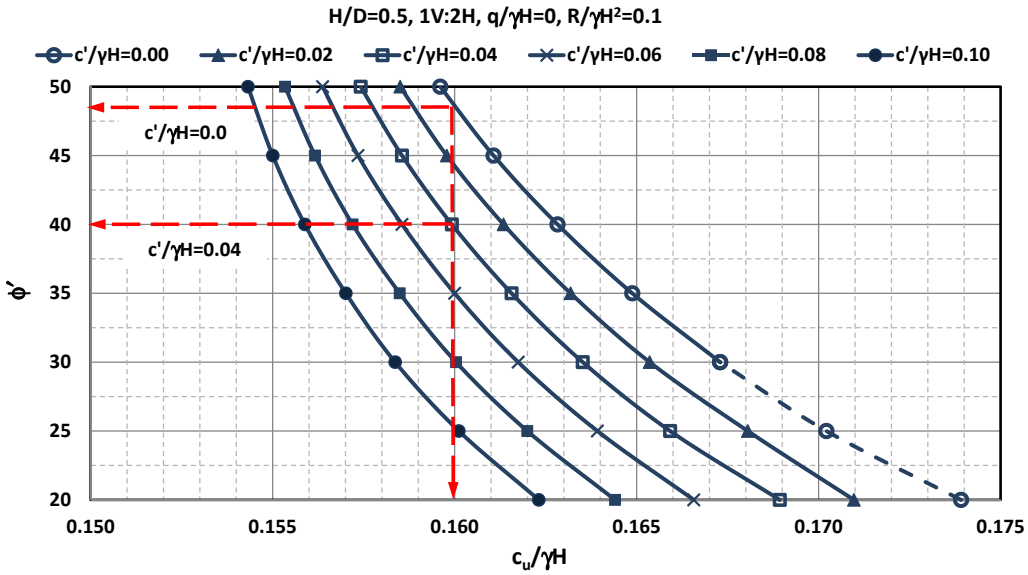

Figure A.12: Example of graph generated from the parametric study discussed in A.5. The long-dashed lines illustrate the design example presented in A.6.

insignificantly affected by the shear resistance generated between the soil and geotextile. These parameters cover most typical embankments which are constructed over soft soil. Due to the symmetry of the model, only half of the cross-section was analysed with a symmetry boundary at one edge. The maximum stable slope angle of a granular material is fundamentally related to the friction angle of the soil. Therefore, an embankment with zero cohesion and angle of friction less than the side slope angle is unstable. In this study, in order to extend the non-dimensional graphs in this area, a small value of c' (equal to 0.1kPa) was set throughout the soil body to avoid local slope instability failure. Where this is done, it is indicated by a dashed line. Finally, for the design charts for the embankment with surcharge, there is no stable solution for a zero value of c' hence these are omitted from the charts.

A.5.2 Reinforcement strength

Two values of $R/\gamma H^2$ were employed in the generic parametric study, 0.1 and 1.0. This was intended to cover a broad range from very weak reinforcement (0.1) and strong reinforcement (1.0). To investigate the effect of reinforcement on stability, specific studies were undertaken over a broad range of values of $R/\gamma H^2$. Figures A.13a and b show how $c_u/\gamma H$ varies with reinforcement strength $R/\gamma H^2$ for a particular parameter set. It can be seen that for the no surcharge case, the solutions are independent of $R/\gamma H^2 > 1.0$ (this value will be defined as the limiting value $R_L/\gamma H^2$, at which the embankment will be said to be fully reinforced), and that there is a generally linear relationship between the parameters between $R/\gamma H^2$=0 to 0.7. Therefore if it is necessary to interpolate for R, a conservative approximation is to linearly interpolate between the values of $R = 0$ to R_L. An example interpolation is indicated in Figure A.13b. In order to ensure conservative results, it can be seen that there will be a small error in the interpolation which is maximum between around $0.5R_L$ to $0.6R_L$. This maximum error is around 8% in c_u or around 20% in R. Further examples of the bilinear fit for a number of different parameter sets are reported in Section A.11 and show similar behaviour.

Furthermore it can be seen that $R/\gamma H^2$ is very sensitive to changes in $c_u/\gamma H$, for values less than 1.0. Ideally the reinforcement should be designed from the horizontal portion of the curves (i.e. using R_L) and in design it would be preferable to apply a (partial) factor of safety to c_u rather than to R, or to both.

A.5.3 Simplified design envelopes

It can be seen from the preceding graphs that the design region between fully stable or fully unstable embankments is relatively small in terms of the values of $c_u/\gamma H$. For example in Figure A.13(b), independent of the value of $R/\gamma H^2$, and assuming that $\phi' = 30^o$ always, the system will always be stable for $c_u/\gamma H > 0.176$ and always unstable for $c_u/\gamma H < 0.125$. Variants in the value of ϕ' would change these values only by around 10% for failure modes where failure in the soft soil layer dominates. Other graphs e.g. Figure A.12 show that additionally $c'/\gamma H$ also has a small effect (<10% on the value of $c_u/\gamma H$).

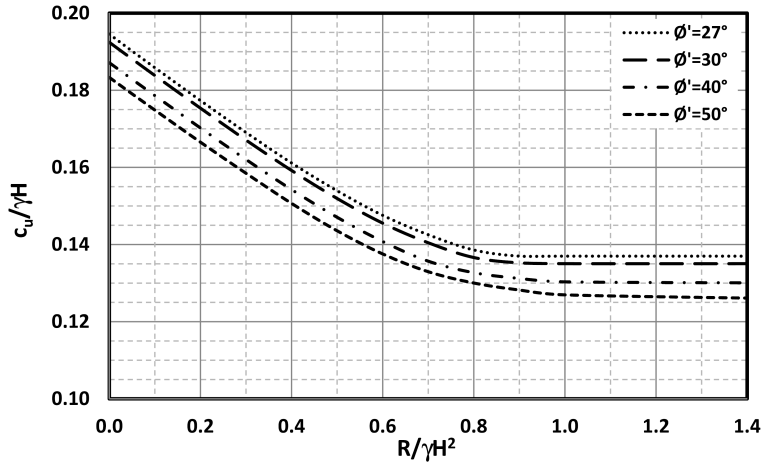

(a) With surcharge, $q/\gamma H = 0.1$

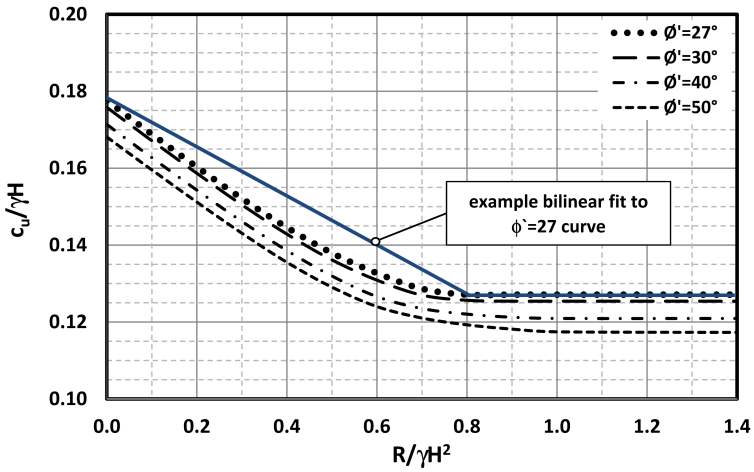

(b) Without surcharge

Figure A.13: Required undrained shear strength for stability plotted against reinforcement strength($H/D = 0.5$, 1V:2H, $c' = 0$ and $\alpha = 0.8$).

It is thus possible to plot a simplified design envelope of $c_u/\gamma D$ vs H/D for $\alpha = 0.8$, shown in Figure A.14a for $\phi' = 30^o$ and $c'/\gamma H = 0.0$ and Figure A.14b for $\phi' = 50^o$ and $c'/\gamma H = 0.1$. Two curves are given. Above the upper value the system is always stable (this corresponds to $R = 0$). Below the lower limit, it is generally always unstable (though minor gains may be made with stronger fill) and this corresponds to $R = R_L$. Values of $R_L/\gamma D^2$ are given on the same graph. In between the values the more detailed design charts must be used, or, as discussed previously, a linear interpolation can be used to provide a good estimate of R. Note that for these graphs the values of c_u and R_L have been normalised using D rather than H since this is expected to be an independent variable. Overall it can be seen that the use of reinforcement allows an embankment of a given size to be constructed on soft soil of around 50-100% the strength of that on which an unreinforced embankment could be constructed, depending on the value of H/D. It can also be seen that stronger fill has a marginal effect on the performance of a reinforced embankment, but a more significant effect on the stability of an unreinforced embankment.

Figure A.14b also indicates that, for this example, an almost unlimited height of a fully reinforced embankment is possible for $c_u/\gamma D > \sim 0.16$ which may seem paradoxical, however this arises because the mechanism of failure is squeezing of the (relatively thin) confined soft soil layer which occurs over a width that extends beyond the embankment crest. Since the side slope width increases in tandem with the height, the bearing resistance in the soft soil layer also increases. It is noted that the reinforcement strength must also increase significantly with the height.

Finally Figure A.15 shows that the limit equilibrium approach recommended by Jewell (1988), for extrusion only, provides a generally good fit to the data and is only slightly conservative compared with the current results for a fully reinforced embankment. The values it recommends involve an approximately 20% higher value of $c_u/\gamma D$ for a given H/D, but an approximately 10% smaller value of $R_L/\gamma D^2$. In combination this should still give a stable state but is slightly overconservative. To confirm this the interpolation method discussed in Section A.5.2 was used on the Jewell value of $c_u/\gamma D$ to predict the corresponding required reinforcement strength $R/\gamma D^2$ using the current method. It can be seen that a value lower than the Jewell value of $R/\gamma D^2$ is predicted.

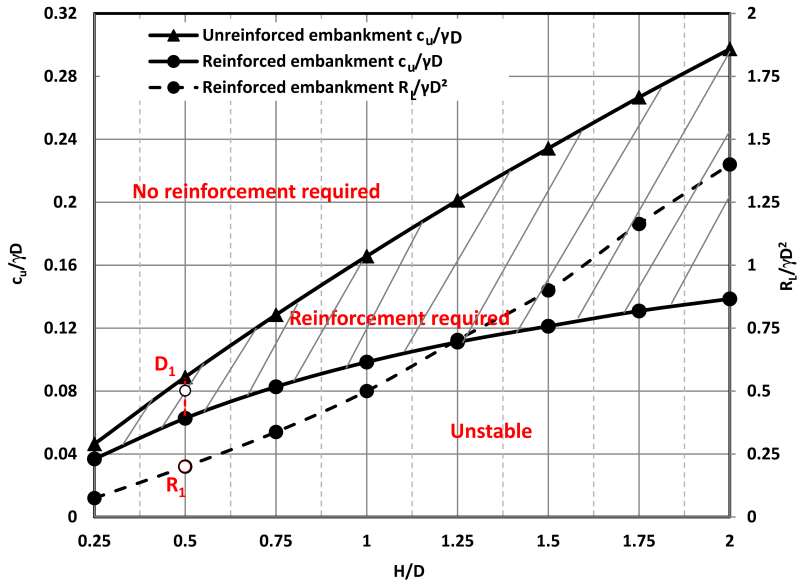

(a) $\phi' = 30°$, $c' = 0$

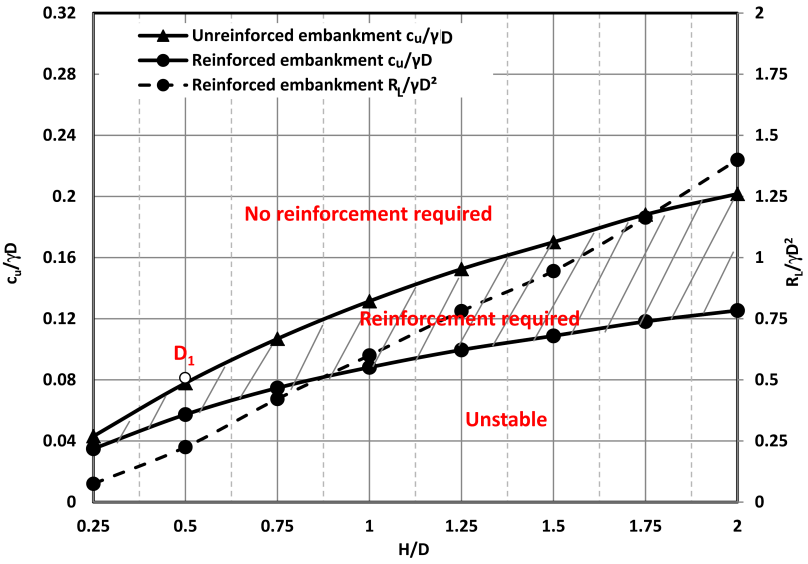

26

(b) $\phi' = 50°$, $\frac{c'}{\gamma H} = 0.1$

Figure A.14: Simplified design domains ($\alpha = 0.8$, $q = 0$ and $n = 2$). The reinforced embankment case uses reinforcement with rupture strength R_L the value of which is given in the same plot. The shaded zone is the design domain where reinforcement is required. Below this zone stability is not possible with a single layer of reinforcement.

However, it is suggested that it would be preferable to design with the value of R_L to avoid the sensitivity to c_u discussed previously. It would also be expected that the extrusion equations would become less valid for values of $H/D < 0.25$, as a deep seated failure mode becomes more dominant.

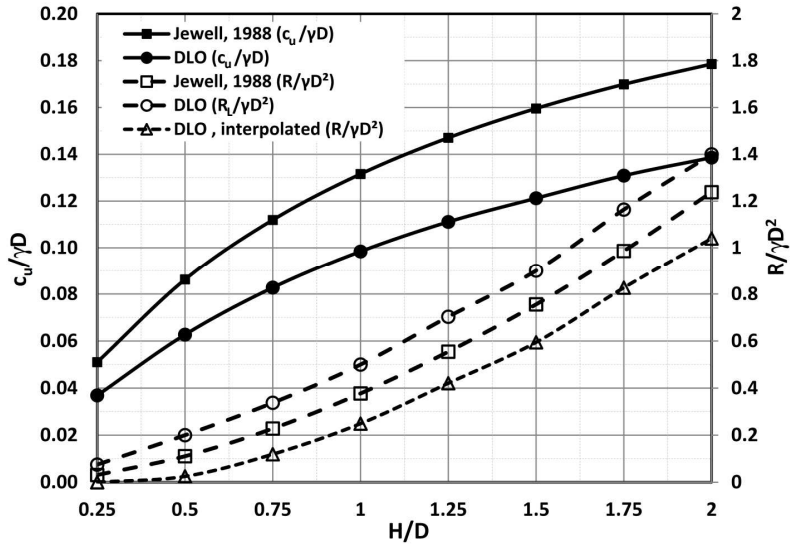

Figure A.15: Comparison of results from the current method and Jewell (1988), equations A.2 and A.3, for determining the required shear strength of soft soil and rupture strength of reinforcement for stability. The 'interpolated' line shows the predicted required value of $R/\gamma D^2$ using the current method based on the value of c_u specified by the method of Jewell (ϕ'=30°, $c' = 0$, $\alpha = 0.8$, $q = 0$ and $n = 2$).

A.6 Design example

Consider an embankment of 5m height and side slope $1V : 2H$ constructed from a coarse grained material of unit weight 17.5kN/m^3 overlying 10m of soft soil of uniform shear strength $c_u = 14kPa$ as shown in Figure A.16. The required soil strength for the embankment fill when using a low rupture strength reinforcement (with $\alpha = 0.8$) without surcharge is determined as follows.

From Figure A.14a, it can be seen that design point D_1 plots at $(H/D,\ c_u/\gamma D) = (0.5,\ 0.08)$ and that this lies between the maximum and minimum curves. In order

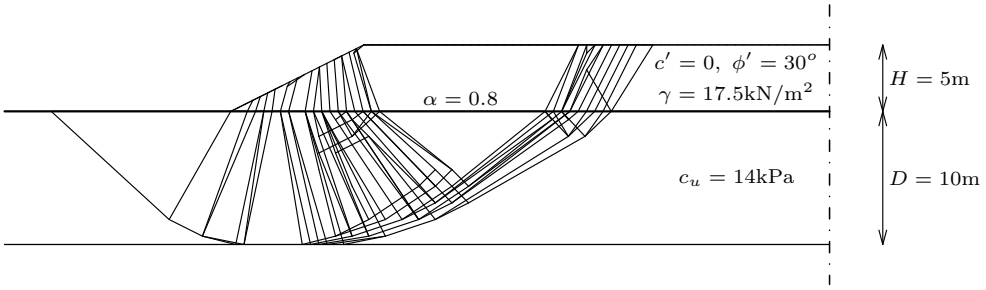

Figure A.16: Design example geometry and failure mechanism associated with the determined geotextile rupture strength $R = 121$ kN/m.

to estimate the required reinforcement strength, the value $R_L/\gamma D^2 = 0.23$ can be read off the same graph (point R_1) for $H/D = 0.5$. This reinforcement strength is sufficient to support an embankment on a soil with $c_u/\gamma H = 0.125$. It is then possible to interpolate as follows:

Taking $c_{u,min}/\gamma D = 0.063$, $c_{u,max}/\gamma D = 0.089$, and $R_L/\gamma D^2 = 0.20$.

$$\frac{R}{\gamma D^2} = \frac{R_L}{\gamma D^2}\frac{c_{u,max} - c_u}{c_{u,max} - c_{u,min}} = 0.20\frac{0.089 - 0.08}{0.089 - 0.063} = 0.069 \tag{A.7}$$

Hence the required reinforcement tensile strength R is 121 kN/m. This result is valid for embankment fill of $\phi' = 30^o$ and $c' = 0$ and will be slightly overconservative due to the linear interpolation approximation. For a stronger fill of $\phi' = 50^o$ and $c' = 0.1\gamma H = 8.8$ kN/m^2, Figure A.14b indicates that no reinforcement is required.

As noted before R has a significant degree of sensitivity to $c_u/\gamma H$, e.g. a reduction in c_u of 10% can lead to a change in R of 60%. However a reduction in c_u of 15% will lead to a situation that cannot be stabilised by reinforcement. For a more detailed study, the case of $R/\gamma H^2 = 0.1$ can be investigated using the charts are available in Section A.10. First the relevant chart is chosen (shown in Figure A.12) based on the values of $H/D = 0.5$, slope $1V : 2H$, and $q/\gamma H = 0$. The graph is therefore determined from a model where the reinforcement rupture strength is a low value of $R = 44$ kN/m. In this case failure is typically by reinforcement rupture, combined with soil failure.

Having selected the graph (Figure A.12), the x-axis can be read off using $c_u/\gamma H = 0.16$. A family of curves then allows different combinations of c' and ϕ' to be selected such as $(c' = 0, \phi' = 48^o)$ or $(c'/\gamma H = 0.04$, ie $c' = 3.5$ kPa, $\phi' = 40^o)$ which is the required shear strength of the embankment soil for a factor of safety of 1.0. This is consistent with the previous result that indicated that reinforcement was not necessary for $\phi' = 50^o$. If higher factors of safety are required then these can be applied as appropriate to the parameters.

A.7 Discussion

The validation studies indicate that the factor of safety computed with the DLO method is typically lower than the conventional limit analysis and limit equilibrium methods. This is due to the critical failure mechanism not being pre-defined. However the DLO results were slightly above those given by the FE analyses of Rowe and Li (1999) and Rowe and Soderman (1987). The reasons for this are not clear but it may be related to the nature of the Limit Analysis approach. The results presented are strictly only valid within this framework which essentially assumes that the soil and reinforcement are rigid-plastic materials. At failure the material must either have not yielded or if it has yielded, it must display a fully ductile plastic response with constant resistance at any strain level.

In practice many geotextiles do display this type of response and so it would be reasonable to assume that soil and geotextile can reach full strength at compatible strain levels at failure. It would be necessary to check that the the limit analysis results indicate reasonably uniform elongation rates along the length of the failing zone, so that high concentrations of strain are not anticipated.

For geotextiles that would rupture rather than stretch at a relatively low strain level, then their (suitably factored) strength should be chosen to be greater than the limiting value R_L. For such cases it is observed that the interface coeffcients α_c and α_s do influence the results (by $\sim 10\%$), whereas below this value the reinforcement will tend to yield before the shear strength on the interface is reached, thus rendering the value of α less significant (as long as it is reasonably large).

A.8 Conclusions

1. The DLO analysis has been shown to find more critical failure mechanisms compared with other limit equilibrium results in the literature for most cases. It was also able to identify a previously unreported bearing type failure mechanism which involves rotational 'snapping' of the embankment.

2. The use of reinforcement allows an embankment of a given height H to be constructed on a depth D of soft soil of around 50-100% the strength of that on which an unreinforced embankment could be constructed, depending on the value of H/D. Use of very strong compared to lower strength embankment fill has only a marginal additional effect of allowing construction on a soft soil of around 10% lower strength.

3. Design charts have been presented that can be used for determining the maximum stable height and required reinforcement strength for fully reinforced (where the reinforcement is not taken to yield) and unreinforced embankments resting over soft soil and the transition between these two states which is shown to result in an approximately linear relationship between the required reinforcement rupture strength and the undrained shear strength of the soft soil.

4. It is recommended that embankments be designed at the point where the reinforcement is not taken to yield to avoid an observed sensitivity to the soft soil strength for cases where reinforcement and soil yield together.

A.9 Appendix I. Precision of DLO solution

Figure A.17 shows the factor of safety on soil strength versus the number of nodes across embankment height. A value of 5 nodes across the embankment height provides an accuracy of 1-2%.

A.10 Appendix II. Design charts

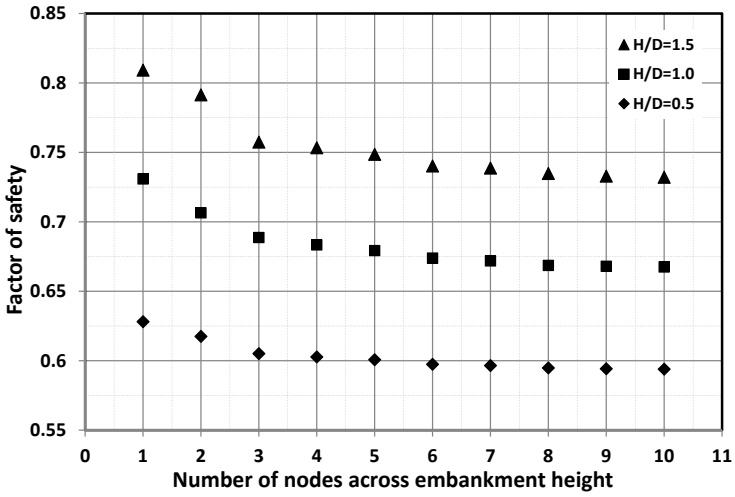

Figure A.17: Variation of factor of safety versus DLO nodal spacing

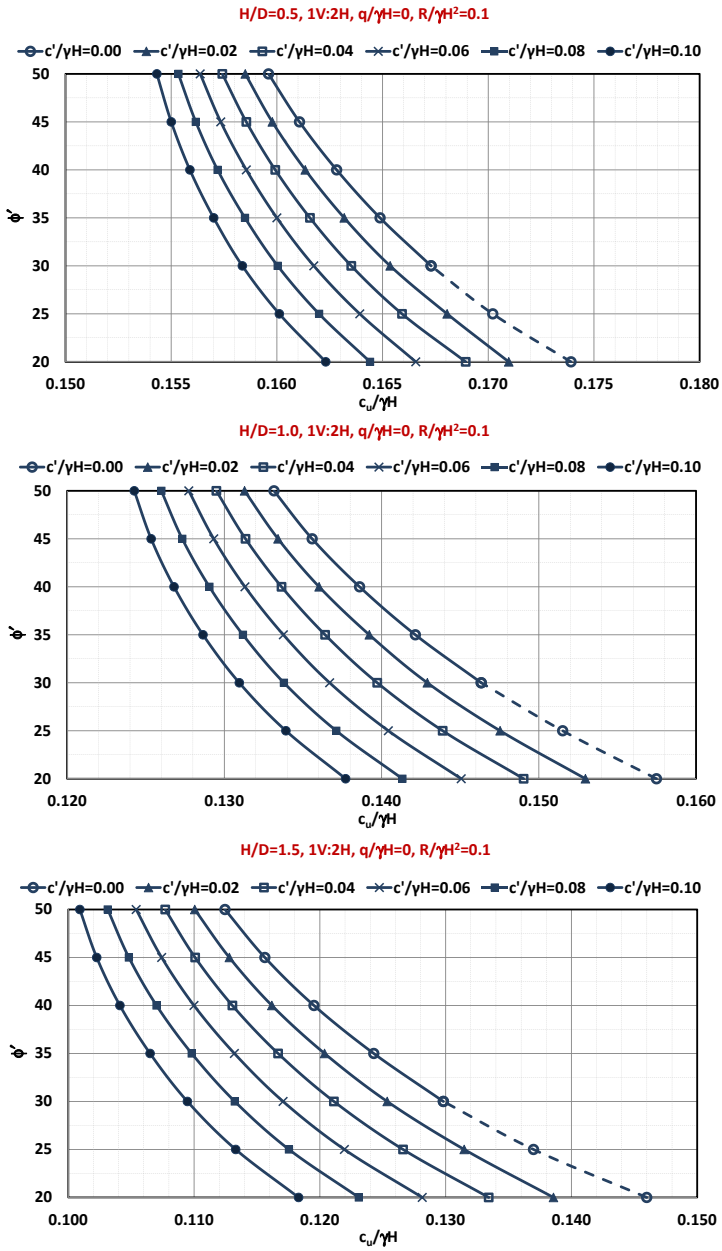

Figure A.18: Required soil properties for embankment without surcharge and low rupture strength reinforcement (n=2) [Note: Dash line part of the graph is unstable with $c' = 0$]

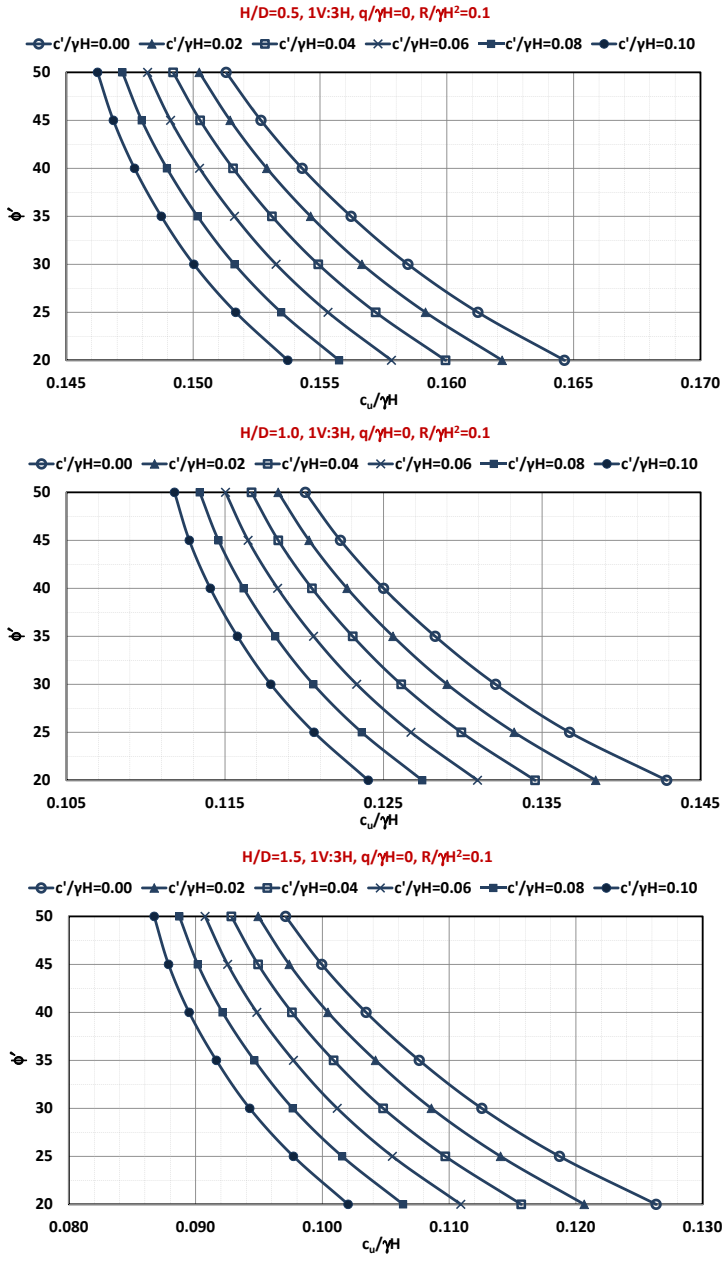

Figure A.19: Required soil properties for embankment without surcharge and low rupture strength reinforcement (n=3)

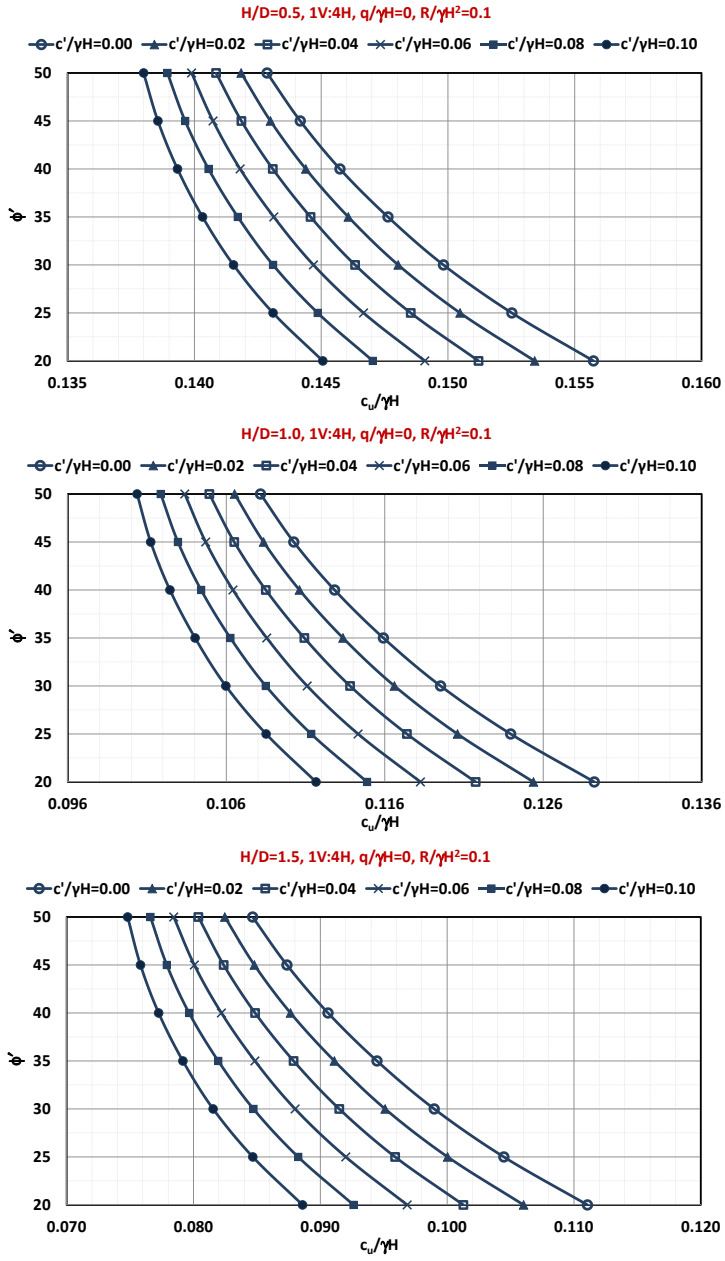

Figure A.20: Required soil properties for embankment without surcharge and low rupture strength reinforcement (n=4)

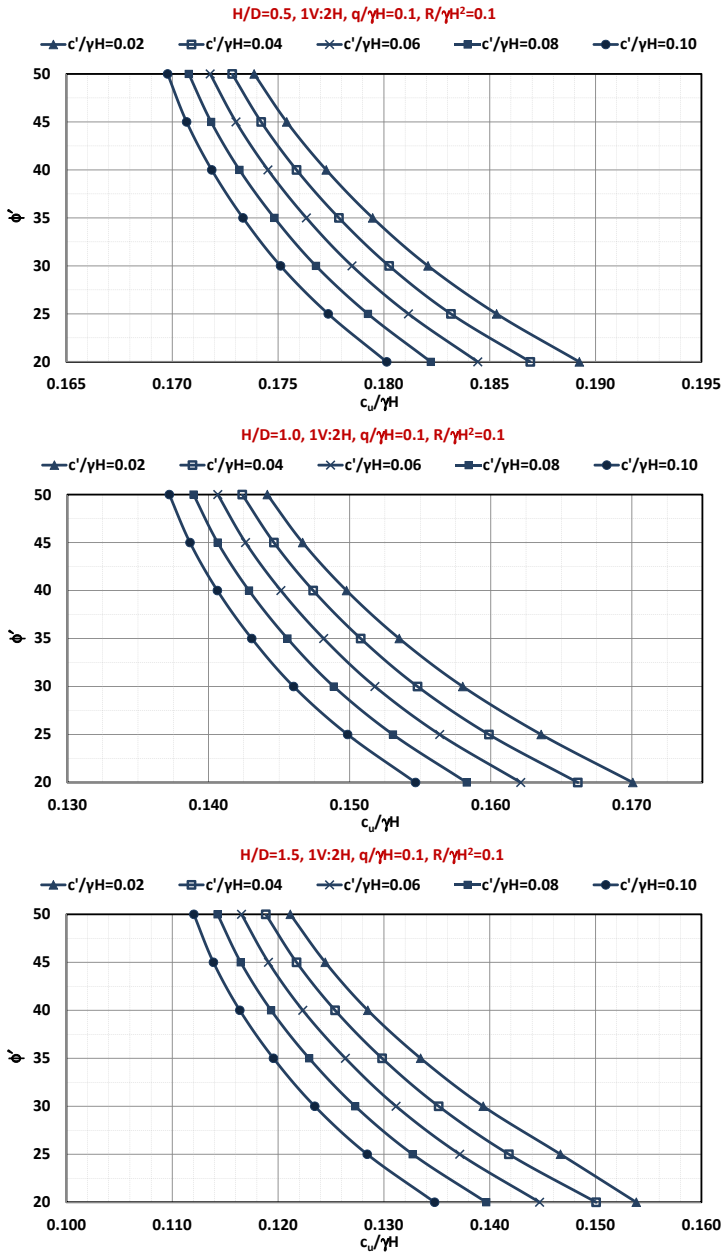

Figure A.21: Required soil properties for embankment with surcharge and low rupture strength reinforcement (n=2)

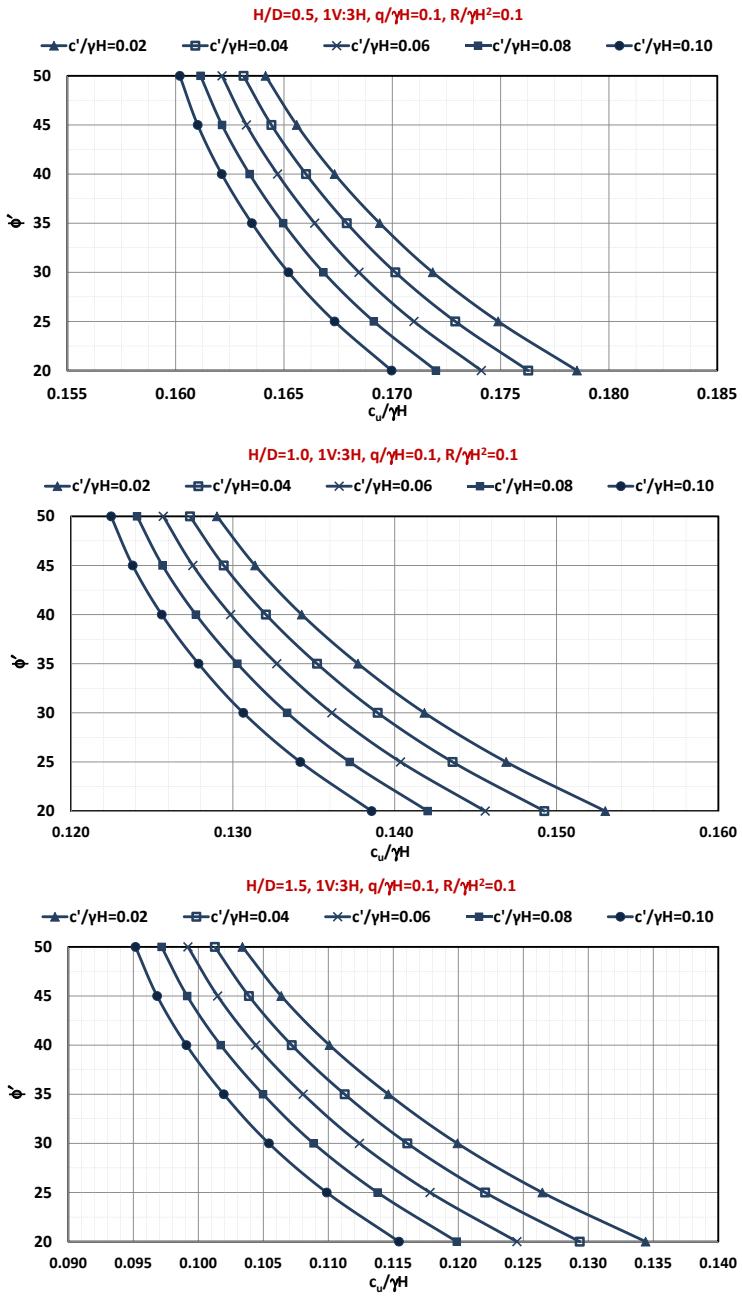

Figure A.22: Required soil properties for embankment with surcharge and low rupture strength reinforcement (n=3)

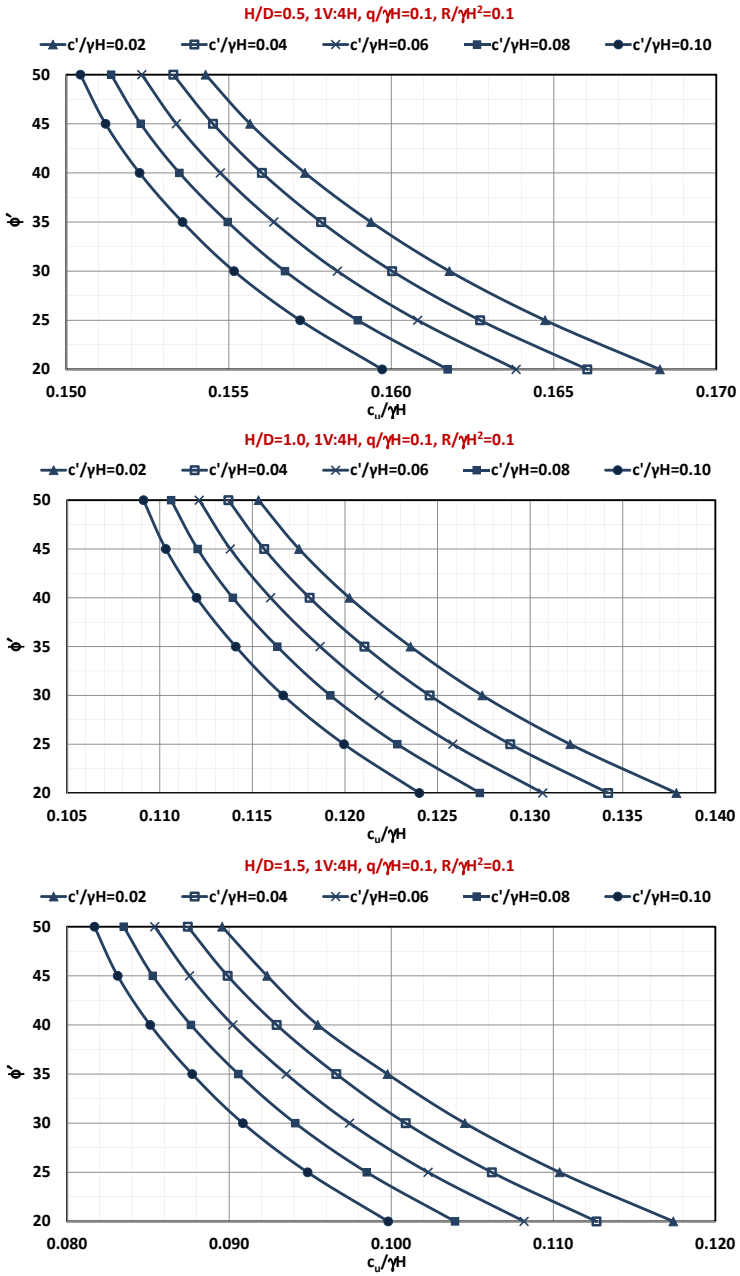

Figure A.23: Required soil properties for embankment with surcharge and low rupture strength reinforcement (n=4)

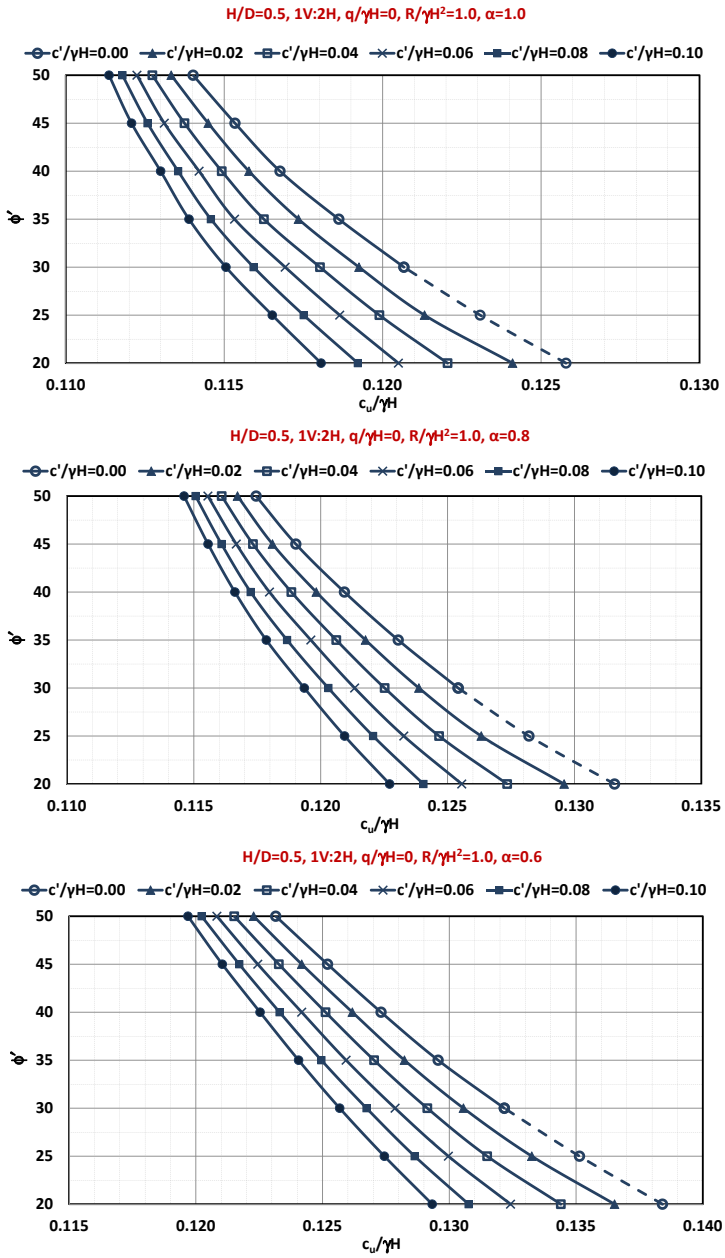

Figure A.24: Required soil properties for embankment without surcharge and high rupture strength reinforcement (n=2,H/D=0.5) [Note: Dash line part of the graph is unstable with $c' = 0$]

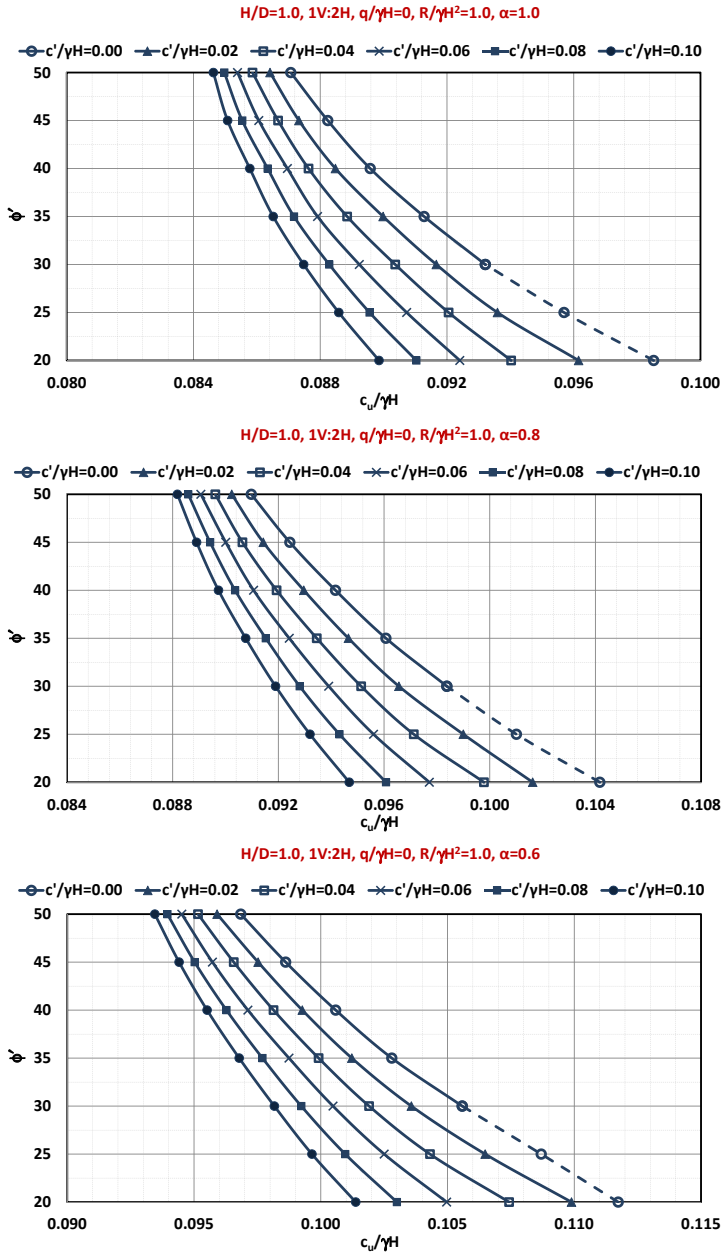

Figure A.25: Required soil properties for embankment without surcharge and high rupture strength reinforcement (n=2,H/D=1.0) [Note: Dash line part of the graph is unstable with $c' = 0$]

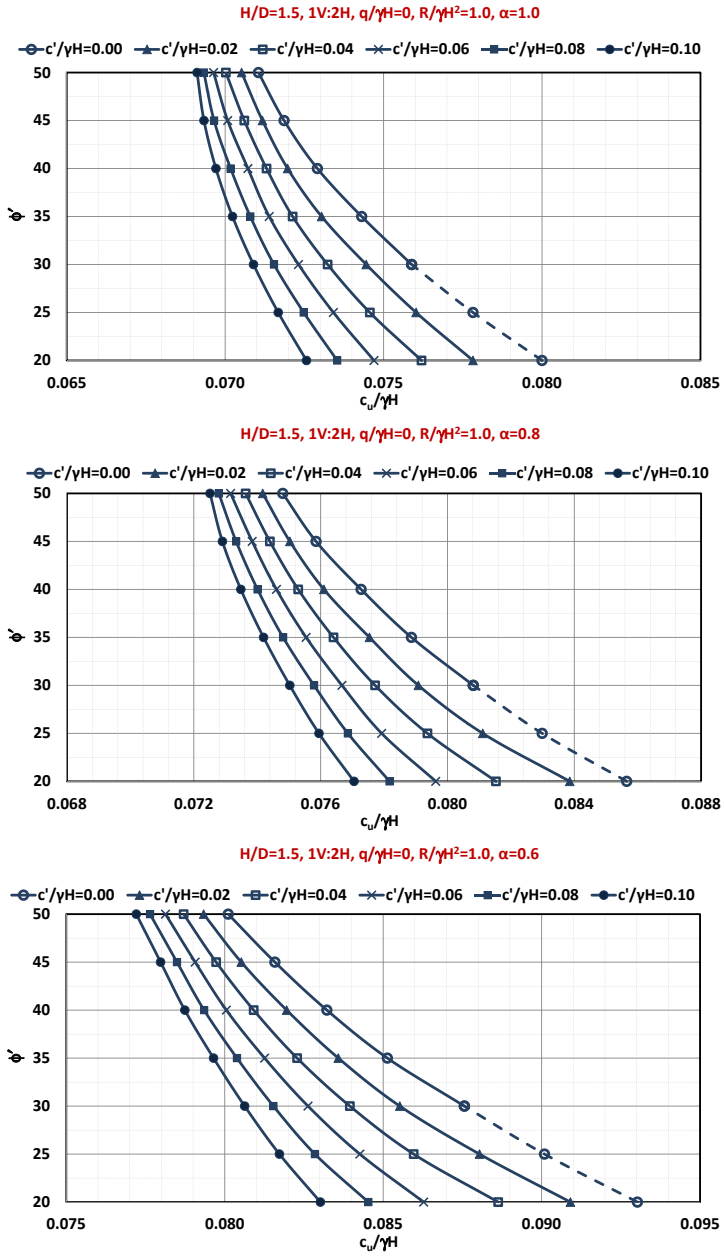

Figure A.26: Required soil properties for embankment without surcharge and high rupture strength reinforcement (n=2,H/D=1.5) [Note: Dash line part of the graph is unstable with $c' = 0$]

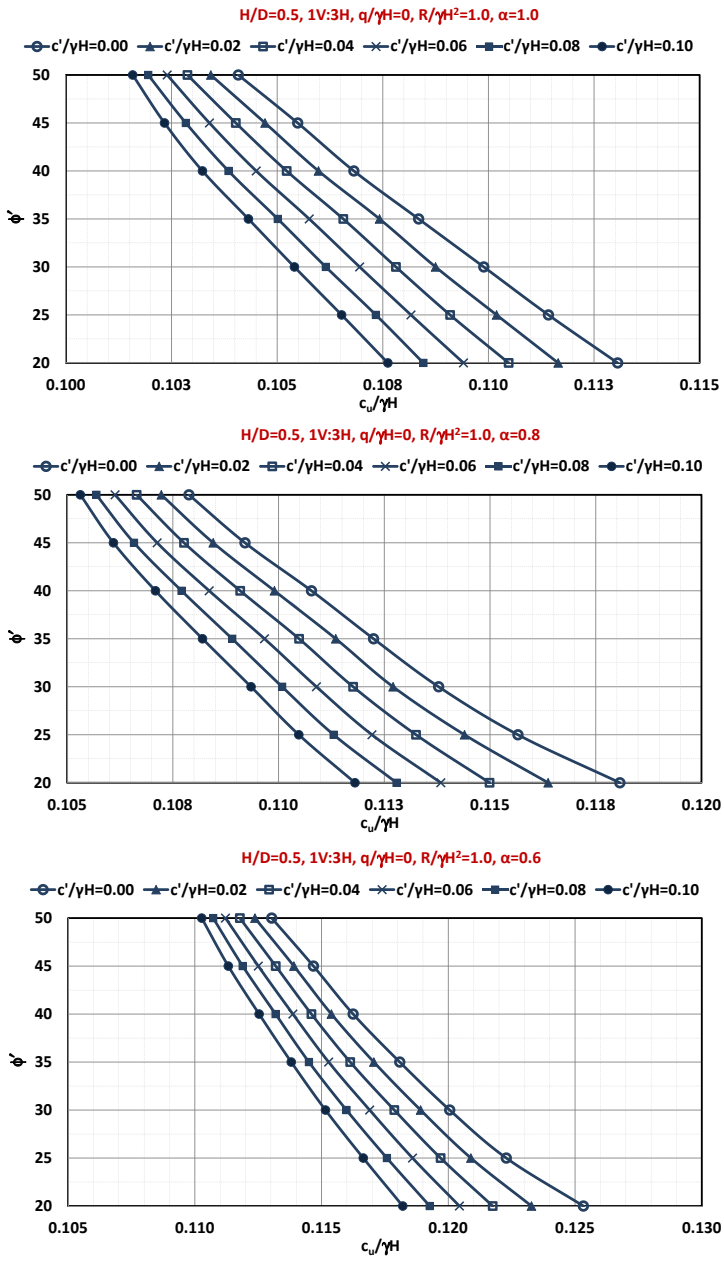

Figure A.27: Required soil properties for embankment without surcharge and high rupture strength reinforcement (n=3,H/D=0.5)

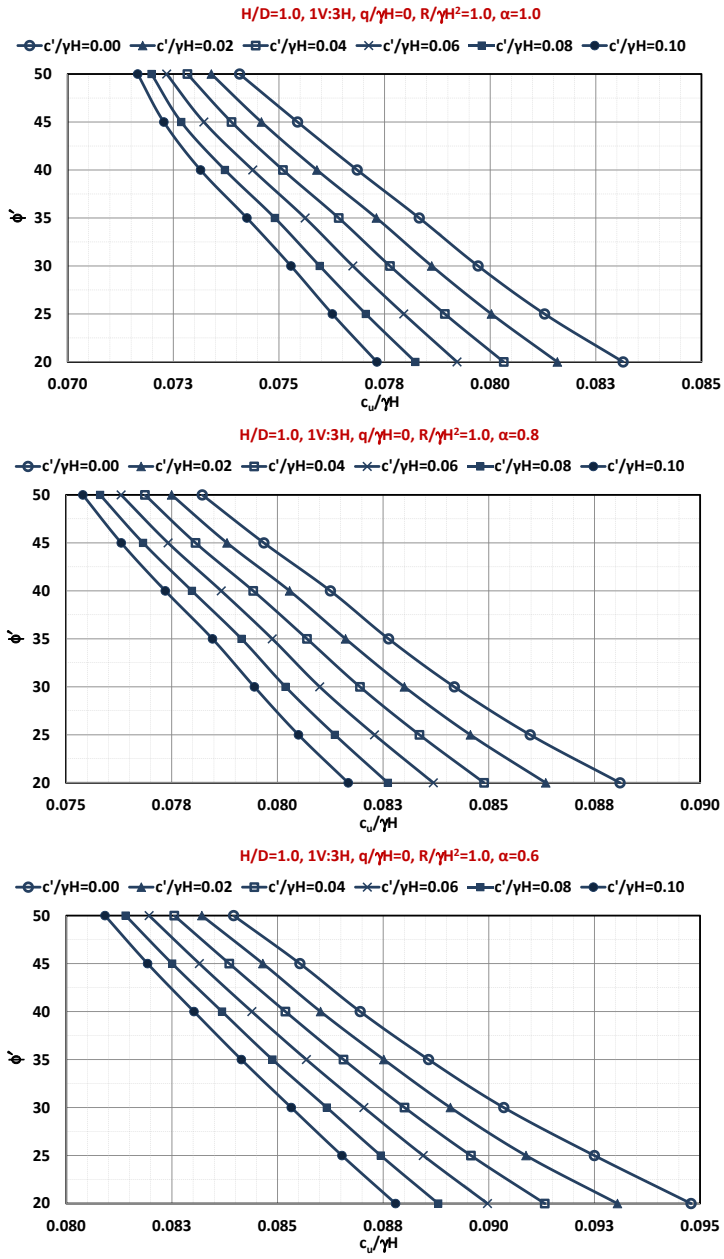

Figure A.28: Required soil properties for embankment without surcharge and high rupture strength reinforcement (n=3,H/D=1.0)

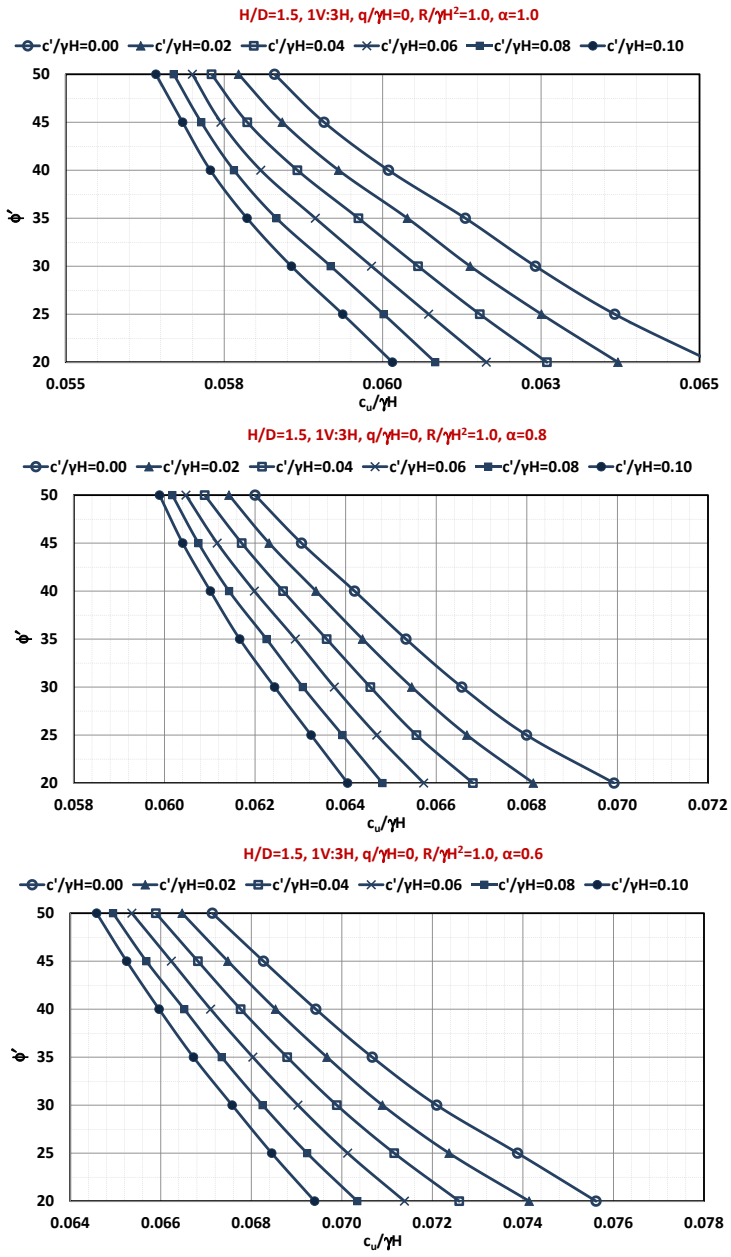

Figure A.29: Required soil properties for embankment without surcharge and high rupture strength reinforcement (n=3,H/D=1.5)

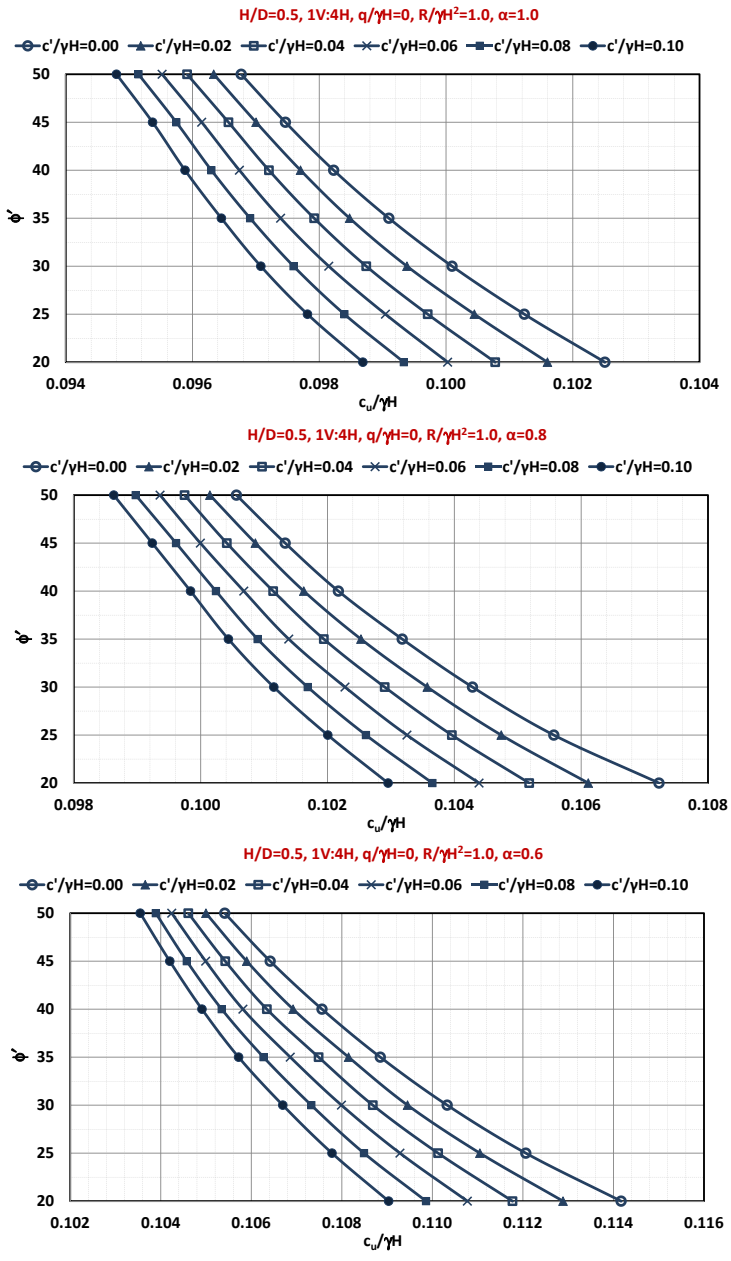

Figure A.30: Required soil properties for embankment without surcharge and high rupture strength reinforcement (n=4,H/D=0.5)

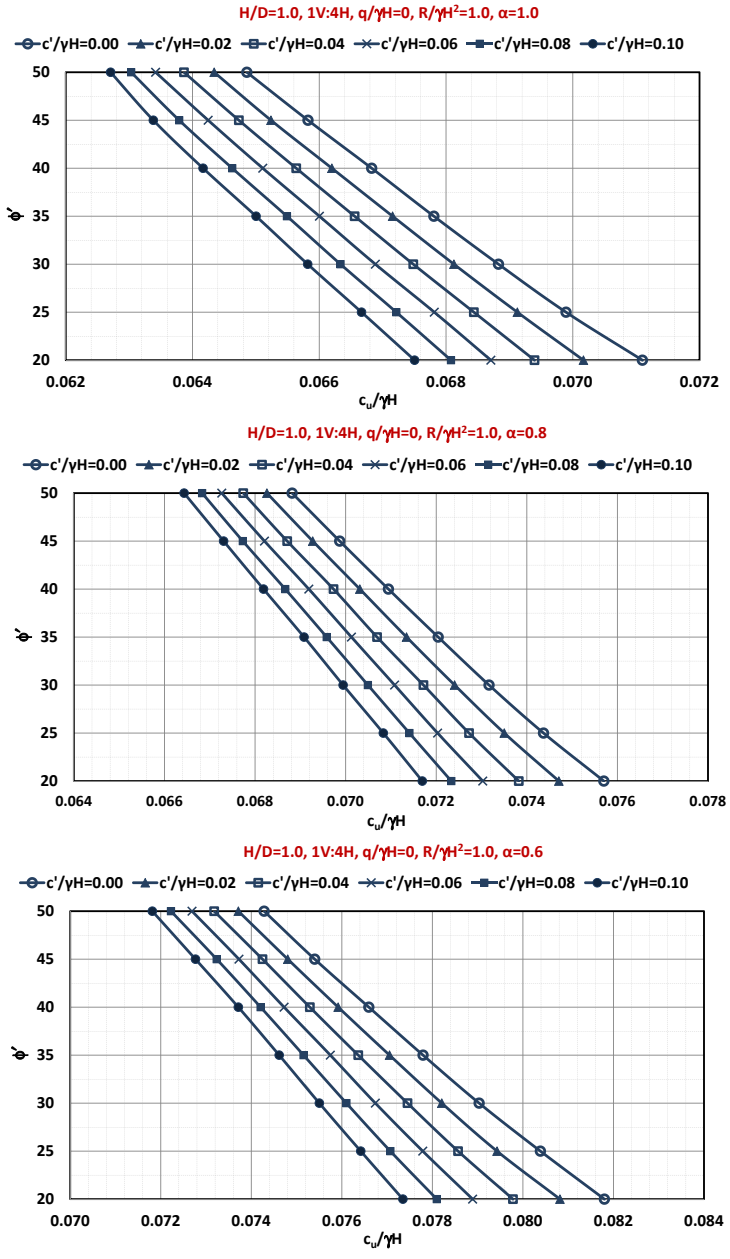

Figure A.31: Required soil properties for embankment without surcharge and high rupture strength reinforcement (n=4,H/D=1.0)

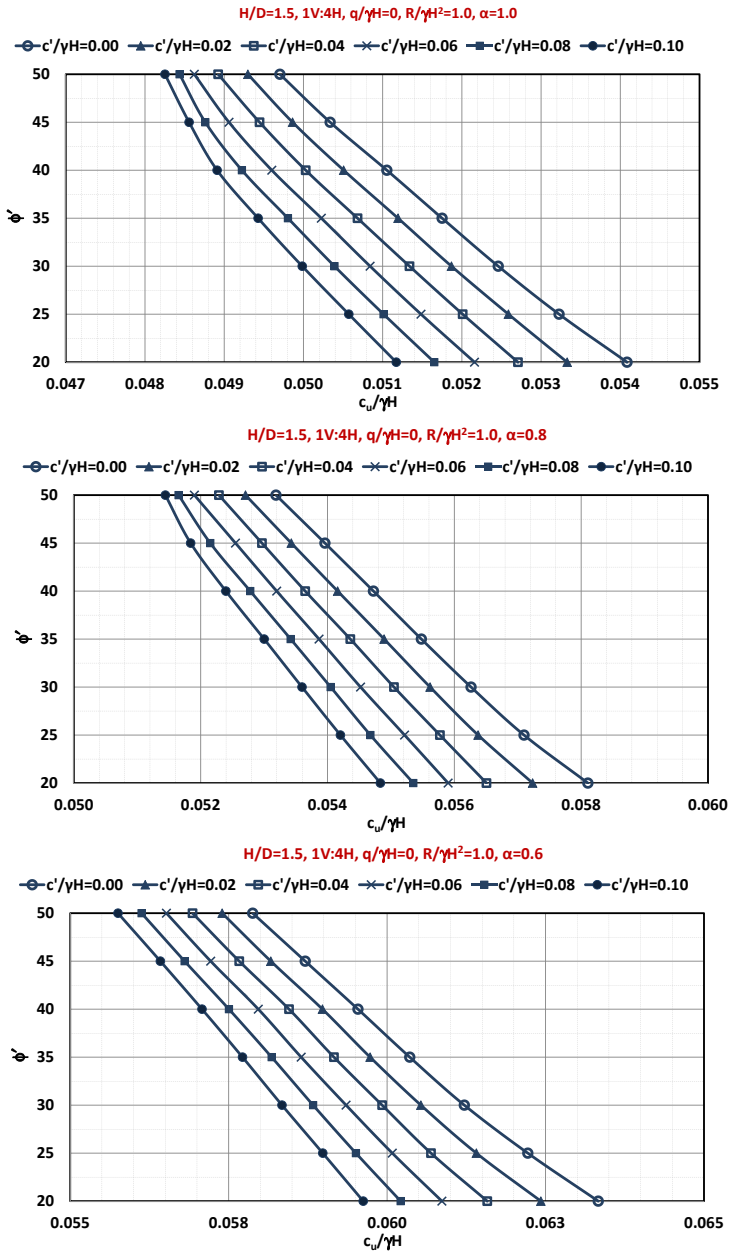

Figure A.32: Required soil properties for embankment without surcharge and high rupture strength reinforcement (n=4,H/D=1.5)

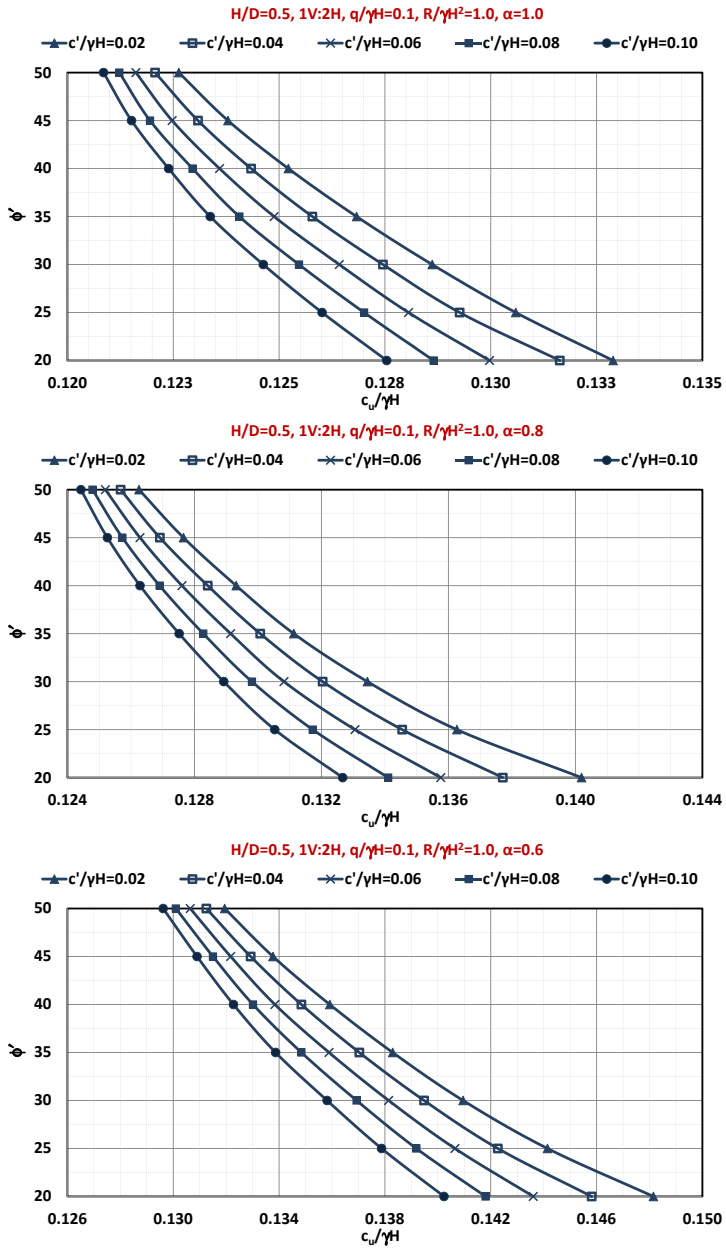

Figure A.33: Required soil properties for embankment with surcharge and high rupture strength reinforcement (n=2,H/D=0.5)

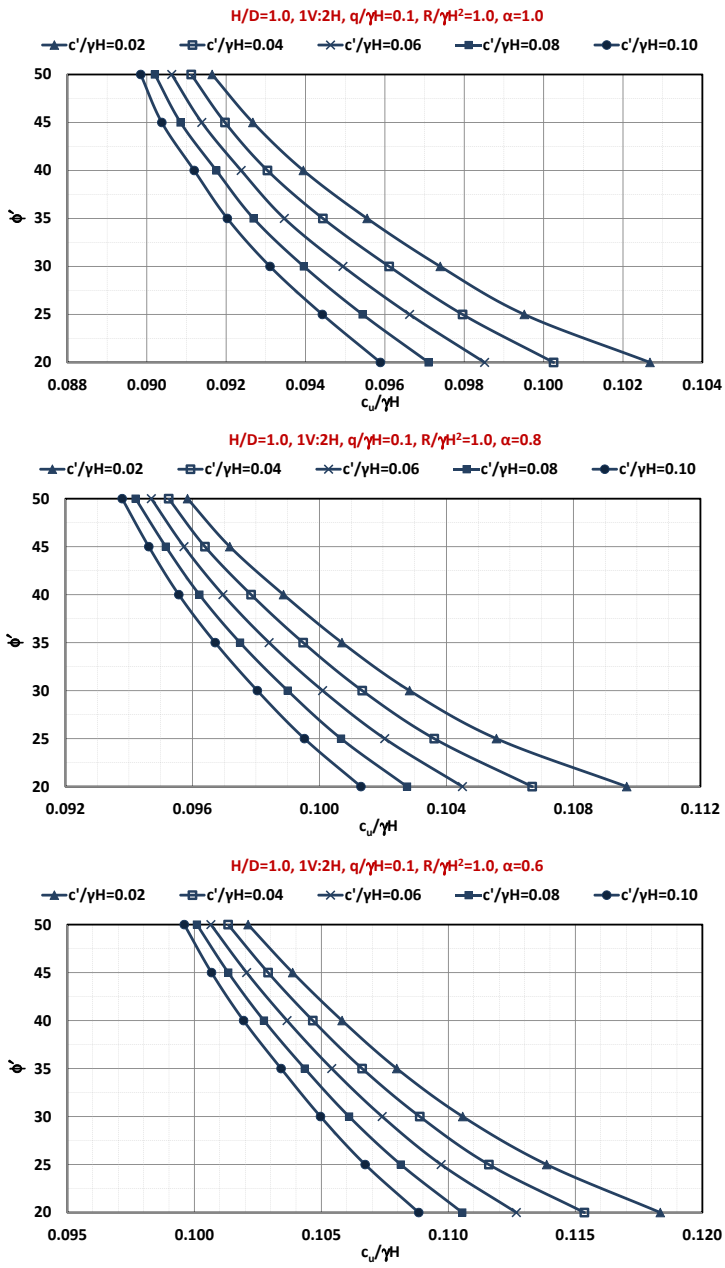

Figure A.34: Required soil properties for embankment with surcharge and high rupture strength reinforcement (n=2,H/D=1.0)

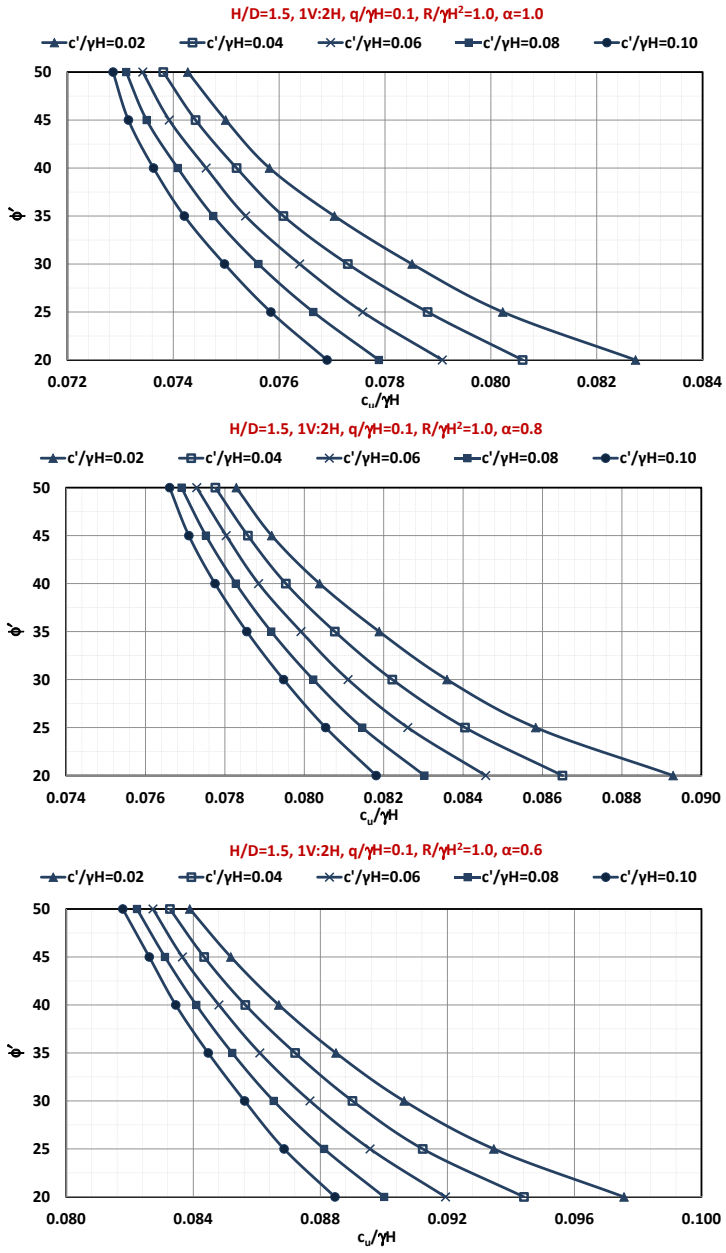

Figure A.35: Required soil properties for embankment with surcharge and high rupture strength reinforcement (n=2,H/D=1.5)

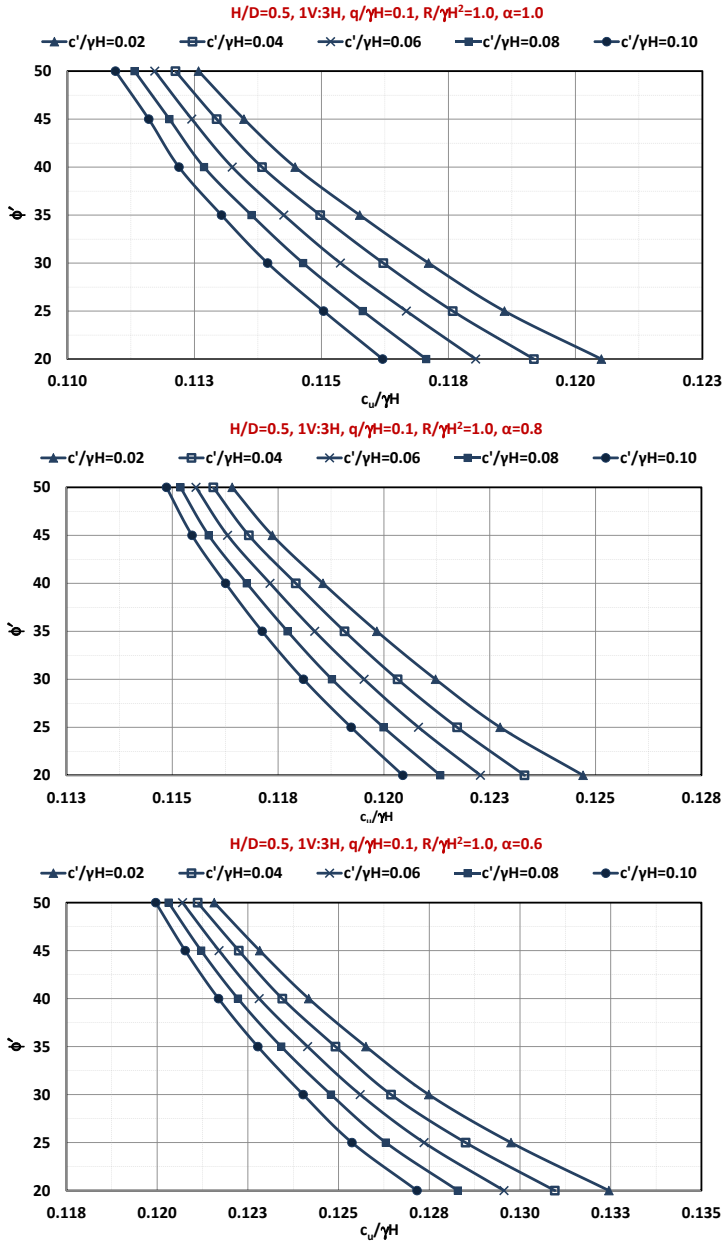

Figure A.36: Required soil properties for embankment with surcharge and high rupture strength reinforcement (n=3,H/D=0.5)

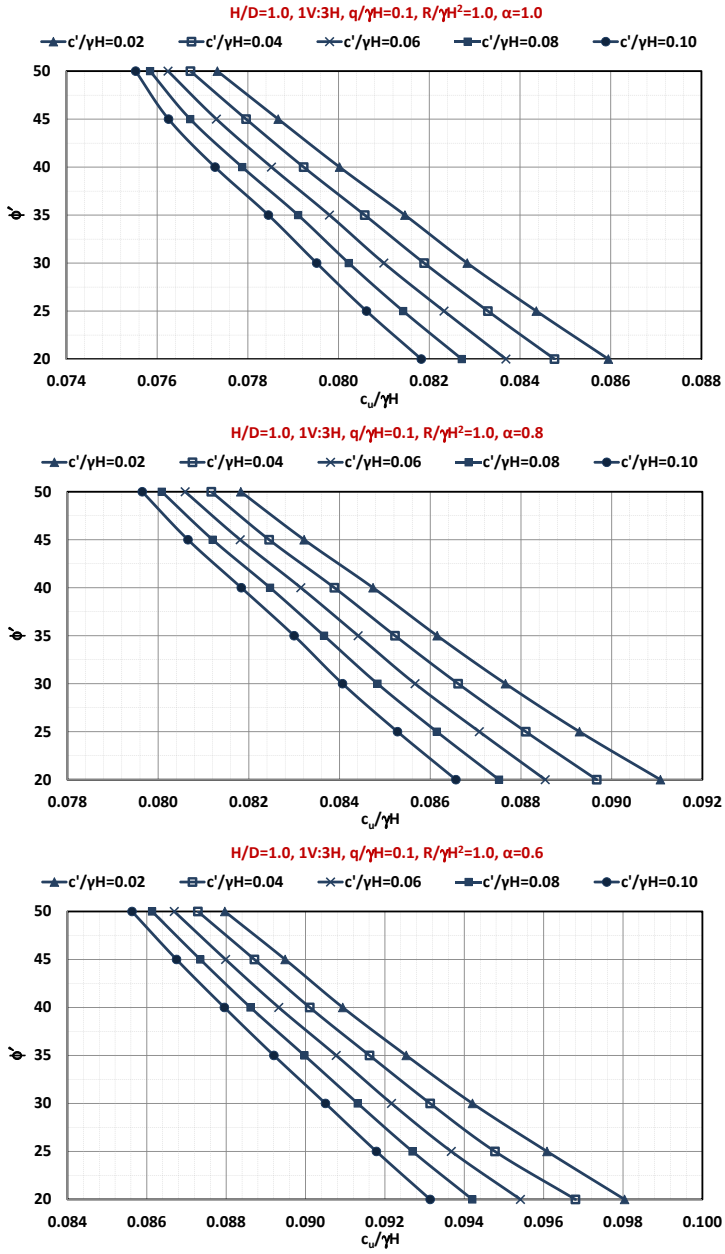

Figure A.37: Required soil properties for embankment with surcharge and high rupture strength reinforcement (n=3,H/D=1.0)

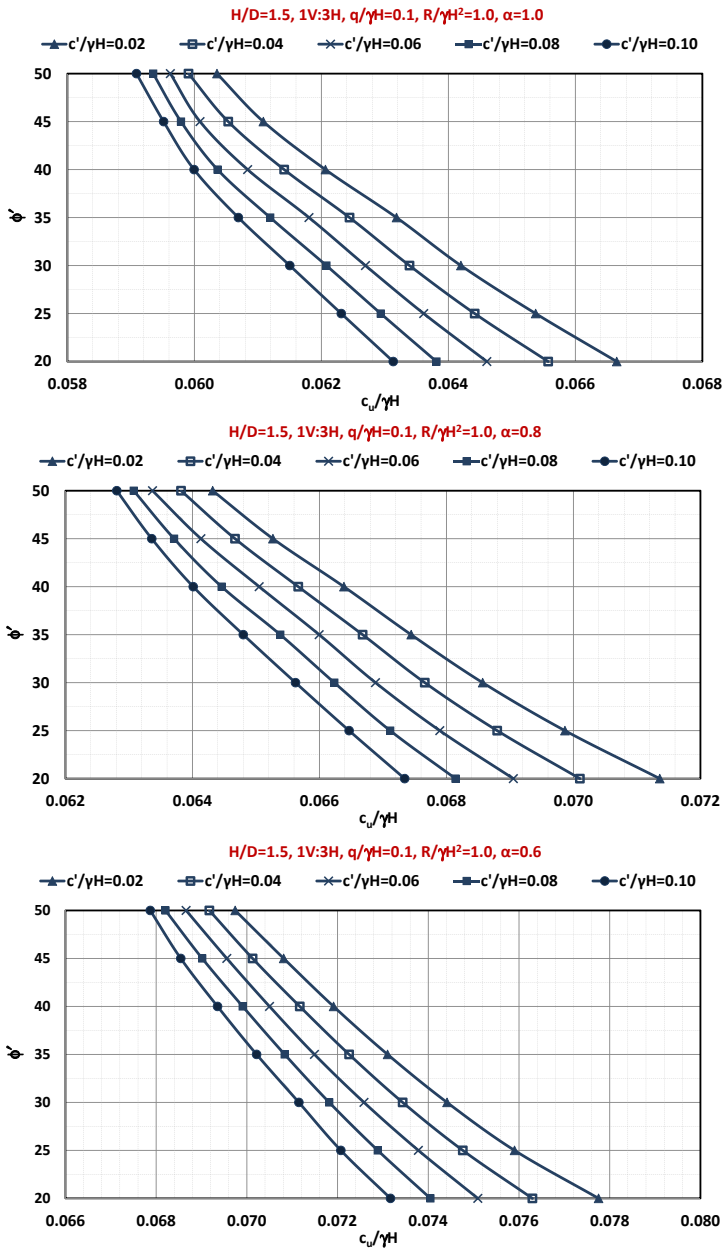

Figure A.38: Required soil properties for embankment with surcharge and high rupture strength reinforcement (n=3,H/D=1.5)

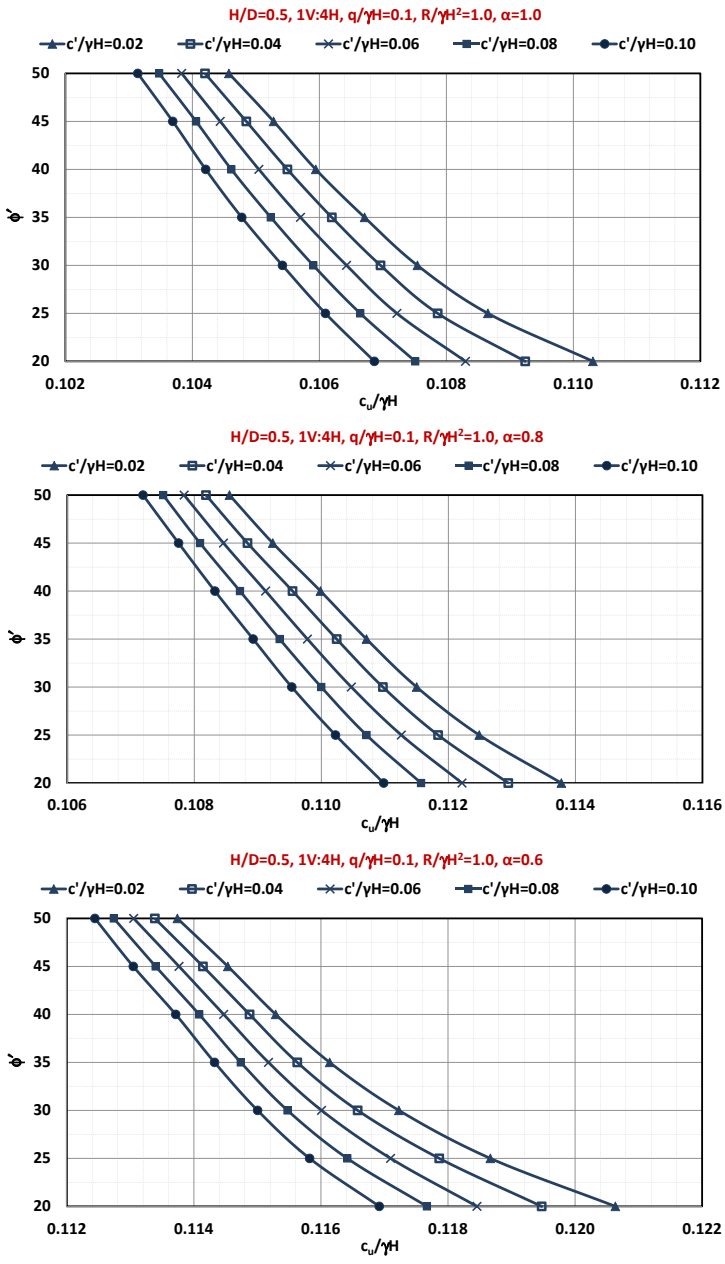

Figure A.39: Required soil properties for embankment with surcharge and high rupture strength reinforcement (n=4,H/D=0.5)

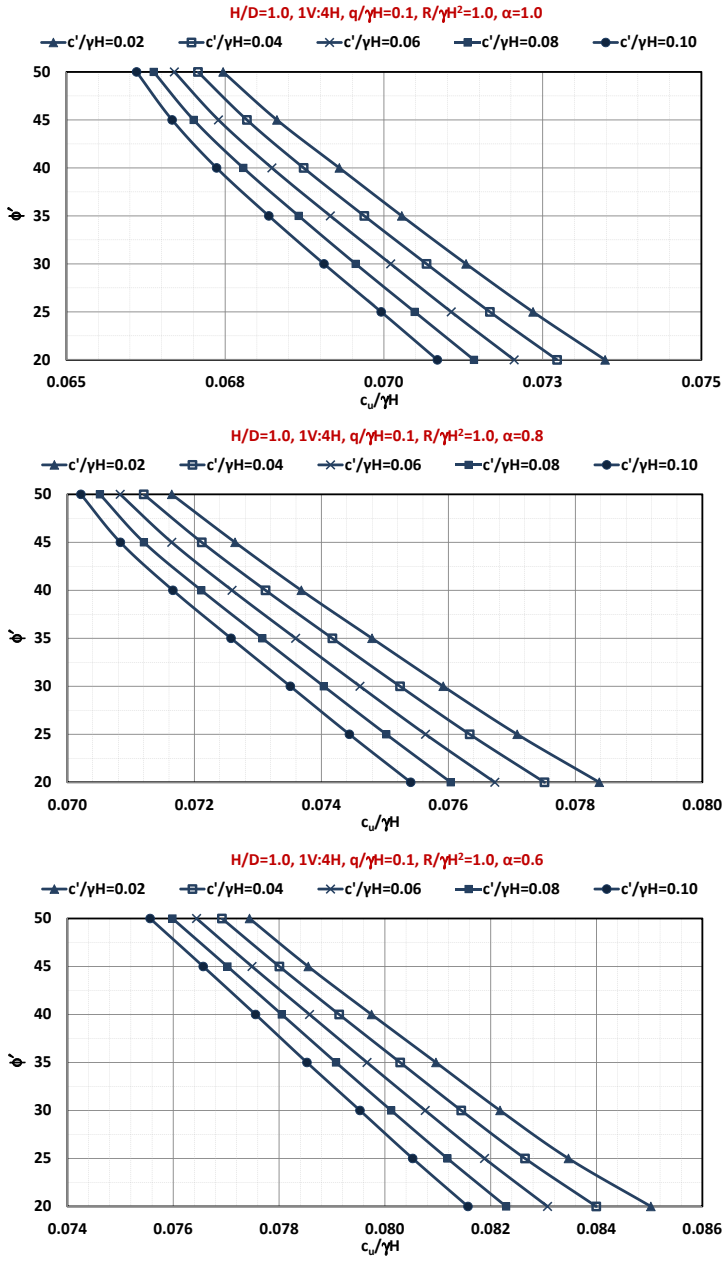

Figure A.40: Required soil properties for embankment with surcharge and high rupture strength reinforcement (n=4,H/D=1.0)

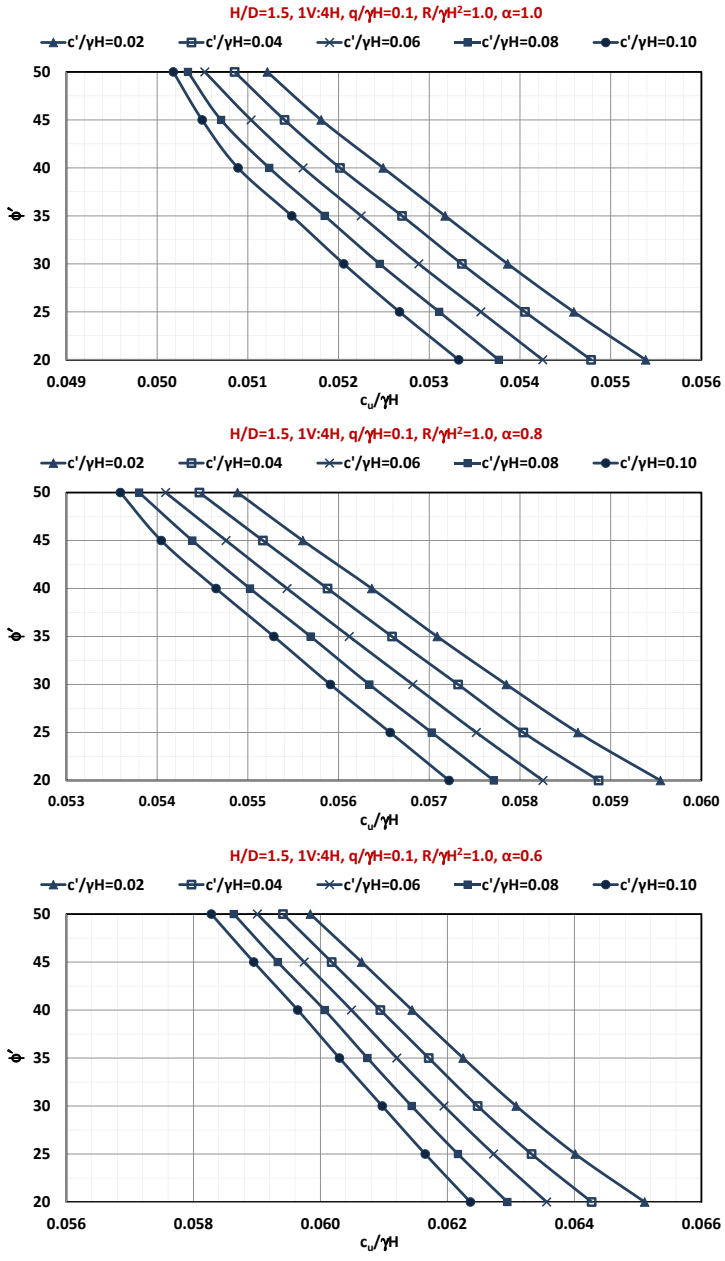

Figure A.41: Required soil properties for embankment with surcharge and high rupture strength reinforcement (n=4,H/D=1.5)

A.11 Appendix III: Relationship between $R/\gamma H^2$ and $c_u/\gamma H$ for various values of H/D

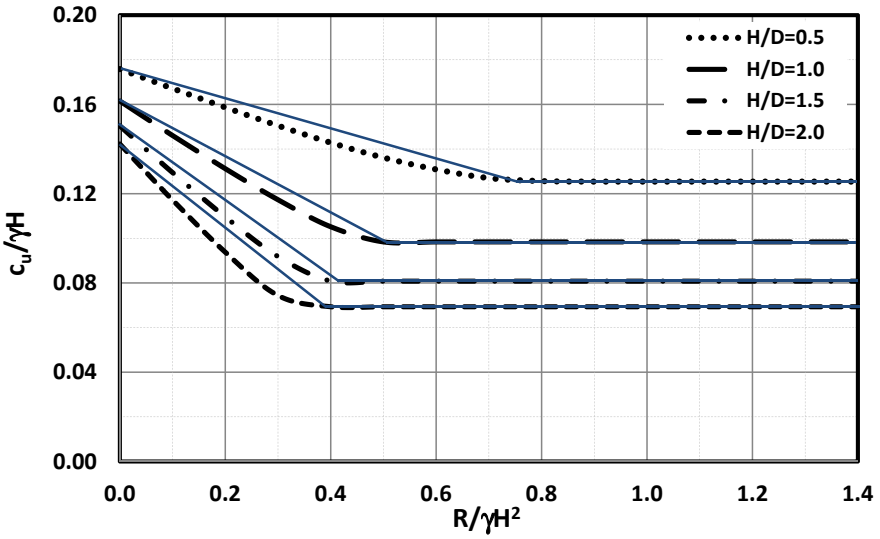

Figure A.42: Required undrained shear strength for stability plotted against reinforcement strength($c'/\gamma H = 0$, $\phi' = 30$, 1V:2H, and $\alpha = 0.8$). Thin lines indicate bilinear fit. The maximum error in using this fit occurs approximately between $0.5 - 0.6R_L$ and is around 8% in $c_u/\gamma H$ or 20% in $R/\gamma H^2$, where R_L is the limiting (lowest) value of R for any curve.

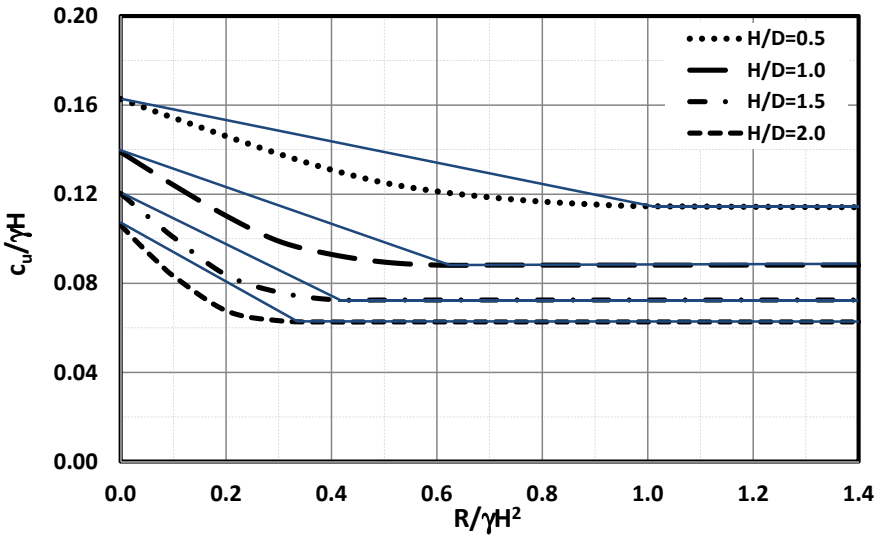

Figure A.43: Required undrained shear strength for stability plotted against reinforcement strength($c'/\gamma H = 0.1$, $\phi' = 50$, 1V:2H, and $\alpha = 0.8$). Thin lines indicate bilinear fit. The maximum error in using this fit occurs approximately between $0.5 - 0.6R_L$ and is around 15% in $c_u/\gamma H$ or 60% in $R/\gamma H^2$, where R_L is the limiting (lowest) value of R for any curve.

Appendix B

Transparent Soil to Model Thermal Process: An Energy Pile Example

This paper published in the Geotechnical Testing Journal ASTM:

Black, J.A. and Tatari, A. (2015). "Transparent Soil to Model Thermal Processes: An energy Pile Example." *Geotechnical Testing Journal ASTM*, 38(**5**):752-764. doi:10.1520/GTJ 20140215

Abstract

Managing energy resources is fast becoming a crucial issue of the 21^{st} century, with ground based heat exchange energy structures targeted as a viable means of reducing carbon emissions associated with regulating building temperatures. Limited information exists about the thermo-dynamic interactions of geothermal structures and soil owing to the practical constraints of placing measurement sensors in proximity to foundations; hence, questions remain about their long-term performance and interaction mechanics. An alternative experimental method using transparent soil and digital image analysis was proposed to visualize heat flow in soil. Advocating the loss of optical clarity as a beneficial attribute of transparent

soil, this paper explored the hypothesis that temperature change will alter its refractive index and therefore progressively reduce its transparency, becoming more opaque. The development of the experimental methodology was discussed and a relationship between pixel intensity and soil temperature was defined and verified. This relationship was applied to an energy pile example to demonstrate heat flow in soil. The heating zone of influence was observed to extend to a radial distance of 1.5 pile diameters and was differentiated by a visual thermal gradient propagating from the pile. The successful implementation of this technique provided a new paradigm for transparent soil to potentially contribute to the understanding of thermo-dynamic processes in soil.

Keywords: transparent soil, thermal modeling, energy pile, energy, image analysis

B.1 Introduction

B.1.1 Energy geotechnics

Managing natural resources is becoming one of the crucial issues of the 21^{st} century and is closely linked to the need to reduce our carbon footprint and become more energy sustainable. Geotechnical energy structures/foundations are believed to offer potential to make a positive contribution to this vision by serving as energy exchange systems to regulate building environmental conditions. In winter, the ground temperature is higher than the air and it therefore provides a potential source of heat energy; alternatively, in summer, the ambient air temperature is higher and the ground can be used as a heat sink to cool the building; thus reducing the reliance on conventional heating and cooling systems.

The concept of ground energy exchange systems has been proposed and implemented for decades, with Brandl (2006) reporting on the first installation of thermal piles in the 1980s. Despite this period since their initial deployment, design methods for their thermal or geotechnical aspects are not yet well established (Loveridge and Powrie, 2012). The lack of a unified approach is largely attributed

to the difficulties in optimizing heat exchange within an energy foundation, current understanding of the effects of temperature on soil behavior, and uncertainty of thermo-mechanical interactions. In this respect, although it is well known that soil behavior is influenced by temperature, the extent of the response is highly variable and dependent on particle size, mineralogy, and stress history of the soil. Many researchers conducted element tests to study the behavior of soils subjected to temperature changes. Campanella and Mitchell (1968) show that an increase in temperature in drained conditions produced a volume reduction of clay soil.

Demars and Charles (1982) documented similar findings and reported that soil behavior was strongly dependent on the overconsolidation ratio in their investigation of a marine undisturbed clay. Similarly, Towhata et al. (1993) reported that normally consolidated clays exhibited thermal contractive behavior, whereas overconsolidated clays can show thermal dilatant behavior. Other studies related to the compression of normally consolidated clays include Mitchell (1964), Plum and Esrig (1969), Habibagahi (1977), and Boudali et al. (1994) who reported that the compression curves obtained at different temperatures are parallel, with lower values of void ratio at higher temperatures.

Variations in shear strength with temperature are also reported. For example, Hueckel et al. (2011) summarised that experimental studies of the triaxial strength of clays show that remolded kaolin clay and natural Boom Clay exhibit temperature dependence of their internal friction, whereas this is not the case for largely smectitic or illitic clays based on works by Hueckel and Baldi (1990), Hueckel and Pellegrini (1992), and Cekerevac and Laloui (2004). Conversely, Houston et al. (1985) reported increases in peak shear strength at elevated temperature under undrained conditions for an illitic and smectitic rich ocean sediment. Hueckel et al. (2009) demonstrated that although numerically small, a 10% temperature-induced increase in the critical state coefficient M over 90°C can produce an increase in compressive strength of up to 25%, compared with the case of a temperature-independent friction angle.

Nomenclature

Symbol	Definition
CCD	charged couple device
cP	centipoise
d_0	pile diameter
D	depth
d_c	direct current
k	thermal conductivity
LED	light emitting diode
l	litres
lp/mm	line pair per mm
MTF	modulation transfer function
n	index of refraction
N	centrifuge acceleration scale
PI	pixel intensity
PID	proportional-integral-derivative
PI_N	normalised pixel intensity
PI_{max}	maximum pixel intensity
PI_{min}	minimum pixel intensity
PIV	particle image velocimetry
r	radius
RI	refractive index
SLR	single lens reflex
USB	universal serial bus
W	width
z	soil depth
$\circ_C$	degree Celsius

Furthermore, it is noteworthy that Hueckel et al. (2011) reported the effects of the thermal variation of internal friction depend heavily on the history of heating and loading. This aspect could have considerable implications on the thermo-mechanical response of foundations (i.e.,energy piles) deployed as energy structures, such that under working stress, deterioration of stability and serviceability

could manifest, leading to uncertainty in long-term performance. In this respect, Loveridge and Powrie (2012) stated that while observations from trial energy pile tests at Lambeth College in London (reported by Bourne-Webb et al., 2009) suggest the thermomechanical response of the pile is reversible, these short term tests would not have identified smaller thermal loading cyclic effects that that could become significant over longer time scales and more heating/cooling cycles.

Owing to the complexity that surrounds assessing the likely thermo-mechanical performance of energy foundations, several field investigations were conducted in an effort to enhance understanding of thermal response of energy structures in the ground. Laloui et al. (2003) conducted heating tests on a $1-m$ diameter energy pile embedded in saturated alluvial sandy soil under different working loads. Without any applied axial load, heating the pile by 21°C induced a heave of 3.5 mm and over 4 MPa of axial stress. Under working load conditions, a threefold increase was recorded in the maximum axial load when the pile was subjected to a 14°C temperature increase. The most widely reported field tests are those previously introduced at Lambeth College, London by Bourne-Webb et al. (2009). The pile had a diameter of 0.55 m, length of 23 m, and was embedded in London clay. The pile was subjected to separate heating and cooling cycles while carrying a working load of 1200 kN. Heating caused an increase in pile axial load of up to 800 kN, while the cooling cycle led to a reduction in load of about 500 kN. Accompanying changes in pile head displacement were small at less than 2 mm. Other field investigations are reported by Wood et al. (2010), who investigated the heat pump performance on a test plot of 21 concrete test piles, 10 m deep for residential buildings. In addition, Pahud and Hubbuch (2007)measured thermal performances of an energy pile system deployed at Zurich Airport confirming that the observed performance was as intended. Gao et al. (2008) and Hepbasli et al. (2003) reported on studies that predominately focused on improving the efficiency and design of heat exchangers in the field. Finally, wider commentary on the broader use of geostructures as heat exchangers in the field such as diaphragm walls, thermal piles, and tunnels are reported by Brandl (2006). While the above field studies were highly beneficial in providing some initial performance data of thermally active foundations,uncertainties in the assessment of energy foundations are exacerbated by the lack of high quality monitoring data from case studies on

which to validate new approaches (Loveridge and Powrie, 2012). Specifically, extensive long-term data relating to the thermo-dynamic interactions of geothermal heat exchange structures and soil is lacking owing to the practical constraints of placing measurement sensors in the soil in close proximity to the geostructure and the data collection time required. As demonstrated in the laboratory element tests, changes in soil characteristics with temperature could affect the performance of geostructures deployed as energy exchange systems. Potential issues could range from increased foundation movement due to the thermal expansion and contraction of the foundation or surrounding soil, or the build-up of internal thermal induced stresses, especially over multiple thermal cycles. Although current field data is limited in duration and number of cycles achieved, several physical model studies were conducted in the centrifuge that evaluated longer-term impacts of multiple thermal cycles. This is possible owing to scaling laws derived by Savvidou (1988), who determined the time scaling factor of N^2 (N being the applied enhanced gravity in the centrifuge) for heat flow in accelerated gravity experiments, which enables multi thermal cycles to be simulated in a shorter duration (hours) that would normally take years at full field scale. Notable centrifuge investigations benefiting from this scaling relationship include Stewart et al. (2014), Ng et al. (2014), Britto et al. (1989), Goode III et al. (2014), and Stewart et al. (2012). These studies considered a range of various soil types with reported observations of increased pile settlements and ratcheting over several thermal cycles. While this behavior has not been observed at full scale, its detection in simulated prototype field stress conditions within the centrifuge is disconcerting and echoes concerns by other authors that thermal loading cyclic effects could become significant over longer time scales and more heating/cooling cycles (Loveridge and Powrie, 2012). Hence, the long-term performance of energy foundations is not well understood and is likely to be the focus of considerable ongoing research in future studies in this field.

B.1.2 Transparent soil modeling

Transparent soil consists of an aggregate and a matched refractive index fluid. When fully saturated, the particles appear invisible and allow light to pass, enabling visualisation through the soil. Both fine (clay) and coarse-grained (sands/gravels) were developed and the materials and their mechanical properties are summarised by Iskander (2010). Many experiments in transparent soil focused on identifying aspects of fluid flow or mechanical response of the soil to enhance understanding of soil structure interaction behavior (Iskander et al. 1994; Iskander et al. 2002; Sadek et al. 2002; Liu et al. 2002;Liu et al. 2003; Ezzein and Bathurst 2014. Investigations of this nature have sought to optimize soil transparency in order to accommodate models of increased geometry and offer greater visualisation of tracking particles within the soil for displacement measurement. Gill (1999) used back illumination to silhouette embedded target markers; however, that has been superseded by modern laser aided imaging in conjunction with digital image correlation techniques (for example Sadek et al. 2003 and Hird et al. 2008). Works using this approach include examination of failure mechanics of helical screw piles Stanier et al. (2013), stone column groups Kelly (2013), and tunnel induced settlements (Ahmed and Iskander, 2010) soil plugging behavior during press-in piling of tubular piles (Black 2012; Forlati and Black 2014).

The success of transparent soil modeling has long been considered reliant on producing a soil surrogate that offers the highest optical clarity, with low transparency being considered detrimental to the modeling technique (Black and Take, 2015). However, recent work by Siemens et al. (2010) and Peters et al. (2011) embraced the loss of soil transparency as a positive characteristic for the purpose of modeling unsaturated soil phenomena. The authors appreciated that fused quartz soil particles appeared white in color when dry, yet were invisible when submerged in suitably matched refractive index pore fluid (i.e., 100% saturation), so that a uniform black background behind the soil would be clearly visible. Intermediate levels of saturation enable only partial transmission of light such that the calibration target no longer would appear uniform black, but gray/white in color at the fluid-air boundaries. Evaluating pixel intensity of the background from fully

saturated to dry conditions enabled the authors to successfully correlate the degree of saturation from digital images. In doing so, the authors provided a new opportunity for transparent soil to offer complementary insight of unsaturated soil problems.

This paper also advocates the loss of optical clarity as a beneficial attribute of transparent soil, focusing on the property of refractive index and its temperature dependency for the purpose of viewing heat flow in soil to model thermo-dynamic problems. It is hypothesized that temperature changes will have a negative impact on soil transparency and the soil will become progressively more opaque as the temperature deviates from the optimum calibrated refractive index match. Hence, changes in transparency can be registered as a shift in pixel intensity of a black background viewed through the soil, which can be related to temperature variations. The aim of this paper is to provide a comprehensive overview of the novel testing protocol that has been developed to fulfil this hypothesis, and to define a relationship for pixel intensity and temperature. The potential for transparent soil to model thermo-dynamic processes is demonstrated using an energy pile application whereby heat flow is quantified through direct visualisation and coupled with image analysis.

B.2 Concept of visualising heat in transparent soil

B.2.1 Refractive index

Refractive index, also called index of refraction (n), is a dimensionless number that describes how light propagates through a medium and is defined as a ratio of the speed of light in the medium relative to its speed in a vacuum. It is also important to note that light changes direction when it travels from one medium to another whereby Snells law can be used to determine the angle of incidence and refraction. Refractive index of a material is affected by factors such as the wavelength of light and temperature. For this reason, refractive index properties of materials are

quoted with respect to the temperature at which they were determined. Variation in temperature affects material density, which in turn affects the speed of light; therefore, increased refraction and dispersion of light rays occur, which manifest as a loss of transparency such that a previously transparent medium may appear as less clear or become opaque as temperature changes.

B.2.2 Image analysis methodology

Individual pixels are the smallest addressable element that combines to form a digital image as a two-dimensional representation of a real object. Each pixel within the image has a pixel intensity value that describes its brightness and color. The most common pixel format is where the pixel number is stored as an 8-bit integer with a range of possible values from 0 (black) to 255 (white). Values in between these extremes describe the spectrum of shades of gray. In color images, separate red, green, and blue components must be specified for each pixel; hence the pixel value is actually a vector of the three individual pixel intensity numbers.

Referring to Figure B.1, when a uniform black background is placed behind transparent soil mixed at its optimum refractive match for a given temperature (i.e., calibrated at 20°C), it will be visible as the soil is transparent and allows the passage of light; therefore, pixel intensities representative of black would be returned in an image. Examining the pixel intensity of a subregion would reveal that the pixel intensity values are not truly black (i.e., zero), but are still sufficiently low to be portrayed as black in the image. It is not uncommon in digital images that the true color information from a real object will not be perfectly transferred to an image due to aberrations and diffraction caused by the camera and lens, illumination conditions, or in this instance, viewing the target through a translucent medium. Conversely, if the soil temperature was increased (i.e., to $50^{o}C$) the refractive index would change and reduce light transmission; therefore, the black target will be less visible or fully obscured. In this instance, the pixel intensity would no longer be close to zero, but increase such that the soil would be considered to be gray in color. Observed changes in pixel intensity provide a clear basis on which to establish a direct visual assessment measurement to detect temperature changes in transparent soil captured in digital images.

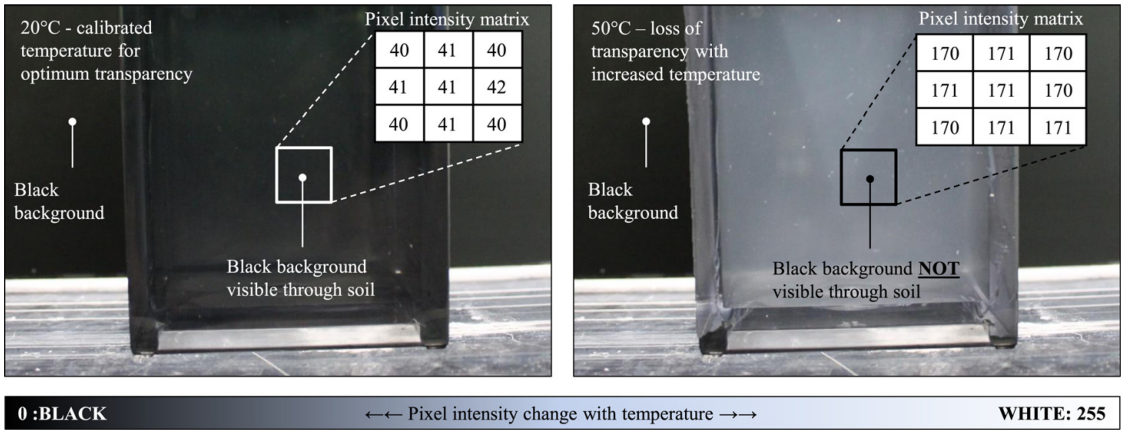

Figure B.1: Concept of pixel-temperature visual based measurement for thermal modeling applications in transparent soil.

The background (referred to herein as "calibration target") implemented in the current research consisted of two distinct regions: (i) black uniform intensity and (ii) alternating black and white stripes at a spatial frequency of 1 line pair per mm (lp/mm). This split target was adopted due to the positive outcome in the work of Siemens et al. (2010) and Peters et al. (2011), who reported success using a black uniform background to detect changes in pixel intensity to capture loss of optical transmission, and striped region due to complementary work by Black and Take (2015) that established a robust quantitative framework for assessing the optical quality of transparent soils using optical method referred to as "modulation transfer function" (MTF). MTF operates by relating the pixel contrast that is transferred from an object to an image and is commonly used to calibrate optical systems. When the transparent soil is of high quality and well optically matched, the modulation contrast between the minimum (black) and maximum (white) pixel intensity is well-defined. However, if transparency is poor or diminishes, then contrast reduces towards a single pixel intensity value (i.e., image blends to gray color). The loss in signal modulation is governed by the transparency; hence, MTF can be used to quantify and evaluate the reduction in clarity that occurs as temperature changes. This process is fully described in Black and Take (2015); however, the main principle is conveyed in Figure B.2, which demonstrates the loss in modulation when temperature increases in transparent soil. This approach offers an alternative method to detect changes in the soil by relating loss in contrast

between successive black and white reciprocating line pairs to variations in soil transparency, induced by temperature changes in this instance.

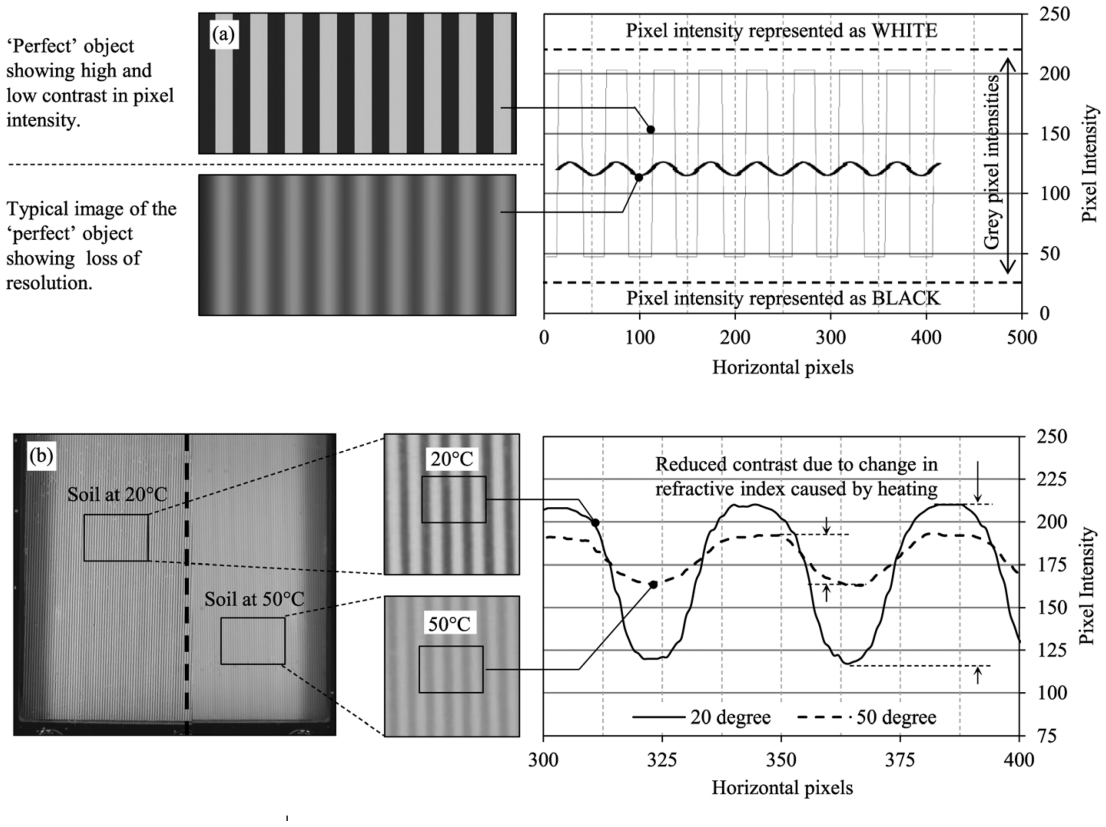

Figure B.2: Concept of using signal modulation to detect changes in contrast from changing refractive index due to temperature changes (a) demonstration using artificial image and (b) verification in transparent soil.

The proposal to use pixel intensity as a measurement framework presents several challenges. Pixel intensity is sensitive to illumination levels and will vary depending on the lighting conditions provided. Moreover, individual pixels located on the camera charged couple device (CCD) sensor will be subjected to varying light intensity owing to the ability of the lens to focus light. Siemens et al. (2010) and Peters et al. (2011) encountered significant challenges when interpreting and correlating pixel intensity to saturation level as the experiment was illuminated using standard fluorescent room lighting and required the use of multiple cameras with overlapping fields of view. Hence, normalization of the pixel intensity was necessary to account for variations in illumination in the field of view due to the

poor lighting conditions. In the current investigation, tests were conducted in a dark room environment under constant illumination, which significantly reduced large variations in measured pixel intensities.

B.3 Experimental program, apparatus and technique

B.3.1 Transparent soil material

The transparent soil used in this investigation consisted of 6% fumed amorphous silica aggregate and 94% pore fluid. The pore fluid was a blend of white oil (Baylube WOM 15) and paraffinic solvent (N-paraffin C10-13) mixed to volumetric proportions of 77:23, giving a refractive index match to the silica aggregates of 1.467 at 20°C. This ratio was previously calibrated by Stanier et al. (2012) using a visual eye chart assessment method; however, as described previously, this was superseded by a newly established quantitative framework proposed by Black and Take (2015) based on an optical calibration method known as MTF. The particle density of the fumed silica was 2200 kg/m^3, with a surface area of 200±25 m^2/g, and particle size D_{50} of 0.014 μm. The density of the fluids was measured to be 845.48 kg/m^3 for Baylube WOM 15 and 764.24 kg/m^3 for N-paraffin C10-13. The dynamic viscosity of the oils was measured using a spindle viscometer in units of centipoises (cP) and determined to be 21.2 cP and 1.2 for the Baylube and Paraffin oils, respectively, and 7.7 cP for the combined fluid mix ratio at 20°C. The volumetric coefficient of thermal expansion of paraffin oil is 7.6×10^{-4} °C^{-1}, and 4.5×10^{-4} °C^{-1} for Baylube oil.

The aggregate and pore fluid were thoroughly mixed using a hand-held food blender to produce a homogeneous slurry and then placed into the test chamber. Samples were located in a vacuum to evacuate the air to produce a two phase continuum which enabled visualisation of the calibration target when placed behind the soil. The soil was consolidated to produce test beds having undrained

shear strength of approximately 10 kPa for the calibration and energy pile application tests. More detailed information about the material consolidation and strength properties are described by Stanier (2011) and Kelly (2013).

B.3.2 Test apparatus

The experimental system is portrayed in Figure B.3 consisted of a water bath of dimensions 600 mm(width) by 400 mm(height) by 500 mm (diameter) that provided a fluid volume capacity of approximately 100 l. A water bath was used to provide a constant temperature boundary to the submerged soil test chamber. The water bath was filled with de-aired water that was warmed using a coil heating element and water pump that circulated the water to maintain a constant temperature. Note, during calibration tests, the temperature of the water in the bath, and hence temperature of the soil, was raised at set increments ensuring thermal equilibrium was achieved at each stage. Alternatively, for the energy pile tests, the water bath was used to provide a constant boundary temperature to the submerged soil test chamber as heat was then applied directly to the energy pile.

The external surfaces were covered in black card to produce a consistent background and to minimize internal light reflections. The system was instrumented with $10LM335Z$ precision temperature sensors (thermocouples) that confirmed equilibrium of the water and soil temperature and to were also used to validate the image-based measurement approach.

As discussed previously, non-uniform illumination conditions are detrimental to producing consistent pixel intensity readings. For this reason, tests were conducted in a dark room environment under constant illumination provided by two LED towers. Each tower consisted of 4 individual LED panels containing 30 surface mount LEDs that were powered at 12V dc. Light diffusers were used to disperse LED hotspots to ensure uniform illumination of the water bath and submerged soil chamber. Precursor trial tests confirmed that large variations in pixel intensity, as reported by Siemens et al. (2010) and Peters et al. (2011), did not occur and hence confirmed the suitability of the control measures implemented to minimize pixel intensity variation caused by poor illumination.

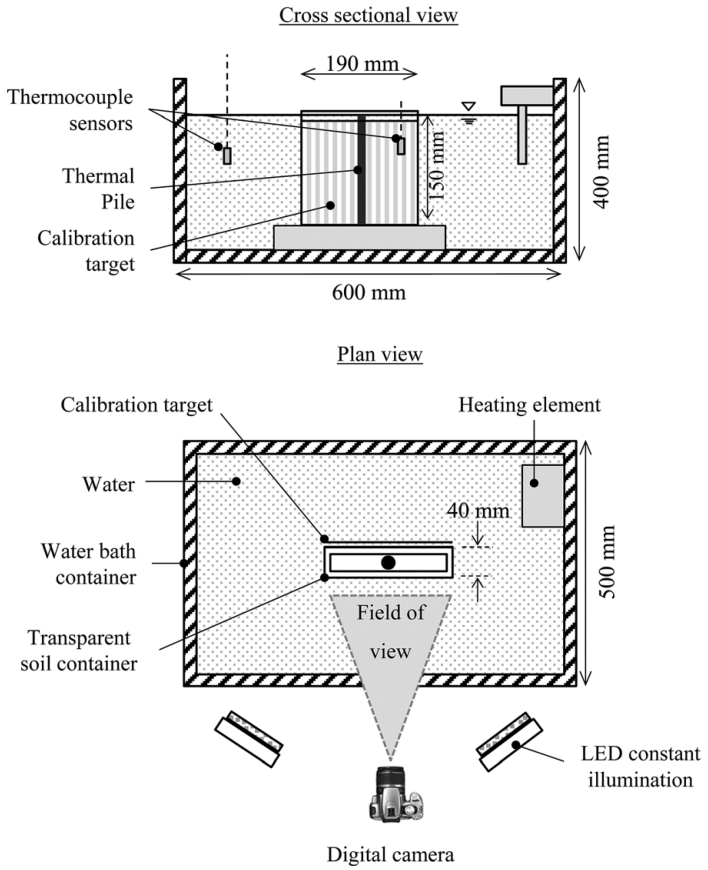

Figure B.3: Transparent soil thermal modeling experimental setup.

Images were captured using a Canon $EOS1100D$ single lens reflex (SLR) with an 1855 mm lens. During the test, the camera was mounted on a tripod at a distance of 0.5 m from the front of the test chamber and was triggered at regular intervals using a digital signal generated from a National Instruments $6211USB$ data acquisition device. This remote trigger capability ensured that it was possible to conduct long term tests without operator intervention, which was beneficial for maintaining constant environmental conditions, and to minimize temporal movements of the camera position between successive images. In addition to illumination variation, pixel intensity can also be affected by camera parameters such as aperture, exposure time, and focus; hence, the camera properties were fixed at focal length of 55 mm, an aperture of $F/16$, shutter speed of $1/5^{th}$ seconds, ISO of 100, auto white balance, and no flash. These parameters were optimized prior to commencing the main test schedule to yield the greatest image clarity. During

testing, an image was initially captured by allowing the camera to auto focus on the target before switching to manual focus to capture the remaining test images. Images were taken at a frequency of between 1 and 10 min depending on the nature of the test, i.e.,calibration or energy pile application. These rigorous precautions ensured that any changes in pixel intensity detected, subsequently interpreted as a change in soil temperature, were attributed solely to loss of transparency of the soil owing to the change in its refractive index as the soil temperature changed.

The soil test chambers used for calibration and the energy pile tests measured 190 by 150 by 40 mm and were constructed from 10-mm thick Perspex sheet. The chambers were fixed using $M8$ bolts and sealed using silicone sealant along the mating surfaces. During calibration, thermocouples were placed inside the chamber to provide temperature readings that were correlated with pixel intensity to verify the pixel-temperature relationship. After vacuuming, the top of the chamber was sealed using a rubber membrane held in place by a top plate. Prior to submerging in the water bath, calibration targets were prepared and waterproofed by laminating and attached to the back of the test chamber. The test chamber was located in the centre of the water bath so as to provide constant temperature boundary conditions.

The experiment was controlled and data was acquired using a National Instruments LabVIEW program that interfaced with the $USB6211$ data acquisition module. The program logged thermocouple signals and triggered the camera at a user defined frequency.

B.3.3 Calibration procedures

Calibration of pixel intensity at various soil temperatures was achieved by submerging the soil chamber in the water bath and allowing it to be heated by the re-circulating water system. Temperature stages ranged from 20 to 50°C in 5°C increments. At each stage, the temperature of the water bath was coarsely set to the desired value and the exact temperature was confirmed precisely by thermocouples submerged both in the water bath and soil. Calibration of the system confirmed the water bath was capable of heating and maintaining constant soil temperature

at each incremental stage and that steady state conditions were achieved after approximately $2h$ of heating exposure.

Correlation of image pixel intensity at various soil temperatures was achieved by capturing images of the calibration target placed behind the test chamber and viewed through the soil across the range of temperatures indicated. Images were captured at the end of each heating stage, ensuring that equilibrium was achieved, and also at regular intervals during the temperature ramp. Changes in soil refractive index due to temperature variations are recorded as changes in image pixel intensity. Post analysis using image processing software in $MATLAB^{TM}$ enabled translation of the recorded pixel intensities to discrete temperatures using the established pixel intensity-temperature relationship described later.

B.3.4 Energy pile application example

The potential of transparent soil to visualize thermo-dynamic problems is demonstrated using an energy pile example. The pile was machined from aluminium and measured 18 mm diameter (d_0) by 150 mm long (Figure B.4). A cartridge heating element, 6.5 mm in diameter by 70 mm long, was inserted in a bored recess in the centre of the pile and fixed in place using thermal epoxy. The heating element had a power rating of 100 W and was interfaced with a CAL 3300 proportional-integral- derivative (PID) relay temperature controller that used feedback from a thermocouple embedded on the surface of the pile to regulate temperature to within ± 0.5 °C. The pile was sprayed matte black to minimize reflections into the soil and also ensure that changes in pixel intensity at the pile-soil interface would be clearly identifiable.

Energy pile tests were conducted by increasing the temperature of the pile to 50°C, while maintaining the temperature of the water bath at 20°C. Typical in situ ground temperatures are in the range of 10°C-15°C, thus the selected valued of 20°C is slightly higher than what may normally be expected. However, higher temperatures in the region of 18°C-20°C were reported by Bourne-Webb et al. (2009), believed to be due to heat radiating from other underground infrastructure; hence, 20°C for the ambient soil temperature was considered viable for

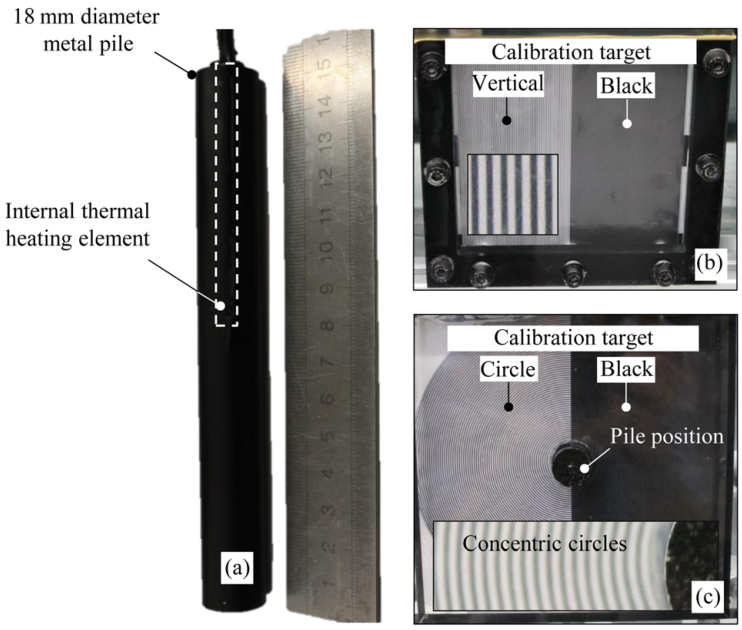

Figure B.4: Energy pile application (a) energy pile, (b) test chamber with vertical stripe and uniform black calibration target regions, and (c) concentric circles and uniform black calibration target.

the preliminary experimental test. This was also advantageous as the laboratory environment was maintained at a temperature of 20°C.

Two pile orientations were considered to show the impact of temperature change and heat flow (i) vertically in the middle of the test chamber to examine the temperature along its length and (ii) horizontally (i.e., end on to the camera principle axis)to evaluate the radial zone of influence. In the case of the vertical pile, the black and vertical stripe calibration target was used; however, for the horizontally placed pile, a specially adapted target was created whereby the vertical lines were changed to concentric circles radiating from the pile centre at the line spacing of 1 lp/mm (Figure B.4(c)).

B.4 Results and discussion

A number of tests were conducted to verify the experimental methodology, calibration of pixel intensity with temperature,and to demonstrate the potential of

this new approach. The main purpose of this paper is to confirm the hypothesis that transparent soil can be used for thermo-dynamic modeling using image-based measurement based on pixel intensity. Note,the energy pile example is provided to demonstrate the potential of this technique to visualize heat flow in and thermal flow processes and not to provide definitive insight of energy pile behavior at this stage. This would require additional testing and verification, which is beyond the scope of this paper.

B.4.1 Calibration of the test environment

The test environment was calibrated by increasing the temperature of the water in the bath and logging the temperature response of the thermocouples. This process was conducted several times, placing the sensors in different locations, to verify the time required to regulate the temperature and confirm that uniform temperature conditions were maintained. The water bath reached a steady temperature after approximately 200 min (Figure B.5(a)) that was also verified independently using a thermometer. In some stages, the final temperature of the water did not precisely reach the desired global value owing to thermal losses from the sides and top of the water bath and the accuracy of the heating coil thermostat. This problem was more pronounced at elevated temperatures above 35°C due to the higher temperature differential of the water relative to the laboratory environment that was controlled at 20°C. This was not considered detrimental to the establishment of a pixel-temperature relationship, as the temperature did reach a point of equilibrium, albeit not precisely the desired value. Moreover, the temperature-pixel relationship was derived using the more accurate thermocouple measurement captured within the soil.

Some lag was observed in the rate at which the water and soil heated owing to the difference in the thermal conductivity of the water, soil test chamber and soil (Figure B.5(b)). The thermal conductivity (k) of water and Perspex are approximately $0.56W.m^{-1}.k^{-1}$ and $0.17W.m^{-1}.k^{-1}$, respectively. A series of tests on the transparent soil using a $KD2Pro$ thermal needle probe indicated it had a thermal conductivity of $0.33W.m^{-1}.k^{-1}$ for the density and saturation conditions tested. This is lower than typical values reported for soils in literature, in the

region of $0.7 - 1.5 W.m^{-1}.k^{-1}$ for sand and clay, respectively (Busby et al., 2009); nevertheless, it was still suitable to model thermo-dynamic problems.

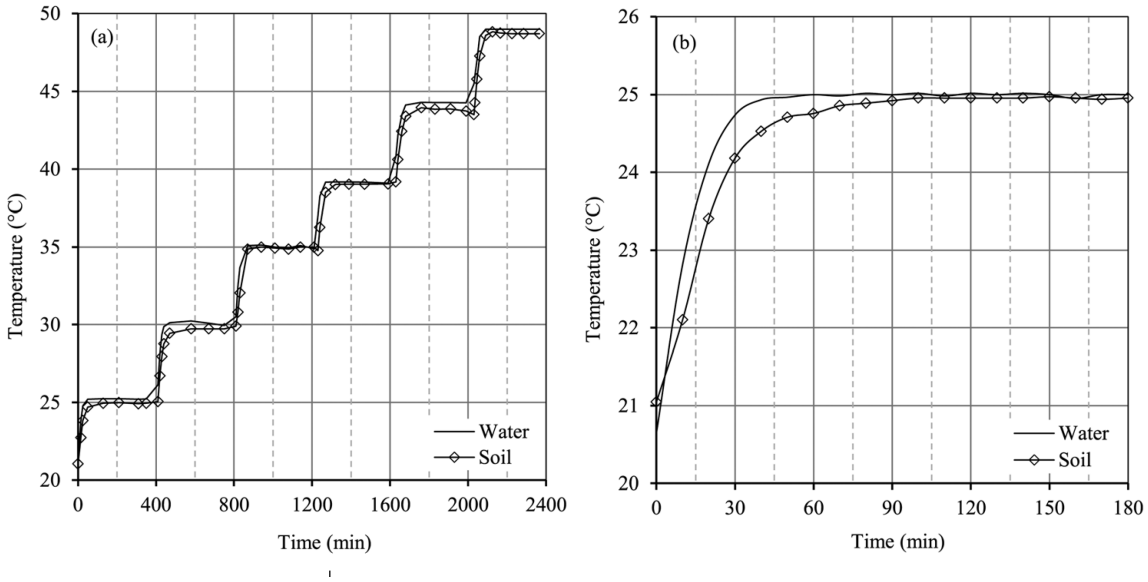

Figure B.5: Calibration of experimental system (a) temperature response over the entire temperature range from 20°C to 50°C and (b)water bath and soil temperature response for 20°C to 25°C temperature increment.

B.4.2 Pixel intensity and temperature relationship

Captured images were processed using (HSG-3-SA-100-L-GG-AB) as this program allowed interrogation of pixel intensities. Despite the improved illumination conditions in the current tests, small variations of up to 10 pixels were observed in pixel intensity measurements across the calibration target in images captured at the extreme 20 and 50°C temperatures. This is significantly lower than the maximum deviation of approximately 50 pixels reported by Peters et al. (2011); however, it still represents a potential error over the pixel range. Any variation in pixel intensity will have a detrimental effect on the interpretation of temperatures using an image-based measure detection system. Hence, pixel intensity normalization was conducted to account for the small anomalies observed at each pixel location using the minimum and maximum intensities determined for images at the extreme

temperatures of 20 and 50°C according to Equation B.1

$$PI_N = \frac{PI - PI_{min}}{PI_{max} - PI_{min}} \tag{B.1}$$

where:

PI_N= the normalised pixel intensity

PI= the captured intensity at a given temperature, and

$PImin$ and $PImax$= the minimum and maximum pixel intensity recorded at 20 and 50°C, respectively.

This normalization was implemented for each temperature increment such that the normalised pixel intensity of the soil varied from 0 to 1 for temperatures of 20 and 50°C, respectively.

The resulting normalised pixel intensity of the uniform black region of the calibration target was correlated with the thermocouple temperature measurements and is displayed in Figure B.6. A strong correlation relating normalised pixel intensity with temperature is evident, with low levels of data scatter present. Between 20 and 30°C, the normalised relationship is non-linear beyond which a linear relation is apparent; although it is not established whether a linear trend will continue over a greater range of temperatures. It is also interesting to note that the trend line turning point corresponds to the temperature at which the material was calibrated to yield optimum transparency (i.e., 20°C). This is in good agreement with previous research reported by Stanier (2011) and Black and Take (2015), and provides further confidence in the pixel intensity temperature relationship established and presented in Figure B.6. This relationship confirms the hypothesis for an image-based measurement approach to observe temperature changes in transparent soil. This discovery presents an exciting new opportunity for transparent soil to contribute to modeling thermo-dynamic processes in soils.

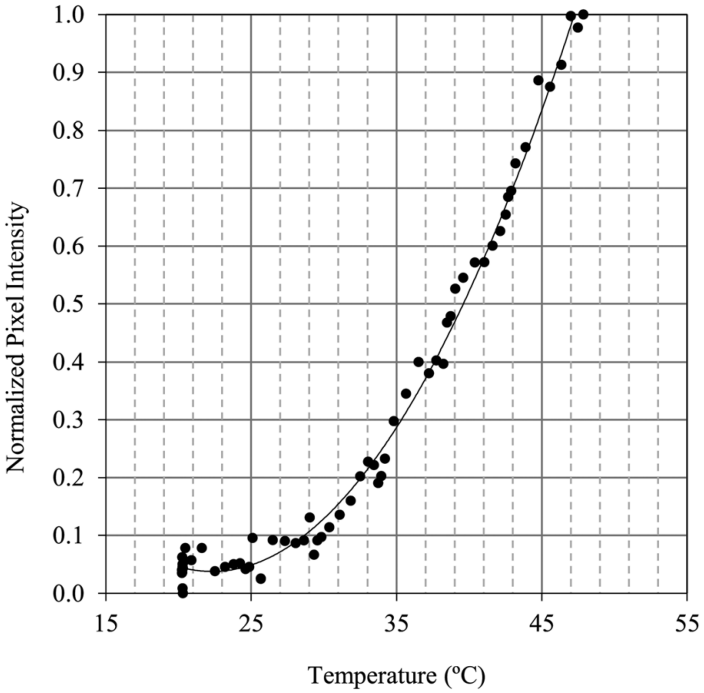

Figure B.6: Normalised pixel intensity with increasing soil temperature.

B.4.3 Energy pile application

The emerging application of an energy pile has been selected to demonstrate the potential of transparent soil and this newly established relationship to model thermo-dynamic processes. Tests were conducted in accordance with the procedure outlined in the section "Energy Pile Application Example". Figure B.7 presents analysis of the soil temperature response for an energy pile vertically embedded in the soil during which the temperature of the pile was activated and increased to a constant temperature of 50°C. Data is presented at time intervals of 10, 30, 60, and 120 min, beyond which no further changes were detected; radial distance away from the pile centreline and depth are normalised by the pile diameter. The heat map shows regions of varying soil temperature and is presented in °C by converting the recorded image pixel intensities using the previously established relationship for normalised pixel intensity and temperature.

Horizontal heat flow propagating radially from the pile is clearly evident. At t=10

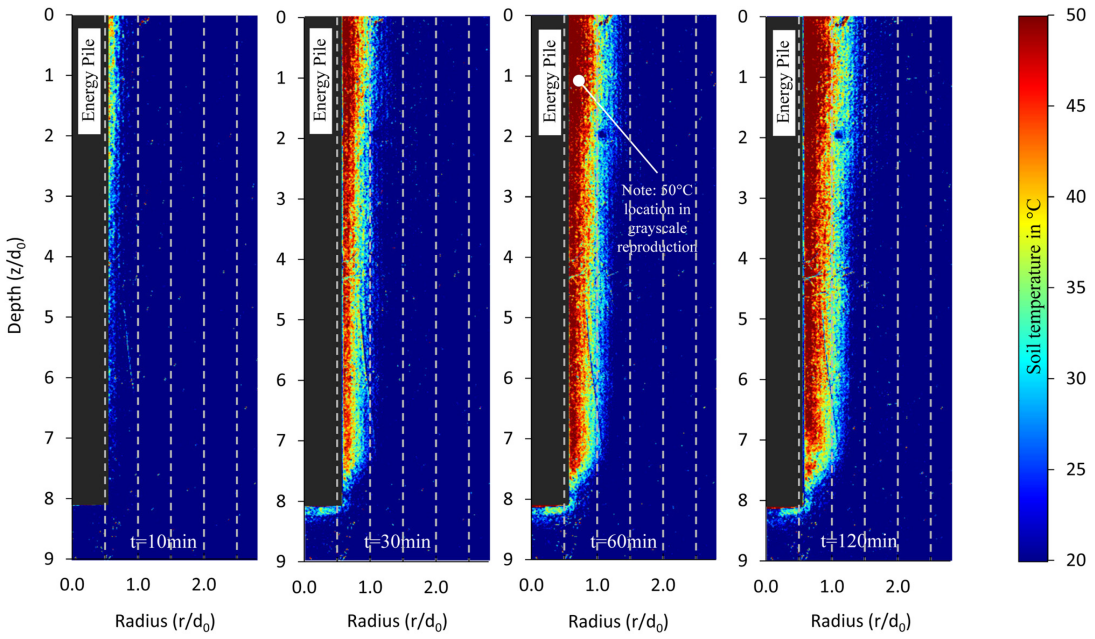

Figure B.7: Horizontal heat flow visualized in transparent soil along the pile length for a 20°C-50°C heating cycle at time intervals t=10, 30, 60, and 120 min depicted as a thermal heat map.

min, only a small region of soil to a depth $z/d_0 = 3$ exhibits an increase in temperature of approximately 35°C. This corresponds with the location of the internal heating element embedded in the pile that extended to a depth corresponding to $z/d_0 = 4$. Significant changes are observed with longer heating exposure time, whereby increased soil temperature is clearly evident along the entire length of the pile. Some small temperature rise is also registered at the pile base. It is also interesting to note that greater thermal heating continues to occur in the upper region of the pile near the heat source. A clear thermal gradient is establish at t_{min}, whereby the temperature at the pile soil interface is the same as the pile at 50°C, and decreases with distance from the pile centreline to the ambient soil background temperature of 20°C that is maintained by the water bath boundary condition. The extent to which this heating zone extends continues to grow up to t=120 min, at which point no further changes were detected. The zone of heating in the soil at the steady state conditions varies slightly along the pile depth from approximately $r/d_0 = 1.5$ up to a depth of $r/d_0 < 1.5$, to $r/d_0 = 1.0$ at $z/d_0 > 4$. It is these observed changes in soil temperature along the length of an energy pile that have been postulated by Laloui et al. (2006), Bourne-Webb et al. (2009), and

Brandl (2006) as the likely contributing factor for increased foundation movements in geothermal structures due to changes in side friction characteristics arising from thermal expansion and contraction of the soil.

Note, the load-displacement performance of the pile or the volumetric response of the soil was not considered in this study; thus, the latter postulation remains an area for further investigation.

The zone of heating influence is more readily portrayed when the pile is viewed end on, as shown in Figure B.8. A second pile test was conducted to examine a cross section of the pile at a pile depth of $z/d_0 = 7$, for the same time increments of t=10 to 120 min. The horizontal and vertical axis are normalised by the pile diameter. During heating, a clear zone of soil up to $z/d_0 = 0.75$ can be seen to be heated to 50°C, which reduces steadily in temperature up to $z/d_0 = 1.25$. Beyond this radial distance, the soil temperature is relatively unaffected.

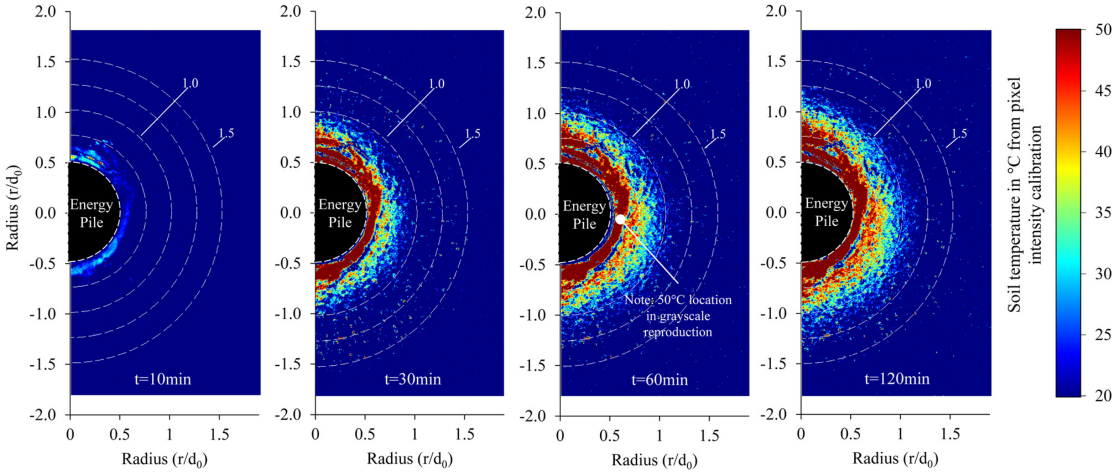

Figure B.8: Radial heat flow visualized in transparent soil at a pile cross section depth z/d$_0$=7, for a 20°C-50°C heating cycle at time intervals t=10, 30, 60, and 120 min depicted as a thermal heat map.

While Figure B.7 and Figure B.8 offers a striking visual portrayal of the soil temperature and thermal gradient, it is difficult to assess the exact zone of heating influence owing to the gradual transition in temperature that occurs. For this purpose, the black and white striped target was used to examine the signal modulation of low and high contrast to ascertain the extent of heating.

Figure B.9 presents images of the concentric black and white circular target at 20 and 50°C, where it is evident that the lines are less distinct at 50°C when the refractive index changed from the calibrated value. This loss in optical transmission is confirmed by the signal modulation spectrum, which appears smaller at the pile interface. As the radial distance increases, the modulation of the normalised pixel intensity amplifies, indicating that the soil refractive index has been less affected by a change in temperature. The signal modulation recovers at approximately $r/d_0 = 1.3$ to match the signature obtained at 20°C, which indicates the heating zone of influence for the energy pile. This method was implemented to determine the increase in the zone of influence with increased time.

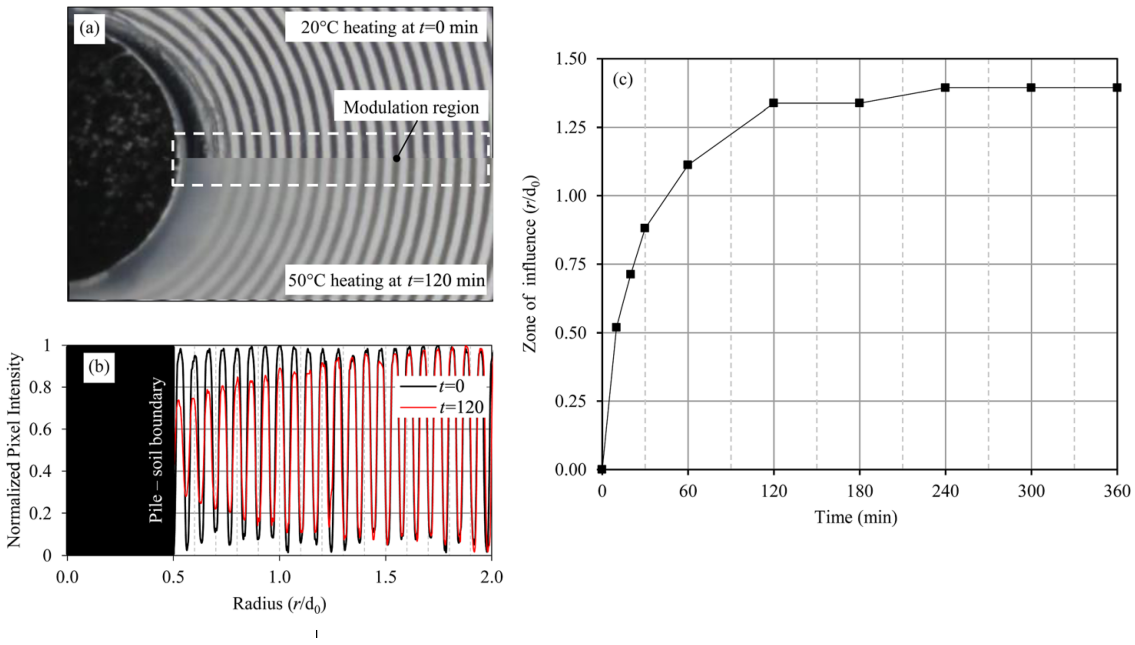

Figure B.9: Zone of influence of heating for a single energy pile determined by signal modulation for a 20°C-50°C heating cycle at t=0 and 120 min; (a) image showing loss of optical transmission of the concentric black/white reference lines,(b) signal modulation and (c) normalised zone of heating influence.

Bourne-Webb et al. (2009) reported that the temperature recorded in a borehole positioned $0.5m$ from the energy pile halved at a radial distance equivalent to $r/d_0 = 1$ and at $r/d_0 = 1.5$ changes where negligible. Cui et al. (2011) reported $r/d_0 = 1.2$ for the zone of influence from a numerical analysis of a pile geothermal heat exchanger. Although similar zones of influence are observed in the present

work, scaling of heat flow from small scale models to prototype field conditions is highly complex. For example, Savvidou (1988) presents a comprehensive investigation pertaining to the modelling of heat flow in soils. Derivation of scaling laws for conduction and convection are presented and verified by results from model experiments conducted on saturated Leighton Buzzard sand at 1 and 100 g in a centrifuge. Comparison of models at 1 g and Ng demonstrated that distinct differences in the heat transfer mechanism occurred; convection was dominant in centrifuge tests, whereas conduction is more significant at 1 g. Hence, based on the complexity associated with modelling heat transfer, it would be inappropriate at this stage to make direct comparisons and draw conclusions with field-based data arising from the embryonic methodology presented in this paper. The authors advocate that considerably more knowledge about the heat transfer mechanisms and associated scaling laws of transparent soil are required before such comparisons could be made. Nevertheless, despite some uncertainties in the correlation with full-scale field behavior, the work has successfully introduced a new modelling paradigm for transparent soil, and with further research, the investigative method could enable new insight and make a positive contribution in modelling thermo-dynamic problems in soil.

B.5 Conclusions

Managing energy resources is fast becoming a crucial issue of the 21st century, with geothermal heat exchange energy structures targeted as a viable means of reducing carbon emissions associated with regulating building temperatures. An alternative experimental method using transparent soil and digital image analysis is presented for the purpose of visualizing heat flow in soil. The research shows that the loss of optical clarity can be used as a beneficial attribute of transparent soil. The work explored and verified the hypothesis that temperature changes of the soil alter its refractive index and therefore progressively reduce its transparency, becoming more opaque. The development of the experimental methodology was discussed and a relationship between pixel intensity and soil temperature is defined and verified. Normalization of pixel intensities was conducted to mitigate changes in illumination observed in the calibration target. This relationship is applied to

an energy pile example in heating mode to demonstrate and visualize heat flow in soil. The heating zone of influence is observed to extend to a radial distance of 1.5 pile diameters, which reflects similar values reported in literature from field and numerical investigations. The paper reported on the successful implementation of this technique, which provides a new paradigm for transparent soil to potentially contribute to greater understanding of thermo-dynamic processes in soil. Although focused on thermal heating, additional works by the authors into cooling effects on transparent soil show early promise that the same experimental framework can be used to investigate cooling problems below ambient temperatures, which may enable both heating and cooling problems to be simulated.